CHALLENGES AND A
COMPUTATIONAL CHEMISTR

Solvat
Molecules and
Computational Meth

Solvation Effects on Molecules and Biomolecules

CHALLENGES AND ADVANCES IN COMPUTATIONAL CHEMISTRY AND PHYSICS

Volume 6

Series Editor:

JERZY LESZCZYNSKI
Department of Chemistry, Jackson State University, U.S.A.

For other titles published in this series, go to
www.springer.com/series/6918

Solvation Effects on Molecules and Biomolecules

Computational Methods and Applications

Edited by

Prof. Sylvio Canuto
University of Sao Paulo, Brazil

Springer

Editor
Prof. Sylvio Canuto
Universidade de São Paulo
Instituto de Física
São Paulo-SP
Brazil
canuto@if.usp.br

ISBN: 978-1-4020-8269-6 e-ISBN: 978-1-4020-8270-2

Library of Congress Control Number: 2008922884

Printed on acid-free paper.

9 8 7 6 5 4 3 2 1

springer.com

CONTENTS

Preface ix

1 Solvation Models for Molecular Properties: Continuum Versus Discrete Approaches 1
Benedetta Mennucci

2 The Multipole Moment Expansion Solvent Continuum Model: A Brief Review 23
Manuel F. Ruiz-López

3 The Discrete Reaction Field Approach for Calculating Solvent Effects 39
Piet TH. van Duijnen, Marcel Swart, and Lasse Jensen

4 Thermochemical Analysis of the Hydration of Neutral Solutes 103
Axel Bidon-Chanal, Jose María López, Modesto Orozco, and F. Javier Luque

5 Electronic Properties of Hydrogen Bond Networks: Implications for Solvent Effects in Polar Liquids 115
Silvia Gomes Estácio, Hugo F. M. C. Martiniano, Paulo Cabral DO Couto, and Benedito José Costa Cabral

6 Solvent Effects on Radiative and Non-Radiative Excited State Decays 135
Aurora Muñoz Losa, Ignacio Fdez. Galván, M. Elena Martín, and Manuel A. Aguilar

7 The Sequential QM/MM Method and its Applications to Solvent Effects in Electronic and Structural Properties of Solutes 159
Kaline Coutinho, Roberto Rivelino, Herbert C. Georg, and Sylvio Canuto

8 Statistical Mechanical Modeling of Chemical Reactions in Condensed Phase Systems 191
Andrea Amadei, Massimiliano Aschi, and Alfredo Di Nola

9 An Explicit Quantum Chemical Solvent Model for Strongly Coupled Solute–Solvent Systems in Ground or Excited State 215
Anders Öhrn and Gunnar Karlström

10 Molecular Dynamics Simulation Methods including Quantum Effects 247
Thomas S. Hofer, Bernhard R. Randolf, and Bernd M. Rode

11 Solvation In Polymers 279
Hossein Eslami and Florian Müller-Plathe

12 Hydrogen Bonds and Solvent Effects in Soil Processes: A Theoretical View 321
Daniel Tunega, Adelia J. A. Aquino, Georg Haberhauer, Martin H. Gerzabek, and Hans Lischka

13 Linear Response Theory in Connection to Density Functional Theory/Molecular Dynamics and Coupled Cluster/Molecular Dynamics Methods 349
Kestutis Aidas, Jacob Kongsted, and Kurt V. Mikkelsen

14 Combined QM/MM Methods for the Simulation of Condensed Phase Processes Using an Approximate DFT Approach 381
Marcus Elstner and Qiang Cui

15 Solvation of Hydrogen Bonded Systems: CH· · ·O, OH· · ·O, and Cooperativity 407
Steve Scheiner

16 Solvation in Supercritical Fluids 433
Ana C. Furlan, Frank W. Fávero, Javier Rodriguez, Daniel Laria, and Munir S. Skaf

17 A Quantum Chemical Approach to Free Energy Calculation for Chemical Reactions in Condensed System: Combination of a Quantum Chemical Method with a Theory of Statistical Mechanics 455
Hideaki Takahashi, Nobuyuki Matubayasi, and Masayoshi Nakano

18 Quantifying Solvation Effects on Peptide Conformations: A QM/MM Replica Exchange Study 507
Gustavo M. Seabra, Ross C. Walker, and Adrian E. Roitberg

Index 519

PREFACE

The incessant development of quantum chemistry since the appearance of the Schrödinger equation has turned this area into a respectable branch of science with unprecedented capabilities. It is now a well-recognized field of research with predictive power that is an important component in physical–chemical laboratories. Very important developments were conducted in the early days by bright theoretical scientists that were ready to absorb the incredible and unpredicted computer revolution which was only just beginning. Isolated medium-size molecular systems can now be accurately studied theoretically by quantum chemical methods. However, it was also long recognized that all biomolecular phenomena necessary to obtain and sustain living systems take place in solution, as well as the vast majority of chemical processes. Indeed solvent and liquid systems are germane in chemistry experiments. In physics, a constant concern is the description of the role played by the environment in modifying the properties of the system as compared to the isolated situation. Hence, the importance of studying atoms, molecules and biomolecules in the solvent environment can hardly be denied. The quantum chemical studies of molecular systems affected by the interaction with a solvent had its own turning point before the end of the 1970s, when some pioneering work was done, including the dielectric properties of the medium in an effective nonlinear Hamiltonian. This naturally led to the development of the so-called continuum models that are important and now popular. Continuum models can be implemented from the simplest to the most sophisticated quantum chemical methods.

The same computer revolution that started in the middle of the last century also plays an important, in fact crucial, role in the development of methods and algorithms to study solvation problems. Dealing, for instance, with a liquid system means the inclusion of explicit molecules, in different thermodynamic conditions. The number of possible arrangements of atoms or molecules is enormous, demanding the use of statistical mechanics. Here is where computer simulation, Monte Carlo (MC) or molecular dynamics (MD), makes its entry to treat liquid systems. Computer simulation is now an important, if not central, tool to study solvation phenomena. The last two decades have seen a remarkable development of methods, techniques and algorithms to study solvation problems. Most of the recent developments have focused on combining quantum mechanics and statistical mechanics using MC or

MD simulations. This led naturally to the so-called QM/MM methods that combine quantum mechanics and molecular mechanics. In the original idea, a part of the system is treated by quantum mechanics and the remaining part by molecular mechanics. Variants of the QM/MM have also been developed adopting the central idea to the particular interest of studies. It is perhaps correct to say that the study of solvation effects in general is the area of physical chemistry research that has recently seen the most spectacular and constant advancements. As such, there is a need for a source material where the important developments and applications are described and directed not only to the specialists, but also for those beginning in this field.

This is the aim of this book. In 18 separate chapters different aspects of the solvation effects in molecules and biomolecules are presented and discussed and applications are shown. Some of the most internationally prominent groups in this field have joined in this project to produce this book that describes some of the important developments that are underway, as well as the achievements that have already been made. Different aspects of the solvation problem are presented, the theoretical methods to solve them are discussed and some perspectives are outlined.

I warmly thank all contributing authors for enthusiastically adhering to the effort to make this book a reality.

Prof. Sylvio Canuto
Instituto de Física, Universidade de São Paulo, Brazil
January 2008

CHAPTER 1

SOLVATION MODELS FOR MOLECULAR PROPERTIES: CONTINUUM VERSUS DISCRETE APPROACHES

BENEDETTA MENNUCCI

Dipartimento di Chimica e Chimica Industriale, via Risorgimento 35, 56126 Pisa, Italy,
e-mail: bene@dcci.unipi.it; web: http:// benedetta.dcci.unipi.it

Abstract: A comparative description of two different hybrid solvation models is presented, both of them describe the solute at quantum-mechanical level while the solvent is treated either through a polarizable molecular mechanics force field or as a polarizable continuum dielectric. The theoretical framework of the two methods is analyzed in terms of common features as well as of eventual differences. An application to the study of solvent effects on NMR properties of solvated molecular systems is used to analyze the relative performances as well as to underline the differences in the corresponding descriptions

1.1. INTRODUCTION

The importance of understanding environment effects on chemical systems is evident in almost all the most active fields of research, such as condensed phase chemistry, biochemistry or material chemistry just to quote a few.

It is thus not strange that, in the years, many different phenomenological approaches and theoretical models aimed at describing the effects of a given surrounding medium on the properties of a selected system have been formulated. However, only with the recent progress achieved in the computational technology, a real step forward has been done in the modelization of the phenomenon giving origin to such effects (which in the following we shall indicate as solvation or embedding). In particular, two have been the successful strategies; on the one hand the availability of fast computers has suggested to try to get a detailed microscopic description of a representative sample of the whole system. This first strategy has led to molecular dynamics (MD) or Monte Carlo (MC) simulations in which a necessarily simplified description of the intra- and intermolecular interactions is introduced in terms of the selected force field.

On the other hand, the development of computers with increasing memory (besides speed) has allowed to increase the realism and the accuracy of the description

S. Canuto (ed.), Solvation Effects on Molecules and Biomolecules, 1–21.
DOI 10.1007/978-1-4020-8270-2_1,

in spite of the dimension of the studied system which now is reduced to a by far smaller part of the whole system, generally called the "solute" even when formed by distinct molecular units. Within this second strategy (which we shall indicate as focussed), the surrounding molecules become the secondary subsystem ("the solvent") and they will be modeled using a less accurate description, in most cases also completely neglecting their microscopic nature. Examples of this second strategy are the hybrid approaches using a quantum-mechanical (QM) description for the solute and a simplified (either Molecular Mechanics, MM [1,2,3,4,5,6] or continuum [7,8,9,10,11]) description for the solvent. In the latter case, the secondary system completely disappears and it is substituted by a macroscopic continuum medium having suitable properties.

It is obvious that the two strategies have different advantages and limits and that their applications are necessarily of different nature. In particular, the first strategy is preferable if a statistically representative picture of the whole system (including its dynamic) is required while the second strategy is necessary if an accurate description of the electronic nature of the solute and how it is changed by the environment is important. The present chapter, devoted to the study of the effects the environment has on the response properties of solvated molecular systems, will thus mainly be focussed on the second strategy even if the importance of an interplay between the two will be made evident.

1.2. FOCUSSED MODELS

There are several approaches to be classified in the family of focussed models. The common characteristic of all of them is that the system is divided into two (or even more) parts (or layers) which are described at different levels of accuracy. The target layer (the solute) is generally described at QM level (either ab initio or semiempirical) while the rest (the solvent) is approximated using an MM description as that used in force fields or a continuum description or both of them in case of more than two layers.

In all cases, the formalism of the in vacuo QM molecular calculations is maintained, including in the solute Hamiltonian an explicit expression of the solute–solvent potential. What distinguishes the different approaches is exactly the form of this potential.

In standard QM/MM approaches, the solvent is treated by assigning partial point charges to the atomic sites and the potential due to these point charges is then introduced into the solute Hamiltonian. However, in such a procedure polarization of the solvent is neglected, i.e., only the solute is polarized. This may be refined, for example, by assigning polarizable sites to the solvent giving rise to induced electrical moments and including their effects in the solute Hamiltonian as a further solvent term.

In the continuum models the solvent is also polarizable and its effect on the solute is again represented by the so-called reaction potential part of the Hamiltonian.

In both cases we can introduce a similar picture in terms of an effective Hamiltonian giving rise to an effective Schrödinger equation for the solvated solute. Introducing the standard Born–Oppenheimer approximation, the solute electronic wavefunction $|\Psi\rangle$ will satisfy the following equation:

$$\hat{H}_{\text{eff}} |\Psi\rangle = \left(\hat{H}_0 + \hat{H}_{\text{env}}\right) |\Psi\rangle = E |\Psi\rangle \tag{1-1}$$

where $\hat{H}_0$ is the Hamiltonian of the solute system when in absence of the rest, and the operator $\hat{H}_{\text{env}}$ introduces the coupling between the solute and the solvent.

The form of the operator $\hat{H}_{\text{env}}$ depends on the particular method used, here, in particular, two alternative schemes are analyzed:

$$\hat{H}_{\text{env}} = \begin{cases} \hat{H}_{\text{QM/MM}} + \hat{H}_{\text{MM}} & \text{QM/MM} \\ V_{\text{cont}} & \text{QM/continuum} \end{cases} \tag{1-2}$$

The details on the operators introduced in the two schemes will be given below, here we only want to add that the addition of $\hat{H}_{\text{env}}$ to the solute Hamiltonian automatically leads to a modification of the solute wavefunction which has now to be determined by solving the effective Eq. (1-1). This can be done using exactly the same methods used for isolated molecules; here in particular we shall mainly focus on the standard self-consistent field (SCF) approach (either in its Hartree–Fock or DFT formulation). Due to the presence of $\hat{H}_{\text{env}}$ the modified SCF scheme is generally known as self-consistent reaction field (SCRF). Historically the term SCRF has been coined for the QM/continuum approach but here, due the parallelism between the two schemes which will be made clear in the following sections, it will be used indistinctly for both.

1.2.1. QM/MM

In QM/MM approaches, the MM system is represented through atomic point charges and (if a polarizable force field is used) atomic or molecular polarizabilities at selected points in the solvent molecules, we thus have

$$\hat{H}_{\text{QM/MM}} = \hat{H}^{\text{el}} + \hat{H}^{\text{pol}} \tag{1-3}$$

We note that the $\hat{H}_{\text{MM}}$ introduced in Eq. (1-2) is the classical MM energy, this term, however, is a contribution only to the energy and not to the wavefunction.

The first term in Eq. (1-3) is the electrostatic interaction between the QM system and the point charges in the MM part of the system, namely

$$\hat{H}^{\text{el}} = \sum_m q_m(\mathbf{r}_m)\hat{\mathbf{V}}(\mathbf{r}_m) \tag{1-4}$$

where $\hat{\mathbf{V}}(\mathbf{r}_m)$ is the electrostatic potential operator due to solute electrons and nuclei at the MM charges q_m. This term is directly included in the one-electron part of the vacuum Hamiltonian.

The second term in Eq. (1-3) is the polarization interaction between the induced dipole moments and the electric field from the QM system. In the following exposition, the approach proposed by Mikkelsen, Kongsted and coworkers will be used [12,13,14]; for such a version of the polarizable QM/MM scheme the acronym DPM (discrete polarizable method) has been introduced and will be used here. In the DPM $\hat{H}^{\text{pol}}$ can be expressed as

$$\hat{H}^{\text{pol}} = \frac{1}{2} \sum_a \mu_a^{\text{ind}} \, \hat{\mathbf{E}}_a^{\text{solute}} \tag{1-5}$$

$$\mu_a^{\text{ind}} = \alpha_a \left(\mathbf{E}_a^{\text{solute}} + \mathbf{E}_a^{\text{solvent}} \left\{ \mathbf{q}; \mu^{\text{ind}} \right\} \right) \tag{1-6}$$

where the summation runs over all the selected polarizability points of the MM molecules and $\hat{\mathbf{E}}^{\text{solute}}$ is the electric field from the electrons and the nuclei in the QM system at those points. To define the induced dipole moments, μ_a^{ind}, in Eq. (1-6) we have assumed a linear approximation, neglected any contribution of magnetic character related to the total electric field and used an isotropic polarizability (α_a) for each selected point in the MM part of the system. Distributed polarizabilities should be introduced, however, for small solvent molecules with low anisotropies in the molecular polarizability, the use of monocenter polarizabilities is usually sufficient; here, for the sake of simplicity we have used a single point for each MM molecule, its center of mass.

In Eq. (1-6), $\mathbf{E}_a^{\text{solvent}}$ refers to the total solvent electric field and it contains a sum of contributions from the point charges and the induced dipole moments in the MM part of the system. Such a field (and hence the induced dipole) depends on all other induced dipole moments in the solvent. This means that Eq. (1-6) must be solved iteratively within each SCF iteration. As an alternative, Eq. (1-6) may be reformulated into a matrix equation

$$\mu^{\text{ind}} = \mathbf{B}\mathbf{E} \tag{1-7}$$

where the matrix $\mathbf{B}$ is of dimension $3N \otimes 3N$, N being the number of polarizable sites, and the vector $\mathbf{E}$ collects the electric field from the solute and the solvent permanent charge distribution, $\left(\mathbf{E}^{\text{solute}} + \mathbf{E}^{\text{solvent}}\{\mathbf{q}\} \right)$. The form of matrix $\mathbf{B}$ will be determined uniquely by the position of the polarizable sites and the polarizability values.

1.2.2. QM/continuum

Moving now to QM/continuum approaches, we shall limit our exposition to the so-called apparent surface charges (ASC) version of such approaches, and in particular to the family known with the acronym PCM (polarizable continuum model) [11]. In this family of methods, the reaction potential V_{cont} defined in Eq. (1-2) has a form completely equivalent to the $\hat{H}^{\text{el}}$ part of the $\hat{H}_{\text{QM/MM}}$ operator defined in Eq. (1-4), namely:

$$V_{\text{cont}} \rightarrow \hat{V}^{\text{PCM}} = \sum_s q_s^{\text{PCM}}(\mathbf{r}_s)\hat{\mathbf{V}}(\mathbf{r}_s) \tag{1-8}$$

Now, however, the point charges q_s^{PCM} are no longer centered on the solvent nuclei as in the MM description but they are placed on selected points placed on the surface of the molecular cavity containing the solute. In addition, such charges are not fixed but they are "apparent" in the sense that they exist only when the solute exists. As the induced dipoles of the polarizable MM description, the PCM charges are determined by total field acting at the selected points on the surface (i.e., the field due to the solute and the charges themselves) but now they also depend on the dielectric properties of the solvent, on the geometry of the cavity and on the number and position of the points chosen to map the cavity surface. In general, these points are determined by partitioning the surface into finite elements (called tesserae) and identifying a representative point for each tessera. The equations giving the charges can be solved iteratively within each SCF cycle or similar to what is done for the induced dipoles (see Eq. 1-7), a single matrix equation can be solved instead:

$$\mathbf{q}^{\text{PCM}} = -\mathbf{K}\mathbf{f}^{\text{solute}} \tag{1-9}$$

where now the field is only that due to the solute. The effect of the self-polarization, in fact, has been reformulated into the matrix **K** exactly as done before in Eq. (1-7) introducing the **B** matrix for the MM-induced dipoles.

Once again, **K** is a square matrix (the dimension being equal to Nts $\otimes$ Nts where Nts is the number of tesserae) and it depends on the geometrical cavity parameters and the dielectric constant of the solvent. It is to be noted that in Eq. (1-9) we have substituted the electric field $\mathbf{E}^{\text{solute}}$ with the more general vector $\mathbf{f}^{\text{solute}}$; in fact different versions of the PCM approach use different electrostatic quantities to define the charges (and correspondingly different forms of the **K** matrix) [11], namely the normal component of the electronic field in its original version (now called DPCM) or the electrostatic potential in its reformulation known as integral equation formalism (IEFPCM) [15,16].

As for the QM/MM description also for PCM, non-electrostatic (or van der Walls) terms can be added to the V_{cont} operator; in this case, besides the dispersion and repulsion terms, a new term has to be considered, namely the energy required to build a cavity of the proper shape and dimension in the continuum dielectric. This further continuum-specific term is generally indicated as cavitation. Generally all the non-electrostatic terms are expressed using empirical expressions and thus their effect is only on the energy and not on the solute wavefunction. As a matter of fact, dispersion and repulsion effects can be (and have been) described at a PCM-QM level and included in the solute-effective Hamiltonian $\hat{H}_{\text{eff}}$ as two new operators modifying the SCRF scheme. Their definition can be found in Ref. [17] while a recent systematic comparison of these contributions determined either using the QM or the classical methods is reported in Ref. [18]

The brief descriptions given here for QM/MM(pol) (in its DPM formulation) and QM/continuum (in its PCM formulation) should make clear the parallelism of the two formulations both from a quantum-mechanical and a computational point of view. There are, however, fundamental differences which are worth being recalled here.

The picture given by a QM/MM approach automatically includes a microscopic description of all the components of the system (solute + solvent) even if with different levels of accuracy (a QM charge distribution for the solute and a set of classical charges and dipole moments for the solvent). A preliminary knowledge of the position in the space of all these components (i.e., the configuration) is thus required. A liquid solution, however, is a very dynamic system which cannot be properly represented in terms of a single (or few) configuration: many different configurations obtained from a correct statistical analysis should thus be introduced and used to get the final averaged picture. These configurations can be obtained as snapshots of a MD (or MC) simulation.

By contrast, the description given by a continuum description does not require any knowledge of the solvent configuration around the solute as a structureless continuum dielectric is introduced instead. The response of such a dielectric to the presence of the solute is determined by its macroscopic properties (namely the dielectric constant and the refractive index) and thus it will be implicitly averaged. Contrary to what happens in a QM/MM approach, here a single calculation on a given solute contained within the continuum dielectric will be sufficient to get the correct picture of the solvated system.

It is evident, however, that this enormous gain in terms of computational time (and simplicity of the protocol) will involve some disadvantages. The main one is the loss of the microscopic nature of the solvent molecules. This issue becomes particularly delicate when solute–solvent specific interactions such as hydrogen bonds are present in the liquid solution: in these cases, the picture obtained using a continuum-only description will be incomplete as it misses an important part of the solute–solvent interactions.

In the following section we shall show how all these specificities of the QM/MM and QM/continuum approaches will affect the quality of the description one can obtain applying them to the study of solvent effects on molecular response properties.

1.3. MODELING SOLVENT EFFECTS ON PROPERTIES

In the previous sections we have briefly summarized the basic theory of QM/MM and QM/continuum methods showing their differences and similarities, now we can move on to describe their applications to the calculation of molecular response properties and the related spectroscopies for a generic solvated system.

As shown above, in both DPM and PCM versions of these schemes, an appropriate interaction operator between the solute and solvent is added to the Hamiltonian of the isolated molecule. Such an operator is the term $\hat{H}_{\mathrm{env}}$ defined in Eq. (1-2) which is obtained by combining one-electron operators and thus no significant increase in

computational effort is introduced. The electronic density is obtained by including self-consistently the polarization of the solvent. Along the same lines as for an isolated molecule, the use of response theory may in the context of solvation be used to study a variety of molecular properties other than the molecular energy. Introducing the concepts of response theory into the PCM or DPM approach leads to a compact and powerful method to calculate molecular properties of a molecule subjected to an environment. In particular, both properties related to external or internal perturbations may be considered. In addition to this, the specific properties may be of either electric or magnetic origin.

Within the DPM the specific contributions due to the polarizable and structured environment will lead to two different sorts of corrections: (i) contributions due to the static multipole moments (here partial charges) and (ii) contributions due to the induced polarization in the environment. In contrast, for the PCM only contributions due to the induced polarization in the solvent are relevant.

The different characteristics of the two solvation models make it interesting to compare their performances when describing the effects of the solvent on given molecular response properties. A very good candidate for such a comparative analysis is the NMR spectroscopy. This is in fact one of the most important techniques available for investigating molecular structures, molecular interactions and the solvation problems. Most NMR measurements are performed on liquid samples and they yield isotropic chemical shifts (related to the nuclear magnetic shielding constants) and scalar spin–spin coupling constants modified by the solvent. NMR parameters (in particular NMR chemical shifts) are, in fact, extremely sensitive to the molecular environment, and especially hydrogen-bonding effects.

1.3.1. QM Evaluation of NMR Nuclear Shieldings

The effects of solvent on nuclear magnetic shielding parameters derived from NMR spectroscopy have been of great interest for a long time. In 1960 Buckingham et al [19] suggested a possible classification in terms of various additive corrections to the shielding arising from (i) the bulk magnetic susceptibility of the solvent, (ii) the magnetic anisotropy of the solvent molecules, (iii) van der Waals interactions and (iv) long-range electrostatic interactions. In the original scheme, strong specific interactions, such as those acting in intermolecular hydrogen bonds, were not specifically dealt with but just mentioned as a possible extreme form of the electrostatic, or, more generally "polar", effect; in the numerous applications that followed Buckingham's classification, however, this further effect has been always included as a separate contribution.

On the basis of such a classification an empirical approach based on the so-called solvent empirical parameters was formulated to evaluate solvent effects on nuclear shieldings. In brief, this approach, originally proposed by Kamlet, Taft and co-workers [20] for electronic excitations, does not involve QM or other types of calculations but introduces a numerical treatment of experimental data obtained for a given reference system to obtain an estimate of solvent effects on various properties.

An extensive study of this type was conducted by Witanowski et al. to interpret the solvent effects on the nitrogen shielding in a large set of compounds (see Ref. [21] and references cited therein).

In the last years, these semiclassical analyses have been substituted by (or supported with) explicit descriptions of the electronic aspects of the solvent effects on NMR properties and in particular on the nuclear shielding. This change of perspective has been made possible by the large development of QM solvation models which have been coupled to QM methodologies initially formulated for isolated systems.

The QM theory of chemical shielding was originally developed many years ago [22,23], but only later have ab initio methods and density functional theories (DFT) been reliably used for the prediction of NMR properties of isolated molecular systems, and finally of solvated systems. The latter step has been achieved by extending the gas-phase theoretical methods to continuum solvation models (see Ref. [11] for a sufficiently updated list of papers).

Here we shall focus on a specific NMR property, namely the nuclear shielding tensor, defined as the second derivatives of the energy with respect to the Cartesian components of the magnetic induction $\mathbf{B}$ and of the nuclear magnetic moment $\mathbf{m}_X$ of nucleus X. Using a SCF description of the solute wavefunction with molecular orbitals (MO) expressed as a linear combination of atomic orbitals (AO) and treating the magnetic field perturbation in an analogous way to the perturbation produced by changes in the nuclear coordinates, the components of the nuclear magnetic shielding tensor are obtained as

$$\sigma_{ij}^{X} = \sum_{\mu\nu} P_{\mu\nu} \frac{\partial^2 h_{\mu\nu}}{\partial B_i \partial m_{X_j}} + \sum_{\mu\nu} \frac{\partial P_{\mu\nu}}{\partial B_i} \frac{\partial h_{\mu\nu}}{\partial m_{X_j}} \tag{1-10}$$

where $P_{\mu\nu}$ is an element of the density matrix in the AO basis and $h_{\mu\nu}$ is a matrix element of the effective one-electron Hamiltonian. The second term in Eq. (1-10) (the paramagnetic contribution) is determined by solving a set of response equations for the three components of the magnetic induction. In order to ensure origin-independent results for the nuclear magnetic shielding constants, *gauge including atomic orbitals*(GIAOs)[24,25,26,27] are generally used, that is, the AO basis functions depend explicitly on the magnetic induction through

$$\chi_\mu(\mathbf{B}) = \exp\left[(-\mathrm{i}/2)(\mathbf{B} \times \mathbf{R}_\mu) \cdot \mathbf{r}\right] \chi_\mu(0)$$

where $\mathbf{R}_\mu$ is the vector giving the position of the nucleus to which the field-dependent basis function is attached relative to the global gauge origin, and $\chi_\mu(0)$ indicates a conventional AO basis function not depending on $\mathbf{B}$.

Equation (1-10) applies both to the case of a molecule in vacuo and in solution. The (polarizable) environment makes contributions both through the density matrix, which is obtained self-consistently including the perturbation from the surroundings, and through the derivative of the density matrix with respect to the magnetic induction, i.e., both terms in Eq. (1-10) contain the effect of the environment.

The first derivative of the density matrix with respect to the magnetic induction ($\partial P_{\mu\nu}/\partial B_i$) is obtained by solving the coupled-perturbed Hartree–Fock (or Kohn–Sham) equations to which the first derivative of the effective Fock (or Kohn–Sham) operator with respect to the magnetic induction contributes. Due to the use of GIAOs, specific corrections arising from the effective operator $\hat{H}_{\text{env}}$ describing the environment effects will appear. We refer to Ref. [28] for the PCM model and to Ref. [29] for the DPM within either a HF or DFT description of the solute molecule.

1.3.2. An Application to Solvated Systems: N Nuclear Shieldings of Diazines

In this section we shall present and compare different computational strategies one can adopt to simulate the effect of the environment on spectroscopic properties of solvated systems. In particular, as a representative example, we shall summarize the results of two studies [30,31] we have published in the last years on the environment effects on the nitrogen nuclear shieldings of a specific class of molecular systems containing sp^2-type nitrogens: three diazines, also known as pyridazine (1,2-diazine), pyrimidine (1,3-diazine) and pyrazine (1,4-diazine).

We have selected these specific studies among the many others we have performed in the years on the effects of the solvent on molecular properties (see for example Ref. [32] for a review published in 2002 and Ref. [33,34,35] for a selection of more recent papers) as they allow to present and discuss all the most important aspects which contribute to define the complex phenomenon of solvation.

Important solvent effects have been observed on the nuclear shielding of diazine nitrogens, for which an increase of up to 40–50 ppm has been measured passing from an apolar solvent to water [36]; we note that this is one of the largest solvent-induced shifts so far observed in nitrogen NMR. Such a sensitivity to the polarity and possible H-bonding properties of the solvent can be easily explained by looking at the electronic charge distribution of diazines in which very polarizable (and H-bonding acceptor) sites are available for the solvent to strongly interact with (see also Figure 1-1 in which the electron density surface painted according to the value of the electrostatic potential is reported for the three diazines).

To try to reproduce the solvent effects on nitrogen nuclear shieldings of diazines and understand the physics beyond them we have applied the QM/continuum (PCM) and QM/MM(pol) (DPM) approaches described in the previous sections.

All QM calculations both in vacuo and in the various solvents have been performed on the basis of the density functional theory (DFT) using the hybrid functional which mixes the Lee, Yang and Parr functional for the correlation part and Becke's three-parameter functional for the exchange (B3LYP) [37,38]. Calculations of nuclear shieldings have been performed exploiting the GIAO method. Within the PCM, the cavities of all the diazines have been obtained in terms of interlocking spheres: in particular, a united atom approach in which hydrogen atoms are inside the sphere centered on the linked carbon atom has been used; the corresponding radii are 1.9 Å for CH and 1.6 Å for N. A cavity scaling factor (f) is introduced to enlarge

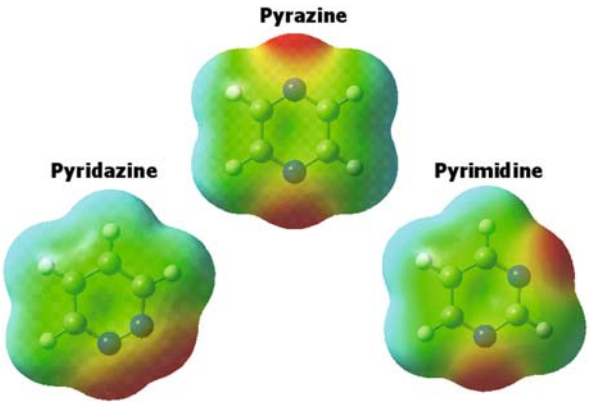

Figure 1-1. Graphical representation of the three diazines, pyridazine (1,2-diazine), pyrimidine (1,3-diazine) and pyrazine (1,4-diazine), in terms of their structure and the electron density surface colored according to the value of the electrostatic potential

the basic radii before the individual spheres are defined; when not explicitly indicated the standard value of 1.2 has been used for *f*.

All calculations on the isolated and the PCM solvated systems have been performed using the Gaussian code [39] while the DPM calculations have been performed using the development version of the Dalton Quantum Chemistry Program [40].

1.3.2.1. QM/continuum: Polarity Versus H-bond

A preliminary description of solvent effects on the nitrogen nuclear shielding of diazines can be obtained by applying a continuum-only description and thus assuming that each diazine is contained in a proper cavity inside an infinite polarizable continuum dielectric. As a result, both the geometry and the electronic charge distribution of each diazine will be modified with respect to the gas-phase case, as well as its response equations determining the NMR properties will be changed. These three effects will give rise to the net solvent effect on the property of interest, namely the nitrogen nuclear shielding. These effects are evaluated here by applying the PCM as described above.

In Figure 1-2 we summarize in a graphical way the results obtained in three different environments, namely cyclohexane, acetone, dimethyl-sulfoxide (DMSO), and water. The data are reported here as a correlation plot between calculated and experimental isotropic nuclear shieldings.

From the plot it is evident that for non-protic solvents, PCM gives gas-to-solution shifts in very good agreement with experiments for all molecules (the regression line presents a R^2 value of 0.998). In contrast, for water such an agreement significantly worsens: in this case, specific H-bonds between water hydrogens and diazine nitrogens are clearly present while the continuum description cannot properly take into

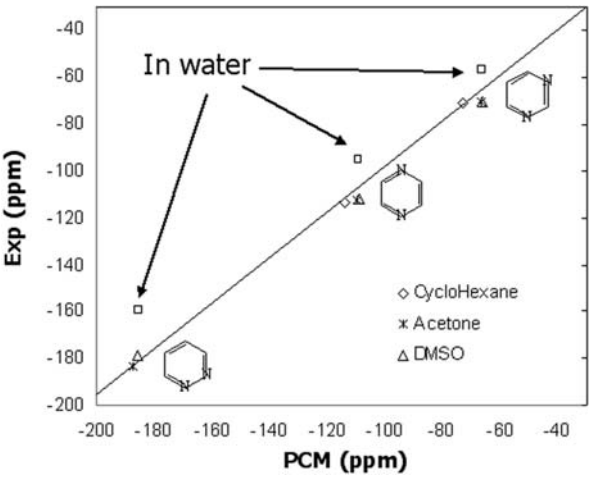

Figure 1-2. Correlation plot between calculated and experimental N nuclear shieldings of diazines obtained in three different environments, namely cyclohexane, acetone, DMSO and water. Calculated shieldings have been obtained at B3LYP/GIAO/6-311+G(d,p) while the geometries were optimized at B3LYP/6-31+G(d,p) in all phases

account their possible effects on the property. To test this analysis, we have optimized H-bonded clusters containing one and two water molecules, without and with an external continuum dielectric; in the latter case an enlarged cavity also containing the water molecules has been introduced using radii equal to 1.2 Å for H and 1.53 Å for O (an example of the cluster structure and of the corresponding PCM cavity is shown in Figure 1-3 for pyridazine). On such optimized geometries we have computed nuclear shieldings at the same level used for the single diazines.

In Figure 1-4 we report the same correlation presented in Figure 1-2 but this time limited to water as a solvent: both isolated and "solvated" (i.e., PCM) diazine–2 w clusters are reported.

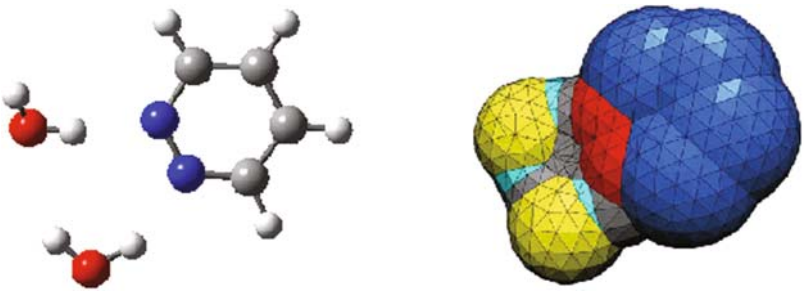

Figure 1-3. Example of diazine–water cluster: pyrimidazine+2 w and the corresponding PCM cavity

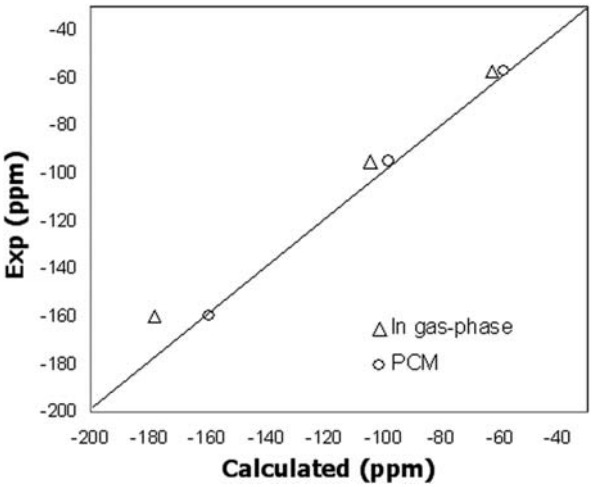

Figure 1-4. Correlation plot between calculated and experimental N nuclear shieldings of diazines in water. Calculated shieldings refer to diazine–2 w clusters in gas-phase and within a PCM continuum. All calculations are at B3LYP/GIAO/6-311+G(d,p) level

From the results obtained for the isolated clusters, it seems evident that even by taking into account the two H-bonds, an important portion of the observed shift is still missing. For all molecules, in fact, the isolated "diazine + 2 waters" clusters seem unable to describe the complete effect due to the whole liquid. Only by adding an external continuum, i.e., including also long-range non-specific polarization effects, the missing gap is filled and a very good agreement with experiments is obtained.

The data reported in Figures 1-2 and 1-4 suggest a possible interpretation of the physics beyond the observed solvent effect on nitrogen nuclear shielding but they still prevent a detailed explanation of the competitive/synergic action of short-range and specific interactions on one side, and long-range and mediated effects on the other side. To do that it is useful to recall that the nuclear magnetic shielding can be partitioned into diamagnetic and paramagnetic terms. This partition is here achieved by considering an NBO analysis [41] and relating the changes in the two contributions to increase or depletion of the population in the nitrogen lone pair due to H-bond and polar effects.

In Table 1-1 we thus report the N nuclear shielding (with its paramagnetic and diamagnetic contributions) and nitrogen lone pair natural population (NP(lp)) for the diazine showing the largest solvent effect, i.e., pyridazine, and its clusters in vacuo (VAC) and in the presence of an external PCM continuum.

To first investigate the effects of H-bonding, we compare lone pair occupancies of monomers and clusters in gas phase: a significant decrease is found passing from the "free" pyridazine to either the one-water or the two-water cluster. This decrease, which indicates that electron population has been removed from the lone pair orbital, is accompanied by an increase of the diamagnetic contribution.

Table 1-1. Nitrogen lone pair natural population (NP(lp)), nuclear shielding (with its paramagnetic and diamagnetic contributions) (ppm) and absorption energies (eV) for pyridazine and water–pyridazine clusters in vacuo (VAC) and in the presence of an external continuum (PCM). For 2 w clusters two values corresponding to the two nonequivalent nitrogens are reported. Calculations are at B3LYP/6-311++G(2d,2p) level for populations and nuclear shielding and at TDB3LYP/6-31+G(d,p) level for absorption energies

	VAC				PCM			
	Free	+1 w	+2 w		Free	+1 w	+2 w	
NP(lp)	1.939	1.921	1.922	1.933	1.943	1.912	1.912	1.924
σ^{par}	–513.52	–513.09	–496.41	–504.49	–482.44	–487.2	–474.83	–475.21
σ^{dia}	296.58	325.07	318.31	313.2	296.9	324.8	319.33	313.95
σ	–216.94	–188.02	–178.1	–191.29	–185.54	–162.4	–155.5	–161.26
$n\pi^*$	3.58	3.74	3.85		3.87	4.00	4.13	

A different analysis involves the comparison between isolated and "solvated" (PCM) systems. For the monomer, the inclusion of a continuum dielectric induces a significant increase in the nitrogen lone pair population, which, however, does not lead to significant changes in the diamagnetic term but instead lead to a less negative σ^{par}. A similar change in the paramagnetic contributions is obtained passing from isolated to solvated clusters, but what is different now is that the introduction of the continuum reduces the lone pair population (indicating a stronger charge transfer from nitrogen lone pair to H-bonded waters). This apparently opposite correlation between orbital population and paramagnetic term reveals that a complex combination of different factors is occurring. Going back to the Ramsey formulation we have that the paramagnetic contributions depend on both ground state and excited states while the diamagnetic contributions are determined by the ground state only. Thus, on passing from isolated to solvated clusters, we can assume that the dominant term in determining σ^{par} is not the lone pair population but the low-lying excited states. If we assume that all other electronic transition energies are much larger than $\Delta E(n\pi^*)$ and therefore make a negligible contribution, the observed decrease in the paramagnetic shielding in the presence of the external continuum can be explained in terms of the parallel changes in the $n\pi^*$ transition energy. In particular, an increase in the transition energy should lead to a less negative σ^{par} the latter being inversely proportional to the former according to the Karplus and Pople model [42].

The $n\pi^*$ transition is a well-known example of H-bond-sensitive property. In such transitions, the electronic density on the heteroatom (either oxygen or nitrogen) decreases upon excitation. This results in a decrease in the capability of this heteroatom to form hydrogen bonds. The effect on absorption should then be similar to that resulting from a decrease in dipole moment upon excitation, and a blue shift of the absorption spectrum is expected; the higher the strength of hydrogen bonding, the larger the shift. From the TDB3LYP results reported in the table an increasing blue shift with respect to the gas-phase-free diazines is observed passing from the

isolated to the solvated clusters; this increase is reflected in a significant decrease in the absolute value of σ^{par} as predicted.

To conclude this first part of the analysis, all the results presented show that H-bond effects and long-range non-specific interactions can combine and give rise to a synergic (or cooperative) action and that the complete picture can only be obtained by taking into account both of them introducing solvated clusters.

It is now interesting to check if this picture is either confirmed or modified by changing the description of the solvent. This check is here realized introducing diazine–water clusters extracted from classical MD simulations and comparing their NMR properties calculated once again with PCM or with the QM/MM(pol) model we have introduced in the previous section with the acronym DPM.

1.3.2.2. QM/MM Versus QM/continuum

In order to generate an appropriate number of solute–solvent clusters to be used in the NMR calculations a series of classical MD simulations of pyrazine, pyrimidine or pyridazine in aqueous solution has been carried out. All the details of the force fields used for the diazines and water as well as computational details of the MD simulation can be found in Ref. [31]. Every 1 ps an MD configuration was dumped so as to obtain 600 different molecular configurations. Then, a spherical cut-off distance equal to 12 Å was applied so as to obtain the final cluster including $\sim$ 230–240 water molecules together with the solute.

In the following electronic calculations, the solute (and potentially a number of the closest water molecules) is treated using DFT/B3LYP while the rest of the solvent is treated either using the same polarizable potential as in the MD simulations (DPM) or introducing an external continuum (PCM). Acronyms like DFT(X)/DPM or DFT(X)/PCM are used here to indicate calculations where X water molecules have been included into the part of the system treated using DFT. The final molecular property in solution is evaluated as a statistical average over all these molecular clusters.

A preliminary necessary check in this kind of calculations is on the convergence of the calculated properties with respect to the number of solute–solvent configurations included in the statistical procedure. Canuto and coworkers have extensively made use of the autocorrelation function of the energy in order to extract uncorrelated solute–solvent configurations to be used in combined QM/MM calculations [43]. The minimum number of solute–solvent configurations to be included in the statistical analysis may, however, depend on the nature of the molecular property in question. The NMR shielding appears to be converged based on around 100 configurations. In this study we have chosen to use 200 configurations in the statistical averaging since this number of configurations clearly provides statistically converged molecular properties. Also, the effect of using a larger number of configurations is to obtain a smaller statistical error in the mean values.

Before moving to the comparison between QM/continuum and QM/MM(pol) results, we briefly comment on differences between the previously QM-optimized clusters and the present MD-derived clusters. The hydrogen coordination number to

the nitrogen site for each solute is almost constant for all the three diazines and is, by spherical integration of the RDFs, found to be around 2: this can be considered as a confirmation of the previous analysis in terms of the diazine–2 w QM clusters. However, in contrast to the QM results, the hydrogen bond distances between the nitrogen site of the solute and the hydrogen of water are all longer in MD-derived configurations. This is not surprising since the outcome from the geometry optimizations are equilibrium structures at T=0 K representing the lowest energies on the potential energy surfaces which physically might be different from the true liquid at finite temperatures. These differences can also be due to possible deficiencies in the underlying force field used in the MD simulations to accurately describe the effect of hydrogen bonding. Due to these geometrical differences, the H-bond effects we shall obtain in the nuclear shielding will be different in the two descriptions. One could thus be suggested to use the comparison between the results presented in the previous section, the present ones obtained from MD-derived clusters and experiments to select the best description. Unfortunately, this is not possible as in all calculations we have neglected other aspects, such as rovibrational averaging, which may be important for accurate evaluation of the solvent-induced shifts and thus represent a potential source of intrinsic uncertainty.

On the basis of these considerations, in the following analysis we shall mainly focus on an internal comparison between the continuum (PCM) and the polarizable MM (DPM) descriptions, so as to explore in more detail their similarities and differences when applied to the evaluation of solvent effects on molecular properties.

The comparison begins with the reaction field produced by either models at specific atomic sites. Both models in fact produce at the solute an electric field which perturbs the solute electronic density and thereby change the properties of the solute. In the case of PCM, the reaction field at site $\mathbf{R}_n$ is a true mean field produced by the ASC distribution represented by point charges, i.e.,

$$\mathbf{E}^{\mathrm{RF}}_{\mathrm{PCM}}(\mathbf{R}_n) = \sum_{k=1}^{\mathrm{Nts}} \frac{q_k^{\mathrm{PCM}}(\mathbf{R}_n - \mathbf{r}_k)}{|\mathbf{R}_n - \mathbf{r}_k|^3} \tag{1-11}$$

On the other hand, for the DPM model the reaction field is calculated by the expression

$$\mathbf{E}^{\mathrm{RF}}_{\mathrm{DPM}}(\mathbf{R}_n) = \sum_{s} \frac{q_s^{\mathrm{DPM}}(\mathbf{R}_n - \mathbf{r}_s)}{|\mathbf{R}_n - \mathbf{r}_s|^3} + \sum_{a} \mu_a^{\mathrm{ind}} \mathbf{T}_{na} \tag{1-12}$$

where the first contribution in Eq. (1-12) is due to the point charges representing the permanent charge distribution of the solvent molecules and the second term represents the contribution from the induced dipoles at the polarizable sites in the solvent region. The symbol $\mathbf{T}$ is the dipole interaction tensor. The reaction field in Eq. (1-12) is calculated for each solute–solvent configuration and thus the MM(pol) includes directly the fluctuations in the reaction field and the consequences this might have for the calculated properties.

Table 1-2. Nonzero components of the reaction field at the nitrogen nuclei in pyrimidine calculated using either DPM or PCM. All calculations are at B3LYP/6-311++G(2d,2p) level. Results are in 10^3 au

Method	E_y^{RF}	E_z^{RF}
DPM	-8.7 ± 0.4	7.3 ± 0.3
PCM ($f = 1.1$)	–7.6	8.6
PCM ($f = 1.2$)	–5.5	6.8
PCM ($f = 1.4$)	–2.9	4.3

In Table 1-2 we report the reaction field at the nitrogen sites of a selected diazine, here pyrimidine, calculated using either DPM or PCM. In the first case the results refer to averaging over 200 solute–solvent configurations; in the second case the reaction field has been calculated for different cavity dimensions obtained using different scaling factors. The molecular coordinate system is defined so that the pyrimidine molecule is confined to the *yz* plane with the internal C_2 axis along the *z*-axis (the two nitrogen sites are indistinguishable).

As seen from Table 1-2 the PCM reaction field depends quite drastically on the cavity scaling factor. Choosing this to be equal to 1.4, which in the literature has been recommended in case of less polar solvents [44,45], clearly underestimates the reaction field as compared to the DPM. This is also expected since water is to be considered as a high dielectric. Choosing the cavity scaling factor to be equal to 1.2 (the standard value) improves very much the results but on average a scaling factor of 1.1 gives the best results. We note, however, that it is not possible to obtain a common scaling factor that reproduces all the DPM reaction field components.

These results provide some information between the differences/similarities in the physics within the PCM and DPM models. Since the bare radii of the nitrogen atom is $\sim$1.5 Å the solvent will in case of the PCM be placed either 1.65 ($f = 1.1$) or 1.80 ($f = 1.2$) Å away from the nitrogen site. In contrast, in the MD simulations, and therefore also in the DPM calculations, the solvent is on average placed 1.96 Å from the nitrogen site as inferred from the nitrogen–hydrogen RDF in pyrimidine. Furthermore, the oxygen site of water will be placed on average around 0.96 Å (the OH bond length in water) even further from the nitrogen site. This means that on average the solvent is placed (much) further away from the solute within the DPM as compared to the PCM. Choosing the cavity dimensions so as to reproduce the structural data from the MD simulation would lead to very underestimated results for the solvent shifts in the NMR shielding constants as compared to either the DPM or experimental data. Thereby, the PCM properly works by effectively placing the solvent closer to the solute as compared to MD data.

An underestimation of the reaction field should lead to an underestimation of the solvent shift in the NMR shielding. In fact, the relation between the reaction field and σ^{N} is in this regime linear. Thereby, choosing the cavity scaling factor to be 1.1

Table 1-3. Diagonal components, and the corresponding isotropic value, of the nitrogen nuclear shielding tensor in pyrimidine calculated using either DPM or PCM. All calculations are at B3LYP/6-311++G(2d,2p) level. Results are in ppm

Method	*xx*	*yy*	*zz*	iso
PCM (f = 1.4)	275.3	–221.8	–250.6	–65.7
PCM (f = 1.2)	275.5	–216.1	–239.0	–59.9
PCM (f = 1.1)	275.9	–212.2	–230.7	–55.7
DFT(2)/PCM	274.2	–211.3	–235.1	–57.4
DPM	273.6	–211.5	–231.3	–56.4
DFT(2)/DPM	273.2	–212	–236.3	–58.4

should result in an improved agreement between the DPM and PCM results. This prediction is confirmed by the data reported in Table 1-3 in which the three components of the NMR shielding tensor and the corresponding isotropic values are reported for the two different solvation models. As for the analysis of the reaction field, in the PCM we have used three different cavity scaling factors (f = 1.1, 1.2 or 1.4).

From the first three entries in Table 1-3 we observe that changing the cavity scaling factor has quite different outcome for the three diagonal components of the NMR shielding tensor. The *xx* component (out of plane) is almost unchanged whereas the magnitudes of the *yy* or *zz* components increases around 10 or 20 ppm, respectively, by changing the cavity scaling factor from 1.1 to 1.4. As already predicted on the bases of the reaction field data in Table 1-2, we find that using f =1.1 gives the best results for the shielding components as compared to DPM. If we also introduce two explicitly treated water molecules (the DFT(2)/PCM entry) the agreement becomes even closer.

Turning to the DPM results we find that introducing two water molecules into the DFT-treated region leads to an average change in each tensor components of around 2 ppm. More evidently than with PCM, the origin of this change is to be found almost entirely due to changes in the *zz* component (along the C_2 axis in pyrimidine). Thus within the DPM model a faster convergence is observed with respect to the number of solvent molecules treated using DFT for both the isotropic value and diagonal components of the NMR shielding tensor.

It is evident that for both the isotropic and each tensor component the DFT(2)/MM results are better reproduced by DFT(2)/PCM than DFT/MM. This clearly illustrates that special (QM) treatment of the solvent molecules very close to the solute may be important whereas the bulk solvent is described equally well using either a PCM or a DPM. It is also interesting to observe that a good agreement is found instead between DFT/PCM (f =1.1) and DFT/MM. Such an agreement might be related to the fact that both models introduce "artificial" short-range solute–solvent interactions (one in terms of a smaller cavity and the other in terms of purely classical dipoles) while an important part of these interactions (charge-transfer, dispersion and other QM effects) is not taken into account.

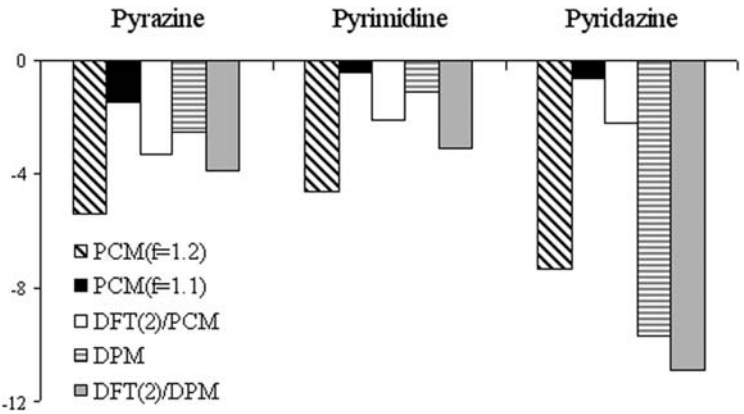

Figure 1-5. QM/continuum and QM/MM(pol) errors with respect to experiments for the N nuclear shielding of the three diazines

We now move to consider the comparison between QM/continuum and QM/MM(pol) results. The results are presented in Figure 1-5 for the error with respect to experiments.

As already observed in the previous section, by combining the explicit consideration of the hydrogen bonded water molecules using the DFT(2) approach, in which the two nearest water molecules are included in the system, with an external PCM (the DFT(2)/PCM entry) a very good agreement with experimental data is found. This shows that for chemical shieldings, both specific and bulk effects are important. Moving to the DPM model, the obtained results are of comparable accuracy as the DFT(2)/PCM model. It also has to be noted that small changes are generally observed passing from completely classical water molecules (DPM) to a description in which explicit water molecules are introduced into the region treated using DFT (DFT(2)/DPM).

1.4. CONCLUSIONS

We have presented and compared different solvation models (continuum, discrete, continuum + discrete) to study solvent effects on molecular properties. In particular, the nitrogen nuclear shielding, which is known to be very sensitive to even small modifications of electronic and/or nuclear charge distributions, has been analyzed. Such alternation/combination of different models has been required to study the complex nature of solute–solvent interactions when both long-range "polar" and shorter-range specific H-bond effects are active.

The study can be summarized as a two-step procedure. The first step is an analysis of the solvent-induced modifications on the property of interest, when obtained through a solvation continuum model. At this level it is fundamental that the continuum model is as accurate as possible: in our case this is realized through the PCM approach. On the basis of the results obtained in this continuum framework

(and, in particular, of possible failures), the following step is defined so as to include all those aspects of the solvation phenomenon which are missing (or are only partially accounted for). In the numerical practice, this means to introduce different approaches and to combine them in order to get an accurate evaluation of the solute response properties and of the way these are modified by the environment.

A single protocol cannot be found. However, some general rules seem to come out: (1) solute–solvent systems not showing strong specific interactions can be reliably described introducing QM/continuum approaches; (2) strongly interacting (and especially H-bonding) solute–solvent systems require a combination of different solvation approaches which has to be chosen in relation to the nature of the interactions on one hand, and to the type of analysis to be done on the other hand; (3) if this analysis is focussed on molecular response properties, then the solute system has to be described at an accurate electronic level, otherwise a complete confidence in the results cannot be obtained; (4) the solvent (or a part of it) can be treated at a lower level but only if all the interactions have been included in the model in a balanced way and including polarization effects; (5) H-bonding effects, to be correctly described, need the inclusion of the long-range interactions due to solvent molecules far beyond the first solvation shells (i.e., the bulk).

An approach which satisfies all these rules is a statistical analysis based on QM/MM(pol) calculations on large clusters obtained through MD simulations. An evident disadvantage is, however, present: the method is quite computationally expensive requiring first a MD simulation and successively many QM calculations on different configurations so as to obtain a statistically reliable result. Here, we have shown that two simplifications are possible.

The first simplification can be introduced any time we have strongly interacting solute–solvents systems (like diazines in water); in these cases in fact, an alternative and still accurate description can be obtained with a single set of small clusters (namely the solute plus the few solvent molecules forming the first solvation shell) obtained in terms of QM geometry optimizations. The second simplification, by contrast, is valid in all cases (i.e., for strongly or weakly interacting systems) and it implies to simulate the bulk effect through a polarizable continuum model. In such a way, the long-range effects of the solvent will be taken into account in an automatically averaged way using a single calculation.

REFERENCES

1. Warshel A, Levitt M (1976) J Mol Biol 103:227
2. Thole BT, van Duijnen PTh (1982) Chem Phys 71:211
3. Singh UC, Kollman PA (1986) J Comput Chem 7:718
4. Field MJ, Bash PA, Karplus M (1990) J Comput Chem 11:700
5. Gao J (1992) J Phys Chem 96:6432
6. Thompson MA (1996) J Phys Chem 100:14492
7. Tomasi J, Persico M (1997) Chem Rev 94:2027
8. Rivail J-L, Rinaldi D (1995) In: Leszczynski J (ed) Computational chemistry review of current trends, World Scientific, New York
9. Cramer CJ, Truhlar DG (1999) Chem Rev 99:2161

10. Orozco M, Luque FJ (2000) Chem Rev 100:4187
11. Tomasi J, Mennucci B, Cammi R (2005) Chem Rev 105:2999
12. Kongsted J, Osted A, Mikkelsen KV, Christiansen O (2002) Mol Phys 100:1813
13. Osted A, Kongsted J, Mikkelsen KV, Christiansen O (2003) Mol Phys 101:2055
14. Nielsen CB, Christiansen O, Mikkelsen KV, Kongsted J (2007) J Chem Phys 126:154112
15. Cancés E, Mennucci B, Tomasi J (1997) J Chem Phys 107:3031
16. Mennucci B, Cancés E, Tomasi J (1997) J Phys Chem B 101:10506
17. Amovilli C, Mennucci B (1997) J Phys Chem B 101:1051
18. Curutchet C, Orozco M, Luque JF, Mennucci B, Tomasi J (2006) J Comp Chem 27:1769
19. Buckingham AD, Schafer T, Schneider WG (1960) J Chem Phys 32:1227
20. Kamlet MJ, Abboud JLM, Taft RW (1980) Prog Phys Org Chem 13:485
21. Witanowski M, Biedrzycka Z, Sicinska W, Grabowski Z, Webb GA (1997) J Magn Res 124:127
22. Ramsey NF (1950) Phys Rev 78, 699
23. Ramsey N F (1953) Phys Rev 91, 303
24. London F (1937) J Phys Radium 8:397
25. Hameka HF (1962) Rev Mod Phys 34:87
26. Ditchfield R (1974) Mol Phys 27:789
27. Wolinski K, Hinton JF, Pulay P (1990) J Am Chem Soc 112:8251
28. Cammi R, Mennucci B, Tomasi J (1999) J Chem Phys 110:7627
29. Kongsted J, Nielsen CB, Mikkelsen KV, Christiansen O, Ruud K (2007) J Chem Phys 126:034510
30. Mennucci B (2002) J Am Chem Soc 124:1506
31. Kongsted J, Mennucci B (2007) J Phys Chem A 111:9890
32. Tomasi J, Cammi R, Mennucci B, Cappelli C, Corni S (2002) Phys Chem Chem Phys 4:5697
33. Klein R, Mennucci B, Tomasi J (2004) J Phys Chem A 108:5851
34. Cappelli C, Mennucci B, Monti S (2005) J Phys Chem A 109:1933
35. Mennucci B, Martinez JM (2005) J Phys Chem B 109:9818, 9830
36. Witanowski M, Stefaniak L, Webb GA (1993) In: Webb GA (ed) Annual reports on NMR spectroscopy, vol 25, Academic Press, London
37. Becke AJ (1993) Chem Phys 98:5648
38. Lee C, Yang W, Parr RG (1988) Phys Rev B 37:785
39. Frisch MJ, Trucks GW, Schlegel HB, Scuseria GE, Robb MA, Cheeseman JR, Montgomery Jr JA, Vreven T, Kudin KN, Burant JC, Millam JM, Iyengar SS, Tomasi J, Barone V, Mennucci B, Cossi M, Scalmani G, Rega N, Petersson GA, Nakatsuji H, Hada M, Ehara M, Toyota K, Fukuda R, Hasegawa J, Ishida M, Nakajima T, Honda Y, Kitao O, Nakai H, Klene M, Li X, Knox JE, Hratchian HP, Cross JB, Bakken V, Adamo C, Jaramillo J, Gomperts R, Stratmann RE, Yazyev O, Austin AJ, Cammi R, Pomelli C, Ochterski JW, Ayala PY, Morokuma K, Voth GA, Salvador P, Dannenberg JJ, Zakrzewski VG, Dapprich S, Daniels AD, Strain MC, Farkas O, Malick DK, Rabuck AD, Raghavachari K, Foresman JB, Ortiz JV, Cui Q, Baboul AG, Clifford S, Cioslowski J, Stefanov BB, Liu G, Liashenko A, Piskorz P, Komaromi I, Martin RL, Fox DJ, Keith T, Al-Laham MA, Peng CY, Nanayakkara A, Challacombe M, Gill PM, Johnson B, Chen W, Wong MW, Gonzalez C, Pople JA (2003) Gaussian 03, Revision C.02, People Gaussian Inc., Wallingford
40. "Dalton, a molecular electronic structure program", Release 2.0 (2005) ed.: see http://www.kjemi.uio.no/software/dalton/dalton.html
41. Weinhold F (1998) Natural bond orbital methods. In: Schleyer PvR, Allinger NL, Clark T, Gasteiger J, Kollman PA, Schaefer III HF, Schreiner PR (eds) Encyclopedia of computational chemistry, vol 3, John Wiley & Sons, Chichester, UK, p 1792
42. Karplus M, Pople JA (1963) J Chem Phys 38:2803

43. See for example Coutinho K, George HC, Fonseca TL, Ludwig V, Canuto S (2007) Chem Phys Lett 437:148 and references therein
44. Luque FJ, Bachs M, Aleman C, Orozco M (1996) J Comput Chem 17:806
45. Cossi M, Crescenzi O (2004) Theor Chem Acc 111:162

CHAPTER 2

THE MULTIPOLE MOMENT EXPANSION SOLVENT CONTINUUM MODEL: A BRIEF REVIEW

MANUEL F. RUIZ-LÓPEZ

Equipe de Chimie et Biochimie théoriques, SRSMC, Nancy-University, BP 239, 54506 Vandoeuvre-lès-Nancy, France, e-mail: Manuel.Ruiz@cbt.uhp-nancy.fr

Abstract: The multipole moment expansion solvent continuum model is being developed by our group for more than 30 years. A pioneer paper by Rinaldi and Rivail in 1973 provided the first self-consistent reaction field model, allowing incorporation of solvation effects in quantum mechanical calculations. It is not the aim of this chapter to make an exhaustive review of the method and its applications, but rather to summarize the main developments achieved during the last three decades and to discuss some particularities of the approach and its potentialities. The question of the solvation energy convergence will be discussed in some detail. Comparison with other polarizable continuum models will be presented too.

Keywords: Solvent Effects, Self-consistent Reaction Field, Continuum, Cavity, Polarizable Continuum model, Multipole Expansion.

2.1. INTRODUCTION

Solvent continuum models are now routinely used in quantum mechanical (QM) studies to calculate solvation effects on molecular properties and reactivity. In these models, the solvent is represented by a dielectric continuum that in the presence of electronic and nuclear charges of the solute polarizes, creating an electrostatic potential, the so-called "reaction field". The concept goes back to classical electrostatic schemes by Martin [1], Bell [2] and Onsager [3] who made fundamental contributions to the theory of solutions. Scholte [4] and Kirkwood [5] introduced the use of multipole moment distributions. The first implementation in QM calculations was reported in a pioneer work by Rivail and Rinaldi [6,7]. Other fundamental investigations were carried out by Tapia and Goscinski [8], Hilton-McCreery et al. [9] and Miertus et al. [10]. Many improvements have been made since then (for a review,

This contribution is dedicated to Dr. Daniel Rinaldi on the occasion of his 65th birthday and his official retirement from the French CNRS.

S. Canuto (ed.), Solvation Effects on Molecules and Biomolecules, 23–38.
DOI 10.1007/978-1-4020-8270-2_2,

see for instance [11,16]). The differences between the methods lie, principally, in the way the reaction field and the solute–solvent interaction energy are computed. This brief review will focus on the model originally proposed by Rivail and Rinaldi [7] that uses multipole moment developments to obtain an analytical expression of the reaction field. Hereafter, the acronym MPE will be employed to design this model (for multipole moment expansion). Such an acronym was proposed by Tomasi and co-workers [11] but has not been systematically used in the literature. The model is sometimes referred to as the "continuum model of Nancy" or simply as the SCRF (self-consistent reaction field) model, though the latter acronym is used for other similar approaches too. Main papers and basic equations will be summarized. A discussion on questions related to the convergence of the multipole moment expansion will be done. Comparison with other models will then be presented.

2.2. DEVELOPMENT OF THE MODEL: MAIN CONTRIBUTIONS

In the earliest version of the model (1973), an extension of the Onsager's formula to a spheroidal cavity for the solvation energy of a polar molecule was incorporated into a semiempirical Hamiltonian to achieve self-consistent reaction field calculations [6]. In that work, modifications of the geometry and dipole moment of the water molecule and water dimers in liquid water were analyzed. Extension to multipole moment distributions was reported in 1976 using spherical cavities and semiempirical approaches [7]. The accuracy of the model was significantly improved by the use of three-axes ellipsoidal cavities together with ab initio Hamiltonians (1982–1983). [17,18] These constant coordinate cavities (sphere, spheroid, ellipsoid) have the advantage of leading to analytical expressions for the solvation energy and the corresponding first and second derivatives with respect to nuclear coordinates [19]. The method was implemented in the Gaussian series of programs [18,20] and in the deMon code [21]. The latter allowed us to perform the first density functional theory calculations with inclusion of solvation effects [22]. However, molecular-shaped cavities are necessary for a proper description of the solute–solvent boundary in most cases and this extension was achieved in the early 1990s [23,24]. As explained below, some quantities that only depend on the cavity shape and solvent dielectric constant have now to be computed numerically, but it is still possible to obtain the first and second derivatives of the energy analytically [25]. The most recent developments of the MPE approach concern the generalization to multicentric multipolar developments in general cavities: the procedure to compute energy and first energy derivatives has been reported in 2004 [26] while second energy derivatives has been reported very recently [27].

The development of the MPE method opened an avenue to the theoretical analysis of solvent effects on chemical and physico-chemical properties. The method was intensively applied to spectroscopical properties in the 1980s [28] including NMR nuclear quadrupole coupling [29,30], spin–spin coupling constants [31], IR spectra [28,32–34] vibrational polarizabilities [35], as well as UV–V and circular dichroism spectra [36–38].

The possibility to investigate chemical reactions in solution strongly contributed to the popularization of continuum models. Experimentally, solvent effects on chemical reactions were well known [39] but their interpretation was usually restricted to modifications of the activation barrier (kinetic constants) through differential solvation between the reactants and the transition structure (TS). Former applications of the MPE method on reactivity focused on modifications of the frontier orbitals [40,41]. The S_N2 reaction [42] and the abnormal basicity order of amines in water constituted very interesting test cases for continuum model calculations [43,44]. A key achievement was the development of analytical algorithms to compute solvation energy derivatives since direct location of TSs in solution became possible. The first work describing a fully optimized TS in solution was reported in the early 1990s for the isomerization of push–pull ethylene derivatives [45,46] and was followed by another application to the Diels–Alder reaction [47,48]. These and other investigations were decisive to demonstrate that solvation effects can induce large changes on the geometry of the TS that do not necessarily occur along the gas-phase reaction coordinate. For instance, in the Diels–Alder reaction, the TS geometry changes along an orthogonal coordinate [49]. Moreover, in processes exhibiting large polarity changes, the nature of the reaction mechanism itself may change. Stepwise vs concerted 2+2 cycloadditions [50–55] and alkene halogenation [56] illustrated this situation. In another paper, the hydrolysis mechanism of the amide bond was analyzed and water assistance vs long-range electrostatic solvation effects were analyzed in detail [57]. The MPE model has also been adapted to deal with non-equilibrium solvation on chemical reactions [58].

2.3. BASIC EQUATIONS

The electrostatic equations for a molecule in a cavity surrounded by a dielectric continuum are solved by considering the conditions the potential must fulfill [59]. The electrostatic potential must obey Poisson's equation inside the cavity:

$$\Delta V_{\text{int}} = -4\pi\rho \tag{2-1}$$

and Laplace's equation outside (no charge assumed):

$$\Delta V_{\text{ext}} = 0 \tag{2-2}$$

Limit conditions at the cavity boundary are defined by

$$V_{\text{int}}(S) = V_{\text{ext}}(S) \tag{2-3}$$

$$[\nabla V_{\text{int}}(S)]_n = \varepsilon[\nabla V_{\text{ext}}(S)]_n \tag{2-4}$$

where n means the normal component to the surface and ε is the static dielectric constant of the continuum. Finally, the external potential must also verify:

$$V_{\text{ext}}(\mathbf{r}) \to 0 \quad \text{for} \quad \mathbf{r} \to \infty \tag{2-5}$$

The general solution of Laplace's equation is given by

$$V(r) = \sum_{l} \sum_{m} \left(A_l^m r^l + \frac{B_l^m}{r^{l+1}} \right) P_l^m(\cos\theta) \mathrm{e}^{\mathrm{i}m\varphi} \tag{2-6}$$

where A and B are constants and P_l^m stand for associated Legendre polynomials. In all these equations, l is assumed to vary from 0 to infinity and m from $-l$ to $+l$. In the following, we assume a multicentric multipole moment expansion of the solute's electrostatic potential, which corresponds to the implementation in current versions of the MPE model [26].

Because of the required behavior at infinity, the general expression for the external potential is

$$V_{\text{ext}}(P) = \sum_{I} \sum_{l} \sum_{m} \sqrt{\frac{4\pi}{2l+1}} \left(\gamma_l^m(I) \frac{1}{r_I^{l+1}} \right) Y_l^m(\theta_I, \varphi_I) \tag{2-7}$$

The sum over I runs over all the centers chosen for the development, usually, all the atomic nuclei. The internal potential is conveniently written by separating the contributions coming from the solute and from the polarized dielectric:

$$V_{\text{int}}(P) = V_{\text{int,solute}}(P) + V_{\text{int,dielectric}}(P) \tag{2-8}$$

$$V_{\text{int,solute}}(P) = \sum_{I} \sum_{l} \sum_{m} \sqrt{\frac{4\pi}{2l+1}} \left(M_l^m(I) \frac{1}{r_I^{l+1}} \right) Y_l^m(\theta_I, \varphi_I) \tag{2-9}$$

$$V_{\text{int,dielectric}}(P) = \sum_{I,J} \sum_{l,l'} \sum_{m,m'} \sqrt{\frac{4\pi}{2l+1}} f_{ll'}^{mm'}(I, J) M_{l'}^{m'}(I) r_J^l Y_l^m(\theta_J, \varphi_J) \tag{2-10}$$

where $M_l^m(I)$ stand for the solute multipole moments computed at center I. There is no unique way to define these distributed multipoles and some possibilities will be mentioned below. In the previous equations, γ_l^m and $f_{ll'}^{mm'}$ are unknowns that must be determined from the limit conditions. These quantities do not depend on the charge distribution but only on the cavity definition and the solvent dielectric constant. To obtain them, the following steps are considered [26]:

1) Define a grid of points at the cavity surface. This can be done using the Gepol program for van der Waals-type surfaces (see below) [60,61].
2) Define a series of probe multipole moments (values and positions are arbitrary, usually unit values at nuclei positions).
3) For each multipole, set down Poisson's and Laplace's equations at each point of the grid using the expressions for the internal and external potentials above.

4) Solve the corresponding overdimensioned system of linear equations. The unknowns can be separated, i.e., one may compute a set of (*l, m*) quantities for fixed *I, J, l′* and *m′*.

Once the reaction field potential $V_{\text{int,dielectric}}$ has been obtained, the total energy of the solvated solute is computed according to the expression

$$E_{\text{s}} = \left\langle \psi^{\text{s}} \right| H^{\text{o}} \left| \psi^{\text{s}} \right\rangle + \frac{1}{2} \left[\sum_{\text{nuclei}} z_i V_{\text{int,dielectric}}(R_i) - \left\langle \psi^{\text{s}} \right| V_{\text{int,dielectric}} \left| \psi^{\text{s}} \right\rangle \right] \tag{2-11}$$

where ψ^{s} is the polarized wavefunction in solution and z_i is the nuclear charge of atom i placed at R_i. The factor $\frac{1}{2}$ comes from the fact that the energy cost to polarize the solvent (positive value) is exactly one half the solute–solvent interaction energy (negative value) [59]. In terms of the solute's multipole moments, the total energy is simply rewritten:

$$E_{\text{s}} = \left\langle \psi^{\text{s}} \right| H^{\text{o}} \left| \psi^{\text{s}} \right\rangle - \frac{1}{2} \sum_{I,J} \sum_{l,l'} \sum_{m,m'} f_{ll'}^{mm'}(I, J) M_{l'}^{m'}(I) M_l^m(J) \tag{2-12}$$

In order to compute the wavefunction of the solute, the standard SCF equations must be modified to minimize this energy and the corresponding Fock operator is

$$F_{\mu\upsilon} = F_{\mu\upsilon}^{\text{o}} - \sum_{I,J} \sum_{l,l'} \sum_{m,m'} f_{ll'}^{mm'}(I, J) M_{l'}^{m'}(I) \left\langle \mu \left| M_l^m(J) \right| \nu \right\rangle \tag{2-13}$$

A similar expression is obtained for the Kohn–Sham operator in density functional. One should note that because of the quadratic nature of these SCRF equations on the molecular orbital coefficients, the $\frac{1}{2}$ factor in the total energy is not present in the Fock operator.

2.4. CAVITY DEFINITION

The definition of the cavity (shape and size) is an intricate and delicate question that may have a considerable influence on the results (even qualitatively). In the original Onsager's theory, the molecular cavity was defined as a sphere and the volume was taken equal to the partial molecular volume of the solute in the solution. In practice, this volume can be assumed to be equal to the average volume in the pure liquid. Experimental values are then easily deduced from the experimental density of the liquid at 20°C when this quantity is available. Obviously, in SCRF applications, it became rapidly necessary to achieve a theoretical definition of the cavity applicable to any molecular structure. In former works carried out by our group [28,62], it was shown that a simple linear relationship exists between the experimental volume derived from the liquid density (Onsager's recipe) and the van der Waals volume, i.e., the volume enclosed by a set of overlapping atomic spheres with Bondi radii [63]. Roughly, this relationship is

$$V_{\text{exp}} \approx 1.7 V_{\text{vdW}} \tag{2-14}$$

This equation provides a way to estimate the molecular cavity volume for any system but the shape of the cavity has also to be defined. Constant coordinate cavities such as the sphere or the ellipsoid are obviously not appropriate for most systems and they have been almost definitively abandoned in favor of molecular-shaped cavities. The majority of current continuum methods, and MPE as well, use van der Waals-type molecular surfaces. Atomic radii are in general larger than standard Bondi radii so that the obtained surface is close to the so-called solvent-excluding surface [64,65]. Consistent with the expression for the volume given above, the order of magnitude of atomic radii should be

$$R \approx (1.7)^{1/3} \; R_{\text{vdW}} \approx 1.2 \quad R_{\text{vdW}} \tag{2-15}$$

This corresponds to the standard definition for atomic radii in MPE applications (some previous versions used values close to 1.3). The factor 1.2 is also used in PCM, where it was introduced empirically on the basis of different tests and considerations [15].

The atomic radii may be further refined to improve the agreement between experimental and theoretical solvation free energies. Work on this direction has been done by Luque and Orozco (see [66] and references cited therein) while Barone et al. [67] defined a set of rules to estimate atomic radii. Further discussion on this point can be found in the review by Tomasi and co-workers [15]. It must be noted that the parameterization of atomic radii on the basis of a good experiment–theory agreement of solvation energies is problematic because of the difficulty to separate electrostatic and non-electrostatic terms. The comparison of continuum calculations with statistical simulations provides another way to check the validity of cavity definition. A comparison between continuum and classical Monte Carlo simulations was reported by Costa-Cabral et al. [68] in the early 1980s and more recently, molecular dynamics simulations using combined quantum mechanics and molecular mechanics (QM/MM) force-fields have been carried out to analyze the case of water molecule in liquid water [69].

An interesting alternative to van der Waals cavities is the use of isodensity or isopotential surfaces. Rivail et al. [70] demonstrated that for a given cavity volume, the electron isopotential surface is the one containing the largest electronic density, thus giving a physical meaning to this surface. Nevertheless, isodensity and isopotential cavities are computationally demanding, as they have to be recomputed at each SCF iteration, and are not quite used in practice.

2.5. DISTRIBUTED MULTIPOLES

As said above, there is no unique way to represent the solute's charge distribution by a multicentric multipole expansion. This point has been discussed by Stone [71] in the general case and by Rinaldi et al. [26] in the context of the MPE method. The

authors proposed to use the definition given by Vigné-Maeder and Claverie [72] and Sokalski and Poirier [73] when the centers of the expansion are the nuclei. In the later case, the components of the multipole moments $M_l^m(I)$ are given by

$$M_l^m(I) = \sum_{\mu \in I} \sum_{\nu} P_{\mu\nu} \left\langle \mu \left| \mathbf{M}_l^m(I) \right| \nu \right\rangle \tag{2-16}$$

where $\mathbf{M}_l^m(I)$ is the multipole moment operator centered on I. The sum runs over all atomic orbitals centered on atom I. The zeroth-order moment $M_0^0(I)$ represents the Mulliken net atomic charge of the atom so that this distribution is called [26] Mulliken–Sokalski–Poirier. A similar definition but using symmetrically orthogonalized orbitals [74], instead of canonical orbitals, was proposed and referred to as the Lowdin–Sokalski–Poirier distribution [26]. Distributed multipoles based on a fitting procedure of the electrostatic potential, as that proposed in the OPEP code [75], would be quite efficient to obtain a faster convergence of the solvation energy but they would be much more time consuming in SCRF calculations. Work is in progress, however, to develop a method in which the multipole distribution is limited to first-order terms, i.e., to point charges, fitting the electrostatic potential [76].

2.6. SOLVATION ENERGY CONVERGENCE

Based on well-known problems in the description of intermolecular interactions though multipole moment expansions, it has been sometimes argued in the literature that the MPE solvation energy converges slowly, creating some confusion about the performances of the model. This point is discussed now but we advance that, in practice, convergence is quite fast provided one applies the model in a proper way. It will be shown that monocentric multipole expansions for the solvation energy may be safely used for small to medium size molecules while multicentric expressions are more adequate for larger systems.

Thanks to efficient recurrence formulae, multipole moments and multipole moment derivatives can be calculated at very high order with a low computational cost. The calculation of reaction field factors, however, may become computationally expensive at high order due to the increasing number of linear equations to be solved. Thus, in practice, the multipole moment expansion is cut off at a maximum value of l ($l_{\max}$), usually taken around 6. In order to get an order of magnitude of the error introduced by the truncation, let us consider Kirkwood's equations [5] for the free energy of a charge distribution of charges q_i and $\boldsymbol{r}_i$ in a spherical cavity of radius a:

$$\Delta G_{\text{elec,solv}} = -\frac{1}{2} \sum_{\ell=0}^{\infty} \sum_{m=-\ell}^{\ell} \frac{(\ell+1)(\varepsilon-1)}{(\ell+1)\varepsilon+\ell} \frac{M_l^{m2}}{a^{2\ell+1}} \tag{2-17}$$

where the multipole moments

$$M_l^m = \sum_i q_i S_l^m(\mathbf{r}_i) \tag{2-18}$$

$$S_l^m(\mathbf{r}_i) = \sqrt{\frac{4\pi}{2l+1}} r_i^l \quad Y_l^m(\theta_i, \varphi_i) \tag{2-19}$$

are computed at the cavity center. Since the charges are assumed to be inside the cavity, $r_i < a$, and the series is convergent. Convergence will be fast for $r_i <<< a$ and will become slower for r_i values approaching a. In other terms, the solvation energy can always be obtained at a desired accuracy using sufficiently high values of l. To further exploit this model, let us consider the case of a single off-centered point charge q placed along the z-axis at a distance r from the cavity center (see Figure 2-1) and a very high dielectric constant. The corresponding solvation energy may be approximated by

$$\Delta G_{\text{solv}} \approx -\frac{q^2}{2a} \sum_{\ell=0}^{\infty} \left(\frac{r}{a}\right)^{2l} \tag{2-20}$$

where we have used

$$M_l^m = q r^{\ell} \tag{2-21}$$

Since

$$\rho = \left(\frac{r}{a}\right)^2 < 1 \tag{2-22}$$

one may sum the series $\sum_{\ell=0}^{\infty} \rho^l$ and write

$$\Delta G_{\text{solv}} \approx -\frac{q^2}{2a\,(1-\rho)} \tag{2-23}$$

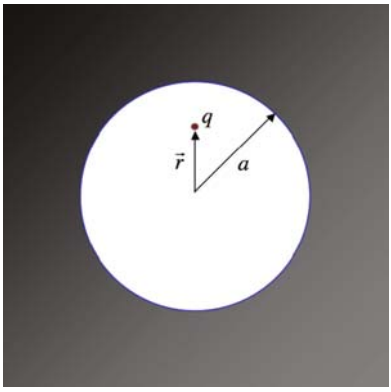

Figure 2-1. Simple model to evaluate convergence speed in multipole expansion of the solvation energy

This expression may be interpreted as a generalized Born formula for an off-centered charge in a spherical cavity. Accordingly, for a development up to the l_{max} order, the percentual error in total energy may easily be shown to be

$$\text{error} \approx 100\rho^{(l_{max}+1)} \tag{2-24}$$

(note that it does not depend on q). In Figure 2-2, this error is represented as a function of r/a and l_{max}. As shown, for a typical l_{max} value of 6, the energy error is small (below 5%) provided r/a does not exceed 0.8. One may roughly estimate the largest molecular size that would satisfy such a condition. Assuming arbitrarily that q represents a hydrogen atom placed at a distance 1.44 Å from the cavity surface (i.e., $1.2^{*}R_{vdw}$ with R_{vdw} = 1.2 Å for H), one obtains a = 7.2 Å and r = 5.8 Å. Therefore, the largest distance of an atom to the cavity center should be slightly smaller than 6 Å. For larger molecules, r/a becomes closer to one for peripheral atomic nuclei and the convergence of monocentric developments will require larger values of l_{max}. In that case, multicentric approaches should be more efficient. The right plot in Figure 2-2 illustrates this. It gives the l_{max} value required to obtain a predetermined error for a charge at a distance r from the center of the development. One should note that l_{max} varies almost linearly with r and that reasonably good results (5% error) may be obtained with $l_{max} \approx r$ with r expressed in Å.

The convergence of the solvation energy in the MPE method has been discussed in previous papers from other points of view. Chalmet and Ruiz-López [69] focused on the convergence of the reaction field for the water molecule in liquid water. Curutchet et al. [77] showed that the error in solvation energy for a series of 18 polar molecules in cyclohexane was smaller than 3% when the multicentric multipole moment development was carried out at l_{max} = 6. The system considered were CH_3F, $CHCl_3$,

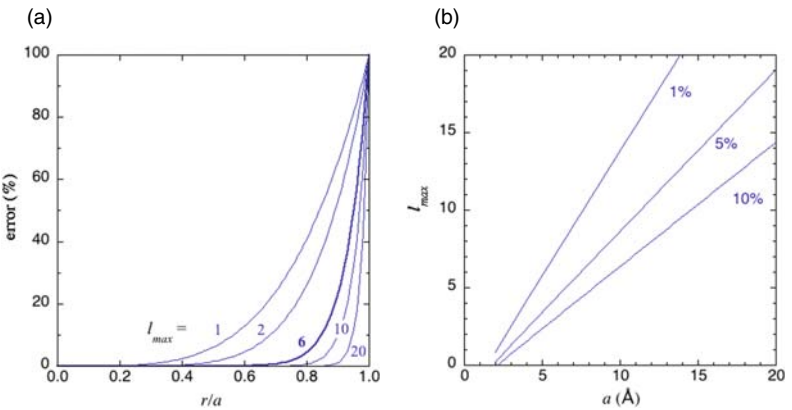

Figure 2-2. Analysis of electrostatic solvation energy error for an off-centered charge in a spherical cavity according to a monocentric multipole moment development. *Left*: error as a function of the ratio r/a and l_{max}. *Right*: required l_{max} value as a function of the charge distance to the cavity center (r) assuming $a = r + 1.44$ Å

C_6H_5SH, CH_3COOCH_3, $CH_3CH_2NO_2$, $CO(CH_3)_2$, CH_3CN, C_6H_5CHO, CH_3NH_2, C_6H_5N, CH_3OH, H_2O, C_6H_5OH, CH_3COOH, CH_3CONH_2, $PO(OH(OCH_3)_2)$, cytosine and guanine. In Figure 2-3, we have detailed the convergence of the electrostatic solvation energy for these systems (HF/6-31 G* calculations). Rinaldi et al. [26] discussed the convergence when different multipole moment distribution types are used in comparison with monocentric expansions.

Before closing this section, a final comment is necessary. In QM calculations, some charge is always present outside the cavity due to electronic density tails, so that the basic hypothesis of the continuum approach is not formally verified. Nevertheless, this "escaped" or "outlying" electronic charge density is usually small and does not introduce specific convergence problems (though there is always an error associated to it). Modifications of the standard PCM continuum model to account for the external density have been proposed using either charge normalization techniques

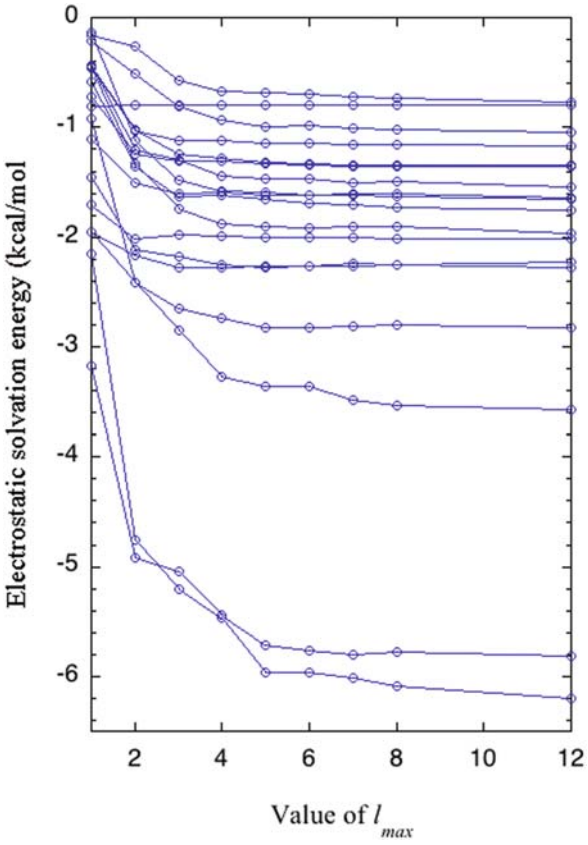

Figure 2-3. Convergence of electrostatic solvation energy in the MPE method for a series of 18 polar molecules in cyclohexane

or the integral equation formalism (see Discussion and References in reference [78]). In the MPE method, no correction for the external charge is in principle necessary since the reaction field factors are independent of the solute charge. One simply assumes that the reaction field computed using the full molecular moments of the solute is valid in all the space [79]. This approximation could become unsuitable for systems exhibiting a large outlying electron density. Such cases may be considered as "pathologic" in SCRF calculations using either MPE or PCM and may require specific adaptations of the model or, alternatively, a discrete-continuum approach.

2.7. NON-ELECTROSTATIC CONTRIBUTIONS

The electrostatic solvation energy is only a part of the total solvation energy. Cavitation, dispersion and repulsion terms must be added. We show below that the MPE method leads to similar electrostatic energies than the polarizable continuum model (PCM) of Tomasi and co-workers [10], provided the same cavities are used. Therefore, non-electrostatic terms in these methods may be computed using the same computational strategies [15]. We emphasize the fact that accurate non-electrostatic contributions are often difficult to compute since they are based on parameterized formulae that cannot be directly compared to experiment. The obtained data must therefore be used with prudence, especially if they are expected to play a major role in the process under study. Fortunately, in many circumstances, non-electrostatic terms are small and/or vary little, so that they can be neglected. Tuñón et al. [80] developed a parameterized expression for the MPE method using an expression of the type

$$\Delta G_{\mathrm{sol}}^{\mathrm{NE}} = \sum_i \gamma_i S_i \tag{2-25}$$

where S_i is the solvent-accessible surface area contribution for the solute's atom i and γ_i is an atom-type parameter obtained from fitting calculations to experimental solvation energies. Parameters were reported for several atom types and for solvation in liquid water.

2.8. COMPARISON WITH OTHER SOLVENT MODELS

Curutchet et al. [77] compared the result obtained by the PCM method, the SM5 method of Cramer, Truhlar and co-workers [81–85] and the MPE method. Calculations with the PCM method were carried out using the MST program (for Miertus–Scrocco–Tomasi) developed by Luque, Orozco and co-workers [66,86–89]. Main conclusion was that the three methods lead to comparable solvation energies. Cavities parameterized for the MST (PCM) model are largely transferable to MPE model. In other words, both methods predict very close solvation energies when they assume identical cavities. The SM5 method must use smaller cavities in order to obtain comparable electrostatic energies, as is the case in the current implementation of this generalized-Born method. Figure 2-4 illustrates the excellent agreement between

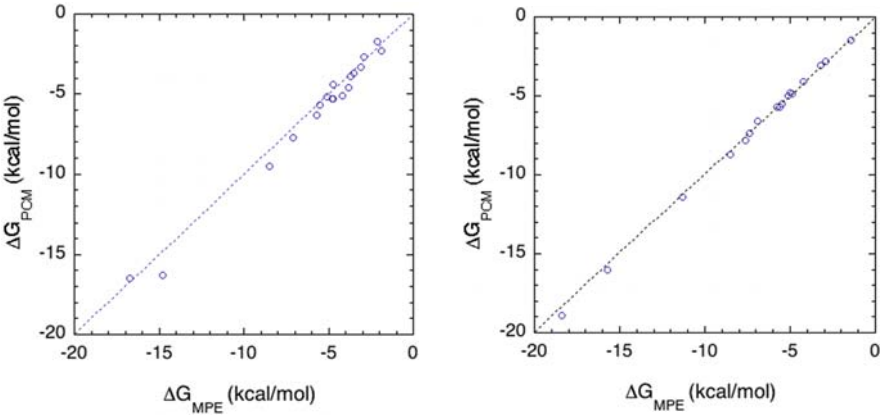

Figure 2-4 Comparison of electrostatic solvation energies obtained with the PCM and MPE methods for 18 polar molecules in aqueous solution (see text). *Left*: self-consistent reaction field calculations at the HF-6-31 G* level. *Right*: calculations using gas-phase CM2 net atomic charges

PCM and MPE calculations for the list of molecules given above. The agreement is especially good when net atomic point charges (gas-phase class IV CM2 [90] values) are used instead of doing a full SCF calculation. This is easily explained by the fact that the external electronic density plays a different role in both methods. When point charges are used, the whole charge distribution is inside the cavity and both methods are formally equivalent.

Further comparison between PCM and MPE was reported in the paper by Rinaldi et al. [26] using several multipole moment distribution types. Again, an excellent agreement was obtained. The authors reported examples for which the computational time with the MPE method represents only 30% of the time required for the equivalent computation with PCM (for details on code versions, see that paper). MPE and PCM results are also found comparable for IR properties [91] as well as for UV spectra [91,92] of substituted coumarins and chromones at the TD-DFT level.

2.9. CONCLUSIONS AND PERSPECTIVES

Continuum models are very useful to evaluate solvent effect on physico-chemical properties and chemical phenomena at a low computational cost. The principles of the MPE and PCM methods are similar and not surprisingly, very close results are obtained when the same cavity definition is used. Probably, the main advantage of the MPE method lies in the independence of the reaction field factors with respect to the charge distribution, which makes SCRF calculations faster (the factors are computed only once for a given geometry) and solvation energy derivatives easier (analytical expressions are obtained). Besides, the use of a multipole moment expansion of the energy allows interpretation of the solvent effect on the basis of quantities that are familiar to the experimental chemist (point charges, local dipoles, etc.). Moreover,

the use of a multicentric expansion allows the application to large molecules without the necessity of using high-order expansions. Difficulties may arise in both MPE and PCM methods when the outlying charge is significant. Thus, particular attention has to be paid when dealing with anions, for which a cavity definition is not trivial: solvent molecules should be closer to the solute sharing the excess electronic charge. Some works have also shown that a continuum representation of the medium may be inaccurate to estimate solvent effects on hydrated zwitterions [93–95]. In all these cases, including a few explicit solvent molecules interacting with the solute represents a straightforward solution. To further reduce the computational time, a three-layer QM/MM/continuum approach [96] in which the solvent molecules are described at the molecular mechanics level might be employed.

Current developments of the MPE continuum model focus on the combination of a multicentric multipole moment expansion of the reaction field combined with a discrete charge representation of the solute charge distribution fitting the electrostatic potential. This scheme leads to a simple formulation that parallels generalized-Born (GB) methods, though in the MPE-GB approach, the only parameter that needs to be defined is the cavity surface [76].

LIST OF ABBREVIATIONS

CM2	Charge model 2
DFT	Density functional theory
GB	Generalized-Born
MM	Molecular mechanics
MPE	Multipole expansion
MST	Miertus–Scrocco–Tomasi model
PCM	Polarizable continuum model
QM	Quantum mechanical
SCRF	Self-consistent reaction field
SM5	Solvation model 5
TD	Time dependent
TS	Transition structure

REFERENCES

1. Martin A (1929) Phil Mag 8:550
2. Bell RP (1931) Trans Faraday Soc 27:797
3. Onsager L (1936) J Am Chem Soc 58:1486
4. Scholte TG (1949) Physica 15:437
5. Kirkwood JG (1934) J Chem Phys 2:351
6. Rinaldi D, Rivail JL (1973) Theor Chim Acta 32:57
7. Rivail JL, Rinaldi D (1976) Chem Phys 18:233
8. Tapia O, Goscinski O (1975) Mol Phys 29:1653
9. Hilton-McCreery J, Christoffersen RE, Hall GG (1976) J Am Chem Soc 98:7198
10. Miertus S, Scrocco E, Tomasi J (1981) Chem Phys 55:117
11. Tomasi J, Persico M (1994) Chem Rev 94:2027

12. Cramer CJ, Truhlar DG (1995) in Lipkowitz KB, Boyd DB (Eds.), Reviews in Computational Chemistry. VCH, New York, p. 1
13. Cramer CJ, Truhlar DG (1999) Chem Rev 99:2161
14. Orozco M, Luque FJ (2000) Chem Rev 100:4187
15. Tomasi J, Mennucci B, Cammi R (2005) Chem Rev 105:2999
16. Luque FJ, Curutchet C, Muñoz-Muriedas J, Bidon-Chanal A, Soteras I, Morreale A, Gelpi JL, Orozco M (2003) Phys Chem Chem Phys 5:3827
17. Rivail JL, Terryn B (1982) J Chim Phys Phys Chim Biol 79:1
18. Rinaldi D, Ruiz-López MF, Rivail JL (1983) J Chem Phys 78:834
19. Rinaldi D, Rivail J-L, Rguini N (1992) J Comput Chem 13:675
20. Rinaldi D, Pappalardo RR (1992) Quantum Chemistry Program Exchange. Indiana University, Bloomington, IN, Program no. 622
21. St-Amant A, Salahub D (1990) Chem Phys Lett 169:387
22. Ruiz-López MF, Bohr F, Martins-Costa MTC, Rinaldi D (1994) ChemPhys Lett 221:109
23. Dillet V, Ángyán JG, Rinaldi D, Rivail JL (1993) Chem Phys Lett 202:18
24. Dillet V, Rinaldi D, Rivail JL (1994) J Phys Chem 98:5034
25. Dillet V, Rinaldi D, Bertrán J, Rivail JL (1996) J Chem Phys 104:9437
26. Rinaldi D, Bouchy A, Rivail JL, Dillet V (2004) J Chem Phys 120:2343
27. Rinaldi D, Bouchy A, Rivail JL (2006) Theoret Chem Acc 116:664
28. Ruiz-López MF (1985) Thesis, Université de Nancy I
29. Ruiz-López MF, Rinaldi D, Rivail JL (1983) J Mol Struct: THEOCHEM 91:373
30. Ruiz-López MF, Rinaldi D, Rivail JL (1986) J Mol Struct: THEOCHEM 148:61
31. Ruiz-López MF, Rinaldi D, Rivail JL, Oliva A (1982) J Chem Res 329
32. Rivail JL, Rinaldi D (1981) in Pullman B (Ed.), Intermolecular Forces. D. Reidel Publishing Company, Dordrecht, p. 343
33. Rivail JL (1981) in Carbó R (Ed.), Current aspects in quantum chemistry. Elsevier, Amsterdam, p. 389
34. Rivail JL, Rinaldi D, Dillet V (1996) Mol Phys 89:1521
35. Rinaldi D, Ruiz-López MF, Martins-Costa MTC, Rivail JL (1986) Chem Phys Lett 128:177
36. Ruiz-López MF, Rinaldi D (1983) J Mol Struct: THEOCHEM 93:277
37. Ruiz-López MF, Rinaldi D (1984) Chem Phys 86:367
38. Ruiz-López MF, Rinaldi D, Rivail JL (1986) Chem Phys 110:403
39. Reichardt C (2003) Solvents and Solvent Effects in Organic Chemistry (Third Edition), Wiley-VCH Verlag GmbH & Co. KGaA, Weinheim
40. Bertrán J, Oliva A, Rinaldi D, Rivail JL (1980) Nouv J Chim 4:209
41. Sánchez-Marcos E, Maraver J, Ruiz-López MF, Bertrán J (1986) Can J Chem 64:2353
42. Bertrán J, Rinaldi D, Rivail JL (1979) C R Acad Sci Paris 289:195
43. Terryn B, Rivail JL, Rinaldi D (1981) J Chem Res-S141
44. Sánchez-Marcos E, Terryn B, Rivail JL (1985) J Phys Chem 89:4695
45. Pappalardo RR, Sánchez-Marcos E, Ruiz-López MF, Rinaldi D, Rivail J-L (1991) J Phys Org Chem 4:141
46. Pappalardo RR, Sánchez-Marcos E, Ruiz-López MF, Rinaldi D, Rivail JL (1993) J Am Chem Soc 115:3722
47. Cativiela C, García JI, Mayoral JA, Royo AJ, Salvatella L, Assfeld X, Ruiz-López MF (1992) J Phys Org Chem 5:230
48. Ruiz-López MF, Assfeld X, García JI, Mayoral JA, Salvatella L (1993) J Am Chem Soc 115:8780
49. Assfeld X, Ruiz-López MF, García JI, Mayoral JA, Salvatella L (1995) J Chem Soc, Chem Commun, 1371

50. Assfeld X, Sordo JA, González J, Ruiz-López MF, Sordo TL (1993) J Mol Struct: THEOCHEM 287:193
51. Assfeld X, Ruiz-López MF, Gonzalez J, López R, Sordo JA, Sordo TL (1994) J Comput Chem 15:479
52. Assfeld X, López R, Ruiz-López MF, González J, Sordo TL, Sordo JA (1995) J Mol Struct: THEOCHEM 331:1
53. López R, Suárez D, Ruiz-López MF, González J, Sordo JA, Sordo TL (1995) J Chem Soc Chem Comm1677
54. López R, Ruiz-López MF, Rinaldi D, Sordo JA, Sordo TL (1996) J Phys Chem 100:10600
55. López R, Suárez D, Sordo TL, Ruiz-López MF (1998) Chemistry Eur J 4:328
56. Assfeld X, Garapon J, Rinaldi D, Ruiz-López MF, Rivail JL (1996) J Mol Struct: THEOCHEM 371:107
57. Antonczak S, Ruiz-López MF, Rivail JL (1994) J Am Chem Soc 116:3912
58. Ruiz-López MF, Rinaldi D, Bertrán J (1995) J Chem Phys 103:9249
59. Böttcher CJF (1973) Theory of electric polarization, Elsevier, Amsterdam
60. Pascual-Ahuir JL, Silla E (1990) J Comput Chem 11:1047
61. Silla E, Tuñón I, Pascual-Ahuir JL (1991) J Comp Chem 12:1077
62. Terryn B, Barriol J (1981) J Chim Phys 78:207
63. Bondi A (1964) J Phys Chem 68:441
64. Richards FM (1977) Annu Rev Biophys Bioeng 6:151
65. Connolly ML (1983) J Appl Crystallogr 16:548
66. Curutchet C, Orozco M, Luque FJ (2001) J Comput Chem 22:1180
67. Barone V, Cossi M, Tomasi J (1997) J Chem Phys 107:3210
68. Costa-Cabral BJ, Rinaldi D, Rivail JL (1982) Chem Phys Lett 93:157
69. Chalmet S, Ruiz-López MF (2001) J Chem Phys 115:5220
70. Rivail JL, Terryn B, Rinaldi D, Ruiz-Lopez MF (1985) J Mol Struct: THEOCHEM 120:387
71. Stone AJ (2000) The Theory of Intermolecular Forces, Oxford University Press, Oxford
72. Vigné-Maeder F, Claverie P (1988) J Chem Phys 88:4934
73. Sokalski WA, Poirier RA (1983) Chem Phys Lett 98:86
74. Löwdin PO (1950) J Chem Phys 18:365
75. Angyán JG, Chipot C, Dehez F, Hättig C, Jansen G, Millot C (2003) J Comput Chem 24:997
76. Rinaldi D, Ruiz-López MF in preparation
77. Curutchet C, Cramer CJ, Truhlar DG, Ruiz-López MF, Rinaldi D, Orozco M, Luque FJ (2003) J Comput Chem 24:284
78. Cancès E, Mennucci B (2001) J Chem Phys 115:6130
79. Rivail JL, Terryn B, Rinaldi D, Ruiz-López MF (1985) J Mol Struct: THEOCHEM 120:387
80. Tuñón I, Bertrán J, Ruiz-López MF, Rinaldi D (1996) J Comput Chem 17:148
81. Li J, Hawkins GD, Cramer CJ, Truhlar DG (1998) Chem Phys Lett 288:293
82. Zhu T, Li J, Hawkins GD, Cramer CJ, Truhlar DG (1998) J Chem Phys 109:9117
83. Li J, Zhu T, Hawkins GD, Winget P, Liotard DA, Cramer CJ, Truhlar DG (1999) Theor Chem Acc 103:9
84. Zhu T, Li J, Liotard DA, Cramer CJ, Truhlar DG (1999) J Chem Phys 110:5503
85. Chuang YY, Radhakrishnan ML, Fast PL, Cramer CJ, Truhlar DG (1999) J Phys Chem A 103:4893
86. Bachs M, Luque FJ, Orozco M (1994) J Comp Chem 15:446
87. Luque FJ, Bachs M, Alemán C, Orozco M (1996) J Comp Chem 17:806
88. Luque FJ, Zhang Y, Alemán C, Bachs M, Gao J, Orozco M (1996) J Phys Chem 100:4269
89. Colominas C, Luque FJ, Orozco M (1999) J Phys Chem A 103:6200
90. Li J, Zhu T, Cramer CJ, Truhlar DG (2000) J Phys Chem A 104:2178

91. Preat J, Loos PF, Assfeld X, Jacquemin D, Perpète EA (2007) Int J Quantum Chem 107:574
92. Preat J, Loos PF, Assfeld X, Jacquemin D, Perpète EA (2007) J Mol Struct: THEOCHEM 808:85
93. Chalmet S, Harb W, Ruiz-López MF (2001) J Phys Chem A 105:11574
94. Gorb L, Asensio A, Tuñón I, Ruiz-López MF (2005) Chemistry Eur J 11:6743
95. Lambert A, Regnouf-de-Vains JB, Ruiz-López MF (2007) Chem Phys Lett 442:281
96. Chalmet S, Rinaldi D, Ruiz-López MF (2001) Int J Quantum Chem 84:559

CHAPTER 3

THE DISCRETE REACTION FIELD APPROACH FOR CALCULATING SOLVENT EFFECTS

PIET TH. VAN DUIJNEN[1], MARCEL SWART[2], AND LASSE JENSEN[3]

[1]*Zernike Institute for Advanced Materials, Rijksuniversiteit Groningen, Nijenborgh 4, 9747 AG, Groningen, The Netherlands, e-mail: p.t.van.duijnen@rug.nl*

[2]*Institució Catalana de Recerca i Estudis Avançats (ICREA), 08010 Barcelona, Spain and Institut de Química Computacional, Universitat de Girona, Campus Montilivi, 17071 Girona, Spain, e-mail: marcel.swart@udg.edu*

[3]*Department of Chemistry, The Pennsylvania State University, University Park, PA 16802, USA, e-mail: jensen@chem.psu.edu*

Abstract: We present here the discrete reaction field (DRF) approach, which is an accurate and efficient model for studying solvent effects on spectra, chemical reactions, solute properties, etc. The DRF approach uses a polarizable force field, which is (apart from the short-range repulsion) based entirely on second-order perturbation theory, and therefore ensures the correct analytical form of model potentials. The individual interaction components are modeled independently from each other, in a rigorous and straightforward way. The required force field parameters result as much as possible from quantum-chemical calculations and on monomer properties, thereby avoiding undesired fitting of these parameters to empirical data.

Because the physical description is correct and consistent, the method allows for arbitrary division of a system into different subsystems, which may be described either on the quantum-mechanical (QM) or the molecular mechanics (MM) level, without significant loss of accuracy. This allows for performing fully MM molecular simulations (Monte Carlo, molecular dynamics), which can subsequently be followed by performing QM/MM calculations on a selected number of representative snapshots from these simulations. These QM/MM calculations then give directly the solvent effects on emission or absorption spectra, molecular properties, organic reactions, etc

3.1. INTRODUCTION

Ballhausen said once, starting his lecture on the Jahn–Teller effect: 'The Jahn–Teller effect does not exist' [1]. J–T, relativistic and quantum effects exist by the grace of incomplete descriptions of systems under study. In contrast, solvent effects are real and part of everyday life of the majority of chemists.

Hence accounting for solvent effects in computational chemistry—or in general, the modeling of molecular properties in the condensed phase—is of paramount

S. Canuto (ed.), Solvation Effects on Molecules and Biomolecules, 39–102.
DOI 10.1007/978-1-4020-8270-2_3,

importance because chemistry overwhelmingly takes place in solution, and molecular properties differ in that environment often considerably in comparison with the gas phase. From a computational chemical point of view, the focus will be on a single molecule (or a molecular system) while the solvent effects are treated as perturbations of the molecular system. The latter (the solute) is then treated with some quantum-mechanical (QM) method while the rest is treated by a much simpler, usually classical, method [2,3,4,5,6,7,8,9,10,11,12,13,14,15,16,17,18].

The classical descriptions can in general be divided into two groups depending on the detail in which the solvent is considered. The first group consists of the continuum models [7,9,14,15] in which the solvent is treated as a continuous medium characterized only by its dielectric constant. Because of their efficiency in terms of computer demands, these methods still dominate the field of computing solvent effects. However, the microscopic structure of the solvent and specific interactions are here completely neglected and therefore provide a poor description of short-range interactions. Moreover, the size and the shape of the cavity in which the solute is embedded affect the results [19]. An ab initio approach for choosing the solvent radius (taking it from the macroscopic density and molecular mass of the solvent) [20] has been suggested recently to avoid ambiguities with empirically adapted solvent radii. However, since the boundary is in principle arbitrary the charge distribution of the solute in all practical cases will extend into the continuum. In particular Chipman [21] but also Mennucci [22] and Cossi [23] discuss this charge penetration and describe methods to account for it. These improvements will make the straight continuum approaches less dependent on the actual size and shape of the cavity. Nevertheless some formal problems will remain. (See Figure 3-1) First, a dielectric continuum can only stabilize a charge distribution and the more so the closer the charges are to the cavity boundary (or it does nothing: for an infinite large cavity, or for $\varepsilon = 1$). This means that the interactions of the electrons of a solute will be larger than that of the nuclei because the former are on average closer to that boundary. The electronic charge distribution will therefore be inflated with respect to the gas phase situation, an effect that is not without consequences [24]. Next, in general the continuum is

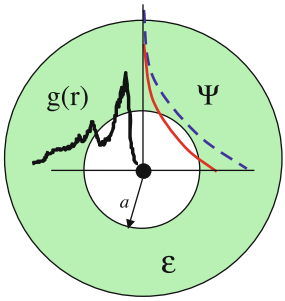

Figure 3-1. Schematic representation of atom in dielectric continuum. Ψ: wave function in vacuo (*solid line*) and solvated (*dashed line*); ε: dielectric constant ; a: cavity radius; $g(r)$: radial distribution of solvent molecules

assumed homogeneous, which should force the cavity to go beyond the second maximum of $g(r)$. Finally, the dielectric constant is a macroscopic property connected with the polarization of the solvent, i.e., with the time- and space-averaged (induced) dipoles. The solute–solvent interaction then will be of type $<\rho_{\text{solute}}> \Leftrightarrow <M_{\text{solvent}}>$, i.e., the average charge density (ρ) interacts with the averaged dipoles (M) of the environment, while in actual experiments results are obtained as (averaged) instantaneous interactions, i.e., of type $<\rho_{\text{solute}} \Leftrightarrow M_{\text{solvent}}>$ which are in general different from the former.

An extension of the continuum model is the inclusion of explicit solvent molecules in the cavity—treated fully quantum-mechanically together with the solute—in order to get a better grip on specific interactions like hydrogen bonding. The best approach to this is to take two or three solvation shells. Of course, some statistical mechanics procedure is needed in order to obtain a reasonable solvent distribution $g(r)$, and that puts this approach into the field of mixed quantum-classical mechanical (QM/MM) models. An early application of this model [25] revealed that only the interaction between the solute and the continuum survives statistically. By adding sufficient solvent shells and increasing the cavity size accordingly, this interaction can be made arbitrarily small, thus making the presence of the continuum superfluous [24,26].

To the second group belong the discrete solvent models in which one or more solvent molecules are treated explicitly. Among these are the supermolecular model [27], the frozen density functional approach [28], ab initio molecular dynamics (AIMD) [29] and the combined quantum and molecular mechanics (QM/MM) models [2,3,4,5,6,8,10,13,18,30,31,32]. In both the supermolecular and the AIMD models all molecules are treated on the same level of theory. This can give highly accurate descriptions of the solute–solvent interactions but due to the computational demands it becomes rapidly impractical so that either only a few of the (small) solvent molecules can be included or the actual level—QM method, basis sets—has to be reduced. Moreover, the definition of the molecular properties requires an arbitrary partitioning of the wave function or the density among the molecules, much in the same way as is necessary for defining atomic charges. Due to this arbitrariness molecular properties cannot be defined for individual molecules [33,34,35] and will depend on the particular partitioning employed. This is for instance shown in an AIMD study of ice I_h [33], where it was found that the average dipole moment ranges from 2.3 to 3.1 D.

In the QM/MM method the system is usually a priori divided into QM (the solute) and classical (MM, the solvent) parts, and an effective operator describes the interaction between the two subsystems. The solvent molecules are treated with a 'classical' force field ('classical' meaning that there are no elementary particles or quantum 'effects') that opens the possibility to take a much larger number of solvent molecules into account. Optionally, the whole system can be embedded in a continuum, e.g., for taking large-range interactions into account. Similar to the continuum approach, the solute is separated from the solvent and its molecular properties are therefore well defined. The remaining problem is to find an accurate approximate representation of

the solvent molecules, the solute–solvent and the solvent–solvent interactions [36]. The discrete representation of the solvent molecules requires sampling of the degrees of freedom of the solvent. This is typically done using Monte Carlo (MC) or molecular dynamics (MD) techniques to generate a large number of possible solvent configurations. This leads to many QM/MM calculations for the solute's properties which must be averaged or represented in another way. Hence the QM/MM method is often employed at a semi-empirical level of the QM theory.

The force fields used in the QM/MM methods are typically adopted from fully classical force fields. While this is in general suitable for the solvent–solvent interactions it is not clear how to model, e.g., the van der Waals interaction between the solute and the solvent. The van der Waals interactions are typically treated as Lennard-Jones (LJ) potentials with parameters for the quantum atoms taken from the classical force field or optimized for the particular QM/MM method for some molecular complexes. However, it is not certain that optimizing the (dispersion and short-range repulsion) parameters on small complexes will improve the results in a QM/MM simulation of liquids [37].

Classical force fields that take polarization into account explicitly, the so-called polarizable force fields [2,3,11,31,32,38,39,40,41,42,43,44,45,46,47,48,49,50,51, 52,53], were originally not popular. The arguments against using them are mostly based on 'efficiency' in terms of computing times. Energy contributions of about 10% to the interaction of (up to) trimers [40,41] were considered of no consequence: instead, polarization in simulations of, e.g., liquid water was taken care of by increasing the monomer dipole moment from the experimental gas phase value of 1.86 D to its condensed phase value of about 2.7 D [40]. Refining this in order to get better agreement with details of the radial distribution led, e.g., to the TIP4P model [54]. Recently the trend is to use (ab initio) QM calculations as a guide, instead of fitting force field parameters (of total energy expressions) to experimental results.

Nowadays, the interest in polarizable force fields has regained ground, both for purely classical and QM/MM simulations. It was shown that it is important to consider also the polarization of the solvent molecules [40,55,56]. Since the inclusion of the solvent polarization leads naturally to an increase in computational time, most studies still ignore this contribution and use the more simple 'effective' pair potentials. If the solvent polarization is included it is usually treated using either an isotropic molecular polarizability [11,39,52] or using distributed atomic polarizabilities [31,32,46,49,53] according to the Applequist scheme [57,58,59]. However, at short distances the Applequist scheme leads to the so-called 'polarization catastrophe' due to the use of a classical description in the bonding regions. Thole [59] avoided this problem by introducing smeared out dipoles, which mimic the overlapping of charge distributions at short distances. Thole's model, which will be discussed in detail later, has been shown to be quite successful in reproducing molecular polarizability tensors using model atomic polarizability parameters independent of the chemical environment of the atoms [59,60]. Karlström et al. [18,36] have a different approach in which solute–solvent and solvent–solvent interactions—including

polarization, dispersion and short-range repulsion—are modeled based on specific QM calculations by keeping a large amount of 'orbital' information.

Recently, we have seen a renewed interest in the development and application of polarizable force fields [61,62,63,64,65,66]. Although these studies are all concerned with a proper description of polarization effects in chemical systems, the philosophy behind the approaches is sometimes substantially different from Thole's. In the paper by Mooij et al. [61], the separate energy terms have a well-defined physical meaning, which enhances transferability to other molecules. Moreover, the parameters were obtained from ab initio calculations on the level of Møller–Plesset second-order perturbation theory (MP2) [67] using large basis sets and corrected for the basis set superposition error (BSSE). In contrast Kaminski et al. [62] fitted atomic polarizabilities either to the change in electrostatic potential (ESP) at a set of grid points outside the van der Waals surface of the molecule or to three-body energies of five small molecules [64]. The use of fitting on a grid, in their first study, makes the polarizabilities depend on the choice of the grid, a similar problem met with ESP charges [48,68,69,70]. In their second paper [64] it is unclear which method has been used to obtain the 'three-body' energies and whether the results have been corrected for BSSE. More importantly, their 'three-body' energies are obtained from intramolecular polarization only, while three-body energies usually concern intermolecular interactions [71], and the polarizabilities will be used to describe intermolecular interactions. One of the main objections to studies such as those by Kaminski et al. [62,64] is that the polarizability enters as a fitting parameter, thereby ignoring the fact that the polarizability is an intrinsic property of an atom or molecule. This is in contrast to the two other papers [61,63], as well as previous work in our group [59].

Without any doubt the most advanced force field is the water potential of Bukowski et al. [72] containing pairwise and many-body interactions and describing the interactions with an accuracy < 0.07 kcal/mol and predicting the properties of the water dimer and of liquid water in excellent agreement with experiments. But it requires 2510 grid points and clusters of up to 32 monomers, CCSD(T) calculations in quadruple-zeta basis (QZ++) to fit all the parameters, and it is highly specific. This is obviously beyond practical use for the large (bio-)organic molecules we have in mind, and for that purpose it is more advantageous to use the transferable model potentials like the polarizable force field used in our group.

In general, the interaction between two systems, having a geometry symbolically represented by **R,** is written as

$$\begin{aligned}\Delta U_{QS}^{\text{int}}(\mathbf{R}) = U_{QS}(\mathbf{R}) - (U_Q^0 + U_S^0) = \Delta U_{QS}^{\text{elst}}(\mathbf{R}) + \Delta U_{QS}^{\text{pol}}(\mathbf{R}) \\ + \Delta U_{QS}^{\text{disp}}(\mathbf{R}) + \Delta U_{QS}^{\text{rep}}(\mathbf{R})\end{aligned} \tag{3-1}$$

with U_{QS} the total energy of the QS system, U_X^0 the ground state energy of system X, $\Delta U_{QS}^{\text{elst}}$, $\Delta U_{QS}^{\text{pol}}$, $\Delta U_{QS}^{\text{disp}}$ and $\Delta U_{QS}^{\text{rep}}$, respectively the electrostatic, polarization, dispersion and (short-range) repulsion energies between two subsystems Q and S.

For multi-molecular assemblies one has to consider whether the total interaction energy can be written as the sum of pairwise interactions. The first-order electrostatic interaction is exactly pairwise additive, the dispersion only up to second order (in third order a generally small three-body Axilrod–Teller term appears [73]) while the induction is not at all pairwise: it is non-linearly additive due to the interference of electric fields from different sources. Moreover, for polar systems the inducing fields are strong enough to change the molecular wave functions significantly.

Fitting of model potentials to supermolecular interactions like in Eq. (3-1) has its disadvantages: the calculations have to be repeated many times and a predefined analytical expression of the model potentials in terms of atomic parameters is required. These parameters are not easily transferred to other situations. The internal state of, e.g., system A depends on the presence of another system *X*, and this will be different near system *Y*. Furthermore, the chosen analytical form of the potential may give rise to problems and errors. For example, Hartree–Fock (HF) calculations fitted to a power series in $1/r$ suggest that the $1/r^6$ terms have to do with dispersion, which is not part of the HF energy. Finally, such empirical potentials are best for describing situations close to those to which the parameters are fitted. Whenever the situation is very different from that, the results will be doubtful.

Our QM/MM model—the discrete (or direct) reaction field (DRF) model—treats the various terms in Eq. (3-1) separately and on the basis of their own intrinsic physical meaning [3,10,31,32,38,59,74]. Historically, DRF was developed to study biochemical problems, in particular for unraveling the reaction mechanism of papain. For that we went stepwise from a model active site [75] to a model active site plus a point charge representation of an α-helix [76,77,78], then to a model with a polarizable helix [78,79], and finally to an all-atom treatment of the enzyme [41]. Furthermore, we extended these studies with an exercise—with the continuum version—to show that a solvent-exposed residue has no effect on the reaction mechanism [80]. Up to then we considered the protein as a peculiar solvent; the 'real' solvents, requiring extensive MC or MD simulations, came later.

In most cases we apply now the method—coined by Coutinho and Canuto [81,82] as *sequential* MC (SMC) or *sequential* MD (SMD)—in which an all-classical simulation is performed from which, after equilibration, a relative small number of snapshots of uncorrelated solute–solvent configurations are collected. In Ref. [81] these authors show that a relatively small number of configurations—small with respect to the total number generated in the simulation—contains all statistically relevant information. Then from QM or QM/MM calculations on the snapshots the (electronic) molecular properties in solution are obtained by averaging, or otherwise collected. In the original paper the saved solute–solvent configurations were subjected to an all-QM calculation. We apply this technique generally with only the solute as QM part for reasons already mentioned above.

The total Hamiltonian in QM/MM is as usual written as

$$\hat{H}(\mathbf{r}_q) = \hat{H}^0(\mathbf{r}_q) + \hat{H}_{QM/MM}(\mathbf{r}_q, \mathbf{r}_s) + \hat{H}_{MM}(\mathbf{r}_s) \tag{3-2}$$

with $\hat{H}^0(\mathbf{r}_q)$ the vacuum Hamiltonian of the QM part, $\hat{H}_{MM}(\mathbf{r}_s)$ the Hamiltonian of the MM part and $\hat{H}_{QM/MM}(\mathbf{r}_q, \mathbf{r}_s)$ the operator describing the interaction between the QM and MM particles. We note that the last two operators contain electrostatic, many-body polarization, short-range repulsion and dispersion terms. Electrostatic potentials are modeled with point charges on atoms (or, if necessary, on additional points, obtained from QM calculations), while polarization and dispersion are described in terms of (model) atomic polarizabilities resulting from calculations or experiment. We want the parameters in the model Hamiltonians to be transferable, and requiring no fitting to energies, structures or thermodynamical properties of the system under study. The parameters of DRF are therefore based on properties of monomers or, if monomers are too large, of model subsystems, and on second-order perturbation theory. The only term so far not coming from perturbation theory is the short-range repulsion, which we have borrowed from other force fields.

The QM/MM version of DRF has been implemented in HONDO [83], ZINDO [84], GAMESS [85] and ADF [86] while DRF90 [87] is our classical statistical mechanics package.

In Section 2 we give the theoretical background and implementation of DRF and in Section 3 some examples to validate the model. Section 4 is dedicated to applications where we address a wide variety of solvent effects.

3.2. THEORY

3.2.1. Perturbation Theory

In a quantum-chemical description of the two subsystems Q and S of the preceding section the total wave function—in the long-range approximation—can be written as

$$\Psi_{QS}(\mathbf{r}_q, \mathbf{r}_s) = \Psi_Q(\mathbf{r}_q) \otimes \Psi_S(\mathbf{r}_s) \tag{3-3}$$

where Ψ_X is the wave function and $\mathbf{r}_X$ the coordinates of particles of system X. Since the short-range repulsion ($\Delta U^{\text{rep}}_{QS}$, cf. Eq. 3-1) in this approximation vanishes, and the total energy of the system is obtained as

$$U_{Q+S} = \left\langle \Psi_Q \Psi_S \right| \hat{H}^0_Q + \hat{H}^0_S + \hat{V}_{QS} \left| \Psi_Q \Psi_S \right\rangle \tag{3-4}$$

where $\hat{H}^0_Q(\mathbf{r}_q)$ and $\hat{H}^0_S(\mathbf{r}_s)$ are the Hamiltonians of the isolated systems and

$$\hat{V}_{QS} = \sum_{\substack{q \in Q \\ s \in S}} \frac{z_q z_s}{|\mathbf{r}_q - \mathbf{r}_s|}. \tag{3-5}$$

the interaction operator, with $\{z\}$ the charges (electrons, nuclei) in the system. Because the overlap is negligible, the integrations involved in Eq. (3-4) can be evaluated locally, e.g.,

$$\Delta U_{\text{int}} = \left\langle \Psi_Q(\mathbf{r}_q) \left| \sum_{q\in Q} z_q \, \langle \Psi_S(\mathbf{r}_s)| \sum_{s\in S} \frac{z_s}{|\mathbf{r}_q - \mathbf{r}_s|} \, |\Psi_S(\mathbf{r}_s)\rangle_S \right| \Psi_Q(\mathbf{r}_q) \right\rangle_Q$$
$$= \left\langle \Psi_Q(\mathbf{r}_q) \left| \sum_{q\in Q} z_q \hat{V}_S(\mathbf{r}_q) \right| \Psi_Q(\mathbf{r}_q) \right\rangle_Q \tag{3-6}$$

so that the problem of Eq. (3-4) is partitioned into smaller ones, for which the equations can be written as

$$U_{QS} = \left\langle \Psi_Q(\mathbf{r}_q) \left| \hat{H}^0_Q(\mathbf{r}_q) + \hat{V}^0_S(\mathbf{r}_q) \right| \Psi_Q(\mathbf{r}_q) \right\rangle = U^0_Q + \Delta U_{\text{int}} \tag{3-7}$$

which is equivalent to solving a Schrödinger equation for system Q in an external potential. The result, Ψ_Q, can obviously be used to define an *effective* potential on S,

$$\hat{V}_Q(r_s) = \left\langle \Psi_Q(\mathbf{r}_q) \right| \sum_{s\in S} \frac{z_q}{|\mathbf{r}_q - \mathbf{r}_s|} \left| \Psi_Q(\mathbf{r}_q) \right\rangle_Q \tag{3-8}$$

leading to a new $\Psi'_S(\mathbf{r}_s)$, etc., a process that can be repeated until self-consistency. This is a simplified sketch of the group function approach originally described by McWeeny [88] and reformulated for non-orthogonal groups by Mehler [89,90,91].

It is better to analyze the interaction energy by means of perturbation theory (PT) [92,93,94,95,96] not only because ΔU_{int} is in general much smaller than the intramolecular U^0_X, but mainly because PT sets the correct analytical form of possible model potentials. Up to second order we have

$$\Delta U^{(1)}_{\text{int}} = \left\langle \Psi^0_Q \Psi^0_S \left| V_{QS} \right| \Psi^0_Q \Psi^0_S \right\rangle \tag{3-9}$$

$$\Delta U^{(2)}_{\text{ind}} = \sum_{k\neq 0} \frac{\left| \left\langle \Psi^0_Q \Psi^0_S \right| V_{QS} \left| \Psi^k_Q \Psi^0_S \right\rangle \right|^2}{U^0_Q - U^k_Q} + \sum_{l\neq 0} \frac{\left| \left\langle \Psi^0_Q \Psi^0_S \right| V_{QS} \left| \Psi^0_Q \Psi^l_S \right\rangle \right|^2}{U^0_S - U^l_S} \tag{3-10}$$

$$\Delta U^{(2)}_{\text{disp}} = \sum_{k,l\neq 0} \frac{\left| \left\langle \Psi^0_Q \Psi^0_S \right| V_{QS} \left| \Psi^k_Q \Psi^l_S \right\rangle \right|^2}{U^0_Q - U^k_Q + U^0_S - U^l_S} \tag{3-11}$$

where U^n_X is the nth excited state of system X. Introducing the multipole expansion about a center $\mathbf{x}$ of the Coulomb potential of X at $\mathbf{y}$:

$$\frac{1}{|\mathbf{r}_y - \mathbf{r}_x|} = \sum_n \left(\frac{1}{n!} \right) T^{(n)}_{yx,\eta_1,\eta_2,\ldots,\eta_n} \tag{3-12}$$

with $T^{(n)}_{xy,\eta_1,\eta_{2,\ldots},\eta_n} = \nabla_{xy,\eta_1} \ldots \nabla_{yx,\eta_n} \left(1/R_{xy}\right)$

$$\begin{aligned} T^{(0)}_{yX} &= \frac{1}{|\mathbf{r}_y - \mathbf{x}|} \;;\; T^{(1)}_{\mathrm{yX},\eta} = -\frac{\left(r_y - x\right)_\eta}{|\mathbf{r}_y - \mathbf{x}|^3} \;; \\ T^{(2)}_{yX,\eta\vartheta} &= \frac{3\left(r_y - x\right)_\eta \left(r_y - x\right)_\vartheta}{|\mathbf{r}_y - \mathbf{x}|^5} - \frac{\delta_{\eta\vartheta}}{|\mathbf{r}_y - \mathbf{x}|^3} \end{aligned} \tag{3-13}$$

Inserting the expansion in the second term in Eq. (3-10) leads to

$$\begin{aligned} &\sum_{l\neq 0} \frac{\left|\left\langle \Psi^0_Q \Psi^0_S | V_{QS} | \Psi^0_Q \Psi^l_S \right\rangle\right|^2}{U^0_S - U^l_S} = \sum_{l\neq 0} \frac{\left|\left\langle \Psi^0_Q \Psi^0_S | \mathbf{T}^{(1)}_{sQ}(\mathbf{r}_q - \mathbf{q}) | \Psi^0_Q \Psi^l_S \right\rangle\right|^2}{U^0_S - U^l_S} \\ &= \left|\left\langle \Psi^0_Q \left| \left(\frac{(\mathbf{r}_q - \mathbf{s})}{|\mathbf{r}_q - \mathbf{s}|^3} \right) \right| \Psi^0_Q \right\rangle\right|^2 \sum_{l\neq 0} \frac{\left|\left\langle \Psi^0_S | (\mathbf{r}_q - \mathbf{q}) | \Psi^l \right\rangle\right|^2}{U^0_S - U^l_S} \\ &= -\frac{1}{2} \left\langle \mathbf{e}_Q(\mathbf{s}) \right\rangle^2 \boldsymbol{\alpha}_S \end{aligned} \tag{3-14}$$

and, hence,

$$\Delta U^{(2)}_{ind} = -\frac{1}{2} \left\langle \mathbf{e}_S(\mathbf{q}) \right\rangle^2 \boldsymbol{\alpha}_Q(\mathbf{q}) - \frac{1}{2} \left\langle \mathbf{e}_Q(\mathbf{s}) \right\rangle^2 \boldsymbol{\alpha}_s(\mathbf{s}) \tag{3-15}$$

where $\mathbf{e}_X(\mathbf{y})$ is the electric field at $\mathbf{y}$ due to the charge distribution of system X, and $\alpha_X(\mathbf{x})$ the polarizability of X centered at $\mathbf{x}$.

The dispersion interaction arises from fluctuations in the charge distribution of Q, leading to transient induction in S and vice versa. By applying the multipole expansion in the dipole approximation in both Q and S, $\Delta U^{(2)}_{disp}$ is reduced to

$$\begin{aligned} \Delta U^{(2)}_{disp} &= \sum_{k,l\neq 0} \frac{\left|\left\langle \Psi^0_Q \Psi^0_S | \mathbf{T}^{(2)}_{sS} \mathbf{T}^{(2)}_{qQ}(\mathbf{r}_s - \mathbf{s})(\mathbf{r}_q - \mathbf{q}) | \Psi^k_Q \Psi^l_S \right\rangle\right|^2}{U^0_Q - U^k_Q + U^0_S - U^l_S} \\ &= \frac{1}{|\mathbf{s} - \mathbf{q}|^6} \left\{ \frac{3\left(\mathbf{s} - \mathbf{q}\right)\left(\mathbf{s} - \mathbf{q}\right)}{|\mathbf{s} - \mathbf{q}|^2} + \mathbf{I} \right\} \\ &\quad \times \sum_{k,l\neq 0} \frac{\left|\left\langle \Psi^0_Q | (\mathbf{r}_q - \mathbf{q}) | \Psi^k_Q \right\rangle\right|^2 \left|\left\langle \Psi^0_S | (\mathbf{r}_s - \mathbf{s}) | \Psi^l_S \right\rangle\right|^2}{U^0_Q - U^k_Q + U^0_S - U^l_S} \end{aligned} \tag{3-16}$$

Due to the excitation energies of both S and Q in the denominator the local integrations do not lead directly to monomer factors, but by invoking the Unsöld approximation [97] it is possible to split the denominator into a product:

$$\frac{1}{U_Q^0 - U_Q^k + U_S^0 - U_S^l} = \left(\frac{\Delta_S \Delta_Q}{\Delta_S + \Delta_Q}\right) \times \left[\frac{-1}{\left(U_Q^0 - U_Q^k\right)\left(U_S^0 - U_S^l\right)}\right]\{1 + \Delta_{kl}\} \tag{3-17}$$

where Δ_S and Δ_Q are chosen so as to minimize the error Δ_{kl}. The expression for the dispersion can hence again be expressed in terms of the polarizabilities of Q and S, leading to the well-known London approximation [98]:

$$\Delta U_{disp}^{(2)} \approx \frac{1}{|\mathbf{s} - \mathbf{q}|^6} \times \left(\frac{\Delta_S \Delta_Q}{\Delta_S + \Delta_Q}\right) \times \frac{1}{2}\boldsymbol{\alpha}_Q \left\{\frac{3\,(\mathbf{s} - \mathbf{q})\,(\mathbf{s} - \mathbf{q})}{|\mathbf{s} - \mathbf{q}|^2} + \mathbf{I}\right\} \frac{1}{2}\boldsymbol{\alpha}_S \tag{3-18}$$

where $\mathbf{I}$ is the 3×3 unit matrix. Another way to write the dispersion energy is the Casimir–Polder integral [99]

$$\Delta U_{disp}^{(2)} = T_{sq,\eta\tau} T_{sq,\xi\theta} \lim_{x \to \infty} \int \alpha_{Q,\eta\xi}(\mathrm{i}u)\alpha_{S,\tau\theta}(\mathrm{i}u)\mathrm{d}u + \text{higher order terms} \tag{3-19}$$

where $\alpha(\mathrm{i}u)$ is the frequency-dependent dipole polarizability at imaginary frequency $\omega = \mathrm{i}u$. By inserting $\alpha(\omega) \approx \frac{n_v(0)}{n_v - \omega^2}$, where n_v the number of valence electrons, in Eq. (3-19) and averaging rotationally, the Slater–Kirkwood approximation [96] is obtained:

$$\Delta U_{disp}^{Slater-Kirkwood} = -\frac{3}{2}\frac{1}{|\mathbf{s} - \mathbf{q}|^6}\frac{\alpha_S \alpha_Q}{\sqrt{(\alpha_S / n_{S,v})} + \sqrt{(\alpha_Q / n_{Q,v})}} \tag{3-20}$$

A semi-classical estimate is obtained by dropping the excitation energy of one of the systems in the denominator in Eq. (3-11), assuming instantaneous instead of frequency-dependent interaction. Then, by means of the closure relation, it is easy to show that in the dipole approximation Eq. (3-11) transforms into [3,38]

$$\Delta U_{disp}^{sc} = -\frac{1}{2}\left\{\mathbf{e_Q}\boldsymbol{\alpha}_S\mathbf{e}_Q \rangle - \langle \mathbf{e}_Q\rangle \boldsymbol{\alpha}_S \langle \mathbf{e}_Q\rangle\right\} \tag{3-21}$$

which has indeed the form of a variation.

At distances between S and Q where the charge distributions overlap the analysis of the interaction energy becomes much more complicated [27,95,100] because the total wave function must obey the Pauli principle:

$$\Psi^0_{QS} = \hat{A}^{as}_{QS}\Psi^0_Q \otimes \Psi^0_S \tag{3-22}$$

with $\hat{A}^{as}_{QS}$ the antisymmetrizing operator, generating a form of $\Delta U^{(2)}_{disp}$ that cannot be separated into fragment wave functions. Starting, e.g., from a Hartree–Fock calculation to get the total energy of the superimposed fragments, corrected for basis set superposition errors (BSSE) [101,102], the first physically meaningful interaction energy can be defined only after satisfying the Pauli principle. This is achieved by orthogonalizing the fragment wave functions, which contributes ΔU^{HF}_{orth} to the interaction energy that can therefore best be written as

$$\Delta U_{\text{int}} = U^{HF}_{Q+S} - \left(U^{HF}_Q + U^{HF}_Q\right) + \Delta U_{orth} \approx \Delta U^{(1)}_{\text{int}} + \Delta U_{rep} + \Delta U_{response} \tag{3-23}$$

Alternatively, one can calculate energies of overlapping charge distributions with symmetry-adapted perturbation theory (SAPT) [95,100], the intermolecular Møller–Plesset (I-MP) perturbation theory [27] or apply schemes as defined by Karlström et al. [36]. However, these procedures require many calculations on specific molecular aggregates which are for systems we have in mind—large (bio)molecules in various solvents—impractical. Because of this the short-range repulsion, which is formally part of $\hat{V}^{\text{response}}_S$, is modeled with ad hoc potentials which in general do not affect the electrons. Hence the QM/MM part of our approach is finding a self-consistent solution for

$$U_{Q+S} = \left\langle \Psi_Q(\mathbf{r}_q) \left| \hat{H}^0_Q(\mathbf{r}_q) + \hat{V}_S(\mathbf{r}_q) \right| \Psi_Q(\mathbf{r}_q) \right\rangle = U^0_Q + \Delta U_{\text{int}} \tag{3-24}$$

with

$$\ddot{V}_S(r_q) = \sum_{\substack{q\in Q \\ s\in S}} \frac{z_s}{|\mathbf{r}_q - \mathbf{r}_s|} + \ddot{V}^{response}_S(\boldsymbol{\alpha}_S, \mathbf{r}_q) \tag{3-25}$$

in which $\ddot{V}^{\text{response}}_S$ contains the many-body polarization and dispersion contributions to the interaction energy. Provided one has a good model for the charge distribution and the polarizability of S, $\ddot{V}^{\text{response}}_S$ can be constructed and used directly for the MM part of the system, while in the QM/MM problem it has to be expressed in terms useful in QM calculations. In the following sections we discuss the modeling of electrostatic potentials and the many-body polarization.

3.2.2. Electrostatic Potentials: The Point Charges

Electrostatic potentials and fields of classical molecules are generated by a collection of point charges—generally on atoms—obtained from QM calculations and defined such that they at least reproduce the vacuum dipole moment [103], or also the quadrupole moment [69], i.e., the first- and second-order sources of the electric field

of neutral molecules. The methods referred to are internal in the sense that no fitting to calculated potentials or fields is necessary. The first one is just an extension of the Mulliken population analysis [104], in which the overlap and dipole integrals are contracted with the density matrix (**D**) to give Mulliken atomic charges and dipoles:

$$q_A^{Mul} = Z_A - \left\{ \sum_{i,j \text{ on } A} D_{ij} \langle \chi_i | \chi_j > + \frac{1}{2} \sum_{\substack{i \text{ on } A \\ j \text{ on } B \neq A}} D_{ij} \langle \chi_i | \chi_j > \right\}$$

$$\mu_A^{Mul} = Z_A \mathbf{r}_A - \left\{ \sum_{i,j \text{ on } A} D_{ij} \langle \chi_i | \mathbf{r} | \chi_j > + \frac{1}{2} \sum_{\substack{i \text{ on } A \\ j \text{ on } B \neq A}} D_{ij} \langle \chi_i | \mathbf{r} | \chi_j > \right\} \tag{3-26}$$

with $\{\chi\}$ the basis functions in which the wave function and operators are expanded, and Z_A the atomic number of A. The next step is to redefine the atomic charges such that the total charge (Q) and the dipole moment of the molecule ($\boldsymbol{\mu}_{\text{mol}}$) are preserved:

$$\sum_A q_A = Q_{mol}; \sum_A q_A \mathbf{r}_A = \mu_{mol} \tag{3-27}$$

We note that ($\boldsymbol{\mu}_A^{Mul} - q_A^{Mul} \mathbf{r}_A$) in Eq. (3-27) is the induced (Mulliken) dipole on atom A which is 'charge free' and hence can be moved or reconstructed in any way one wishes. Additional expansion centers may be defined if required, e.g., by symmetry. Equations (3-27) can be satisfied in many ways. We choose to take the smallest possible charges, placed on the nearest atoms, compatible with Eq. (3-27). This can be achieved by minimizing

$$\sum_A q_A^2 / 2 w_A \tag{3-28}$$

with w_A a weighting function that decreases more or less rapidly with the distance relative to the position of A. Thole and van Duijnen [103] took Gaussians with interatomic distances as parameter for defining the weights. Swart et al. [70] applied the same technique—implemented so far only in the Amsterdam density functional theory (ADF) package [86]—for representing the atomic multipoles up to the quadrupole moment. These moments result directly from the numerical integrations in ADF and they obviously add up to the molecular moments. These atomic moments are used also for generating the electric potential *inside* a molecule accurately and hence are even better for generating the *external* potential. For obtaining the redistributed charges that reproduce as well as possible the total charge (Q), dipole ($\mu_{i,A}^M$) and quadrupole ($\theta_{jk,A}^M$) moment components Swart et al. [70] minimize the function

$$g_A = \sum_s \frac{q_{s,A}^2}{2w_{s,A}} + \xi_A \left(q_A^M - q_A^{repr}\right) + \sum_i \tau_{i,A} \left(\mu_{i,A}^M - \mu_{i,A}^{repr}\right) + \sum_{j,k} \eta_{jk,A} \left(\theta_{jk,A}^M - \theta_{jk,A}^{repr}\right) \cdots \tag{3-29}$$

with ξ_A, $\tau_{i,A}$ and $\eta_{jk,A}$ Lagrange multipliers, $\{i,j,k \in x,y,z\}$ and $w_{s,A}$ the weight factor defined by

$$w_{s,A} = \exp\left(\frac{-\zeta\,(|\mathbf{r}_s - \mathbf{r}_A|)}{d_A}\right) \tag{3-30}$$

with d_A the distance between center A and its nearest neighbor, and ζ an exponential prefactor. The redistributed charges then are

$$q_{s,A} = w_{s,A}\left(\xi_A + \sum_i \tau_{i,A} r_{sA,i} + \sum_{j,k} \eta_{jk,A}\left\{\frac{3}{2} r_{sA,j} r_{sA,k} - \frac{1}{2}\delta_{jk} r_{sA}^2\right\} + \cdots\right) \tag{3-31}$$

For each site in the set there is a set of linear equations which are solved by a standard **Ax=b** routine. The prefactor ζ in Eq. (3-30) must in principle be large for the reproduced multipoles to be as local as possible, but if it is very large the weight function approaches a delta function, leading to the loss of freedom to distribute the charges over other atoms. The 'optimal' value was chosen such as to make the errors in the represented multipoles (due to machine precision and numerical accuracy) smaller than the accuracy required for the numerical integration of some typical cases (a set of amino acid residues). The best choice turned out to be 3.0. The resulting MDC-q charges is for a number of small molecules given in Table 3-1.

These internal procedures for obtaining point charges are preferred over, e.g., potential-derived charges [105,106,107] since the latter require the definition of a grid of points where the quantum-chemical potential is fitted to the static potential of the point charges. The drawbacks are manifold: strong dependence on the size and form of the grid, the fitting method, numerical instability, etc. Furthermore, there are uncertainties in assigning charges to buried atoms, because the atoms near the grid mainly determine the potential outside of the molecule. Finally, these methods are very CPU intensive because of the many times that the inverse distance ($1/r$) between grid points and charges has to be evaluated. In contrast, the internal methods described above are almost trivial in terms of CPU costs: they take slightly more than the usual Mulliken analysis and can be done 'on the fly', e.g., inside SCF iterations whenever needed.

3.2.3. The Many-Body Polarization

For a collection of (atomic) polarizabilities in an electric field, assuming linear response, the induced dipole moment at site s is

Table 3-1. MDC-q charges for some molecules

Molecule	Charges	Molecule	Charges
Benzene		Hexafluorobenzene	
q_C	−0.123	q_C	0.094
q_H	0.123	q_F	−0.094
Ethylene		Ammonia	
q_C	−0.250	q_N	−0.444
q_H	0.125	q_H	0.148
Carbondioxide		Carbondisulfide	
q_C	0.574	q_C	−0.351
q_O	−0.287	q_S	0.185
Methylcyanide		Thiophene	
$q_{C\text{-}Me}$	0.692	q_S	0.051
q_H	−0.157	$q_{C'}$	−0.229
q_C	0.203	$q_{H'}$	0.206
q_N	−0.425	$q_{C''}$	−0.176
		$q_{H''}$	0.173

$$\mu_{s,i}^{ind} = \alpha_{s,ij}\left[e_{s,i}^{init} + \sum_{i,j} T_{st,ij}^{(2)}\mu_{t,j}^{ind}\right]; \quad i, j \in x, y, z \tag{3-32}$$

where $\alpha_{s,ij}$ is a component of the polarizability tensor at site s, which for an isotropic atom is $\alpha_{s,ij} = \delta_{ij}\alpha_s$. In Eq. (3-32) $\mathbf{e}^{\text{init}}$ is the initial field at site s and the last term is the field from the induced dipoles at the other sites. The self-consistent solution of Eq. (3-32) for all induced dipoles **M** can be written as a matrix equation:

$$\mathbf{M} = \mathbf{E}\,\mathbf{B} \tag{3-33}$$

where **B** is the relay matrix defined in supermatrix notation as

$$\mathbf{B} = \left[\mathbf{A}^{-1} - \mathbf{T}^{(2)}\right]^{-1} \tag{3-34}$$

in which $\mathbf{A}^{-1}$ is the block-diagonal matrix of the site-inverse polarizabilities, and $\mathbf{T}^{(2)}$ the off-diagonal interaction tensors, **M** the supervector of all induced dipoles in the system and **E** the vector of all initial local fields. Equation (3-33) can be solved by means of an exact inversion constructing **B** explicitly, or by iteration using $\mathbf{MB}^{-1} = \mathbf{E}$. We note that **B** in Eq. (3-33) behaves as a 'normal' (but many-center) polarizability. We note that the polarization energy is given by

$$\Delta U_{ind} = -1/2\left(\mathbf{E}^0\right)^T \mathbf{B}\mathbf{E}^o = -1/2\sum_i (\mathbf{e}_i^0)^T \boldsymbol{\mu}_i = -1/2\sum_i (\mathbf{e}_i^0)^T \boldsymbol{\alpha}_i \mathbf{e}_i \tag{3-35}$$

which, due to the self-consistency, is quadratic neither in the permanent fields $\mathbf{e}_i^0$nor in the total fields $\mathbf{e}_i$.

The matrix **B** can be reduced to smaller dimensions by summing over (groups of) atoms:

$$\alpha_{ij}^G = \sum_{p,q}^{N^G} (B_{pq})_{ij}\,; i, j \in \{x, y, z\} \tag{3-36}$$

resulting in a 3×3 *molecular* polarization if the summation comprises all the atoms in the group.

The polarizabilities parallel ($\alpha_{//}$) and perpendicular ($\alpha_{\perp}$) to the axis connecting two interacting atoms p and q—are given by Silberstein's equations [58] which are the exact solutions of Eq. (3-34):

$$\alpha_{//} = \frac{\alpha_p + \alpha_q + 4\alpha_p\alpha_q/r^3}{1 - 4\alpha_p\alpha_q/r^6}; \alpha_{\perp} = \frac{\alpha_p + \alpha_q - 2\alpha_p\alpha_q/r^3}{1 - \alpha_p\alpha_q/r^6} \tag{3-37}$$

Even for the case of isotropic polarizabilities, where $\alpha_p = \alpha_q = \bar{\alpha}$, it follows from Eq. (3-36) that the total polarizability will be anisotropic. If we want to define *effective* polarizabilities from Eq. (3-37) for the members, we must (arbitrarily!) distribute the interaction term. For $\alpha_p = \alpha_q$ equipartitioning could work, leading to local anisotropy with $\alpha_{//}$ (local)$>\bar{\alpha}$ and $\alpha_{\perp}$ (local)$<\bar{\alpha}$, but for $\alpha_p \neq \alpha_q$ no scheme is obvious.

One possibility is weighting the partitioning with the original polarizabilities [108]. This may work better in the general case, but it is just as arbitrary. What will happen to local (anisotropic) polarizabilities in the condensed phases is hard to estimate without calculations. Some typical model systems can be found in Ref. [24]. It is also demonstrated by the work of Augspurger and Dykstra [109] on acetylene clusters where for *linear* complexes an *increase* of the axial components of the linear and second hyperpolarizabilities are found, while van Duijnen et al. [110] for *parallel* clusters of butadienes and Kirtman et al. [111] for hexatrienes obtained a *decrease* in the same properties. These authors also show that well-constructed fully classical electrostatic models are able to reproduce these results.

Here we note that only a single polarizability or susceptibility exists for any system. The reconstruction from local contributions is in fact an abstraction, the result of which depends on the detail wanted: macroscopic with local susceptibilities or microscopic with local polarizabilities and—more importantly—on the partitioning of such properties. However, experimental chemists are used to such procedures: from well-chosen series of compounds they derive 'bond energies' as 'local' contributions to heats of formation and 'ionic radii' from crystal structures. Theoretical chemists obtain 'atomic charges' from, e.g., a Mulliken analysis of their wave functions. We are able, following similar reasoning, to construct molecular polarizabilities from atomic ones [38,60], although there is formally no connection between them. In an opposite direction we can 'decompose' a molecular polarizability into a many-center

matrix of effective local contributions, in which a one-to-one assignment of the interaction blocks to the corresponding diagonal 'local' blocks looks like the Mulliken scheme. A weighted assignment, e.g., with the traces of the diagonal blocks [108], will look like the Löwdin scheme for a population analysis. In this sense we can at least assess the local contributions to the system's polarizability, although only within an arbitrary but well-defined framework.

From Eq. (3-36) we learn that for r approaching $(4\alpha_p\alpha_q)^{1/6}$, $\alpha_{//}$ goes to infinity and becomes negative for smaller distances. In order to avoid this unphysical situation, Thole [59] introduced a damping scheme by rewriting the interaction tensor in terms of a reduced distance $u_{pq}=R_{pq}/(\alpha_p\alpha_q)^{1/6}$ as

$$T^{(2)}_{pq,ij} = (\alpha_p\alpha_q)^{1/2}\frac{\partial^2\phi(u_{pq})}{\partial u_{pq,i}\partial u_{pq,j}} \tag{3-38}$$

with $\Phi(u)$ the potential of a point charge at u.

The screened dipole interaction tensor (taking $\mathbf{r} = \mathbf{R}_{pq}$ for clarity) then becomes

$$T^{(2)}_{pq,ij} = \frac{3f_T r_i r_j}{r^5} - \frac{f_E r_i \delta_{ij}}{r^2} \tag{3-39}$$

with f_T and f_E damping functions depending on the particular form of ρ. Thole tried a number of forms for ρ, but in practice only an exponentially decaying charge distribution

$$\rho(u) = \frac{a^3}{8\pi}\exp(-au) \tag{3-40}$$

survived, with a the screening length. The following expressions define consistently the damped potential, field, field gradient and gradient-of-the-gradient of a point charge:

$$\begin{aligned}
v &= au \\
V &= f_V/r;\ f_V = 1 - \left(\frac{1}{2}v + 1\right)e^{-v} \\
E_i &= f_E r_i/r^3;\ f_E = f_V - \left(\frac{1}{2}v^2 + \frac{1}{2}v\right)e^{-v} \\
T_{ij} &= \frac{3r_i r_j f_T - \delta_{ij} r^2 f_E}{r^5};\ f_T = f_E - \frac{1}{6}v^3 e^{-v} \\
D_{ijk} &= \frac{3r^2(r_i\delta_{jk} + r_j\delta_{ik} + r_k\delta_{ij})f_T - 15 r_i r_j r_k f_D}{r^7}; \\
f_D &= f_T - \frac{1}{30}v^4 e^{-v}
\end{aligned} \tag{3-41}$$

With this method, Thole fitted isotropic model polarizabilities for H, C, N and O to 16 experimental molecular polarizabilities, using a single screening length and only one polarizability for each atom type, regardless of the chemical environment.

With the parameters thus obtained, the polarizabilities of six other molecules—not in the training set—containing these atoms were calculated within experimental accuracy. Van Duijnen and Swart [60] re-parameterized the same atomic polarizabilities using restricted Hartree–Fock (RHF)-optimized geometries, extended the training set to 52 molecules, the control set to 18 molecules and the set of atoms with sulfur and the halogens. Also computed molecular polarizabilities were parameterized for enabling comparison with fully quantum-chemical calculations.

The resulting atom polarizabilities fitted to experiment are summarized in Table 3-2 together with numerical Hartree–Fock results for the free atoms [112].

Comparing the fitted values with the HF results it appears that the former have more physical contents than one can expect from mere fitting parameters. The differences with the HF values are obviously related to the fact that the fitted values hold for atoms bound in molecules, which is conspicuous for H with its short bond lengths, and for C, which is in most compounds bonded to (up to four) other atoms. In Table 3-3 the polarizabilities of the control set (resulting from the fit to 52 experimental values) are listed.

In appraising the average accuracy one must bear in mind that experimentally the mean polarizabilities are usually obtained from the refractive index n (at 5893 Å, the sodium D-line) and the Lorenz–Lorentz equation (with M molecular weight, ρ macroscopic density, N_{av} Avogadro's number):

$$\frac{n^2-1}{n^2+2}\frac{M}{\rho} = \frac{4\pi}{3}N_{av}\bar{\alpha} \tag{3-42}$$

Table 3-2. Effective atomic polarizabilities (Bohr^3) from various fits

Atom	Fit to 16 molecules		Fit to 52 molecules[a]	
	Thole[b]	Geom. optimized[a]		Num. HF[c]
H	2.8815	3.0588	2.7927	4.52[d]
C	8.6716	8.7939	8.6959	11.7
N	6.5256	6.6704	6.5565	6.75
O	5.3042	5.6480	5.7494	4.93
F	–	–	3.0013	3.58
S	–	–	16.6984	23.2
Cl	–	–	16.1979	17.6
Br	–	–	23.5714	25.6
I	–	–	36.9880	42.6
a	2.089	1.9088	2.1304	–

Data from: [a]Ref. [60], [b]Ref. [59], [c]Ref. [112], [d]exact.

Table 3-3. Experimental and calculated polarizabilities for compounds *not* in the 52-membered training set of molecules[a]

Molecule		Exp	Calculated	Dev (%)
Cyclohexanol	$C_6H_{11}OH$	78.01	77.97	0.0
Dodecane	$C_{12}H_{26}$	153.86	157.76	2.4
Neopentane	$C(CH_3)_4$	68.83	65.49	4.8
Acetylene	C_2H_2	23.55	21.90	8.3
m-Dichlorobenzene	$C_6H_4Cl_2$	96.03	89.65	6.6
o-Dichlorobenzene	$C_6H_4Cl_2$	95.62	89.03	6.9
N, *N*-dimethylformamide	$HCON(CH_3)_2$	52.70	51.77	1.8
N-methylacetamide	$CH_3CONHCH_3$	52.77	51.95	1.8
Carbonylchloride	$COCl_2$	45.75	44.30	3.2
Chloromethylcyanide	CH_2ClCN	41.16	42.87	4.2
Isopropylcyanide	$(CH_3)_2CHCN$	54.32	54.54	0.4
Trichloromethylcanide	CCl_3CN	70.32	69.56	1.1
Dichloromethane	CH_2Cl_2	46.02	43.55	5.4
Difluoromethane	CH_2F_2	18.42	18.56	0.8
Tribromomethane	$CHBr_3$	79.90	75.99	3.8
Trichlorofluoromethane	$CFCl_3$	55.61	56.45	1.5
Triiodomethane	CHI_3	121.74	111.74	8.2
Nitrous oxide	N_2O	20.24	17.81	12.0
			Average	4.0

[a]Data from Ref. [60].

This equation is accurate in the gas phase but the refractive index should first be extrapolated to infinite wavelength (or zero frequency) to obtain the static polarizability:

$$n(\lambda) = n^*_\infty + \frac{a}{\lambda^2} + \frac{b}{\lambda^4} + \cdots \tag{3-43}$$

The polarizabilities decrease in this extrapolation by about 2–4% [113] which gives an estimate of the uncertainty in the experimental values. From Kerr constants [113] for small, symmetric molecules also the anisotropy and the frequency dependence can be determined, but the assumptions about the geometry add an uncertainty of 5–10%, giving a total uncertainty of 6–14%. Hence, an average deviation of 4% in Table 3-3 is considered to be within experimental error. From this table we also learn that the effective atomic polarizabilities work fine within Thole's model for predicting polarizabilities of virtually any system comprising these atoms. If no experimental data are available, one may predict molecular polarizabilities. In Table 3-4 polarizabilities of various molecules are collected as obtained from different computational approaches together with the experimental values. Calculation of polarizabilities is based on a Taylor expansion of the total energy (or the dipole moment) of a system in an external field:

Table 3-4. Some experimental and calculated molecular polarizabilities[a]

Molecule	α_{exp}	α_{DRF}	α_{CPHF}(TZP)	α_{DFT}(TZ2P++)
Acetamide	40.5	38.6	31.1	43.1
Acetylene	22.4	21.9	18.0	23.1
Benzene	70.1	61.9	61.9	72.6
Chlorine	31.1	31.2	18.7	31.7
Cyclohexane	80.0	78.0	69.2	82.7
Dimethylether	79.9	35.4	27.6	36.3
Formaldehyde	16.5	18.3	13.5	18.3
Hydrogen	5.33	4.90	2.62	5.76
Methylcyanide	29.7	29.8	24.6	31.1
Neopentane	69.0	655	59.0	1.3
Propane	42.4	42.2	35.9	44.1
TCFM	57.5	56.5	40.0	60.9
TCMC	70.5	68.3	54.0	75.2
TFM	19.0	19.0	13.1	18.9
Water	9.94	10.1	5.56	9.38
Deviation	–	±4.8%	±12%	±3%
Time	–	< 1 s	57 h	80 h

[a]Data from Ref. [60].

$$U = U^{(0)} - \mu_i^{(0)} e_i - \frac{1}{2!}\alpha_{ij} e_i e_j - \frac{1}{3!}\beta_{ijk} e_i e_j e_k - \frac{1}{4!}\gamma_{ijkl} e_i e_j e_k e_l$$

or

$$\mu_i = \mu_i^{(0)} e_i - \alpha_{ij} e_j - \frac{1}{2!}\beta_{ijk} e_j e_k - \frac{1}{3!}\gamma_{ijkl} e_j e_k e_l; \; i, j, k, l \in \{x, y, z\} \tag{3-44}$$

with $U^{(0)}$the unperturbed total energy, $\mu^{(0)}$ the permanent dipole moment and α, β and γ the linear polarizability and the first and second hyperpolarizabilities. For molecules with closed-shell ground states the coupled perturbative Hartree–Fock (CPHF) equations [83] can be used. However, RHF results give an average difference with experiment of about 25% for small- to medium-sized basis sets [60]. It is known that specially constructed [114,115,116] or very large basis sets (including very diffuse functions) [117] are needed, in particular for planar and linear molecules. Furthermore, taking electron correlation into account is essential in order to get results comparable with the experimental values. Configuration interaction (CI), multi-configuration SCF (MCSCF), coupled cluster (CC) or Møller–Plesset (MP) methods, combined with the required large basis sets, are computationally very demanding. Promising and accurate are density functional theory (DFT) results. Depending on the exchange–correlation (XC) potentials and the basis set, a deviation of 3% can be obtained, which is about the experimental accuracy, although DFT

polarizabilities of conjugated systems [118,119] and systems with large charge transfer character [120,121] tend to be too large. Table 3-4 is clear: one has to spend a fair amount of computing time by doing high-quality QM calculations for gaining about 0.6% accuracy for relatively small molecules. For large (bio-)organic molecules QM calculations of this quality are obviously beyond practical possibilities and therefore methods like Thole's are the best approach.

There are other parameterizations possible. Thole noted, in his original paper, that it would be more elegant to describe the interaction—between induced dipoles—in terms of two interacting charge distributions instead of his 'one-particle' ansatz. Jensen et al. [35] took up this suggestion in order to arrive at traceless interaction tensors. He started from the interaction between two isotropic Gaussian charge distributions on a distance r:

$$V = \int\int \frac{\rho(r_1)\rho(r_2)}{r_{12}} \mathrm{d}r_1 \mathrm{d}r_2 = \frac{\mathrm{erf}(\mathrm{r}\sqrt{\mathrm{b}})}{r} \tag{3-45}$$

Here is b the reduced exponent $b = a_p\, a_q \,/\, (a_p + a_q)$ and erf $\left(r\sqrt{b}\right)$ the regular error function which tends to unity when the argument goes to infinity, and hence the usual potential between two point charges is obtained. The results with the Gaussians are only slightly better [66] than that of Thole's original method. Another approach is that of Pircaud et al. [122] who start from partial charges for water reproducing the vacuum dipole moment that are 'inflated' by Gaussians and used together with the experimental polarizability. This amounts to the use of the screened potential of Eq. (3-41).

Concluding this section, we are confident that the present treatment of the many-body polarization gives transferable and reliable effective polarizabilities and screening factors.

3.2.4. Bulk Effects: The Dielectric Continuum

The collective properties of bulk material typically reflect the behavior of tens of thousands of molecules in a volume of at least 10^6 Å^3 [123]. The description of the electrostatic and response properties of such volumes is obviously beyond any discrete approach and one has to resort to experimental information, i.e., the dielectric constant. In the Introduction we argued that if sufficient solvation shells are included in a calculation, the effect of an enveloping continuum can be neglected. Nevertheless we give here, for completeness' sake, an explicit formulation of the coupling between a set of point charges and polarizabilities and a dielectric continuum.

The extension of Eq. (3-32) is straightforward: for a discretized enveloping surface (**S**) with the boundary element method (BEM) the final result can be expressed in a set of linear equations [124]:

$$\begin{bmatrix} \mathbf{M}_p \\ \mathbf{\Omega}_I \end{bmatrix} = \mathbf{B}' \begin{bmatrix} \mathbf{e}_p \\ \dfrac{\mathbf{v}_I}{2\pi(\varepsilon+1)} \end{bmatrix} \tag{3-46}$$

where in the lhs vector **M** represents the induced dipoles at the polarizable points and **Ω** a set of induced dipoles on the surface **S**. In the rhs **e** and **v** are, respectively, the source fields at the polarizable points and the potentials at the N^{BEM} representative points of **S**. The matrix $\mathbf{B}'$ is given by

$$\mathbf{B}' = \begin{bmatrix} \boldsymbol{\alpha}_p^{-1} - \mathbf{T}_{pq}^{(2)} & \nabla \mathbf{K}_{Ip} S_I \\ \dfrac{-\mathbf{e}_{pI}}{2\pi(\varepsilon+1)} & \mathbf{1} - \dfrac{\mathbf{K}_{IJ}}{2\pi(\varepsilon+1)} \end{bmatrix}^{-1} \tag{3-47}$$

with ε the dielectric constant of the continuum. In Eqs. (3-46) and (3-47) we have added (redundant) indices for clarity: lower case indices for discrete polarizable points and capitals for boundary elements. In the top left of Eq. (3-47) the matrix of Eq. (3-34) will be recognized, while **K** and ∇**K** are more or less complicated potential and field-like kernels, depending on ε and the geometry of **S,**while **1** is the unit matrix of dimension N^{BEM} [10,124]. Hence, leaving out the continuum Eq. (3-34) alone remains, while for the continuum only, just the right bottom part of Eq. (3-47) remains and we are left with a method like the polarizable continuum model (PCM) [9,17]. Like **M** in Eq. (3-33) the lhs of Eq. (3-46) is a self-consistent solution and all information about the reaction potentials is contained in a single relay matrix.

3.2.5. Implementations

In the preceding sections, we have shown that our point charges and polarizabilities can generate trustworthy electrostatic and response properties for any system. The working expression for the DRF/QM/MM method is

$$\hat{H}(r) = \hat{H}_{QM} + \hat{H}_{QM/MM} + \hat{H}_{MM} \tag{3-48}$$

The interaction operator at any point $\mathbf{r}_\mathrm{i}$ is given by

$$\begin{aligned} \hat{H}_{QM/MM}(\mathbf{r}_i) = \sum_i \hat{v}^{DRF}(\mathbf{r}_i, \omega) = \sum_i \hat{v}^{elst}(\mathbf{r}_i) \\ + \sum_i \hat{v}^{pol}(\mathbf{r}_i, \omega) + \left[\sum_i \hat{v}^{disp}(\mathbf{r}_i) \right] \end{aligned} \tag{3-49}$$

where v^{elst} is the electrostatic operator, which describes the Coulombic interaction between the QM system and the permanent charge distribution of the solvent molecules. The polarization operator describes the many-body polarization of the solvent molecules, i.e., the change in the charge distribution of the solvent molecules due to interaction with the QM part and other solvent molecules. The dispersion operator v^{disp} is bracketed in Eq. (3-47) because it may optionally be made part of $H_{\mathrm{QM/MM}}$ or not.

The charge distribution of the solvent is represented by the atomic point charges (z_s), hence the electrostatic operator is given by

$$\hat{v}^{elst}(\mathbf{r}_i) = \sum_s \frac{z_s}{R_{si}} = \sum_s z_s \hat{T}^{(0)}_{si} \tag{3-50}$$

with R_{si} the distance between points s and i, and $T^{(0)}$ the zeroth order interaction of Eq. (3-12). Depending on the particular QM method the operator $\hat{v}^{elst}$ for the electrostatic interaction energy

$$\Delta U^{elst} = \int \rho(r_i)\hat{v}^{elst}(\mathbf{r}_i)\mathrm{d}\mathbf{r}_i \tag{3-51}$$

has to be evaluated, e.g., in ADF [86] in all integration points, or leads to additional 'nuclear attraction'-type integrals in conventional wave function methods where the operators are expanded in basis functions $\{\chi\}$:

$$\left(v^{elst}\right)_{kl} = \sum_s \int \chi_k(r_i)\frac{f_V z_s}{|\mathbf{r}_i - \mathbf{r}_s|}\chi_l(r_i)\mathrm{d}\mathbf{r}_i = \sum_s <\chi_k|\frac{f_V z_s}{R_{si}}|\chi_l> \tag{3-52}$$

The atom pairs determining the screening factor f_V of Eq. (3-52) are taken as the atoms at $\mathbf{r}_s$ and the atom(s) on which χ_k and χ_l are centered. In ADF the screening is achieved by scaling the distance between grid points and classical atoms R_{pq}:

$$S_{pq} = c_{pq} R_{pq} = f(R_{pq}) \tag{3-53}$$

where c_{pq} is a factor and $f(R_{pq})$ an appropriately chosen function of R_{pq}. Furthermore, each component of R_{pq} is also scaled by c_{pq}, so the reduced distance becomes

$$S_{pq} = \sqrt{S_{pq,\kappa} S_{pq,\kappa}} = c_{pq}\sqrt{R_{pq,\kappa} R_{pq,\kappa}} = c_{pq} R_{pq}; \kappa \in \{\mathrm{x}, \mathrm{y}, \mathrm{z}\} \tag{3-54}$$

i.e., consistent with the definition in Eq. (3-53). For Greek indices the Einstein summation convention is employed. The damped operator can thus be obtained by modifying the interaction tensors in Eqs. (3-19), which is equivalent to replacing R_{pq} by S_{pq} and $R_{ij,\kappa}$ by $S_{ij,\kappa}$ in the regular formulae for the interaction tensors:

$$T^{(n)}_{pq,\eta_1,\eta_2,\ldots,\eta_n} = \nabla_{yx,\eta_1} \ldots \nabla_{yx,\eta_n}\left(1/S_{pq}\right) \tag{3-55}$$

The particular form of the scaling function employed here is

$$f(r_{pq}) = \frac{r_{pq}}{\mathrm{erf}(r_{pq})} \tag{3-56}$$

which was obtained by considering the interaction between two Gaussian charge distributions with unit exponents. The damping ensures that the quantum part is not overpolarized due to the interactions.

The damping depends on the width of the Gaussian charge distribution, which in this work was taken to be unit (a.u.). However, both a slightly smaller width [125] and a slightly larger width [126] have been suggested.

For $\hat{v}^{pol}$ a similar route is followed:

$$\hat{v}^{pol}(r_i, \omega) = -\sum_s \mu_s^{ind}(\omega)\mathbf{T}_{si}^{(1)} \tag{3-57}$$

with $\boldsymbol{\mu}_s^{\mathrm{ind}}(\omega)$ the induced dipole moment at atom s, obtained from Eqs. (3-33) and (3-34):

$$\mathbf{M}(\omega) = \mathbf{E}^{\mathrm{init}}(\omega)\mathbf{B} \tag{3-58}$$

The initial field consists of four terms:

$$\mathbf{e}_s^{\mathrm{init}}(\omega) = \mathbf{e}_s^{\mathrm{QM,el}}(\omega) + \mathbf{e}_s^{\mathrm{QM,nuc}} + \mathbf{e}_s^{\mathrm{MM}} + \mathbf{e}_s^{\mathrm{mac}}(\omega) \tag{3-59}$$

where $\mathbf{e}_s^{\mathrm{QM,el}}(\omega)$ is the electric field arising from the electronic charge distribution of the QM part:

$$\mathbf{e}_s^{\mathrm{QM,el}}(\omega) = -\int \rho(\mathbf{r}_i, \omega)\mathbf{T}_{si}^{(1)}\mathrm{d}\mathbf{r}_i \tag{3-60}$$

and $\mathbf{e}_s^{\mathrm{QM,nuc}}$ is the field arising from the QM nuclei,

$$\mathbf{e}_s^{\mathrm{QM,nuc}} = -\sum_n Z_n \mathbf{T}_{ns}^{(1)} \tag{3-61}$$

and $\mathbf{e}_s^{\mathrm{MM}}$ is the field arising from the point charges of the solvent molecules,

$$\mathbf{e}_s^{\mathrm{MM}} = -\sum_t{}' q_s \mathbf{T}_{st}^{(1)} \tag{3-62}$$

The prime in Eq. (3-62) indicates that the sum is restricted to sites that do not belong to the same molecule. Depending on the specific implementation the tensors $\mathbf{T}^{(1)}$ are multiplied with appropriate f_E factors for the associated atoms. The last term in Eq. (3-59), $\mathbf{e}_s^{\mathrm{mac}}(\omega)$, is the macroscopic electric field. This completes the most usual form of $\hat{v}^{pol}$, i.e., the potential of the dipoles due to the total field at the polarizable sites is made a part of the effective Hamiltonian and Eq.(3-24) is solved self-consistently. Since the induced dipoles $\mathbf{M}$ in the solvent (MM) part are self-consistent for any field $\mathbf{E}$, i.e., also for intermediate fields during the iterative process for solving Eq. (3-24), in this way we obtain an overall self-consistent solution, similar to, e.g., the HF or Kohn–Sham procedure. Extension to post-HF methods are straightforward because the reaction potential (RP) is formally a one-particle

operator and in, e.g., the configuration interaction (CI) method only the diagonal CI-matrix elements are affected which can be evaluated by calculating $\mathbf{e}_s^{\mathrm{QM,el}}$ for the various determinants. The final CI states thus obtained are not strictly self-consistent but for a small number of solutions one may recalculate the RP and reiterate.

The electronic contribution to ΔU^{int} is $\Delta U_{el}^{\mathrm{int}} = -1/2\,(\mathbf{E}^{QM,el})\,\mathbf{B}\mathbf{E}^{QM,el}$ and in its earliest form of DRF (the *direct* reaction field approach [3,38]) v^{DRF} was of the form

$$\ddot{v}^{pol} = -1/2 \sum_{i,j} \ddot{\mathbf{E}}_i \mathbf{B} \ddot{\mathbf{E}}_j \tag{3-63}$$

where the summation runs over all particles in QM. If i or j is related with an electron, the integral of Eq. (3-52) appears naturally, but in addition integrals for the *screened self-interaction* appears:

$$I_{km}^{self} = -\frac{1}{2} \int\int \chi_k(\mathbf{r}_1) \left[\ddot{\mathbf{T}}^{(1)}(\mathbf{r}_1) \mathbf{B} \ddot{\mathbf{T}}^{(1)}(\mathbf{r}_1) \right] \chi_m(\mathbf{r}_1) \mathrm{d}\mathbf{r}_1 \tag{3-64}$$

and, if i and j both refer to electrons, screened 2-electron integrals are

$$\begin{aligned} I_{klmn}^{two} &= -\frac{1}{2} \int\int \chi_k(\mathbf{r}_1)\chi_l(\mathbf{r}_2) \ddot{\mathbf{T}}^{(1)}(\mathbf{r}_1) \mathbf{B} \ddot{\mathbf{T}}^{(1)}(\mathbf{r}_2) \chi_m(\mathbf{r}_1)\chi_n(\mathbf{r}_2) \mathrm{d}\mathbf{r}_1 \mathrm{d}\mathbf{r}_2 \\ &= -\frac{1}{2} \left\{ \int \chi_k(\mathbf{r}_1) \ddot{\mathbf{T}}^{(1)}(\mathbf{r}_1) \chi_m(\mathbf{r}_1) \mathrm{d}\mathbf{r}_1 \right\} \times \left\{ \int \chi_l(\mathbf{r}_2) \mathbf{B} \ddot{\mathbf{T}}^{(1)}(\mathbf{r}_2) \chi_n(\mathbf{r}_2) \mathrm{d}\mathbf{r}_2 \right\} \end{aligned} \tag{3-65}$$

They may be added to the standard integrals used in, e.g., a standard HF calculation and, after contracting the integrals in Eq. (3-65) with the density matrix, this gives the following contributions to the energy in terms of MOs:

$$<\mathrm{self}> = -\frac{1}{2} \sum_{K_{\mathrm{occ}}} <K \left| \left[\mathbf{T}^{(1)}(\mathbf{r}_1) \mathbf{B} \mathbf{T}^{(1)}(\mathbf{r}_1) \right] \right| K> \tag{3-66}$$

and

$$\begin{aligned} <\mathrm{scoul}> &= a \sum_{K,L=1,n_{\mathrm{occ}}} -\frac{1}{2} <K(1)L(2) \left| \frac{1}{2} \left[\mathbf{T}^{(1)}(\mathbf{r}_1) \mathbf{B} \mathbf{T}^{(1)}(\mathbf{r}_2) \right] \right| K(1)L(2)> \\ <\mathrm{sexch}> &= -b \sum_{K,L=1,n_{\mathrm{occ}}} -\frac{1}{2} <K(1)L(2) \left| \frac{1}{2} \left[\mathbf{T}^{(1)}(\mathbf{r}_1) \mathbf{B} \mathbf{T}^{(1)}(\mathbf{r}_2) \right] \right| K(2)L(1)> \end{aligned} \tag{3-67}$$

where $a/b = 2.0$ for a closed-shell determinant but varies for open shells. It is clear that <scoul> is just the electronic reaction field contribution obtained above. The

presence of <sexch>, missing in the molecular field approach from which we started above, is correct because it removes energy contributions that violate the Pauli principle. The new one is <self> that describes the stabilization of an electron in its own reaction field . The operator in Eq. (3-64) can always be rewritten as

$$\left[\hat{\mathbf{T}}(\mathbf{r}_1)\hat{\mathbf{BT}}(\mathbf{r}_1)\right] = \hat{\mathbf{G}}^2(\mathbf{r}_1) \tag{3-68}$$

and by applying the closure rule we obtain

$$\begin{aligned}\langle \text{self}\rangle &= -\frac{1}{2}\sum_{K=1,\text{nocc}} \left\langle K\left|\left[G^2(\mathbf{r}_1)\right]\right|K\right\rangle \\ &= -\frac{1}{2}\sum_{\substack{K=1,\text{nocc}\\ L=1,\infty}} \langle K|\left[G(\mathbf{r}_1)\right]|L\rangle\,\langle L|\left[G(\mathbf{r}_1)\right]|K\rangle\end{aligned} \tag{3-69}$$

so that in the total energy the sum of the screened self-energy and the exchange becomes

$$\langle \text{self}\rangle + \langle \text{sexch}\rangle = -\frac{1}{2}\sum_{\substack{K=1,\text{nocc}\\ L=\text{nocc}+1,\infty}} \langle K|G(\mathbf{r})_1|L\rangle\langle L|G(\mathbf{r})_1|K\rangle \tag{3-70}$$

We note that **G** is associated with the polarizability of the classical system, for which we may write $\boldsymbol{\alpha} = \frac{|\langle 0|\mathbf{r}|n\rangle|^2}{U^{(0)}-U^{(n)}}$, i.e., a sum of matrix elements connecting singly excited states. In Eq. (3-70) we see similar matrix elements connecting ground state and singly excited states of the quantum system, and hence formally the self-consistent result there is a representation of second-order terms of perturbation theory (cf. Eq. 3-16) up to third order. However, in Eq. (3-70) the energy denominators are absent and, hence, this is only an upper bound for the dispersion. Moreover, integrals that appear in ⟨self⟩ are divergent: the quadratic operator is of type $f(r)/r^4$, with r the distance between a source and a polarizability, while the integrating volume is only $\sim r^3$. There are several methods to cure this problem. In one the reaction field is expanded, e.g., to second order, so that all integrals can be expressed in combinations of overlap and dipole integrals [3,10,38]. In another, a small region around the center of the polarizabilities is excluded [127]. In order to repair the absence of the energy denominators of the QM part of the system in Eq. (3-70) we use the factor

$$\gamma = \frac{U_S}{U_Q + U_S} \tag{3-71}$$

with U_S and U_Q the experimental or computed ionization energies, respectively, to arrive at a London-like ground state dispersion energy:

$$\Delta U_{\text{int}}^{\text{two-el}} = \langle \text{scoul}\rangle + \gamma\,\{\langle \text{self}\rangle + \langle \text{sexch}\rangle\} \tag{3-72}$$

If $\gamma = 0$, the procedure is equivalent to the molecular or *average* reaction field (ARF) according to Eq. (3-57).

The direct approach looks at first sight complicated, but it is in fact very efficient because by incorporating reaction field integrals in the standard set of integrals no 'external' cycles for computing fields, etc., are necessary: the whole process described in Eq. (3-52) is gone through once to obtain the necessary integrals and afterward the programs do not know the difference. The direct reaction field operator can always be used *after* an ARF calculation in order to get an estimate of the dispersion. The *direct* and *average* methods are available in HONDO [83], ZINDO [84] and GAMESS [85] while in ADF [86] only ARF is possible.

The MM Hamiltonian contains obviously the same $\hat{v}^{elst}$ and $\hat{v}^{pol}$ but acting on classical sites:

$$\hat{v}^{elst}(\mathbf{r}_p) = \sum_s{}' \frac{z_s}{R_{sp}} f_{V_{sp}} = \sum_s{}' z_s f_{V,sp} \hat{T}^{(0)}_{sp} \tag{3-73}$$

$$\hat{v}^{pol}(\mathbf{r}_p, \omega) = -\sum_s{}' \mu^{ind}_s(\omega) f_{E,sp} \mathbf{T}^{(1)}_{sp} \tag{3-74}$$

where the prime indicates that interactions between sites belonging to the same molecule or group are excluded.

For the classical dispersion interaction we use the Slater–Kirkwood expression of Eq. (3-20):

$$\Delta U^{disp}_{sp} = -\frac{1}{4} \frac{\mathrm{Trace}[\boldsymbol{\alpha}_p \mathbf{T}^{(2)}_{sp} \mathbf{T}^{(2)}_{sp} \boldsymbol{\alpha}_p]}{\sqrt{\alpha_s/n_s} + \sqrt{\alpha_p/n_s}} \tag{3-75}$$

with α the average polarizability. This interaction can be between two atomic or group polarizabilities, which may be treated as isotropic or anisotropic. In the isotropic case, Eq. (3-75) reduces to a simpler form:

$$\Delta U^{disp}_{sp} = -\frac{6}{4} \frac{\alpha_s \alpha_p}{\sqrt{\alpha_s/n_s} + \sqrt{\alpha_p/n_s}} \frac{\frac{3}{2} f^2_{T,sp} - f_{T,sp} f_{E,sp} - \frac{1}{2} f^2_{E,sp}}{R^6_{sp}} \tag{3-76}$$

while in the anisotropic case the expression is slightly more complicated [87].

The expression for the short-range repulsion is closely connected to Eq. (3-75):

$$\Delta U^{rep}_{sp} = -\frac{1}{2} \Delta U^{disp}_{sp} \frac{\left(R_{vdw,s} + R_{vdw,p}\right)^6}{R^6_{sp}} \tag{3-77}$$

that can be taken either as isotropic or anisotropic. Furthermore, the dispersion term within Eq. (3-77) may include screening factors that account for overlapping charge

densities (consistent with Eqs. (2.4.28) and (2.4.29)), or without these factors as done typically in standard force fields such as CHARMM, and our early work).

When taken together with dispersion, the short-range repulsion is thus modeled by the Lennard-Jones potential:

$$U_{\mathrm{LJ}} = D_0 \left[\rho^{-12} - 2\rho^{-6}\right] \tag{3-78}$$

with $\rho = r/R_0$. In this representation, the potential has a minimum with well depth D_0 and equilibrium distance R_0 ($\rho = 1$). It can easily be transformed into an X6-form, which uses a more realistic exponential short-range repulsion:

$$U_{\mathrm{X6}} = D_0 \left[\frac{6}{\zeta - 6} e^{\zeta(1-\rho)} - \frac{\zeta}{\zeta - 6} \rho^{-6} \right] \tag{3-79}$$

By choosing a value of ζ=12, the long-range dispersion does not change with respect to the LJ formula of (3-78), while a value of ζ = 13.772 results in a second derivative at the equilibrium distance R_0 that is equal to the LJ value ($72 \cdot D_0$). Hence, the latter value (13.772) does not change the shape of the energy curve around the equilibrium and is therefore chosen as default in DRF90 [87], since we are interested in the condensed phase, i.e., the region around the equilibrium. Note that the well depth and equilibrium distance are equal to that of the LJ form, irrespective of the choice for ζ.

For the atomic radii needed in Eq. (2.4.30), there exist many options but the default in DRF90 [87] is to use charge-dependent atomic radii using Frecer's model [128] in which a polynomial of third order is used to describe the change in atomic radii due to the atomic charge. If the atomic charge is positive, it means that less electrons are surrounding this atom, and therefore the radius is smaller. When negative, the radius increases following the same reasoning.

Both dispersion and repulsion contributions—although basically belonging to $\hat{H}_{MM}$—should of course be added to the QM/MM interactions when doing QM/MM geometry optimizations or MD simulations, using the same parameters for the QM atoms. However, in single-point energy calculations they add only to the total energy since the operators do not affect the electrons. Since the effective atomic charges can be obtained 'on the fly' during any QM calculation it is possible to let them have influence on the results, e.g., in calculations of spectra (if total energies are used) or in structure optimizations.

For MD and/or QM/MM geometry optimizations gradients of the energies are needed. They follow naturally from the energy expressions by replacing electrostatic potential and field operators by, respectively, the corresponding field and field gradient operators.

3.2.6. Macroscopic and Microscopic Properties

It is obviously useful to compare calculated and experimental values for response properties like (frequency-dependent) polarizabilities α, and hyperpolarizabilities β

and γ. This comparison is not without problems—in particular for β and γ—because of the many different conventions and experimental techniques that are used [129]. The linear polarizabilities, α, are experimentally usually obtained from refractive indices applying the Lorenz–Lorentz equation (3-42). For the hyperpolarizabilities different conventions used in calculations and experiments can lead to differences up to 300%, and that apart from different references used experimentally. All this can be avoided by clearly stating the convention used. In a macroscopic electric field

$$F_J^{mac}(t) = F_{0,J}^{mac} + F_{\omega,J}^{mac}\cos(\omega t) \tag{3-80}$$

the polarization, i.e., the dipoles averaged over a macroscopic volume, is usually expressed as a power series in the field strength:

$$\begin{aligned} P_I^{\omega_s} = {} & \delta_{\omega_s,0}P_I^0 + \chi_{IJ}^{(1)}(-\omega_s;\omega_s)F_{\omega_s,J}^{mac} \\ & + C(-\omega_s;\omega_a,\omega_b)\chi_{IJK}^{(2)}(-\omega_s;\omega_a,\omega_b)F_{\omega_a,J}^{mac}F_{\omega_b,K}^{mac} \\ & + C(-\omega_s;\omega_a,\omega_b,\omega_b)\chi_{IJKL}^{(3)}(-\omega_s;-\omega_s;\omega_a,\omega_b,\omega_b)F_{\omega_a,J}^{mac}F_{\omega_b,K}^{mac}F_{\omega_c,L}^{mac} \end{aligned} \tag{3-81}$$

where the output frequency $\omega_s = \sum_a \omega_a$ and $\chi^{(n)}$ is the nth order susceptibility. The numerical coefficients $C(-\omega_s;\omega_a,\ldots)$ arise from the Fourier expansion of the field and ensure that all susceptibilities of the same order have the same static limit. A tabulation can be found in Ref. [130]. Each of the susceptibilities corresponds to different physical processes: $\chi^{(1)}$ governs the refractive index, $\chi^{(2)}(-2\omega;\omega,\omega)$ the second harmonic generation (SHG), $\chi^{(3)}(-3\omega;\omega,\omega,\omega)$ the third harmonic generation (THG) and $\chi^{(3)}(-\omega;\omega,\omega,-\omega)$ the degenerate four-wave mixing (DFWN) or the intensity dependency of the refractive index.

The microscopic polarization of a molecule in an external field (or the dipole moment, i.e., the positions of the charges in the molecules averaged over the molecular volume) can be expanded in a Taylor series:

$$\begin{aligned} \mu_i^{\omega_s} = {} & \delta_{\omega_s,0}\mu_i^0 + \alpha_{ij}(-\omega_s;\omega_s)F_{\omega_s,j}^{tot} \\ & + \frac{1}{2}C(-\omega_s;\omega_a,\omega_b)\beta_{ijk}(-\omega_s;\omega_a,\omega_b)F_{\omega_a,j}^{tot}F_{\omega_b,k}^{tot} \\ & + \frac{1}{6}C(-\omega_s;\omega_a,\omega_c)\gamma_{ijkl}(-\omega_s;\omega_a,\omega_b,\omega_c)F_{\omega_b,j}^{tot}F_{\omega_b,k}^{tot}F_{\omega_c,l}^{tot} \end{aligned} \tag{3-82}$$

where the numerical coefficients C are the same as for the macroscopic polarization.

For extracting microscopic properties from experiment the so-called local field factors are needed [131], and, vice versa, also to obtain macroscopic values from computed (microscopic) results. The concept of relating the macroscopic field and the actual (or local) field experienced by a molecule goes back to Lorentz [113,132].

The idea is that only the field from molecules near to the solute has to be considered, so that the complete system can be separated into microscopic and macroscopic regions. The molecules in the latter can be described by the average macroscopic properties. Lorentz derived a simple relation between the local field and the macroscopic polarization, which is still in use [113,133,134,135].

DRF has been implemented such that all necessary information is available. To that end, we distinguish between 'solute' and 'effective' properties. The first coming from the action of a field solely on the solute in a cluster, but embedded in its classical environment. For the latter, the field acts on the whole discrete system, hence generating the field of dipoles induced by the field that counteract the inducing field.

From the effective properties the macroscopic polarization can be calculated as

$$P_I^{\omega_s} = N_\mathrm{d}\delta_{\omega_s,0}\left\langle \mu_i^{\mathrm{eff}} \right\rangle_I \tag{3-83}$$

with N_d the number density, and from there the local field factors, the refractive index and the susceptibilities. For details the reader is referred to Ref. [136].

3.3. SOME VALIDATION

Many applications of new force fields and new QM/MM methods of necessity focus on 'agreement' with experimental or otherwise calculated results. Also in this section we will first show that DRF indeed gives a reliable model for static and response potentials and can lead to QM/MM—or even completely MM calculations—that are as good as, e.g., SCF calculations. To that end we point at some results for simple systems like the water and benzene dimers, and the three- and four-body interactions in several systems.

3.3.1. The Water Dimer

The hydrogen-bonded water dimer is without any doubt the most used system to study intermolecular interactions, be it from the QM [34,72] QM/MM [13,26,31,32,40,52,108], or MM [25,42,45,48,50,72] perspective. In the past we have also used it to show that the DRF model indeed gives static and response potentials that are as good as, e.g., SCF calculations [74,137]. Of course, if this is the case, it allows for arbitrary separation of the total system into different subsystems, which can then be arbitrarily described at the QM or MM level; e.g., for a simple system like the water dimer, one may treat both monomers at the QM level, one monomer at QM and the other at MM, or both monomers at MM. Hence, we may go from the computationally expensive fully QM to QM/MM and to MM, without significant loss of accuracy. Alternatively, we can do MD simulations at the MM level, take snapshots from them and submit these to QM/MM (or QM) calculations to obtain UV-Vis spectra, excitation energies, NLO properties, etc., for the solute in solvent, i.e., *sequential* MD.

In order to show that this interchangeability is indeed feasible, we focus on the hydrogen-bonded water dimer (see Figure 3-2). We treated it first completely with

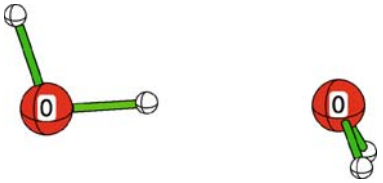

Figure 3-2. The hydrogen-bonded water dimer. The *x*-axis coincides with O–H–O

QM at the RHF level with Dunning's DZP basis set [138], and corrected for basis set superposition errors (BSSE) [102]. Next we treated it at the fully classical MM level, using the force field parameters as obtained from the RHF/DZP calculations on the monomer. Hence, we used atomic polarizability values (3.3791 a.u. for oxygen, 1.3333 a.u. for hydrogen) and an *a*-factor of 2.445 that result directly from polarizabilities calculated at the same level of theory (see, e.g., Table 4 in Ref. [60]). The partial charges on the atoms (–0.7886 on oxygen, 0.3943 on hydrogen) reproduce the dipole moment of the monomer at RHF/DZP calculation (2.28 D). Finally, the atomic radii (3.5587 a.u. for oxygen, 0.9637 a.u. for hydrogen), needed for the short-range repulsion (cf., Eq. 3-77), were taken from the atomic quadrupole moments (or rather, the expectation values of R^2) also from the RHF/DZP calculation.

With these force field parameters we calculated the potential energy surfaces for the water dimer (without taking dispersion into account since this is absent in RHF calculations) at the MM level using three different choices for the short-range repulsion. As already mentioned in the Section 3.2.5, the latter term is the only energy term that does not result directly from second-order perturbation theory. So far, we have been using the CHARMM expression Eq. (3-77) that takes the expression for the dispersion energy and 'corrects' it to give the Lennard-Jones repulsion term that goes as R^{-12}. In our early work, we took the CHARMM expression directly, i.e., without including the screening factors in the dispersion part that account for overlapping charge densities. More recently, we have moved on to including the screening factors to make it consistent with the other energy terms. Here, we explore for the first time also exponential repulsion, which should be more appropriate for the short-distance range.

In Figure 3-3 the excellent agreement between the fully QM and the fully MM data is seen, having minima at the same O–O distance with the same well depth. As anticipated, screening the repulsion for overlapping charge densities improves the agreement with the reference RHF/DZP data to some extent, but not much. The use of exponential repulsion does not play a major role here, but this may be resulting from using RHF as a method for obtaining the force field parameters.

In Figure 3-4 the experimental radial distribution [139] of water is plotted together with the one obtained with a 257 molecules MD simulation (with the same parameters as above) in which the central water molecule is the solute. The comparison is not bad: the first maxima for MM and experiment are almost at the same position. The second maximum (MM) is too far out, and the third maximum is virtually not

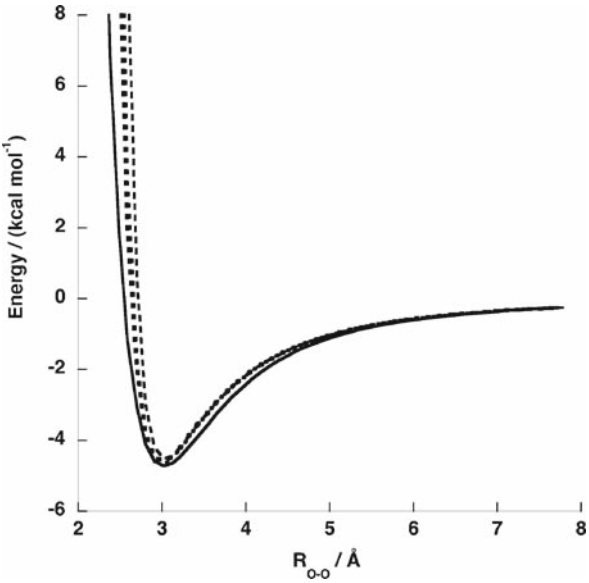

Figure 3-3. Potential energy surface for the water dimer obtained at RHF/DZP and fully classical MM levels with various repulsion models. *Solid line*: RHF. Repulsion; *dashed line*: unscreened LJ; *dotted*: screened LJ ; *bold dotted*: unscreened X6

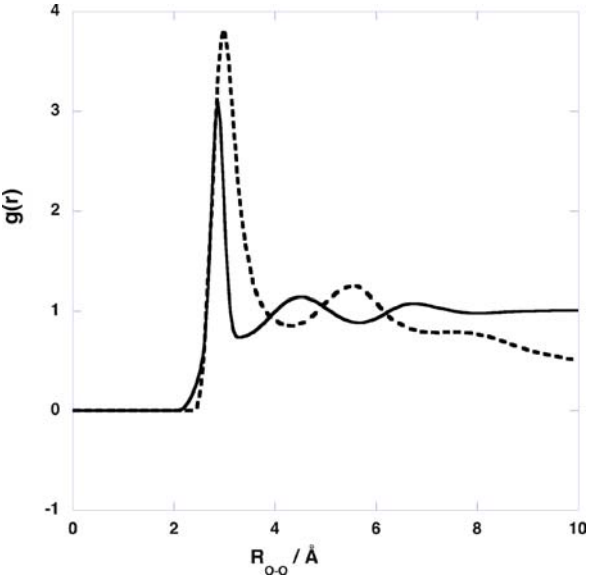

Figure 3-4. Radial distribution of 126 water molecules around the central water molecule from a MD simulation at 298 K with parameters from RHF/DZP calculation (*dashed line*) and experimental $g(r)$ (*solid line*) from Ref. [139]

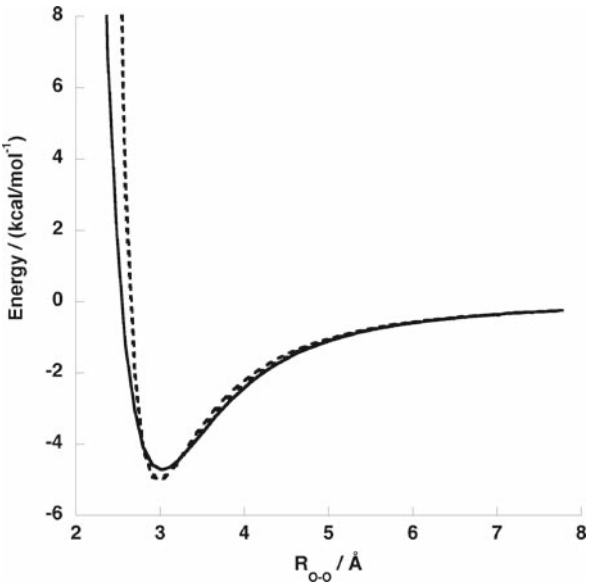

Figure 3-5. Potential energy surface for the water dimer obtained at RHF/DZP and QM/MM levels. *Solid line*: RHF; *dotted*: donor QM; *dashed*: acceptor QM

present. All these differences have to do with the parameterization based on the RHF results, and the size of the sample.

With this good agreement between the fully QM and fully MM results in mind, we went a step further and performed QM/MM calculations for the water dimer. There are two ways for separating the water dimer, i.e., either with the hydrogen-bond donor or the H-bond acceptor in the QM part. We calculated the PES for either QM/MM option, using the same force field parameters as before, and the 'exact' version of HONDO/DRF, i.e., (reaction) potentials and fields, were obtained as expectation values of the appropriated operators. In Figure 3-5 the QM/MM potential energy curves are plotted, together with the fully QM one.

The excellent agreement between the MM, QM/MM and QM PES results directly from the consistent and consequent screening of the interactions for overlapping charge densities. Therefore, as was already shown previously [74,137], our model gives static and response potentials that are as good as SCF calculations (and better if the dispersion is accounted for) which let us separate the total system into different subsystems.

3.3.2. Benzene Dimer

While the water dimer serves as the prototype system for studying hydrogen-bonding interactions, the benzene dimer serves this same purpose for π–π stacking. The latter may also be relevant for technological applications, but it is mainly associated with

biological systems such as deoxyribonucleic acid (DNA) or proteins. The benzene dimer proved to be a challenge for quantum-chemical methodologies. On the one hand, the system was too large for treatment with highly sophisticated ab initio methods such as CCSD(T) with large basis sets (which are necessarily large because the BSE is of the same order of magnitude or larger than the interaction itself), while more efficient QM methods (RHF, DFT) had intrinsic problems in describing accurately the dispersion interaction which is the major component of the interaction energy [140]. More recently, with improvements in computational power and DFT functionals, it has become possible to study these complexes more accurately [141,142].

Many different structures can be envisaged for the benzene dimer, but three stand out: parallel (P), parallel-displaced (PD) and T-shaped perpendicular (T) while for PD and T there are various orientations possible (See Figure 3-6).

We have studied the benzene dimer several times previously [74,87]. In the first one [74] only two structures (P1 and T2) were investigated, for which the geometry was taken directly from another study, with force field parameters obtained from a RHF/DZP calculation on the monomer. In the second, we studied five structures from Figure 3-6 [143], taking force field parameters from a DFT (BP86/TZ2P) calculation of the monomer, and performed a PES-scan for each of them. The dimer was investigated at the MM level in both studies, using different choices for the atomic charges and atomic polarizabilities.

The first non-vanishing multipole moment of the benzene molecule is the quadrupole moment, so the charges used within the MM calculations should give a good representation of it. The dipole-preserving charges (DPC) resulting from RHF/DZP, as used in the first study, give a molecular quadrupole moment of –2.82 a.u. (reported here is Θ_{zz}; because of symmetry $\Theta_{xx} = \Theta_{yy} = -1/2\ \Theta_{zz}$). This is a significant underestimation of the expectation value of the quadrupole at the same level, which amounts to –7.10 a.u. On the other hand, the multipole-derived (MDC-q) charges used in the second study represent by construction the computed molecular quadrupole moment (–5.59 a.u.), which is only slightly lower than the experimental value of –6.46 a.u. [143].

Because dispersion is an important component of the intermolecular interaction—in fact the most important for the relative stability of benzene dimers [140]—the value of the (molecular) polarizability is most likely very important for the stability

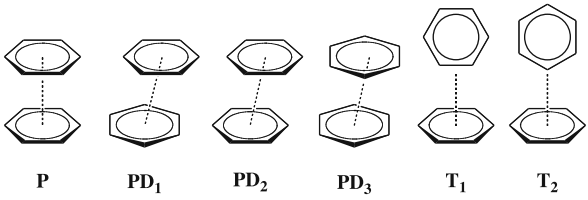

Figure 3-6. Structures of the various benzene dimers. For symbols used, see text

Table 3-5. Interaction of the benzene dimers (kcal/mol)

method	monomer properties		energies					
	α	θ	P	P1	P2	P3	T1	T2
DPC-[a]	61.5	–4.66	–	−2.20	–	–	–	–1.92
EE	70.1	–6.64	–	−3.18	–	–	–	–3.38
SMDC_vDS	70.1	–5.59	−1.63	−2.49	–2.56	–	–2.28	–2.26
CCSD(T)	–	–	−1.70	–	–	–2.63	–	–2.61
exp	70.1	–6.64			1.67±0.24[a,b]			

[a]Ref. [144]; [b]+ZPE: 1.87 kcal/mol.

of the isomers. The benzene molecule is a special molecule (like any other arene) in that the nuclear framework is planar, but an important portion of the electron density resides outside this plane. One-electron basis sets tied to the nuclei provide insufficient opportunity to distribute electrons in the regions above and below the molecular plane. The same holds for Thole's model, in which polarizabilities too are centered on atoms. This deficiency may lead to the underestimation of the out-of-plane component of the molecular polarizability tensor. The importance for the benzene dimer, and the relative stability of the different structures is, a priori, unclear. Therefore, in the first study, a set of polarizabilities outside of the nuclear plane was used, together with point charges fitted to give the experimental values. In Table 3-5 the results for the various choices are summarized.

The computed interaction energies for the different structures of the benzene dimer varies from ca. –1.6 to –3.4 kcal/mol, depending on the particular form and model used. From Table 3-5 we learn also that 'simply' choosing parameters that match experimental values (EE) does not work: these values are beyond any other results. Better are those of good QM calculations generating values for polarizabilities and charges being close to experiment, i.e., with the charges of Ref. [69] and the polarizabilities of Ref. [60] (SMC-vdDS) being in the range of high-quality ab initio calculations. Surprisingly, the most simple approximation (DPC) is closest to experiment: a dissociation energy of 1.92 kcal/mol at 5.03 Å, to be compared with 1.67 kcal/mol [140]—or rather 1.87 kcal/mol after correcting it for the zero point energy (ZPE) of 0.2 kcal/mol—for a T-shaped dimer at a distance of 4.96 Å [144]. The ZPE was obtained by fitting the CCSD(T) curve for the T-shaped dimer in Figure 4 of Ref. [141] to a Morse potential. The DPC result may be a fluke, but if so, and if we have to put more confidence in the numbers coming from, e.g., the CCSD(T) calculations, that would not be the first time that good ab initio calculations suggesta re-interpretation of the experimental findings [145]. More support for the DPC parameterization is collected in Table 3-6, where the results of MC-PESs are compared with experimental dissociation energies [140] of various benzene derivatives. Even if the numbers in Table 3-6 are corrected with ca. 0.2 for the ZPE, they are reasonably good.

Table 3-6. Interaction energies of benzene and derivative dimers (kcal/mol)

System	Structure	U_{MC}[a]	Experiment[b]
B–B	T2	−1.92	−1.67±0.24
B–T	P1	−3.35	−3.11±0.48
T–T	P1	−3.58	−3.35±0.48
T–X	P1	−4.18	−4.06±0.72
X–X	P1	−4.86	−5.02±0.72
F–F	P1	−3.66	

[a]Minimum of MC from Ref. [74] PES; [b]from Ref. [140].

3.3.3. Many-Body Interactions

Reacting on a remark of Chalasinski and Szczesniak [146] that classical polarization is a 'too poor model' to describe many-body effects, Grozema et al. [71] performed SCF and classical DRF calculations which showed that this insufficiency has probably more to do with particular polarization models than with classical models in general. The following partitioning of the total interaction energy was used:

$$\Delta U_{tot} = U^{(abc)} - U^{(abc)}(a) - U^{(abc)}(b) - U^{(abc)}(c) \tag{3-84}$$

with $U^{(abc)}(a)$ the energy of component a in the trimer (abc) basis set. All interactions were corrected for the BSSE applying the Boys–Bernardi counterpoise scheme [101,102]. The correlation-consistent basis set of Dunning [147] was used. For the classical calculations point charges giving the monomer dipoles and polarizabilities obtained from monomers with the same basis sets were used. For details, see Ref. [71]. Here some results are summarized in Table 3-7.

Extending this to a HF tetramer, the three- and four-body interactions were calculated, respectively, as –2.109 and –0.090 kcal/mol with SCF, and 2.055 and 0.126 kcal/mol with DRF. The relative success of the DRF model is most likely due to the fact that we always use self-consistent solutions of the expression in Eq. (3-47).

Table 3-7. Three-body interactions in some trimers (kcal/mol)

Method	HF	H_2O	Urea
SCF	−0.951	−0.987	−0.467
DRF	−0.920	−1.131	−0.498
Diff.	3%	15%	7%

3.3.4. Concluding the Validation

In the foregoing sections we have shown that the parameterization of DRF, based on good quality QM calculations (large basis set, correlated wave functions, multipole derived charges and polarizabilities fitted to experiment) on monomers, gives for two difficult and extreme examples, i.e., the water and benzene dimers, results good enough to define it as 'default' for QM/MM and MM calculations.

3.4. APPLICATIONS

In this section we present summaries of the DRF approach in various fields of computational chemistry, ranging from spectra and (hyper-)polarizabilities to chemical reactions in solution.

3.4.1. Sudden Polarization in Excited States of Symmetric Ethylenes

An interesting phenomenon is the so-called 'sudden polarization' in low-lying excited states of symmetric alkenes like (substituted) ethylenes. One aspect of the behavior of the excited states of these systems is the existence of a polarized (or charge separated) state in which two electrons are localized at one side of the molecules—as opposed to the initial 'biradical' state in which the unpaired electrons are distributed—and thus leading to a considerable dipole moment. Direct and indirect experimental evidence of such a 'phantom' state comes from time-resolved photo-induced excitation experiments on tetraphenylethylene (TPE) [148]. Other studies on TPE have revealed a strong correlation between the lifetime of this polarized excited state and solvent polarity. Schilling and Hilinsky [149] observed a dramatic drop in TPE excited state lifetime from several nanoseconds in non-polar solvents to only a few hundreds of picoseconds in (di)polar solvents. Picosecond optical calorimetric studies by Ma and Zimmt [150] showed a decrease of the energy gap between the ground and excited states of several (para-substituted) TPEs with increasing solvent polarity, which has led to the suggestion that the energy difference between ground and excited states is a measure of the coupling between the two states, thus explaining the decrease in lifetime of CT states in polar solvents.

After the vertical excitation of an electron from the D_{2h} ground state of ethylene, the C–C bond length will increase and a twist around this bond will be initiated. On progressing twisting, three low-lying excited singlet states arise, which at the perpendicular D_{2d} geometry are denoted as $N(^1B_1;ab)$, $V(^1B_2;a^2–b^2)$ and $Z(^1A_1;a^2+b^2)$ and are very sensitive to the twist angle. The N state is destabilized in going from the D_{2h} to the D_{2d} geometry, while in this process the V and Z states are stabilized, coming close together and—in the Born–Oppenheimer approximation—cross for $\theta \approx 80^\circ$. Around the near perpendicular geometry the V and Z are (nearly) degenerate and linear combinations of V and Z like $V \pm Z$ are equally acceptable solutions of the Schrödinger equation leading to localized states of type a^2 or b^2 which have a considerable dipole moment.

As a first effort to investigate the influence of solvents on the properties of these states, we prepared non-symmetrical reaction potentials in a continuum with various dielectric constants generated by putting a localized charge distribution for $\theta \approx 90^\circ$, obtained from a RHF procedure from which an a^2 solution was obtained with a dipole moment of about 4.0 D. This was done for dielectric constants ε = 2.0, 4.0, 6.0 and 10.0, which are typical for a range of organic solvents with increasing polarity. Configuration interaction with single and double excitations (CISD) in vacuo calculations on all valence electrons with the ROHF wave function as reference lead to perfectly zero dipoles for all states. With the polarized continuum present and starting from the localized RHF wave function at the D_{2d} geometry, a dipole moment of about 3.2 D was obtained, the strong polarization occurring near the crossing between the 'pure' V and Z states. It was found that a weak dielectric is unable to maintain a large dipole on progressive twisting beyond the $\theta \approx 80^\circ$ point, and we concluded that relatively strongly polar solvents are needed to trap polarized states in the near perpendicular geometry. Next we used DRF with ethylene in six different solvents [151]. First we calculated the polarizability of ethylene in its first excited state in the 70–90° twist angle area with the finite field method. From this we learned that an electric field of about 5×10^{-5} a.u. is sufficient for a full charge separation. The polarizability increases almost stepwise from 'normal' to about the unphysical value of 80,000 a.u. around the 81° twist. For other twist angles the dipole moment was linear in the applied field. Solvation effects were investigated by SMC calculations on ethylene embedded in 50 solvent molecules, followed by QM/MM, as before, with CISD. In Table 3-8 the average solvent-induced dipole moments are listed.

Table 3-8 shows that, as expected, only polar solvents are capable of breaking the symmetry of the ethylene excited states. This led to new experimental work on TPE in which the dynamics of the charge separation was studied [152]. A similar theoretical study on the solvent effect on the formation of charge transfer states in 9,9'-bianthryl [153] led to similar results and conclusions.

Table 3-8. Average solvent-induced dipole moments in the N, Z and V states for 81° twist angle

Solvent	$\lvert\mu_z\rvert$/ D		
	N-state	Z-state	V-state
Ethane	0.0	0.09	0.08
Tetrachloromethane	0.01	0.72	0.70
Chloroform	0.05	2.07	1.93
Carbon dioxide	0.09	2.62	2.37
Acetone	0.10	2.61	2.38

3.4.2. Spectra

Spectra are in most cases calculated as help by the interpretation of experiments, like by assigning (orbital) transitions. On the other hand, computed spectra are obviously an excellent way to validate QM and QM/MM procedures. Calculated vertical transitions may be convoluted to bands, thus mimicking the internal movements in a molecule. Sometimes solvent effects are accounted for by adding a single or a few solvent molecules, thus missing any 'bulk' effects. Also in this field the continuum approach is popular, then, however, only a single set of vertical transitions is obtained, which may be broadened, now to mimic also the band structure usually obtained for spectra in the condensed phases. Applying the SMC or SMD and QM/MM techniques one may average the excitations and oscillator strengths and use standard deviations in either to indicate the margins.

In several cases DRF has been successfully applied for calculating spectra of molecules in solution. Of late, we add the oscillator strengths of all transitions in equal-width energy intervals, the width depending on the required resolution, and—if different conformers of the solute are present—scaled with appropriate Boltzmann factors. The individual transitions may be convoluted for the vibrations. In this way the bands appear 'naturally' and this is about the closest one can come to simulate a real spectrometer. Here we summarize some results.

3.4.2.1. The n→ π transition in acetone*

Our first effort to compute a spectrum was on the solvent shift of the $n \rightarrow \pi^*$ transition in acetone [154] in various solvents by calculating the ground state and first excited state as restricted and open shell Hartree–Fock (RHF and ROHF) single determinant wave functions. The solvent was for comparison modeled by both the dielectric continuum and by discrete solvent molecules in which the solute/solvent configurations were obtained from Monte Carlo (MC) simulations. This was done the 'hard way' by using the DRF-QM/MM ground state energy in the MC procedure, i.e., for each accepted step also a ROHF calculation was done on the excited state. Due to the extremely high CPU demands of this procedure only a limited number of solvents (water, acetonitrile (MeCN) and tetrachloromethane (CCl_4)), solvent molecules (ca. 30) and MC steps (ca. 7000) were possible with a minimum basis (STO-3 G) [138] for the solute. In Table 3-9 some of the results are collected.

From Table 3-9 one learns that the continuum-only results are only for water in reasonable agreement with experiment. In contrast, the discrete solvent model leads, even in this very limited version, to shifts that compare well with experiment. Notice also that going from water to MeCN and CCl_4, the dispersion is of increasing importance: MeCN has an appreciable dipole moment but is also more polarizable than water, especially along the CN triple bond, while for CCl_4 the polarizability is the only parameter of importance.

In the next effort [187] to compute the same $n \rightarrow \pi^*$ excitation in acetone we applied the SMC technique: completely classical MC calculations produced 100 solvent-solute configurations that were afterwards subjected to DRF-QM/MM

Table 3-9. Computed excitation shifts (cm^{-1}) of acetone[a] relative to the gas-phase result in water, MeCN and CCl_4

Solvent model	Shift in H_2O[b]	Shift in MeCN[b]	Shift in CCl_4[b]
Continuum[c]	−1803 (+1624)	–1848 (+1579)	−2403 (+675)
Discrete[d]	+1639 (+2788)	+620 (+1597)	−216 (+411)
Discrete, MC average	+1821 ± 330	+ 922 ±310	−381 ±75
Experimental[e]	+1700 ± 200	+ 400 ±200	−350 ±200

[a]Vacuum excitation energy 26,962 cm^{-1} (exp. 36, 100 ±100 cm^{-1}, [180]).
[b]A negative value indicates a red shift. The values in parentheses are without dispersion.
[c]Boundary at 1.2 times the van der Waals radii.
[d]At lowest energy solute–solvent configuration from an all-classical MC run.
[e]From [181,180,182].

calculations. The advantages are clear: more solvents (eight), more solvent layers (about two, i.e., 40–52 solvent molecules), more MC steps (50,000) and a better basis set (DZP instead of STO). The results are depicted in Figure 3-7.

Although the still relatively small basis and the use of HF wave functions result in absolute excitations far away from the experimental value, the solvent shifts are very well reproduced. The need for dispersion is probably disputable, because it might only be connected with the uncorrelated wave functions. Wave functions that

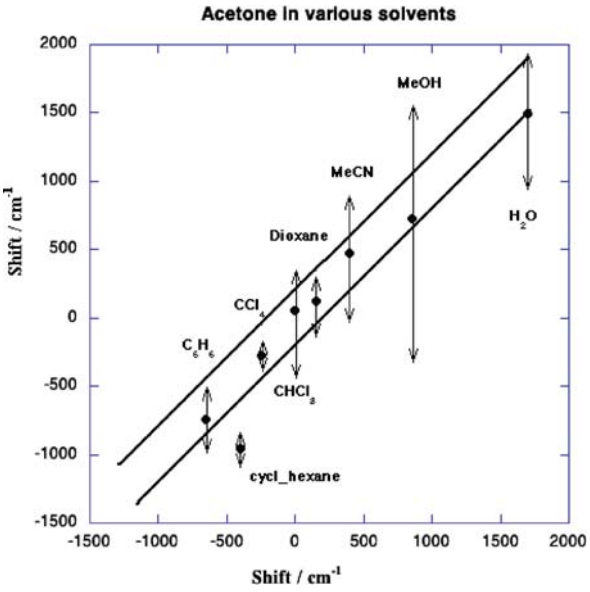

Figure 3-7. Calculated shifts of the $n \rightarrow \pi^*$ transition of acetone in various solvents. The *solid lines* indicate the experimental margins. The arrows indicate the standard deviations from the MC simulations. Data from Ref. [187]

do not violate the Pauli principle for the part in which there is overlap with charge distributions of solvent molecules, and in which electron correlation is accounted for, are more tight and lead possibly to less dispersion interaction. The most important issue here is the fact that all calculations were done with a single set of parameters, i.e., without reparameterization for, e.g., the excited state. The only difference was the adaptation of γ of Eq. (3-71), in which in the denominator the ionization energy of the solute was reduced by subtracting the calculated excitation energy, for use in the dispersion contribution of the excited state.

3.4.2.2. Absorption and emission spectra of N-(1-pyrenyl)-methyluracil-5-carboxamide-1-aminopyrene (PAU_{Me})

A more recent application is the calculation of the absorption and emission spectrum of a pyrenyldeoxyuridine nucleoside model [155] (see Figure 3-8). The interest was here to find an explanation for the stronger pyrenyl emission quenching in the polar solvents (MeCN and MeOH) than in the less polar solvent tetrahydrofuran (THF) [156]. This is consistent with the formation of intramolecular $Py^{\bullet+}/dU^{-}$ charge transfer (CT) states.

The absorption and emission spectra of *N*-acetyl-1-aminopyrene (PAAc) and PAU_{Me} immersed in 200 MeCN molecules were calculated using ZINDOs/CIS [84] and DRF [157] for the QM/MM parts. Eight conformers of both molecules were used, for PAAc obtained 'by hand' by rotating the Ac moiety, for PAU_{Me} as local minima in a classical MC calculation [156]. Each of the conformers was treated in a SMD simulation equilibrated to the vacuum ground state charge distribution as modeled by the ZDO [84] charges that reproduce the dipole moment, and a simulation equilibrated to the charge distribution of the first (vacuum) CT state. For each conformer 20 vertical transitions were calculated. The oscillator strengths were then scaled by appropriate Boltzmann factors, based on ground state energies calculated with the Amsterdam density functional package (ADF) [86], and then the ca. 15,000 transitions were collected in 200 equal-width energy intervals, leading to Figure 3-9 (PAAc) and Figure 3-10 (PAU_{Me}) in which we compare the calculated and experimental spectra. From Figure 3-9 we see that the combination ZINDO/DRF does reasonably well for PAAc, which made us going on with PAU_{Me}. Comparing the two spectra we see that the absorption bands for PAU_{Me} are much broader than for PAAc, which agrees with the experimental findings [156].

Both absorption and emission spectra are somewhat blue shifted, which we attributed to the difference between the spectroscopic model (PAUMe) and the compound actually used in the experiments (PAdU). Furthermore, the dispersion interaction was neglected, mainly because the choice of the scaling parameter γ Eq. (3-71) for states beyond the first excited state is cumbersome. Reducing the ionization energy of the solute by the excitation energy leads rapidly to a value smaller than zero, and hence to a positive dispersion interaction. In order to avoid this unphysical situation it is better to neglect the dispersion completely. Moreover, it is sometimes assumed that in semi-empirical wave functions electron correlation is accounted for because the parameters come from experiment. (The CIS

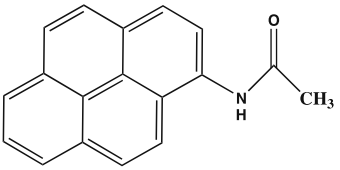

PAAc

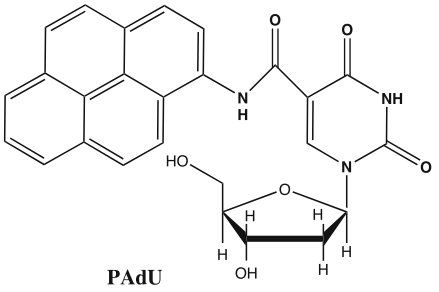

PAdU

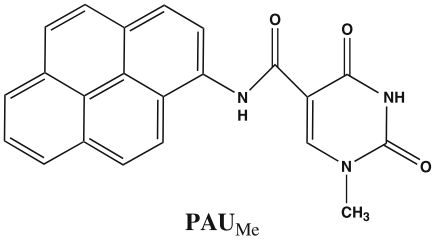

PAU$_{Me}$

Figure 3-8. Structural drawings of *N*-acetyl-1-aminopyrene (PAAc), 5-(*N*-carboxyl-1-aminopyrenyl)-2'-deoxyuridine (PAdU) and *N*-(1-pyrenyl)-1-methyluracyl-5-carboxamide (PAU$_{Me}$)

procedure of course, considering only single electron excitations, does not contribute to this). Reproduction of experimental spectra was not the main goal of this study, however satisfactory the results of Figure 3-10 may be. The events in the femtosecond experiments in Ref. [156] were rationalized as schematically pictured in Figure 3-11.

The left side of Figure 3-11 gives a qualitative impression of the computed spectrum for the solvent being equilibrated with the solute's ground state charge distribution. A relatively high-lying excited state is present with a very large dipole moment. The left side relates to a calculation for which the solvent is first equilibrated with the CT_1 state (in the gas phase). The effects are twofold: first the ground state shifts up,

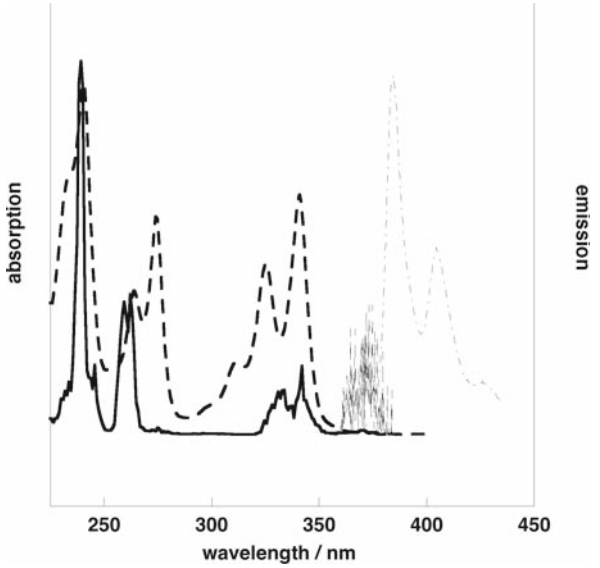

Figure 3-9. (Normalized) calculated (*solid*), experimental (*dashed*) absorption, and calculated (*dash-dot*) and experimental (*fine dash*) emission spectra of PAAc in MeCN

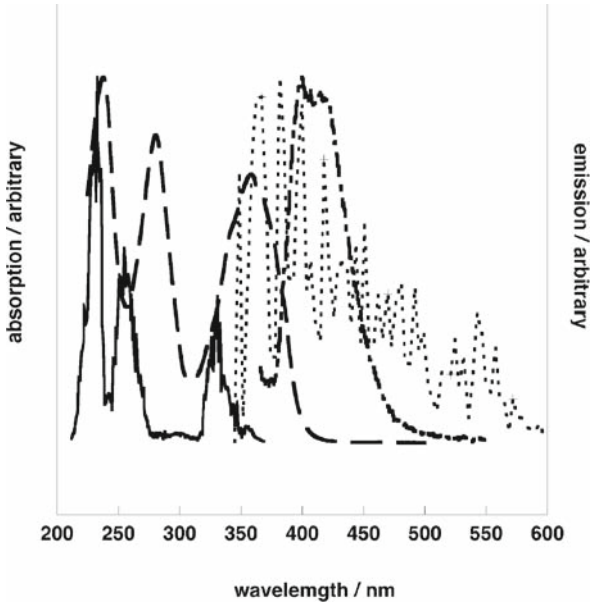

Figure 3-10. (Normalized) experimental (PAdU) and calculated (PAU_{Me}) absorption and emission spectra in MeCN. *Dashed line*: experimental absorption; *dash-dot*: experimental emission. *Solid line*: calculated absorption; *dotted line*: experimental emission

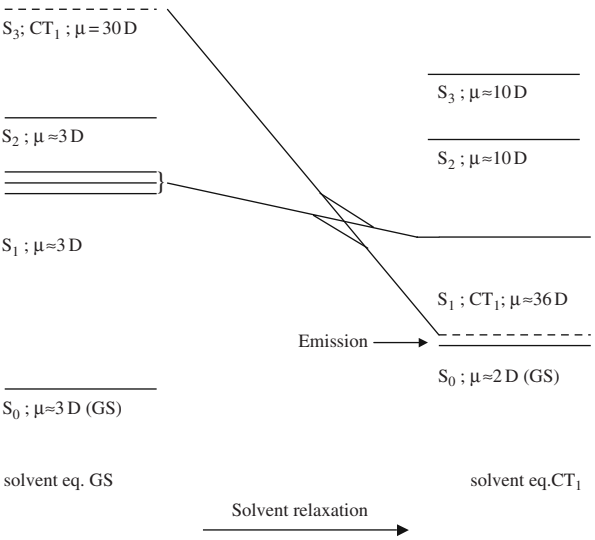

Figure 3-11. Schematic representation of two transition energy manifolds, showing some low-energy electronic states (S_n) of PAU_{Me} in MeCN. *Left*: solvent equilibrated with ground state charge distribution. *Right*: solvent equilibrated with charge distribution of (vacuum) CT_1 state

because it is not in equilibrium with the solvent. The other states may go up or down, depending on how much they 'like' their new environment. However, the CT_1 state is stabilized by almost 1 eV and actually ends up as the first excited state. This state lies very close to the (new) ground state, thus explaining the emission quenching of such states. For the details we refer the reader to Ref. [155].

3.4.2.3. The visible spectrum of Fe-(PyPepS)$_2^-$

Another numerical experiment involved a model active site of Fe-dependent nitrile-hydratase (Nhase), a non-heme Fe^{III} enzyme that catalyzes the hydration of nitriles to amides. The mechanism is as yet unknown and computational chemistry may be important to help unraveling it, provided the methods used are adequate, and the idea was that calculating the spectrum is a good check on the computational method. Of the model compound, $[Fe^{III}(PyPepS)_2]^-$ (see Figure 3-12) the spectrum in aqueous solution is known.

The spectrum is very similar to that of the native enzyme, showing strong absorption in the 400–500 nm region and a weaker band around 700–800 nm. An early effort to calculate it from a combination of time-dependent density theory TDDFT and MM (geometry optimization of the complex surrounded by 50 water molecules), followed by ZINDOs/CIS in which the whole sample was treated quantum-mechanically, failed for several reasons. Semi-empirical methods like INDO are minimal basis set approaches that are unable to describe negative ions. In the analysis of the charge distribution of the resulting SCF wave function all

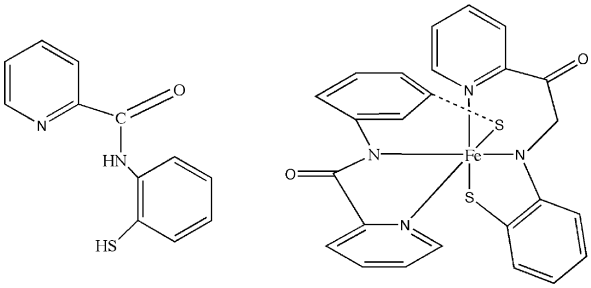

Figure 3-12. Structural drawings of $PyPepSH_2$ (*left*) and $[Fe^{III}(PyPepS)_2]^-$

water molecules were slightly negative to the extent that the complex 'lost' about two electrons and, hence, the calculated spectrum was that of a positive ion, rather than the original negative one. We turned to DRF that has been implemented in ZINDO for open shell ground states within the Rumer-CI scheme [158,159]. In the usual SMD/ZINDO/DRF procedure the spectrum was calculated for the complex immersed in 200 water molecules. The result was half satisfying: the 400–500 nm band was in perfect agreement with experiment but beyond 500 nm the spectrum was empty. This is probably due to the use of a minimal basis set for a negative ion, and the parameterization for Fe. Then we turned to TDDFT, using a DZ basis of Slater-type orbitals and arrived at the spectra in Figures 3-13 and 3-14 [160].

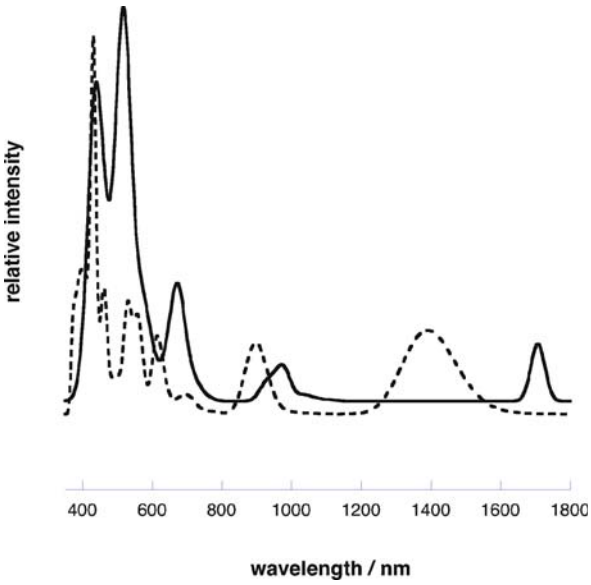

Figure 3-13. Gas phase spectrum (*solid line*) and spectrum of a single solute–solvent configuration (*dashed line*). Vertical transitions are convoluted by Gaussians with a width of 0.14 eV. Data from Ref. [160]

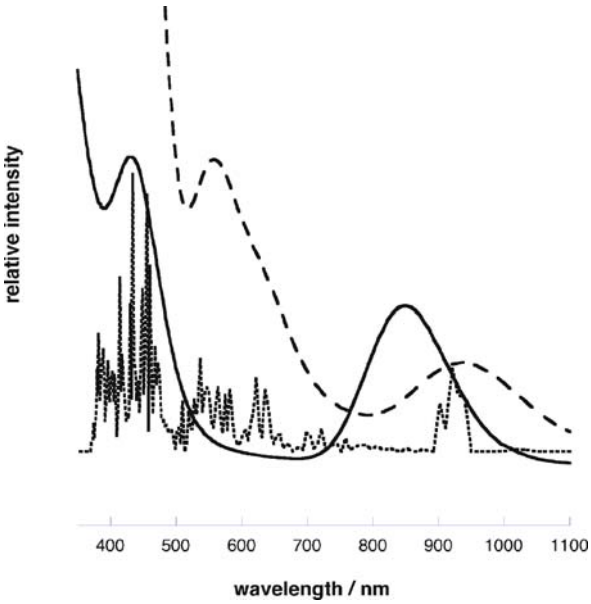

Figure 3-14. Experimental (*solid line*) and calculated (*dashed line*) spectra of $[Fe^{III}(PyPepS)_2]^-$ in water. Calculated spectrum obtained by collecting the vertical transitions of 25 solute–solvent configurations in 60 equal energy intervals, then convoluted with Gaussians with width of 0.3 eV. The dotted spectrum is collected in 200 intervals without convoluting

In Figure 3-13 the vacuum spectrum, comprising 100 vertical transitions, is superimposed on that of a single solute–solvent configuration. The latter shows the expected blue shift with respect to the gas phase: the excited state charge distribution sees a solvent polarization belonging to the ground state. In Figure 3-14 the spectrum is collected from 25 solute–solvent configurations and is compared with the experimental spectrum. It shows an overall red shift of about 70–120 nm. This means errors of ca. 0.3 eV in the high-energy part of the spectrum and ca. 0.1 eV in the low-energy region. This is more or less normal in spectra calculated with TDDFT [161,162,163]. The overall agreement with the experimental spectrum is satisfactory, and our conclusion is that this combination of TDDFT and DRF is promising for further investigations on the actual enzyme.

3.4.2.4. Circular dichroism spectrum of $[Co(en)_3]^{3+}$ in water

Chirality is an important topic in chemistry and biochemistry, due to the natural occurrence of chiral molecules in living organisms. In circular dichroism (CD) one measures the differential absorption of left- and right-handed circularly polarized light, which for chiral species are different. Therefore, CD has turned out to be a powerful tool which provides information on the electronic and geometric structure of chiral molecules. Since most CD spectra are measured in solution we extended our DRF/TDDFT method to also calculate such properties. As a first example we studied

the CD spectrum of a transition metal complex, $[Co(en)_3]^{3+}$, in aqueous solution [164]. Transition metal complexes are often chiral, so CD is used experimentally to characterize the compounds. The complex $[Co(en)_3]^{3+}$ represents a good benchmark system since there are several theoretical and experimental studies and since the CD spectrum of the complex is dominated by a single conformer.

The CD spectrum of the complex in aqueous solution was obtained by averaging over several snapshot configurations obtained from classical polarizable MD simulations. The convergence of the CD spectrum was shown to be quick with a required number of snapshots of the order of 50. It was demonstrated that by using mixed coarse/fine grained parallel computation this kind of averaging can be obtained within a few hours of turnaround time in a routine fashion.

Although, the DRF model predicts a blue shift of the CD bands above 35×10^3 cm^{-1}, a perfect agreement with experiment was not obtained since all the calculated intensities are much larger than what is found experimentally. Also, the DRF method predicts a weak band around 40×10^3 cm^{-1} which is not visible experimentally. The DRF results were compared with results obtained from the much simpler COSMO model, which showed very similar trends although larger shifts were found with the COSMO model. It was suggested that the weak band around 40×10^3 cm^{-1} was very sensitive to the local structure of the solvent, but this could be ruled out since the DRF results did not show a significant lowering of this band.

Although, the agreement with experiments did not show a significant improvement over the simpler COSMO model we are still confident that the combination of DRF with TDDFT is computationally an attractive solution for calculating chiro-optical properties of molecules in solution when the explicit solvent structure is of interest.

3.4.3. (Hyper-)polarizabilities and Macroscopic Properties in Solution

Non-linear optical (NLO) properties of molecules are very sensitive to solvent effects and it is therefore essential to include these effects directly in the calculations in order to accurately describe NLO properties. This makes the accurate prediction of molecular response properties in the condensed phase of great interest, both from a theoretical and a technological point of view, since materials exhibiting NLO effects are of fundamental technological importance for use in future application within electronics and photonics. Accurate calculations of NLO properties of molecules are difficult due to the strict requirements of the level of theory used, i.e., correlation and basis set with many diffuse functions are required. Attempts to calculate effective static (hyper)polarizabilities in the condensed phase go, in our group, 10 years back [110] in which we showed that it is to be expected that such properties are smaller than in the gas phase. The next one describes the static (hyper)polarizability of acetone in 11 different solvents, modeled with both the continuum and the discrete approach [24]. The conclusion was that in the continuum approach all values are larger, e.g., like in the work of Cammi et al. [165], Luo et al. [166] and Dehu et al. [167]. The latter two even suggest a strong correlation between the (non-)linear

Table 3-10. Comparison of the molecular properties of water in the gas phase. All results are in a.u.

Method	μ	α	β	γ
CCSD (gas)	0.73	9.52	−19.26	1942
DFT (gas)	0.71	9.97	−20.41	2021.3
Exp. (gas)	0.73	9.83	−19.2±5%	1800±8%
CCSD/MM	1.07	10.04	12.21	2169
DFT/DRF	1.04	10.13	8.57	2117.6

Data from Refs. [26,31,32].

properties and the dielectric constant of the solvent. This is a consequence of the inflation of density in a stabilizing-only environment, and the neglect of the role of the local fields. Wortmann and Bishop [131] pointed out that errors in the local field factors can lead to significant errors, both in calculated and experimental values. In contrast with the continuum approach, with discrete solvents [24,168] all effective static properties appeared to be smaller than in the gas phase for all solvents, and virtually independent of the dielectric constant. For example, α^{sol} is expected to be larger than α^{vac} for the reason given above: for a real solution the molecular charge distribution is stabilized. In contrast, $\alpha^{\text{eff}} < \alpha^{\text{vac}}$ due to the field from the dipoles induced in the immediate environment. At the time, in Ref. [24], a small basis set was used and all interaction (reaction) potentials and fields were expanded around the solute's nuclei [10]. With a single calculation using a large basis set and 'exact' potentials and fields, i.e., expectation values of the appropriate QM operators, the difference with the gas phase was much smaller.

Next, DRF was introduced in the response module of ADF [32] and the local field problem was reformulated and used to study solvent effects on the NLO properties of water, acetonitrile [26], *p*-nitroaniline (pNA) [169] and fullerene clusters. Here we summarize results for water and pNA since they are representative of the method.

3.4.3.1. Response properties of liquid water

Although water is not the first material that springs to mind when talking about NLO properties it has certain interesting properties. First, the size of the molecule is small, so that large basis sets and high-level theory can be used which provides a means of benchmarking new methods, a feature particularly important when dealing with TDDFT. In addition to this, water exhibits a sign change in the first hyperpolarizability upon solvation [170], a trend not reproduced with simple continuum models. As a benchmark of the DRF model we compared the results with coupled cluster (CCSD) results obtained both in the gas phase and for a single average water structure obtained from MD simulations [16]. The experimental and calculated results are summarized in Table 3-10.

From Table 3-10 it is clear that the DRF model compares extremely well with the results obtained from the more computational demanding CCSD method, both

in the gas phase and for the average liquid structure. The only exception seems to be the first hyperpolarizability where the DFT/DRF result is smaller than that of CCSD/MM. However, this difference probably arises from the short-range damping of the many-body polarization operator which is not included in the CCSD/MM model. The good agreement indicates that one needs only to benchmark the DFT in the gas phase. Although the small water cluster did not provide a realistic model of liquid water, it did provide a benchmark for the DRF model.

To go beyond a single average water structure, and capture the dynamic fluctuations of the properties of water molecules in liquid water, we selected 101 different water structures from a 50-ps SMD simulation of 256 water molecules. By comparing results from different configurations, information is obtained about the sensitivity of different response properties due to the dynamic fluctuations in the local molecular environment. This is illustrated in Figure 3-15 where the calculated linear polarizability, first hyperpolarizability and second hyperpolarizability are plotted as a function of the different configurations. All the properties show significant fluctuations, illustrating the importance of sampling over several molecular configurations in order to describe the solvent effect. This is particularly clear when considering the first hyperpolarizability that shows particularly large fluctuations. In fact, only on average does the first hyperpolarizability show the experimentally observed sign change [170], whereas many of the individual configurations retain a negative value.

While the above discussion clearly highlights the importance of including solvent effects in the calculations , the calculated properties cannot be compared directly with experimental results. This is mainly caused by the many different conventions used for representing hyperpolarizabilities and susceptibilities. However, the calculated properties can be combined with appropriate, calculated Lorentz/Onsager local field factors to obtain macroscopic susceptibilities that can be compared with experimental results. For water, we used this to calculate the refractive index and the third harmonic generation (THG) and the electric field-induced second harmonic (EFISH) non-linear susceptibilities. The results are collected in Table 3-11.

In order to make possible the comparison presented in Table 3-11 we converted the experimental values to match the conventions used in this work. Due to a myriad of different conventions used in defining the NLO properties this conversion is rather complicated but necessary when comparing with literature values. In addition to correcting for differences in conventions [129], we also adopted a different reference value for THG experiments on fused silica and EFISH experiments on quartz [171,172]. The combined effects of these, clearly makes a comparison between theory and experiments more difficult, since differences in convention and accuracy of reference values can obscure any agreement.

The agreement between the TDDFT/DRF results and experiment is very good for the refractive index and for the THG susceptibility. However, for EFISH we find that the theoretical results are smaller by almost a factor of three as compared with thewill be reflected in the snapshots and, therefore, hopefully describe the rotational contribution to the susceptibility.

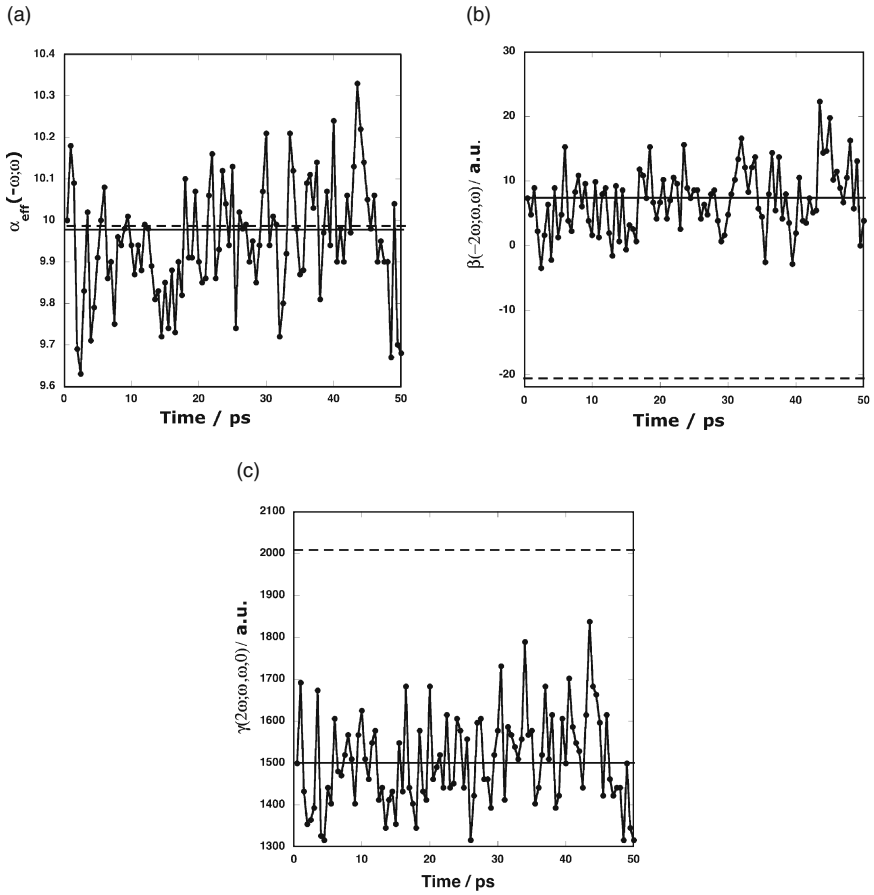

Figure 3-15. Fluctuations in effective linear polarizability (**a**), first (**b**) and second (**c**) hyperpolarizability as function of simulation time from 50 ps MD runs. Vacuum values (*dashed lines*) and average values (*solid lines*) are included

Table 3-11. Macroscopic response properties of liquid water. The frequency is $\omega = 0.0428$ a.u. $\chi^{(3)}$ is in units of 10^{-14} esu

	$n(\omega)$	$n(2\omega)$	$\chi^{(3)}_{\mathrm{THG}}$	$\chi^{(3)}_{\mathrm{EFISH}}$
DFT/DRF[a]	1.334	1.342	1.07	4.1
Exp.	1.326[b]	1.333[c]	1.29[b]	10.5[d]

[a]Ref. [26]; [b]Ref. [183]; [c]Ref. [184]; [d]Ref. [185].

3.4.3.2. The first hyperpolarizability of pNA in 1,4-dioxane solution

Molecules which contain donor and acceptor groups connected by some conjugated bridge (so-called push–pull molecules) are important candidates for new materials based on their strong NLO properties, particularly as SHG material. The prototypical push–pull molecule is *p*-nitroaniline (pNA) and it is therefore no surprise that there are numerous studies, both experimentally and theoretically, of its NLO properties. The molecular quantity that governs the SHG properties of materials is the first hyperpolarizability, $\beta(-2\omega; \omega, \omega)$, a quantity which can be measured using either with EFISH or hyper-Rayleigh scattering (HRS) techniques. In the gas phase the experimental value for the first hyperpolarizability of pNA is found to be 1072 ± 44 a.u. using the EFISH technique. In 1,4-dioxane solution values are found between 1359 and 1482 a.u. at 1064 nm using both HRS and EFISH measurements [129,171,173]. The increase in the first hyperpolarizability upon solvation in 1,4-dioxane is therefore found experimentally to be around 30%. We were therefore interested in seeing whether the DFT/DRF method can accurately describe the NLO properties of pNA and the increase due to solvation. Again, we performed SMD simulations of pNA in 1,4-dioxane solution, where 100 different solvent configurations, well separated in time, were selected. The results of the QM/MM calculations are presented in Table 3-12.

From Table 3-12 we see that the calculated solvent shift for β is calculated to be 30%, which is in excellent agreement with the experimental data. It is also evident that the calculated β is larger by a factor of two, both in the gas phase and in the solution. Several different possible causes of the differences between theory and experiments were explored. Calculations of β of a series of small molecules were all found to be in good agreement with experiments in the gas phase, indicating that the TDDFT method used can accurately describe the NLO properties [169]. To test the TDDFT/DRF model we also calculated the refractive index of 1,4-dioxane which shows good agreement with the experimental value. In the calculations we assumed that the structure of pNA is close to being planar which could explain some of the discrepancy between theory and experiment. Calculating β as an average over many pNA conformations is possibly the solution to this problem. On the other hand, this may also have to do with the problems TDDFT has with pull–push systems: in the

Table 3-12. Static and frequency-dependent properties of pNA in gas phase and 1,4-dioxane solution

Method	μ/D	β^{SHG}
DFT(gas)	7.73	2127
Exp(gas)	6.87	1072±44
DFT/DRF(1,4-dioxane)	10.62±0.06	2771±26
Exp. (1,4-dioxane)[a]	–	1359[a], 1409[a], 1482[b]

[a]Ref. [173]; [b]Ref. [186].

series of test calculations nitro-benzene also showed a β value from DFT that is more than twice the experimental one.

3.4.4. Chemistry in Solution

DRF is also used for modeling chemical events in solution. One example was used as a test to see if it could describe the simple dissociation of *ter*-butyl-chloride in water. The other is a numerical experiment on tautomerism of biologically important compounds, done because experiments are difficult or impossible.

3.4.4.1. The dissociation of ter*-butyl-chloride in water*

For describing the dissociation of *ter*-butyl-chloride (*t*ButCl), we performed MC calculations on $t\text{But}^+$, Cl^- and tetramethylammonium, $(CH3)_4N^+$ (TMA^+). TMA^+ is used as a benchmark because the experimental hydration energy of $t\text{But}^+$ is unknown. We calculated the 'solvated' minimal energy reaction path (MERP) as obtained from the gas phase, i.e., the Cl atom is stepwise removed from the central carbon atom, while the geometry of the *t*But group was optimized.

First Cl^-, $t\text{But}^+$ and TMA^+ were solvated by 62 water molecules, the temperature was 298 K, for equilibration 5×10^5 steps and for sampling 1×10^6 steps were used. This was repeated for the waters without solute, as reference. We used the Metropolis scheme without any sophistication. The charges on water were taken from ab initio calculations, the polarizabilities were set at the experimental values [60]. For the long-range interactions we added—for a number of accepted MC configurations—a dielectric continuum with $\varepsilon\approx80$. As boundary we took the solvent-accessible Connolly surface [174]. The free energy of cavitation was estimated from Pierotti's expression [175]. The results are given in Table 3-13.

The parameterization for Cl^- is apparently not perfect, most likely because the size is somewhat off. Noting that the experimental entropy change $\Delta S_{solv}(Cl^-)$ = –18.4 cal/(mol K) [176] the experimental change in enthalpy will—at 298 K—be $\Delta U_{solv}(Cl^-)$ = –81.4 kcal/mol, a number that must be compared with the –74 kcal/mol in Table 3-13.

The calculated free energy of TMA^+ is in good agreement with experiment, and therefore we had confidence in that for $t\text{But}^+$ as well. Next, we solvated 15 points along the vacuum MERP of the dissociation of *ter*-ButCl. We applied the MC

Table 3-13. Solvation energies (kcal/mol)

	ΔU_{int} [a]	ΔG_{solv} [a]	ΔG_{solv} [b]	ΔG_{tot}	ΔG_{exp}
$t\text{But}^+$	−43	−30	−15	−45	–
Cl^-	−74	–62	−19	−81	−76.0
TMA^+	−40	−34	−17	−51	−50.4

[a] From the MC calculations on the discrete system.
[b] Continuum contribution: $\Delta G_{solv} = \Delta G_{es} + \Delta G_{cav}$.

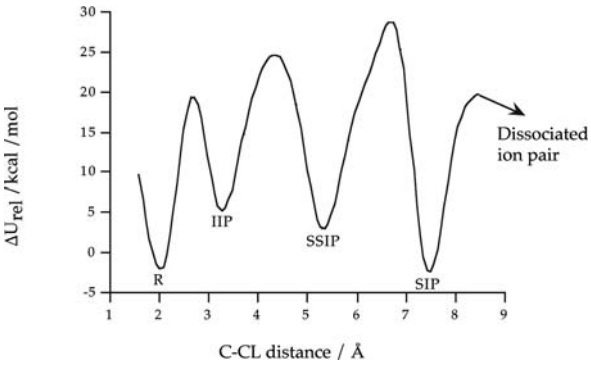

Figure 3-16. Minimum energy reaction path (MERP) for hydrolysis of *ter*-butyl-chloride (tBut) in water. Calculated was the potential of mean force for 15 points along the vacuum MERP of tBut immersed in 124 water molecules. For symbols see text

sampling again, now with 124 water molecules, adding the solvation energies to the corresponding values of the MERP energies, to arrive at the potential of mean force in solution by equilibrating each point on the MERP. Figure 3-16 gives an impression of the results.

From Figure 3-16, the four stages of Winstein [177] emerge clearly: the reactants (R), the intimate ion pair (IIP) at a longer C–Cl distance without water yet inserted, the solvent-separated IP with about a single water molecule between *t*But and the chloride ion, the solvent-separated IP (SSIP) and the separated IP(SIP) where both ions are solvated, but still strongly interacting, and, finally, the dissociated IP at infinite dilution. The calculated energy of activation (20 kcal/mol) for the rate-determining step, R→IIP, is in good agreement with the experimental value of Winstein et al. [176]. Even with this modest simulation the results are satisfactory, in particular because no specific parameterization was used. A similar study on the structure and stability of Li- and Na-carboxylate, -sulfate and -phosphate complexes is reported in Ref. [178].

3.4.4.2. Tautomerism of substituted cyclic imidazoline

The amidine group, –NH–C(R)=N– , occurs in numerous biologically active compounds, which include amino acids, antivirial, antibacterial, antifungal, antihypertensive drugs, and pesticides. Prototropic tautomerism in compounds containing this group is exceptionally difficult to study using the current experimental physicochemical methods because the proton transfer from the amino to the imino nitrogen is very fast and separation of individual tautomers is impossible. 2-Amino-2-imidazoline, 2-amino-2-oxazoline and 2-amino-2-thiazoline moieties are part of many important drugs (e.g., agonists and antagonists of α-adrenoreceptors, drugs binding to imidazoline receptors and inhibitors of neuronal Na^+ channels) and could be present in two tautomeric forms (amino and imino species). The absence of experimental energetic and structural data of amino–imino tautomeric equilibrium presents a

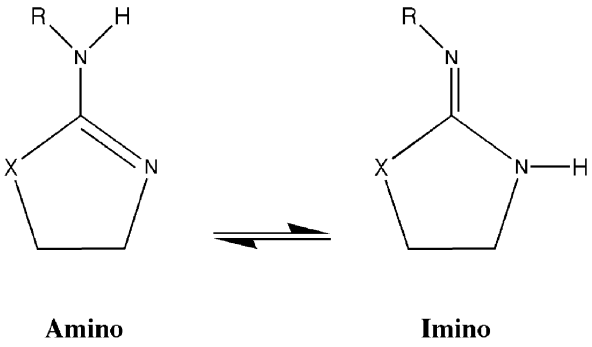

Figure 3-17. Scheme of amino–imino tautomerism, X=N, O; R=CH_3, Phenyl

challenge to quantum-chemical methods to obtain some insight into the reactivity of these compounds.

Here we summarize the results of a systematic theoretical examination of amino and imino tautomers in the systems schematically shown in Figure 3-17 based on DFT model chemistry in the gas phase and in water. In particular the equilibrium constant K_T = [amino tautomer]/[imino tautomer] for the process of Figure 3-17 was studied. The imino tautomers exhibit in general larger dipole moments and, hence are expected to have greater affinity to water and therefore a smaller K_T. In Table 3-14 the K_T values in the gas phase and in aqueous solution, obtained applying the MD module of DRF90 [87] for the solutes in 100 water molecules, are listed.

The values support the expectations on the shift of the equilibrium toward the imino form going from vacuum to solution with the exception of methyl derivatives of oxazoline and thiazoline of which the amino tautomers appear to be most

Table 3-14. Gas phase Gibbs energies and equilibrium constants[a]

	System	ΔG (kJ/mol)	K_T
1	Gas phase	−6	10
	Solution	30	6×10^{-6}
2	Gas phase	15	445
	Solution	3	4
3	Gas phase	−9	39
	Solution	−73	6×10^{12}
4	Gas phase	10	0
	Solution	70	6×10^{-13}
5	Gas phase	−9	44
	Solution	54	4×10^{-10}
6	Gas phase	8	23
	Solution	74	7×10^{-33}

[a]Data from Ref. [179].

stable in water. Probably the strong intramolecular hydrogen bonds of the N—H···O and N—H···S type, not present in the imino forms, play an important role. More information can be found in Ref. [179].

3.5. SUMMARY AND CONCLUSION

In this chapter we described the discrete reaction field (DRF) approach for handling condensed phase problems in computational chemistry. DRF focuses on a quantum-chemical treatment of the system of interest (the solute) while the rest of the (large) system is represented by discrete molecules or groups of atoms (the solvent) which are treated classically (QM/MM approach). The discrete parts are modeled by point charges and explicit polarizabilities obtained from high-level quantum-mechanical calculations on monomers without (or with minimal) fitting to experimental or to otherwise obtained results. This makes the parameters very transferable. Degrees of freedom of the solvent (MM) are treated by statistical mechanics techniques (e.g., molecular dynamics) with a force field that is parameterized in the same way. Although resulting in reasonable results, the least satisfying part of the force field used lies in the ad hoc short-range repulsion potentials needed to keep molecules sufficiently apart in (half) classical simulations. Because such potentials do not affect the electrons in QM/MM calculations, the electronic charge distributions are most likely too diffuse. This is a matter of further development.

We discussed DRF in perspective with other methods, gave the theoretical background and addressed the implementation. In a short section on the validation of DRF we showed that we can treat a system with QM, MM or QM/MM without significant loss of accuracy. A set of examples of its application ranges from simple solvation energies, spectra to (hyper)polarizabilities and processes of excited states of molecules in solution. These examples employ DRF in combination with—ab initio or semi-empirical—conventional wave function and DFT techniques.

We conclude that DRF is a flexible and reliable method for the treatment of condensed phase systems in computational chemistry.

ABBREVIATIONS

a.u.	atomic units energy: 1 a.u. = 1 Hartree = 627.5 kcal/mol = 2625.5 kJ/mol length: 1 a.u. = 1 Bohr = 52.917726 10^{-12} m charge: 1 a.u. = 1e = 1.60217733 10^{-19} C
ADF	Amsterdam density functional
AIMD	Ab initio molecular dynamics
ARF	Average reaction field
BSSE	Basis set superposition error
CT	Charge transfer
CCSD(T)	Coupled cluster with singles and doubles (+ perturbative triplets)
CD	Circular dichroism

CISD	Configuration interaction with singles and doubles
DFT	Density functional theory
DRF	Discrete (or direct) reaction field
DZP	Double-zeta + polarization functions
EFISH	Electric field induced second harmonic generation
ESP	Electrostatic potential
e.s.u	Electrostatic units
HF	Hartree-Fock
lhs	left hand side
MC	Monte Carlo
MCSCF	Multi-configurational self consistent field
MD	Molecular dynamics
MM	Molecular mechanics
MPn	Møller Plesset n-order perturbation
PCM	Polarizable continuum model
PES	Potential energy surface
PT	Perturbation theory
QM/MM	Quantum mechanics/molecular mechanics
RHF	Restricted Hartree-Fock
rhs	right hand side
ROHF	Restricted open shell Hartree-Fock
RP	Reaction potential
SAPT	Symmetry adapted perturbation theory
SCF	Self consistent field
SMC	Sequential Monte Carlo
SMD	Sequential molecular dynamics
TDDFT	Time dependent density functional theory
TZP	Triple zeta + polarization basis set

REFERENCES

1. Ballhausen, C., (1965) private communication.
2. Warshel, A. and Levitt M., *Theoretical studies of enzymatic reactions: dielectric, electrostatic, and steric stabilization of the carbenium ion in the reaction of Lysozyme.* J. Mol. Biol.: (1976) **103** 227–249.
3. Thole, B.T. and Duijnen P.Th. van, *On the quantum mechanical treatment of solvent effects.* Theor. Chim. Acta: (1980) **55** 307–318.
4. Singh, U.C. and Kollman P.A., *A combined ab initio quantum mechanical and molecular mechanical method for carrying out simulations on complex molecular systems: applications to the $CH_3Cl + Cl^-$ exchange reaction and gas phase protonation of polyethers.* J. Comput. Chem.: (1986) **7** 718–730.
5. Bash, P.A., Field M.J. and Karplus M., *Free Energy Perturbation Method for Chemical Reactions in the Condensed Phase: A Dynamical Approach Based on a Combined Quantum and Molecular Mechanics Potential.* J. Am .Chem.Soc.: (1987) **109** 8092–8094.

6. Field, M.J., Bash P.A. and Karplus M., *A combined quantum mechanical and molecular mechanical potential for molecular dynamics simulations.* J. Comput. Chem.: (1990) **11** 700–733.
7. Karelson, M.M. and Zerner M.C., *Theoretical treatment of solvent effects on electronic spectroscopy.* J.Phys.Chem.: (1992) **96** 6949–6957.
8. Luzhkov, V. and Warshel A., *Microscopic models for quantum mechanical calculations of chemical processes in solutions: LD/AMPAC and SCAAS/AMPAC calculations of solvation energies.* J. Comput. Chem.: (1992) **13** 199–213.
9. Tomasi, J. and Persico M., *Molecular interactions in solution: an overview of methods based on continuous distributions of the solvent.* Chem. Rev.: (1994) **94** 2027–2094.
10. Vries, A.H. de, Duijnen P.Th. van, Juffer A.H., Rullmann J.A.C., Dijkman J.P., Merenga H. and Thole B.T., *Implementation of reaction field methods in quantum chemistry codes.* J. Comput. Chem.: (1995) **16** 37–55;1445–1446.
11. Jansen, G., Colonna F. and Ángyán J.G., *Mixed Quantum-Classical Calculations on the Water Molecule in Liquid Phase: Influence of a Polarizable Environment on Electronic Properties.* Int. J. Quantum Chem.: (1996) **58** 251.
12. Gao, J., *Hybrid Quantum and Molecular Mechanical Simulations: An Alternative Avenue to Solvent Effects in Organic Chemistry.* Accounts of Chemcal Research: (1996) **29** 298–305.
13. Tuñón, I., Martins-Costa M. T. C, Millot C., Ruiz-López M. F. and Rivail J. L., *A Coupled Density Functional-Molecular Mechanics Monte Carlo Simulation Method: The Water Molecule in Liquid Water.* J.Comput.Chem.: (1996) **17** 19–29.
14. Cramer, C.J. and Truhlar D.G., *Implicit Solvation Models: Equilibria, Structure, Spectra, and Dynamics.* Chem. Rev.: (1999) **99** 2161–2200.
15. Orozco, M. and Luque F.J., *Theoretical Methods for the Description of the Solvent Effect in Biomolecular Systems.* Chem. Rev.: (2000) **100** 4187–4225.
16. Poulsen, T.D., Ogilby P.R. and Mikkelsen K.V., *Linear repsonse for solvated molecules MC/SCF/MM.* J.Chem.Phys.: (2002) **116** 3730–3738.
17. Tomasi, J., *Thirty years of continuum solvation chemistry: a review, and prospects for the near future.* Theor.Chem.Acc: (2004) **112** 112–203.
18. Öhrn, A. and Karlström G., *A theoretical study of the solvent shift to the n-p transition in formaldehyde with an effective discrete quantum chemical solvent model including non-electrostatic perturbation.* Mol. Phys.: (2006) **104** 3087–3099.
19. Barone, V., Cossi M. and Tomasi J., *A new definition of cavities for the computation of solvation free energies by the polarizable continuum model.* J. Chem.Phys.: (1997) **107** 3210–3221.
20. Swart, M., Rösler E. and Bickelhaupt F.M., *Proton Affinities in Water of Maingroup-Element Hydrides. Effects of Hydration and Methyl Substitution.* Eur. J. Inorg. Chem.: (2007) 3646–3654.
21. Chen, F. and Chipman D.M., *Boundary element methods for dielectric cavity construction and integration.* J. Chem.Phys.: (2003) **119** 10289–10297.
22. Mennucci, B. and Tomasi J., *Continuum solvation models: A new approach to the problem of solute's charge distribution and cavity boundaries.* J. Chem.Phys.: (1997) **106** 5151–5158.
23. Cossi, M., Rega N., Scalmani G. and Barone V., *Polarizable dielectric model of solvation with inclusion of charge penetration effects.* J. Chem.Phys.: (2001) **114** 5691–5701.
24. Duijnen, P.Th. van, Vries A.H. de, Swart M. and Grozema F.C., *Polarizabilities in the Condensed Phase and the Local Fields Problem. A Direct Reaction Field formulation.* J.Chem.Phys.: (2002) **117** 8442–8453.
25. Rullmann, J.A.C. and Duijnen P.Th. van, *Analysis of discrete and continuum dielectric models; application to the calculation of protonation energies in solution.* Mol. Phys.: (1987) **61** 293–311.
26. Jensen, L., M.Swart and Duijnen P.Th. van, *Microscopic and macroscopic polarization within a combined quantum mechanics and molecuar mechanics model.* J. Chem.Phys.: (2005) **122** 034103.

27. Chalasinski, G. and Szczesniak M.M., *Origins of Structure and Energetics of van der Waals Clusters from ab Initio Calculations.* Chem. Rev.: (1994) **94** 1723–1765.
28. Wesolowski, T. and Warshell A., *Ab Initio Free Energy Perturbation Calculations of Solvation Free Energy Using the Frozen Density Functional Approach.* J.Phys.Chem: (1994) **98** 5183–5187.
29. Car, R. and Parinello M., *Unified approach for molecular dynamics and density-functional theory.* Phys.Rev.Lett.: (1985) **55** 2471–2474.
30. Gao, J. and Thompson M.A., eds. Combined Quantum Mechanical and Molecular Mechanics Methods. Vol. 712. 1998, ACS: Washington, DC.
31. Jensen, L., Duijnen P.Th. van and Snijders J.G., *A discrete solvent reaction field model for calculating molecular linear response properties in solution.* J.Chem.Phys.: (2003) **119** 12998–13006.
32. Jensen, L., Duijnen P.Th. van and Snijders J.G., *A discrete reaction field model within density functional theory.* J.Chem.Phys.: (2003) **118** 514–521.
33. Batista, E.R., Xantheas S.S. and Jónsson H., *Multipole moments of water molecules in clusters and ice Ih from first principles calculations.* J. Chem.Phys.: (1999) **111** 6011–6015.
34. DelleSite, L., Alevi A. and Lynden-Bell R.M., *The electrostatic properties of water molecules in condensed phases: an ab initio study.* Mol. Phys.: (1999) **96** 1683–1693.
35. Jensen, L., Astrand P.-O., Osted O., Kongsted J. and Mikkelsen K.V., *A dipole interaction model for the polarizability.* J. Chem. Phys.: (2002) **116** 4001–4010.
36. Engkvist, O., Åstrand P.-O. and Karlström G., *Accurate Intermolecular Potentials Obtained from Molecular Wave Functions: Bridging the Gap between Quantum Chemistry and Molecular Simulations.* Chem. Rev.: (2000) **100** 4087–4108.
37. Tu, Y. and Laaksonen A., *On the effect of Lennard-Jones parameters on the quantum mechanical and molecular mechanical coupling in a hybrid molecular dynamics simulation of liquid water.* J. Chem.Phys.: (1999) **111** 7519–7525.
38. Thole, B.T. and Duijnen P.Th. van, *The direct reaction field hamiltonian: analysis of the dispersion term and application to the water dimer.* Chem.Phys.: (1982) **71** 211–220.
39. Brooks, B.R., Bruccoleri R.E., Olafson B.D., States D.J., Swaminathan S.J. and Karplus M., *CHARMM: a program for macromolecular energy, minimization and dynamical calculations.* J. Comput. Chem.: (1983) **4** 187–217.
40. Rullmann, J.A.C. and Duijnen P.Th. van, *A polarizable water model for calculation of hydration energies.* Mol. Phys.: (1988) **63** 451–475.
41. Rullmann, J.A.C., Bellido M.N. and Duijnen P.Th. van, *The active site of Papain. All-atom study of interactions with protein matrix and solvent.* J. Mol. Biol.: (1989) **206** 101–118.
42. Ahlström, P., Wallqvist A., Engström S. and Jönsson B., *A molecular dynamics study of polarizable water.* Mol. Phys.: (1989) **68** 563–581.
43. Kuwajima, S. and Warshel A., *Incorporating Electric Polarizabilities in Water-Water Interaction Potentials.* J.Phys. Chem.: (1990) **94** 460–466.
44. Dang, L.X., *Development of nonadditive intermolecular potentials using molecular-dynamics - solvation of Li+ and F- ions in polarizable water.* J. Chem.Phys.: (1992) **96** 6970–6977.
45. Soetens, J.-C. and Milot C., *Effect of distributing multipoles and polarizabilities on molecular dynamics simulations of water.* Chem. Phys. Lett.: (1995) **235** 22–30.
46. Thomson, M.A. and Schenter G.K., *Excited States of the Bacteriochlorophyll b Dimer of Rhodopseudomonas viridis: A QM/MM Study of the Photosynthetic Reaction Center That Includes MM Polarization.* J. Phys. Chem.: (1995) **99** 6374–386.
47. Day, P.N., Jensen J.H., Gordon M.S., Webb S.P., Stevens W. J., Krauss M., Garmer D., Bash H. and Cohen D., *An effective fragment method for modeling solvent effects in quantum mechanical calculations.* J. Chem.Phys.: (1996) **105** 1968–1986.

48. Dang, L.X. and Chang T.-M., *Molecular dynamics study of water clusters, liquid, and liquid–vapor interface of water with many-body potentials.* J. Chem.Phys.: (1997) **106** 8149–8159.
49. Gao, J., *Energy components of aqueous solution: Insight from hybrid QM/MM simulations using a polarizable solvent model.* J. Comput. Chem.: (1997) **18** 1061–1071.
50. Burnham, C.J., Li J., Xantheas S. and Leslie M., *The parametrization of a Thole-type all-atom polarizable water model from first principles and its application to the study of water clusters (n=2–21) and the phonon spectrum of ice Ih.* J. Chem.Phys.: (1999) **110** 4566–4581.
51. Halgren, T.A. and Damm W., *Polarizable force fields.* Curr. Opin. Struct. Biol.: (2001) **11** 236–242.
52. Poulsen, T., Kongsted J., Osted A., Ogilby P.R. and Mikkelsen K.V., *The combined multiconfigurational self-consistent-field/molecular mechanics wave function approach.* J. Chem.Phys.: (2001) **115** 2393–2400.
53. Dupuis, M., Aida M., Kawahsima Y. and Hirao K., *A polarizable mixed Hamiltonian model of electronic structure for micro-solvated excited states. I. Energy and gradients formulation and application to formaldehyde..* J.Chem.Phys.: (2002) **117** 1242–1255.
54. Jorgensen, W.L., Chandraskhar J., Madura J.D., Impey R.W. and Klein M.L., *Comparison of simple potential functions for simulating liquid water.* J.Chem.Phys.: (1983) **79** 926–935.
55. Rullmann, J.A.C. and Duijnen P.Th. van, *Potential energy models of biological macromolecules: a case for ab initio quantum chemistry.* CRC Reports in Molecular Theory: (1990) **1** 1–21.
56. Kongsted, J., Osted A., Mikkelsen K.V. and Christiansen O., *Molecular electric properties of liquid water calculated using the combined coupled cluster/molecular mechanics method.* J. Mol.Struct. (THEOCHEM): (2003) **632** 207–225.
57. Applequist, J., Carl J.R. and Fung J.K., *Atom dipole interaction model for molecular polarizability. Application to polyatomic molecules and determination of atom polarizabilities.* J.Am.Chem.Soc.: (1972) **94** 2947–2952.
58. Silberstein, L., *Molecular refractivity and atomic interaction. II.* Philos.Mag: (1917) **33** 521–533.
59. Thole, B.T., *Molecular polarisabilities calculated with a modified dipole interaction.* Chem.Phys.: (1981) **59** 341–350.
60. Duijnen, P.Th. van and Swart M., *Molecular and atomic polarizabilities.* J.Phys.Chem.A.: (1998) **102** 2399–2407.
61. Mooij, W.T.M., Duijneveld F.B. van, Rijdt J.G.C.M. van Duijneveldt-van de and Eijck B.P. van, *Transferable ab Initio Intermolecular Potentials. 1. Derivation from Methanol Dimer and Trimer Calculations.* J. Phys. Chem. A: (1999) **103** 9872–9882.
62. Kaminski, G. A., Stern H. A., Berne B. J., Friesner R. A., Cao Y. X., Murphy R. B., Zhou R. and Halgren T. A., *Development of a Polarizable Force Field For Proteins via Ab Initio Quantum Chemistry: First Generation Model and Gas Phase Tests.* J.Comput.Chem.: (2002) **23** 1515–1531.
63. Ren, P. and Ponder J.W., *Consistent Treatment of Inter- and Intramolecular Polarization in Molecular Mechanics Calculations.* J. Comput. Chem.: (2002) **23** 1497–1506.
64. Kaminski, G. A., Friesner R. A. and Zhou R., *A Computationally Inexpensive Modification of the Point Dipole Electrostatic Polarization Model for Molecular Simulations.* J.Comput.Chem.: (2003) **24** 267–276.
65. Yu, H. and Gunsteren W.F. van, *Accounting for polarization in molecular simulation.* Comp. Phys. Comm.: (2005) **172** 69–85.
66. Elking, D., Darden T. and Woods R.J., *Gaussian Induced Dipole Polarization Model.* J. Comput. Chem.: (2006) **28** 1261–1274.
67. Møller, C. and Plesset M.S., *Note on an Approximation Treatment for Many-Electron Systems.* Phys.Rev.: (1934) **46** 618–622.

68. Breneman, C.M. and Wiberg K.B., *Determining atom-centered monopoles from molecular electrostatic potentials. The need for high sampling density in formamide conformational analysis.* J. Comput. Chem.: (1990) **11** 361–373.
69. Swart, M., Duijnen P.Th. van and Snijders J.G., *A charge analysis derived from an atomic multipole expansion.* J.Comput.Chem.: (2001) **22** 79–88.
70. Bachrach, S. M., ed. *Population Analysis and Electron Densities from Quantum Mechanics*. Reviews of Computational Chemistry, ed. K.B. Lipkowitz and D.B. Boyd. Vol. 5. 1994, VCH: Weinheim. 171–227.
71. Grozema, F., Zijlstra R.W.J. and Duijnen P.Th. van, *Many-body interactions calculated with the direct reaction field model.* Chem.Phys.: (1999) **246** 217–227.
72. Bukowski, R., Szalewicz K., Groenenboom G.C. and Avoird A.van der, *Predictions of the Properties of Water from First Principles.* Science: (2007) **315** 1249–1252.
73. Axilrod, P. M. and Teller E., *Interaction of the van der Waals Type Between Three Atoms.* J. Chem. Phys.: (1943) **11** 299–300.
74. Duijnen, P.Th. van and Vries A.H. de, *The "direct reaction field" force field: a consistent way to connect and combine quantum-chemical and classical descriptions of molecules.* Int. J. Quantum Chem.: (1996) **60** 1111–1132.
75. Broer, R., Duijnen P.Th. van and Nieuwpoort W.C., *Ab initio molecular orbital calculations on the active site of papain.* Chem. Phys. Lett.: (1976) **42** 525–529.
76. Thole, B.T., Duijnen P.Th. van and Hol W.G.J., *On the role of the active site a-helix in papain.* Biophys. Chem.: (1979) **9** 273–280.
77. Duijnen, P.Th. van, Thole B.T., Broer R. and Nieuwpoort W.C., *Active-site a-helix in papain and the stability of the ion-pair* $RS^{-}\ldots ImH^{+}$. Int. J. Quantum Chem.: (1980) **17** 651–671.
78. Thole, B.T. and Duijnen P.Th. van, *Reaction field effects on proton transfer in the active site of Actinidin.* Biophysical Chemistry: (1983) **18** 53–59.
79. Duijnen, P.Th. van and Thole B.T., *Environmental effects on proton transfer. Ab initio calculations on systems in a semi-classical, polarizable environment.*, in Quantum Theory of Chemical Reactions., R. Daudel, et al., Editors. 1982, D.Reidel Publishing Company: Dordrecht. p. 85–95.
80. Dijkman, J.P. and Duijnen P.Th. van, *Papain in aqueous solution and the role of Asp-158 in the mechanism: an ab initio SCF+DRF+BEM study.* International Journal of Quantum Chemistry, Quantum Biology Symposium: (1991) **18** 49–59.
81. Coutinho, K., Oliveira M.J.D. and Canuto S., *Sampling configurations in Monte Carlo simulations for quantum mechanical studies of solvent effects.* Int. J. Quantum Chem.: (1998) **66** 249–253.
82. Coutinho, K. and Canuto S., *The sequential Monte Carlo-quantum mechanics methodology. Application to the solvent effects in the Stokes shift of acetone in water.* J. Mol.Struct. (THEOCHEM): (2003) **632** 235–246.
83. Dupuis, M., Farazdel A., Karma S.P. and Maluendes S.A., *HONDO: a general atomic and molecular electronic structure system*, in MOTECC-90, E. Clementi, Editor. 1990, ESCOM: Leiden. p. 277–342.
84. Zerner, M.C., *ZINDO, A General Semi-empirical Program Package*. 1990, Quantum Theory Project, University of Florida: Gainesville (Fl.) USA.
85. Guest, M.F., Lenthe J.H. van, Kendrick J. and Sherwood P., *GAMESS(UK)*. 1999, Daresbury Laboratory: Cheshire England.
86. Baerends, E.J., Autschbach J., Bérces A., Bickelhaupt F.M., Bo C., Boerrigter P.M., Cavallo L., Chong D.P., L. Deng, Dickson R.M., Duijnen P.Th. van, Ellis D.E., Faassen M. van, L. Fan T.H. Fischer, Guerra C. Fonseca, Gisbergen S.J.A. van, Groeneveld J.A., Gritsenko O.V., Grüning M., Harris F.E., Hoek P. van den, Jacob C.R., Jacobsen H., Jensen L., Kessel G. van, Kootstra F., Lenthe E. van, McCormack D.A., Michalak A., Neugebauer J., Nicu V.P.,

Osinga V.P., Patchkovskii S., Philipsen P.H.T., Post D., Pye C.C., Ravenek W., Ros P., Schipper P.R.T., Schreckenbach G., Snijders J.G., Solà M., Swart M., Swerhone D., Velde G. te, Vernooijs P., Versluis L., Visscher L., Visser O., Wang F., Wesolowski T.A., Wezenbeek E.M. van, Wiesenekker G., Wolff S.K., Woo T.K., Yakovlev A.L. and Ziegler T., *Amsterdam Density Functional Theory*. 2007, SCM: Amsterdam.

87. Swart, M. and Duijnen P.Th. van, *DRF90: a Polarizable Force Field.* Mol. Simul.: (2006) **32** 471–484.
88. McWeeny, R., *Methods of Molecular Quantum Mechanics*. 1989, London: Academic Press.
89. Mehler, E.L., *Self-consistent, nonorthogonal group function approximation for polyatomic systems. I. Closed shells.* J.Chem.Phys.: (1977) **67** 2728–2739.
90. Mehler, E.L., *Self-consistent, nonorthogonal group function approximation for polyatomic systems. II. Analysis of noncovalent interactions.* J.Chem.Phys.: (1981) **74** 6298–6306.
91. Mehler, E.L., *Self-consistent, nonorthogonal group function approximation: An ab initio approach for modelling interacting fragments and environmental effects.* J. Mathematical Chemistry: (1992) **10** 57–91.
92. Stone, A. J., *The Theory of Intermolecular forces*. 1996, Oxford: Clarendon.
93. Kutzelnigg, W., *Stationary perturbation theory.* Theor. Chim. Acta: (1992) **83** 263–312.
94. Buckingham, A.D., *Basic theory of intermolecular forces: applications to small molecules*, in Intermolecular Interactions: From Diatomics to Biopolymers, B. Pullman, Editor. 1978, John Wiley & Sons: Chichester. p. 1–67.
95. Avoird, A. van der, Wormer P.E.S., Mulder F. and Berns R.M., *Ab initio studies of the interactions in van der Waals molecules*, in Topics in Current Chemistry, F.L. Boschke, Editor. 1980, Springer Verlag: Berlin. p. 1–51.
96. Margenau, M. and Kestner N. R., *Theory of Intermolecular forces*. 1969, Oxford: Pergamon.
97. Unsöld, A., *Quantentheorie des Wasserstoffmolekülions und der Born-Landéschen Abstoßungskräfte.* Z.Phys.: (1927) **43** 563–574.
98. London, F., *Theory and systematics of molecular forces.* Z.Phys.: (1930) **63** 245–279.
99. Casimir, H.B.G. and Polder D., *The Influence of Retardation on the London-van der Waals Forces.* Phys. Rev.: (1948) **73** 360–372.
100. Claverie, P., *Elaboration of approximate formulas for the interaction between large molecules: application in organic chemistry*, in Intermolecular Interactions: From Diatomics to Biopolymers, B. Pullman, Editor. 1978, John Wiley & Sons: Chichester. p. 69–305.
101. Boys, S.F. and Bernardi F., *The calculation of small molecular interactions by the differences of separate total energies. Some procedures with reduced errors.* Mol. Phys.: (1970) **19** 553–566.
102. Duijneveldt, F.B. van, Rijdt J.G.C.M. van Duijneveldt-van de and Lenthe J.H. van, *State of the art in counterpoise theory.* Chem. Rev.: (1994) **94** 1873–1885.
103. Thole, B.T. and Duijnen P.Th. van, *A general population analysis preserving the dipole moment.* Theor. Chim. Acta: (1983) **63** 209–221.
104. Mulliken, R.S., *Electronic population analysis on LCAO–MO molecular wave functions II. Overlap populations, bond orders, and covalent bond energies.* J.Chem.Phys.: (1955) **23** 1841–1846.
105. Jensen, F., *Introduction to Computational Chemistry*. 1999, Chichester, UK: Wiley.
106. Wiberg, K.B. and Rablen P.R., *Comparison of atomic charges derived via different procedures.* J.Comput.Chem.: (1993) **14** 1504–1518.
107. Sigfridsson, E. and Ryde U., *Comparison of methods for deriving atomic charges from the electrostatic potential and moments.* J.Comput.Chem.: (1998) **19** 377–395.
108. Jensen, L., Swart M., Duijnen P.Th. van and Snijders J.G., *Medium perturbations on the molecular polarizability calculated with a localized dipole interaction model.* J.Chem.Phys.: (2002) **117** 3316–3320.

109. Augspurger, J.D. and Dykstra C.E., *Evolution of polarizabilities and hyperpolarizabilities with molecular aggregation: A model study of acetylene clusters.* Int.J. Quantum Chem.: (1992) **43** 135–146.
110. Duijnen, P.Th. van, Swart M. and Grozema F., *QM/MM calculation of (hyper)polarizabilities with the DRF approach.*, in Hybrid Quantum Mechanical and Molecular Mechanics Methods, J.Gao and M.A. Thompson, Editors. 1999, ACS Books: Washington, DC. p. 220–232.
111. Kirtman, B., Dykstra C.E. and Champagne B., *Major intermolecular effects on nonlinear electrical response in a hexatriene model of solid state polyacetylene.* Chem.Phys.Lett.: (1999) **305** 132–138.
112. Fraga, S., Saxena K.M.S. and Karwowski J., *Handbook of Atomic Data*. Physical Sciences Data 5. 1976, Amsterdam: Elsevier.
113. Böttcher, C.J.F. and Bordewijk P., *Theory of electric polarization*. 2nd ed. Vol. II. 1978, Amsterdam: Elsevier.
114. Sadlej, A.J., *Medium-size polarized basis-sets for high-level-correlated calculations of molecular electric properties. 4. Third row atoms - Ge through Br.* Theor. Chim. Acta: (1991) **81** 45–63.
115. Sadlej, A.J., *Medium-size polarized basis-sets for high-level-correlated calculations of molecular electric properties. 5. Fourth row atoms - Sn through I.* Theor. Chim. Acta: (1991) **81** 339–354.
116. Werner, H-H. and W.Meyer, *Static dipole polarizabilities of small molecules.* Mol. Phys.: (1976) **31** 855–872.
117. Gisbergen, S.J.A. van, Osinga V.P., Gritsenko O.V., Leeuwen R. van, Snijders J.G. and Baerends E.J., *Improved density functional theory results for frequency-dependent polarizabilities, by the use of an exchange-correlation potential with correct asymptotic behavior.* J.Chem.Phys.: (1996) **105** 3142–3161.
118. Champagne, B., Perpète E.A., Gisbergen S.J. A. van, Baerends E.J., Snijders J.G., Soubra-Ghaoui C., Robins K.A. and Kirtman B., *Assessment of conventional density functional schemes for computing the polarizabilities and hyperpolarizabilities of conjugated oligomers: An ab initio investigation of polyacetylene chains.* J.Chem.Phys.: (1998) **109** 0489–10498.
119. Gisbergen, S.J.A. van, Schipper P.R.T., Gritsenko O.V., Baerends E.J., Snijders J.G., Champagne B. and Kirtman B., *Electric Field Dependence of the Exchange-Correlation Potential in Molecular Chains.* Phys. Rev. Lett.: (1999) **83** 694–697.
120. Gritsenko, O. and Baerends E.Jan., *Asymptotic correction of the exchange – correlation kernel of time-dependent density functional theory for long-range charge-transfer excitations.* J.Chem.Phys.: (2004) **121** 655–660.
121. Neugebauer, J., Gritsenko O. and Baerends E.J., *Assessment of a simple correction for the long-range charge-transfer problem in time-dependent density-functional theory.* J.Chem.Phys.: (2006) **124** 214102.
122. Paricaud, P., Predota M., Chialvo A.A. and Cummings P.T., *From dimer to condensed phases at extreme conditions: Accurate predictions of the properties of water by a Gaussian charge polarizable model.* J. Chem. Phys.: (2005) **122** 244511.
123. Jackson, J.D., *Classical Electrodynamics*. 1975, New York: John Wiley & Sons.
124. Juffer, A.H., Botta E.F.F., Keulen B.A.M. van, Ploeg A. van der and Berendsen H.J.C., *The electric potential of a macromolecule in a solvent: a fundamental approach.* J.Comput.Phys.: (1991) **97** 144–171.
125. Eichinger, M., Tavan P., Hutter J. and Parrinello M., *A hybrid method for solutes in complex solvents: Density functional theory combined with empirical force fields.* J. Chem. Phys.: (1999) **110** 10452–10467.
126. Takahashi, H., Hori T., Hashimoto H. and Nitta T., *A hybrid QM/MM method employing real space grids for QM water in the TIP4P water solvents.* J.Comput.Chem.: (2001) **22** 1252–1261.

127. Müller, W., Flesch J. and Meyer W., *Treatment of intershell correlation effects in ab intio calculations by use of core potentals. Method and application to alkali and earth atoms.* J. Chem. Phys.: (1984) **80** 3297–3310.
128. Frecer, V. and Miertus S., *Polarizable continuum model of solvation for biopolymers.* Int. J.Quant. Chem.: (1992) **42** 1449–1468.
129. Willetts, A., Rice J.E., Burland D.M. and Shelton D.P., *Problems in the comparison of theoretical and experimental hyperpolarizabilities.* J. Chem Phys.: (1992) **97** 7590–7599.
130. Shelton, D.P. and Rice J.E., *Measurements and Calculations of the Hyperpolarkabilities of Atoms and Small Molecules in the Gas Phase.* Chem. Rev.: (1994) **94** 3–29.
131. Wortmann, R. and Bishop D.M., *Effective polarizabilities and local field corrections for nonlinear optical experiments in condensed media.* J.Chem.Phys.: (1998) **108** 1001–1007.
132. Lorentz, H.A., *The Theory of Electrons*. 1st. ed. 1909, Leizig: B.G. Teubner.
133. Boyd, R.W., *Nonlinear Optics*. 1992, San Diego: Academic Press.
134. Prasad, P.N. and Williams D.J., *Introduction to Nonlinear Optical Effeects in Molecules and Polymers*. 1991, New York: Wiley.
135. Butcher, P..N and Cotter D, *The Elements of Nonlinear Optics*. 1st ed. 1990, Cambridge: Cambridge University Press.
136. Jensen, L. and Duijnen P. Th. van, *The Discrete Solvent Reaction Field model: A Quantum mechanics/Molecular mechanics model for calculating nonlinear optical properties of molecules in the condensed phase.*, in Atoms, molecules and clusters in electric fields. Theoretical approaches to the calculation of electric polarizability, G. Maroulis, Editor. 2006, Imperial College Press: London. p. 1–43.
137. Duijnen, P.Th. van and Rullmann J.A.C., *Intermolecular interactions with the direct reaction field method.* Int. J. Quantum Chem.: (1990) **38** 181–189.
138. Dunning, T.H. and Hay P.J., *Gaussian basis sets for molecular calculations*, in Methods in Electronic Structure Theory, H.F. Schaefer III, Editor. 1977, Plenum: New York. p. 1–27.
139. Soper, A.K., *The radial distribution functions of water and ice from 220 to 673 K and at pressures up to 400 MPa.* Chem. Phys.: (2000) **258** 121–137.
140. Neusser, H.J. and Krause H., *Binding Energy and Structure of van der Waals Complexes of Benzene.* Chem. Rev.: (1994) **94** 1829–1843.
141. Sinnokrot, M.O. and Sherrill C.D., *Highly Accurate Coupled Cluster Potential Energy Curves for the Benzene Dimer: Sandwich, T-Shaped, and Parallel-Displaced Configurations.* J. Phys. Chem. A: (2004) **108** 10200–10207.
142. Swart, M., Wijs T. van der, Guerra C.Fonseca and Bickelhaupt F. M., *π-π stacking tackled with density functional theory.* J. Molec. Model.: (2007) in press.
143. Battaglia, M.R., Buckingham A.D. and Williams J.H., *The electric quadrupole moments of benzene and hexafluorobenzene.* Chem. Phys. Lett.: (1981) **78** 421–423.
144. Arunan, E. and Gutowsky H.S., *The rotational spectrum, structure and dynamics of a benzene dimer.* J.Chem.Phys.: (1993) **98** 4294–4296.
145. Kolos, W. and Roothaan C.C J., *Accurate Electronic Wave Functions for the H2 Molecule.* Rev. Mod. Phys.: (1960) **32,** 219–232.
146. Chalasinski, G., Szczesniak M.M., Cieplak P. and Scheiner S., *Ab initio study of intermolecular potential of Hz0 trimer.* J. Chem. Phys.: (1991) **94** 2873–2882.
147. Dunning, T.H., *Gaussian basis sets for use in correlated molecular calculations. I. The atoms boron through neoen and hydrogen.* (1989) **90** 1007–1023.
148. Schuddeboom, W., Jonker S.A., Warman J.M., Haas M.P. de, Vermeulen M.J.W., Jager W.F., Lange B. de, Feringa B.L. and Fessendens R.W., *Sudden Polarization in the Twisted, Phantom*

State of Tetraphenylethylene Detected by Time-Resolved Microwave Conductivity. J. Am. Chem. SOC: (1993) **115** 3286–3290.

149. Schilling, C.L. and Hilinski∗ E.F., *Dependence of the Lifetime of the Twisted Excited Singlet State of Tetraphenylethylene on Solvent Polarity.* J. Am .Chem.SOc.: (1988) **110** 2296–2298.
150. Ma, J. and Zimmt M.B., *Equilibration between the fluorescent and zwitterionic phantom states in alkyl-substituted tetraphenylethylenes.* J. Am .Chem.SOc.: (1992) **114** 9723–9724.
151. Zijlstra, R. W.J., Grozema F. C., Swart M., Feringa B. L. and Duijnen P. Th. van, *Solvent Induced Charge Separation in the Excited States of Symmetrical Ethylene: A Direct Reaction Field Study.* J.Phys.Chem.A: (2001) **105** 3583–3590.
152. Zijlstra, R.W.J., Duijnen P.Th. van, Feringa B.L., Steffen T., Duppen K. and Wiersma D.A., *Excited state dynamics of tetraphenylethene: ultrafast Stoke shift, isomerization and charge separation.* J.Phys.Chem.A: (1997) **101** 9828–9836.
153. Grozema, F.C., M.Swart, Zijlstra R.J.W., Piet J.J., Siebbeles L.D.A. and Duijnen P. Th. van, *QM/MM study of the role of the solvent in the formation of the charge separated excited state in 9,9'-bianthryl.* J. Am .Chem.SOc.: (2005) **127** 11019–11028.
154. Vries, A.H. de and Duijnen P.Th. van, *Solvatochroism of the $\pi*¨n$ transition of acetone by combined quantum mechanical–classical mechanical calculations.* Int. J. Quantum Chem.: (1996) **57** 1067–1076.
155. Duijnen, P.Th. van and Netzel T.L., *Explicit Solvent DRF INDOs/CIS Computations of Charge Transfer State Energetics in a Pyrenyldeoxyuridine Nucleoside Model.* J.Phys. Chem. A: (2006) **110** 2204–2213.
156. Mitchell, C.D. and Netzel T.L., *CIS INDO/S SCRF study of electron transfer excige states in a 1-pyrenyl substituted 1-methyluracil-5-carboxamide nucleoside: dielctric continuum solvation effects on electron transger states.* J.Phys.Chem. B: (2000) **104** 125–136.
157. Duijnen, P.Th. van, *ZINDO/DRF*, in *ZINDO, A General Semi-empirical Program Package*, M.C. Zerner, Editor. 1998, Quantum Theory Project, University of Florida: Gainesville (Fl.) USA. p. unpublished.
158. Duijnen, P.Th. van, *ZINDO/DRF_RUMER_CI*, in *ZINDO, A General Semi-empirical Program Package*, M.C. Zerner, Editor. 2003, Quantum Theory Project, University of Florida: Gaines-Gainesville (Fl.) USAville. p. unpublished.
159. Manne, R. and Zerner M.C., *Matrix elements of spin-dependent one-electron operators between bonded functions.* Int. J. Quantum Chem.Quantum Chemistry Symposium: (1986) **19** 165–172.
160. Duijnen, P.Th. van, Greene S.N. and Richards N.G.J., *Time dependent density functional theory/discrete reaction field spectra of open-shell systems: the visual spectrum of $[Fe^{III}(PyPepS)_2]^-$ in aqueous solution.* J.Chem.Phys.: (2007) **127** 045105.
161. Hirata, S. and Head-Gordon M., *Time-dependent density functional theory within the Tamm– Dancoff approximation.* Chem.Phys.Lett.: (1999) **314** 291–299.
162. Rinkevicius, Z., Tunell I., Salek P., Vahtras O. and Ågren H., *Restricted DFT theory of linear time-depnendent properties in open- shell molecules.* J. Chem. Phys.: (2003) **119** 34–46.
163. Wang, F. and Ziegler T., *Excitation energies of some d1 systems calculated using time-dependent density functional theory: an implementation of open-shell TDDFT theory for doublet–doublet excitations.* Mol.Phys: (2004) **102** 2585 – 2595.
164. Jensen, L., M.Swart, Duijnen P.Th. van and Autschbach J., *The circular dichroism spectrum of [Co(en)3] 3+ in water.* Int. J. Quantum Chem.: (2006) **106** 2479–2488.
165. Cammi, R., Cossi M. and Tomasi J., *Analytical derivatives for molecular solutes. III. Hartree – Fock static polarizability and hyperpolarizabilities in the polarizable continuum model.* J. Chem Phys.: (1996) **104** 4611–4620.

166. Luo, Y., Norman P. and Ågren H., *A semiclassical approximation model for properties of molecules in solution.* J. Chem. Phys.: (1998) **109** 3589–3595.
167. Dehu, C., Geskin V., Persoons A. and Brédas J.-L., *Effect of medium polarity on the secnd order polarizabiity of an ocupolar chromophore: an ab initio reation field study.*. Eur. J. Org. Chem.: (1998) 1267–1269.
168. Morita, A. and Kato S., *An ab initio analysis of medium perturbation on molecular polarizabilities.* J.Chem.Phys.: (1999) **110** 11987–11998.
169. Jensen, L. and Duijnen P.Th. van, *The first hyperpolarizability of p-nitroaniline in 1,4-dioxane: A quantum mechanical/molecular mechanics study.* J. Chem. Phys.: (2005) **213** 074307.
170. Mikkelsen, K.V., Luo Y., H.Ågren and Jørgensen P., *Sign change of hyerpolarizablities of solvated water.* J. Chem Phys.: (1995) **102** 9362–9367.
171. Kaatz, P. and Shelton D.P., *Polarized hyper-Rayleigh light scattering measurements of nonlinear optical chromophores.* J. Am .Chem.SOc.: (1996) **105** 3918–3929.
172. Shoji, I., Kondo T. A. and Ito R., *Second-order nonlinear susceptibilities of various dielectric and semiconductor materials.* Opt.Quantum Electr.: (2002) **34** 797–833.
173. Stähelin, M., Burland D.M. and Rice J.E., *Solvent dependence of the second order hyperpolarizability in p-nitroaniline.* Chem. Phys. Lett.: (1992) **191** 245–250.
174. Connolly, M.L., *Solvent-accessible surface of proteins and nucleic acids.* Science: (1983) **221** 709–713.
175. Pierotti, R.A., *A scaled particle theory of aqueous and nonaqueous solutions.* Chem. Rev.: (1976) **76** 717–726.
176. Winstein, S. and Fainberg A.H., *Correlation of Solvolysis Rates. 1 V.l Solvent Effects on Enthalpy and Entropy of Activation for Solvolysis of &Butyl Chloride2.* J. Am .Chem.Soc.: (1957) **79** 5937–5950.
177. Winstein, S., Clippinger E., Fainberg A.H. and Robinson G.C., *Salt effexts of ion-pairs in solvolysis.* J.Am.Chem.Soc.: (1954) **76** 2597.
178. Remko, M., Duijnen P.Th. van and Lieth C-W. von der, *Structure and stability of Li (I) and Na(I) - carboxylate, sulfate and phosphate complexes.* J.Mol.Struct. (THEOCHEM): (2007) **814** 119–125.
179. Remko, M., Duijnen P.Th. van and Swart M., *Theoretical study of molecular structure, tautomerism, and geometrical isomerism of N-methyl and N-phenyl substituted cyclic imidazolines, oxazolines and thiazolines.* Struct.Chem.: (2003) **14** 271–278.
180. Calvert, J. G. and Pitts J. N., *Photochemistry*. 1966, New York: Wiley. 377.
181. Hayes, W.P. and Timmons C.J., *Solvent and substituent effects on the nÆπ∗ absorption bands of some ketones.* Spectrochim. Acta: (1965) **21** 529–541.
182. Bayliss, N.S. and Wills-Johnson G., *Solvent effects on the intensities and weak ultraviolet spectra of ketones and nitroparaffins - I.* Spectrochim. Acta: (1968) **24A** 551–661.
183. Kajzar, F. and J.Messier, *Third-harmonic generation in liquids.* Phys. Rev. A: (1985) **32** 2352–2363.
184. Levine, B. F. and Bethea C. G., *Effects on hyperpolarizabilities of molecular interactions in associating liquid mixtures.* J. Chem. Phys.: (1976.) **65** 2429–2438.
185. Thormahlen, I., Straub J. and Grigul. U., *Refractive Index of Water and Its Dependence on Wavelength, Temperature, and Density.* J. Phys. Chem. Ref. Data: (1985) **14** 933–945.
186. Teng, C.C. and Garito A.F., *Dispersion of the nonlinear second-order optical susceptibility of organic systems.* Phys. Rev. B: (1983) **28** 6766–6773.
187. Grozema, F.C. and Duijnen P.Th. van, *Solvent effects on the π∗◇n transition in various solvents.* J.Phys.Chem.A: (1998) **102** 7984–7989.

CHAPTER 4

THERMOCHEMICAL ANALYSIS OF THE HYDRATION OF NEUTRAL SOLUTES

AXEL BIDON-CHANAL[1], JOSE MARÍA LÓPEZ[1], MODESTO OROZCO[2], AND F. JAVIER LUQUE[1]

[1]*Departament de Fisicoquímica and Institut de Biomedicina (IBUB), Facultat de Farmàcia, Universitat de Barcelona, Avgda. Diagonal 643, Barcelona 08028, Spain, e-mail: fjluque@ub.edu*
[2]*Institut de Recerca Biomèdica and Instituto Nacional de Bioinformática, Parc Científic de Barcelona, c/. Josep Samitier 1, 08028 Barcelona, Spain; Departament de Bioquímica i Biología Molecular, Facultat de Biología, Avgda Diagonal 647, Barcelona 08028, Spain; Computational Biology Program, Barcelona Supercomputer Center, Jordi Girona 31, Edifici Torre Girona, Barcelona 08028, Spain, e-mail: modesto@mmb.pcb.ub.es*

Abstract: The enthalpic and entropic contributions to the free energy of hydration of a series of neutral solutes are analyzed by means of continuum solvation methods based on the Miertus–Scrocco–Tomasi (MST) method. Particular attention is paid to the partitioning of the enthalpic and entropic components of the hydration free energy into its electrostatic and non-electrostatic terms. The results provide a basis to design further refinements of continuum solvation models

4.1. INTRODUCTION

The solvation of a solute reflects the subtle balance between two opposite components. First, the interaction between solute and solvent molecules, which is a favorable contribution arising from the different intermolecular forces that can be formed depending on the chemical nature of both solute and solvent. Second, the interaction between solvent molecules, which is an unfavorable term due to the disruption of the internal structure of the bulk solvent caused by the presence of the solute. The key magnitude to characterize the transfer of solute from gas phase to solution is the free energy of solvation, ΔG_{sol}, which can be defined as the reversible work required to transfer the solute from the ideal gas phase to solution at a given temperature, pressure and chemical composition [1]. This definition allows us to compute ΔG_{sol} as the difference in the reversible works necessary to "build up" the solute both in solution and in the gas phase.

To determine the coupling work between solute and solvent, it is convenient to decompose ΔG_{sol} into separate, more manageable terms, which typically involves

S. Canuto (ed.), Solvation Effects on Molecules and Biomolecules, 103–113.
DOI 10.1007/978-1-4020-8270-2_4,

electrostatic (ΔG_{ele}) and non-electrostatic ($\Delta G_{n\text{-}ele}$) contributions (Eq. 4-1). The former accounts for the work required to assemble the electric charge distribution of the solute in solution, while the latter is typically used to account for van der Waals interactions (ΔG_{vW}) between solute and solvent molecules, as well as for cavitation (ΔG_{cav}), i.e., the work required to create the cavity that accommodates the solute:

$$\Delta G_{sol} = \Delta G_{ele} + \Delta G_{n\text{-}ele} = \Delta G_{ele} + \Delta G_{cav} + \Delta G_{vW} \tag{4-1}$$

The partitioning scheme shown in Eq. 4-1 has been widely adopted by theoretical chemists to face the challenging question of determining ΔG_{sol} [2,3,4,5,6]. In particular, the adoption of such scheme has been extremely fruitful in the framework of quantum mechanical (QM) self-consistent reaction field (SCRF) continuum models, [7,8,9,10,11] where the solvent is treated as a continuum polarizable medium characterized by suitable macroscopic properties. After a careful parametrization, QM-SCRF models are able to predict with a remarkable accuracy the solvation free energy of a large variety of solutes in different solvents, including water [12,13,14,15,16]. Unfortunately, high accuracy in the total ΔG_{sol} does not necessarily imply the same level of accuracy in the different free energy components, due to the neglect of mutual coupling between the different solvation components [17,18].

An alternative procedure to gain deeper insight into the physico-chemical basis of solvation consists of the partitioning of ΔG_{sol} into its enthalpic, ΔH_{sol}, and entropic, ΔS_{sol}, components. Taken together, these quantities represent a substantial reservoir of information about the interactions between solute and solvent molecules. Moreover, these quantities are state functions and can be rigorously derived by using standard thermodynamic relationships, as noted in Eqs. 4-2 and 4-3. Finally, the availability of experimentally measured data for the enthalpy and entropy of solvation makes it possible to calibrate the reliability of theoretical models to predict those thermodynamic quantities.

$$\Delta G_{sol} = \Delta H_{sol} - T\Delta S_{sol} \tag{4-2}$$

$$\Delta H_{sol} = \Delta G_{sol} - T\left(\frac{\partial G_{sol}}{\partial T}\right)_P \tag{4-3}$$

It can be anticipated that the computation of ΔH_{sol} and ΔS_{sol} is more delicate than the prediction of ΔG_{sol}, which benefits from the enthalpy–entropy compensation. Accordingly, the suitability of the QM-SCRF models to predict the enthalpic and entropic components of the free energy of solvation is a challenging issue, which could serve to refine current solvation continuum models. This contribution reports the results obtained in the framework of the MST solvation model [15] to estimate the enthalpy (and entropy) of hydration for a set of neutral compounds. To this end, we will first describe the formalism used to determine the MST solvation free energy and its enthalpic component. Then, solvation free energies and enthalpies for a series of typical neutral solutes will be presented and analyzed in light of the available experimental data. Finally, collected data will be used to discuss the differential trends of the solvation in water.

4.2. THE MST-PCM CONTINUUM METHOD

Following the formalism of the polarizable continuum model originally developed by Miertus, Scrocco and Tomasi, [19,20] the electrostatic component (ΔG_{ele}) of the total solvation free energy (Eq. 4-1) is determined by using a set of apparent charges spread over the cavity surface (Eq. 4-4), which account for the reaction field created in the solvent by the presence of the solute's charge distribution. Such charges are obtained by solving the Laplace equation with suitable boundary conditions, as noted in Eq. 4-5, where V_T is the total electrostatic potential, which includes both solute and solvent contributions, n is the unit vector normal to the surface element j, S_j is the area of the surface element j and ϵ is the solvent dielectric constant:

$$V_R = \sum_{j=1}^{M} \frac{q_j}{|r_j - r|} \tag{4-4}$$

where V_R is the perturbation operator used to couple the solute's charge distribution and the solvent reaction field, M is the total number of surface elements, j, into which the solute/solvent boundary is divided and q_j is the apparent charge at the j surface element, which is centered at r_j:

$$q_j = -\frac{\varepsilon - 1}{4\pi\varepsilon} S_j \left(\frac{\partial V_T}{\partial \boldsymbol{n}} \right)_j \tag{4-5}$$

The cavitation contribution is determined following Pierotti's scaled particle theory, where ΔG_{cav} is expressed as an expansion series in powers of the radius of the sphere which excludes the centers of the solute molecules from the solute, R_{MS} (i.e., the sum of the solute and solvent radii; Eq. 4-6). The expansion coefficients K_i (i = 0–3) are expressed in terms of properties of the solvent (the radius of the solvent molecule and the numeral density) and of the solution (temperature and pressure):

$$\Delta G_{cav} = K_0 + K_1 R_{MS} + K_2 R_{MS}^2 + K_3 R_{MS}^3 \tag{4-6}$$

Since Pierotti's theory was developed for solutes with spherical shape, its implementation to molecular-shaped cavities is performed by using the procedure proposed by Claverie (Eq. 4-7), [21] where the cavitation free energy of a given atom i is determined from the contribution of the isolated atom, $\Delta G_{cav,i}$, and a weighting factor, w_i, determined from the ratio between the surface of such an atom and the total surface of the sphere generated by that atom:

$$\Delta G_{cav} = \sum_{i=1}^{N} w_i \Delta G_{cav,i} \tag{4-7}$$

where N is the number of atoms.

Finally, the van der Waals term (G_{vW}) is computed using a linear relationship to the solvent-exposed surface of each atom, as noted in Eq. 4-8, where the atomic surface tensions, ξ_i, are determined by fitting to the experimental free energies of solvation for large series of solutes. Note then that those surface tensions not only account for dispersion–repulsion interactions between solute and solvent, but also correct for the implicit assumptions introduced in the evaluation of the remaining components of ΔG_{sol}:

$$\Delta G_{vW} = \sum_{i=1}^{N} \xi_i S_i \tag{4-8}$$

Molecular-shaped GEPOL cavities [22,23] are used to define the solute/solvent interface for the calculations of electrostatic and non-electrostatic (cavitation, van der Waals) terms. In the last parametrization of the MST-PCM model, a dual-cavity strategy was used, [24] so that non-electrostatic contributions are determined by using a van der Waals surface mainly built up from Pauling's radii (in Å; polar hydrogen: 0.9, apolar hydrogen: 1.2, C and N: 1.5, O: 1.4, F: 1.35, S: 1.75 and Cl: 1.80), whereas the electrostatic term is determined by using a solvent-exposed surface created by scaling the atomic radii by a solvent-dependent factor, which for neutral molecules adopts values of 1.25, 1.50, 1.60 and 1.80 for the solvation of neutral compounds in water, octanol, chloroform and carbon tetrachloride [15].

4.3. THE ENTHALPY OF SOLVATION

By analogy with free energy, the solvation enthalpy can be represented by the addition of the corresponding enthalpy components, as noted in Eq. 4-9, where each term might be determined a priori by using the Gibbs–Helmholtz relationship (Eq. 4-3):

$$\Delta H_{sol} = \Delta H_{ele} + \Delta H_{n\text{-}ele} = \Delta H_{ele} + \Delta H_{cav} + \Delta H_{vW} \tag{4-9}$$

Since the electrostatic component of ΔG_{sol} depends on the permittivity of the solvent, ε, and on the cavity size (represented by means of the vector normal to the cavity surface, n), the electrostatic contribution to the enthalpy of solvation, ΔH_{ele}, can be determined as indicated in Eq. 4-10:

$$\Delta H_{ele} = \Delta G_{ele} - T\left[\left(\frac{\partial G_{ele}}{\partial \varepsilon}\right)_{\lambda}\left(\frac{\partial \varepsilon}{\partial T}\right)_{P} + \left(\frac{\partial G_{ele}}{\partial \boldsymbol{n}}\right)_{\varepsilon}\left(\frac{\partial \boldsymbol{n}}{\partial T}\right)_{P}\right] \tag{4-10}$$

The temperature dependence of the solvent permittivity, $(\partial\varepsilon/\partial T)_P$, and of the cavity size, $(\partial \boldsymbol{n}/\partial T)_P$, for water were approximated by empirical values equal to –0.3554 and 2.56 10^{-4} K^{-1},respectively [25]. The values of $(\partial G_{ele}/\partial\varepsilon)$ and $(\partial G_{ele}/\partial \boldsymbol{n})$ were estimated numerically from the ΔG_{ele} values calculated by varying both ε and κ (i.e., the scaling factor used to modulate the size of the cavity;

see above). Numerical derivatives were performed by using increments of ±0.5 and ±1.0 for ε and of ±0.01 and ±0.05 for κ, but the calculated ΔH_{ele} values were little affected by the magnitude of those increments.

Finally, the non-electrostatic components of the hydration enthalpy ($\Delta H_{\text{n-ele}}$) and entropy ($-T\Delta S_{\text{n-ele}}$) can be determined by subtracting the electrostatic enthalpy, ΔH_{ele}, and entropy $-T\Delta S_{\text{ele}}$ from the known experimental quantities.

4.4. EXPERIMENTAL DATA AND COMPUTATIONAL DETAILS

A series of 16 molecules, which include different monofunctional compounds, were chosen to determine the enthalpy of solvation in water. Besides four hydrocarbons (hexane, heptane, octane and cyclohexane) and water, the series of molecules include alcohols (2-methylpropan-2-ol, 1-butanol and 2-butanol), ethers (diethylether, tetrahydrofuran and tetrahydropyran), amines (propylamine, butylamine, diethylamine and dibutylamine) and piperidine. This choice allows us to examine the differences between different functional groups, as well as the influence of the molecular size on the enthalpic contributions for a given series of monofunctional compounds. Free energies of hydration as well as the corresponding enthalpies taken from the data compiled by Cabani and coworkers [26] are shown in Table 4-1.

All MST-PCM calculations were performed at the HF/6-31 G(d) level. As usual in MST calculations the gas phase geometry of the molecules was fully optimized and subsequently used for calculations in solution. Calculations were performed using a locally modified version of Monstergauss [27].

Table 4-1. Experimental free energy, enthalpy and entropy of hydration (kcal/mol) for the series of neutral molecules considered in this study

Compound	ΔG_{exp}	ΔH_{exp}	$-T\Delta S_{\text{exp}}$
Hexane	2.5	−7.6	10.1
Heptane	2.6	−8.1	10.7
Octane	2.9	−9.5	12.4
Cyclohexane	1.2	−7.9	9.2
Water	−6.3	−8.9	2.6
2-Methylpropan-2-ol	−4.5	−15.3	10.8
1-Butanol	−4.7	−14.7	10.0
2-Butanol	−4.6	−15.0	10.4
Diethylether	−1.6	−11.2	9.6
Tetrahydrofuran	−3.5	−11.3	7.8
Tetrahydropyran	−3.1	−11.7	8.6
Propylamine	−4.4	−13.3	8.9
Butylamine	−4.3	−14.1	9.8
Diethylamine	−4.1	−15.6	11.5
Dibutylamine	−3.3	−18.2	14.9
Piperidine	−5.1	−15.6	10.5

To further check the magnitude of the electrostatic enthalpy determined from MST calculations, a series of Monte Carlo (MC) free energy perturbations (FEP) were performed in explicit solvent to determine the dependence of solvation free energy (minus the reversible work needed to annihilate solute charge distribution) on the temperature. For this purpose, MC-FEP estimates of the electrostatic component of the hydration free energy of a small series of solutes were determined at 273, 298 and 323 K. The electrostatic enthalpy, ΔH_{ele}, at 298 K was calculated using the Gibbs–Helmholtz relationship, where the temperature dependence of ΔG_{ele} was estimated numerically from the free energy values obtained at 273 and 323 K. The simulated systems contained a single solute immersed in a cubic box containing around 500 TIP3P water molecules [28,29]. Electrostatic potential-derived atomic charges computed at the HF/6-31 G(d) level were used with standard OPLS van der Waals parameters. A residue-based non-bonded cutoff of 9 Å was used to evaluate intermolecular interactions. The internal geometry of the solute was kept fixed in all simulations. Rotations and translations of the solute and solvent molecules were adjusted to give 40–50% acceptance. MC simulations were run considering 6 million configurations for equilibration of the solute–solvent system. The final structure was used as the starting point in MC-FEP simulations. All simulations were done in the isothermal–isobaric ensemble.

MC-FEP simulations were performed in 21 windows where charges were gradually annealed using the double-wide sampling technique. For each window the system was equilibrated over at least 10 million configurations, and the average was done for 10 million configurations. In all cases the hysteresis and the standard deviations were small, which lends confidence to the protocol of the simulation.

4.5. THERMOCHEMICAL ANALYSIS OF THE HYDRATION

Table 4-2 reports the electrostatic and non-electrostatic components of ΔG_{sol} in water for the series of compounds included in the study computed from MST calculations. The deviation between experimental and calculated free energies of hydration is in general small, as noted in a mean signed errors (mse) close to zero and a root-mean square deviation around 0.9 kcal/mol, which compares with the statistical parameters obtained in the parametrization of the MST model [15].

Inspection of the free energy components points out the dominant role of ΔG_{ele} in water, which amounts to around 145% of the experimental hydration free energy (Table 4-1). In turn, the non-electrostatic term, $\Delta G_{n\text{-}ele}$, gives rise to an unfavorable contribution to the hydration of these compounds, which reflects the larger magnitude of the cavitation term compared to the van der Waals one in water [15]. Overall, except for hydrocarbons, the transfer of polar solutes from the gas phase to water is a favorable process, which mainly originates from the electrostatic interactions between solute and water molecules.

Experimental values indicate that hydration is enthalpically favored, even for hydrocarbons (see Table 4-1). For these compounds, the hydration enthalpy must be ascribed to the dispersion forces between alkanes and water molecules, which do

Table 4-2. Electrostatic and non-electrostatic components of the free energy of solvation in water (kcal/mol) determined at the HF/6-31 G(d) level from MST-PCM calculations

Compound	ΔG_{ele}	$\Delta G_{n\text{-}ele}$	ΔG_{cav}	ΔG_{vW}	ΔG_{sol}
Hexane	0.0	2.5	24.1	–21.6	2.5
Heptane	–0.1	2.8	27.6	–24.7	2.7
Octane	–0.1	3.1	30.9	–27.8	3.0
Cyclohexane	0.0	1.7	20.6	–19.0	1.7
Water	–6.4	–0.3	4.6	–4.9	–6.7
2-Methylpropan-2-ol	–6.0	2.1	18.1	–16.0	–3.9
1-Butanol	–6.4	1.6	18.3	–16.7	–4.8
2-Butanol	–6.0	2.0	18.2	–16.2	–4.1
Diethylether	–3.9	3.2	18.5	–15.3	–0.6
Tetrahydrofuran	–5.0	2.4	15.6	–13.2	–2.6
Tetrahydropyran	–4.6	2.7	4.6	–4.9	–1.9
Propylamine	–6.2	1.5	15.4	–13.9	–4.7
Butylamine	–6.4	1.7	18.8	–17.1	–4.6
Diethylamine	–4.7	2.2	19.2	–17.0	–2.6
Dibutylamine	–5.9	3.2	32.8	–29.6	–2.6
Piperidine	–4.8	1.5	19.0	–17.5	–3.3
mse[a]					–0.5
Rmsd					0.9

[a]Mean-signed error (mse) and root-mean square deviation (rmsd) between experimental and calculated free energies of hydration.

not suffice to compensate the change in entropy, leading to an unfavorable hydration free energy. For polar solutes, nevertheless, the electrostatic interactions with water molecules increase the magnitude (in absolute value) of the hydration enthalpy, which thus counterbalances the entropic term and makes the transfer from gas phase to water solution to be a favorable process.

Table 4-3 shows the enthalpic and entropic components of the electrostatic term of the hydration free energy computed by using Eq. 4-10. The ΔH_{ele} values determined from MST-PCM calculations are similar to the corresponding data derived from MC-FEP calculations for the subset of molecules representative of the different functional groups (2-butanol, tetrahydropyran, dibutylamine and piperidine; see above), thus giving strong support to the reliability of the values reported here. For polar compounds, the electrostatic term plays a significant contribution to the hydration enthalpy, since it accounts on average for $\sim 60\%$ of ΔH_{exp}. Nevertheless, it is clear that even for these compounds the non-electrostatic enthalpy plays a significant stabilizing contribution, as can be noted in the $\Delta H_{n\text{-}ele}$ values obtained by subtracting ΔH_{ele} from ΔH_{exp} (see Table 4-3).

Table 4-3 also shows that the electrostatic entropy term (expressed as $-T\Delta S_{ele}$) has a destabilizing contribution, thus reflecting the decrease in the configurational flexibility of the water molecules arising from the electrostatic forces exerted by the polar solute. This term, however, is notably smaller than the non-electrostatic

Table 4-3. Enthalpic and entropic components of the electrostatic and non-electrostatic terms of the hydration free energy (kcal/mol). The non-electrostatic enthalpy and entropy were determined by subtracting the electrostatic enthalpy and entropy from the corresponding experimental data

Compound	ΔH_{ele} MST	ΔH_{ele} MC-FEP	$-T\Delta S_{ele}$	$\Delta H_{n\text{-}ele}$	$-T\Delta S_{n\text{-}ele}$
Hexane	0.0	–	0.0	–7.6	10.1
Heptane	0.0	–	–0.1	–8.1	10.8
Octane	0.0	–	–0.1	–9.5	12.4
Cyclohexane	–0.1	–	0.1	–7.8	9.1
Water	–7.9	–	1.5	–1.0	1.0
2-Methylpropan-2-ol	–7.8	–	1.8	–7.5	9.0
1-Butanol	–8.3	–	1.9	–6.4	8.1
2-Butanol	–7.8	–8.4	1.8	–7.2	8.6
Diethylether	–5.6	–	1.7	–5.6	7.9
Tetrahydrofuran	–6.6	–	1.7	–4.7	6.2
Tetrahydropyran	–6.0	–4.7	1.5	–5.7	7.1
Propylamine	–8.1	–	2.0	–5.2	6.9
Butylamine	–8.6	–	2.1	–5.5	7.7
Diethylamine	–6.5	–	1.8	–9.1	9.7
Dibutylamine	–8.1	–7.3	2.2	–10.1	12.7
Piperidine	–6.8	–5.5	2.0	–8.8	8.6

entropic term, $-T\Delta S_{n\text{-}ele}$, which can be mainly attributed to the rearrangement of the water molecules originated from the creation of the solute cavity.

Previous studies have shown that there is a correlation between the enthalpy of hydration of alkanes and their accessible surface area [30,31] or related magnitudes. Moreover, relationships between the hydration numbers calculated from discrete simulations for hydrocarbons and both the free energy and enthalpy of hydration of these molecules have also been reported [32] and have been often used to evaluate solvation enthalpies. Analysis of our results, illustrates the existence of a linear relationship between $\Delta H_{n\text{-}ele}$ and the surface of the van der Waals cavity, S_{vW}, defined in MST computations for the calculation of the non-electrostatic contributions (Figure 4-1). In contrast, no relationship was found for the electrostatic component of the hydration enthalpy (ΔH_{ele}; data not shown). Clearly, in a first approximation, one can assume that the electrostatic interactions between solute and solvent can be decoupled from the interactions formed between *uncharged* solutes and solvent molecules.

As noted above for the non-electrostatic component of the hydration enthalpy, a linear relationship between the non-electrostatic component of the entropy, $-T\Delta S_{n\text{-}ele}$, and the van der Waals surface is also found (see Figure 4-1), indicating that this term increases with the size of the compounds. Again, no similar relationship was found for the electrostatic component of the hydration enthalpy. This finding suggests that the entropic reorganization of the water molecules associated

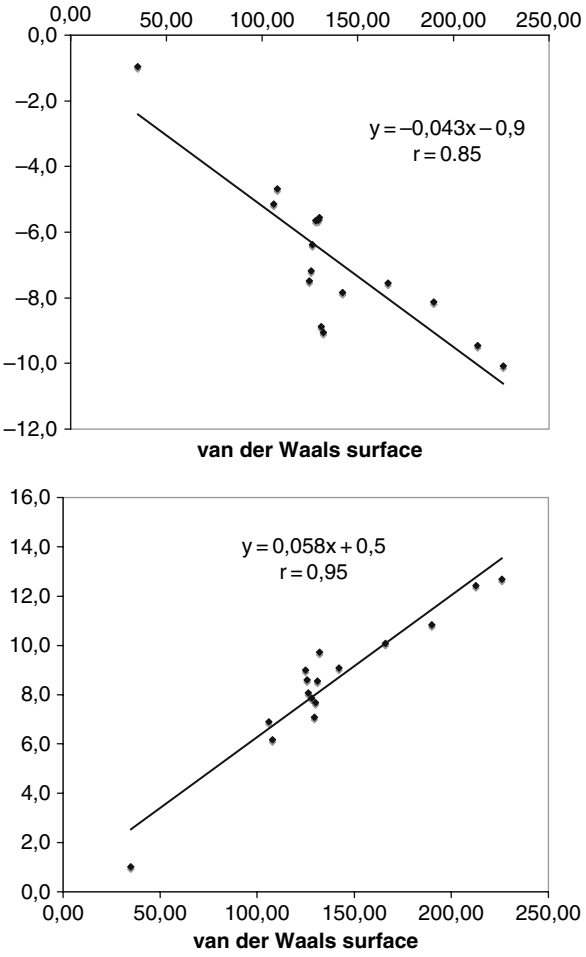

Figure 4-1. Representation of the change in the non-electrostatic component (kcal/mol) of the hydration enthalpy ($\Delta H_{\text{n-ele}}$) and entropy ($-T\Delta S_{\text{n-ele}}$) versus the surface (Å) of the van der Waals cavity used in MST computations

with the hydration of the *uncharged* solutes is largely decoupled from the entropic contribution due to the charging up of the polar compounds in water.

4.6. CONCLUDING REMARKS

The availability of computational procedures to determine the electrostatic and non-electrostatic components of the thermodynamic quantities is necessary to gain a deeper understanding of the processes associated with the transfer of solutes from the gas phase into the bulk solvent. In this work we have examined the partitioning of the

free energy of hydration into its enthalpic and entropic components, paying particular attention to the balance between the electrostatic and non-electrostatic contributions to both enthalpy and entropy.

The results point out the relevant contribution played by electrostatic interactions to the hydration enthalpy of polar solutes. Nevertheless, even for these compounds the non-electrostatic term plays a significant contribution to the hydration enthalpy. The entropic contribution to the hydration is mainly associated with the non-electrostatic terms, which can be mainly attributed to the reorganization of the solvent molecules around the solute cavity, as van der Waals terms are assumed to be essentially enthalpic [31,33].

Interestingly, the results point out that the non-electrostatic enthalpic and entropic components of the hydration process are linearly related with the size of the solutes, and that this relationship holds for both the alkane compounds as well as for the *uncharged* polar molecules examined here. Since only the total free energy of solvation (and its enthalpic and entropic contributions) is experimentally measurable, this finding gives support to the widely used strategy of partitioning the solvation free energy into electrostatic and non-electrostatic components, which is convenient from a practical point of view, but necessarily neglects the coupling between the various components of the solute-solvent interaction potential.

Finally, present results suggest that calibration of solvation models by using not only solvation free energies, but also their enthalpic and entropic components would yield to better balanced and more accurate models, which will be extremely useful to provide a more comprehensive understanding of the forces that mediate the solvation of solutes in diverse solvents.

ACKNOWLEDGMENTS

We are grateful to Prof. J. Tomasi for providing us with his original code of the PCM model, which was modified by us to carry out the MST calculations. This work has been supported by the Ministerio de Ciencia y Tecnología (CTQ2005-08797-C02-01/BQU) the Centre de Supercomputació de Catalunya and the Barcelona Supercomputing Center.

REFERENCES

1. Ben-Naim A (1987) Solvation thermodynamics, Plenum Press, New York
2. Jorgensen WL (1989) Acc Chem Res 22:184
3. Warshel A (1991) Computer modeling of chemical reactions in enzymes and solutions, Wiley, New York
4. Kollman PA (1993) Chem Rev 93:2395
5. Tomasi J, Mennucci B, Cammi R, Cossi M (1997) In: Náray-Szabó G, Warshel A (eds) Computational approaches to biochemical reactivity, Kluwer, Dordrecht, p 1
6. Orozco M, Luque F (2000) J Chem Rev 100:4187
7. Tomasi J, Persico M (1994) Chem Rev 94:2027
8. Rivail JL, Rinaldi D (1995) In: Leszczynski J (ed) Computational chemistry, reviews if current trends, World Scientific, Singapore, p 139

9. Cramer CJ, Truhlar DG (1999) Chem Rev 99:2161
10. Luque F J, Curutchet C, Muñoz-Muriedas J, Bidon-Chanal A, Soteras I, Morreale A, Gelpí JL, Orozco M (2003) Phys Chem Chem Phys 5:3827
11. Tomasi J, Mennucci B, Cammi R (2005) Chem Rev 105:2999
12. Tuñón I, Ruiz-López MF, Rinaldi D, Bertrán J (1996) J Comput Chem 17:148
13. Barone V, Cossi M, Tomasi J (1997) J Chem Phys 107:3210
14. Kelly CP, Cramer CJ, Truhlar DG (2005) J Chem Theory Comput 1:1133
15. Curutchet C, Orozco M, Luque FJ (2001) J Comput Chem 22:1180
16. Forti F, Barril X, Orozco M, Luque FJ (2008) J Comput Chem 29:578
17. Curutchet C, Cramer CJ, Truhlar DG, Ruiz-López MF, Rinaldi D, Orozco M, Luque FJ (2003) J Comput Chem 24:284
18. Curutchet C, Orozco M, Luque FJ, Mennucci B, Tomasi J (2006) J Comput Chem 27:1769
19. Miertus S, Scrocco E, Tomasi J (1981) Chem Phys 55:117
20. Miertus S, Tomasi J (1982) Chem Phys 65:239
21. Claverie P, Daudey JP, Langlet J, Pullman B, Piazzola D, Huron MJ (1978) J Phys Chem 82:405
22. Pascual-Ahuir JL, Silla E, Tomasi J, Bonaccorsi R (1987) J Comput Chem 8:778
23. Silla E, Tuñón I, Pascual-Ahuir JL (1991) J Comput Chem, 9:1077
24. Colominas C, Luque FJ, Teixidó J, Orozco M (1999) Chem Phys 240:253
25. Lide DR (ed) (1999) CRC handbook of chemistry and physics, 80th edn. CRC Press, Boca Raton
26. Cabani S, Gianni P, Mollica V, Lepori L (1981) J Solut Chem 10:563
27. Peterson M, Poirier R (1986) MonsterGauss; Department of Biochemistry, Univ. of Toronto, Canada. Version modified by Cammi R, Tomasi J (1987); and by Curutchet C, Orozco M, Luque FJ (2003)
28. Jorgensen WL, Maxwell DS, Tirado. Rives J (1996) J Am Chem Soc 118:11225
29. Jorgensen WL (1999) BOSS 4.2, Yale University, New Haven, CT
30. Rashin AA, Young L, Topol IA (1994) Biophys Chem 51:359
31. Gallichio E, Kubo MM, Levy R M (2000) J Phys Chem B 104:6271
32. Jorgensen WL, Gao J, Ravimohan C (1985) J Phys Chem 89:3450
33. Amovili C, Mennucci B (1997) J Phys Chem B 101:1051

CHAPTER 5

ELECTRONIC PROPERTIES OF HYDROGEN BOND NETWORKS: IMPLICATIONS FOR SOLVENT EFFECTS IN POLAR LIQUIDS

SILVIA GOMES ESTÁCIO[1], HUGO F. M. C. MARTINIANO[1],
PAULO CABRAL DO COUTO[1], AND BENEDITO JOSÉ COSTA CABRAL[1,2]

[1]*Grupo de Física Matemática da Universidade de Lisboa, Av. Prof, Gama Pinto, 2, 1649-003 Lisboa, Portugal, e-mail: silvia@cii.fc.ul.pt(Silvia Gomes Estácio); hugo.cii.fc.ul.pt(Hugo F. M. C. Martiniano); pcouto@cii.fc.ul.pt(Paulo Cabral do Couto); ben@cii.fc.ul.pt (Benedito José Costa Cabral)*
[2]*Departamento de Química e Bioquímica, Faculdade de Ciências da Universidade de Lisboa, Portugal, e-mail: ben@cii.fc.ul.pt (Benedito José Costa Cabral)*

Abstract: The electronic properties of polar liquids where the structures are characterized by hydrogen bond networks are reviewed. Emphasis is placed on theoretical predictions of liquid state electronic properties such as the electric dipole moment, electron binding energies, and electronic density of states. A discussion on the relationship between the structure of the hydrogen bond (HB) network and the electronic properties of water is presented. Born–Oppenheimer molecular dynamics results for proton transfer (PT) in ionized phenol–water clusters illustrate the link between charge fluctuations of the HB network and the PT dynamics

5.1. INTRODUCTION

Chemical reactions in solution are, in general, processes assisted by the solvent. The reaction mechanisms and kinetics are dependent on structural and energetic fluctuations of the solvent. The classical example is proton transfer in liquid water, which is a fluctuation-induced chemical reaction [1,2]. Several polar solvents are characterized by hydrogen bond (HB) networks and in these cases, solvent effects on the chemical reactivity are strongly dependent on the structure and electronic properties of the network. The water HB network has been the subject of several investigations, which were mainly focused on topological aspects [3,4,5,6]. The HB network is a complex system, characterized by a rich dynamics involving breaking and forming of hydrogen bonds, specific vibrational and diffusion dynamics, which are controlled by collective motions [2,7,8]. The dynamics of the HB network controls reactivity in solution. The slowdown of the water dynamics confined in supramolecular

S. Canuto (ed.), Solvation Effects on Molecules and Biomolecules, 115–133.
DOI 10.1007/978-1-4020-8270-2_5,

assemblies may retard reactions in confined water [9]. Cooperative effects associated with many-body interactions [10] are, in the case of water, the possible explanation for the value of its effective dipole moment in the liquid phase (∼2.6–3.1 D), which corresponds to an increase of ∼40–67% in comparison to the gas phase value (1.855 D). Another relevant feature that illustrates the ability of the HB network of water to reorganize around charged species is that hydrated electrons can be produced by photoabsorption at ∼6.5 eV [11]. This energy is significantly lower than the threshold energy for photoelectron emission by liquid water (10.06 eV) [12]. It is also ∼6 eV below the first ionization potential of the gas phase water molecule (12.62 eV) [13]. The understanding of hydration effects, or solvent effects in water, should rely on the correct description of the electronic properties of the HB network.

Specifically, it should be expected that chemical reactivity in HB solvents is dependent on fluctuations of the HB network [1,14]. Moreover, the ability of water to reorganize about charged species is associated with the dynamics of the HB network, which seems to be controlled by thermal-induced fluctuations [2,8].

Relevant structural information based on first principles molecular dynamics have been reported for water [15,16,17,18,19,20] and ammonia, [21,22] and several recent works were dedicated to the study of the water electronic properties [23,24,25,26,27,28]. On the other hand, the relationship between the local structure of the HB network and electronic properties such as the effective dipole moment in solution or electron binding energies is not well understood and deserves further investigation. The effective molecular dipole moment in solution is related to polarization effects and charge transfer. Electron binding energies are important because they reflect the ability of the HB network to stabilize an excess charge and it is known that electron attachment to polar clusters depends on the total electric multipole moments of the aggregates [29,30].

In this chapter we review recent investigations on the electronic properties of HB liquids, with emphasis on the calculation of the dipole moment and electron binding energies (EBEs) in liquid phase. For liquid water an analysis of the relationship between the local environment of the HB network and the electronic properties is presented. Most of the present results are based on sequential statistical mechanics simulations/quantum mechanics calculations [31,32]. We are also reporting Born–Oppenheimer molecular dynamics [33,34,35] results for neutral phenol–water clusters as well as for the corresponding ionized structures, which are model systems of acid–base reactions. The proton transfer (PT) dynamics in ionized phenol–water clusters and its dependence on charge and energy fluctuations of the water molecules were investigated.

5.2. POLARIZATION EFFECTS AND CHARGE FLUCTUATIONS IN POLAR HYDROGEN BONDING LIQUIDS

5.2.1. Electronic Polarization and the Dipole Moment in Liquid Phase

The increase of the dipole moment in the liquid relative to the gas phase value is related to electronic polarization effects. The experimental dipole moment of

a molecule in the liquid phase is usually based on dielectric measurements [36]. More recently, the electronic density distribution relative to the nuclear positions determined by x-ray diffraction was used to estimate the dipole in liquid water [37]. However, the theoretical estimate of the dipole moment in liquid phase remains a controversial subject [38]. In the specific case of pure water, values in the 2.3–3.1 D range were reported [38]. Different approaches were used to calculate the dipole moment in liquid phase: sequential statistical mechanics/quantum mechanics calculations, [39,40] quantum mechanics/molecular mechanics (QM/MM), [41,42] first principles molecular dynamics, [43] and cluster calculations [44,45,46,47].

One fundamental issue concerns the partitioning of the electronic density and the estimation of the charges associated with a specific molecular unit because different partitioning schemes of the electronic density lead to different values of electric multipoles [48]. This is still a matter of debate and has been discussed by different authors [38].

Sequential statistical mechanics/quantum mechanics (SM/QM) calculations are usually based on the assumption that the structure of the liquid phase is correctly reproduced by the simulation. Therefore, supermolecular structures extracted from the simulation can be used for the QM calculations of the electronic properties. However, when a sequential SM/QM approach is adopted, some issues should be addressed. How does the results depend on the size of the supermolecular structures used in the QM calculations? When a supermolecular structure is defined, an outer surface is introduced and if we are interested in bulk properties it is important to discuss how surface effects can be minimized. This can be carried out by embedding the quantum supermolecular system in the electrostatic field of the surrounding solvent molecules. Usually, the charges representing the liquid environment are those that describe the electrostatic interactions for a given intermolecular potential model [24,25]. Recently, an alternative approach where the embedding charges are determined through an iterative self-consistent procedure has been proposed [49].

It is known that first principles molecular dynamics may overcome the limitations related to the use of an intermolecular interaction model. However, it is not clear that the results for the structure of hydrogen bonding liquids predicted by first principles molecular dynamics simulations are necessarily in better agreement with experiment than those relying on classical simulations, and recent first principles molecular dynamics simulations of liquid water indicated that the results are dependent on the choice of different approximations for the exchange–correlation functional [50]. Cluster calculations are an interesting alternative, although surface effects can be important and extrapolation to bulk phase remains a controversial issue.

The previous discussion pointed out some well-known limitations of the different theoretical approaches currently used to analyse polarization effects and estimate the dipole moment in the liquid phase. We will focus the present analysis of polarization effects in HB liquids on results obtained by using the sequential statistical mechanics/quantum mechanics approach.

Recent sequential molecular dynamics/quantum mechanics (MD/QM) calculations of the water dipole moment [51] using a polarizable model for water [52] indicate that the average dipole moment in the liquid is not dependent on the number

of molecules used in the QM system. On the other hand, this property is more dependent on embedding or inclusion of long-ranged polarization effects of the liquid environment. These conclusions are supported by results for the average dipole moment in liquid water using supermolecular structures (quantum system) with a different number of water molecules. The quantum system can be isolated (non-embedded) or embedded in the charge distribution of the surrounding water molecules. The dependence of the average dipole moment of water on the number of water molecules explicitly included in the quantum system and on the presence of embedding charges is illustrated in Figure 5-1.

In comparison with water, studies on polarization effects in liquid ammonia are scarce [53,54]. Recent sequential molecular dynamics/QM calculations [54] predict that the average dipole moment in liquid ammonia is 2.05 ± 0.09 D, which corresponds to an increase of 27% compared to the gas phase value for the isolated molecule (1.57 D). The dependence of the ammonia dipole moment on the number of ammonia molecules in the supermolecular structures and on the presence of embedding charges representing the liquid environment is illustrated in Figure 5-1 and follows the same trends observed for liquid water. Although polarization effects in liquid ammonia are less important than those observed in liquid water, they are significant enough to be taken into consideration. In conclusion, sequential statistical mechanics/quantum mechanics calculations suggest that the electric dipole moment of liquid water and ammonia can be estimated as a local property and that it is essentially dependent on the adequate treatment of long-ranged polarization effects.

Another very important hydrogen bond solvent is acetonitrile that is characterized by a strong gas phase dipole moment (3.92 D), which may lead to the formation of

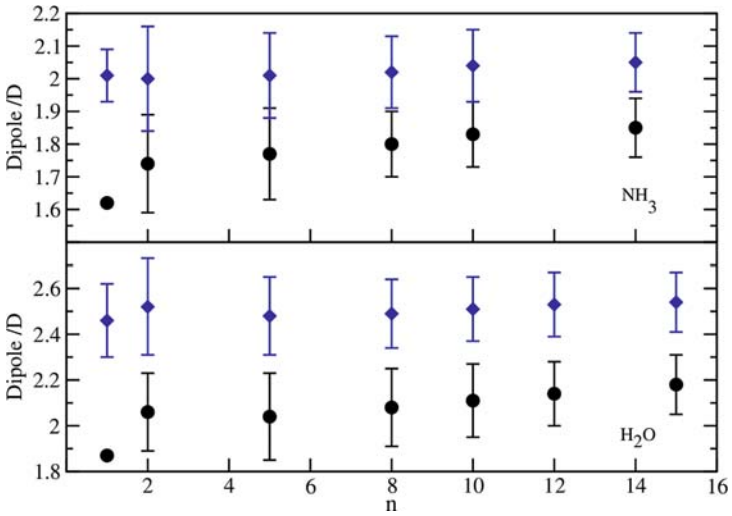

Figure 5-1. Dependence of the average dipole moment (in D) of the water and ammonia molecule on the number of molecules (*n*) included in the quantum mechanics calculations. Circles (diamonds) are for non-embedded (embedded) clusters

dipole-bound states and charge transfer to solvent (CTTS) in excited states of anionic species solvated in acetonitrile [55]. In contrast with water and ammonia that can play the role of hydrogen donor and acceptor species, the ability of acetonitrile as a proton donor is a controversial issue [56]. Polarization effects in acetonitrile were investigated by using cluster calculations [47] and sequential Monte Carlo/quantum mechanics simulations [40]. These studies indicate that the average dipole moment of acetonitrile in liquid phase (4.65 ± 0.19 D) is increased by ∼16–18% relative to the gas phase value. The theoretical estimates are in good agreement with an experimental value of 4.5 ± 0.1 D [57].

5.2.2. Charge Fluctuations in Hydrogen Bonding Liquids

The importance of charge fluctuations coupled to rearrangements of the HB network can be assessed through the calculation of the average *total* dipole moment of clusters with different number (n) of molecules. Results for this property in liquid water and ammonia are reported in Figure 5-2, where strong fluctuations that increase with the cluster size can be observed. Long-range polarization effects which are included for the embedded clusters contribute, as expected, to increase the average total dipole of the clusters. The magnitude of the fluctuations is similar for embedded and non-embedded aggregates. These fluctuations are related to structural and electronic density reorganization of the HB network and can be of relevance for understanding

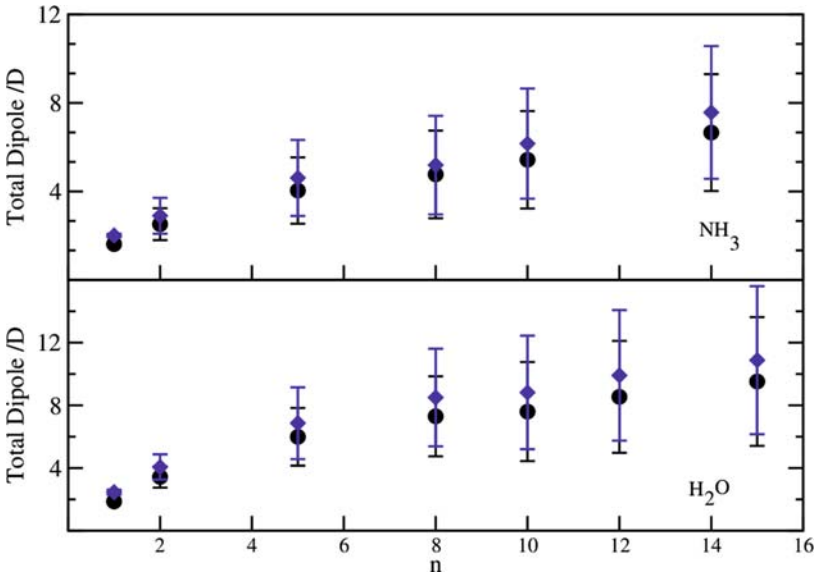

Figure 5-2. Dependence of the average total dipole moment (in D) of the water and ammonia clusters on the number of molecules (n) included in the quantum mechanics calculations. Circles (diamonds) are for non-embedded (embedded) clusters

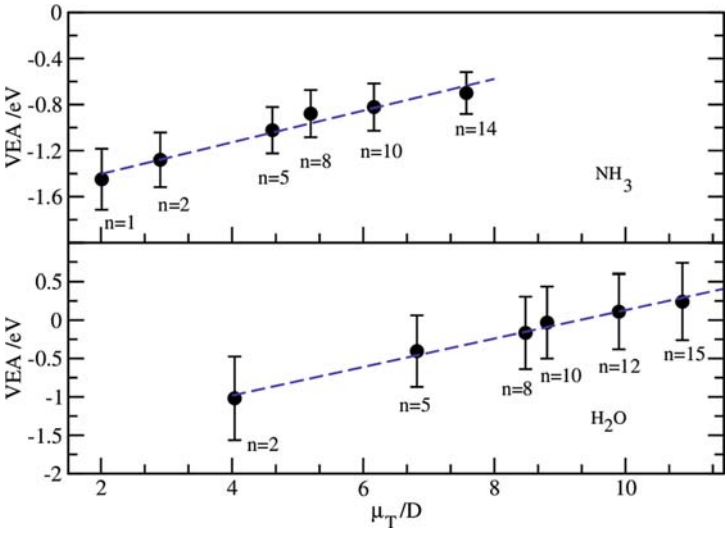

Figure 5-3. Dependence of the vertical electron affinity (VEA in eV) of ammonia and water on the average total dipole moment (μ_T in D) for clusters with different number of molecules (n). The dashed lines are fitting to the raw data with correlation coefficients $r = 0.99$ (water) and $r = 0.98$ (ammonia)

chemical reactivity in solution. For example, strong local multipole moments of the aggregates in the liquid can contribute to the stabilization of an excess charge through the formation of multipole-bound anionic states [58]. The relationship between the *vertical* electronic affinity (VEA) and the average total dipole moment (μ_T) of hydrogen bond systems is illustrated in Figure 5-3. For small water and ammonia clusters of different size (n) the ability of the HB network to vertically stabilize an excess electron correlates with μ_T. These results are for clusters embedded in the charge distribution of the liquid environment and indicate that the VEA of ammonia is negative for small aggregates. In contrast with ammonia, the VEA of water clusters become positive for $n \geq 10$. Another closely related problem of interest, where solvent fluctuations contribute to stabilize an specific charge distribution, concerns the zwitterion formation in hydrated amino acids, [59] where it is expected that charge fluctuations of the HB network play a relevant role for the energetic stabilization of the polar zwitterionic structures.

5.3. STRUCTURE OF THE HYDROGEN BOND NETWORK AND ELECTRONIC PROPERTIES OF WATER

5.3.1. Hydrogen Bonding and the Dipole Moment of Liquid Water

The structure of water is characterized by hydrogen bonding. Therefore, it should be expected that its electronic properties are dependent on the topological features

of the HB network, [60] which are related to the definition of hydrogen bond. To investigate this dependence, 1000 uncorrelated configurations corresponding to each different possibility of coordination in clusters with five water molecules were extracted from a *NpT* Monte Carlo (N = 512) simulation at normal conditions (T = 298 K; p = 1 atm). The simulation was carried out with the DICE program [32] and the TIP5P intermolecular potential [61] was used.

There are different criteria for defining a hydrogen bond [6,62]. Usually, for water, the definition relies on energetic [63,64,65] and geometric parameters [66,67]. A mixed criterion (energetic and geometric) was defined by Sutmann and Vallauri [68] and we have adopted a very similar one. Two water molecules are considered to be hydrogen bonded when (a) the interaction energy is ≤ 0.1 eV; (b) the distance O. . .O is ≤ 3.5 Å; and (c) the O–H. . .O angle is $\leq 35^{\circ}$.

By using the present criterion, the hydrogen bond distribution per water molecule is shown in Figure 5-4, and the results indicate that three and fourfold coordination are dominant with a total average relative frequency of ∼0.7. The presence of "HB defects" (zero coordination) has a very small average relative frequency (less than 1%). The calculated average number of H bonds per molecule is 3, which is lower than recent predictions (3.2–3.7) based on different criteria using the SPC/E model for liquid water [62]. A given water molecule can accept (a) or donate (d) a hydrogen. Then, for each configuration with five water molecules, the central molecule can form zero, one (a;d), two (aa;ad;dd), three (aad;add), or four (aadd) hydrogen bonds with the other four molecules. For the quantum mechanical calculations (over the 9000 selected configurations) only the central molecule is explicitly included. The surrounding molecules, including not only the hydrogen bonded ones, are represented by their charge distribution, which corresponds to the charges of the TIP5P

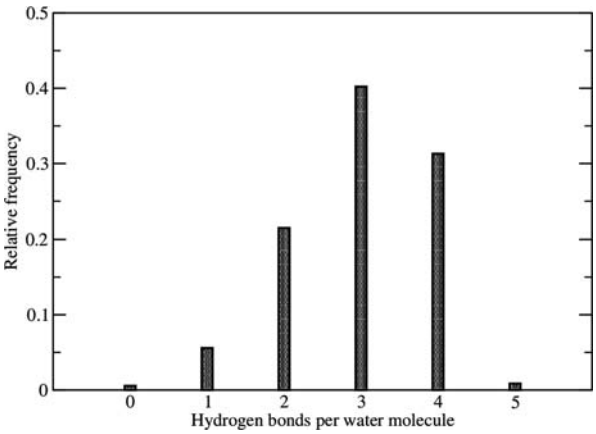

Figure 5-4. Distribution of H bonds per water molecule for the TIP5P intermolecular potential of liquid water at T = 298 K

interaction model. Thus, the central molecule is embedded in the electrostatic field of the surrounding water molecules (204 in total).

The average values of the dipole moment (μ in D) for a central water molecule forming different number of HB are reported in Table 5-1. As it should be expected, the smaller value (2.37 $\pm$ 0.02 D) corresponds to a "HB defect" or to zero H bonds. On the other hand, μ in liquid water increases with the number of H bonds and this trend is in keeping with a recent study of water clusters reported by McGrath et al. [69]. For a given number of H bonds, no significant differences are observed between the role played by the central water molecules as hydrogen acceptor (a) or donor (d). If the average dipole moment is calculated for all the configurations without any restriction on the number of H bonds, then μ is 2.59 $\pm$ 0.01 D, which practically coincides with the average value for a central molecule with 3 H bonds.

5.3.2. Hydrogen Bonding and Electron Binding Energies

Results for the average electron binding energies (EBE) of a central water molecule hydrogen bonded to the surrounding ones are reported in Table 5-2. The energy of the highest occupied molecular orbital ($1b_1$) is more dependent on the role played by the water molecule as acceptor (a) or donor (d) of hydrogen. This can be illustrated by analysing the $1b_1$ EBE when the central molecule is hydrogen bonded to one water molecule. In this case, the $1b_1$ EBE is 11.66 $\pm$ 0.02 eV when the central molecule is a hydrogen donor (d) and 11.98 $\pm$ 0.01 eV when it is a hydrogen acceptor (a). The same trend can be observed for all the other cases with a larger

Table 5-1. Dependence of the average [(a)] dipole moment (μ in D) of a central water molecule on the number of hydrogen bonds (n_{HB})

n_{HB}	Type of HB	M
0		2.37 $\pm$ 0.02
1	a	2.44 $\pm$ 0.01
	d	2.43 $\pm$ 0.01
2	aa	2.53 $\pm$ 0.01
	ad	2.52 $\pm$ 0.01
	dd	2.53 $\pm$ 0.01
3	aad	2.59 $\pm$ 0.01
	add	2.59 $\pm$ 0.01
4	aadd	2.67 $\pm$ 0.01

[(a)] Averages were calculated with a re-parametrized [25] MPW1PW91 hybrid functional and the aug-cc-pVDZ basis set. One thousand uncorrelated structures from Monte Carlo simulations were used for averaging.

Table 5-2. Dependence of the electron binding energies (in eV) [(a)] of a central water molecule on the number of hydrogen bonds (n_{HB})

n_{HB}	Type	$4a_1$	$1b_1$	$3a_1$	$1b_2$	$1b_1$–$4a_1$ gap
0		–0.67 ± 0.02	11.80 ± 0.02	13.95 ± 0.03	17.52 ± 0.03	12.47 ± 0.01
1	a	–0.64 ± 0.01	11.98 ± 0.01	14.15 ± 0.01	17.66 ± 0.01	12.61 ± 0.01
	d	–0.79 ± 0.02	11.66 ± 0.02	13.80 ± 0.02	17.33 ± 0.02	12.37 ± 0.01
2	aa	–0.62 ± 0.02	12.18 ± 0.03	14.37 ± 0.03	17.80 ± 0.03	12.80 ± 0.02
	ad	–0.68 ± 0.01	11.83 ± 0.03	13.99 ±0.04	17.46 ± 0.04	12.50 ± 0.03
	dd	–0.70 ± 0.01	11.54 ± 0.03	13.66 ± 0.03	17.16 ± 0.03	12.25 ± 0.02
3	aad	–0.66 ± 0.02	12.03 ± 0.02	14.21 ± 0.02	17.61 ± 0.02	12.69 ± 0.02
	add	–0.70 ± 0.02	11.69 ± 0.03	13.84 ± 0.03	17.27 ± 0.03	12.39 ± 0.02
4	aadd	–0.67 ± 0.02	11.89 ± 0.02	14.06 ± 0.02	17.43 ± 0.02	12.57 ± 0.01

[(a)] Averages were calculated with a re-parametrized [25] MPW1PW91 hybrid functional and the aug-cc-pVDZ basis set. One thousand uncorrelated structures from Monte Carlo simulations were used.

number of H bonds and reflects the stabilization of $1b_1$ orbital when the interaction with the surrounding molecules involves directly the oxygen atom of the central molecule.

The $4a_1$ EBE is not significantly dependent on the number of H bonds nor on the role played by the central water molecule as a hydrogen donor (d) or acceptor (a). There is some stabilization of the $4a_1$ EBE when the central molecule is accepting a hydrogen atom, but this effect is rather small (less than 0.1 eV). We are also reporting in Table 5-2 the $1b_1$–$4a_1$ (HOMO–LUMO) energy gap. The gap increases with the hydrogen acceptor character of the H bond and this tendency simply reflects the stabilization of the $1b_1$ orbital.

For a molecule in liquid water, the dependence of the electronic density of states (DOS) on hydrogen bonding is illustrated in Figure 5-5. In keeping with the stabilization of the $1b_1$ orbital previously discussed, when the central water molecule is hydrogen bonded to two water molecules, the valence DOS corresponding to (aa) configurations is shifted to lower energies in comparison with (ad) or (dd) configurations. Moreover, a slight shift to higher energies of the $1b_1$ band can be observed for (dd) configurations indicating a small reduction of the $1b_1$–$4a_1$ (HOMO–LUMO) gap for a water molecule playing the role of double hydrogen bond donor. The DOS for virtual orbitals is not dependent on the number of H bonds nor on the role played by the central water molecule as hydrogen bond donor or acceptor. However, this is possibly related to the fact that in the present approach only polarization effects are being taken into account. No charge transfer to virtual orbitals is possible, and it is known that the EBEs of virtual orbitals cannot be estimated as a local property [25,54].

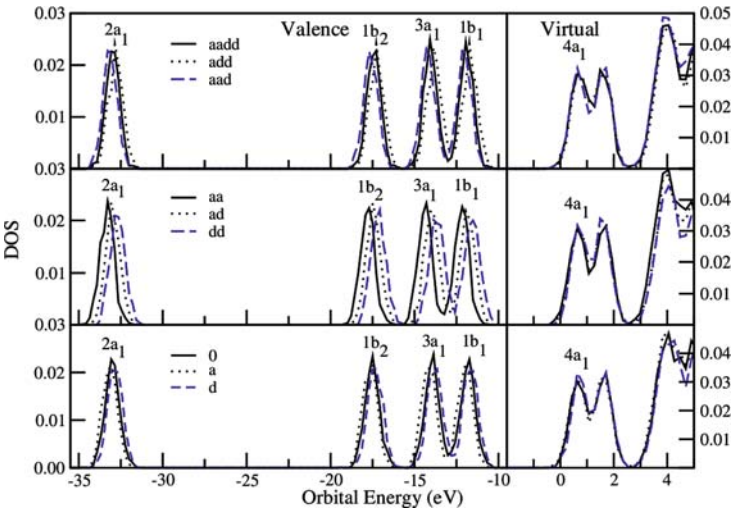

Figure 5-5. Dependence of the electronic density of states (DOS) on the number of H bonds for a water molecule in liquid water

5.4. CHARGE FLUCTUATIONS OF THE HYDROGEN BOND NETWORK AND PROTON TRANSFER ASSISTED BY THE SOLVENT IN PHENOL–WATER CLUSTERS

5.4.1. Born–Oppenheimer Molecular Dynamics of Proton Transfer in Phenol–Water Clusters

The acidity of some aromatic molecules may exhibit significant changes upon excitation or ionization [70]. This behaviour, known as photoacidity, has been the subject of several investigations [70,71]. The change of the acidity of a given species is related to its ability to transfer a proton to the nearby solvent molecules and the PT mechanism is triggered by the electronic density reorganization coupled to the solvent fluctuations. Small hydrogen bonded solute–solvent clusters are model systems for investigating acid–base reactions [72,73]. One interesting system is phenol–water clusters, where phenol is a weak acid in the ground state but may exhibit an increased acidity when it is excited or ionized. Therefore, several works on proton transfer in phenol–water aggregates were reported [74,75,76,77,78] and provided evidence that no proton transfer from phenol to water occurs in small neutral phenol–water clusters [77,78]. However, proton transfer to water takes place in $[C_6H_5OH{-}(H_2O)_n]^{\bullet+}$ clusters for $n \geq 3$ [72,73,77,78,79].

The proton transfer in ionized phenol–water clusters is strongly dependent on the number of water molecules and their specific organization, i.e., the PT is a process assisted by the solvent [72]. Most of the theoretical studies of PT in $[C_6H_5OH{-}(H_2O)_n]^{\bullet+}$ clusters were focused on the structure, vibrational, [79,80,81] and energetic aspects [77,78]. However, much less is known on the dynamics of PT.

Moreover, the PT mechanism, specifically the role played by the water molecules, is not well understood from the microscopic point of view and deserves further analysis.

With the purpose of investigating proton transfer in the phenol–water system we have carried out Born–Oppenheimer molecular dynamics (BOMD) of $[C_6H_5OD{-}(H_2O)_4]$ clusters. Several applications of first principles molecular dynamics to the study of PT reactions were reported [81,82,83,84,85,86,87]. By adopting this approach polarization effects and charge transfer are implicitly taken into account. Although this system is small to model solvation, it should be expected that some of the basic features that control PT in solution are correctly represented. Quantum effects on the proton dynamics [84,88,89] were not included. To reduce their importance on the PT dynamics the hydrogen of the phenol OH group has been deuterated (we will use, however, PT for describing the charge migration of the deuterium in the aggregates).

Initially, we carried out BOMD for the neutral $[C_6H_5OD{-}(H_2O)_4]$ system. BOMD simulations were carried out with a velocity-Verlet integration scheme coupled to the Gaussian-03 package [90]. Velocity scaling was used to equilibrate the system to the desired temperature of 298 K during 6000 steps of 0.5 fs, which correspond to a total time of 3 ps. After this time, scaling was turned off and the dynamics of the system in the microcanonical ensemble was propagated through another 2 ps. In a second phase, the system has been ionized at different time-steps (A–H in Figure 5-6) of the equilibrium trajectory. Then, starting from these different configurations, the dynamics of the $[C_6H_5OD{-}(H_2O)_4]^{\bullet+}$ cluster was followed during 3 ps.

The quantum mechanical calculations (energies and forces on each atom) were carried out with the B3LYP functional [91,92] and the 6-31 G(d) basis set [93].

5.4.2. Dynamics of PT in Phenol–Water Clusters

The time evolution of the phenol O−D distance between the phenolic oxygen and the deuterium and the D−O_w distance between the deuterium and the oxygen of the nearest water molecule in the neutral (left panel at the bottom) and ionized clusters (right panels) is shown in Figure 5-6.

In agreement with previous studies [78], no PT is observed in the neutral system, where very small changes of the O−D distance are observed. The time evolution of the D−O_w distance reflects the reorganization of the water molecules around the phenol O−D group. The average O−D and D−O_w distances are 0.98 ± 0.14 and 2.00 ± 0.14 Å, respectively.

The time evolution of the O−D and D−O_w distances in the ionized clusters is also shown in Figure 5-6 (A–H right panels). In contrast with the neutral system, significant changes of the distances can be observed. These variations describe the occurrence of proton transfer from the phenolic moiety to water and also recombination of the transferred proton with the phenoxy moiety. As expected, the PT dynamics is dependent on the initial configuration.

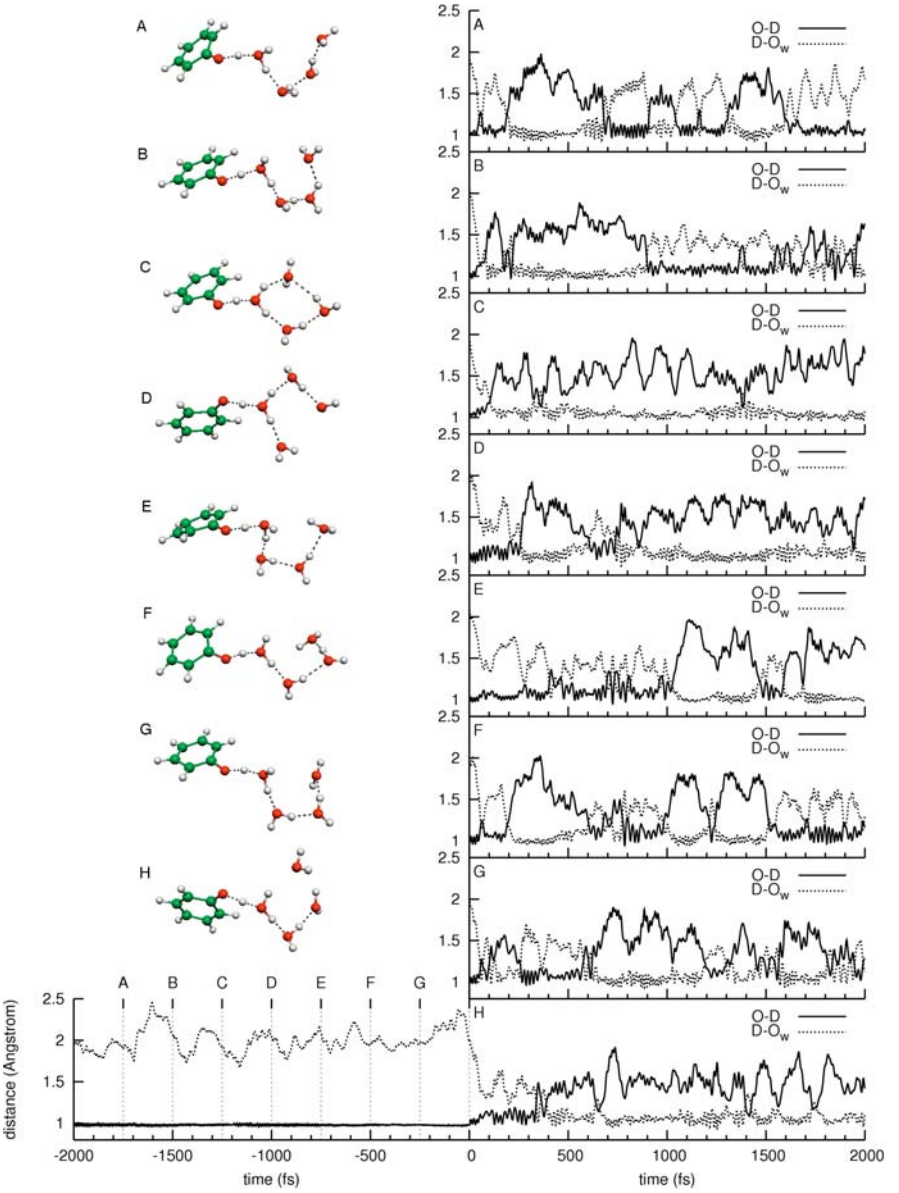

Figure 5-6. Time evolution of the O−D distance (*full lines*) between the phenol oxygen and the deuterium and the D−O_w distance (*dotted lines*) between the PhOD deuterium and the oxygen of the nearest water molecule in the neutral (*left panel at the bottom*) and ionized clusters (A–H *right panels*). The $t = 0$ time corresponds to the ionization of the $[C_6H_5OD{-}(H_2O)_4]$ cluster at different (A–H) equilibrium configurations. The snapshots show for each trajectory the structure of the $[C_6H_5OD{-}(H_2O)_4]^{\bullet+}$ cluster corresponding to the configuration where the O−D and D−O_w distances are the same before the first PT following ionization

For the set of trajectories (A–H) shown in Figure 5-6, the time for the first PT from phenol to water after ionization is defined in a 100–400 fs window. Snapshots for the configurations where the O−D and D−O_w distances are the same before the first PT following ionization are represented in Figure 5-6. For most of the trajectories, a significant number of PT from phenol to water as well as migration of the proton from water to the phenoxyl radical are observed. Therefore, the results indicate that the dynamics of PT in $[C_6H_5OD{-}(H_2O)_4]^{\bullet+}$ is described by a bidirectional kinetics scheme, [94,95] where PT from phenol to water is reversible and competes with PT from the H_3O^+ moiety to the phenoxyl radical. However, the PT dynamics should be dependent on the number of water molecules in the cluster, and proton propagation along the HB network [20,70] may significantly modify the kinetics of proton transfer/recombination mechanisms.

5.4.3. Proton (Deuterium) Transfer in Phenol–Water Clusters and Fluctuations of the HB Network

It should be expected that PT is dependent on the electrostatic field at the proton position [41,96,97,98]. This field can be created by the phenoxy moiety and by the water molecules and these two contributions were calculated by using charges fitted to the electrostatic potential [99,100]. Figure 5-7 shows the time evolution of the electrostatic field (in a.u.) at the proton position due to the phenoxy radical moiety (full lines) and water molecules (dotted lines). In the ionized clusters (panels A–H) the electrostatic field due to water is characterized by strong fluctuations. A qualitative relationship between these fluctuations and the number of proton transfer and recombination can be established by comparing the different trajectories shown in Figure 5-6, and it appears that thermal-induced fluctuations play a relevant role on the PT dynamics [2]. This issue can be further addressed by calculating the fluctuations of the electrostatic field $\delta E(t) = [(E(t) - < E >)^2]^{\frac{1}{2}}$ due to the charge distributions of the phenoxy moiety and water. The time evolution of $\delta E(t)$ is shown in Figure 5-8. The fluctuations of the electrostatic field due to the water molecules are significantly higher than those corresponding to the electrostatic field of the phenoxy moiety and are related to the reorganization of the HB network. The kinetics of PT/recombination seems to reflect, at least qualitatively, the magnitude of the fluctuations, which are smaller for trajectories C and D (see Figure 5-8). Interestingly, C and D also exhibit, in comparison with the other trajectories, the smaller number of PT/recombination (Figure 5-6). The role played by charge fluctuations in water on the PT dynamics in $[C_6H_5OD{-}(H_2O)_4]^{\bullet+}$ clusters seems to be in keeping with the view that relates the specific and anomalous behaviour of water to the nature of their energy fluctuations [2,8]. In our case, it is important to investigate the time evolution of the deuterium kinetic energy, which is illustrated in Figure 5-9. In agreement with the analysis of Ohmine and collaborators for the fluctuations of the total energy in liquid water, [2,8] the deuterium kinetic energy exhibits strong fluctuations. Although PT in ionized phenol–water clusters can be related to fluctuations of the

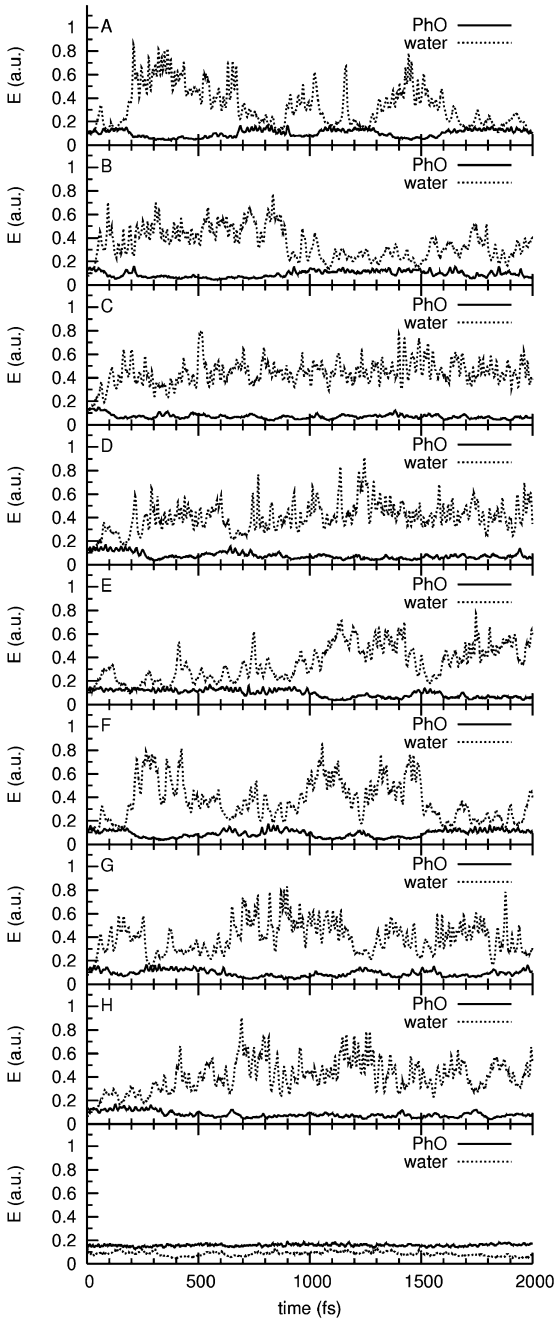

Figure 5-7. Time evolution of the electrostatic field $E(t)$ (in a.u.) at the deuterium position in the neutral $[C_6H_5OD{-}(H_2O)_4]$ (*bottom panel*) and $[C_6H_5OD{-}(H_2O)_4]^{\bullet+}$ (panels A–H) clusters due to the phenoxy moiety (*full lines*) and water molecules (*dotted lines*)

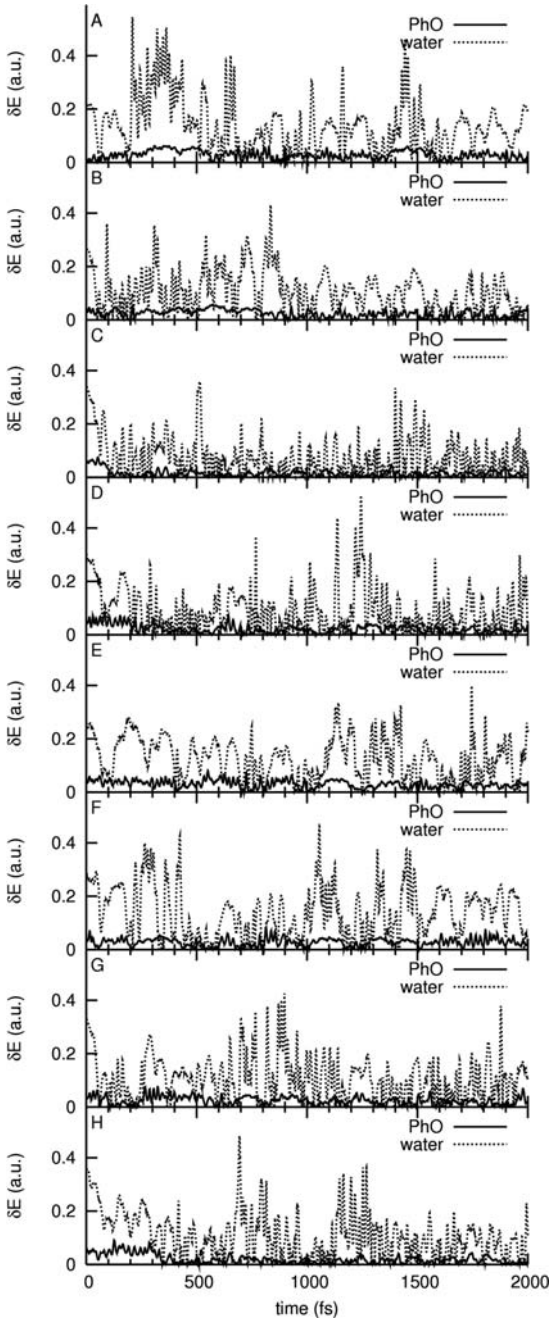

Figure 5-8. Time evolution of the electrostatic field fluctuation $\delta E(t) = \left[(E(t) - < E >)^2\right]^{\frac{1}{2}}$ (in a.u.) at the deuterium position in $[C_6H_5OD{-}(H_2O)_4]^{\bullet+}$ clusters (panels A–H) due to the phenoxy moiety (*full lines*) and water molecules (*dotted lines*)

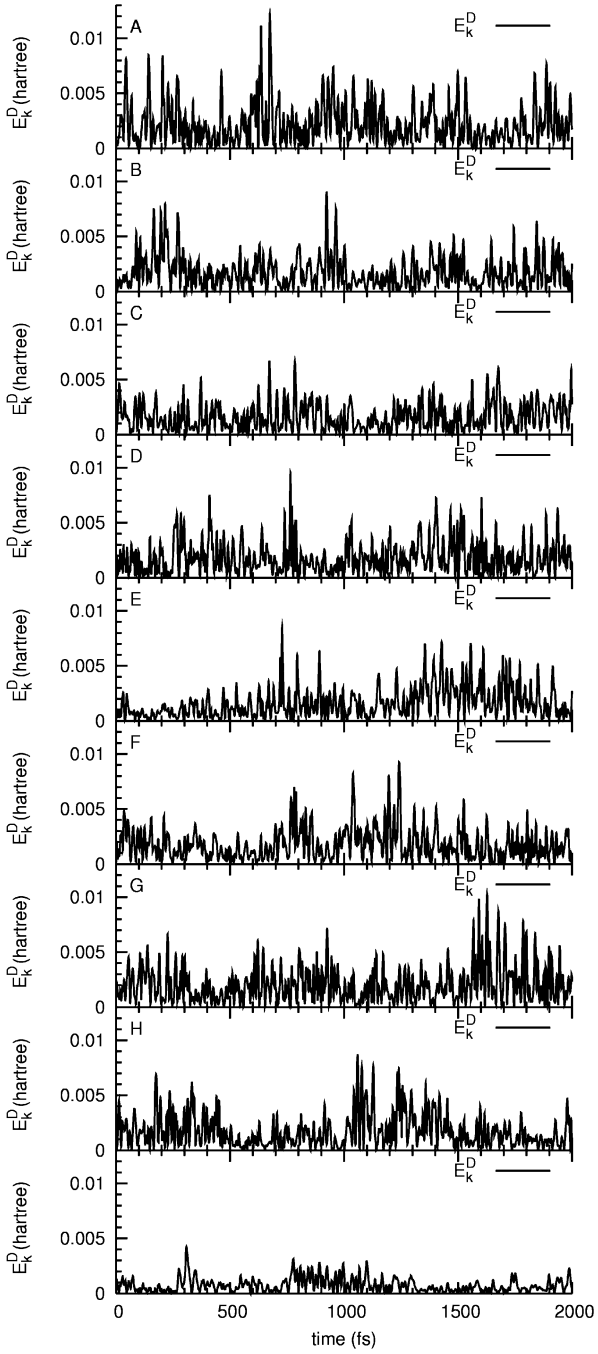

Figure 5-9. Time evolution of the deuterium kinetic energy $E_k^D(t)$ (a.u.) in $[C_6H_5OD{-}(H_2O)_4]$ (*bottom panel*) and $[C_6H_5OD{-}(H_2O)_4]^{\bullet+}$ clusters (panels A–H)

water HB network, the interplay between energy and charge fluctuations as well as their relationship with the kinetics of PT deserves further attention.

5.5. CONCLUSIONS

The electronic properties of polar liquids including water and ammonia, whose structures are characterized by HB networks were reviewed. Emphasis was placed on the analysis of polarization effects, charge fluctuations, and electron binding energies.

Polarization effects in liquid water and ammonia are very important and lead to a significant increase of the average dipole moment relative to the gas phase values. Moreover, polarization effects are related to fluctuations of the electronic density of the HB network and a strong correlation between the total dipole moment of small water and ammonia clusters and the vertical electron affinity can be established.

The relationship between the local structure of the HB network and electronic properties was investigated and it was concluded that the water dipole moment and electron binding energies exhibit some dependence on the local environment of the network. Specifically, the dipole moment in liquid water increases with the number of H bonds, although it is not dependent on the role played by the water molecule as H donor or acceptor. On the other hand, the $1b_1$ EBE increases when the interaction with the surrounding water molecules involves directly the oxygen atom of the central water molecule, which then plays the role of H bond acceptor.

Born–Oppenheimer molecular dynamics simulations for neutral and ionized phenol–water clusters are reported. The results for $[C_6H_5OD{-}(H_2O)_4]^{\bullet+}$ illustrate how the PT dynamics is coupled to fluctuations of the solvent. The kinetics of PT/recombination in $[C_6H_5OD{-}(H_2O)_4]^{\bullet+}$ clusters is related to strong fluctuations of the electrostatic field of the water molecules and this relationship points out the relevance of investigating the electronic properties of the HB network for understanding chemical reaction in solution.

REFERENCES

1. Kobayashi C, Iwahashi K, Saito S, Ohmine I (1996) J Chem Phys 105:6358
2. Ohmine I, Saito S (1999) Acc Chem Res 32:741
3. Bergman DL (2000) Chem Phys 253:267
4. Franzese G, Stanley HE (2002) Physica A 314:508
5. Kumar P, Franzese G, Buldryev SV, Stanley HE (2006) Phys Rev E 73:041505
6. Matsumoto M (2007) J Chem Phys 126:054503
7. Ohmine I, Tanaka H (1993) Chem Rev 93:2545
8. Ohmine I (1995) J Phys Chem 99:6767
9. Bhattacharyya K (2003) Acc Chem Res 36:95
10. Xantheas SS (2000) Chem Phys 258:225
11. Bartels M, Crowell RA (2000) J Phys Chem A 104:3349
12. Delahay P, Von Burg K (1981) Chem Phys Lett 83:250

13. Dutuit O, Tabche-Fouhaile A, Nenner I, Frolich H, Guyon PM (1985) J Chem Phys 83:584
14. Li G-S, Martins Costa MTC, Millot C, Ruiz-López MF (1999) Chem Phys 240:93
15. Sprik M, Hutter J, Parrinello M (1996) J Chem Phys 105:1142
16. Hura G, Russo D, Glaeser RM, Head-Gordon T, Krack M, Parrinello M (2003) Phys Chem Chem Phys 5:1981
17. Lee HS, Tuckerman ME (2006) J Chem Phys 125:154507
18. Mantz YA, Chen B, Martyna GJ (2005) Chem Phys Lett 405:294
19. Mantz YA, Chen B, Martyna GJ (2006) J Phys Chem B 110:3540
20. Marx D (2006) Chem Phys Chem 7:1848
21. Diraison M, Martyna GJ, Tuckerman ME (1999) J Chem Phys 111:1096
22. Boese AD, Chandra A, Martin JML, Marx D (2003) J Chem Phys 119:5965
23. Winter B, Faubel M (2006) Chem Rev 106:1176
24. Couto PC, Estácio SG, Cabral BJC (2005) J Chem Phys 123:054510
25. Couto PC, Cabral BJC, Canuto S (2006) Chem Phys Lett 429:129
26. Couto PC, Cabral BJC (2007) J Chem Phys 126:014509
27. Turi L, Madarász A, Rossky PJ (2006) J Chem Phys 125:014308
28. Sobolewski AL, Domcke W (2007) Phys Chem Chem Phys 9:3818
29. Abdoul-Carime H, Schermann JP, Desfrançois C (2002) Few-Body Syst 31:183
30. Seydou M, Modelli A, Lucas B, Konate K, Desfrançois C, Schermann JP (2005) Eur Phys J D 35:199
31. Coutinho K, Canuto S (1997) Adv Quantum Chem 28:89
32. Coutinho KS, Canuto S (2000) DICE: A general Monte Carlo program for liquid simulation, Universidade de São Paulo, Brazil
33. Barnett RN, Landman U (1993) Phys Rev B 48:2081
34. Cheng HP (1998) J Phys Chem A 102:6201
35. Sadeghi RR, Cheng HP (1999) J Chem Phys 111:2086
36. Bøttcher CJF, (1973) Theory of electric polarization, Elsevier, Amsterdam
37. Badyal YS, Saboungi M-L, Price DL, Shastri SD, Haeffner DR (2000) J Chem Phys 112:9206
38. Devereux M, Popelier PLA (2007) J Phys Chem A 111:1536
39. Coutinho K, Guedes RC, Cabral BJC, Canuto S (2003) Chem Phys Lett 369:345
40. Rivelino R, Cabral BJC, Coutinho K, Canuto S (2005) Chem Phys Lett 407:13
41. Tuñón I, Martins-Costa MC, Millot C, Ruiz-López MF, Rivail JL (1996) J Comp Chem 17:19
42. Kongsted J, Oested A, Mikkelsen KV, Christiansen O (2002) Chem Phys Lett 364:379
43. Silvestrelli PL, Parrinello M (1999) J Chem Phys 111:3572
44. Gregory JK, Clary DC, Liu K, Brown MG, Saykally RJ (1997) Science 275:814
45. Tu Y, Laaksonen L (2000) Chem Phys Lett 329:283
46. Cabral BJC, Guedes RC, Pai-Panandiker RS, Nieto de Castro CA (2001) Phys Chem Chem Phys 3:4200
47. Mata RA, Cabral BJC (2004) J Mol Struct – Theochem 673:155
48. Batista ER, Xantheas SS, Jonsson H (1999) J Chem Phys 111:6011
49. Georg HC, Coutinho K, Canuto S (2006) Phys Lett 429:119
50. Todorova T, Seitsonen AP, Hutter J, Kuo I-FW, Mundy CJ (2006) J Phys Chem B 110:3685
51. Millot C, Cabral BJC, to be submitted
52. Niesar U, Corongiu G, Clementi E, Kneller GR, Bhattacharya DK (1990) J Phys Chem 94:7949
53. Deng Z, Martyna GJ, Klein ML (1994) J Chem Phys 100:7590
54. Almeida TS, Coutinho K, Cabral BJC, Canuto S (2008) J Chem Phys 128:014506
55. Timerghazin QK, Peslherbe GH (2002) Chem Phys Lett 354:31
56. Scheiner S (1997) Hydrogen bonding: A theoretical perspective, Oxford University Press, New York

57. Ohba T, Ikawa S (1991) Mol Phys 73:985
58. Defrançois C, Schermann JP (2002) Chem Soc Rev 31:269
59. Xu S, Nilles M, Bowen KH (2003) J Chem Phys 119:10696
60. Myneni S, Luo Y, Näslund LÅ, Cavalleri M, Ojamäe L, Ogasawara H, Pelmenschikov A, Wernet Ph, Väterlein P, Heske C, Hussain Z, Pettersson LGM, Nilsson A (2002) J Phys: Condens Matter 14:L213
61. Mahoney MW, Jorgensen WL (2000) J Chem Phys 112:8910
62. Kumar R, Schmidt JR, Skinner JL (2007) J Chem Phys 126:204107
63. Stillinger FH (1980) Science 209:451
64. Stanley HE, Teixeira J (1980) J Chem Phys 73:3404
65. Jorgensen WL, Chandrasekhar J, Madura JD, Impey RW, Klein ML (1983) J Chem Phys 79:926
66. Luzar A, Chandler D (1993) J Chem Phys 98:8160
67. Smith JD, Cappa CD, Wilson KR, Messer BM, Cohen RC, Saykally RJ (2004) J Science 306:851
68. Sutmann G, Vallauri R (2002) J Mol Liquids 98–99:213
69. McGrath MJ, Siepmann JI, Kuo I-FW, Mundy CJ (2007) Mol Phys 105:1411
70. Agmon N (2005) J Phys Chem A 109:13
71. Ebata T, Mizuochi N, Watanabe T, Mikami N (1996) J Phys Chem 100:546
72. Sato S, Mikami N (1996) J Phys Chem 100:4765
73. Sawamura T, Fujii A, Sato S, Ebata T, Mikami N (1996) J Phys Chem 100:8131
74. Tanabe S, Ebata T, Fujii M, Mikami N (1993) Chem Phys Lett 215:347
75. Hobza P, Burcl R, Špirko V, Dopfer O, Müller-Dethlefs K, Schlag EW (1994) J Chem Phys 101:990
76. Watanabe T, Ebata T, Tanabe S, Mikami N (1996) J Chem Phys 105:408
77. Sodupe M, Oliva A, Bertran J (1997) J Phys Chem A 101:9142
78. Re S, Osamura Y (1998) J Phys Chem A 102:3798
79. Martiniano HFMC, Cabral BJC, Simões JAM (2007) Chem Phys Lett 442:451
80. Jensen A, Gerhards M (2001) J Chem Phys 115:5445
81. Yamashita T, Takatsuka K (2007) J Chem Phys 126:074304
82. Tuckerman MK, Laasonen K, Sprik M, Parrinello M (1995) J Chem Phys 103:150
83. Sagnella DE, Laasonen K, Klein ML (1996) Biophys J 71:1172
84. Kim SY, Hammes-Schiffer S (2003) J Chem Phys 119:4389
85. Leung K, Rempe SB (2005) J Chem Phys 122:184506
86. Choe Y-K, Tsuchida E, Ikeshoji T (2007) J Chem Phys 126:154510
87. Degtyarenko IM, Jalkanen KJ, Gurtovenko AA, Nieminen RM (2007) J Phys Chem B 111:4227
88. Borgis D, Hynes JT (1993) Chem Phys 170:315
89. Hammes-Schiffer S, Tully JC (1994) J Chem Phys 101:4657
90. Frisch MJ et al (2003) Gaussian-03, Rev. C.02, Gaussian Inc., Pittsburgh, PA
91. Becke AD (1993) J Chem Phys 98:5648
92. Lee C, Yang W, Parr RG (1988) Phys Rev B 37:785
93. Hariharan PC, Pople JA (1974) Mol Phys 27:209
94. Pines E, Huppert D (1986) J Chem Phys 84:3756
95. Pines E, Huppert D, Agmon N (1988) J Chem Phys 88:5620
96. Morillo M, Cukier RI (1990) J Chem Phys 92:4833
97. Cukier RI, Zhu J (1997) J Phys Chem B 101:7180
98. Tuñón I, Martins-Costa MC, Millot C, Ruiz-López MF (1997) J Chem Phys 106:3633
99. Singh UC, Kollman PA (1984) J Comput Chem 5:129
100. Besler BH, Merz Jr KM, Kollman PA (1990) J Comput Chem 11:431

CHAPTER 6

SOLVENT EFFECTS ON RADIATIVE AND NON-RADIATIVE EXCITED STATE DECAYS

AURORA MUÑOZ LOSA, IGNACIO FDEZ. GALVÁN, M. ELENA MARTÍN, AND MANUEL A. AGUILAR

Química Física, Universidad de Extremadura, Avda. de Elvas s/n. 06071 Badajoz (Spain)

Abstract: An extended version of the ASEP/MD method that permits the unified treatment of solvent effects on both radiative and non-radiative excited state decays is presented. The method combines a high-level quantum-mechanic description of the ground and excited states of the solute molecule with molecular dynamics simulations of the solvent. De-excitations are intrinsically dynamic processes where there exists an interplay between electronic structure and nuclear dynamics. We have undertaken this problem by establishing two limit situations, which we have characterized as equilibrium and non-equilibrium solvation regimes. In the former, we suppose decay times long enough to allow a complete relaxation of the solute and the solvent structure. In the latter, we suppose the decay process is fast enough to prevent the solvent equilibration. As an example of application of the methodology the solvent effects on radiative and non-radiative de-excitation processes in acrolein are studied

6.1. INTRODUCTION

The study of solvent effects on the appearance of UV-vis absorption spectra has a long history [1]. From the first qualitative (classical) description based on the changes in the dipole moment and polarizability during the excitation until the current quantitative models where the solute charge distribution is described through high-level quantum-mechanics techniques, a great number of theoretical models have been proposed [2,3,4,5] in such a way that, at present, the chemists have at their disposition a wide range of methods that permit the prediction of the position and intensity of the absorption bands of chromophores in solution. Comparatively, less attention has been paid to the study of solvent effects on emission spectra (fluorescence and phosphorescence) [6,7] where only recently we have begun to have available accurate methods that permit to optimize the geometry and charge distribution of excited states and to describe its interaction with the solvent. Solvent effects on emission spectra follow qualitative rules similar to those applied to absorption spectra [8,9]: a band in the fluorescence or phosphorescence spectrum will

S. Canuto (ed.), Solvation Effects on Molecules and Biomolecules, 135–157.
DOI 10.1007/978-1-4020-8270-2_6,

shift to higher frequencies (blue shift) if the dipole moment of the excited state is smaller than the ground state dipole moment and it will be red shifted if the dipole moment of the excited state is larger than the ground state dipole moment. In general, the magnitude of the solvent shift will increase with the solvent polarity and with the variation of the dipole moment during the transition. However, even when one has the dipole moment values for the solute molecule in the different states (something not always easy because they must be calculated at the excited state optimized geometry) these approximate rules could fail when applied to molecules with complex charge distributions or when specific solute–solvent interactions are involved.

Unlike UV-vis absorption spectra where all molecules display one or more active bands, many molecules do not present emission spectra or if they do, they exhibit exceedingly small quantum yield values. To understand this behaviour, one must realize that radiative decay always competes with non-radiative decay pathways, mainly internal conversion (IC), intersystem crossing (ISC) and quenching. Solvents can favour the activation of non-radiation pathways, consequently, they can have a dramatic influence on the fluorescence quantum yields. So, for instance, molecules can display fluorescence spectra in some solvent but not in another [10]. Despite the proved importance of the molecular environment, the theoretical study of solvent effects on IC and ISC (quenching is a phenomenon that depends on the presence in the solvent of certain type of molecules, oxygen for instance and not on the characteristics of the excited state) has received little attention [11,12,13,14,15,16,17,18]. The reasons are obvious: to the difficulties inherent to the study of non-adiabatic processes (processes that imply more than one potential energy surface) in vacuo one must add the complications associated to the presence of a solvent, that is, the great number of surrounding molecules that interact with the solute molecule and the existence of a manifold of configurations thermally accessible that must be included to obtain statistically significant results.

Furthermore, when one studies emission spectra it is necessary to take into account the subtle interplay between the time evolution of the excited state and the dynamics of the solvent, something that does not occur in the study of UV-vis absorption spectra. A photophysical or photochemical process usually begins with the excitation from the minimum energy configuration of the ground state to the Franck–Condon (FC) point on the excited state free energy surface. The classical formulation of this principle establishes that in the time required for a radiative process to occur ($\approx 10^{-15}$ s), the geometry of the molecule, and of the solvent around it, remains fixed. This means that, at the FC point, the solvent is in a non-equilibrium situation whose structure corresponds to the equilibrium with the solute in its ground state. After the absorption process, and as time goes on, the solvent modifies its structure and after a long enough time it becomes equilibrated with the charge distribution of the solute excited state. The time scale of the different processes involved in the evolution of an excited state can be very different. For instance, the lifetimes of most emitting states are sufficiently long (1 ns or larger) to permit a complete

relaxation of the solute and the solvent. Only when the emission involves excited states characterized by very short lifetimes or solvents with high viscosity must we expect an incomplete relaxation of the solvent. Radiationless processes are usually faster, they can take place on the femtosecond time scale, a scale in which, in general, the solvent equilibration will not be complete. However, in systems where the geometry of the surface crossing points is very different from the FC point the de-excitation will take place only after a great part of the solvent reorganization has occurred.

We can hence define two limit cases depending on whether the solvent is in an equilibrium or non-equilibrium situation. In a real system, and depending on the specific characteristics of the process, we can find the solvent structure at any point between these two limits. It is important to stress that, actually, the solvent dynamics is characterized by different response times, associated to different solvent degrees of freedom. Traditionally, it has become usual to distinguish between an inertial component, associated to nuclear movements (vibrations, rotations and translations) and an inertialess or electronic component, associated to the response of the electronic degrees of freedom of the solvent (although more complex classifications are possible) [6,19,20]. In general it is supposed that the electronic response is fast enough so as to be always in equilibrium with the solute charge distribution even in the FC point. In dielectric continuum models [19,21] these two types of response have been usually characterized by the square of the index of refraction in the case of the electronic component or by the dielectric constant at zero frequency in the case of the complete response (inertial plus electronic). In molecular solvent models, the electronic component can be conveniently represented through electronic polarizabilities on the individual solvent molecules.

In the following, we present a sequential quantum mechanics/molecular mechanics (QM/MM) method, known as ASEP/MD [22,23,24,25,26], oriented to the study of solvent effects on absorption and emission spectra and on non-radiative excited state decay. The method combines a high-level quantum-mechanic description of the ground and excited states of the solute molecule with a molecular mechanics description of the solvent and allows the mutual equilibration of the solute charge distribution and the solvent structure around it. Furthermore, it permits the study of electron transitions in equilibrium and non-equilibrium conditions. The rest of the chapter is organized as follows: Section 2 details the main characteristics of the method, paying special attention to the evaluation of the gradients (ground and excited state gradients, gradient difference, derivative coupling) used in the search of minima and surface crossing points. In Section 3, and taking the acrolein molecule in aqueous solution as a model, we show how the ASEP/MD method permits the study of solvent shifts in absorption and emission spectra as well as the characterization of the competitive radiationless de-excitation pathways. Special attention is dedicated to the comparison between the results obtained assuming equilibrium and non-equilibrium solvation.

6.2. METHOD

6.2.1. Fundament of the ASEP/MD Method

ASEP/MD, acronym for average solvent electrostatic potential obtained from molecular dynamics data, is a sequential QM/MM method that makes extensive use of the mean field approximation (MFA) [24]. In solution, any static property A of the system must be calculated by averaging over the configurational space $\{X\}$ defined by all the configurations thermally accessible to the system:

$$\langle A\rangle = \frac{\sum_i \exp(-E_i/kT)\,\langle\Psi_i|\,\hat{a}\,|\Psi_i\rangle}{\sum_i \exp(-E_i/kT)} \tag{6-1}$$

where $\hat{a}$ is the quantum-mechanic operator for the property A and Ψ_i represents the quantum state i. This means that, in principle, hundreds or thousands of quantum calculations are necessary to obtain results that are statistically significant. In the mean field approximation this average is replaced by the value obtained in the presence of an average perturbation or configuration. The main advantage of MFA is that it greatly reduces the number of quantum calculations needed, the cost that has to be paid is the neglect of the correlation between the motion of the solvent nuclei and the response of the solute electron polarizability, i.e., the MFA does not allow the solute to polarize in response to instantaneous changes in the solvent nuclear configurations as consequence of the thermal fluctuations. It has been shown, both theoretically [24] and experimentally [27] that this correlation energy, usually known as Stark component [28,29], does not contribute significantly to the solvent shift. Many of the most frequently used methods for the study of solvent effects make use of the MFA: the different quantum versions of dielectric continuum models (SCRF [30], PCM [2], multipole expansions [3,4], etc.), the methods based on Langevin dipoles [31] or more elaborated methods such as RISM/SCF [32] are representative examples of this.

In the MFA the average value, $\langle A\rangle$, of any quantity is approximated as

$$\langle A\rangle \approx \bar{A} = \int \bar{\Psi}^* \hat{a} \bar{\Psi}\, \mathrm{d}r \tag{6-2}$$

where $\bar{\Psi}$ is the solute wavefunction perturbed by the solvent and calculated by solving the following effective Schrödinger equation:

$$\left(\hat{H}_{\mathrm{QM}} + \left\langle \hat{H}_{\mathrm{int}}^{\mathrm{elect}} \right\rangle\right) \left|\bar{\Psi}\right\rangle = \bar{E}\, \left|\bar{\Psi}\right\rangle \tag{6-3}$$

$\hat{H}_{QM}$ being the "in vacuo" solute molecular Hamiltonian and where the solute–solvent electrostatic interaction energy reads

$$\left\langle \hat{H}_{\mathrm{int}}^{\mathrm{elect}} \right\rangle = \int \mathrm{d}r \cdot \hat{\rho} \cdot \langle V_S(r;\rho)\rangle_{\{X\}} \tag{6-4}$$

here $\hat{\rho}$ is the solute charge density operator and the term $\langle V_S(r;\rho)\rangle_{\{X\}}$ is the average solvent electrostatic potential (ASEP) or reaction potential generated by the solvent at the r position. The brackets denote an average on the configurational space $\{X\}$. In general, the ASEP depends on ρ, the solute charge density, consequently, Eqs. (6-3) and (6-4) must be solved iteratively. In defining (6-4) only the electrostatic component was considered, although other components of the solute–solvent interaction energies, dispersion or repulsion terms for instance, can also be included.

Different solvation methods can be obtained depending on the way the $\langle V_S(r;\rho)\rangle_{\{X\}}$ term is calculated. So, for instance, in dielectric continuum models $\langle V_S(r;\rho)\rangle_{\{X\}}$ is a function of the solvent dielectric constant and of the geometric parameters that define the molecular cavity where the solute molecule is placed. In ASEP/MD, the information necessary to calculate $\langle V_S(r;\rho)\rangle_{\{X\}}$ is obtained from molecular dynamics calculations. In this way $\langle V_S(r;\rho)\rangle_{\{X\}}$ incorporates information about the microscopic structure of the solvent around the solute, furthermore, specific solute–solvent interactions can be properly accounted for. For computational convenience, the potential $\langle V_S(r;\rho)\rangle_{\{X\}}$ is discretized and represented by a set of point charges $\{q_i\}$ that simulate the electrostatic potential generated by the solvent distribution. The set of charges $\{q_i\}$ is obtained in three steps [26]:

(1) Each selected solute–solvent configuration is translated and rotated in such a way that all of the solvent coordinates are referred to a reference system centred on the centre of mass of the solute with the coordinate axes parallel to the principal axes of inertia of the solute.

(2) Next, one explicitly includes in the ASEP the charges belonging to solvent molecules that, in any of the molecular dynamics (MD) configurations selected, lie inside a sphere of radius a and that includes at least the first solvation shell. The value of every charge is then divided by the number of solvent configurations included in the determination of the ASEP. Next, in order to reduce the number of charges, one adds together all the charges separated from each other by less than a certain distance. This distance is generally taken as 0.5 a.u.

(3) Finally, one includes a second set of charges representing the effect of the solvent molecules lying outside the first solvation shell. These charges are obtained by a least squares fit to the values of the ASEP originated by the outer solvent molecules in a three-dimensional grid defined inside the volume occupied by the solute molecule. The solute volume is defined through a set of interlocking spheres of radius $f{\cdot}R_{\mathrm{vdw}}$, where f is a numerical factor close to one and R_{vdw} are the Bondi radii [33]. The total number of charges introduced into the perturbation Hamiltonian is generally between 25 000 and 35 000.

The basic scheme of ASEP/MD is displayed in Figure 6-1. ASEP/MD alternates high-level quantum calculations and MD simulations in an iterative procedure. During the MD simulations the internal geometry and charge distribution of the solute molecule, as well as those of the solvent molecules, are considered as fixed. From the MD data one obtains the average solvent electrostatic potential, $\langle V_S(r,\rho)\rangle$ that is introduced as a perturbation into the solute molecular Hamiltonian. By solving the associated Schrödinger equation, one gets a new solute charge distribution that

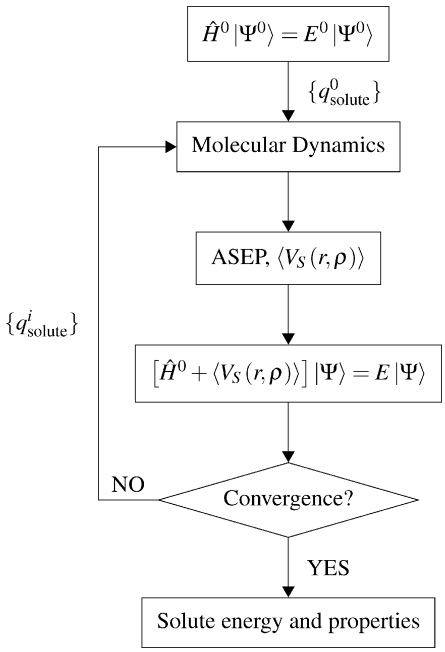

Figure 6-1. Scheme of the ASEP/MD method

serves as input for a new MD calculation. The process is repeated until convergence in the solute charges and in the solute energy is reached. At the end of this process the solute charge distribution and the solvent structure around it become mutually equilibrated. The charges that represent the solute molecule during the MD simulation can be obtained from the in solution molecular wavefunction by using the CHELPG method [34,35] or any of the many methods currently available.

In ASEP/MD, the MD simulations can be performed using polarizable or non-polarizable solvents. However, it is known that simulations employing effective charges can reproduce adequately the solvent structure and are more effective from a computational point of view than those using polarizable force fields. Because of this, in ASEP/MD the solvent polarization is made a posteriori. The determination of the solvent electron polarization with the ASEP/MD method involves two steps [36]. During the first step the solvent structure around the solute is equilibrated, but it is supposed that the charge distribution of every solvent molecule remains fixed, that is, during the simulations one considers a non-polarizable solvent. In the second step, the solvent structure is kept fixed but now the electron degrees of freedom of the solvent polarize in response to the changes in the solute charge distribution originated, for instance, by an electron transition in the solute. That is, using the solvent structure and solute geometry obtained in the first step, in the second one the quantum-mechanical solute and the solvent electron polarization are coupled. To this end, we assign a molecular polarizability to every solvent molecule and,

simultaneously, replace the effective solvent charge distribution used in the MD calculation (TIP3P [37] for instance, if the solvent is water) with the gas phase charge distribution. This is necessary because effective charges include a certain degree of implicit solvent polarization; when one considers a polarizable model it is necessary to use the in vacuo charges of the solvent molecules in order to avoid accounting twice for this effect.

6.2.2. Ground and Excited State Gradients

Any method dedicated to the study of solvent effects on electron spectra must permit the geometry optimization of the solute both in the ground and excited states in presence of the perturbation originated by the solvent. ASEP/MD uses a variant of the free energy gradient method [38,39,40] for the calculation of the gradients that drive the optimization process. The bases of the method are the following: Let $G = -kT \ln Z_{\mathrm{NVT}}$ be the Helmholtz free energy of a system formed by one solute molecule and N–1 solvent molecules. Z_{NVT} is the quasi-classical canonical partition function defined by:

$$Z_{\mathrm{NVT}} = \frac{1}{N!}\frac{1}{h^{3N}} \int \mathrm{d}R^N \mathrm{d}p^N \exp\left[-\frac{E(p^N, r^N)}{kT}\right] \tag{6-5}$$

where E is the energy of the system, which, by convenience, can be split into three terms:

$$E = E_{\mathrm{QM}} + E_{\mathrm{int}} + E_{\mathrm{solv}} \tag{6-6}$$

corresponding to the solute, E_{QM}, the solvent, E_{solv}, and the interaction between them, E_{int}. The force, F, on the free energy surface (the force felt by the solute molecule) is

$$F(R) = -\frac{\partial G}{\partial R} = -\left\langle \frac{\partial E}{\partial R} \right\rangle = -\left\langle \frac{\partial E_{\mathrm{QM}}}{\partial R} \right\rangle - \left\langle \frac{\partial E_{\mathrm{int}}}{\partial R} \right\rangle \tag{6-7}$$

R being the nuclear coordinates of the solute and where we have assumed that E_{solv} does not explicitly depend on the nuclear solute coordinates. The brackets denote a configurational average.

In the same way the Hessian reads

$$\begin{aligned} H(R, R') &= \left\langle \frac{\partial^2 E}{\partial R \partial R'} \right\rangle - \beta \left\langle \frac{\partial E}{\partial R} \right\rangle \left\langle \frac{\partial E}{\partial R} \right\rangle^{\mathrm{T}} + \beta \left\langle \frac{\partial E}{\partial R} \right\rangle \left\langle \frac{\partial E}{\partial R} \right\rangle^{\mathrm{T}} \\ &= \left\langle \frac{\partial^2 E}{\partial R \partial R'} \right\rangle - \beta \left[\left\langle F^2 \right\rangle - \langle F \rangle^2 \right] \end{aligned} \tag{6-8}$$

where the superscript T denotes the transposition and β=1/kT. The last term in Eq. (6-8) is related to the thermal fluctuations of the force.

Next, we use the MFA to simplify the gradient and Hessian expressions. Thus, we replace the configurational average of the derivatives with the derivative of the average configuration, furthermore we neglect the force fluctuation terms (given that the Hessian is used only to accelerate the optimization procedure, this approximation has no effect on the optimized geometries but it can affect the harmonic frequencies evaluation). The validity of these approximations has been checked elsewhere [41]. The force and Hessian now read

$$F(R) = -\left\langle \frac{\partial E}{\partial R} \right\rangle \approx -\frac{\partial \bar{E}}{\partial R} = -\frac{\partial \bar{E}_{\mathrm{QM}}}{\partial R} - \frac{\partial \bar{E}_{\mathrm{int}}}{\partial R} \tag{6-9}$$

$$H(R, R') \approx \frac{\partial^2 \bar{E}}{\partial R \partial R'} = \frac{\partial^2 \bar{E}_{\mathrm{QM}}}{\partial R \partial R'} + \frac{\partial^2 \bar{E}_{\mathrm{int}}}{\partial R \partial R'} \tag{6-10}$$

where $\bar{E}$ and its components are calculated as the solution of the Eq. (6-3).

From a computational point of view, it is convenient to split the interaction term into two components, one associated to the electrostatic interaction and the other to the van der Waals contribution:

$$\hat{H}_{\mathrm{int}} = \hat{H}_{\mathrm{int}}^{\mathrm{elect}} + \hat{H}_{\mathrm{int}}^{\mathrm{vdw}} \tag{6-11}$$

The $\hat{H}_{\mathrm{int}}^{\mathrm{elect}}$ term is calculated using Eq. (6-4), while the $\hat{H}_{\mathrm{int}}^{\mathrm{vdw}}$ term is represented by a Lennard-Jones (LJ) potential. This last term depends only on the nuclear coordinates and hence has no effect on the solute wavefunction but it contributes to the final value of the gradient and Hessian. The final expression for the force is

$$F(R) = -\frac{\partial \bar{E}_{\mathrm{QM}}}{\partial R} - \frac{\partial \bar{E}_{\mathrm{int}}^{\mathrm{elect}}}{\partial R} - \left\langle \frac{\partial E_{\mathrm{int}}^{\mathrm{vdw}}}{\partial R} \right\rangle \tag{6-12}$$

with an equivalent expression for the Hessian. As we can see, electrostatic and van der Waals contributions are calculated in a different way. In the case of the electrostatic term the gradient is calculated quantum-mechanically as the gradient of the average solvent configuration, however, the van der Waals contribution is calculated with a classical force field during the MD simulation as the average value of the gradient over all solvent configurations selected.

When one supposes equilibrium solvation, the different terms appearing in Eq. (6-12) are calculated using the configurational space of each state. For instance, for an excited state we have

$$F^{\mathrm{ex}}(R) = -\nabla \bar{E}(R) = -\frac{\partial \bar{E}_{\mathrm{QM}}(\rho^{\mathrm{ex}})}{\partial R} - \frac{\partial \bar{E}_{\mathrm{int}}^{\mathrm{elect}}(\rho^{\mathrm{ex}}, \{X^{\mathrm{ex}}\})}{\partial R} - \left\langle \frac{\partial E_{\mathrm{int}}^{\mathrm{vdw}}}{\partial R} \right\rangle_{\{X^{\mathrm{ex}}\}} \tag{6-13}$$

where we have made explicit the functional dependence of the energy with the solute charge density and where $\{X^{\mathrm{ex}}\}$ indicates that the average solvent structure is calculated using the solvent configurations in equilibrium with the charge distribution of the solute excited state, ρ^{ex}. However, in FC points, characterized by a non-equilibrium solvation situation, the configurational space used is that of the ground state (for an absorption process), and the force can then be written as

$$F^{\mathrm{FC}}(R) = -\nabla \bar{E}(R) = -\frac{\partial \bar{E}_{\mathrm{QM}}(\rho^{\mathrm{ex}})}{\partial R} - \frac{\partial \bar{E}_{\mathrm{int}}^{\mathrm{elect}}(\rho^{\mathrm{ex}}, \{X^{\mathrm{gr}}\})}{\partial R} - \left\langle \frac{\partial E_{\mathrm{int}}^{\mathrm{vdw}}}{\partial R} \right\rangle_{\{X^{\mathrm{gr}}\}} \tag{6-14}$$

where now $\{X^{\mathrm{gr}}\}$ is the solvent configuration in equilibrium with the charge distribution of the solute ground state.

6.2.3. Location of Conical Intersections and Singlet–Triplet Crossing Points in Solution

To locate a minimal energy conical intersection (MECI) between two electronic states K and L we combine the ASEP/MD method with an algorithm due to Bearpark et al. [42]. The algorithm simultaneously minimizes the in solution energy difference between the two intersecting states and the energy of the crossing seam between the two potential energy surfaces. The final form taken by the gradient used in the location algorithm is

$$\mathbf{f}_{KL} = 2(E_K - E_L)\hat{g}_{KL} + \left[\nabla E_K - (\nabla E_K \cdot \hat{g}_{KL})\,\hat{g}_{KL} - \left(\nabla E_K \cdot \hat{h}_{KL}\right)\hat{h}_{KL}\right] \tag{6-15}$$

here E_K and E_L are the energies of the intersecting surfaces, ∇E_K is the gradient of the upper state and $\hat{g}_{KL}$ and $\hat{h}_{KL}$ are the two versors that define the branching space or g–h plane [43], i.e., the subspace of nuclear coordinates in which the degeneracy between the two intersecting surfaces is lifted linearly in displacements from the intersection. When the two intersecting states have different spin symmetry as in the case of singlet–triplet crossing (STC), the $\hat{h}_{KL}$ term vanishes and only one coordinate defines the branching space. The expression of $\mathbf{g}_{KL}$, the energy difference gradient vector, is

$$\mathbf{g}_{KL} = \nabla(E_K - E_L) \tag{6-16}$$

while $\mathbf{h}_{KL}$, the derivative coupling vector, reads

$$\mathbf{h}_{KL} = \langle \Psi_K \,|\nabla|\, \Psi_L \rangle \tag{6-17}$$

where the gradient ∇ is a vector in the nuclear space and Ψ_I are the adiabatic electronic wavefunctions, eigenfunctions of the electronic Hamiltonian, $\hat{H}$, with energies E_I. The corresponding versors are defined as $\hat{g}_{KL} = \mathbf{g}_{KL} / |\mathbf{g}_{KL}|$ and $\hat{h}_{KL} = \mathbf{h}_{KL} / |\mathbf{h}_{KL}| - \left(\mathbf{h}_{KL}\hat{g}_{KL} / |\mathbf{h}_{KL}|\right) \hat{g}_{KL}$.

Equation (6-15) is valid both for in vacuo and in solution systems. Obviously, in this last case we must include the perturbation due to the solvent in each one of the terms: interstate energy difference, excited state gradient, energy difference gradient and derivative coupling.

The energies of the K and L states are obtained by solving Eqs. (6-3) and (6-4), the excited state gradient is calculated with Eq. (6-13). The same expression is used in the calculation of the energy difference gradient, $\mathbf{g}_{KL}$, however, in this case some simplifications are possible because we suppose that the Lennard-Jones coefficients are the same for all the states of one molecule. Furthermore, taking into account that the two states K and L are calculated at the same geometry we obtain

$$\begin{aligned}\mathbf{g}_{KL} = \nabla(E_K - E_L) = \frac{\partial \bar{E}_{\mathrm{QM}}(\rho^K)}{\partial R} - \frac{\partial \bar{E}_{\mathrm{QM}}(\rho^L)}{\partial R} \\ + \frac{\partial \bar{E}^{\mathrm{elect}}_{\mathrm{int}}(\rho^K, \{X^K\})}{\partial R} - \frac{\bar{E}^{\mathrm{elect}}_{\mathrm{int}}(\rho^L, \{X^K\})}{\partial R}\end{aligned} \tag{6-18}$$

where the van der Waals terms vanish because they depend only on nuclear coordinates and hence take the same values for all the electronic states. Note that we use the configurational space of the excited state K in the determination of the solute–solvent interaction energy difference.

The complete scheme of the process followed to locate CI or STC of molecules in solution using ASEP/MD is shown in Figure 6-2. We begin by equilibrating the solvent and the solute and getting a set of point charges that represent the charge distribution of the solute molecule in the initial state, generally the ground state. These charges are then used as input for an MD simulation of the solute and solvent molecules, the remaining parameters for the solute (LJ coefficients) and solvent (charges and LJ coefficients) are obtained from the literature. N representative solvent configurations (N usually taken between 500 and 1000) are selected from the MD simulation. From these configurations the average solvent potential, Eq. (6-4), generated by the solvent in the volume occupied by the solute is calculated. Next, one solves the electronic Schrödinger equation of the solute molecule, Eq. (6-3), in presence of the average perturbation generated by the solvent. The energies and wavefunctions of the crossing points are calculated and the gradient $\mathbf{f}_{KL}$ is obtained. A new solute geometry, closer to the crossing point, can be obtained by using a quasi-Newton method. In this point we have two possibilities depending on whether the solvent is in an equilibrium or non-equilibrium situation. In the former case the solvent must be equilibrated with the solute charge distribution of the upper state and hence a new MD must be performed, the procedure is continued until the solvent distribution and the charge distribution of the upper state are mutually equilibrated. Although strictly speaking it is necessary to perform an MD calculation for each new

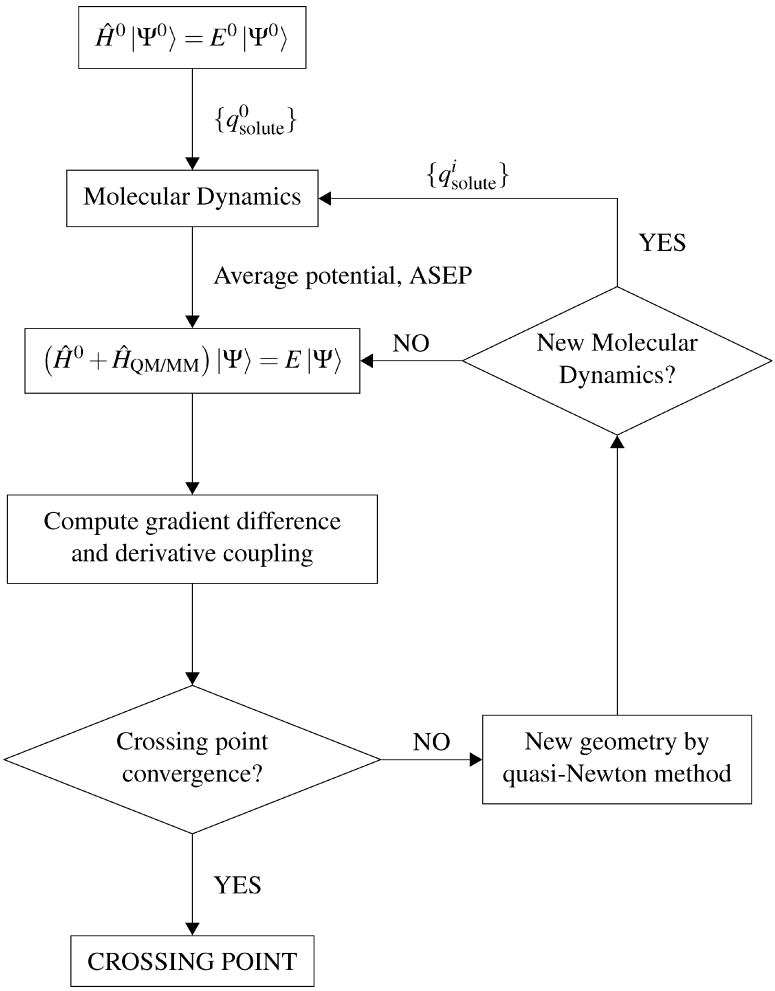

Figure 6-2. Conical intersection and singlet–triplet crossing location scheme

solute geometry, this is a very inefficient procedure. It has been verified [44] that it is computationally more efficient to perform several steps of the crossing point search procedure before equilibrating the solvent again. We update the solvent structure only after 10–20 iterations of the crossing point search procedure.

In the case of non-equilibrium conditions, the crossing point is located for a frozen solvent structure. During an electron transition the Franck–Condon principle is applicable and the solvent nuclei remain fixed during the transition. Consequently, the solvent structure is in equilibrium with the charge distribution of the solute in its ground state. The crossing point search procedure is performed in presence of this solvent structure.

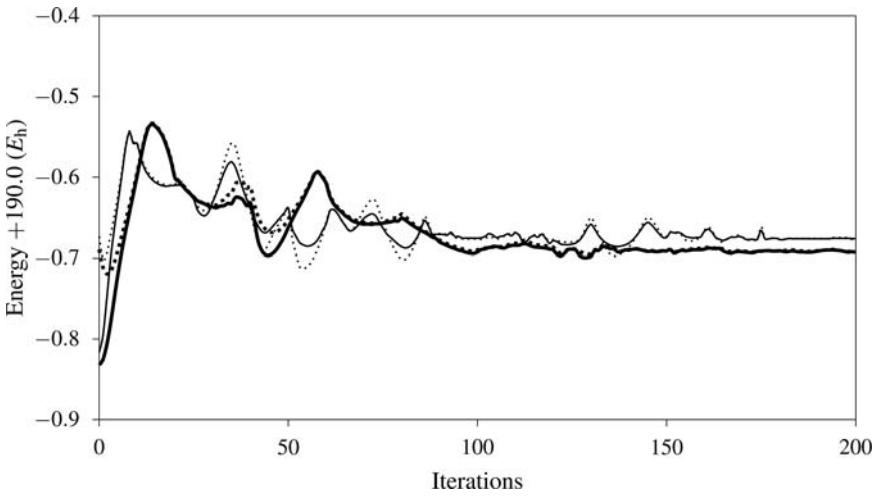

Figure 6-3. Evolution during the search procedure of the S_0 and S_1 energies of acrolein (in Hartree) in vacuum (*thin lines*, *continuous* and *dotted*, respectively), and in water solution (*thick lines*, *continuous* and *dotted*, respectively)

Figure 6-3 displays the evolution of the total energy in vacuo and in solution of the S_0 and S_1 acrolein states as a function of the number of cycles of the search procedure. In the first steps the energy difference between the two crossing states decreases until the system is close to the CI seam. Then the energy decreases until the MECI is reached. Each time a new ASEP/MD is performed the solvent structure is recalculated. If this change is important the position of the crossing seam changes and the energies begin to fluctuate until they are again stabilized in a new plateau. The final in solution values (energies, geometries, dipoles, etc.) are calculated by averaging over the results obtained with the last few cycles of ASEP/MD.

6.2.4. Free Energy Differences

Once the different minima, MECI and MESTC points have been located, it is necessary to determine their relative stabilities. For in solution systems the relevant quantity is the free energy difference. The standard free energy difference between two states, *i* and *f*, in solution can be written as the sum of two terms [45]

$$\Delta G_{\text{diff}} = \Delta G_{\text{solute}} + \Delta G_{\text{int}} \tag{6-19}$$

where ΔG_{int} is the difference in the solute–solvent interaction free energy between the two QM states, and

$$\Delta G_{\text{solute}} = \Delta E_{\text{solute}} + \Delta V_{\text{solute}} \tag{6-20}$$

where

$$\Delta E_{\text{solute}} = E^{f}_{\text{QM}} - E^{i}_{\text{QM}} = \left\langle \bar{\Psi}^{f} \middle| \hat{H}_{\text{QM}} \middle| \bar{\Psi}^{f} \right\rangle - \left\langle \bar{\Psi}^{i} \middle| \hat{H}_{\text{QM}} \middle| \bar{\Psi}^{i} \right\rangle \tag{6-21}$$

is the ab initio difference between the two QM states calculated using the in vacuo solute molecular Hamiltonian, $\hat{H}_{\text{QM}}$, and the in solution wavefunctions. ΔV_{solute} is the solute's vibrational and thermal contribution to the free energy (usually evaluated with the harmonic approximation).

In order to clarify the role played by the solvent in the stabilization of the different structures it is useful to split the ΔG_{int} term into two terms: ΔE_{int} and ΔG_{solv}. The last term, ΔG_{solv}, provides the solvent distortion energy, i.e., the energy spent in changing the solvent structure from the initial to the final state. The term ΔE_{int} accounts for the difference in the solute–solvent interaction energy between the final and initial states. For a non-polarizable solvent this term reads

$$\Delta E_{\text{int}} = E^{f}_{\text{int}} - E^{i}_{\text{int}} = \left\langle \bar{\Psi}^{f} \middle| \hat{H}_{\text{int}} \middle| \bar{\Psi}^{f} \right\rangle - \left\langle \bar{\Psi}^{i} \middle| \hat{H}_{\text{int}} \middle| \bar{\Psi}^{i} \right\rangle \tag{6-22}$$

If one wants to consider explicitly the electron polarization of the solvent it is necessary to add to Eq. (6-22) the energy spent in polarizing the solvent dipoles. In a previous work [36], we have shown that for a polarizable solvent, the final expression that the solute–solvent interaction energy takes is

$$\Delta E^{\text{pol}}_{\text{int}} = \frac{1}{2}\Delta E_{q\mu} + \Delta E_{\rho q} + \frac{1}{2}\Delta E_{\rho\mu} \tag{6-23}$$

Here, q refers to the permanent charges of solvent molecules, μ the induced dipoles on the solvent and ρ the solute charge density.

In solvent effect studies, a fundamental quantity is the solvent shift, δ, on the energy, defined as the difference between the energy gap values calculated in solution and in vacuo:

$$\delta = \Delta G_{\text{diff}} - \Delta G^{0}_{\text{solute}} \tag{6-24}$$

If we suppose, as it is usually the case, that the solvent has only a small influence on the solute's thermal contribution, ΔV_{solute}, then, using Eqs. (6-19) and (6-20), Eq. (6-24) can be simplified to

$$\delta = \Delta G_{\text{int}} + (\Delta E_{\text{solute}} - \Delta E^{0}_{\text{solute}}) \tag{6-25}$$

where the term in parentheses is the distortion energy of the solute: the energy spent in the solute polarization during the solvation process. Splitting the different contributions to ΔG_{int} one obtain the following expression for the solvent shift on a solute embedded in a polarizable solvent:

$$\delta = \frac{1}{2}\Delta E_{\mu q} + \Delta E_{\rho q} + \frac{1}{2}\Delta E_{\rho\mu} + (\Delta E_{\text{solute}} - \Delta E^{0}_{\text{solute}}) + \Delta G_{\text{solv}} \tag{6-26}$$

In the case of vertical transitions the term ΔG_{solv} cancels out because the Franck–Condon approximation is applicable and the solvent structure is the same in both the ground and excited states. For non-vertical transition, ΔG_{solv} must be explicitly calculated. We calculate this term as difference between ΔG_{int} and ΔE_{int}. This last term is calculated quantum-mechanically using Eq. (6-22). The ΔG_{int} can be calculated using free energy perturbation method [46]. The solute geometry is assumed to be rigid and a function of the perturbation parameter (λ) while the solvent is allowed to move freely. When λ=0 the solute geometry and charges and the solute–solvent interaction parameters correspond to the initial state. When λ=1 the charges and geometry are those of the final state. For intermediate values a linear interpolation is applied.

6.3. DE-EXCITATION PATHWAYS IN ACROLEIN

As an example of application of the ASEP/MD method described in the previous section, in this section we proceed to the discussion of solvent effects on radiative and non-radiative processes in acrolein. Acrolein or propenal is the smallest α,β-unsaturated carbonyl compound. The presence of the carbonyl group and the C=C double bond makes it a compound of marked interest from a spectroscopic and photochemical points of view. In solution, acrolein displays a strong absorption band corresponding to a $^1(\pi\rightarrow\pi^*)$ transition and a weak band, at lower frequencies associated to a dipole forbidden $^1(n\rightarrow\pi^*)$ transition. The fluorescence spectrum shows a band, which overlaps the first absorption peak, and which is assigned as originating from the S_1 state. The molecule presents also a phosphorescence spectrum, but the assignation of the observed band to one specific transition is not clear. Finally, the small values of the quantum yields for both fluorescence and phosphorescence (0.007 and 0.00004, respectively [47]) point to the existence of important non-radiative decay pathways.

In what follows, the ground and excited states of acrolein have been described using CASSCF and CASPT2 levels of theory. In previous papers [36,48] it was shown that the inclusion of the dynamic correlation component through CASPT2 calculations is compulsory if one desires to reproduce the transition energy. However, in the acrolein case this component does not appreciably modify the solvent shift and, in general, a good description of the solvent effects can be obtained at CASSCF level. The complete active space was spanned by all the configurations arising from six valence electrons in five orbitals (6e/5o). The quantum calculations were performed using two basis sets: the 6-31 G* basis set and an atomic natural orbitals (ANO) [49] basis set (the contraction scheme used was C,O [4s3p1d]/H [2s1p]). The initial geometry for acrolein was obtained by CASSCF optimization both in vacuum and in solution with the aforementioned basis sets. A total of one acrolein molecule and 250 TIP3P water molecules [37] were simulated with fixed intramolecular geometry by combining LJ interatomic interactions with electrostatic interactions in a cubic box of 18.7 Å side. Periodic boundary conditions were applied, and spherical cutoffs were used to truncate the molecular interactions at 9.0 Å. A time step of 0.5 fs

was used. The electrostatic interaction was calculated with the Ewald method. The temperature was fixed at 298 K by using a Nosé-Hoover thermostat. Each MD calculation simulation was run for 75 ps (25 ps equilibration, 50 ps production). Solvent effects were treated with the ASEP/MD program [26,41] using the data provided by Gaussian 98 [50] (quantum calculations) and MOLDY [51] (MD simulations). CASPT2 calculations were performed with the Molcas [52] program.

6.3.1. Absorption Spectra

To understand the nature of the solvent shift in the absorption process it is interesting to analyse first the solvent structure around the acrolein molecule. The radial distribution functions (rdf) O(water)–O(acrolein) and H(water)–O(acrolein) for S_0 and S_1 states are shown in Figures 6-4 and 6-5, respectively. They were obtained as average values over the last 10 ASEP/MD cycles. For the S_0 state, the H(w)–O(a) rdf displays a well-defined peak at 1.85 Å, indicating a strong hydrogen bond between acrolein and a water molecule. The first peak of the O(w)–O(a) rdf appears at 2.75 Å, and given that the H–O distance in water is 0.957 Å, one can conclude that the hydrogen bond is almost linear. In Figure 6-4, it can also be observed that the radial distribution function has several peaks at long distances, indicating that acrolein imposes a considerable order on the water structure. The calculated coordination number is 2.1. The two electron lone pairs of the acrolein oxygen seem to be involved in the formation of hydrogen bonds.

Table 6-1 lists the solvent shift on the $^1(n\rightarrow\pi^*)$ transition and its different contributions (see Eq. (6-26)). The first column corresponds to the solvent shift due to

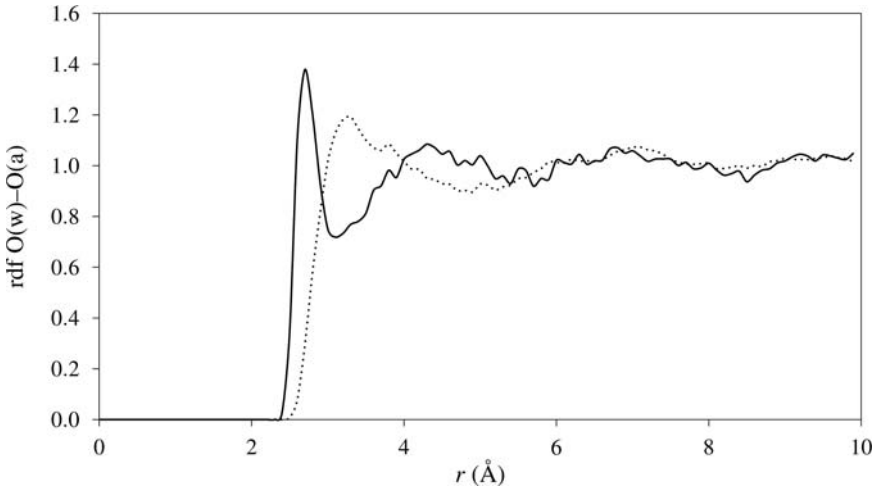

Figure 6-4. Oxygen (water)–oxygen (acrolein) radial pair distribution function of the S_0 (*continuous line*) and S_1 (*dotted line*) states of acrolein

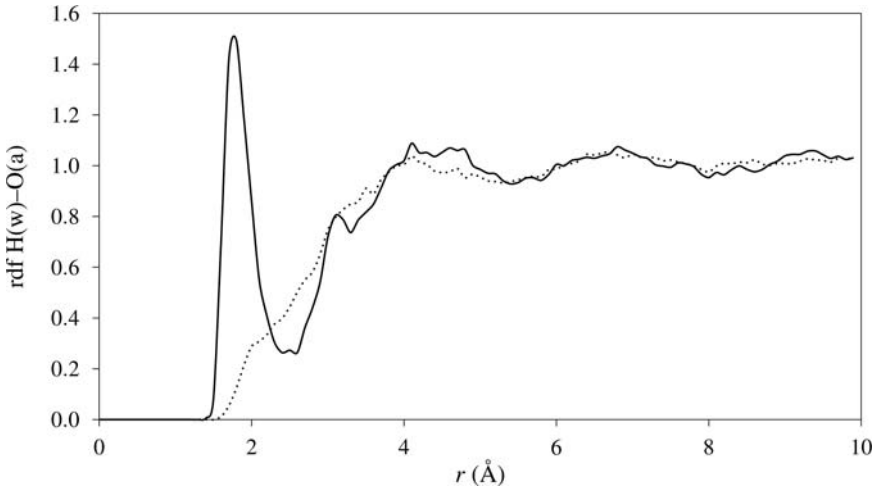

Figure 6-5. Hydrogen (water)–oxygen (acrolein) radial pair distribution function of the S_0 (*continuous line*) and S_1 (*dotted line*) states of acrolein

the electrostatic interaction between the solute charge distribution and the permanent charges of the solvent. The second and third columns correspond to the interaction between the induced solvent dipoles (μ) and the solute charge distribution (ρ) and permanent solvent charges (q). The fourth column is the contribution of the solute distortion energy. The total solvent shift is given in the last two columns. Given that the dipole moment, and hence the solute–solvent interaction energy, decreases in about 2.2 D during the excitation, the band position is blue shifted in 5.0 kcal/mol (6-31 G* basis set), very close to the value, 4.5 kcal/mol, obtained at CASPT2 level and using ANO basis sets and to the experimental value [53], 4.4 kcal/mol. The largest contribution to the solvent shift comes from the interaction between the solute and the permanent charges of the solvent. However, the contribution from the solvent polarization (components associated to the induced dipoles) is also important, representing about 26% of the total solvent shift.

In solution, the strongest band of the absorption spectrum is associated with the $^1(\pi\rightarrow\pi^*)$ transition. During this transition the dipole moment increases in about 2.0 D, and the position of the band is red shifted by 6.2 kcal/mol.

Table 6-1. Solvent shift values and its components in kcal/mol

	$\delta_{\rho q}$	$\frac{1}{2}\delta_{q\mu}$	$\frac{1}{2}\delta_{\rho\mu}$	δ_{sol}^{dist}	δ	δ_{CASPT2}
Absorption	5.9±0.4	0.04±0.02	1.1±0.1	–2.7±0.4	4.3±0.2	4.5±0.2

6.3.2. Emission Spectra

As was indicated above the fluorescence band overlaps the $^1(n\rightarrow\pi^*)$ absorption band, this fact and the very low value of the fluorescence quantum yield allows the assignation of the band to the de-excitation from the S_1 state. The charge flux that accompanies the electron transition has an influence on the solvent structure around the excited state of the acrolein molecule. Figures 6-4 and 6-5 display the O(water)–O(acrolein) and H(water)–O(acrolein) radial pair distribution function in the S_1 excited state with dotted lines. In the O(w)–O(a) rdf the height of the first peak decreases with the excitation and its position is shifted to longer distances, the same is valid for the rest of the peaks, the solvent is less structured around the excited state than around the ground state. The number of solvent molecules included in the first solvation shell (calculated by integration until the first minimum of the ground state rdf) are 2.1 and 1.2 for the ground and excited states, respectively. The behaviour of the H(w)–O(a) rdf is even more striking, the solvent structure found around the solute ground state is completely lost in the solute excited state. One can conclude that the $^1(n\rightarrow\pi^*)$ excitation produces the partial desolvation of acrolein. This desolvation determines the energetic features of the emission process in solution.

Compared to the corresponding in vacuo transition, the solvent originates a blue shift in the fluorescence band of 1.8 kcal/mol (polarizable solvent). The results obtained with polarizable solvent are similar to that obtained with an effective charges model, the computational cost being notably lower in the latter case. The difference in solvent shift values found for the absorption and emission processes is related to the different strengths of the solute–solvent interaction in the ground and first excited states. As it was indicated above, the charge flux that accompanies the excitation yields a lower dipole moment, weaker solvent structure around the solute and as a consequence lower solute–solvent interaction energy (and energy differences) when the solvent is in equilibrium with the excited state. The inclusion of dynamic electron correlation increases the solvent shift by only 0.2 kcal/mol for the absorption process but by 0.6 kcal/mol for the emission process. On a percentage basis, the contribution of the dynamic electron correlation to the solvent shift represents 33% of the total solvent shift in the emission process but less than 5% of the total solvent shift in the absorption process.

The phosphorescence band is more complicated to assign. Table 6-2 displays the energy of the singlet and triplet states both in vacuo and in solution. In both cases, the most stable triplet is the $T_{\pi\pi^*}$ state. This state has in its minimum a geometry twisted 90° around the C=C bond. At this geometry the $T_{\pi\pi^*}$ state crosses the ground state and hence it relaxes non-radiatively through an intersystem crossing. Consequently, the phosphorescence emission must be associated to the de-excitation from the $T_{n\pi^*}$ state. Experimentally, the maximum of the phosphorescence band appears at 2.46 eV, our calculations places the emission from the $T_{n\pi^*}$ state at 2.24 eV. The solvent originates a blue shift of about 0.73 kcal/mol. The solvent structure around the $T_{n\pi^*}$ is similar to that of S_1. Like for the S_1 state, the $T_{n\pi^*}$ state is characterized by a charge flux from the oxygen to the carbon skeleton, this charge flux decreases the dipole moment of the excited triplet state with respect to the ground state value. At the

Table 6-2. Energy results in a.u. ΔE and ΔG in kcal/mol

		Vacuum		Solution		
		E	ΔE	ΔG eq	ΔE non-eq	Geometry
S_1	FC	–190.6788	0.0	0.0	0.0	
S_0	Min	–190.8235	–90.8	–95.8		Planar
S_1	Min	–190.7081	–18.4	–20.7		Planar
$T_{n\pi^*}$	Min	–190.7131	–21.5	–22.3		Planar
$T_{\pi\pi^*}$	Min	–190.7278	–35.7	–36.4		Twisted
$S_1/T_{\pi\pi^*}$	STC	–190.7044	–16.1	–19.2	–17.7	Planar
$T_{n\pi^*}/T_{\pi\pi^*}$	CI	–190.7055	–16.7	–19.1	–18.4	Planar
$T_{\pi\pi^*}/S_0$	STC	–190.7275	–30.5	–33.7	–34.2	Twisted
S_1/S_0	CI	–190.6762	+1.6	–1.4	+6.4	Twisted

same time it produces a partial desolvation of the excited state. These two effects destabilize the excited state with respect to the ground state and explain the blue shift.

6.3.3. Non-radiative Excited State Decay

In the radiationless relaxation of acrolein there are at least four states involved [54], the ground state, S_0, the first singlet excited state, S_1, and two triplet states, $T_{\pi\pi^*}$ and $T_{n\pi^*}$. Two paths have been proposed in order to explain the radiationless de-excitation of acrolein in gas phase: (1) a direct de-excitation through a S_1/S_0 IC and (2) an indirect path starting with a $S_1/T_{\pi\pi^*}$ ISC. From here we have several possibilities: (a) the system can return to the ground state through a $T_{\pi\pi^*}/S_0$ ISC, (b) the system can pass to $T_{n\pi^*}$ through a $T_{\pi\pi^*}/T_{n\pi^*}$ IC. From $T_{n\pi^*}$ acrolein relaxes non-radiatively to $T_{\pi\pi^*}$ and from here it returns to S_0 through a $T_{\pi\pi^*}/S_0$ ISC. When the system is in $T_{n\pi^*}$ state it can relax radiatively originating the phosphorescence band.

Table 6-2 provides the relative stability of the different minima, MECI and MESTC points, calculated in vacuo and in solution, and in the latter case, in equilibrium and non-equilibrium conditions. Figure 6-6 displays the geometries of the minima, and minimal energy CI and STC points.

We first analyse the influence of the solvent on the different geometries supposing solvent equilibrium conditions. In all the cases analysed – minima, MECI and MESTC – the solvent increases the C–O distance and decreases the two C–C distances. This behaviour can be explained by the formation of hydrogen bonds between the carbonyl oxygen and the hydrogen of the water molecules. The larger distance variations appear in the $S_0/T_{\pi\pi^*}$ STC and $T_{\pi\pi^*}/T_{n\pi^*}$ CI. In order to understand the variation of the geometrical parameters it is necessary to consider two variables: the bond order of the carbonyl group and the in vacuo dipole moment value. The

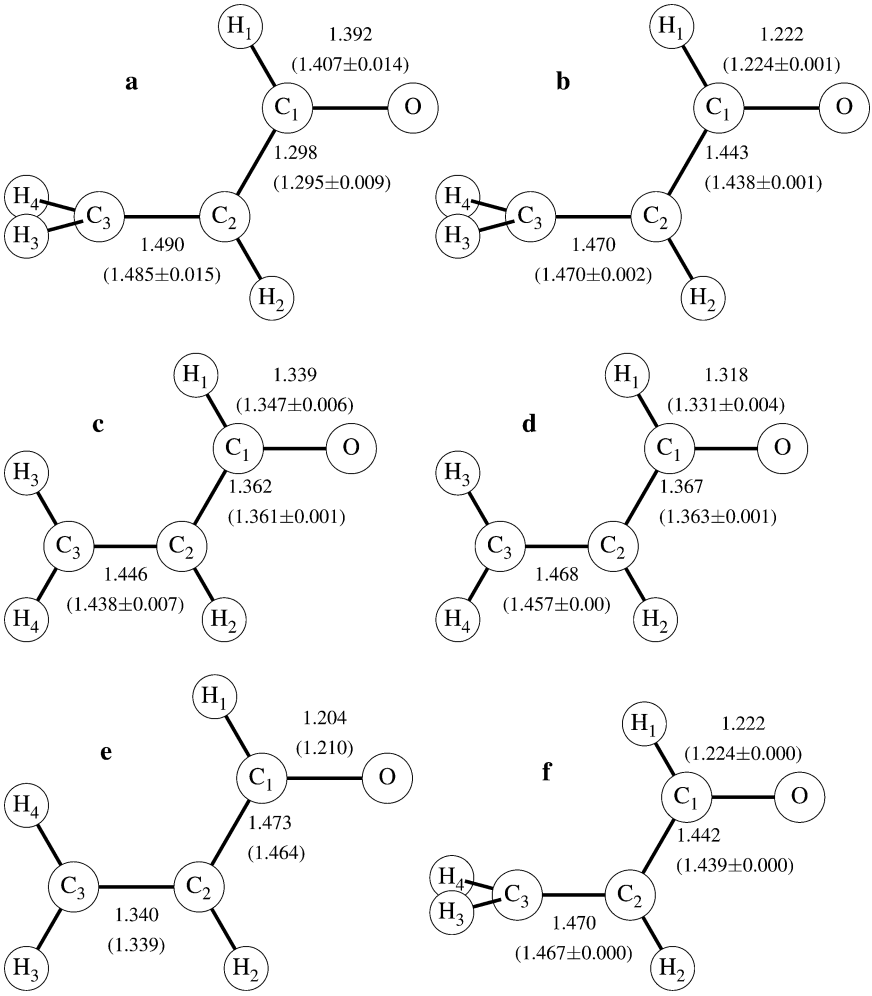

Figure 6-6. (a) S_1/S_0 CI geometry in vacuo and in solution (in parentheses). (b) The $T_{\pi\pi^*}/S_0$ STC geometry in vacuo and in solution (in parentheses). (c) $S_1/T_{\pi\pi^*}$ STC geometry in vacuo and in solution (in parentheses). (d) $T_{n\pi^*}/T_{\pi\pi^*}$ CI geometry in vacuo and in solution (in parentheses). (e) FC geometry in vacuo and in solution (in parentheses). (f) $T_{\pi\pi^*}$ minimum geometry in vacuo and in solution (in parentheses) Distances in Å

larger variations of distances appear in those structures where the C–O bond has a single bond character and the dipole moment is high. In these conditions the bond is more labile and hence easier to elongate. In twisted structures, the solvent affects the $C_1C_2C_3H_6$ torsion angle value, which, in the S_0/S_1 CI structure, for instance, increases from 100° to 103°.

The solvent has also effects on the relative energies of the minima and crossing points. In Table 6-2, all data have been referred to the FC points (in vacuo and in solution), being the points where the de-excitation process initiates. As a general rule and when compared with the in vacuo values, the solvent stabilizes the energy of all the minima and crossing points of acrolein. In the FC point the solvent is in a non-equilibrium situation, however, in the rest of points, minima, CI and STC, the solvent is in equilibrium with the corresponding solute charge distribution. The relaxation of the solvent from a non-equilibrium situation to an equilibrium situation explains the additional stability obtained in solution.

The main conclusion that one can obtain from Table 6-2 is that, in solution, the radiationless relaxation can follow the same path as in vacuo. The direct de-excitation, path 1, through the S_0/S_1 CI is improbable but possible, it is 1.6 kcal/mol above the gas phase FC point but 1.3 kcal/mol below the FC point in solution. However, this path involves an appreciable reorganization of the solvent structure. As for the gas phase process the most probable path passes through the $S_1/T_{\pi\pi^*}$ STC. This de-excitation path supposing an equilibrium solvent situation implies also a large reorganization of the solvent structure around acrolein and hence one can expect that it will be slower in solution than in vacuo.

The different crossing points have also been located for a non-equilibrium solvation situation. Depending on the case, the search procedure can be more complicated than in the equilibrium solvation situation, see Figure 6-7. In non-equilibrium solvation all the crossing points are less stable than the corresponding equilibrium points. For instance, the S_0/S_1 CI is 3.2 kcal/mol above the FC point. However,

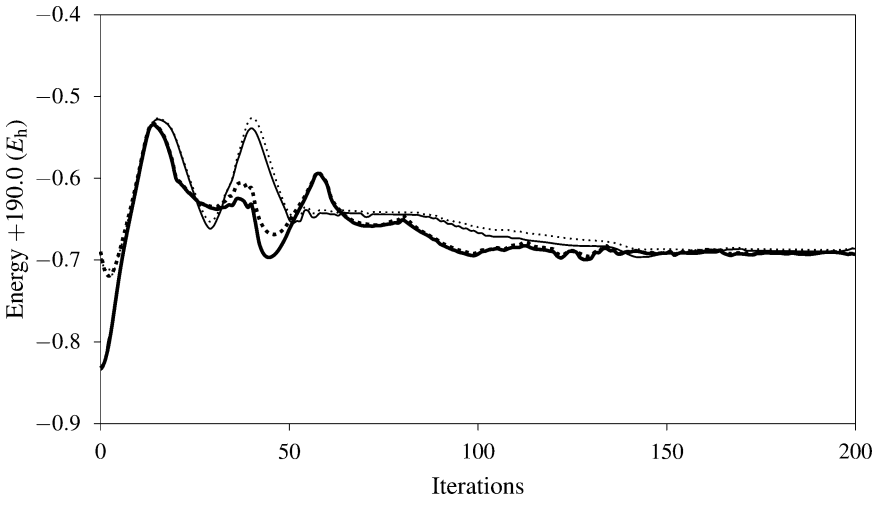

Figure 6-7. Evolution during the search procedure of the S_0 and S_1 energies (in Hartree) in non-equilibrium conditions (*thin lines*, *continuous* and *dotted*, respectively), and in equilibrium conditions (*thick lines*, *continuous* and *dotted*, respectively)

the path that involves the $S_1/T_{\pi\pi^*}$ and $T_{\pi\pi^*}/S_0$ STC is still energetically possible. This path does not imply solvent reorganization, only solute movements and hence can take place, in principle, at practically the same speed as in vacuo. In conclusion, the radiationless relaxation of acrolein in aqueous solution can follow the same path as that of the in vacuo system and must proceed with almost the same speed.

6.4. CONCLUDING REMARKS

In the last decades, the theoretical study of solvent effects has known a great development. New and improved models have been proposed that have permitted to extend the range of problems treated and improve the accuracy of the predictions made. The new models are characterized by a quantum-mechanics high-level description of the solute molecule and a detailed description of the microscopic structure of the solvent. Among this trend is placed the method proposed by our group, the ASEP/MD method: a sequential QM/MM method that has as a distinct feature the use of the mean field approximation. ASEP/MD has been successfully applied to the study of solvent effects on chemical reactions, conformational equilibrium and absorption spectra. In this chapter, we have presented an extended version that permits a first approximation to the study of solvent effects on the radiative and non-radiative decay of excited states. These are intrinsically dynamic processes where it is necessary to take into account the interplay between electronic structure and nuclear dynamics. We have undertaken this problem by establishing two limit situations, which we have characterized as equilibrium and non-equilibrium solvation regimes. In the former, we suppose decay times long enough to allow a complete relaxation of the solute and the solvent structures. In the latter, we suppose the decay process is fast enough to prevent the solvent equilibration (although we assume a complete relaxation of the solute). In some situations the solvent behaviour will be halfway between these two limits and an adequate treatment would require the use of more advanced techniques such as ab initio molecular dynamics. We believe, however, that in many cases, the two limits indicated above would be a good approximation to the real situation and valid and interesting information about the solvent effects on the decay processes could be obtained.

As an example of application of the method we have considered the case of the acrolein molecule in aqueous solution. We have shown how ASEP/MD permits a unified treatment of the absorption, fluorescence, phosphorescence, internal conversion and intersystem crossing processes. Although, in principle, electrostatic, polarization, dispersion and exchange components of the solute–solvent interaction energy are taken into account, only the firsts two terms are included into the molecular Hamiltonian and, hence, affect the solute wavefunction. Dispersion and exchange components are represented through a Lennard-Jones potential that depends only on the nuclear coordinates. The inclusion of the effect of these components on the solute wavefunction is important in order to understand the solvent effect on the red shift of the bands of absorption spectra of non-polar molecules or the disappearance of

the Rydberg bands of chromophores in solution. Furthermore, it is supposed that the LJ parameters are the same for all the electron states. Consequently, in our model, LJ components do not contribute to the transition energies. These approximations constitute a limitation of the method that we will try to overcome in the near future.

REFERENCES

1. Bayliss NS, McRae EG (1954) J Phys Chem 58:1002
2. Tomasi J, Persico M (1994) Chem Rev 94:2027
3. Rivail JL, Rinaldi D (1995) In: Leszczynski J (ed) Computational chemistry: review of current trends, World Scientific Publishing, Singapore
4. Cramer CJ, Truhlar DG (1995) In: Lipkowitz KB, Boyd DB (eds) Reviews in computational chemistry, vol VI. VCH Publishers, New York, p 1
5. Martín ME, Sánchez ML, Olivares del Valle FJ, Aguilar MA (2000) J Chem Phys 113:6308
6. Caricato M, Mennucci B, Tomasi J, Ingrosso F, Cammi R, Corni S, Scalmani G (2006) J Chem Phys 124:124520
7. Improta R, Barone V, Santoro F (2007) Angew Chem Int Ed 46:405
8. Lippert E (1957) Z Elektrochem Ber Bunsenges Phys Chem 61:962
9. Lippert E (1961) Angew Chem 73:695
10. Whery EL (1990) In: Guilbault GG (ed) Practical fluorescence, 2 nd edn. Marcel Dekker, Inc., New York, p 127
11. Toniolo A, Ben-Nun M, Martínez TJ (2002) J Phys Chem A 106:4679
12. Toniolo A, Granucci G, Martínez TJ (2003) J Phys Chem A 107:3822
13. Burghardt I, Cederbaum L, Hynes JT (2004) Faraday Discuss 127:395
14. Spezia R, Burghardt I, Hynes JT (2006) Mol Phys 104:903
15. Garavelli M, Rugen F, Ogliano F, Bearpark MJ, Bernardi F, Olivucci M, Robb MA (2003) J Comput Chem 24:1357
16. Frutos LM, Andruniów T, Santoro F, Ferré N, Olivucci M (2007) Proc Natl Acad Sci USA 104:7764
17. Yamazaki S, Kato S (2005) J Chem Phys 123:114510
18. Yamazaki S, Kato S (2006) J Am Chem Soc 129:2901
19. Tomasi J, Mennucci B, Cammi R (2005) Chem Rev 105:2999
20. Caricato M, Ingrosso F, Mennucci B, Tomasi J (2005) J Chem Phys 122:154501
21. Aguilar MA (2001) J Phys Chem A 105:10393
22. Sánchez ML, Aguilar MA, Olivares del Valle FJ (1997) J Comput Chem 18:313
23. Sánchez ML, Martín ME, Aguilar MA, Olivares del Valle FJ (2000) J Comput Chem 21:705
24. Sánchez ML, Martín ME, Fdez. Galván I, Olivares del Valle FJ, Aguilar MA (2002) J Phys Chem B 106:4813
25. Martín ME, Sánchez ML, Olivares del Valle FJ, Aguilar MA (2002) J Chem Phys 116:1613
26. Fdez. Galván I, Sánchez ML, Martín ME, Olivares del Valle FJ, Aguilar MA (2003) Comput Phys Commun 155:244
27. Ghoneim N, Suppan P (1995) Spectrochim Acta 51A:1043
28. Linder B (1967) Adv Chem Phys 12:225
29. Karlström G, Halle B (1993) J Chem Phys 99:8056
30. Tapia O, Goscinski O (1975) Mol Phys 29:1653
31. Warshel A (1991) Computer modelling of chemical reactions in enzymes and solutions, Wiley Interscience Publication, New York
32. Ten-no S, Hirata F, Kato S (1993) Chem Phys Lett 214:391

33. Bondi A (1964) J Phys Chem 68:441
34. Chirlian LE, Francl MM (1987) J Comput Chem 8:894
35. Breneman CM, Wiberg KB (1990) J Comput Chem 11:361
36. Martín ME, Muñoz Losa A, Fdez. Galván I, Aguilar MA (2004) J Chem Phys 121:3710
37. Jorgensen WL, Chandrasekhar J, Madura JD, Impey RW, Klein ML (1983) J Chem Phys 79:926
38. Okuyama-Yoshida N, Nagaoka M, Yamabe T (1998) Int J Quantum Chem 70:95
39. Okuyama-Yoshida N, Nagaoka M, Yamabe T (2000) J Chem Phys 113:3519
40. Hirao H, Nagae Y, Nagaoka M (2001) Chem Phys Lett 348:350
41. Fdez. Galván I, Sánchez ML, Martín ME, Olivares del Valle FJ, Aguilar MA (2003) J Chem Phys 118:255
42. Bearpark MJ, Robb MA, Schlegel HB (1994) Chem Phys Lett 223:269
43. Yarkony DR (2004) In: Domcke W, Yarkony DR, Köppel H (eds) Conical intersections, Advanced Series in Physical Chemistry no. 15, World Scientific, Singapore, p 42
44. Muñoz Losa A, Martín ME, Fdez. Galván I, Aguilar MA (2007) Chem Phys Lett 443:76
45. Fdez. Galván I, Martín ME, Aguilar MA (2004) J Comput Chem 25:1227
46. Kollman PA (1993) Chem Rev 93:2395
47. Becker RS, Inuzuka K, King J (1970) J Chem Phys 52:5164
48. Muñoz Losa A, Fdez. Galván I, Martín ME, Aguilar MA (2006) J Phys Chem B 110:18064
49. Widmark P-O, Malmqvist P-Å, Roos BO (1990) Theor Chim Acta 77:291
50. Frisch MJ, Trucks GW, Schlegel HB, Scuseria GE, Robb MA, Cheeseman JR, Zakrzewski VG, Montgomery Jr. JA, Stratmann RE, Burant JC, Dapprich S, Millam JM, Daniels AD, Kudin KN, Strain MC, Farkas O, Tomasi J, Barone V, Cossi M, Cammi R, Mennucci B, Pomelli C, Adamo C, Clifford S, Ochterski J, Petersson GA, Ayala PY, Cui Q, Morokuma K, Malick DK, Rabuck AD, Raghavachari K, Foresman JB, Cioslowski J, Ortiz JV, Baboul AG, Stefanov BB, Liu G, Liashenko A, Piskorz P, Komaromi I, Gomperts R, Martin RL, Fox DJ, Keith T, Al-Laham MA, Peng CY, Nanayakkara A, Gonzalez C, Challacombe M, Gill PMW, Johnson B, Chen W, Wong MW, Andres JL, Gonzalez C, Head-Gordon M, Replogle ES, Pople JA (1998) Gaussian 98, Rev. A11.3, Gaussian, Inc., Pittsburgh, PA
51. Refson K (2000) Comput Phys Commun 126:310
52. Andersson K, Barysz M, Bernhardsson A, Blomberg MRA, Carissan Y, Cooper DL, Fülscher MP, Gagliardi L, de Graaf C, Hess BA, Hagberg D, Karlström G, Lindh R, Malmqvist P-Å, Nakajima T, Neogrády P, Olsen J, Raab J, Roos BO, Ryde U, Schimmelpfennig B, Schütz M, Seijo L, Serrano-Andrés L, Siegbahn PEM, Stålring J, Thorsteinsson T, Veryazov V, Widmark P-O (2006) Molcas Version 6, University of Lund, Lund, Sweden
53. Moskvin AE (1966) Theor Exp Chem 2:175
54. Reguero M, Olivucci M, Bernardi F, Robb MA (1994) J Am Chem Soc 116:2103

CHAPTER 7

THE SEQUENTIAL QM/MM METHOD AND ITS APPLICATIONS TO SOLVENT EFFECTS IN ELECTRONIC AND STRUCTURAL PROPERTIES OF SOLUTES

KALINE COUTINHO[1], ROBERTO RIVELINO[2], HERBERT C. GEORG[1], AND SYLVIO CANUTO[1]

[1] *Instituto de Física, Universidade de São Paulo, CP 66318, 05315-970 São Paulo, SP, Brazil, e-mail: kaline@if.usp.br*

[2] *Instituto de Física, Universidade Federal da Bahia, 40210-340 Salvador, BA, Brazil*

Abstract: The combination of molecular mechanics and quantum mechanics (QM/MM) is gaining increasing application in solvation problems. One possibility that has been explored is to use the MM and QM sequentially. This has the advantage that statistically converged results can be ensured. In addition, convergence with the size (number of explicit solvent molecules) can also be easily explored. The disadvantage is that uncoupling the QM and the MM imposes special consideration for including the solute polarization. These aspects are considered here, where a detailed analysis is made of the statistical correlation and the statistical inefficiency. An iterative procedure to include the solute polarization is discussed and examples are presented. Examples are also given to illustrate the different aspects, especially the size and statistical convergence. Finally, the possibility and implementation of using just one average configuration to obtain, from a single QM calculation, the same average of the statistically converged value is discussed

7.1. INTRODUCTION

The study of atomic and molecular properties in a liquid environment is a problem deserving increasing theoretical interest. The modifications of the atomic or molecular properties are a sensitive probe of the interaction between the reference system and the environment. Interesting examples of this are found in the analysis of liquid helium [1,2,3] and physical–chemical solvation problems [4]. In the past decade we have seen an enormous increase in the theoretical possibilities to study solvation and solvent effects in general. This is a consequence of persistent and systematic improvements since the early pioneering days of Onsager [5] and Kirkwood [6]. This is the origin of the continuum methods that found an interesting development in the self-consistent reaction field [7,8,9,10]. An important extension has been developed by the Pisa group that led to the polarizable continuum model [11,12,13],

S. Canuto (ed.), Solvation Effects on Molecules and Biomolecules, 159–189.
DOI 10.1007/978-1-4020-8270-2_7,

termed as PCM, and later also extended to include isodensity PCM [14]. Because of its simplicity PCM is one of the most used theoretical methods to study solvent effects. Continuum methods can now be used with the most sophisticated quantum chemistry methods [15,16] and a discrete reaction field method has also been developed [17,18]. An interesting variant of the continuum approach is the conductor-like screening model (COSMO) developed by Klamt and Schüürmann [19] which can now be used with the multi-reference configuration interaction method [20]. Further progress can be achieved by considering the inclusion of explicit solvent molecules, a procedure that normally requires the use of statistical mechanics computer simulation. An influent work has been made nearly 20 years ago by Blair and co-workers [21] where they performed a spectroscopic analysis of formaldehyde in water combining quantum mechanics (QM) and molecular simulation (MM). Another well-recognized work is that of Warshell and Levitt [22] that is considered to be in the origin of the QM/MM methods [23,24]. By combining quantum mechanics and molecular mechanics with a proper partition they have laid the foundation to systematic theoretical studies of biological systems. The combined use of statistical mechanics computer simulation with quantum mechanics is perhaps the theoretical tool that has seen the most spectacular recent advances. These have been the subjects of some recent reviews [10,23,25,26,27]. The use of computer simulation is the natural way to obtain the diversity of configurations that characterizes a liquid system [28]. A liquid is statistical by nature and its properties should be obtained by statistical averages. As such only statistically converged average values are of any significance. All properties of a liquid are represented by a statistical distribution that reflects the simple fact that temperature imposes structural fluctuations.

The sequential QM/MM (S-QM/MM) is a variant of the conventional QM/MM approach that aims at obtaining statistically converged values for all properties of interest. This is particularly interesting because it uses a very efficient sampling procedure, thus reducing considerably the number of QM calculations to obtain proper statistically converged average values. It thus consists of two steps. In the first one, computer simulations are made to generate the configurations and, in the second one, QM calculations are made on these configurations. Of course the use of separate computer simulation and quantum mechanics is a natural idea and in fact it has been used already in the pioneering work of Blair and co-authors [21] and in the early works of Zeng and co-authors [29,30]. One of the greatest advantages of using the two-step procedure is that between them, after concluding the MM part, a statistical analysis can be made to select configurations that are of relevance to the final average value. This can be done in two, technically, different ways, either by analyzing the statistical correlation interval from the auto-correlation function of the energy or from the statistical inefficiency. These are in fact related but they are obtained by using different computational procedures. Both will be discussed later in this chapter. In this sense, the S-QM/MM methodology was proposed by Canuto and Coutinho [31,32] to study solvent effects in electronic and structural properties of solutes. In this type of study, two important ingredients are necessary. First, as the electronic properties are of interest, it is necessary to use quantum mechanics to describe the solute and its interactions with the solvent. Second, as the whole system

is a solution, usually studied in a given condition of temperature and pressure, it is also necessary to include the thermodynamic effects on the solute–solvent and solvent–solvent interactions. This is the recognition that a liquid system is statistical in essence and that all of its properties, classical or quantum (spectroscopic, for instance) are derived from a statistical distribution. These effects of temperature and pressure are frequently obtained using computer simulations of molecular systems in liquid phase or in solutions. Therefore, the commonly used QM/MM hybrid method [22,23,33,34] joins together quantum mechanics and computer simulation to study solvent effects on electronic properties of molecules. In this method, one part of the simulated system uses a quantum Hamiltonian and the remainder uses classical force fields. Usually the classical part interacts with the quantum part by the inclusion of an electrostatic field – generated by the atomic point charges of the solvent molecules not included in the quantum part – in the quantum Hamiltonian. Thus, in each step of the simulation, one quantum calculation should be performed and, even at a semiempirical level, this method may be computationally very demanding for a large quantum part, because thousands of quantum calculations may be needed. Another important aspect is that the separation between the classical (MM) and the quantum (QM) parts may not be so clear. In the case of considering the active site of an enzyme it seems justifiable that the separation should include the active site as the QM part. However, in a liquid considering different properties of the solute this is a subtle problem. The NMR shielding of an atom in the solute is a more localized property than a solvatochromic shift of a polar molecule in a polar environment. For the chemical shielding the solute and the nearest neighbors are very likely to be enough to characterize the solvent contribution. On the other hand, the $n–\pi^*$ transition of a polar organic molecule in a liquid environment seems to be affected by solvent molecules located well beyond the first solvation shell. Hence, making the QM/MM in a two-step procedure, avoiding a previous partition may be a more flexible procedure. Different properties may require a different partition and the number of explicit solvent molecules to be considered in a S-QM/MM will be extracted from the same simulation. The MM part has mostly been made using Monte Carlo simulation but molecular dynamics can, of course, also be used [35]. The QM model is also flexible and different methods may be used for different properties. An application of the sequential QM/MM has used the TDDFT QM model to obtain excitation energies within a subset of the orbitals to save on computation time [36]. Finally, we should also mention that an important ingredient to ensure statistical convergence is the calculation of the correlation interval, and that is obtained after a long simulation (normally after concluding the simulation). These aspects will be considered in this chapter that includes several illustrative examples.

7.2. METHODOLOGY

The idea of the sequential QM/MM method is thus to join the quantum calculations and the computer simulations in an efficient way to reduce the number of QM calculations and hence the computational cost. Therefore, in the two-stage procedure the system is first simulated using classical force fields for all interactions,

solute–solvent and solvent–solvent. Then, a statistical analysis is performed and two important analyses are made. One is related to the statistical correlation between successive configurations of the system generated by the simulation and the other is related with the structural distribution of the solvent around the solute. Taking this information into account, the second stage is to perform the quantum calculations in a few sampled statistically important configurations (typically less than 100) composed of the solute surrounded by some solvent molecules. In this procedure, the computer simulations are performed by using the Monte Carlo Metropolis [28] method, where the configurations are generated taking into account the Boltzmann factor so that having the results of the QM calculations on these structures, a *simple average* is performed and the electronic property of interest is obtained. It is important to note that with this two-step procedure, proposed in the sequential QM/MM method, the effects of temperature and pressure, which show up in the configurations generated by the simulations, are automatically included in the QM calculation through the diversity of configurations. Another important aspect to be noted is that once the quantum calculations are performed in a supermolecular system composed of the solute and some solvent molecules, all the interactions in these sub-systems are in principle considered. This includes electrostatic, induction, dispersion, charge transfer, etc. Therefore, this method provides a realistic treatment of the system including all the important aspects of the solute–solvent interactions in the liquid phase. However, there are two points that need special consideration. One is that by uncoupling the classical simulation and the quantum treatment one suppresses the mutual polarization between the solute and the solvent. In particular, the polarization of the solute by the solvent is important for a proper treatment of the solute properties. This point will be considered below in this chapter. We will show that it is possible to include the solute polarization in some average way. The second drawback is a little more delicate and subtle and it refers to the consistency of the configuration space that is sampled by a classical and a quantum simulation. It is still an open question whether the energy surface generated by the classical force field and sampled by the computer simulation properly describes the true systems in their microscopic states. It is acceptable that classical force fields may well describe the real systems, on the average, once they can reproduce the experimental thermodynamic data such as density, heat of vaporization, specific heat, etc. Also, structural properties such as the radial distribution function and structure factor are important properties that have been used to gauge the quality of force field parameters. But, rigorously it is still unknown whether the microscopic states are equivalent. This is a topic that needs special consideration.

7.2.1. Description of the Statistical Analyses

In this section we present in some detailed form the statistical correlation between the values of a property in a chain of successive values generated by computer simulation. Two concepts are used, the statistical correlation and the statistical inefficiency. Although these two concepts are related they are obtained by using different

computational strategies that are analyzed in the following. Additionally, we discuss the use of the radial distribution function (RDF) and the minimum-distance distribution function (MDDF) to determine the structural distribution of the solvent around the solute.

7.2.1.1. Statistical correlation or statistical inefficiency

After performing a computer simulation of a system composed of several entities (atoms or molecules) in a given ensemble, thousands or millions of configurations are generated. Each configuration is a set of coordinates for all atoms. The instantaneous value of a property, f, is calculated using these configurations, which generates a chain of successive values, $\{f_i\}$. The average, $\langle f \rangle$, and the variance of the average, $\langle \delta f^2 \rangle$, are obtained by

$$\langle f \rangle_L = \frac{1}{L} \sum_{i=1}^{L} f_i \tag{7-1}$$

and

$$\text{var}(\langle f \rangle_L) = \langle \delta f^2 \rangle_L = \frac{1}{L} \sum_{i=1}^{L} (f_i - \langle f \rangle_L)^2 = \langle f^2 \rangle_L - \langle f \rangle_L^2, \tag{7-2}$$

where L is the size of the chain, $\{f_i\} = f_1, f_2, \cdots, f_L$. The statistical error due to the finite size of the chain $\{f_i\}$, generated by the simulation, is obtained as

$$\text{err}(\langle f \rangle_L) = \sqrt{\frac{\langle \delta f^2 \rangle}{L}}. \tag{7-3}$$

The variance of the average tends to a constant when the size of the chain $\{f_i\}$ tends to infinity and it is easy to see that, on the same condition, the error tends to zero. However, Eq. (7-3) is correct only when the successive values of the chain $\{f_i\}$ are independent, or statistically uncorrelated. If there exists statistical correlation between the values this equation changes to

$$\text{err}(\langle f \rangle_L) = \sqrt{\frac{\langle \delta f^2 \rangle}{(L/s)}}, \tag{7-4}$$

where s is the interval necessary to obtain statistically uncorrelated configurations. As discussed before [31,37], two methods can be used to calculate the interval to obtain statistically uncorrelated configurations: the statistical correlation and the statistical inefficiency.

The statistical correlation between two different quantities can be calculated through the correlation coefficient [38,39] and this concept is usually extended by

considering these two quantities as the same property evaluated in different times or, in a chain $\{f_i\}$ separated by an interval k, that is known as an auto-correlation coefficient for a fixed k or an auto-correlation function, $C(k)$, for any interval k:

$$\begin{aligned} C(k) &= \frac{\langle \delta f_i \delta f_{i+k} \rangle_{L-k}}{\sqrt{\langle \delta f_i^2 \rangle_{L-k} \langle \delta f_{i+k}^2 \rangle_{L-k}}} \\ &= \frac{\langle (f_i - \langle f_i \rangle_{L-k})(f_{i+k} - \langle f_{i+k} \rangle_{L-k}) \rangle_{L-k}}{\sqrt{\langle (f_i - \langle f_i \rangle_{L-k})^2 \rangle_{L-k} \langle (f_{i+k} - \langle f_{i+k} \rangle_{L-k})^2 \rangle_{L-k}}}, \end{aligned} \tag{7-5}$$

where i varies from 1 to $L- k$. Considering that the interval k is much smaller than the total size of the chain L (typically we vary k from 1 to 0.5% of L), the variance of the first set of values, f_i, and the second, f_{i+k}, shown in the denominator, are approximately equal to the variance of the total chain. Thus, Eq. (7-5) can be rewritten approximately as

$$C(k) \cong \frac{\langle f_i f_{i+k} \rangle_{L-k} - \langle f_i \rangle_{L-k} \langle f_{i+k} \rangle_{L-k}}{\langle f^2 \rangle_L - \langle f \rangle_L^2} \tag{7-6}$$

which has values below 1. Values close to 1 indicate a very high degree of correlation (close to 100%). The correlation time, τ, is then obtained by integrating this auto-correlation function

$$\tau = \int_0^\infty C(k) \mathrm{d}k. \tag{7-7}$$

When successive values of the chain $\{f_i\}$ differ by small fluctuations, which is the case of macroscopic properties obtained from successive configurations generated by molecular simulations, the auto-correlation function follows an exponential decay [38,40,41]

$$C(k) = \sum_i c_i \mathrm{e}^{-k/\tau_i}, \tag{7-8}$$

where τ_i represents characteristic correlation times of the system. For simulations performed with Monte Carlo Metropolis method, it was found that the auto-correlation function of the potential energy [32,42] and of other properties [40,43,44] can be well represented by one or two exponential functions. Therefore, the correlation time τ can be easily obtained by fitting the auto-correlation function $C(k)$, calculated by Eq. (7-6), by using a double exponential decaying function (see Eq. 7-8) and integrating it from zero to infinity. That gives $\tau = c_1\tau_1 + c_2\tau_2$, where typically $\tau_2 >> \tau_1$. An example of this behavior is shown in Figure 7-1.

Rigorously, fully uncorrelated configurations ($C(k) \approx 0$) require an infinite interval ($k \to \infty$). In general, for an interval larger than 2τ, the statistical correlation is less

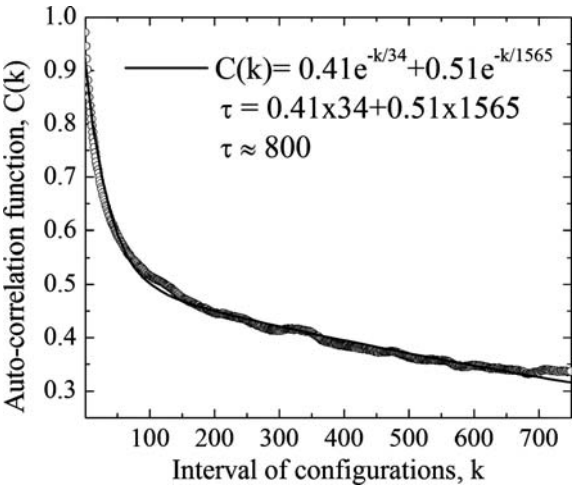

Figure 7-1. Typical auto-correlation function of the energy. In this example it is calculated for the case of benzophenone in water simulated with Monte Carlo Metropolis method. The calculated auto-correlation function (*circles*) is fitted to the exponential decay (*line*) and the correlation time τ is obtained using Eq. (7-7) applied in the fitted function shown in Eq. (7-8)

than 13%, i.e., $C(k) < 0.13$. The values of the chain $\{f_i\}$ separated by this interval can be considered as statistically uncorrelated and we call $k \approx 2\tau$ as the correlation interval. In our applications efficient statistical convergence has been obtained for correlation less than 15%, i.e., $C(k) < 0.15$.

The second method used to calculate the necessary interval to obtain statistically uncorrelated configurations is the statistical inefficiency. As defined by Friedberg and Cameron [45], it is based on the variance of averages taken over blocks of a chain $\{f_i\}$. Dividing the chain into n_b blocks with L_b successive values, where $L = n_b L_b$, then the average taken over the bth block is

$$\langle f \rangle_b = \frac{1}{L_b} \sum_{b_{\text{start}}}^{b_{\text{end}}} f_i, \tag{7-9}$$

where $b_{\text{start}} = (b - 1)L_b + 1$, $b_{\text{end}} = bL_b$ and b can assume values from 1 to n_b. The variance of the averages taken over the blocks is

$$\langle \delta f^2 \rangle_{n_b} = \frac{1}{n_b} \sum_{b=1}^{n_b} (\langle f \rangle_b - \langle f \rangle_L)^2 \tag{7-10}$$

and the statistical inefficiency s is given by

$$s = \lim_{L_b \to \infty} \left(\frac{L_b \langle \delta f^2 \rangle_{n_b}}{\langle \delta f^2 \rangle_L} \right) = \lim_{L_b \to \infty} S(L_b) \tag{7-11}$$

For chains of statistically correlated values, $S(L_b)$ increases with the increasing of L_b until it approaches a limiting value s. The limiting value of $S(L_b)$ means that the block size L_b has become so large that there is no correlation from block to block, i.e., a correlation interval. Therefore, by performing a graphic of $S(L_b)$ versus L_b the value of s can be estimated. But as the chain is finite ($L = n_b L_b$), when the block size L_b increases the number of blocks n_b decreases and it generates an increasing error in the calculation of $S(L_b)$ and an imprecision in the estimate of the best value of s. Thus, it is necessary to perform an analysis of s with respect to the size of the chain L. An example of this analysis is shown in Figure 7-2.

For those chains $\{f_i\}$ where the auto-correlation function follows an exponential decay, it is called a first-order autoregressive or Markovian chain [38] and in this case the statistical inefficiency and the correlation time are related by $s \approx 2\tau$ [28]. These two methods are used independently in a complementary way to obtain the best estimate for the interval to obtain statistically uncorrelated configurations generated by molecular simulations, i.e., to obtain the correlation interval. Applications of this statistical analysis to study solvent effects in molecular spectroscopy have been made in some detailed form [42]. Numerical applications have shown that the average obtained using all successive values of $\{f_i\}$ is the same as the average obtained using only statistically uncorrelated values [37], that is, values that are separated by an interval $s \approx 2\tau$, regardless of the starting value f_i. This is of considerable interest when applying to QM calculations (see, e.g., [46,47,48]).

The correlation interval s, or 2τ, gives the information of how many Monte Carlo (MC) cycles, or molecular dynamics time steps Δt, are necessary to obtain configurations that are statistically uncorrelated, i.e., with less than ~13% of

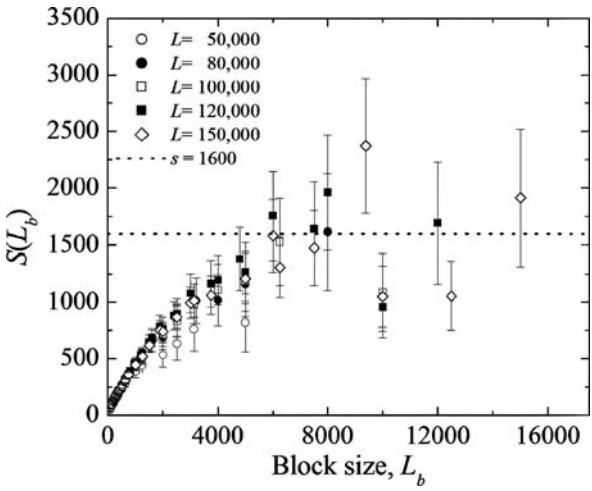

Figure 7-2. Typical graphic of the statistical inefficiency. In this example it is calculated for the case of benzophenone in water simulated with Monte Carlo Metropolis method. The behavior of $S(L_b)$ versus L_b for chains with different sizes L. The *dashed line* represents the asymptotic value s of uncorrelated blocks as shown in Eq. (7-11)

correlation. Hence, instead of selecting a total of thousands of successive configurations generated by the simulations, it is possible to select only a few statistically uncorrelated configurations that are obtained considering the configurations separated by an interval of *s*, where *s* is typically 1000 MC cycles when the solvent is water. Typically we have been able to obtain statistically converged values after 60–80 QM calculations (see, e.g., [32,46]). Examples will be discussed later in this chapter. In all cases the statistical correlation has been calculated using the program *Correlation*, that is available from the authors, and is part of the *DICE* package [49].

7.2.1.2. Structural analysis: solvent distribution

One important aspect is the distribution of the solvent molecules around the solute, i.e., the solvation shells and the hydrogen bonds. They are usually analyzed through the radial distribution function (RDF). The RDFs can be calculated between any atom of the solute and any atom of the solvent [28]. It can also be obtained between their centers of mass (CM). Among all possibilities, the RDF between the CMs, RDF(CM), are frequently used to define the solvation shells. Figure 7-3 shows a typical RDF(CM), which represents the distribution of water molecules around a C_{60} fullerene. It is possible to identify three peaks that define the solvation shells. These can be used to obtain the coordination number. In the case of a liquid system this coordination is the average number of molecules in any given solvation shell. Hence, by a spherical integration of each peak, it is possible to obtain the average number of solvent molecules in each shell. Figure 7-4 shows an illustration of one configuration of the C_{60} fullerene surrounded by its first hydration shell with 63 water molecules.

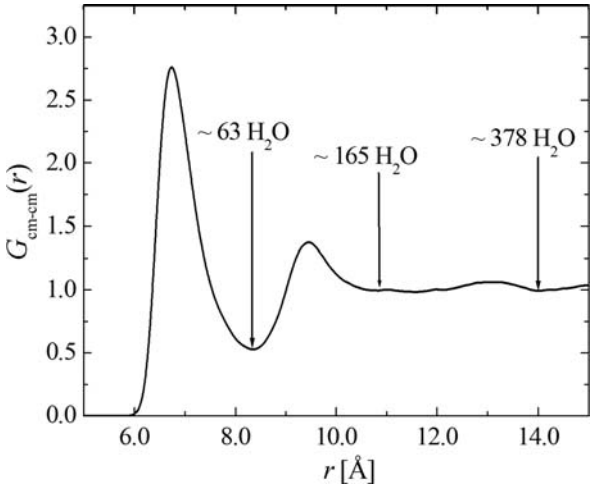

Figure 7-3. RDF between the center of mass of C_{60} and water. Three peaks are shown indicating the number of water molecules in the hydration shells, obtained by spherical integration of $G_{cm\text{-}cm}(r)$ from the solute center of mass up to the limit of their respective minima

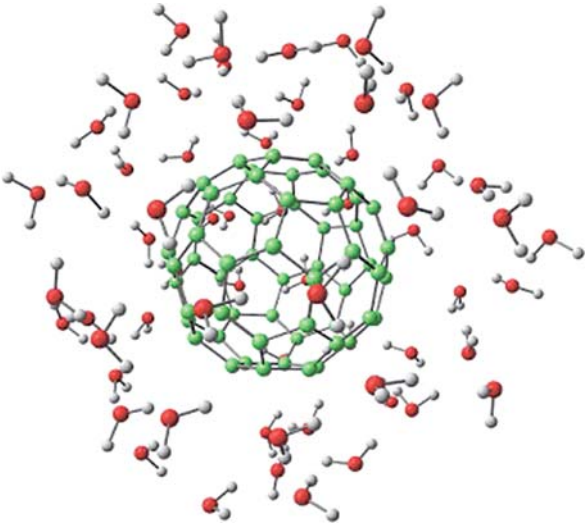

Figure 7-4. Illustration of one MC configuration of C_{60} surrounded by 63 water molecules that form the first hydration shell

However, the RDF(CM) is not appropriate when the solute is an elongated molecule, as it was discussed before, for the case of β-carotene in several solvents [47] and benzophenone in water [50]. In these cases of elongated solutes, an appropriate function is the *minimum-distance distribution function* (MDDF), where the histogram used to calculate the distribution function is not the distance between the CMs of solute–solvent, but the minimum distance between them. The MDDF is defined as

$$G(r) = \frac{\text{HISTOGRAM}[r_-, r_+]}{L\ \rho\ \delta V}, \tag{7-12}$$

where $r_+ = r + (\delta r/2)$, $r_- = r - (\delta r/2)$, L is the number of configurations used for computing the histogram, $\rho = N/V$ is the density of the system, δr is the width of the bin of the histogram and δV is the normalization volume. In a RDF, δV is the volume of the spherical shell with radius between the range $[r_-, r_+]$ and is given by

$$\delta V = \frac{4\pi}{3}[(r_+)^3 - (r_-)^3] \tag{7-13}$$

However, the MDDF is not spherical. It follows the shape of the solute and there is no obvious choice for the normalization volume δV. One possible choice was proposed [50] and it was used in the case of benzophenone, which is a parallelepiped normalization, where the molecule is represented by a box of dimensions a, b, c that characterize its size. For benzophenone, these dimensions were 11.5, 7.0 and 4.0 Å [50], and the δV is a parallelepiped shell between $[r_-, r_+]$ given by

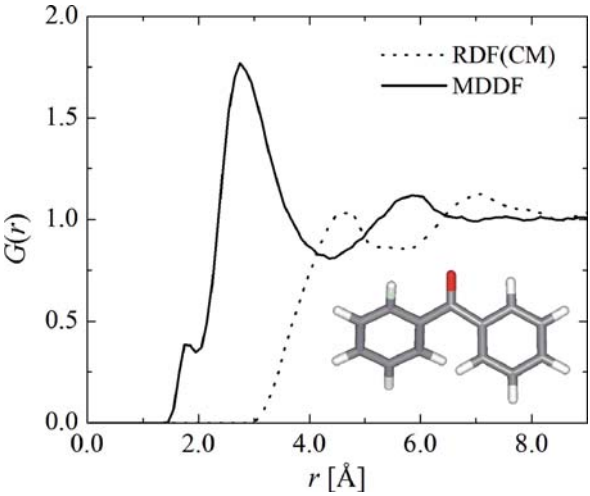

Figure 7-5. The RDF between the center of mass (*dashed line*) and the minimum-distance distribution function (*solid line*) between the benzophenone (shown in the inset) and the water molecules

$$\delta V = (a+2r_+)(b+2r_+)(c+2r_+)-(a+2r_-)(b+2r_-)(c+2r_-). \quad (7\text{-}14)$$

For illustration, Figure 7-5 shows the two distribution functions of the benzophenone in water. The dotted line is the RDF(CM) and the solid line is the MDDF. In this latter case, the distribution of the water molecules around the benzophenone is clear: (i) a small peak, ending at 2.0 Å, that characterizes the hydrogen bonds, (ii) a large peak, between 2.0 and 4.3 Å, that characterizes the first solvation shell and (iii) another peak, between 4.3 and 7.0 Å, that characterizes the second solvation shell.

In Figure 7-6, for comparison, two configurations of benzophenone surrounded by 45 water molecules are shown. In Figure 7-6(a) the distribution is spherical with

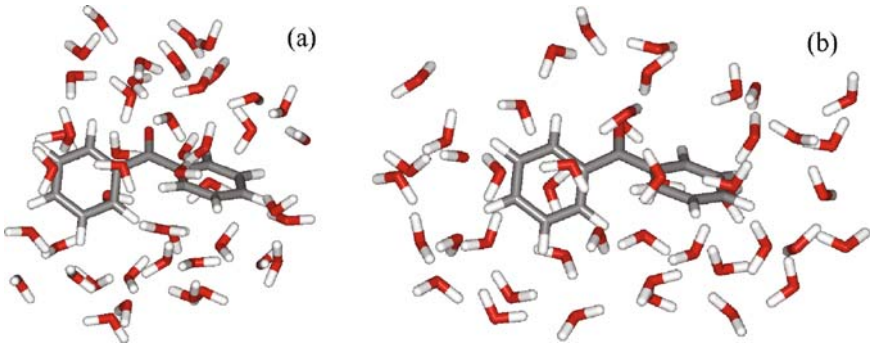

Figure 7-6. Illustration of one MC configuration of the benzophenone molecule surrounded by 45 water molecules selected with respect to (**a**) the center of mass distance and (**b**) the minimum distance

respect to the CM distance and in Figure 7-6(b) the distribution is with respect to the minimum distance.

In Figure7-6(b), it is possible to note a better distribution of the solvent molecules, particularly on the edges of the solute. An important case in this direction is that of β-carotene where the solvent molecules selected using a spherical distribution is a severe limitation [47]. On the other hand for small solutes, such as formaldehyde, the solvation shells selected with the MDDF and the RDF(CM) are very similar.

7.3. APPLICATIONS

Since the suggestion of the sequential QM/MM hybrid method, Canuto, Coutinho and co-authors have applied this method with success in the study of several systems and properties: shift of the electronic absorption spectrum of benzene [42], pyrimidine [51] and β-carotene [47] in several solvents; shift of the ortho-betaine in water [52]; shift of the electronic absorption and emission spectrum of formaldehyde in water [53] and acetone in water [54]; hydrogen interaction energy of pyridine [46] and guanine–cytosine in water [55]; differential solvation of phenol and phenoxy radical in different solvents [56,57]; hydrated electron [58]; dipole polarizability of F^- in water [59]; tautomeric equilibrium of 2-mercaptopyridine in water [60]; NMR chemical shifts in liquid water [61]; electron affinity and ionization potential of liquid water [62] and liquid ammonia [35]; dipole polarizability of atomic liquids [63]; etc.

In this section, we will present some illustrative applications of the S-QM/MM methodology in the study of solvent effects.

7.3.1. Nonpolar Solutes

Nonpolar molecules polarize less the solvent environment and generally lead to small solvation effects, for instance, small solvatochromic shifts. The general rule is that upon excitation a decrease in the dipole moment leads to an increase in the excitation energy and hence a blue shift. This is the case of most $n–\pi^*$ transitions. On the other hand, an increase in the dipole moment leads to a smaller separation of the ground and excited states and therefore a red shift. The blue shift of the $\pi–\pi^*$ transition of 1H-benzotriazole in water, for instance, can be completely understood in terms of the variation of the in-water dipole moments of the ground and first excited states [64]. However, for nonpolar molecules such as benzene where the spectrum is characterized by $\pi–\pi^*$ transitions, both the ground and the excited states have zero dipole moments. Hence the dipole interaction that is normally the dominant contribution cannot be sufficient in the qualitative analysis. It is expected that these excitations are associated to small red shifts that come from the induced dipole moments rather than from the permanent dipole moments. As the dipole polarizability of the excited state is expected to be larger than for the ground state the induced dipole interaction (dispersion) will solvate the excited state better than the ground state and hence will contribute to a red shift. This is the reason why dispersion interactions are so important for describing nonpolar molecules and its contribution to solvatochromism

normally leads to a red shift [65]. In the next two sections we will then consider the very interesting cases of benzene and C_{60} in different solvents. We will also take the opportunity to illustrate the application of the sequential QM/MM methodology where one of the concerns is to obtain statistically converged results. In addition we also analyze the convergence with respect to the number of solvent molecules explicitly considered. For nonpolar molecules, as we will see, size convergence of the solvatochromic shifts are achieved after including all solvent molecules within the first solvation shell.

7.3.1.1. Solvent effects on the UV-vis spectra of benzene

Here, we address the solvatochromic shifts of benzene in different solvents. The experimental results for the first absorption band of benzene in water, cyclohexane and carbon tetrachloride and for homogeneous liquid benzene [66] show clear red shifts as compared to the gas phase results. As benzene is a neutral molecule and has no permanent dipole moment in the ground state and in the π–π^* excited state, the dipolar self-consistent reaction field is essentially zero and no spectral shift of these bands can be expected using this model. Of course, higher moments can be used but these give lower contribution. Using the explicit model of the solvent with the S-QM/MM, we obtained excellent results in comparison with the experimental data [42]. Initially, the Monte Carlo simulation was performed for four systems: liquid benzene (at 0.8990 g/cm^3), benzene in cyclohexane (at 0.7785 g/cm^3), in carbon tetrachloride (at 1.5867 g/cm^3) and in water (at 0.9966 g/cm^3). Standard procedures were used for the Metropolis sampling in the *NVT* ensemble [28], with temperature of 25°C and volume of the cubic box determined by the density, considering the system composed of one benzene molecule surrounded by 343 solvent molecules of water and CCl_4 and 124 of cyclohexane and benzene. As usual, the periodic boundary conditions, the minimum image method and the cutoff radius, with the half-length of the box, were used. All the simulations were performed using the DICE program [49]. The geometry of the molecules were kept rigid during the simulations and the intermolecular interaction was described by the Lennard-Jones plus Coulomb potential with parameters obtained from the OPLS force field for benzene and cyclohexane [67], for carbon tetrachloride from McDonald and co-authors [68] and for water we used the SPC model [69]. During the simulation, after each MC cycle, i.e., the attempt to move N molecules, one configuration was generated. In total, 80000 configurations were generated for each system and the statistical correlation analysis was performed, as described in the previous section. Correlation intervals, s, of 800 and 500 were obtained, respectively, for liquid benzene and benzene in water and for benzene in cyclohexane and in CCl_4. Thus, from the 80000 successive configurations (L = 80000) generated by the simulation, only 100 statistically uncorrelated configurations ($l = L/s$ = 100) were selected for posterior QM calculations of liquid benzene and benzene in water and 160 for benzene in cyclohexane and CCl_4.

Additionally, as each configuration generated by the simulation contains hundreds of solvent molecules, a QM treatment of the solvent requires a reduction of the total number of solvent molecules included. Therefore, we performed an analysis of

the saturation, or convergence, of the solvatochromic shift in the first $^1B_{2u}$ π–π^* absorption transition of benzene with respect to the number of solvent molecules, n, included in the QM calculations. The solvatochromic shift of the transition is calculated by

$$\langle \Delta E \rangle_l = \frac{1}{l} \sum_{i=1}^{l} (E_i(\text{solv}) - E(\text{gas})) = \frac{1}{l} \sum_{i=1}^{l} \Delta E_i, \tag{7-15}$$

where l is the number of statistically uncorrelated configurations, E_i(solv) is the transition energy calculated for one uncorrelated configuration composed by one solute surrounded by n solvent molecules, E_i(gas) is the transition energy calculated for the isolated solute. In the QM calculations, first an intermediate neglect of differential overlap (INDO) self-consistent field equations with spectroscopic parametrization [70] are solved for the entire solute–solvent supermolecular configuration. This means that the wavefunction is antisymmetric with respect to the entire function. Then, singly excited configuration interaction (CIS) calculations are performed to obtain the transition energies, using the program *ZINDO* developed by Zerner [71].

Figure 7-7 shows the convergence of the $^1B_{2u}$ π–π^* transition shift obtained for benzene in water varying the number of water molecules included in the QM calculations. As it can be seen, for n larger than 18 water molecules the shift reaches a converged value. Analyzing the radial distribution function between the carbon atoms of the benzene and the oxygen atom of the water molecules, we observed that the first solvation shell of benzene in water is composed of 18 water molecules. Thus, we note that the shift in the π–π^* transition of benzene in the presence of water is converged with respect to the size of the solute–solvent system when the first solvation shell is included in the QM calculations. The same behavior was found for

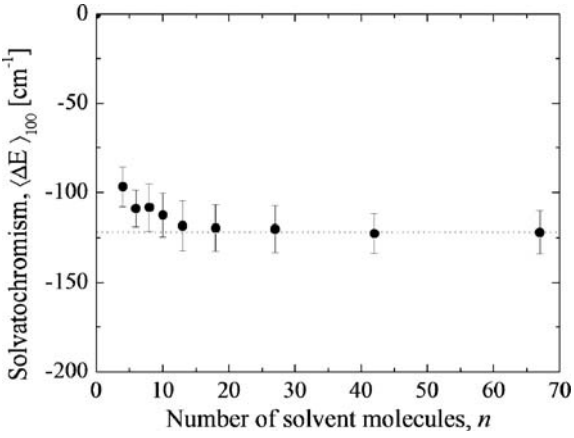

Figure 7-7. The convergence of the calculated shift of the first $^1B_{2u}$ π–π^* transition of benzene in water with respect to the number of solvent molecules included in the quantum mechanical calculations

the other solvents, as reported in detail by Coutinho and co-authors [42] and also for another nonpolar solute, the β-carotene, in several solvents [47]. Then, we conclude with these results that the solvatochromism in the absorption transitions of nonpolar solutes is given by the first solvation shell and shows that the interactions between them are of short range.

In Figure 7-8, the calculated values of the solvatochromic shift for each statistically uncorrelated supermolecular configuration, composed of one benzene and 18 water molecules, are shown. The average value of $-122 \pm 7\,cm^{-1}$ and the experimental value of $-143 \pm 20\,cm^{-1}$ are also shown for comparison. As it can be seen they are in excellent agreement taking into account the experimental and the statistical errors. The individual values are spread between –10 and $-360\,cm^{-1}$ and show that the thermodynamic effects, such as temperature and pressure, that are considered in the present method through the statistical distribution, produce a natural transition broadening. In the case of molecular systems it is known that the vibrational movements also contribute to the transition broadening, but for atomic systems the thermodynamic effects are the only contribution. Ludwig and co-authors [3] used the S-QM/MM to study the excitation lineshift and linewidth of the principal resonance line of Na embedded in liquid He and obtained values that are close to the experimental expectations.

Another statistical analysis that shows the robustness of our results was done for the number of uncorrelated configurations selected for the QM calculations. Figure 7-9 shows the convergence of the average value of the solvatochromic shift of the $^1B_{2u}$ π–π^* transition obtained for benzene in water when varying the number of uncorrelated configurations sampled for the QM calculations. As it can be seen, after 40 uncorrelated configurations the average value fluctuates around the final average

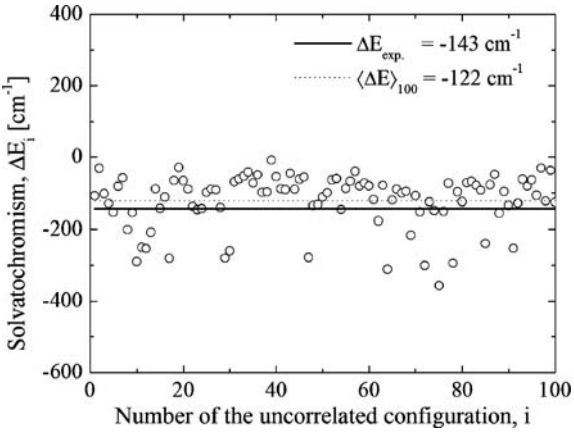

Figure 7-8. The individual values of the solvatochromic shift of the first $^1B_{2u}$ π–π^* transition of benzene in water obtained for each one of the 100 statistically uncorrelated configurations, composed of benzene surrounded by the first solvation shell of water

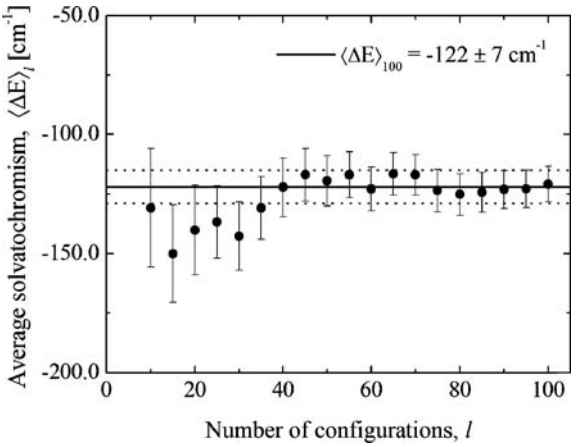

Figure 7-9. The convergence of the average solvatochromic shift of the first $^1B_{2u}$ π–π^* transition of benzene in water with respect to the number of uncorrelated configurations included in the quantum mechanical calculations. The *solid line* represents the final average value and the *dotted lines* the interval of the statistical error (see Eq. 7-4)

within the statistical error, $-122 \pm 7\,cm^{-1}$, and they can be considered as converged. We performed the same analysis for benzene in the other solvents and we found that for all studied systems around 50 uncorrelated configurations are necessary to obtain converged averages.

In Table 7-1, we summarize the results obtained for the solvatochromic shift of the first $^1B_{2u}$ π–π^* transition of benzene in four different environments. As can be seen, the final calculated solvatochromic shifts $\langle E \rangle_{100}$ are in excellent agreement with the experimental results in all cases studied. For instance, in the case of liquid benzene 100 QM calculations were performed in uncorrelated supermolecular configuration selected in an interval of 800 successive configurations, each one composed of one benzene surrounded by 13 nearest benzene molecules.

Table 7-1. Calculated solvatochromic shift of the first $^1B_{2u}$ π–π^* transition of benzene in different solvents. s is the correlation interval and $\langle \Delta E \rangle_{100}$ is the calculated average solvatochromic shift (in cm^{-1}) obtained with 100 uncorrelated configurations. The error in $\langle \Delta E \rangle_{100}$ is obtained from Eq. (7-4) and the experimental results are obtained from Bayliss and Hulme [66]

System	Solute+ *n* solvent	*s*	$\langle \Delta E \rangle_{100}$	ΔE_{exp}
Liquid benzene	1+13	800	−306±11	−332±30
Benzene in cyclohexane	1+11	500	−268±20	−308±20
Benzene in carbon tetrachloride	1+14	500	−456±27	−458±20
Benzene in water	1+18	800	−122±7	−143±20

As Table 7-1 shows, the final average result for the solvatochromic shift of the $^1B_{2u}$ π–π^* transition of homogeneous liquid benzene is calculated to be –306± 11 cm^{-1}, in excellent agreement with the experimental result of –332 ±30 cm^{-1} [66].

7.3.1.2. Hydration effects on the structure, band gap and UV-vis spectrum of C_{60}

Another nonpolar system of considerable interest is the C_{60} fullerene molecule. Structural and electronic properties of C_{60} in liquid water are interesting cases that have been recently investigated using the S-QM/MM [72,73]. This will now be considered. The molecular configurations of the solution were generated at room temperature and atmospheric pressure by using MC simulations in the *NPT* ensemble with solute–solvent interaction described by a realistic Lennard-Jones (LJ) potential [72,74,75], and solvent–solvent interactions modeled by TIP5P potential [76]. In this limit of very dilute solutions, containing one fullerene molecule immersed in thousands of solvent molecules, statistically uncorrelated structures were selected from the fullerene aqueous solution (C_{60}FAS) using the auto-correlation function of energy [53]. QM calculations were then performed to study the effects of solvation on the optical properties of the hydrated C_{60} molecule, using the CIS and density-functional theory (DFT) approximations.

Thus, the UV-vis spectra of C_{60} in water have been calculated using the INDO/CIS method [77]. These were performed to obtain the excitation energies of $C_{60}@\{H_2O\}_n$ cluster with *n* explicit water molecules, thus taking into account part of the dispersion interaction [78] between the solute and solvent. Using the same set of uncorrelated configurations of C_{60}FAS, DFT calculations were also performed by employing the *SIESTA* program [79,80]. Two approaches have been used: (a) the local density approximation (LDA) [81,82] and (b) the gradient-corrected approximation (GGA) with the BLYP functional [83,84]. A nonlocal norm-conserving scalar Troullier–Martins [85] pseudopotential has been included to replace the core electrons and the Kohn–Sham (KS) eigenstates were expanded with a linear combination of numerical atomic orbitals (NAO) as the basis set [86,87,88]. An equivalent plane-wave cutoff radius of 200 Ry for the grid integration was utilized to represent the charge density and only the Γ point was sampled in these calculations [73].

In Figure 7-3 the calculated pairwise radial distribution function, $G_{cm-cm}(r)$, between C_{60} and water is shown. This RDF(CM) is similar to those obtained using other models for water [72,74,89]. As indicated in Figure 7-3, the first peak, corresponding to the first hydration shell, starts at 6.0 Å and ends at the minimum value of 8.3 Å. This shell is composed of an average of ca. 63 water molecules (for an illustration of one configuration see Figure 7-4). Thus, after the MC simulation we separated 160 statistically uncorrelated hydrated configurations of the $C_{60}@\{H_2O\}_{63}$ type. These structures have shown that preferential interactions between water and fullerene, such as O–H$\cdots\pi$ hydrogen bonds [90], are less probable to occur in solution under ambient conditions. Indeed, according to Andrievsky and co-authors [91] the stabilization of supramolecular $C_{60}@\{H_2O\}_n$ clusters should be explained

by a weak C_{60}–oxygen interaction, for which we have calculated, using the classical force field, the interaction energy value of –0.65 ± 0.27 kcal/mol taking $n = 63$. These configurations present sphere-like hydrated shells around the fullerene, ordered due to water–water hydrogen bonds formation. By considering all uncorrelated $C_{60}@\{H_2O\}_{63}$ configurations, we have calculated the minimum distance between the C_{60} surface and water in the aqueous solution as 3.3 ± 0.5 Å.

If one considers the existence of larger hydrated clusters, Figure 7-3 also shows a second hydration shell starting approximately at 8.3 Å and extending until 10.9 Å. In this case, the spherical integration of $G_{cm-cm}(r)$ gives a total number of 185 water molecules on average, from the solute center of mass up to the limit of the second shell. Also, by considering the calculated number of H-bonds in the solvent, the second shell is less ordered around C_{60} than the first one. This is most expected in C_{60}FAS because of the short-range interaction between C_{60} and water. On the other hand, the second hydration shell has a diameter that is within the predicted size [91] for a single hydrated C_{60}, lying in the range of 16–17 Å, as obtained experimentally. Therefore, our prediction of larger supramolecular structures, of the $C_{60}@\{H_2O\}_{185}$ type, seems to be in agreement with the supposed existence of highly hydrated single fullerene configurations, as estimated by means of electron micrograph [92]. Actually, these $C_{60}@\{H_2O\}_n$ configurations are expected to be formed by a large layer of water molecules [93] in comparison with the crystalline hydrates obtained in colloidal solutions of C_{60} fullerene. More interesting, our results reinforce the supposed existence of supramolecular hydrated clusters in aqueous environments, which has more recently been proposed to be in connection with DNA damage in human lymphocytes [94].

The transition energies calculated with INDO/CIS converge rapidly with the number of configurations considered in the averages. For instance, taking the $C_{60}@\{H_2O\}_{60}$ configurations into account, we obtain average values of 268 ± 5 and 350 ± 9 nm. These transitions are in good agreement with the experimental UV-vis absorption spectra of aqueous solutions [91,95], exhibiting peaks at 265 and 345 nm. The intermolecular interaction between C_{60} and water is expected to be dominated by dispersion interactions and this is normally responsible for red shifts in the optical absorption spectrum [65]. This emphasizes the importance of including dispersion interaction for a proper description of nonpolar solutes. Here, the calculated absorption spectra of the hydrated C_{60} seems to explain well the UV-vis spectra of C_{60}FAS in a wide range of concentration, because the optical absorbance of C_{60}–water system has a linear behavior with the concentration [91].

To better understand the influence of the aqueous environment on the ground-state electronic properties of fullerene, we now use DFT calculations to analyze the band gap. In our analysis we have considered the dielectric screening of the first hydration shell on the band gap and density of states (DOS) of C_{60} at room temperature and atmospheric pressure [72,73]. As obtained from the RDF(CM), given in Figure 7-3, there are 63 water molecules present in each configuration representing the first hydration shell of C_{60}. The calculations are performed over uncorrelated configurations composed of $C_{60}@\{H_2O\}_{63}$ (for illustration see Figure 7-4).

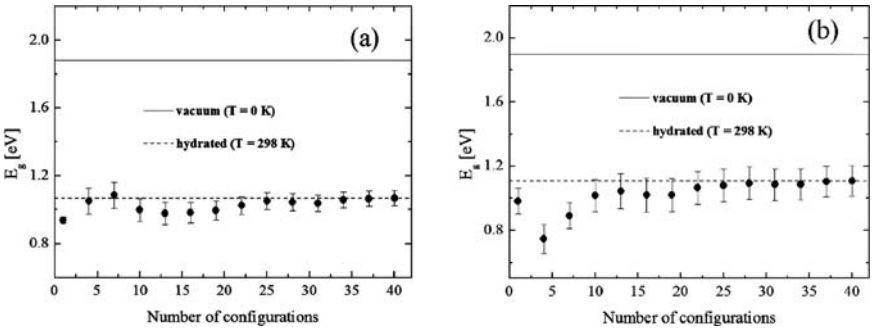

Figure 7-10. Band gap convergence of the hydrated system $C_{60}@\{H_2O\}_{63}$ under ambient conditions: (**a**) using LDA and (**b**) using BLYP levels of DFT. The average values are shown (*dashed line*) and also the corresponding gap of the isolated C_{60} (*solid line*)

Figure 7-10 shows the convergence of the calculated band gap (E_g) of the hydrated fullerene as a function of the number of uncorrelated MC configurations included in the averaging. The calculated average E_g is a mean difference between the Kohn–Sham (KS) eigenvalues of the highest occupied molecular orbital (HOMO) and lowest unoccupied molecular orbital (LUMO) of the ground-state electronic structure of the hydrated system over statistically uncorrelated configurations. Our results are converged at both levels of DFT calculations (LDA and GGA) with 40 uncorrelated configurations. In a similar fashion, the DOS of the solvated system was averaged over uncorrelated configurations up to the convergence limit. Thus, the average band gap of the hydrated system was calculated as 1.07 ± 0.28 eV with LDA and 1.11 ± 0.31 eV with GGA. Both levels of DFT also yielded good estimates for the HOMO–LUMO gap of C_{60} in vacuum, i.e., 1.88 and 1.86 eV, respectively. For comparison, this energy gap determined for C_{60} configurations from direct forbidden optical transitions data is 1.77 eV [96].

In Figure 7-11 the charge densities related to the KS eigenstates near the Fermi level of the hydrated C_{60} are shown. The HOMO of the solvated system

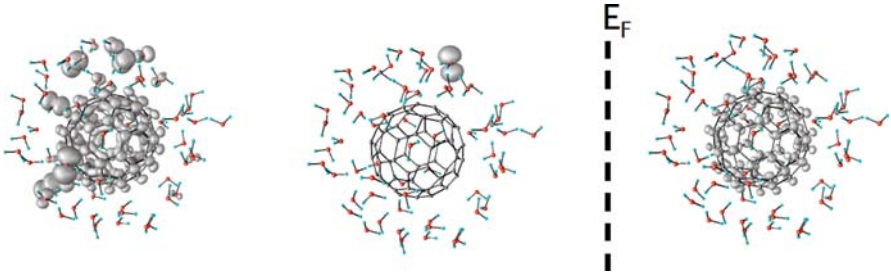

Figure 7-11. Top of the valence band of the hydrated fullerene. The range of –1.67 to –0.97 eV, the lone pairs of water and the LUMO are represented from the *left* to the *right*. The dashed line represents the Fermi level (E_F)

is localized in lone pairs of oxygen atoms of the hydrating molecules, whereas its LUMO is qualitatively similar to the LUMO of the isolated solute [73]. This analysis is in line with the expected high electron affinity of C_{60} in the presence of available oxygen and water [91,97]. This feature reveals the weak donor–acceptor character of the interactions involving electron lone pairs of oxygen atoms in H_2O and the fullerene surface. However, taking the finite temperature effect into account for the isolated C_{60}, we expect that no appreciable changes in the electronic structure may be observed due to the rigid surface of this molecule. Thus, the calculated 0.8 eV of red shift in the band gap of the hydrated fullerene, from that of the solute in vacuum, indicates that the disordering of water only affects the ground-state electronic structure of the whole system at higher temperature.

In summary, these C_{60}FAS studies have successfully described the spectral properties of $C_{60}@\{H_2O\}_n$ considering only the first solvation shell around C_{60}. We have obtained converged averages for the transition energies at 268 ± 5 and 350 ± 9 nm (with INDO/CIS) for the hydrated state of C_{60}. The results for the aqueous solution are in very good agreement with previous experiments and reinforce that the water layers cause only a mild perturbation in the absorption spectra of fullerene. Moreover, the results show that including only the first hydration shell around C_{60} is enough to analyze the spectral properties of this hydrated fullerene. At the DFT level, we found that thermal fluctuations of the aqueous environment around the fullerene surface are the most likely sources of the calculated 0.8 eV red shift in the band gap of the hydrated system. On the other hand, by considering the projected DOS of C_{60} in the presence of water it is clear that the influence of the first hydration shell produces a mild polarization effect on the fullerene surface. This is in agreement with the experimental prediction from both direct and indirect optical transitions data for C_{60} in aqueous environment.

7.3.2. Including Solute Polarization

Using the S-QM/MM procedure has the disadvantage that the classical and quantum parts are uncoupled. The solute cannot be polarized by the subsequent QM calculations. But it is clear that the mutual polarization between the solute and the solvent can be very important [98]. In this section we consider how the solute polarization can be considered in the context of the sequential procedure.

When a molecule is placed in a liquid environment, it is polarized, i.e., its electrostatic moments are changed giving rise to induced multipole moments. The amount of polarization will depend on several factors including, of course, the polarizability of the solute and the electric field provided by the environment.

In a conventional QM/MM simulation, where the quantum and classical parts are made simultaneously, this polarization will be taken into account naturally, as the solute will be polarized during the simulation. Furthermore the polarization fluctuates in different configurations generated. In the S-QM/MM approach, on the other

hand, the quantum and classical stages are uncoupled and the treatment of the solute polarization is not so straightforward. It is clear that in the QM calculations of the supermolecule (solute + solvent) such polarization will be taken into account. But the solvent configurations have been determined by the precedent unpolarized classical simulation.

In molecular mechanics simulations in general, a fixed set of parameters is assumed for modeling the intermolecular interaction. Most simulations use the Lennard-Jones plus Coulomb potential to mimic this interaction, where the Coulomb term, consisting of point charges, takes into account the electrostatic part of the interaction. Therefore, these point charges should somehow include the solute polarization. But there is a natural difficulty to establish the solute polarization. Experimentally, there is no direct way to determine the dipole moment of a specific molecule in the liquid environment although it can be indirectly estimated by, for instance, integrating infrared intensities [99]. Experimental reports on this, however, are very scarce. Hence, this is a property that largely relies on theoretical estimates and the inclusion of polarization or polarizable force fields is one of the great concerns at present (see the special issue in [98,100]).

An approach that became widely used in the past has been to account for the polarization of the solute molecule assuming an increase of ~20% over the experimental gas-phase dipole moment [101,102]. Indeed, such an "implicit polarization" model has been very successful for simulating a wide range of systems. Such polarization can be achieved simply by performing HF/6-31 G(d) calculations on the isolated molecule, as shown by Jorgensen and co-authors [103]. As for the nonpolar molecules, the usual procedure is to use the gas-phase charges, since they are not expected to suffer significant polarization. The same is generally done for polar molecules in nonpolar environments. This approach has been successful for simulating many liquid systems (see, e.g., [104]). However, the use of fixed-charge models for the intermolecular electrostatic potential, neglecting the actual polarization, may lead to errors that may be significant. It has been shown, for instance, that in the case of polar molecules in nonpolar environments, the use of fixed charges in the solvent may lead to errors in the potential energy profile and therefore to wrong conclusions about the conformational stability of the molecule in a medium (see, for instance [105],). Similar problems may arise for ion solvation [106,107] and also for peptide folding [108].

On the other hand, for polar molecules in polar environments, this approach may lead to errors because the actual polarization of the molecule may significantly surpass any modest estimate (e.g., 20%) and the extra polarization may be responsible for important differences in the solute–solvent interaction. Hence, one needs a strategy to account more systematically for the solute polarization. It would be especially interesting to do it in a way to preserve the main advantage of the sequential QM/MM methodology, that is, performing only statistically relevant QM calculations.

One way to do that is through an iterative use of the sequential QM/MM methodology. We perform a MC simulation, using some initial model for the point charges, make the statistical analysis and select uncorrelated configurations to perform the QM calculations, just in the usual sequential QM/MM. Next, we calculate for each configuration the electronic density of the solute in the presence of the solvent, the latter being represented by point charges. Then, based on the calculated electronic density, the atomic point charges of the solute are fitted for each configuration. In our real applications we have made use of the fit of the charges from electrostatic potential in a grid (CHELPG) of Breneman and Wiberg [109] or the Merz–Kollman [110] electrostatic mapping. Now, in the next simulation we use the average point charges (representing the solute average dipole moment in the presence of the solvent). Hence, we simulate the solution again, make the statistical analysis and select configurations for the next QM calculations. The procedure is repeated until the charge density of the solute is converged (monitored by the dipole moment). This iterative procedure is described in detail in Georg and co-authors [111] and is similar to that used by Martín and co-authors [112].

In each step we introduce in the simulation the average charge density over a number of configurations enough to converge the induced dipole moment. This convergence is achieved typically with less than 100 configurations. Note also that we are using a solvent model – in the cases below the SPC model for water [69] – that was developed to account for the properties of the liquid state, and therefore implicitly includes some polarization effect in an averaged way. Therefore our concern here is to describe more accurately the polarization of the solute molecule. After the convergence of the iterative procedure the solute is in electrostatic equilibrium with the solvent. The *average* polarization of the solute is used and in recent applications this has given improved results [50,111].

Now, as experimental estimates of dipole moments of molecules in solution are scarce, we must probe the calculated converged charge density by analyzing results for other properties. One possibility is to analyze the solute–solvent interaction, and that can be obtained by solvent shifts in UV-vis or NMR spectra for example.

Good test cases would be the solvent effects on the UV-vis absorption spectra of formaldehyde and acetone that have been the subject of innumerous theoretical studies. Innovative theoretical methods have been applied to formaldehyde (see also the compilation of results in [20,32,113,114,115,116]). Unfortunately the experimental result for formaldehyde in water is not clear because of chemical problems mostly associated to the aggregation and formation of oligomers. Therefore a better test case is the UV-vis spectra of acetone, because reliable experimental solvent shifts and several theoretical results are available (see the compilation of results in [117]). The Stokes shift of the n–π^* transition of acetone has been critically discussed by Öhrn and Karlström [118]. Grozema and van Duijnen [17] studied the solvatochromic shift of the absorption band of acetone in as much as eight different solvents. Acetone is known to shift the maximum of the n–π^* band by 1500–1700 cm^{-1} when immersed in water [119,120,121]. Using the conventional HF/6-31 G(d) point charges, Coutinho and Canuto [54] simulated acetone in water and performed INDO/CIS

calculations for uncorrelated configurations. They obtained a blue shift of 1300 cm^{-1}, which is very close to the experimental range of 1500–1700 cm^{-1}.

Now we consider the solute polarization with the charge distribution of acetone equilibrated with the water environment, as obtained in the iterative procedure described above. We start with the gas-phase point charges, calculated with MP2/aug-cc-pVDZ using the *Gaussian-03* program [122]. This method gives a dipole moment of 2.98 D, which is very close to the experimental dipole moment of 2.93 D [123]. We then perform a MC simulation and after selecting 100 uncorrelated configurations we obtain an average dipole moment of 4.05 D, representing an increase of 38%. These new charges can then be used in another MC simulation to obtain new values of the electrostatic parameters. By continuing the process we reach the convergence on the dipole moment at around 4.80 D, 60% larger than the gas-phase dipole (Figure 7-12). This induction surpasses substantially the estimate of 20%, but our equilibrated dipole moment is comparable to other theoretical estimates that obtained 4.44, 4.52 and 4.90 D [112,117,124]. In particular the last value, obtained with a Car–Parrinello MD simulation, is very close to our result. They also obtained the same 60% of polarization and the same amount for the induced dipole, 1.8 D.

Note that using the polarizable continuum model (PCM) the dipole moment of acetone is calculated as 3.98 D with the same MP2/aug-cc-pVDZ level. This is equivalent to the first average dipole moment, obtained in the first step (see Figure 7-12), and represents a polarization of 34%, about half of that obtained with the iterative process. This case indicates that the PCM calculation could be used as a good estimate of the polarization or for starting the iterative procedure.

Once the charges are equilibrated, we perform one last simulation and extract uncorrelated configurations to perform the QM calculations. The solvatochromic shift is now calculated as $1650 \pm 40\,cm^{-1}$ [111]. This is a small improvement over the previous result of 1300 cm^{-1}, but it shows that the use of polarized solute gives a

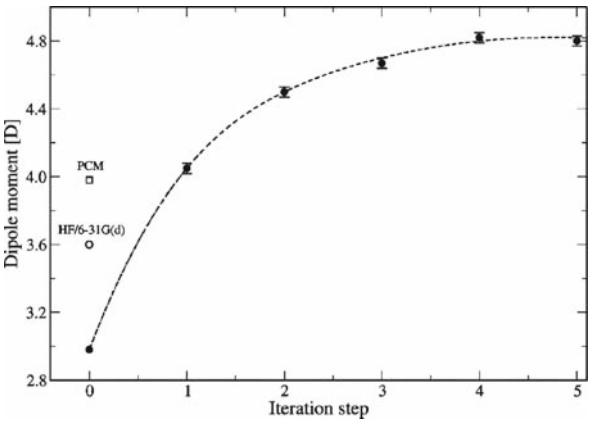

Figure 7-12. Evolution of the dipole moment of acetone with the iteration step (see text)

better description of the solvatochromic shift. This is corroborated by other studies like in the case of benzophenone that will be considered next.

Benzophenone (see Figure 7-5) is another example of the importance of the solute polarization. This molecule is more polarizable than acetone. Benzophenone has polarizable π clouds in the rings and larger dipole polarizability estimated as 144 ea_0^3 [125], compared to 43 ea_0^3 [126] for acetone.

The absorption spectrum of benzophenone is characterized by two distinct and broad bands [127], a weak n–π^* band and a strong π–π^* band. The n–π^* band suffers a shift of around 2200 cm^{-1} when going from *n*-hexane to water, while the π–π^* band is shifted by nearly –1600 cm^{-1}. The description of these distinct solvatochromic shifts is therefore a good theoretical challenge.

In the MC simulations of benzophenone in water we have used a previous geometry optimized with MP2/3-21 G. One important parameter is the interplanar angle between the phenyl rings and that is in good agreement with the experiment, as described elsewhere [128]. The gas-phase dipole moment of benzophenone is calculated in the MP2/6-31++G(d,p) level as 3.11 D, in good agreement with the experimental value of 2.98 D [125]. Using the iterative procedure we obtained a converged dipole moment of 5.84 D for benzophenone in water (see Figure 7-13). This represents a large polarization of nearly 90%.

Using the atomic charges obtained from a CHELPG fit of the isolated molecule in the MC simulation results in calculated subsequent INDO/CIS solvatochromic shifts of approximately 990 cm^{-1} for the n–π^* band and –950 cm^{-1} for the π–π^*. These values are disappointingly small compared to the experimental values of 2000 and –1600 cm^{-1}, respectively. Using, in turn, the implicit polarization obtained with the HF/6-31 G(d) we calculated a solvent shift of approximately 1400 cm^{-1} for the n–π^* band and –1200 cm^{-1} for the π–π^*, corresponding to an improved picture

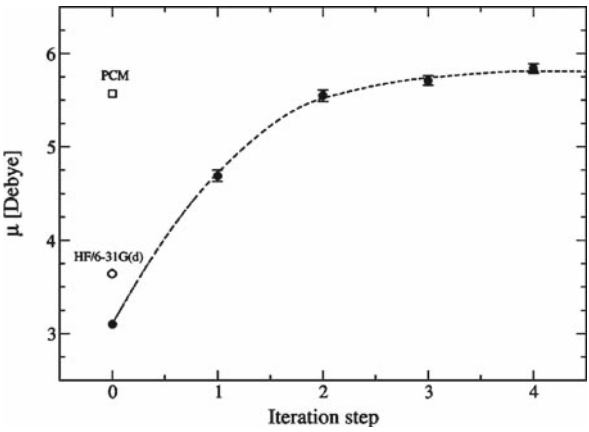

Figure 7-13. Evolution of the dipole moment (in the MP2/6-31++G(d,p) level) of benzophenone in water with the iteration step. The *open circle* corresponds to the dipole obtained with a HF/6-31 G(d) and the open square to PCM calculations

but still in poor comparison with experiment. Now, using finally the configurations obtained from the simulation with the converged solute polarization we obtained shifts of 2045 and –1790 cm^{-1} for the n–π^* and π–π^* bands, respectively, in much better agreement with the experimental values. This shows that in this case the solute polarization is very important for the correct description of the solvatochromic shift and the solute–solvent interaction (see [50] for details).

As several simulations and correspondingly several QM calculations are involved in this iterative polarization scheme it is worthwhile to discuss some simple alternative procedures. The results so far obtained seem to indicate that given the computational simplicity PCM could give a good approximation to the solute polarization either as the final value or to start the iterative procedure (see Figures 7-12 and 7-13). Note that for benzophenone PCM gives a very good estimate of its in-water dipole moment (5.57 D), which is close to the value obtained with the iterative procedure (5.84 D). Whether this is general still needs further investigation. Another simple possibility has been developed by Couto and co-workers [129] that uses some electrostatic fitting (CHELPG or Merz–Kollman, for instance) to calculate the charges of all atoms, solute and solvent, in all statistically uncorrelated configurations and therefrom the average value. For homogeneous ammonia liquid this has given essentially the same result as the iterative procedure described above [35]. Finally, one possibility that we discuss in the next section is to use one average configuration to obtain the average dipole moment in the intermediate points of the iterative procedure, thus using just one QM calculation for each iteration.

7.3.3. Average Solvent Electrostatic Configuration

As described in the previous sections, one of the advantages of performing the QM/MM calculations sequentially is that after the simulation statistical information permits an efficient protocol for the QM calculations. Hence, statistically converged results have been obtained with a relatively small number of QM calculations. In most cases, we have been able to obtain statistically converged averages with 60–80 QM calculations. Although this is a relatively small number, compared to conventional methodologies, it is still large enough to preclude the incursion into very large molecules. For biological molecules or for higher-level calculations, for instance, this could still be a severe limitation. Therefore, it would be very desirable to overcome this by reducing further the necessary number of QM calculations to obtain any average property. In more dramatic terms it would be desirable to perform *just one* QM calculation. One possibility would be to have an average solute–solvent potential that could reproduce the collection of available configurations, even if unphysical, but reproducing the average of any property involved. This possibility has been developed by Sánchez and co-authors [130,131,132] in the form of an average solvent electrostatic potential (ASEP). This has been further explored using a simpler and efficient implementation [133] facilitated by the use of statistically uncorrelated solute–solvent configurations. If for the QM calculations the liquid solvent around the solute can be represented by classical point charges the applications have shown

that the use of one average configuration alone is sufficient to obtain the average value, although at the inevitable expense of the statistical distribution. Indeed, in many situations we are only interested in the statistical average. This is particularly the case if one considers the intermediate steps in the iterative procedure of the solute polarization described above (see for instance Figure 7-13).

Because the configurations sampled from the simulations are statistically uncorrelated, using a relatively small number of them will give convergent results. Thus we simply superpose the coordinates of all n solvent molecules, within a given cut-off radius, in the l configurations, with the solute fixed. In other words, the average configuration is obtained by simply superposing all the l configurations of the solvent atomic charges, and scaling by $1/l$. The scaling is important for giving the proper normalized average configuration. We thus have *one configuration* composed of the solute molecule surrounded by $l \times n$ solvent molecules represented by atomic charges of values scaled by $1/l$. Only this average configuration is used in the QM calculations and hence in the following we shall term this as the average solvent electrostatic configuration (ASEC). Illustrative examples are given by Coutinho and co-authors [133] for solvatochromic shifts, NMR chemical shieldings and in-solution dipole moments, using different quantum chemical methods. In every case considered the ASEC has given the same average as that obtained using the entire set of statistically uncorrelated configurations. In Figure 7-14 the histogram of the statistical distribution of 100 MP2/aug-cc-pVDZ calculations of the ^{17}O isotropic chemical shift of acetone in water obtained from uncorrelated configurations is shown.

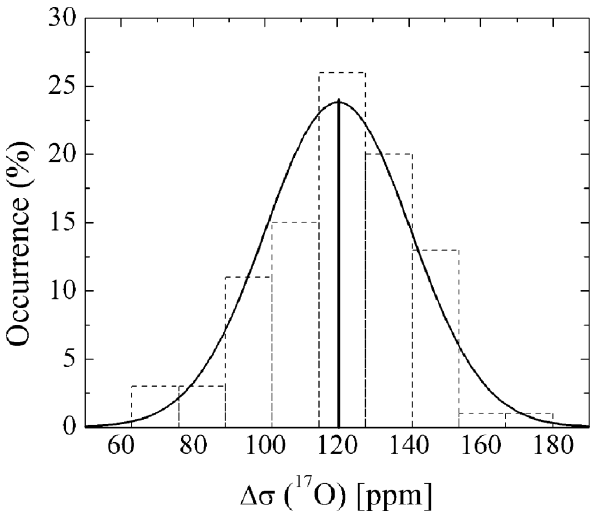

Figure 7-14. Comparison between the statistical distribution and the average value obtained using the average solvent electrostatic configuration (*central vertical line*)

The solvent contribution to the nuclear shielding constant is $\Delta\sigma = \sigma^{\text{water}} - \sigma^{\text{vacuum}}$. Figure 7-14 then compares the histogram of the statistical distribution of calculated values for $\Delta\sigma^{\text{iso}}(^{17}\text{O})$ and the single average value obtained with ASEC. The solvent effect on the shielding is calculated as $\Delta\sigma^{\text{iso}}(^{17}\text{O}) = 120.3 \pm 2.1$ ppm. The mean value obtained from one ASEC calculation is 120.5 ppm, in sharp agreement. This result is in good agreement with the direct result of 121.8 ppm obtained from Car–Parrinello molecular dynamics [134]. But it neglects the so-called indirect effects [134] and the possible effect of nuclear vibrations, a topic that has been analyzed by Mennucci and co-authors [135]. As the main objective here is to show the performance of the ASEC it is clearly seen that *one QM calculation* using ASEC reproduces precisely the statistical average using all configurations selected. Further discussions and examples can be found in Coutinho and co-authors [133].

As the ASEC replaces the statistical distribution by just one average configuration it suppresses the statistical distribution. Hence one will not succeed in the study of inhomogeneous broadening and line width of the absorption spectra of liquid systems, for instance. But ASEC will be very efficient and accurate for obtaining average solute properties in the electrostatic field of the solvent.

7.4. SUMMARY AND CONCLUSIONS

The sequential QM/MM methodology is a simple procedure to study solvent effects in general taking advantage of some statistically important aspects. By performing first the classical part to generate the liquid structures all the important statistical information is available. After the simulation the analysis of the statistical correlation can then be made. Hence, the sampling of configurations for subsequent QM calculations can be made in a very efficient manner. Having the liquid configurations the convergence of the QM calculated average with respect to the size of the system can also be easily obtained. These aspects have been analyzed here. First we reviewed the statistical analysis where the correlation can be studied from the auto-correlation function of the energy or from the statistical inefficiency. These two quantities are related but computationally obtained in different procedures. Next, examples have been given to demonstrate the feasibility and accuracy of the applications. We have first considered the case of nonpolar solutes in different solvents. Convergence has been analyzed with respect to both the statistical averages and the size of the solute + solvent system. It has been seen by explicit numerical applications that for nonpolar molecules the effects are restricted to the first solvation shell of explicit solvent molecules.

One drawback of the sequential procedure is that by adopting a two-step procedure, the MM part is uncoupled from the QM part. The mutual polarization between the solute and the solvent is thus precluded. To include the solute polarization by the solvent we have used an iterative procedure that brings the solute to the electrostatic equilibrium with the solvent. Using this scheme we have obtained some in-solution dipole moments of the solute that are in very good agreement with other theoretical results. Using these polarized solutes has improved the accuracy of the solvent

effects considered. Finally, we discussed and presented an illustrative example of how to obtain the same average value of the statistical distribution by using just one average configuration. This is a very efficient procedure but at present it is limited for obtaining average values of the solute properties with the solvent represented by point charges, i.e., the solute in the average electrostatic field of the solvent. But with this possibility we could consider studying larger solute systems aiming at biological molecules.

ACKNOWLEDGMENT

This work has been partially supported by the Brazilian agencies FAPESP, CNPq, RENAMI and CAPES.

REFERENCES

1. Yabuzaki T, Kinoshita T et al (1995) Z Phys B 98:367
2. Tabbert B, Günther H et al (1997) J Low Temp Phys 109:653
3. Ludwig V, Mukherjee PK, et al (2005) Phys Rev A 72:062714–1
4. Reichardt C (2003) Solvents and solvent effects in organic chemistry, 3rd edn. Wiley-VCH, Weinheim
5. Onsager L (1936) J Am Chem Soc 58:1486
6. Kirkwood JG (1934) J Chem Phys 2:351
7. Tapia O, Goscinski O (1975) Mol Phys 29:1653
8. Rivail JL, Rinaldi D (1976) Chem Phys 18:233
9. Rinaldi D, Rivail JL (1973) Theor Chim Acta 32:57
10. Tomasi J (2004) Theor Chem Acc 112:184
11. Miertus S, Scrocco E et al (1981) Chem Phys 55:117
12. Tomasi J, Persico M (1994) Chem Rev 94:2027
13. Tomasi J, Mennucci B et al (2005) Chem Rev 105:2999
14. Foresman JB, Keith TA et al (1996) J Phys Chem 100:16098
15. Mikkelsen KV, Ågren H, et al (1988) J Chem Phys 89:3086
16. Kongsted J, Osted A et al (2003) J Chem Phys 119:10519
17. Grozema FC. van Duijnen Th P (1998) J Phys Chem A 102:7984
18. Jensen L, van Duijnen Th P et al (2003) J Chem Phys 118:514
19. Klamt A, Schüürmann G (1993) J Chem Soc Perkins *T* 2:799
20. Monte SA, Muller T et al (2004) Theor Chem Acc 111:78
21. Blair JT, Krogh-Jespersen K et al (1989) J Am Chem Soc 111:6948
22. Warshell A, Levitt M (1976) J Mol Biol 103:227
23. Gao JL (1996) in: Lipkowitz KB, Boyd DB (eds) Reviews of Computational Chemistry, vol 7. New York, p. 119
24. Ruiz-López MF (ed) (2003) J Mol Struct (Theochem) 632, special issue on Combined QM/MM calculations in chemistry and biochemistry, p 1
25. Orozco M, Luque FJ (2000) Chem Rev 100:4187.
26. Cramer CJ (2004) Essentials of computational chemistry: Theories and models, 2 nd edn. Wiley, Chichester
27. Lin H, Truhlar DG (2007) Theor Chem Acc 117:185
28. Allen MP, Tildesley DJ (1987) Computer Simulation of Liquids, Oxford, Clarendon

29. Zeng J, Hush NS et al (1993) J Chem Phys 99:1508
30. Zeng J, Craw JS et al (1994) J Phys Chem 98:11075
31. Canuto S, Coutinho K (1997) Adv Quantum Chem 28:89
32. Canuto S, Coutinho K (2000) Int J Quantum Chem 77:192
33. Field MJ, Bash PA et al (1990) J Comput Chem 11:700
34. Gao JL, Luque FJ et al (1993) J Chem Phys 98:2975
35. Almeida TS, Coutinho K et al (2007) J Chem Phys 128:014506
36. Besley NA, Oakley MT et al (2004) J Am Chem Soc 126:13502
37. Coutinho K, Oliveira MJ et al (1998) Int J Quantum Chem 66:249
38. Chatfield C (1984) The analysis of time series. An introduction, Chapman and Hall, London
39. Kendal MG (1973) Time Series, Griffin, London
40. Krätschmer R, Binder K et al (1976) J Stat Phys 15:267
41. Caprihan A, Seymour JD (2000) J Mag Res 144:96
42. Coutinho K, Canuto S et al (2000) J Chem Phys 112:9874
43. Müller-Krumbhaar H, Binder K (1973) J Stat Phys 8:1
44. Tang S, Landau DP (1987) Phys Rev B 36:567
45. Friedberg R, Cameron JE (1970) J Chem Phys 52:6049
46. Malaspina T, Coutinho K et al (2002) J Chem Phys 117:1692
47. Canuto S, Coutinho K et al (2002) Adv Quantum Chem 41:161
48. Coutinho K, Cabral BJC et al (2004) Chem Phys Lett 399:534
49. Coutinho K, Canuto S (1997) DICE: A Monte Carlo program for molecular liquid simulation, University of São Paulo, Brazil
50. Georg HC, Coutinho K et al (2007) J Chem Phys 126:034507
51. Almeida KJ, Coutinho K et al (2001) Phys Chem Chem Phys 3:1583
52. Hernandez MZ, Longo R et al (2004) Phys Chem Chem Phys 6:2088
53. Coutinho K, Canuto S (2000) J Chem Phys 113:9132
54. Coutinho K, Canuto S (2003) J Mol Struct (Theochem) 632:235
55. Coutinho K, Ludwig V et al (2004) Phys Rev E 69:619021–1
56. Guedes RC, Coutinho K et al (2003) J Phys Chem B 107:4304
57. Guedes RC, Coutinho K et al (2003) J Phys Chem A 107:9197
58. Ludwig V, Coutinho K et al (2004) Phys Rev B 70:214110–1
59. Canuto S, Coutinho K et al (2005) Adv Quantum Chem 48:141
60. Lima MCP, Coutinho K et al (2006) J Phys Chem A 110:7253
61. Fileti EE, Georg HC et al (2007) J Braz Chem Soc 18:74
62. Couto PC, Cabral BJC et al (2006) Chem Phys Lett 429:129
63. Coutinho K, Canuto S (2006) in: Maroulis G (ed) Atoms, Molecules and Clusters in Electric Fields. Theoretical Approaches to the Calculation of Electric Polarizability. Imperial College Press, London, p 405
64. Ludwig V, Coutinho K et al (2003) Int J Quantum Chem 95:572
65. Liptay W (1966), in: Sinanoglu O (ed) *Modern quantum chemistry*, Acad. Press, N.Y., Part II, p 173
66. Bayliss NS, Hulme L (1953) Aust J Chem 6:257
67. Jorgensen WL, Chandrasekhar J et al (1984) J Am Chem Soc 106:6638
68. McDonald IR, Bounds DG et al (1982) Mol Phys 45:521
69. Berendsen HJC, Postman JPM et al (1981) Interaction models for water in relation to protein hydration. In: Pullman B (ed) Intermolecular forces. Dordrecht, Reidel, p. 331
70. Ridley J, Zerner MC (1973) Theor Chim Acta 32:111

71. Zerner MC (2000) ZINDO: A semi-empirical program package, University of Florida, Gainesville, FL, USA
72. Rivelino R, Maniero AM et al (2006) Carbon 44:2925
73. Rivelino R, Mota FB (2007) Nano Lett 7:1526
74. Li L, Bedrov D et al (2005) Phys Rev E 71:011502
75. Werder T, Walther JH et al (2003) Phys Chem B 107:1345
76. Mahoney MW. Jorgensen WL (2000) J Chem Phys 112:8910
77. Zerner MC (1990) Semiempirical molecular orbital methods. In: Lipkowitz KB Boyd DB (eds) Reviews of computational chemistry, VCH, New York, vol 25, p. 313
78. Canuto S, Coutinho K et al (2000) J Chem Phys 112:7293
79. Ordejón P, Artacho E, et al (1996) Phys Rev B 53:10441
80. Soler JM, Artacho E et al (2002) Phys: Condens Matter 14:2745
81. Ceperley DM, Alder BJ (1980) Phys Rev Lett 45:566
82. Perdew JP, Zunger A (1981) Phys Rev B 23:5048
83. Becke AD (1998) Phys Rev A 38:3098
84. Lee C, Yang W et al (1998) Phys Rev B 37:785
85. Troullier N, Martins JL (1991) Phys Rev B 43:1993
86. Junquera J, Paz O et al (2001) Phys Rev B 64:235111
87. Artacho E, Sánchez-Portal D et al (1999) Phys Status Solidi B 215:809
88. Ordejón P (2000) Phys Status Solidi B 217:335
89. Choudhury NJ (2006) Chem Phys 125:034502
90. Steiner T (2002) Biophys Chem 95:195
91. Andrievsky GV, Klochkov VK et al (2002) Chem Phys Lett 364:8
92. Andrievsky GV, Klochkov VK et al (1999) Chem Phys Lett 300:392
93. Andrievsky GV, Klochkov VK et al (2005) Fullerenes, Nanotubes, Carbon Nanostruct 13:363
94. Dhawan A, Taurozzi JS et al (2006) Environ Sci Technol 40:7394
95. Scharff P, Risch K et al (2004) Carbon 42:1203
96. Prylutskyy YI, Durov SS et al (2001) Int J Thermophys 22:943
97. Sayes CM, Fortner JD et al (2004) Nano Lett 4:1881
98. Jorgensen WL (ed) special issue no. 6 (2007) J Chem Theo Comput 3:1877–2145
99. Ohba T, Ikawa S (1991) Mol Phys 73:985
100. Jensen L, Swart M et al (2005) J Chem Phys 122:034103
101. Cornell WD, Cieplack P et al (1995) J Am Chem Soc 117:5179
102. Jorgensen WL. Tirado-Rives J (1988) J Am Chem Soc 110:1657
103. McDonald NA, Carlson HA et al (1997) J Phys Org Chem 10:563
104. Rivelino R, Cabral BJC et al (2005) Chem Phys Lett 407:13
105. Jorgensen WL, McDonald NA et al (1995) J Am Chem Soc 117:11809
106. Dang LX, Rice JE et al (1991) J Am Chem Soc 113:2481
107. Meng EC, Cieplak V et al (1994) J Am Chem Soc 116:12061
108. Soto P, Mark AE (2002) J Phys Chem B 106:12830
109. Breneman CM, Wiberg KB (1990) J Comput Chem 11:361
110. Besler BH, Merz KM et al (1990) J Comput Chem 11:431
111. Georg HC, Coutinho K et al (2006) Chem Phys Lett 429:119
112. Martín ME, Sánchez ML et al (2000) J Chem Phys 113:6308
113. Ten-no S, Hirata F et al (1994) J Chem Phys 100:7443
114. Kongsted J, Osted A et al (2004) J Chem Phys 121:8435
115. Öhrn A, Karlström G (2006) Mol Phys 104:3087
116. Kawashima Y, Dupuis M et al (2002) J Chem Phys 117:248

117. Aidas K, Kongsted J et al (2005) J Phys Chem A 109:8001
118. Öhrn A, Karlström G (2007) Theor Chem Acc 117:441
119. Hayes WP. Timmons CJ (1965) Spectrochim Acta 21:529
120. Bayliss NS, McRae EG (1954) J Phys Chem 58:1006
121. Bayliss NS, Wills-Johnson G (1968) Spectrochim Acta, Part A 24:551
122. Frisch MJ et al (2004) Gaussian 03, Revision D.01; Gaussian, Inc., Wallingford CT
123. Peter R, Dreizler H (1965) Z Naturforsch A 20:301
124. Röhrig UF, Frank I, et al (2003) Chem Phys Phys Chem 4:1177
125. Barker JW, Noe LJ (1972) J Chem Phys 57:3035
126. Lide DR (1993) Handbook of Chemistry and Physics, CRC Press, Boca Raton
127. Dilling WL (1966) J Org Chem 31:1045
128. Urahata S, Canuto S (2000) Int J Quantum Chem 80:1062
129. Couto PC, Guedes RC et al (2003) J Chem Phys 119:7344
130. Sánchez ML, Aguilar MA et al (1997) J Comput Chem 18:313
131. Sánchez ML, Aguilar MA et al (1998)J Mol Struct (Theochem) 426:181
132. Sánchez ML, Martín ME et al (2002) J Phys Chem 106:4813
133. Coutinho K, Georg HC et al (2007) Chem Phys Lett 437:148
134. Pavone M, Crescenzi O et al (2006) Theor Chem Acc 116:456
135. Mennucci B, Martinez JM et al (2001) J Phys Chem A 105:7287

CHAPTER 8

STATISTICAL MECHANICAL MODELING OF CHEMICAL REACTIONS IN CONDENSED PHASE SYSTEMS

ANDREA AMADEI[1], MASSIMILIANO ASCHI[2], AND ALFREDO DI NOLA[3]

[1] *Dipartimento di Scienze e Tecnologie Chimiche, Università di Roma "Tor Vergata", via della Ricerca Scientifica 1, 00133 Roma, Italy, e-mail: andrea.amadei@uniroma2.it*

[2] *Dipartimento di Chimica, Ingegneria Chimica e Materiali, Università dell'Aquila, via Vetoio, 67010 l'Aquila, Italy, e-mail: aschi@caspur.it*

[3] *Dipartimento di Chimica, Università di Roma "La Sapienza", P.le A. Moro 5, 00185 Roma, Italy, e-mail: dinola@caspur.it*

Abstract: In this contribution it will be outlined the basic theoretical framework and two applications of a new theoretical–computational approach specifically designed for evaluating free-energy profiles (and related observables such as equilibrium and rate constants) for chemical reactions taking place in condensed phase. The methodology, based on the use of molecular dynamics simulations and perturbed matrix method, if combined with basic statistical mechanics, may represent a useful tool complementary to other approaches for addressing chemical processes occurring in complex atomic–molecular environments

8.1. INTRODUCTION

Most of the chemical processes of biological and technological relevance take place in condensed phase. For this reason their modeling, at atomistic level, has always represented one of the major challenges of theoretical and computational physical chemistry. In this respect, because of the recent advances in the theoretical modeling of solution [1,2,3], accurate calculations of the equilibrium constants of many reactions have become accessible [4], and now we are in a position of explaining why, and sometimes to predict if, a chemical reaction in condensed phase does actually occur. The picture becomes less optimistic as far as we are interested in elucidating, at the atomistic detail, how a chemical reaction takes place [5,6]. Whatever "mechanistic" information may be obtained by relating the phenomenological analysis of the reaction course with the theoretical prediction of the microscopic rate constants which, beyond a physically sound modelization, requires a proper evaluation of the reaction free-energy profile. Accurate evaluation of the reaction free energy, which is essentially a statistical quantity, depends on the level of sampling of the system configurational space. Hence, when dealing with the course of chemical reactions,

S. Canuto (ed.), Solvation Effects on Molecules and Biomolecules, 191–213.
DOI 10.1007/978-1-4020-8270-2_8,

one should in principle carry out statistical averages over the ensembles defined by a huge number of trajectories connecting the reactant state to the product one. This is obviously undoable for systems in solution because of the prohibitively large phase-space dimensions. For this reason, in the last years, several investigators have proposed different theoretical–computational methods [7,8,9,10,11,12,13]. Essentially all the above methodologies show a common strategy based on the predefinition of a portion of the entire system to be explicitly treated at the electronic level (quantum center, QC), with the rest of the system acting as an electrostatic perturbation, and the predefinition of a generalized (semi-classical) coordinate, within the QC, which is called the reaction coordinate (RC). Beyond the drawbacks and limitations characterizing the above procedures calculation of free-energy profiles requires an accurate outline of the RC, typically provided by quantum chemical calculations, and a proper sampling of the perturbing environment, typically obtained through force field-based molecular dynamics (MD) or Monte Carlo (MC) simulations. Some of the proposed methodologies provide a very accurate quantum chemical picture at the price of reducing the statistical sampling [14] or, sometimes, to treat it as a mean field [15,16]. Other approaches enhance the statistics of the fluctuating environment making use of relatively cheap semi-empirical description of the QC [17,18,19]. The necessity of maintaining a good level of electronic accuracy for QC characterization while ensuring a proper statistical sampling of the atomistic environment inspired us to propose the perturbed matrix method (PMM) [20,21]. Based on the very first principles of quantum mechanics, PMM seems very promising for treating systems where usual procedures are computationally problematic and, if combined with basic statistical mechanics, actually provides a powerful, rigorous approach to treat chemical reactions in complex systems [22,23,24,25]. In this chapter, the bases of PMM and related theoretical procedures for evaluating the reaction free-energy surface and kinetics for a chemical transition defined by a set of classical generalized coordinates will be reviewed, extending and generalizing the statistical mechanical framework and discussing in detail the approximations which may be used.

8.2. PMM BASIC DERIVATIONS

Consider a quantum center (i.e., a molecule or a subpart of a molecule) embedded in a classical molecular environment. Defining with $\mathbf{r}_n$ the nuclear coordinates of the quantum center and with $\mathbf{x}$ the coordinates of the atoms providing the (classical) perturbing field we can expand [26] the perturbed Hamiltonian matrix $\tilde{H}$ of the quantum center on the Born–Oppenheimer surface as

$$\tilde{H} = \tilde{H}^0 + \tilde{I} q_T \mathcal{V}(\mathbf{r}_0) + \tilde{Z}_1(\mathbf{E}) + \tilde{Z}_2(\tilde{\Theta}) + \cdots \tag{8-1}$$

$$\left[\tilde{Z}_1\right]_{l,l'} = -\mathbf{E} \cdot \langle \Phi_l^0 | \hat{\boldsymbol{\mu}} | \Phi_{l'}^0 \rangle \tag{8-2}$$

$$\left[\tilde{Z}_2\right]_{l,l'} = \frac{1}{2} Tr\left[\tilde{\Theta}\ \tilde{Q}_{l,l'}\right] \tag{8-3}$$

$$\Theta_{k,k'} = -\left(\frac{\partial E_k}{\partial r_{k'}}\right)_{\mathbf{r}=\mathbf{r}_0} \tag{8-4}$$

$$\hat{\boldsymbol{\mu}} = \sum_j q_j \left(\mathbf{r}_j - \mathbf{r}_0\right) \tag{8-5}$$

where $\tilde{H}^0$ and q_T are the unperturbed Hamiltonian matrix and total charge of the quantum center, $\tilde{Q}_{l,l'}$, is the l, l' transition quadrupoles matrix [21], $\mathcal{V}(r_0, x)$ is the perturbing electric potential at r_0 position of the quantum center, E is the perturbing electric field at r_0 and Φ_l^0 the lth unperturbed electronic Hamiltonian eigenfunction (we use these eigenfunctions as basis set). Note that we consider the total charge as invariant in the presence of the perturbation, and hence a constant defined by the unperturbed condition.

For a quantum center where the perturbing electric field is almost constant, at least neglecting local atomic interactions typically described by short-range potentials such as the Lennard-Jones one, we can write [26] the perturbed Hamiltonian matrix $\tilde{H}$ of the quantum center on the Born–Oppenheimer (BO) surface as

$$\tilde{H}(\mathbf{r}_n, \mathbf{x}) \cong \tilde{H}^0(\mathbf{r}_n) + q_\mathrm{T}\mathcal{V}(\mathbf{r}_0, \mathbf{x})\tilde{I} + \tilde{Z}_1(\mathbf{E}, \mathbf{r}_n) + \Delta V(\mathbf{r}_n, \mathbf{x})\tilde{I} \tag{8-6}$$

where $\Delta V(r_n, x)$ approximates the perturbation due to all the terms from the quadrupoles on, as a simple short-range potential. For more complex perturbing field we can use a similar expression, although by inserting higher order multipole terms, e.g., the quadrupole term $\tilde{Z}_2$. Hence the perturbed BO Hamiltonian eigenvalues ε_i are, within this approximation,

$$\varepsilon_i = \varepsilon_i'(\mathbf{r}_n, \mathbf{x}) + q_\mathrm{T}\mathcal{V}(\mathbf{r}_0, \mathbf{x}) + \Delta V(\mathbf{r}_n, \mathbf{x}) \tag{8-7}$$

where

$$\left(\tilde{H}^0 + \tilde{Z}_1\right)\mathbf{c}_i = \varepsilon_i'\mathbf{c}_i \tag{8-8}$$

and c_i is the *i*th perturbed eigenvector. Note that from the set c_i we can in principle obtain any possible perturbed property; e.g., the perturbed (transition) dipole [26] $\mu_{i,j} = \langle \Phi_i \,|\hat{\mu}|\, \Phi_j \rangle$ is

$$\mu_{i,j} = \mathbf{c}_i^{*\mathrm{T}}\tilde{\Lambda}_x^0\mathbf{c}_j\ \mathbf{i} + \mathbf{c}_i^{*\mathrm{T}}\tilde{\Lambda}_y^0\mathbf{c}_j\ \mathbf{j} + \mathbf{c}_i^{*\mathrm{T}}\tilde{\Lambda}_z^0\mathbf{c}_j\ \mathbf{k} \tag{8-9}$$

$$\left[\tilde{\Lambda}_x^0\right]_{l,l'} = \langle \Phi_l^0 \,|\hat{\mu}_x|\, \Phi_{l'}^0 \rangle \tag{8-10}$$

$$\left[\tilde{\Lambda}_y^0\right]_{l,l'} = \langle \Phi_l^0 \,\big|\hat{\mu}_y\big|\, \Phi_{l'}^0 \rangle \tag{8-11}$$

$$\left[\tilde{\Lambda}_z^0\right]_{l,l'} = \langle \Phi_l^0 \,|\hat{\mu}_z|\, \Phi_{l'}^0 \rangle \tag{8-12}$$

where obviously Φ is the perturbed Hamiltonian eigenfunction and $\mathbf{c}^{*\mathrm{T}}$ is the transpose of the complex conjugate of $\mathbf{c}$ (typically from quantum chemical calculations $\tilde{H}$ has only real elements and hence $\mathbf{c} = \mathbf{c}^*$ is a real eigenvector).

8.3. STATISTICAL MECHANICS IN THE INFINITE DILUTION CONDITIONS

The partition function of a solute–solvent system for a given electronic state, where for the N solutes we use as (classical) molecular coordinates the center of mass position $\mathbf{r}_G$, the eulerian angles θ, ϕ, ψ providing the orientation of the molecular frame and the internal coordinates $\mathbf{x}_{\text{in}}$ providing the atom positions in the molecular frame, is [27,28]

$$
\begin{aligned}
Q_{\text{T}} &= \sum_{l} \int \frac{\mathrm{e}^{-\beta \mathcal{K}_{\text{T},s}} \mathrm{e}^{-\beta \mathcal{K}_{\text{T}}} \mathrm{e}^{-\beta \mathcal{U}_{\text{T},}}}{(1+\gamma_s)^{N_s}(1+\gamma)^{N} N_s! N! h^{(Nd+N_s d_s)}} \mathrm{d}\mathbf{p}_s \mathrm{d}\mathbf{x}_s \\
&\quad \prod_{i=1}^{N} |\sin\theta_i| \mathrm{d}\mathbf{x}_i \mathrm{d}\mathbf{p}_i \\
\mathbf{p}_i &= \tilde{M}_i \mathbf{x}'_i \\
\mathbf{x}_i &= \begin{pmatrix} \mathbf{r}_{i,G} \\ \theta_i \\ \phi_i \\ \psi_i \\ \mathbf{x}_{i,\text{in}} \end{pmatrix} \quad \dot{\mathbf{x}}'_i = \begin{pmatrix} \dot{\mathbf{r}}_{i,G} \\ \omega_{i1} \\ \omega_{i2} \\ \omega_{i3} \\ \dot{\mathbf{x}}_{i,\text{in}} \end{pmatrix}
\end{aligned}
\tag{8-13}
$$

where $\mathcal{K}_{T,s}$ is the kinetic energy of the N_s solvent molecules, x_s and p_s are the classical coordinates and conjugated momenta of the solvent, and the kinetic energy of the N solute molecules is

$$
\mathcal{K}_T = \frac{1}{2} \sum_{i=1}^{N} \mathbf{p}_i^T (\tilde{M}_i)^{-1} \mathbf{p}_i \tag{8-14}
$$

Furthermore, $\mathbf{x}_i$ are the classical coordinates of the ith solute molecule, rototranslational ones plus a subset of the internal coordinates here defined as $\mathbf{x}_{i,\text{in}}$, $\mathcal{U}_{T,l}$ is the total potential energy including the lth quantum vibrational term and $1+\gamma$ and $1+\gamma_s$ are the symmetry coefficients per molecule for the solute and solvent molecules necessary to correct the partition function from the rotations and intramolecular atomic displacements which correspond to permutations of identical particles which do not change the physical state of the system [29,30]. Note that quantum nuclear coordinates (responsible for quantum vibrations) are equivalent to classical constrained coordinates, as shown in a previous paper [21], and hence disappear in the semiclassical partition function. For each ith solute we used the corresponding transformed momenta, given by the Jacobian $|\sin\theta_i|$, associated with the transformation of the angular velocity from the time derivatives of the Eulerian angles $(\dot{\theta}_i, \dot{\phi}_i, \dot{\psi}_i)$ to the projections of the angular velocity vector onto the molecular axes $(\omega_{i1}, \omega_{i2}, \omega_{i3})$, i.e., time derivatives of the rotation angles, defined by

$$
\omega_{i1} = \dot{\theta}_i \cos\psi_i + \dot{\phi}_i \sin\theta_i \sin\psi_i \tag{8-15}
$$

$$
\omega_{i2} = -\dot{\theta}_i \sin\psi_i + \dot{\phi}_i \sin\theta_i \cos\psi_i \tag{8-16}
$$

$$
\omega_{i3} = \dot{\phi}_i \cos\theta_i + \dot{\psi}_i \tag{8-17}
$$

Note that the mass tensor $\tilde{M}_{\mathrm{i}}$, providing the kinetic energy associated to the classical degrees of freedom, is expressed in the form which is appropriate for using $\omega_{i1}, \omega_{i2}, \omega_{i3}$. Finally, h is the Planck constant, d and d_s are the number of classical degrees of freedom in the solute molecules and solvent molecules, respectively N_s is the number of solvent molecules and $\beta = 1/kT$. For a given configuration we can solve the integral over the solutes momenta using the orthogonal transformations of these momenta which diagonalize each $(\tilde{M}_i)^{-1}$ obtaining

$$\int \mathrm{e}^{-\beta \frac{1}{2}\mathbf{p}_i^T(\tilde{M}_i)\mathbf{p}_i} d\mathbf{p}_i = \left[(2\pi kT)^d \det \tilde{M}_i\right]^{1/2} \tag{8-18}$$

Using this last equation we then have

$$\begin{aligned} Q_T = \sum_l \int & \frac{\mathrm{e}^{-\beta \mathcal{K}_{T,s}} \mathrm{e}^{-\beta \mathcal{U}_{T,l}} (2\pi kT)^{(Nd)/2}}{(1+\gamma_s)^{N_s}(1+\gamma)^N N_s! N! h^{(Nd+N_s d_s)}} \mathrm{d}\mathbf{p}_s \mathrm{d}\mathbf{x}_s \\ & \prod_{i=1}^{N} (\det \tilde{M}_i)^{1/2} |\sin\theta_i| \mathrm{d}\mathbf{x}_i \end{aligned} \tag{8-19}$$

If the N solutes are in the infinite dilution condition, we can simplify the integral in the previous equation considering that there is no interaction among the solute molecules. Hence for the great majority of the solutes rototranslational configurations, the integral on the other coordinates and solvent momenta is a constant (note that in the solute mass tensor no elements depend on the center of mass position and the Eulerian angles). Therefore

$$\begin{aligned} & \int \mathrm{e}^{-\beta(\mathcal{U}_{T,l}+\mathcal{K}_{T,s})} \mathrm{d}\mathbf{p}_s \mathrm{d}\mathbf{x}_s \prod_{i=1}^{N} (\det \tilde{M}_i)^{1/2} |\sin\theta_i| \mathrm{d}\mathbf{x}_i \cong \\ & (V 8\pi^2)^N \int \mathrm{e}^{-\beta(\mathcal{U}_{T,l}+\mathcal{K}_{T,s})} \mathrm{d}\mathbf{p}_s \mathrm{d}\mathbf{x}_s \prod_{i=1}^{N} (\det \tilde{M}_i)^{1/2} \mathrm{d}\mathbf{x}_{i,\mathrm{in}} \end{aligned} \tag{8-20}$$

where in this last equation we used

$$8\pi^2 = \int_0^{\pi} |\sin\theta| \, \mathrm{d}\theta \int_0^{2\pi} \mathrm{d}\phi \int_0^{2\pi} \mathrm{d}\psi \tag{8-21}$$

$$V = \int \mathrm{d}\mathbf{r}_G \tag{8-22}$$

and $\mathcal{U}_{T,l}$ is now evaluated at fixed rototranslational coordinates of the solute molecules being homogeneously distributed in the volume V of the full system. Note that in the special case where we deal with a linear solute molecule the integral over the Eulerian angles must be performed at fixed ψ and hence reduces to 4π. Finally, considering again that N/N_s is almost zero we have

$$\begin{aligned} & \int \mathrm{e}^{-\beta(\mathcal{U}_{T,l}+\mathcal{K}_{T,s})} \mathrm{d}\mathbf{p}_s \mathrm{d}\mathbf{x}_s \prod_{i=1}^{N} (\det \tilde{M}_i)^{1/2} \mathrm{d}\mathbf{x}_{i,\mathrm{in}} \cong \\ & \frac{N_s!}{(n_s!)^N} \left(\int \mathrm{e}^{-\beta(\mathcal{U}_l+\mathcal{K}_s)} (\det \tilde{M})^{1/2} \mathrm{d}\mathbf{p}_s \mathrm{d}\mathbf{x}_s \mathrm{d}\mathbf{x}_{\mathrm{in}} \right)^N \end{aligned} \tag{8-23}$$

where $\mathcal{U}_l$ is the potential energy including the lth quantum vibrational term of a subsystem defined by a single solute molecule with fixed rototranslational coordinates, in the center of the subsystem, and n_s solvent molecules (n_s is given by the closest integer number to N_s/N) with $\mathcal{K}_s$ the corresponding solvent molecules' kinetic energy. The right-hand integral in the last equation is taken over the volume V/N of the subsystem, and $\mathbf{x}_s$ and $\mathbf{p}_s$ are now the coordinates and momenta of the n_s solvent molecules of the subsystem. Clearly $\mathbf{x}_{\text{in}}$ and $\tilde{M}$ represent the internal coordinates and the mass tensor of the single solute molecule. Note that the factor $N_s!/(n_s!)^N$ is a simple degeneration factor due to the number of ways we can distribute n_s out of N_s solvent molecules in N subsystems. Hence, using $N! \cong N^N \mathrm{e}^{-N}$ we can rewrite the whole partition function as $Q_T = (Q'V)^N/N! \cong (\mathrm{e}Q'V/N)^N = (Q/\mathrm{e}^{-1})^N$ with $Q = Q'V/N$ the partition function of a single subsystem and

$$\begin{aligned} Q' &= \Theta \sum_l \int \mathrm{e}^{-\beta(\mathcal{U}_l+\mathcal{K}_s)}(\det \tilde{M})^{1/2}\mathrm{d}\mathbf{x}_s\mathrm{d}\mathbf{p}_s\mathrm{d}\mathbf{x}_{\text{in}} \\ &\cong \Theta Q_{v,s}^{n_s} Q_v \int \mathrm{e}^{-\beta(\mathcal{U}'+\mathcal{K}_s)}(\det \tilde{M})^{1/2}\mathrm{d}\mathbf{x}_s\mathrm{d}\mathbf{p}_s\mathrm{d}\mathbf{x}_{\text{in}} \end{aligned} \tag{8-24}$$

$$\Theta = \frac{(2\pi kT)^{d/2}8\pi^2}{(1+\gamma)(1+\gamma_s)^{n_s}n_s!h^{(n_s d_s+d)}} \tag{8-25}$$

Note that in Eq. 8-24 we have used the typical approximation to factorize the partition function [28,32] and hence $Q_{v,s}$, Q_v are the (quantum) vibrational partition functions of the solvent and solute molecule, respectively, and $\mathcal{U}' = \Phi + \Delta\mathcal{U}_{v,0}$ with Φ the system potential energy (i.e., electronic ground state energy surface) and $\Delta\mathcal{U}_{v,0}$ the system vibrational ground state energy shift from a reference value [28,32], typically negligible.

This last result states that we can obtain the exact statistical mechanics for whatever dilute solute (including of course a reactive molecular complex), by simply investigating a single solute at a given rototranslational configuration embedded in the solvent (the environment).

8.4. THE FREE-ENERGY REACTION SURFACE

In order to deal with a chemical reaction it is convenient to express the energy $\mathcal{U}'$ by the perturbed Hamiltonian matrix as a function of the reaction coordinates $\boldsymbol{\eta}$. Expressing the nuclear coordinates of the quantum center (we consider it as the solute or a part of the solute) as $\mathbf{r}_n = \{\mathbf{x}_{\text{q}}, \boldsymbol{\eta}, \boldsymbol{\zeta}\}$ where $\mathbf{x}_{\text{q}}$ are the internal quantum vibrational coordinates, $\boldsymbol{\eta}$ the reaction coordinates (belonging to the solute classical internal coordinates $\mathbf{x}_{\text{in}}$) and $\boldsymbol{\zeta}$ the remaining classical coordinates. Defining with $\boldsymbol{\xi}$ all the solute classical internal coordinates except $\boldsymbol{\eta}$, i.e., $\mathbf{x}_{\text{in}} = \{\boldsymbol{\xi}, \boldsymbol{\eta}\}$, we have that the free-energy change for a chemical transition defined by $\boldsymbol{\eta}_a \rightarrow \boldsymbol{\eta}_b$ is

$$\begin{aligned} \Delta A &= -kT \ln \left[\frac{Q_{v,b} \int \mathrm{e}^{-\beta(\mathcal{K}_s+\mathcal{U}'_b)}(\det \tilde{M}_b)^{1/2}\mathrm{d}\boldsymbol{\xi}\mathrm{d}\mathbf{x}_s\mathrm{d}\mathbf{p}_s}{Q_{v,a} \int \mathrm{e}^{-\beta(\mathcal{K}_s+\mathcal{U}'_a)}(\det \tilde{M}_a)^{1/2}\mathrm{d}\boldsymbol{\xi}\mathrm{d}\mathbf{x}_s\mathrm{d}\mathbf{p}_s} \right] \\ &= -kT \ln\langle \mathrm{e}^{-\beta(\mathcal{U}'_b-\mathcal{U}'_a)}(\det \tilde{M}_b/\det \tilde{M}_a)^{1/2}\rangle_a^0 - kT \ln \frac{Q_{v,b}}{Q_{v,a}} \end{aligned}$$

where

$$\langle \mathrm{e}^{-\beta(\mathcal{U}'_b-\mathcal{U}'_a)}(\det \tilde{M}_b/\det \tilde{M}_a)^{1/2}\rangle_a^0 = \frac{\int \mathrm{e}^{-\beta(\mathcal{U}'_b-\mathcal{U}'_a)}\mathrm{e}^{-\beta(\mathcal{K}_s+\mathcal{U}'_a)}(\det \tilde{M}_b/\det \tilde{M}_a)^{1/2}(\det \tilde{M}_a)^{1/2}\mathrm{d}\boldsymbol{\xi}\,\mathrm{d}\mathbf{x}_s\mathrm{d}\mathbf{p}_s}{\int \mathrm{e}^{-\beta(\mathcal{K}_s+\mathcal{U}'_a)}(\det \tilde{M}_a)^{1/2}\mathrm{d}\boldsymbol{\xi}\,\mathrm{d}\mathbf{x}_s\mathrm{d}\mathbf{p}_s}$$

and the subscripts a and b mean that the property is evaluated at $\boldsymbol{\eta}_a$ or $\boldsymbol{\eta}_b$.

For those molecular systems where the chemical transition considered is, as usual, not accessible within a simulation (i.e., the Hamiltonian used provides that $\boldsymbol{\eta}$ fluctuations are confined within a very small range around $\boldsymbol{\eta}_a$) the ensemble average of the last equation can in principle be obtained by a molecular simulation taking into account only the configurations where $\boldsymbol{\eta} \cong \boldsymbol{\eta}_a$. However, such a procedure is in general statistically not very efficient since it utilizes only a subpart of the sampling obtained by the simulation and when Molecular Dynamics simulations are concerned, often the use of a rather short time step is required, as $\boldsymbol{\eta}$ typically involve bond length coordinates. The use of a constrained simulation where $\boldsymbol{\eta} = \boldsymbol{\eta}_a$ would then be very convenient. However, it must be noted that in the previous equations $\tilde{M}_a$ and $\tilde{M}_b$ are not in general identical to the mass tensors of a constrained system where $\boldsymbol{\eta} = \boldsymbol{\eta}_a$ or $\boldsymbol{\eta} = \boldsymbol{\eta}_b$ [28,32] and hence we must consider with care when the ensemble average of the previous equations can be obtained using a constrained simulation. In fact we can rewrite the ensemble average as

$$\begin{aligned}
&\langle \mathrm{e}^{-\beta(\mathcal{U}'_b-\mathcal{U}'_a)}(\det \tilde{M}_b/\det \tilde{M}_a)^{1/2}\rangle_a^0 \\
&= \frac{\langle(\det \tilde{M}_b/\det \tilde{M}_{\boldsymbol{\xi},b})^{1/2}\rangle_{\boldsymbol{\eta}_b}^0}{\langle(\det \tilde{M}_a/\det \tilde{M}_{\boldsymbol{\xi},a})^{1/2}\rangle_{\boldsymbol{\eta}_a}^0}\langle \mathrm{e}^{-\beta(\mathcal{U}'_b-\mathcal{U}'_a)}d(\det \tilde{M}_{\boldsymbol{\xi},b}/\det \tilde{M}_{\boldsymbol{\xi},a})^{1/2}\rangle_{\boldsymbol{\eta}_a}^0 \\
&\langle \mathrm{e}^{-\beta\cdots\cdots}(\det \tilde{M}_{\boldsymbol{\xi},b}/\det \tilde{M}_{\boldsymbol{\xi},a})^{1/2}\rangle_{\boldsymbol{\eta}_a}^0 \\
&= \frac{\int \mathrm{e}^{-\beta(\mathcal{U}'_b-\mathcal{U}'_a)}\mathrm{e}^{-\beta(\mathcal{K}_s+\mathcal{U}'_a)}(\det \tilde{M}_{\boldsymbol{\xi},b}/\det \tilde{M}_{\boldsymbol{\xi},a})^{1/2}(\det \tilde{M}_{\boldsymbol{\xi},a})^{1/2}\mathrm{d}\boldsymbol{\xi}\,\mathrm{d}\mathbf{x}_s\mathrm{d}\mathbf{p}_s}{\int \mathrm{e}^{-\beta(\mathcal{K}_s+\mathcal{U}'_a)}(\det \tilde{M}_{\boldsymbol{\xi},a})^{1/2}\mathrm{d}\boldsymbol{\xi}\,\mathrm{d}\mathbf{x}_s\mathrm{d}\mathbf{p}_s} \\
&\langle(\det \tilde{M}_b/\det \tilde{M}_{\boldsymbol{\xi},b})^{1/2}\rangle_{\boldsymbol{\eta}_b}^0 \\
&= \frac{\int \mathrm{e}^{-\beta(\mathcal{K}_s+\mathcal{U}'_b)}(\det \tilde{M}_b/\det \tilde{M}_{\boldsymbol{\xi},b})^{1/2}(\det \tilde{M}_{\boldsymbol{\xi},b})^{1/2}\mathrm{d}\boldsymbol{\xi}\,\mathrm{d}\mathbf{x}_s\mathrm{d}\mathbf{p}_s}{\int \mathrm{e}^{-\beta(\mathcal{K}_s+\mathcal{U}'_b)}(\det \tilde{M}_{\boldsymbol{\xi},b})^{1/2}\mathrm{d}\boldsymbol{\xi}\,\mathrm{d}\mathbf{x}_s\mathrm{d}\mathbf{p}_s} \\
&\langle(\det \tilde{M}_a/\det \tilde{M}_{\boldsymbol{\xi},a})^{1/2}\rangle_{\boldsymbol{\eta}_a}^0 \\
&= \frac{\int \mathrm{e}^{-\beta(\mathcal{K}_s+\mathcal{U}'_a)}(\det \tilde{M}_a/\det \tilde{M}_{\boldsymbol{\xi},a})^{1/2}(\det \tilde{M}_{\boldsymbol{\xi},a})^{1/2}\mathrm{d}\boldsymbol{\xi}\,\mathrm{d}\mathbf{x}_s\mathrm{d}\mathbf{p}_s}{\int \mathrm{e}^{-\beta(\mathcal{K}_s+\mathcal{U}'_a)}(\det \tilde{M}_{\boldsymbol{\xi},a})^{1/2}\mathrm{d}\boldsymbol{\xi}\,\mathrm{d}\mathbf{x}_s\mathrm{d}\mathbf{p}_s}
\end{aligned} \tag{8-26}$$

where $\det \tilde{M}_{\boldsymbol{\xi},a}$, $\det \tilde{M}_{\boldsymbol{\xi},b}$ are the mass tensor (diagonal) blocks corresponding to the $\boldsymbol{\xi}$ velocities, obtained at $\boldsymbol{\eta}_a$ and $\boldsymbol{\eta}_b$. For a non-highly flexible solute (where the rotational coupling can be neglected) [27] if we consider a limited range for the reaction

coordinates such that the $\boldsymbol{\eta}$ transition does not alter much the solute structure and therefore its mass tensor determinant, we may assume

$$\langle(\det \tilde{M}_a / \det \tilde{M}_{\boldsymbol{\xi},a})^{1/2}\rangle^0_{\boldsymbol{\eta}_a} \cong \langle(\det \tilde{M}_b / \det \tilde{M}_{\boldsymbol{\xi},b})^{1/2}\rangle^0_{\boldsymbol{\eta}_b} \tag{8-27}$$

and hence

$$\Delta A \cong -kT \ln\langle e^{-\beta(\mathcal{U}'_b-\mathcal{U}'_a)}(\det \tilde{M}_{\boldsymbol{\xi},b} / \det \tilde{M}_{\boldsymbol{\xi},a})^{1/2}\rangle^0_{\boldsymbol{\eta}_a} - kT \ln \frac{Q_{v,b}}{Q_{v,a}} \tag{8-28}$$

where $\langle e^{-\beta(\mathcal{U}'_b-\mathcal{U}'_a)}(\det \tilde{M}_{\boldsymbol{\xi},b} / \det \tilde{M}_{\boldsymbol{\xi},a})^{1/2}\rangle^0_{\boldsymbol{\eta}_a}$ is evaluated in the true constrained ensemble and so it may be obtained by a constrained molecular simulation with $\boldsymbol{\eta} = \boldsymbol{\eta}_a$.

Moreover, considering $\Delta\mathcal{U}_{v,0}$ as virtually independent of the $\boldsymbol{\eta}$ coordinates, we have

$$\mathcal{U}'_b - \mathcal{U}'_a \cong \varepsilon_b - \varepsilon_a + \mathcal{U}_{\text{env},b} - \mathcal{U}_{\text{env},a} \tag{8-29}$$

where ε comes from Eq. 8-7 and $\mathcal{U}_{\text{env},a}, \mathcal{U}_{\text{env},b}$ are the internal energies of the atomic and molecular environment (excluding the interaction with the QC and the quantum vibrational energy) obtained when the quantum center is at $\boldsymbol{\eta}_a$ and $\boldsymbol{\eta}_b$, respectively. Note that the QC electronic ground state energy ε at each $\boldsymbol{\eta}$, $\boldsymbol{\xi}$ position is obtained with energy-minimized $\mathbf{x}_q$ coordinates. If the environment energy is basically independent of the internal state of the quantum center, as typically in MD simulations where the atomic polarization is neglected, then (see Eq. 8-7)

$$\begin{aligned}\mathcal{U}'_b - \mathcal{U}'_a &\cong \varepsilon_b - \varepsilon_a = \varepsilon'_b - \varepsilon'_a + q_T(\mathcal{V}_b - \mathcal{V}_a) + \Delta V_b - \Delta V_a \\ &= \Delta(\varepsilon' + q_T\mathcal{V}) + \Delta V_b - \Delta V_a\end{aligned}$$

Hence, we may write

$$\begin{aligned}&\langle e^{-\beta(\mathcal{U}'_b-\mathcal{U}'_a)}(\det \tilde{M}_{\boldsymbol{\xi},b} / \det \tilde{M}_{\boldsymbol{\xi},a})^{1/2}\rangle^0_{\boldsymbol{\eta}_a} \cong \\ &e^{-\beta\Delta A_{\Delta V}}\langle e^{-\beta\Delta(\varepsilon'+q_T\mathcal{V})}(\det \tilde{M}_{\boldsymbol{\xi},b} / \det \tilde{M}_{\boldsymbol{\xi},a})^{1/2}\rangle^0_{\boldsymbol{\eta}_a} \\ &e^{-\beta\Delta A_{\Delta V}} = \frac{\int e^{-\beta(\mathcal{U}'_b+\mathcal{K}_s)}(\det \tilde{M}_{\boldsymbol{\xi},b})^{1/2} d\boldsymbol{\xi} d\mathbf{x}_s d\mathbf{p}_s}{\int e^{-\beta(\mathcal{U}'_b+\mathcal{K}_s)} e^{-\beta(\Delta V_a-\Delta V_b)}(\det \tilde{M}_{\boldsymbol{\xi},b})^{1/2} d\boldsymbol{\xi} d\mathbf{x}_s d\mathbf{p}_s} \\ &\langle e^{-\beta\Delta(\varepsilon'+q_T\mathcal{V})}(\det \tilde{M}_{\boldsymbol{\xi},b} / \det \tilde{M}_{\boldsymbol{\xi},a})^{1/2}\rangle^0_{\boldsymbol{\eta}_a} = \\ &\frac{\int e^{-\beta(\mathcal{U}'_a+\mathcal{K}_s)} e^{-\beta\Delta(\varepsilon'+q_T\mathcal{V})}(\det \tilde{M}_{\boldsymbol{\xi},b} / \det \tilde{M}_{\boldsymbol{\xi},a})^{1/2}(\det \tilde{M}_{\boldsymbol{\xi},a})^{1/2} d\boldsymbol{\xi} d\mathbf{x}_s d\mathbf{p}_s}{\int e^{-\beta(\mathcal{U}'_a+\mathcal{K}_s)}(\det \tilde{M}_{\boldsymbol{\xi},a})^{1/2} d\boldsymbol{\xi} d\mathbf{x}_s d\mathbf{p}_s}\end{aligned} \tag{8-30}$$

providing

$$\Delta A \cong -kT \ln\langle e^{-\beta\Delta(\varepsilon'+q_T\mathcal{V})}(\det \tilde{M}_{\boldsymbol{\xi},b} / \det \tilde{M}_{\boldsymbol{\xi},a})^{1/2}\rangle^0_{\boldsymbol{\eta}_a} \tag{8-31}$$

$$-kT \ln \frac{Q_{v,b}}{Q_{v,a}} + \Delta A_{\Delta V}$$

Moreover, for any electronic property χ of the quantum center, the average at $\boldsymbol{\eta}_b$ is

$$\begin{aligned}\langle \chi_b \rangle_b &= \frac{\int \mathrm{e}^{-\beta(\mathcal{U}'_b + \mathcal{K}_s)} (\det \tilde{M}_b)^{1/2} \chi_b \mathrm{d}\boldsymbol{\xi} \mathrm{d}\mathbf{x}_s \mathrm{d}\mathbf{p}_s}{\int \mathrm{e}^{-\beta(\mathcal{U}'_b + \mathcal{K}_s)} (\det \tilde{M}_b)^{1/2} \mathrm{d}\boldsymbol{\xi} \mathrm{d}\mathbf{x}_s \mathrm{d}\mathbf{p}_s} \\ &= \frac{\langle \mathrm{e}^{-\beta(\mathcal{U}'_{b,} - \mathcal{U}'_{a,})} (\det \tilde{M}_b / \det \tilde{M}_a)^{1/2} \chi_b \rangle_a^0}{\langle \mathrm{e}^{-\beta(\mathcal{U}'_b - \mathcal{U}'_a)} (\det \tilde{M}_b / \det \tilde{M}_a)^{1/2} \rangle_a^0}\end{aligned}$$

with

$$\begin{aligned}&\langle \mathrm{e}^{-\beta(\mathcal{U}'_{b,} - \mathcal{U}'_{a,})} (\det \tilde{M}_b / \det \tilde{M}_a)^{1/2} \chi_b \rangle_a^0 \\ &= \frac{\langle (\det \tilde{M}_b / \det \tilde{M}_{\boldsymbol{\xi},b})^{1/2} \chi_b \rangle_{\boldsymbol{\eta}_b}^0 \langle \mathrm{e}^{-\beta(\mathcal{U}'_b - \mathcal{U}'_a)} (\det \tilde{M}_{\boldsymbol{\xi},b} / \det \tilde{M}_{\boldsymbol{\xi},a})^{1/2} \chi_b \rangle_{\boldsymbol{\eta}_a}^0}{\langle (\det \tilde{M}_a / \det \tilde{M}_{\boldsymbol{\xi},a})^{1/2} \rangle_{\boldsymbol{\eta}_a}^0 \langle \chi_b \rangle_{\boldsymbol{\eta}_b}^0}\end{aligned}$$

On the basis of the previous approximations and using derivations similar to the ones for the free-energy change, we can write

$$\frac{\langle \mathrm{e}^{-\beta(\mathcal{U}'_b - \mathcal{U}'_a)} (\det \tilde{M}_{\boldsymbol{\xi},b} / \det \tilde{M}_{\boldsymbol{\xi},a})^{1/2} \chi_b \rangle_{\boldsymbol{\eta}_a}^0 \cong \langle \chi_b \rangle_{\boldsymbol{\eta}_b}^0 \langle \mathrm{e}^{-\beta\Delta(\epsilon' + q_T \mathcal{V})} (\det \tilde{M}_{\boldsymbol{\xi},b} / \det \tilde{M}_{\boldsymbol{\xi},a})^{1/2} \chi_b \rangle_{\boldsymbol{\eta}_a}^0}{\langle \mathrm{e}^{-\beta(\Delta V_a - \Delta V_b)} \chi_b \rangle_{\boldsymbol{\eta}_b}^0}$$

and hence

$$\langle \chi_b \rangle_b \cong \frac{\mathrm{e}^{\beta \Delta A_{\Delta V}} \langle (\det \tilde{M}_b / \det \tilde{M}_{\boldsymbol{\xi},b})^{1/2} \chi_b \rangle_{\boldsymbol{\eta}_b}^0 \langle \mathrm{e}^{-\beta\Delta(\epsilon' + q_T \mathcal{V})} (\det \tilde{M}_{\boldsymbol{\xi},b} / \det \tilde{M}_{\boldsymbol{\xi},a})^{1/2} \chi_b \rangle_{\boldsymbol{\eta}_a}^0}{\langle (\det \tilde{M}_a / \det \tilde{M}_{\boldsymbol{\xi},a})^{1/2} \rangle_{\boldsymbol{\eta}_a}^0 \langle \mathrm{e}^{-\beta(\Delta V_a - \Delta V_b)} \chi_b \rangle_{\boldsymbol{\eta}_b}^0 \langle \mathrm{e}^{-\beta\Delta(\epsilon' + q_T \mathcal{V})} (\det \tilde{M}_{\boldsymbol{\xi},b} / \det \tilde{M}_{\boldsymbol{\xi},a})^{1/2} \rangle_{\boldsymbol{\eta}_a}^0}$$

The last equation can be simplified by considering that the small $\boldsymbol{\eta}$ transition and the short-range nature of ΔV often make it possible to assume

$$\begin{aligned}&\langle (\det \tilde{M}_b / \det \tilde{M}_{\boldsymbol{\xi},b})^{1/2} \chi_b \rangle_{\boldsymbol{\eta}_b}^0 \cong \langle (\det \tilde{M}_b / \det \tilde{M}_{\boldsymbol{\xi},b})^{1/2} \rangle_{\boldsymbol{\eta}_b}^0 \langle \chi_b \rangle_{\boldsymbol{\eta}_b}^0 \\ &\langle \mathrm{e}^{-\beta(\Delta V_a - \Delta V_b)} \chi_b \rangle_{\boldsymbol{\eta}_b}^0 \cong \langle \mathrm{e}^{-\beta(\Delta V_a - \Delta V_b)} \rangle_{\boldsymbol{\eta}_b}^0 \langle \chi_b \rangle_{\boldsymbol{\eta}_b}^0 = \mathrm{e}^{\beta \Delta A_{\Delta V}} \langle \chi_b \rangle_{\boldsymbol{\eta}_b}^0\end{aligned}$$

readily providing

$$\langle \chi_b \rangle_b \cong \frac{\langle \mathrm{e}^{-\beta\Delta(\epsilon' + q_T \mathcal{V})} (\det \tilde{M}_{\boldsymbol{\xi},b} / \det \tilde{M}_{\boldsymbol{\xi},a})^{1/2} \chi_b \rangle_{\boldsymbol{\eta}_a}^0}{\langle \mathrm{e}^{-\beta\Delta(\epsilon' + q_T \mathcal{V})} (\det \tilde{M}_{\boldsymbol{\xi},b} / \det \tilde{M}_{\boldsymbol{\xi},a})^{1/2} \rangle_{\boldsymbol{\eta}_a}^0} \tag{8-32}$$

For typical solutes where the mass tensor determinant at each $\boldsymbol{\eta}$ position can be considered as essentially independent of the other coordinates, we may then write

$$\begin{aligned}\Delta A \cong & -kT \ln\langle \mathrm{e}^{-\beta\Delta(\varepsilon'+q_T\mathcal{V})}\rangle^0_{\boldsymbol{\eta}_a} - kT \ln\left(\frac{\det \tilde{M}_{\boldsymbol{\xi},b}}{\det \tilde{M}_{\boldsymbol{\xi},a}}\right)^{1/2} \\ & -kT \ln \frac{Q_{v,b}}{Q_{v,a}} + \Delta A_{\Delta V}\end{aligned} \tag{8-33}$$

$$\langle \chi_b\rangle_b \cong \frac{\langle \mathrm{e}^{-\beta\Delta(\varepsilon'+q_T\mathcal{V})}\chi_b\rangle^0_{\boldsymbol{\eta}_a}}{\langle \mathrm{e}^{-\beta\Delta(\varepsilon'+q_T\mathcal{V})}\rangle^0_{\boldsymbol{\eta}_a}} \tag{8-34}$$

It is worth noting that in the free-energy change the terms $-kT \ln\left(\frac{\det \tilde{M}_{\boldsymbol{\xi},b}}{\det \tilde{M}_{\boldsymbol{\xi},a}}\right) - kT \ln \frac{Q_{v,b}}{Q_{v,a}}$ and $\Delta A_{\Delta V}$ are typically small and for usual reactions involving the disruption/formation of a chemical bond, they should be characterized by an opposite sign: The first term is typically negative/positive for a bond disruption/formation as a result of the lower frequencies and larger mass tensor determinant in the QC stretched bond state; the second term is typically positive/negative in a bond disruption/formation reaction as a consequence of the reduced available configurational volume for the environment atoms in the QC stretched bond state. Such a fact may often be used [23,24,25] to further simplify the free-energy change expression by setting $-kT \ln\left(\frac{\det \tilde{M}_{\boldsymbol{\xi},b}}{\det \tilde{M}_{\boldsymbol{\xi},a}}\right) - kT \ln \frac{Q_{v,b}}{Q_{v,a}} + \Delta A_{\Delta V} \cong 0$ which provides

$$\Delta A \cong -kT \ln\langle \mathrm{e}^{-\beta\Delta(\varepsilon'+q_T\mathcal{V})}\rangle^0_{\boldsymbol{\eta}_a} \tag{8-35}$$

Equations 8-34 and 8-35 are more suited for calculations based on simulation data as require a constrained simulation, considering only the vibrational ground state condition, where the energy shift does not include the short-range term which is likely to be not properly sampled in a constrained simulation with a fixed subset of classical coordinates.

Finally, when we deal with a reaction involving a quantum state transition, like in a spin transition reaction, we may easily obtain the reaction free energy for the general $\boldsymbol{\eta}_{\mathrm{ref}} \rightarrow \boldsymbol{\eta}$ transition via a simple generalization of Eq. 8-35:

$$\begin{aligned}\Delta A(\boldsymbol{\eta}) &= -kT \ln\left[\sum_l \mathrm{e}^{-\beta\Delta_l A(\boldsymbol{\eta})}\right] \\ &\cong -kT \ln\left[\sum_l \left\langle \mathrm{e}^{-\beta\Delta_l(\varepsilon'+q_T\mathcal{V})}\right\rangle^0_{\boldsymbol{\eta}_a,l_{\mathrm{ref}}}\right]\end{aligned} \tag{8-36}$$

$$\Delta_l A(\boldsymbol{\eta}) = A_l(\boldsymbol{\eta}) - A_{l_{\mathrm{ref}}}(\boldsymbol{\eta}_{\mathrm{ref}}) \tag{8-37}$$

$$\Delta_l(\varepsilon' + q_T\mathcal{V}) = \varepsilon'_l(\boldsymbol{\eta}) - \varepsilon'_{l_{\mathrm{ref}}}(\boldsymbol{\eta}_{\mathrm{ref}}) + q_T\left[\mathcal{V}(r_0(\boldsymbol{\eta})) - \mathcal{V}(r_0(\boldsymbol{\eta}_{\mathrm{ref}}))\right] \tag{8-38}$$

where the index l runs over all the quantum states involved in the reaction and l_{ref} and η_{ref} are the reference quantum state and reaction coordinates position used to define the reference energy, free-energy and ensemble in the last equations.

Note that the free-energy variation as defined by the previous equations exactly corresponds to the change of the solute chemical potential along the reaction coordinates for a given fixed solute density, i.e., $\Delta A(\boldsymbol{\eta}) = \Delta\mu^{\ominus}(\boldsymbol{\eta})$ with $\mu^{\ominus}$ the solute standard chemical potential.

8.5. MODELING THE REACTION KINETICS

In order to define proper reaction coordinates for describing the kinetics of the chemical process and not only its thermodynamics, we need to use classical degrees of freedom such that all their orthogonal coordinates are well equilibrated during the reaction coordinates relaxation (here we do not consider reactive processes which may relax faster or at a similar rate than the environment as they may typically occur at very high temperature). Hence, it is possible that according to the initial conditions of the kinetic relaxation (i.e., the coordinates/observables equilibrated at the beginning of the process) and the exact definition of the reactant and product states, different reaction coordinates should be used. This also clearly implies that a certain variation of the reaction free-energy profile is possible, as a consequence of the different choice of the reaction coordinates and hence of the orthogonal planes used to obtain the corresponding free-energy. In principle, each set of reaction coordinates, if properly defined, should provide the correct kinetic relaxation for the corresponding process, modeled as a diffusion along the reaction free-energy surface. Note that for a highly diluted solute, including the QC, the reaction free energy is independent of the solute rototranslational coordinates [22] and the solvent, provided an initial equilibrium condition, is expected to relax instantaneously in the ensemble of reactive trajectories at each reaction coordinate position [24].

8.5.1. The Diffusion Equation

Consider, in general, a set of reaction coordinates η providing the kinetic relaxation of the system, i.e., all the other degrees of freedom are assumed to be fully equilibrated along the η relaxation. The equations of motion for the η degrees of freedom when averaging over the ensemble defined by the molecules (typically the solute molecules) within a tiny η volume (equivalent to a numerical differential) can be approximated as

$$\langle \dot{\boldsymbol{\pi}}_{\eta}(\boldsymbol{\eta})\rangle \cong \mathbf{F}(\boldsymbol{\eta}) - \tilde{\Gamma}(t, \boldsymbol{\eta})\langle \boldsymbol{\pi}_{\eta}(\boldsymbol{\eta})\rangle \tag{8-39}$$

$$\langle \boldsymbol{\pi}_{\eta}(\boldsymbol{\eta})\rangle = \tilde{M}_{\eta,\eta}(\boldsymbol{\eta})\langle \dot{\boldsymbol{\eta}}(\boldsymbol{\eta})\rangle \tag{8-40}$$

where $\boldsymbol{\pi}_{\eta}$ are the $\boldsymbol{\eta}$ conjugated momenta; $\mathbf{F}$ is the systematic, i.e., equivalent to an external field, force in the $\boldsymbol{\eta}$ space; and $\tilde{\Gamma}$ and $\tilde{M}_{\eta,\eta}$ are the friction matrix and (classical) mass tensor block corresponding to the $\boldsymbol{\eta}$ coordinates. We assumed a virtually fixed mass tensor for a given $\boldsymbol{\eta}$ position and hence $\tilde{M}_{\eta,\eta}$ provides the only non-zero terms of $\boldsymbol{\pi}_{\eta}$ after averaging, as the other degrees of freedom are considered as fully

equilibrated with hence zero mean velocities. Within the approximation given by the previous equations, the work due to the systematic force only should coincide with the maximum work along the transition, i.e., the work obtained for a reversible transition with then $\langle \dot{\boldsymbol{\eta}} \rangle = 0$. Hence, for a molecule passing from a tiny volume centered at $\boldsymbol{\eta}_a$ to another one centered at $\boldsymbol{\eta}_b$ we can write

$$\begin{aligned} \Delta A(\mathbf{n}) &= \left(\frac{\partial A}{\partial n_{\boldsymbol{\eta}_b}}\right) + \left(\frac{\partial A}{\partial n_{\boldsymbol{\eta}_a}}\right)\left(\frac{\partial n_{\boldsymbol{\eta}_a}}{\partial n_{\boldsymbol{\eta}_b}}\right) \\ &= \mu(n_{\boldsymbol{\eta}_b,\boldsymbol{\eta}_b)} - \mu(n_{\boldsymbol{\eta}_a,\boldsymbol{\eta}_a)} = -\int_{\boldsymbol{\eta}_a}^{\boldsymbol{\eta}_b} F(\boldsymbol{\eta}) \cdot \mathrm{d}\boldsymbol{\eta} \end{aligned} \tag{8-41}$$

providing

$$\mathbf{F}(\boldsymbol{\eta}) = -\nabla_{\boldsymbol{\eta}} \mu(n_{\boldsymbol{\eta}}, \boldsymbol{\eta}) \tag{8-42}$$

In the last equations $A(\mathbf{n})$ is the Helmholtz free energy of the total NVT system fully defined by the vector $\mathbf{n} = n_{\boldsymbol{\eta}_1}, n_{\boldsymbol{\eta}_2}, \ldots$ providing the molecular number in each tiny volume and $\mu(n_{\boldsymbol{\eta}}, \boldsymbol{\eta})$ is the chemical potential at a given $\boldsymbol{\eta}$ position, i.e., within the corresponding tiny volume. Note that the molecular number can be used as a continuous variable, given the fact that for any thermodynamic property in a macroscopic system the variation due to a single molecule is virtually equivalent to a differential. From the definition of the chemical potential and probability density in the $\boldsymbol{\eta}$ space $\rho(t, \boldsymbol{\eta})$, we readily have

$$\mu(n_{\boldsymbol{\eta}}, \boldsymbol{\eta}) = \Delta\mu^o(\boldsymbol{\eta}) + kT \ln \frac{n_{\boldsymbol{\eta}}}{n_{\boldsymbol{\eta}_R}} + \mu(n_{\boldsymbol{\eta}_R}, \boldsymbol{\eta}_R) \tag{8-43}$$

$$= \Delta\mu^o(\boldsymbol{\eta}) + kT \ln \frac{\rho(t, \boldsymbol{\eta})}{\rho(t, \boldsymbol{\eta}_R)} + \mu(n_{\boldsymbol{\eta}_R}, \boldsymbol{\eta}_R) \tag{8-44}$$

which used together with $\langle \dot{\boldsymbol{\pi}}_\eta \rangle \cong 0$ (the linear regime condition) provides

$$\langle \dot{\boldsymbol{\eta}}(\boldsymbol{\eta}) \rangle \cong -\left[\tilde{\Gamma}(t, \boldsymbol{\eta}) \tilde{M}_{\eta,\eta}(\boldsymbol{\eta})\right]^{-1} \nabla_{\boldsymbol{\eta}} \Delta\mu^{\ominus}(\boldsymbol{\eta}) - \left[\tilde{\Gamma}(t, \boldsymbol{\eta}) \tilde{M}_{\eta,\eta}(\boldsymbol{\eta})\right]^{-1} kT \frac{\nabla_{\boldsymbol{\eta}} \rho(t, \boldsymbol{\eta})}{\rho(t, \boldsymbol{\eta})} \tag{8-45}$$

Hence from the definition of the flux density vector $\mathbf{J}(\boldsymbol{\eta}) = \rho(t, \boldsymbol{\eta}) \langle \dot{\boldsymbol{\eta}}(\boldsymbol{\eta}) \rangle$ and setting

$$\tilde{D}(t, \boldsymbol{\eta}) = kT \left[\tilde{\Gamma}(t, \boldsymbol{\eta}) \tilde{M}_{\eta}(\boldsymbol{\eta})\right]^{-1} \tag{8-46}$$

we obtain, via the divergence theorem,

$$\left(\frac{\partial \rho}{\partial t}\right)_{\boldsymbol{\eta}} = -\nabla_{\boldsymbol{\eta}} \cdot \mathbf{J} \cong \nabla_{\boldsymbol{\eta}} \cdot \left[\tilde{D}(kT)^{-1} \rho \nabla_{\boldsymbol{\eta}} \Delta\mu^o + \tilde{D} \nabla_{\boldsymbol{\eta}} \rho\right] \tag{8-47}$$

This last equation, when considering a one-dimensional $\boldsymbol{\eta}$ space with then $\tilde{D} = D$, provides the diffusion equation used in this chapter within the assumption $\partial D/\partial t, \partial D/\partial \eta \cong 0$. For the sake of simplicity and without loss of generality, hereon we will always consider a single reaction coordinate to describe the chemical transition.

8.5.2. Evaluation of the Reaction Rate Constants

Using the reaction free-energy profile, $\Delta A(\eta) = \Delta\mu^{\ominus}(\eta)$, and the diffusion coefficient D of the reaction coordinate (if available), it is possible to obtain the reaction (classical) kinetics by solving a diffusion equation (DE) in the reaction coordinate space [33]

$$\left(\frac{\partial\rho}{\partial t}\right)_{\eta} = \frac{D}{kT}\left[\rho\frac{\mathrm{d}^2\Delta\mu^{\ominus}}{\mathrm{d}\eta^2} + \frac{\mathrm{d}\Delta\mu^{\ominus}}{\mathrm{d}\eta}\left(\frac{\partial\rho}{\partial\eta}\right)_t\right] + D\left(\frac{\partial^2\rho}{\partial(\eta)^2}\right)_t \tag{8-48}$$

where $\rho(t, \eta)$ is the probability density in η and we assumed $\partial D/\partial t, \partial D/\partial\eta \cong 0$.

The time–space behavior of ρ can provide in principle all the kinetic/thermodynamic information on the chemical reaction. Therefore, in order to schematize the kinetic process, we may define three chemical states: the transition state (TS) defined by a tiny interval $[\eta_{\mathrm{TS}} - \delta, \eta_{\mathrm{TS}} + \delta]$ (typically about 0.1 Å centered on the reaction free-energy maximum η_{TS}, the reactant (R) defined by one of the η range neighbor to the TS (here the right one) and the product (P) defined by the other neighbor η range (here the left one). Hence, within such a scheme the complete reaction can be described by the time dependence of these three chemical state probabilities, as obtained by

$$P_{\mathrm{TS}}(t) = \int_{\eta_{\mathrm{TS}}-\delta}^{\eta_{\mathrm{TS}}+\delta} \rho(t, \eta)\mathrm{d}\eta \tag{8-49}$$

$$P_{\mathrm{R}}(t) = \int_{\eta_{\mathrm{TS}}+\delta}^{\eta_{\mathrm{U}}} \rho(t, \eta)\mathrm{d}\eta \tag{8-50}$$

$$P_{\mathrm{P}}(t) = \int_{\eta_{\mathrm{L}}}^{\eta_{\mathrm{TS}}-\delta} \rho(t, \eta)\mathrm{d}\eta \tag{8-51}$$

where $\eta_{\mathrm{L}}, \eta_{\mathrm{U}}$ are the lower and upper limits of the reaction coordinate range used to define the complete reaction. Note that as the η range is finite $\Delta\mu^{\ominus}$ used in the diffusion equation must provide two infinite free-energy barriers at the extremes of such a range. These infinite barriers do not correspond in general to physical free-energy barriers, they are used simply to restrict the reaction kinetics to the chemical step of interest. Once we obtain $P_{\mathrm{TS}}(t)$, $P_{\mathrm{R}}(t)$, $P_{\mathrm{P}}(t)$ by the DE solution, we may construct a kinetic model via the following procedure. Consider the general reaction scheme for the three chemical states R, P and TS

$$\mathrm{R} \overset{k_1}{\rightarrow} \mathrm{TS} \overset{k_{-2}}{\rightarrow} \mathrm{P} \tag{8-52}$$

$$\mathrm{P} \overset{k_2}{\rightarrow} \mathrm{TS} \overset{k_{-1}}{\rightarrow} \mathrm{R} \tag{8-53}$$

and the stationary condition

$$\dot{P}_{\mathrm{TS}} = k_1 P_{\mathrm{R}} - k_{-1} P_{\mathrm{TS}} + k_2 P_{\mathrm{P}} - k_{-2} P_{\mathrm{TS}} \cong 0 \tag{8-54}$$

$$P_{\mathrm{TS}} \cong \frac{k_1 P_{\mathrm{R}} + k_2 P_{\mathrm{P}}}{k_{-1} + k_{-2}} \tag{8-55}$$

valid for $t \geq t_0$ (t_0 is the time interval required to achieve the steady state), providing

$$\dot{P}_{\mathrm{R}} \cong -K_{\mathrm{R}} P_{\mathrm{R}} + K_{\mathrm{P}} P_{\mathrm{P}} \tag{8-56}$$

$$\dot{P}_{\mathrm{P}} \cong K_{\mathrm{R}} P_{\mathrm{R}} - K_{\mathrm{P}} P_{\mathrm{P}} \tag{8-57}$$

$$K_{\mathrm{R}} = \frac{k_{-2} k_1}{k_{-1} + k_{-2}} \tag{8-58}$$

$$K_{\mathrm{P}} = \frac{k_{-1} k_2}{k_{-1} + k_{-2}} \tag{8-59}$$

where K_{R} and K_{P} can be considered as the rate constants for the R $\rightarrow$ P and P $\rightarrow$ R transitions, respectively.

From the obvious relation $1 = P_{\mathrm{R}}(t) + P_{\mathrm{P}}(t) + P_{\mathrm{TS}}(t)$, we have $P_{\mathrm{P}}(t) = 1 - P_{\mathrm{R}}(t) - P_{\mathrm{TS}}(t)$ and hence $\forall\, t \geq t_0$:

$$P_{\mathrm{TS}}(t) \cong \frac{(k_1 - k_2) P_{\mathrm{R}} + k_2}{k_{-1} + k_{-2} + k_2} \tag{8-60}$$

$$\dot{P}_{\mathrm{R}} \cong -K P_{\mathrm{R}} + K' \tag{8-61}$$

$$K = \frac{k_1 k_{-2} + k_1 k_2 + k_2 k_{-1}}{k_{-1} + k_{-2} + k_2} \tag{8-62}$$

$$K' = \frac{k_2 k_{-1}}{k_{-1} + k_{-2} + k_2} \tag{8-63}$$

The general solution of the previous ordinary linear differential equation is, in the time range $t \geq t_0$,

$$\begin{aligned} P_{\mathrm{R}}(t) &\cong P_{\mathrm{R}}(\infty) + [P_{\mathrm{R}}(t_0) - P_{\mathrm{R}}(\infty)]\ \mathrm{e}^{-K(t-t_0)} \\ P_{\mathrm{R}}(\infty) &= \frac{K'}{K} = \frac{k_2 k_{-1}}{k_1 k_{-2} + k_1 k_2 + k_2 k_{-1}} \end{aligned} \tag{8-64}$$

From the last expressions we readily obtain (using again $P_{\mathrm{P}}(t) = 1 - P_{\mathrm{R}}(t) - P_{\mathrm{TS}}(t)$ and the stationary condition)

$$\begin{aligned} P_{\mathrm{P}}(t) &\cong P_{\mathrm{P}}(\infty) - \frac{k_{-1} + k_{-2} + k_1}{k_{-1} + k_{-2} + k_2} [P_{\mathrm{R}}(t_0) - P_{\mathrm{R}}(\infty)]\ \mathrm{e}^{-K(t-t_0)} \\ P_{\mathrm{P}}(\infty) &= \frac{k_{-1} + k_{-2} - (k_{-1} + k_{-2} + k_1) P_{\mathrm{R}}(\infty)}{k_{-1} + k_{-2} + k_2} = \frac{k_1 k_{-2}}{k_1 k_{-2} + k_1 k_2 + k_2 k_{-1}} \end{aligned} \tag{8-65}$$

$$P_{\mathrm{TS}}(t) \cong P_{\mathrm{TS}}(\infty) + \frac{k_1 - k_2}{k_{-1} + k_{-2} + k_2} \left[P_{\mathrm{R}}(t_0) - P_{\mathrm{R}}(\infty)\right] \, \mathrm{e}^{-K(t-t_0)}$$

$$P_{\mathrm{TS}}(\infty) = \frac{(k_1 - k_2)P_{\mathrm{R}}(\infty) + k_2}{k_{-1} + k_{-2} + k_2} = \frac{k_1 k_2}{k_1 k_{-2} + k_1 k_2 + k_2 k_{-1}} \tag{8-66}$$

It is also instructive to consider two special cases of this general model. If we deal with a reaction where $k_2 \cong 0$ then we have $K \cong K_{\mathrm{R}} = k_1 k_{-2}/(k_{-1} + k_{-2})$ and

$$\frac{P_{\mathrm{TS}}}{P_{\mathrm{R}}} \cong \frac{k_1}{k_{-1} + k_{-2}} \tag{8-67}$$

corresponding to a simple steady state for the R $\rightarrow$ P reaction alone. This case is typical in systems where the free energy of the product is much lower than the reactant one or the product is instantaneously removed in some way (e.g., in enzymatic reactions). When $k_2, k_{-2} \cong 0$ we obtain a further condition with $K \cong k_1 k_{-2}/k_{-1}$ and $P_{\mathrm{TS}}/P_{\mathrm{R}} \cong k_1/k_{-1}$ which clearly corresponds to a pre-equilibrium between the R and TS species, as required by the Eyring theory. However, this last case is rather unusual as k_{-2} is typically larger than or of the same order of k_{-1} when $k_1 \gg k_2$, and hence Eyring theory should not be used as a general model to describe chemical reactions.

8.6. APPLICATIONS

In the present section some applications of the previously outlined theoretical framework, recently reported in literature [24,25], will be illustrated. In particular we will focus our attention on two benchmark reactions of computational–theoretical chemistry, namely the carbon monoxide (CO) binding–unbinding reaction in myoglobin (Mb) and the unimolecular tautomeric proton transfer in aqueous malonaldehyde.

8.6.1. Binding–Unbinding Reaction of CO in Myoglobin

CO–Mb reaction, extensively studied in the last decades under a variety of experimental techniques [34,35,36,37,38,39,40], is characterized by CO diffusion within Mb leading to a heme–CO geminate pair eventually interconverting to the heme–CO covalent complex. This last step has become the most investigated biochemical process by means of computational–theoretical methods [41,42,43,44,45,46,47] and has been selected as a good test for appreciating the performances of the present methodology.

First we selected, as QC, the CO–heme–histidine complex shown in Figure 8-1 with a schematic view of the Mb.

Configuration interaction calculations including single and double excitations (CISD) were carried out on the QC using as reference state (reference Slater determinant) the one obtained by the previous B3LYP/BS ground state evaluation and

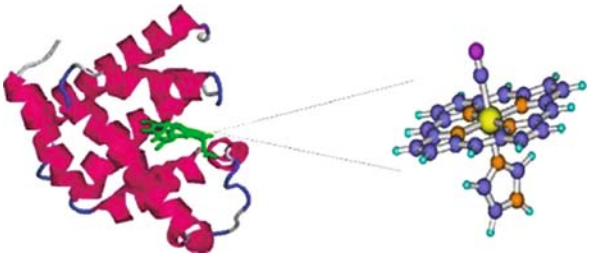

Figure 8-1. Quantum center used in our PMM calculation (reaction center), defined by the heme–CO complex and including the proximal histidine side chain. The figure refers to the reference QC condition, i.e., with the heme–CO distance at 1.8 Å

using the 6-311++G(p,d) atomic basis set (BS) for the four nitrogens and CO, 6-31G BS for the remaining atoms and effective core potential from Los Alamos for iron.

The above calculations provided the electronic ground and the first nine excited energies as well as the corresponding (transition) dipoles, at each point of the above reaction path. Such unperturbed Hamiltonian eigenstates defined the basis set used to construct the perturbed Hamiltonian matrix, Eq. 8-1, which was then diagonalized at each simulation frame, leading to the reaction free energy and related properties.

At this purpose N,V,T MD simulations of 10 ns each, were performed at 300 and 293 K, constraining Mb–CO in the center of the simulation box, filled with water molecules, at the proper liquid density. The rototranslational constraint [27] was used to keep the Mb–CO rototranslationally fixed at the center of the simulation box.

In Figure 8-2 we show the reaction free energy for the singlet and quintet surfaces as obtained by PMM and MD simulations as described in the previous sections.

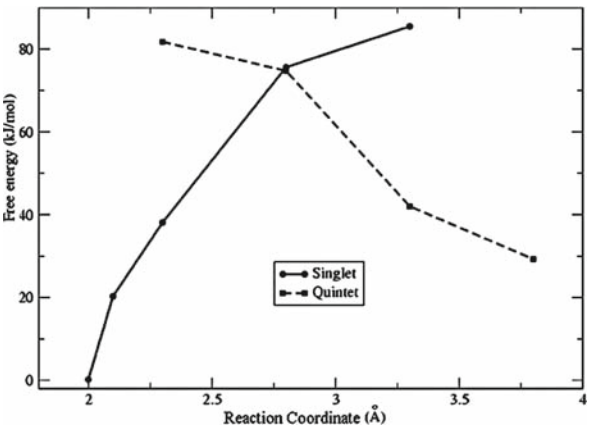

Figure 8-2. Singlet and quintet reaction free-energy surfaces, as obtained by PMM using the 293 K MD simulation

Similar to the results for the isolated QC [43], the transition state of the reaction in Mb is determined by the singlet–quintet free-energy surface crossing. The triplet surface is, in our calculations, thermodynamically too unstable to affect the reaction and, therefore, we omitted such a surface in our calculations. Interestingly, the perturbed QC free-energy absolute minimum, at about 2.0 Å, is slightly shifted from the unperturbed one (our reference condition) indicating a corresponding slight variation of the Fe–CO equilibrium distance.

From Table 8-1 it is evident that the protein provides a "catalytic" effect lowering the barriers by about 10 kJ/mol with respect to the unperturbed condition. Moreover, the free-energy barriers at the two temperatures are, within the noise, almost identical suggesting low activation entropies.

Using the reaction free energy we are now in the position of calculating the reaction (classical) kinetics by means of the equations outlined in Section 5.2. In particular, for solving DE using Eq. 8-49, it is first necessary to evaluate the related diffusion coefficient D of the reaction coordinate.

For this purpose we performed short (110 ps) MD trajectories at constant energy (i.e., with no temperature coupling) of the overall system, utilizing unconstrained bond lengths and a reduced time step of 0.1 fs. By using a large number of (constant energy) trajectory subparts, starting close to the carbon–iron equilibrium distance, we evaluated the reaction coordinate diffusion coefficient via the corresponding computed carbon–iron distance mean square displacement in time. The obtained value of D equal to 4.2×10^{-3} nm^2/ps was then utilized to solve (numerically) the DE. For addressing the DE we modeled $\Delta\mu^{\ominus}(\eta)$ as a simple polynomial function reproducing the PMM/MD free-energy barriers and the positions of minima and transition state. Moreover we considered that, for the system and time interval considered, $P_{\mathrm{R}}(t) - P_{\mathrm{R}}(\infty) \cong P_{\mathrm{R}}(t)$, $P_{\mathrm{TS}}(t) - P_{\mathrm{TS}}(\infty) \cong P_{\mathrm{TS}}(t)$ (i.e., $P_{\mathrm{R}}(\infty)$, $P_{\mathrm{TS}}(\infty)$ are negligible).

The result is reported in Figure 8-3 where we show the time dependence of the reactant (the geminate complex) and transition state probabilities.

The result demonstrates that the steady-state model described in the theory section is very accurate to provide the kinetics of the reaction in terms of a simple reactant–TS–product scheme, as typically used to interpret experimental data. By using such time courses as well as the reactant to TS ($\Delta A_{\mathrm{R}}^{\ddagger} = A_{\mathrm{TS}} - A_{\mathrm{R}}$) and product to TS ($\Delta A_{\mathrm{P}}^{\ddagger} = A_{\mathrm{TS}} - A_{\mathrm{P}}$) free-energy differences

Table 8-1. Free-energy barriers as obtained by different MD/PMM conditions as well as from in vacuo calculations. The noise shown corresponds to a standard deviation

Ensemble	Binding barrier (kJ/mol)	Unbinding barrier (kJ/mol)
MD/PMM 300 K	43.8 ± 0.6	74.1 ± 0.9
MD/PMM 293 K	41.9 ± 0.6	74.2 ± 0.9
MD/PMM 300 K	41.4 ± 0.4	76.3 ± 0.7
DFT vacuum	47.6	87.6

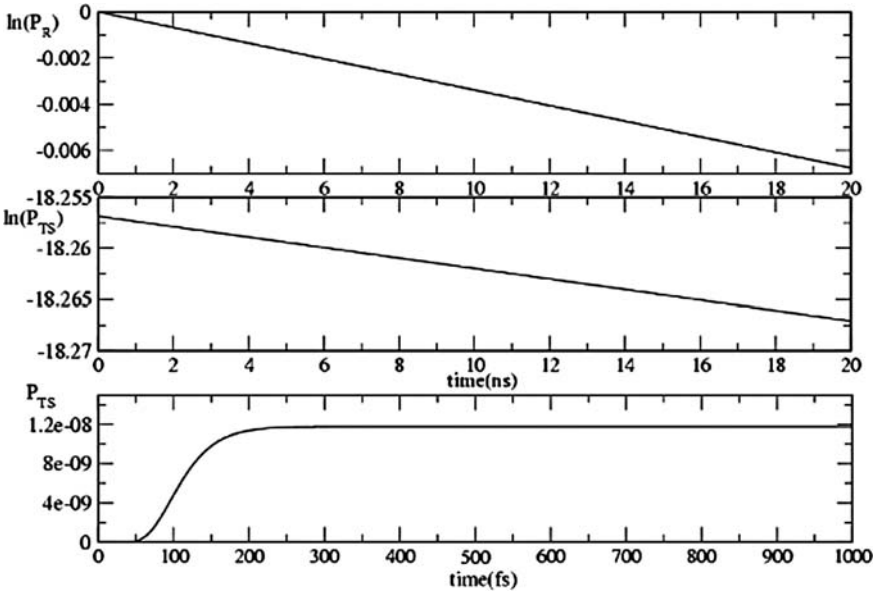

Figure 8-3. Kinetics of the reactant (the geminate complex), *upper panel*, and transition, *middle* and *lower panels*, states as obtained by the DE solution for the system at 293 K

$$\Delta A_{\mathrm{R}}^{\ddagger} = -kT \ln \frac{P_{\mathrm{TS}}(\infty)}{P_{\mathrm{R}}(\infty)} = -kT \ln \frac{\int_{\eta_{\mathrm{TS}}-\delta}^{\eta_{\mathrm{TS}}+\delta} \mathrm{e}^{-\beta \Delta A(\eta)} \mathrm{d}\eta}{\int_{\eta_{\mathrm{TS}}+\delta}^{\eta_{\mathrm{U}}} \mathrm{e}^{-\beta \Delta A(\eta)} \mathrm{d}\eta}$$

$$\Delta A_{\mathrm{P}}^{\ddagger} = -kT \ln \frac{P_{\mathrm{TS}}(\infty)}{P_{\mathrm{P}}(\infty)} = -kT \ln \frac{\int_{\eta_{\mathrm{TS}}-\delta}^{\eta_{\mathrm{TS}}+\delta} \mathrm{e}^{-\beta \Delta A(\eta)} \mathrm{d}\eta}{\int_{\eta_{\mathrm{L}}}^{\eta_{\mathrm{TS}}-\delta} \mathrm{e}^{-\beta \Delta A(\eta)} \mathrm{d}\eta}$$

it is possible to obtain all the kinetic rate constants involved in the reaction step studied. In fact, from the overall rate constant $K = 10.2 \times 10^{-7}$ ps^{-1}, evaluated by the slope of the logarithmic reactant decay (top of Figure 8-3), the TS probability at the beginning of the stationary condition (starting after 200–300 fs) and the relations $k_{-1} = k_1 \, \mathrm{e}^{\beta \Delta A_{\mathrm{R}}^{\ddagger}}$, $k_{-2} = k_2 \, \mathrm{e}^{\beta \Delta A_{\mathrm{P}}^{\ddagger}}$, we obtain the four rate constants for the reactant–TS–product interconversion which then provide for the reactant to product and inverse rate constants $K_{\mathrm{R}} = 3.4 \times 10^{-7}$ ps^{-1}, $K_{\mathrm{P}} = 9.2 \times 10^{-13}$ ps^{-1} corresponding to about 3 μs and 1 s, respectively. Note that from our calculations $K_{\mathrm{R}} \cong K$, as expected by the large free-energy difference between the reactant and product states, and a rough estimate of the error of the K_{R} and K_{P} rate constants, essentially due to the noise in the free-energy barriers, provides a maximal possible excursion (evaluated using $\pm$ 4 standard deviations of the free-energy barrier) corresponding to $0.7 - 12.0$ μs and $0.3 - 3.0$ s, respectively. Such results can be compared to the experimental

data at 293 K [48,49], considering that the R $\rightarrow$ P and the P $\rightarrow$ R transitions are reaction steps involved in either the geminate binding kinetics (obtained after photolization of the heme–CO covalent complex) or the thermal heme–CO dissociation. Interestingly the experimental rate constant for the dissociation process is equal to 1.9×10^{-14} ps^{-1}, reasonably close, within the noise, to our K_P value (note that only 9–10 kJ/mol variation in the unbinding barrier would account for the $\simeq$ 50 times variation of K_P with respect to the experimental overall dissociation constant). This suggests that in the heme–CO thermal dissociation the P $\rightarrow$ R transition (i.e., the Heme–CO chemical bond disruption) is probably the rate-limiting step of the whole kinetic process and no slow conformational transitions [40,50] seem to be involved. In fact the supposed distal histidine opening–closing side chain transition, often considered as the slow conformational change involved in the reaction, results from MD simulation data [51] as largely equilibrated within a few nanoseconds. Note that for the geminate binding, with an experimental rate constant of 5.6×10^{-6} ps^{-1} close to our K_R, no simple comparison is possible because of the complex non-sequential reaction scheme involved.

8.6.2. Intramolecular Proton Transfer in Aqueous Malonaldehyde

Tautomeric equilibrium in aqueous *cis*-malonaldehyde, see reaction 1 in Figure 8-4, is a prototypical reaction extensively studied in the gas phase but still relatively unknown in solution. In fact, despite the large number of NMR experiments [52,53,54] and quantum chemical calculations [55] with the polarized continuum model (PCM), [1] the actual stability of *cis*-malonaldehyde is not well clarified, although the *trans* isomer should be the predominant form in water. Secondly, the involvement of the light proton in the reaction may in principle provide relevant quantum effects even in condensed phase. All these complications did not prevent this reaction to be used as a prototypical system for theoretical studies of intramolecular proton transfer in condensed phase by several investigators [56,57,58,59,60] including ourselves.

Differently from the previous case (CO–Mb), the reaction path associated to such a tautomeric process may be less intuitive. For this reason we calculated the intrinsic reaction coordinate (IRC) [61] in vacuum which provided a linear generalized degree

Figure 8-4. Schematic picture of tautomeric intramolecular proton transfer in malonaldehyde

of freedom (i.e., defined by a single unit vector in configurational space) [24]. This coordinate, essentially involving the migrating proton, was selected as the proper reaction coordinate in condensed phase also.

At this purpose we spanned reaction 1 unperturbed IRC using the CCSD(T)/6-311++G(p,d)//B3LYP/6-311++G(p,d) level of theory.

In correspondence to each point of the IRC grid, i.e., the QC structures along the reaction coordinate, ten states (i.e., the ground plus nine excited states) were optimized for the unperturbed QC, using time-dependent density functional theory shifts added to the CCSD(T) ground state energies. Such unperturbed Hamiltonian eigenstates defined the basis set used to construct the perturbed Hamiltonian matrix, Eq. 8-1, which was then diagonalized at each simulation frame, leading to the reaction free-energy and related properties.

In this respect, MD simulations (3,000,000 of steps) were performed over a wide temperature range (280–1200 K), constraining the Malonaldehyde in the reactant configuration in the center of the simulation box, filled with water molecules, at the proper liquid density.

In Figure 8-5 we report the perturbed free-energy surface, as obtained by PMM and the MD simulation at 300 K, together with the CCSD(T) vacuum free-energy profile and the 300 K reaction free energy as obtained by PCM using the same procedure and level of quantum chemical calculations (i.e., adding the PCM/B3LYP free-energy shifts to the CCSD(T) curve). It is evident from PMM results that solvent provides a free-energy barrier (activation free-energy) of about 2 kJ/mol lower than the vacuum one. PCM reaction free-energy profile, although showing a similar shape to the PMM curve, presents a free-energy barrier slightly higher than the vacuum one and predicts a local minimum in correspondence of the vacuum transition structure. Such an unphysical condition is probably due to the macroscopic

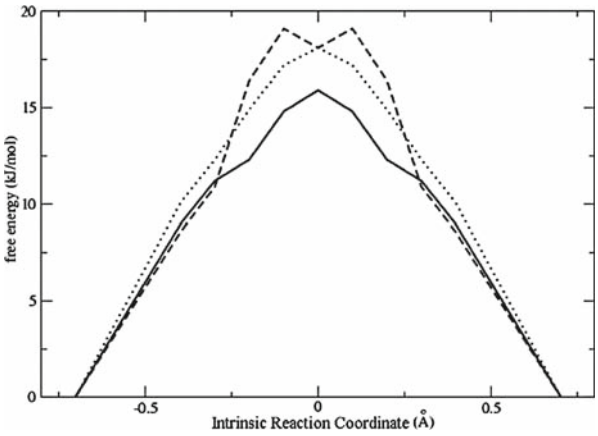

Figure 8-5. Reaction free-energy surfaces as provided by PMM and the MD simulation at 300 K (*solid line*), CCSD(T) (vacuum) calculations (*dotted line*) and 300 K PCM calculations (*dashed line*)

dielectric polarization used in PCM to model solute–solvent interaction, which may be rather unrealistic Similar to CO–Mb reaction, using the above results within the same theoretical–computational framework, we evaluated the kinetics of such a reaction within the classical view of the diffusion along the reaction free-energy surface. Using a value of $D = 4.1 \times 10^{-3} \pm 10^{-4}$ nm^2/ps for the diffusion coefficient, provided by a set of short constant energy MD simulations, we could obtain the detailed time course of the proton transfer reaction from the reactant to the product state.

In Figure 8-6 we show the time courses of R, P and TS probabilities as obtained by the DE solution. R and P probabilities converge to their equilibrium values within 120–150 ps, clearly indicating a rather fast kinetics. From the figure it is also clear that the TS reaches a stationary condition within $t_0 = 300$ fs, providing in the following time range a completely symmetric reactant and product kinetics (i.e., identical relaxation rates and final equilibrium values), as expected by the free-energy symmetric shape. Interestingly, the R and P relaxations, when subtracted of the equilibrium value, are perfectly exponential (beyond t_0) for virtually the complete reaction time course with a rate constant $K = 0.038 \pm 0.001$ ps^{-1} corresponding to the mean life $\tau \cong 26$ ps (the noise indicated is the error upper limit). Remarkably, the obtained rate constant well matches the experimentally observed kinetics of this reaction in solution [62,63] (picoseconds range in $CFCl_3/CD_2Cl_2$) and suggests that tunneling might not be relevant in liquid-phase conditions, as also indicated by the theoretical–computational estimate of the tunneling rate in liquid water [60] (nanoseconds range). Our results, obtained in condensed phase, are also in agreement with the data obtained in a previous computational attempt to investigate malonaldehyde proton transfer in vacuum [59], leading to similar conclusions for the gas-phase reaction.

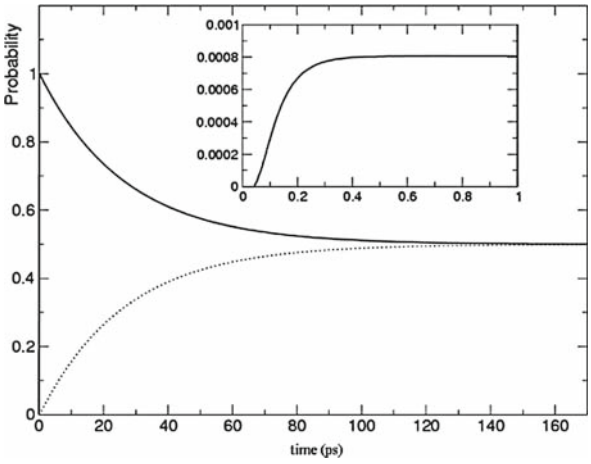

Figure 8-6. Time course of the reactant (*solid line*), product (*dotted line*) and transition state (*inset*) probabilities as obtained by solving the diffusion equation

REFERENCES

1. Tomasi J, Persico M (1994) Chem Rev 94:2027
2. Tongraar A, Liedl KR, Rode BM (1997) J Phys Chem A 101 6299–6309
3. Cramer CJ, Truhlar DG (1999) Chem Rev 99:2161–2200
4. D'Abramo M, Aschi M, Marinelli F, Di Nola A, Amadei A (2007) J Mol Struct THEOCHEM 811:197–201
5. Matyushov DV (2007) Acc Chem Res 40:294–301
6. Pu J, Gao J, Truhlar DG (2006) Chem Rev 106:3140–3169
7. Gao J (1996) Acc Chem Res 29:298–305
8. Friesner R, Beachy MD (1998) Curr Opin Struct Biol 8:257–262
9. Schwartz SD (ed) (2000) Theoretical methods in condensed phase chemistry, Springer, Dordrecht
10. Yamazaki S, Kato S (2005) J Chem Phys 123:114510
11. Losa AM, Martn ME, Galvn IF, Aguilar MA (2007) Chem Phys Lett 443:76–81
12. Lima MCP, Coutinho K, Canuto S, Rocha WR (2006) J Phys Chem A 110:7253–7261
13. Watney JB, Soudackov AV, Wong KF, Hammes-Schiffer S (2006) Chem Phys Lett 418:268–271
14. Derat E, Cohen S, Shaik S, Altun A, Thiel W (2005) J Am Chem Soc 127:13611–13621
15. Rivail JL, Rinaldi D, Ruiz-Lopez MF (1991) In: Formosinho SJ, Arnaut L, Csizmadia I (eds) Theoretical and computational models of organic chemistry, Kluwer, Dordrecht
16. Jug K, Klle C, Neumann F (1999) J Comp Chem 20:301–304
17. Bash PA, Field MJ, Karplus M (1987) J Am Chem Soc 109:8092
18. Liu H, Muller-Plathe F, van Gunsteren WF (1995) J Chem Phys 102:1722
19. Strajbl M, Sham YY, Vill J, Chu ZT, Warshel A (2000) J Phys Chem B 104:4578–4584
20. Aschi M, Spezia R, Di Nola A, Amadei A (2001) Chem Phys Lett 344:374–380
21. Spezia R, Aschi M, Di Nola A, Amadei A (2002) Chem Phys Lett 365:450–456
22. Amadei A, D'Alessandro M, Aschi M (2004) J Phys Chem B 118:16250–16254
23. Amadei A, D'Alessandro M, Paci M, Di Nola A, Aschi M (2006) J Phys Chem B 110:7538–7544
24. Aschi M, D'Abramo M, Ramondo F, Daidone I, D'Alessandro M, Di Nola A, Amadei A (2006) J Phys Org Chem 19:518
25. Amadei A, D'Abramo M, Daidone I, D'Alessandro M, Di Nola A, Aschi M (2007) Theor Chem Acc 117:637–647
26. Amadei A, D'Abramo M, Zazza C, Aschi M (2003) Chem Phys Lett 381:187–193
27. Amadei A, Chillemi G, Ceruso MA, Grottesi A, Di Nola A (2000) J Chem Phys 112:9–23
28. Amadei A, Apol MEF, Brancato G, Di Nola A (2002) J Chem Phys 116:4437–4449
29. Landau LD, Lifshitz EM (1980) Statistical physics. Part 1, 3rd (edn). Pergamon press, Oxford
30. Amadei A, Apol MEF, Berendsen HJC (1998) J Chem Phys, 109:3004–3016
31. Amadei A, Apol MEF, Berendsen HJC (1997) J Chem Phys 106:1893–1912
32. Fixman M (1974) Proc Nat Acad Sci USA 69:1527
33. Mc Quarrie DA (1976) Statistical mechanics, Harper Collins Publishers, New York
34. Austin RH, Beeson KW, Eisenstein L, Frauenfelder H, Gunsalus IC (1975) Biochemistry 14:5355
35. Steinbach PJ, Ansari A, Berendzen J, Braunstein D, Chu K, Cowen BR, Ehrenstein D, Frauenfelder H, Johnson JB, Lamb DC, Luck S, Mourant GU, Nienhaus GU, Ormos P, Philipp R, Xie AH, Young RD (1991) Biochemistry 30:3988
36. Srajer V, Ren Z, Teng TY, Schmidt M, Ursby T, Bourgeois D, Pradervand C, Schildkamp W, Wulff M, Moffat K (2001) Biochemistry 40:13802
37. Bourgeois D, Vallone B, Scotte F, Arcovito A, Miele AE, Sciara G, Wulff M, Anfinrud P, Brunori M (2003) Proc Natl Acad Sci USA 100:8704

38. Sottini S, Abbruzzetti S, Viappiani C, Ronda L, Mozzarelli A (2005) J Phys Chem B 109: 19523–19528
39. Chen E, Goildberg RA, Kliger DS (1997) Annu Rev Biophys Biomol Struct 26:327
40. Angeloni L, Feis A (2003) Photochem Photobiol Sci 2:730–740
41. McMahon BH, Stojkovic BP, Hay PJ, Martin RL, Garcia AE (2000) J Chem Phys 113:6831
42. Franzen SJ (2002) Phys Chem B 106:4533
43. Harvey JN (2000) J Am Chem Soc 122:12401
44. Harvey JN (2004) Faraday Discuss 127:156
45. Sigfridsson E, Ryde UJ (2002) Inorg Biochem 91:101
46. De Angelis F, Jarzecki AA, Car R, Spiro TG (2005) J Phys Chem B 109:3065
47. Rovira C, Schultze B, Eichinger M, Evanseck JD, Parrinello M (2001) Biophys J 81:435
48. Springer BA, Sligar SG, Olson SJ, Phillips JN Jr (1994) Chem Rev 94:699–714
49. Olson SJ, Phillips JN Jr (1996) J Biol Chem 271:17593–17596
50. Kleinert T, Doster W, Leyser H, Petry W, Schwarz W, Settles M (1998) Biochemistry 37:717–733
51. Bossa C, Anselmi M, Roccatano D, Amadei A, Vallone B, Brunori M, Di Nola A (2004) Biophys J 86:3855–3862
52. Bothner-By A, Harris RK (1965) J Org Chem 30:254
53. George WO, Mansell VG (1968) J Chem Soc B 132
54. Bertz SH, Dabbagh G (1990) J Org Chem 55:5161
55. Buemi G (2002) Chem Phys 277:241
56. Berendsen HJC, Mavri J (1993) J Phys Chem 97:13464
57. Borgis D, Hynes JT (1991) J Chem Phys 94:3619
58. Garcia-Viloca M, Alhambra C, Truhlar DG, Gao J (2001) J Chem Phys 114:9953
59. Wolf K, Mikenda W, Nusterer E, Schwartz K, Ulbricht C (1998) Chem Eur J 4:1418
60. Mavri J, Berendsen HJC, van Gunsteren WF (1993) J Phys Chem 97:13469
61. Gonzales C, Schlegel HB (1989) J Chem Phys 90:2154
62. Brown SR, Tse A, Nakashima T, Haddon RC (1979) J Am Chem Soc 101:3157
63. Perrin CL, Kim YJ (1998) J Am Chem Soc 120:12641

CHAPTER 9

AN EXPLICIT QUANTUM CHEMICAL SOLVENT MODEL FOR STRONGLY COUPLED SOLUTE–SOLVENT SYSTEMS IN GROUND OR EXCITED STATE

ANDERS ÖHRN AND GUNNAR KARLSTRÖM

Department of Theoretical Chemistry, Chemical Centre, P.O.B. 124, S-221 00 Lund, Sweden, e-mail: anders.ohrn@teokem.lu.se, gunnar.karlstrom@teokem.lu.se

Abstract: A detailed account of the explicit quantum chemical solvent model QMSTAT is given. The model is presented in terms of three coupled aspects of relevance for all types of quantum chemical solvent models: the quantum chemical method, the intermolecular interactions and the statistical mechanical method. The quantum chemical method is either a compact natural orbital formulation of the standard Hartree–Fock method or a compact multiconfigurational method with a state basis. The latter method can describe excited states apart from the ground state and is for most systems an excellent approximation to the complete active space self-consistent field method. Both static and induced electrostatic interaction terms between the quantum chemical region and the solvent are included. Further, a non-electrostatic term is added to describe effects which derive from the Pauli principle. This term models both the exchange repulsion between solute and solvent and the packing effects an environment has on a molecule, in particular on diffuse states of the molecule. The statistical mechanical problem is solved with an exact Metropolis–Monte Carlo simulation that requires several similar quantum chemical problems to be solved. Since the quantum chemical problem and the statistical mechanical problem are solved as a coupled problem, the present model is especially useful for problems where electronic degrees of freedom of the solute strongly depend on the solvent distribution and vice versa. Three applications are summarized, which highlight this type of coupling present in QMSTAT and the non-electrostatic contribution. The examples are the solvation of four monatomic ions, the solvation of para-benzoquinone and the solvation of indole and the solvent shift to its absorption and fluorescence spectra

9.1. INTRODUCTION

Much of chemistry, as we know it, is suitably represented as a process of limited spatial extent taking place in an environment of some sort. The molecular interactions, which link the different constituents of the system together (solvent to solute, enzyme to substrate, molecule to molecule), differ with respect to length scale, strength, angular features and, consequently, relevance for the process under study.

S. Canuto (ed.), Solvation Effects on Molecules and Biomolecules, 215–246.
DOI 10.1007/978-1-4020-8270-2_9,

An outstanding toolbox for studies of these interactions has been provided to the scientific community through the development, implementation and optimization of the array of quantum chemical methods which exist nowadays. Our knowledge of the interactions has thus improved greatly over the last decades and significant advancements have been achieved in both scope and detail of the theory of intermolecular forces [1,2,3,4,5,6,7,8,9]. However, this does not mean that no problems remain to be tackled. First of all, the theory of intermolecular forces is very accurate in describing interactions between dimers, but much more molecular matter is usually found in chemical systems, and hence many-body terms are bound to appear. They are usually more difficult to understand and model than pair interactions. Second, with the possible exception of crystals and solid-state cryogenic solvents, chemical processes can significantly depend on entropy or, in other words, how the molecules distribute in the space of possible configurations. This means that not only are interactions in optimal intermolecular configurations (from an energetic point of view) in need of an adequate description, out also, interactions over a greater variety of energies and separations, as well as their interplay in defining the "volume" of available configurations, require a satisfactory treatment in order to describe the free energy of the system. Third, in a world of finite computational resources, molecular modelling is, with very few exceptions, practically restricted to simpler and more approximate descriptions of the relevant interactions than theoretically possible. State-of-the-art quantum chemistry, after all, scales very unfavourably with molecular size, which prompts the molecular modeller to develop efficient approximations to discard the most costly features, but at the same time keep the essentials intact. Finally, the scientific pursuit is a search for relevant causes and simple explanations of their connections to the observed effects, according to some philosophical schools at least. To know *how* something is tends to be more valued than only to know *that* something is. Therefore, a quantitatively less accurate, but physically more transparent theoretical model can be of greater scientific value to many chemists than a model of the inverse characteristics, as discussed in the context of quantum chemistry by theoretical chemists in the past [10,11,12]. To determine the relevant causes can be quite a challenge in terms of formulating and testing hypotheses. To conclude, these four problems show that there is much potential for improvements, extensions and re-evaluations of chemical models and our understanding of chemistry. Below, we will present one particular model, called QMSTAT, which uses quantum chemistry, the theory of intermolecular interactions and statistical mechanics to contribute to the understanding of chemistry in a condensed environment.

QMSTAT is an effective quantum chemical solvent model with an explicit solvent representation. "Effective" here means that the quantum chemical electronic Hamiltonian only pertains to a small subset of the total system (typically the solute), with the solvent entering as a perturbation operator to the Hamiltonian; "explicit solvent" means that the solvent is described with a set of spatial coordinates and parametrized physical features significantly simplified compared to a full quantum chemical description. The explicit solvent representation implies that it is possible to go beyond the mean-field approximation inherent in the often used continuum

solvent models [13,14,15,16,17,18]. On the other hand, more detail in the model also implies a greater variation of possible models: The number of model variables subject to the previous experiences and goals of the research of the individual developers grows in going from the continuum models to the explicit solvent models (or discrete solvent models, as they are sometimes called to clarify the contrast to the continuum models). Therefore, different researchers have come up with different models, all with their particular strengths as well as weaker sides. To be able to put the different models in a bigger picture, we have previously suggested that the models are discussed with respect to three different but connected aspects: their quantum chemical approach, their treatment of the intermolecular interactions (both solute–solvent and solvent–solvent) and the technique used in solving the statistical mechanical problem [19]. Before an overview of QMSTAT is given, this three-way picture of explicit solvent models will be reiterated. That way, we think, the meaning of the particular model variables in QMSTAT will, on a qualitative level, become clearer as will the advantages and limitations of the model.

The following chain of relations will establish the meaning and merit of the three-way picture: The influence an environment has on a molecule and on properties of that molecule is determined by the perturbation the environment exerts on the molecule. For a given configuration of solute and solvent coordinates, the accuracy of the description of the perturbation is determined by the accuracy of the direct solute–solvent intermolecular interaction. If sufficient details are included, the effective solute Hamiltonian is good. This defines the Schrödinger equation to be solved. For molecules some quantum chemical method is required to approximately solve that equation, and the quality of the method will influence the quality of the solution. Further, the perturbation is a function of the relative orientation of the solute and solvent, and at temperatures around 300 K a system with weak intermolecular forces will never adopt a single structure. Therefore, a statistical mechanical method of certain accuracy is needed to obtain the distribution of relative orientations, i.e. the particle distribution function. On the other hand, the particle distribution is a function of the intermolecular interactions between solute and solvent as well as solvent and solvent, where the former also depends on the quality of the quantum chemical method. Consequently, if one of the three aspects – quantum chemical method, description of the intermolecular interactions, statistical mechanical method – is poor for a given system, the quality of the results obtained will be limited by the most poorly modelled aspect, since the other two model aspects will, on account of the established interdependence, perform below their potential. To obtain an efficient and accurate model, balance between the three aspects is mandatory. It should be noted that where this balance lies will depend on the properties of the system under study and what questions are asked.

Before details of QMSTAT are formulated in the sections below, a brief overview is given. The molecular system in QMSTAT in divided into three parts: One region described with a quantum chemical method, one region of water molecules described with a polarizable force-field and a dielectric continuum that encompasses the other two regions, see Figure 9-1. To refer to the discussion in the first paragraph,

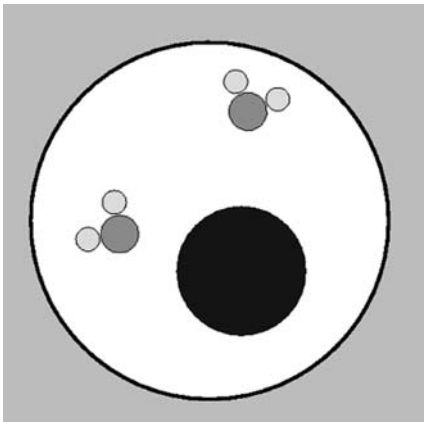

Figure 9-1. A two-dimensional projection of the modelled system in QMSTAT. The *dark spherical region* represents the quantum chemical region, and two solvent molecules are shown. Around the region of discrete molecular matter is a dielectric continuum; the explicit water molecules and the quantum chemical region are prevented from migrating into the continuum

the limited spatial region where high accuracy is sought is the first of these three regions, and the remaining two are regions where significant simplifications have been made compared to a full quantum chemical description in order to focus the computational resources on other, more relevant, aspects of the solvation phenomena. Two quantum chemical methods are currently implemented in QMSTAT: a compact Hartree–Fock (HF) formulation and a compact many-state model for multiconfigurational problems. For the connection between the central quantum chemical region and the solvent region, the quantum–classical intermolecular potential is formulated. It takes into account electrostatics, induction, dispersion and repulsive interactions. This combined quantum chemical classical mechanical potential is then used to construct the particle distribution with the Monte Carlo method. Therefore, QMSTAT uses a so-called hybrid approach to solve its statistical mechanical problem in contrast to the sequential approach, which first constructs the particle distribution with a simple fully classical force-field, then substitutes the simple solute representation with the quantum chemical solute representation. It should finally be noted that all simulations with QMSTAT have so far taken place under constant temperature, pressure and particle number conditions (the isobaric–isothermic ensemble). The second condition is achieved by a variable radius of the dielectric cavity and a volume–pressure term in the total energy and the third by putting a repulsive barrier between the explicit solvent and the boundary of the cavity (vide infra).

In the next section, QMSTAT is thoroughly presented and explained. As will be seen, we will return to the three aspects of explicit solvent models presented above. We continue with some previously published representative results obtained with QMSTAT. The results are mainly meant to illustrate features of the model; other perspectives on the result are omitted and the reader is referred to the original

publications. At the end, a short summary is given of QMSTAT in its present state of development.

9.2. THE MODEL, QMSTAT

The combined quantum chemical statistical mechanical method QMSTAT was originally published in 1996 for Hartree–Fock (HF) quantum chemistry [20]. This formulation has been applied in a number of studies, to which we will return in a later section. In 2006, an extension of QMSTAT was published with another quantum chemical method which enabled studies of excited states and multiconfigurational systems [21]. The two formulations have a lot in common and the discussion below applies to both formulations except when stated otherwise.

9.2.1. Intermolecular Interactions

An effective electronic Hamiltonian is formulated for the solute:

$$\widehat{H}_{\text{eff.}} = \widehat{H}_0 + \widehat{V}_{\text{solv.}} \tag{9-1}$$

where $\widehat{H}_0$ is the Hamiltonian for the isolated solute and $\widehat{V}_{\text{solv.}}$ is some operator that characterizes how the solvent affects the electronic structure of the solute. In QMSTAT three different terms contribute to $\widehat{V}_{\text{solv.}}$: permanent electrostatics, induced electrostatics and repulsive interactions. They are dealt with in turn below.

But before this is possible, the description of the solvent molecules and the interactions with the continuum have to be summarized. So far, QMSTAT has only been applied with water as solvent and the classical description of the water molecules which has been used is an early version of the NEMO force-field [22]. Each water molecule is equipped with four point-charges: one on each hydrogen atom and two charges close to the oxygen atom, but displaced slightly along the symmetry axis towards the hydrogen atoms and slightly off the molecular plane. This construction was found to perform significantly better than the more intuitive construction with three point-charges. The significant quadrupole moment of the water molecule is the reason for this, a moment which cannot be reproduced without charges off the molecular plane. Four-centre water models have been used before, for example in the early and well-cited study by Stillinger and Rahman [23]. To describe the electronic polarization of water, there is on each atom a point-polarizability α, which when subjected to an electric field, $\mathcal{E}$, generates a dipole of magnitude and orientation $\mu = \alpha\mathcal{E}$. The polarization of water molecules in aqueous solution is known to be significant and a proper description of this effect requires a polarizable solvent; effective pair potentials that modify permanent properties to emulate the polarized state do not perform as well [24]. The solution of the coupled polarization equations is obtained through iteration [25,26]. However, they will need to be coupled with the polarization of the quantum chemical systems as well, which means that a so-called generalized self-consistent reaction field (GSCRF) problem is to be solved

(vide infra) [27,28,29]. To complete the water–water intermolecular potential, van der Waals terms are included of the form

$$\sum_{i,j}\left(a_{ij}\mathrm{e}^{-b_{ij}r_{ij}}+\left(\frac{c_{ij}}{r_{ij}}\right)^{20}-\frac{d_{ij}}{r_{ij}^{6}}S(r_{ij})\right) \tag{9-2}$$

where a_{ij}, b_{ij}, c_{ij} and d_{ij} are atom-pair parameters, r_{ij} the separation and $S(r_{ij})$ a function which will damp the dispersion interaction at short distances; for parameter values, the reader is referred to the original publication [22]. Observe that this part of the potential only pertains to the solvent–solvent interaction.

A model for bulk solvation has also to account for long-range effects. In QMSTAT a non-periodic boundary condition is used, in contrast to the more common periodic boundary conditions. The explicitly represented molecules are put inside a spherical dielectric cavity. For all structures, save a few idealized ones, some approximate method has to be used to describe the interaction between the charge distribution and the dielectric continuum [30]. We use the image-charge approximation of Friedman [31]. The advantages of this type of boundary condition in simulations have been discussed by Wallqvist and more recently by Petraglio et al. [32,33]. In practice, all charges and dipoles inside the cavity give rise to image-charges and image-dipoles of certain location and magnitude outside the cavity. They define the reaction field. The method is obtained by truncation of an infinite series and is hence only an approximation to the true interaction with a dielectric continuum. The quality of the approximation improves, however, with increasing cavity radius and dielectric constant. Since the cavity in QMSTAT contains a lot of molecular matter, the radius will be large, and since the solvent is water, the dielectric constant is also large, hence the image-charge approximation is expected to perform well.

We now return to the task of formulating the solvent perturbation operator in Eq. (9-1). To formulate ourselves in terms of matrix elements, we introduce a real and orthogonal basis set for the quantum chemical region, $\{\psi_i\}_{i=1,\ldots,n}$. When the discussion turns to the quantum chemical method, the details of this basis will be dealt with, but for the moment the discussion is kept general. The permanent electrostatic contribution to $\widehat{V}_{\mathrm{solv.}}$, called $\widehat{V}_{\mathrm{perm.}}$, comes from the interaction between the quantum chemical charge distribution and the point-charges of the solvent. In other words,

$$\langle\psi_i|\widehat{V}_{\mathrm{perm.}}|\psi_j\rangle=\sum_{k=1}^{4N}\int\psi_i(\mathbf{r})\psi_j(\mathbf{r})\frac{q_k}{|\mathbf{r}-\mathbf{r}_k|}\mathrm{d}\mathbf{r} \tag{9-3}$$

where k counts over the $4N$ point-charges q_k in the explicit solvent, located at $\mathbf{r}_k$. To facilitate the evaluation of this integral, each density element $\psi_i(\mathbf{r})\psi_j(\mathbf{r})$ is multicentre multipole expanded. This means that each unique density pair $\psi_i(\mathbf{r})\psi_j(\mathbf{r})$ is made to correspond to a set of charges, $\{q_{ij}^a\}_a$, dipoles, $\{\boldsymbol{\mu}_{ij}^a\}_a$, and Cartesian quadrupoles, $\{Q_{ij}^a\}_a$, in n_{C} number of centres, $\{\mathbf{r}_a\}_a$ in the quantum chemical region. To keep the number of distances in need of computation minimal, the set of centres is the same for all basis function pairs. With the quadrupole in the Buckingham convention, Eq. (9-3) becomes [34]

$$\langle\psi_i|\widehat{V}_{\text{perm.}}|\psi_j\rangle \approx \sum_{k=1}^{4N}\sum_{a=1}^{n_C} q_k \left(q_{ij}^a \frac{1}{|\mathbf{r}_k - \mathbf{r}_a|} + (\boldsymbol{\mu}_{ij}^a)_\alpha \left(\nabla \frac{1}{|\mathbf{r}_k - \mathbf{r}_a|} \right)_\alpha + \frac{1}{3}(Q_{ij}^a)_{\alpha\beta} \left(\nabla\nabla \frac{1}{|\mathbf{r}_k - \mathbf{r}_a|} \right)_{\alpha\beta} \right) \tag{9-4}$$

where the nabla operator ∇ has been used in the differentiation of the separations. Tensors for charge–dipole and charge–quadrupole interactions of rank one and two, respectively, are thus obtained; the Greek indices designate the elements in the tensors and the Einstein summation convention has been used for these indices.

The advantage of using Eq. (9-4) is that it is faster to evaluate than Eq. (9-3). The error that the multicentre multipole expansion (MME) introduces is connected to the degree of overlap between the solute and solvent charge distributions. A large overlap, as for solvent molecules very close to the quantum chemical region, will lead to a larger error than for a configuration with smaller overlap. By distributing the multipole expansion, the range in which Eq. (9-4) is of acceptable quality is significantly larger than if only a single-centre multipole expansion had been used. It should be noted, though, that the error for a given separation does not necessarily tend to zero if the order of the MME is increased. This follows from the fact that a $\frac{1}{r}$-expansion like this only is semi-convergent [35]. This justifies our choice to truncate the expansion at quadrupolar order: Higher-order terms will lead to tensors of higher rank and thus require a greater computational effort, without leading to any certain improvement of the model. Observe also that already in Eq. (9-3) an error has been introduced, since the charge density of the solvent is multipole expanded. The true reference equation would involve two-electron Coulomb integrals. We therefore argue that the use of Eq. (9-4) instead of Eq. (9-3) is a good choice with respect to efficiency. To further develop the model with respect to its electrostatic interaction would involve removing the multipole expansion for both solute and solvent. Clearly, an efficient density-fitting method would then be required to avoid having to evaluate all two-electron integrals. Today this is being researched by several groups [36,37,38,39,40,41]. At this stage, however, QMSTAT uses Eq. (9-4).

Since the solvent molecules are polarizable, there will be a contribution to $\widehat{V}_{\text{solv.}}$ on account of the induced dipoles, $\widehat{V}_{\text{pol.}}$. The same type of equation as in Eq. (9-4) is used, but with dipoles interacting with the charges, dipoles and quadrupoles of the quantum chemical region. This, of course, requires additional tensors, but the principle is the same as before. There is one important difference, however. The induced dipoles of the solvent depend on the density of the quantum chemical region, which in turn depends on the induced dipoles. This non-linear problem is solved by iteration with the previously mentioned GSCRF method [27,28,29]. The practical procedure goes like this: Some initial guess of the induced dipoles defines $\widehat{V}_{\text{pol.}}$, which together with the other contributions to $\widehat{V}_{\text{solv.}}$ gives rise to a specific density $\rho(\mathbf{r})$ for the quantum chemical region; it exerts a new electric field on the solvent polarizabilities, thus

new induced dipoles are obtained and hence a new $\widehat{V}_{\text{pol.}}$ is defined; the procedure is iterated until a convergence criterion is satisfied.

This procedure suffers from the same problem as fully classical polarizable force-fields, namely the risk of polarization catastrophe [26,42,43]. Thole introduced polarizability damping which for short separations removes the discontinuity which causes the catastrophe [43,44]. For most applications, no catastrophe appears and we manage without damping. There are a few situations when damping is introduced, however. Since the quantum chemical system does not have any ordinary polarizabilities, the damping is best formulated as a damping of the electric field from the quantum region on the polarizabilities, and, correspondingly, as a damping of the electric potential, field and field gradient from the induced dipoles on the charges, dipoles and quadrupoles in the quantum chemical region, respectively:

$$(\mathcal{E}_{\text{charge}})_\alpha(\mathbf{r}_k) = q_a \left(\nabla \frac{1}{|r_k - r_a|} \right)_\alpha \cdot \left(1 - \mathrm{e}^{-c|r_k - r_a|}\right)^m \tag{9-5}$$

$$(\mathcal{E}_{\text{dipole}})_\alpha(\mathbf{r}_k) = (\mu_a)_\beta \left(\nabla\nabla \frac{1}{|r_k - r_a|} \right)_{\alpha\beta} \cdot \left(1 - \mathrm{e}^{-c|r_k - r_a|}\right)^m \tag{9-6}$$

$$(\mathcal{E}_{\text{quadr.}})_\alpha(\mathbf{r}_k) = (Q_a)_{\beta\gamma} \left(\nabla\nabla\nabla \frac{1}{|r_k - r_a|} \right)_{\alpha\beta\gamma} \cdot \left(1 - \mathrm{e}^{-c|r_k - r_a|}\right)^m \tag{9-7}$$

These equations show the damped expression for the αth component of the electric field from the solute multipoles in $\mathbf{r}_a$ on the solvent centre in $\mathbf{r}_k$ where a polarizability is located; observe that once more the Einstein summation convention has been used with respect to the Greek indices. The parameter c determines the range of the damping, and the integer parameter m determines for how high orders n of $\left(\frac{1}{|r_k - r_a|} \right)^n$ the discontinuity is removed, as seen by Taylor-expanding the damping function.

The dielectric continuum also contributes to both $\widehat{V}_{\text{perm.}}$ and $\widehat{V}_{\text{pol.}}$. Since we use the image-charge approximation, one possibility to include the continuum perturbation is by using the same equations as above, but now for image-charges and image-dipoles. That would more than double the computational effort in evaluating matrix elements of $\widehat{V}_{\text{perm.}}$ and $\widehat{V}_{\text{pol.}}$ since a dipole gives rise to both an image-charge and an image-dipole. As will be seen below, the quantum chemical region will be kept close to the centre of the cavity. This suggests that for the quantum chemical region (but not the explicit solvent) a less demanding procedure to include the continuum contribution can be used without appreciable loss of accuracy: The charge distribution of all molecular matter inside the cavity is multipole expanded in a single centre, then the dipole term is allowed to engender a reaction field which is added to the perturbation on the quantum chemical region. This procedure would be poor if the cavity was small or if the reaction field close to the boundary is sought. For the evaluation of the aforementioned matrix elements, neither condition is fulfilled, and the present approach will be both good and efficient.

The last contribution to $\widehat{V}_{\text{solv.}}$ comes from a repulsive term, which we usually call the non-electrostatic perturbation or sometimes the pseudo-potential, $\widehat{V}_{\text{nel.}}$. First the formulation of $\widehat{V}_{\text{nel.}}$ is given. After that, previous applications of pseudo-potentials are reviewed, which leads to the purpose and justification of this potential in QMSTAT. For the same general basis set as above, a matrix element of $\widehat{V}_{\text{nel.}}$ equals

$$\langle \psi_i | \widehat{V}_{\text{nel.}} | \psi_j \rangle = d \sum_{k \in \Omega} \sum_{l} \epsilon_l \langle \psi_i | \chi_l^k \rangle \langle \chi_l^k | \psi_j \rangle \tag{9-8}$$

where χ_l^k is the lth occupied orbital of the kth solvent molecule, ϵ_l is the corresponding negative orbital energy, Ω is a subset of solvent molecules with a significant overlap with the quantum chemical region and d is a parameter. The parameter d always takes negative values, which means that the expectation value of $\widehat{V}_{\text{nel}}$. will always be positive. In other words, it will give a repulsive contribution to the total energy. Observe also that the solvent orbitals are frozen: A translation and a rotation will map the lth orbital of the kth molecule on the lth orbital of any other solvent molecule, in any other configuration.

The concept of a pseudo-potential in quantum chemistry was first introduced by Hellmann in connection with frozen core calculation on atoms and further elaborated in that context over the following years [45,46,47,48,49,50,51,52,53]. A pseudo-potential is a "quantum mechanical technique in which the Pauli exclusion principle is replaced by operators and potential functions [50]." In the context of atoms, this is a way to simplify the treatment of the core and only describe it as, on the one hand, a shielding of the nuclear charge acting on the chemically active valence electrons and, on the other hand, a constraint to keep the valence electrons out of a certain region of space. Seijo and Barandiarán have taken the application of pseudo-potentials (or embedding potentials) to studies of impurities in solid-state problems [54,55,56,57]. The impurity is treated as being embedded in a solid-state host. It is obvious that the electrons of the impurity must be kept outside of the forbidden regions of the host. If this is not done, there is a significant risk that the electrons of the impurity will occupy the space around the nearby host charges, which usually are of large magnitude. The idea of pseudo-potentials has also been used for calculations on molecules, where certain less important parts of the molecule are removed from the explicit consideration and only indirectly included through a pseudo-potential [58,59,60,61,62]. The purpose of the non-electrostatic operator, or pseudo-potential, in QMSTAT is the same as above. If electrons in the important solute part escape to the less important parts, the electronic structure of the important part will deteriorate significantly. Further, in the modelling of intermolecular interactions, the Pauli exclusion principle has to be included somehow, since it is the cause of the repulsive intermolecular interaction. It is not common, however, to explicitly couple it to the electronic structure through some potential in the Hamiltonian. Instead a phenomenological term is usually added to the total energy. Apart from QMSTAT, there are some other models in the literature which depart from this description [63,64,65,66,67,68]. The work on the hydrated electron by Schnitker and Rossky as well as Wallqvist et al. is especially interesting in this respect, since without repulsive electron–water interactions

that restrict the electron, it would remain unbound and have no spectrum, which it is experimentally known to have [69]. It should be noted, though, that in methods which use supermolecular clusters for their description of the intermolecular interactions, like the Car–Parrinello method or the QM/MM method of Rode and co-workers, the Pauli effects are included, but through the anti-symmetry requirements in the optimization of the density or the wave function [70,71].

The expression in Eq. (9-8) can be justified in another way, using results from symmetry-adapted perturbation theory (SAPT). In SAPT the polarization approximation in the common Rayleigh–Schrödinger perturbation theory is removed and some partial anti-symmetry forcing between the interacting monomers is included [5,7]. One result that the different theories share is that the leading repulsive intermolecular term is proportional to the wave function overlap between the monomers raised to the power of two [1,72,73]. This observation has been used in some fully classical force-fields to model the repulsion with some approximate overlap or with the related, but not equivalent, charge-density overlap [74,75,76,77,78,79,80,81]. As is seen from Eq. (9-8), each basis function has a repulsive interaction with the solvent with a quadratic dependence on the overlap. The orbital energy, from that perspective, becomes a weight that makes stronger bound orbitals on the solvent penalize basis functions that overlap much with them more than weaker bound orbitals. In solving the quantum chemical problem with the effective Hamiltonian, the wave function will thus be "pushed away" from the solvent.

To conclude the discussion of $\widehat{V}_{\mathrm{nel}}$., its purpose will be briefly addressed. The physics that the pseudo-potential models should be clear from the discussion above. The question is whether the coupling between the interacting molecules is of such nature that the electronic degrees of freedom of the quantum chemical systems really have to be directly coupled to the repulsion. For solvated anions, at least, the answer is unambiguously affirmative. It has long been known experimentally that the polarizability of anions in an environment is markedly different from the polarizability in gas phase [82,83]. The reason is that in an environment the diffuse charge distribution of the anion is significantly restricted by the anti-symmetry requirements to the environment, which leads to less flexibility and thus less polarizability. An implication of this is that simulations of polarizable anions which neglect the explicit coupling between repulsion and electronic degrees of freedom have to underestimate the polarizability, either by assigning it a lower value or by using small basis sets that do not reproduce the full polarizability. This problem has been analysed and highlighted in a number of recent theoretical works, including one study with QMSTAT (vide infra) [84,85,86,87,88]. Another instance where experiment has led to discussions of more direct influence of repulsive forces on electronic properties is spectroscopy in simple environments such as rare gas liquids [89,90,91,92]. The idea is that when a molecule is electronically excited the charge distribution is instantaneously altered, which leads to a different repulsive interaction with the surrounding, and thus a non-electrostatic contribution to the shift of the absorption or fluorescence peak is recorded. In a general theoretical discussion of solvent shifts to UV- and visible spectra, Bayliss and McRae name this effect *packing strain* [93]. For the same process,

Dobrosavljević et al. also conclude with simple models that the modification of the repulsive interaction can contribute to spectra [94,95]. They use boundary conditions to prevent the solute electrons from occupying forbidden space in the solvent. A pseudo-potential is an alternative way to include this effect. These are some of the physical effects a pseudo-potential is meant to model, but there are also model defects that a pseudo-potential can alleviate or remove. Since the representation of the solvent uses partial point-charges, there is a risk, if diffuse basis functions are used for the quantum chemical region, that an excessive accumulation of electrons at the point-charges occurs when the quantum chemical problem is solved [96,97]. As a consequence, the performance of the model can deteriorate with increasing quality of the basis set. This final point amplifies the importance of balance in solvation models: Improving the quantum chemical description (by improving the basis set) without simultaneously improving the intermolecular description can lead to poorer model performance.

This concludes the formulation of $\widehat{V}_{\text{solv.}}$. Two terms remain, though, in the intermolecular interaction potential between quantum chemical region and solvent. These terms are only added to the total energy and therefore only indirectly influence the electronic structure. The first term is a consequence of the finding that the pseudo-potential in Eq. (9-8) does not lead to sufficient repulsion at short separations. With SAPT it is shown that higher-order repulsive terms will appear, terms which have a fourth, sixth and so forth order dependence on the overlap. In QMSTAT, these terms are not included in $\widehat{V}_{\text{solv.}}$, instead terms like

$$E_{S^4} = \beta_4 \left(\sum_{k \in \Omega} \sum_{l} \langle \psi | \chi_l^k \rangle \langle \chi_l^k | \Psi \rangle \right)^2 \tag{9-9}$$

are added to the total energy; Ψ is the wave function for the quantum chemical region described in terms of the basis set $\{\psi_i\}_{i=1,\ldots,n}$, and β_4 is a parameter. Second, the dispersion interaction between solute and solvent is phenomenologically included through a distributed $\frac{1}{r^6}$ expression:

$$E_{\text{disp.}} = -\sum_{k,l} \frac{C_{kl}}{r_{kl}^6} f_{kl}(r_{kl}) \tag{9-10}$$

Indices k and l count over all solvent and solute atoms, respectively; C_{kl} is a parameter; r_{kl} is the separation between the kth solvent atom and the lth solute atom. $f_{kl}(r_{kl})$ is a damping function active at short separations; we use the variant derived by Tang and Toennies [98]:

$$f_{kl}(r_{kl}) = 1 - \left(\sum_{i=0}^{6} \frac{(b_{kl} r_{kl})^i}{i!} \right) \mathrm{e}^{-b_{kl} r_{kl}} \tag{9-11}$$

The parameter b_{kl} determines the range of the damping. Instead of fitting this parameter we use an empirical expression involving localized second-moments and charges

[99]. In a note from 1942, London criticises expressions as that in Eq. (9-10) from two perspectives: [100] First, in a molecule the dispersion interaction centres do not have to be spherically symmetric, as they have to be in atoms for which London originally derived his now well-known formula for the dispersion interaction or the van der Waals attraction [101,102]. Second, the oscillations in distributed centres in a molecule do not have to remain local. Instead of only transition dipoles in the different centres, also transition charges *between* different centres can occur, which implies that additional non-local terms (in the nomenclature of Stone and Tong) of order $\frac{1}{r^2}$ and $\frac{1}{r^4}$ appear [7,103]. Still, the current literature is replete with expression of the same form as that in Eq. (9-10). It is therefore reasonable to conclude that despite its formal deficiencies, the present expression for the dispersion interaction energy is a good compromise between simplicity and accuracy. Finally, in this context, the direct reaction field (DRF) method by van Duijnen and co-workers merits special attention [104,105,106]. In DRF the dispersion interaction is included as a term in the solvent perturbation to the quantum chemical region, which also means that dispersion interactions in different states can be accounted for. This method can potentially go beyond the phenomenological description of the dispersion interaction, but it should also be noted that there are indications that the DRF method tends to overestimate the dispersion interaction [107,108].

9.2.2. The Quantum Chemical Methods

As stated in the preamble to this section, two quantum chemical methods are implemented in QMSTAT. The first is the well-known HF method, the cornerstone of ab initio quantum chemistry. For an excellent account of the HF method, see the textbook by Szabo and Ostlund [109]. The standard way to solve the HF equations nowadays is to use a basis set for expanding the orbitals, as first suggested by Hall and Roothan [110,111]. The basis sets that are used in most cases are Gaussian atom-centred basis functions, which for molecules constitute a non-orthogonal basis. The bottleneck in HF calculations is the number of two-electron integrals. This has led developers to construct a multitude of methods to speed up the treatment of the two-electron integrals, with the aim of making HF calculations feasible for increasingly larger systems. The limitations faced by QMSTAT simulations with the HF method are similar to the gas-phase quantum chemical calculations, with one minor, but, as will be seen, decisive difference: We have to do many repeated quantum chemical calculations on systems with very similar effective Hamiltonians. Below we will describe how this can be utilized in the expansion in a basis to acquire a work-saving solution to the HF equations. The postponed discussion of how the MME practically is performed will also be given. Then we will turn to the other quantum chemical method.

The common atom-centred basis sets (ACBS) are designed to be applicable for a range of different geometries, covalent bonds, environments and methods. This generality is both their strength and weakness. The weakness becomes apparent in QMSTAT where, on account of the statistical mechanical procedure (vide infra),

many very similar quantum chemical problems have to be solved; the largest contribution to the Hamiltonian in Eq. (9-1), the intramolecular $\widehat{H}_0$, is constant in our frozen geometry approximation while only the small intermolecular $\widehat{V}_{\text{solv}}$. changes between different configurations. Thus, the basis for the orbital expansion does not have to be as versatile as the full ACBS since it is already known pretty well before the nth quantum chemical calculation is done what it should be. We use the following procedure to construct a different, less redundant basis set: A set of HF calculations on the molecule later to be solvated with QMSTAT are done with a usual ACBS of dimension N. The calculations differ in terms of the Hamiltonian; a calculation with only $\widehat{H}_0$ is included, but a number of calculations with generic perturbations are added, $\widehat{H}_0 + \widehat{V}$. The different perturbations are usually homogeneous electric fields, sometimes size penalties (see reference [112]) and inhomogeneous fields; their purpose is to span a space of perturbations in which the full solvent perturbation is well contained. Each calculation generates a density matrix, D_a, slightly different from the other density matrices. An average density matrix is constructed:

$$D_{\text{aver.}} = \sum_{a=1}^{N_{\text{calc.}}} \omega_a D_a \tag{9-12}$$

where the sum of the weights, ω_a, is unity. The average density matrix is symmetrically orthogonalized ($S^{1/2} D S^{1/2}$, S overlap matrix) and diagonalized. This procedure generates a set of average natural orbitals of dimension N, with some fractional occupation numbers, $\{\eta_i\}_i$. At this point a subset of the natural orbitals is obtained by only including orbitals with occupation numbers greater than some threshold, t_{d}. This subset is used as the basis set, $\{\psi_i\}_{i=1,\ldots,M} (M \langle N)$, in the simulation. The one- and two-electron integrals needed in the construction of matrix elements to $\widehat{H}_0$ are transformed to this basis; the expression for the effective Fock matrix becomes

$$\begin{aligned} \langle \psi_i | \widehat{F}_{\text{eff.}} | \psi_j \rangle = {} & \langle \psi_i | \widehat{T} + \widehat{H}_{\text{nuc.}} | \psi_j \rangle + \langle \psi_i | \widehat{V}_{\text{solv.}} | \psi_j \rangle \\ & + \sum_{k,l}^{M} \tilde{D}_{kl} \left((\psi_i \psi_j | \psi_k \psi_l) - \frac{1}{2} (\psi_i \psi_l | \psi_k \psi_j) \right) \end{aligned} \tag{9-13}$$

where $\widehat{T}$ and $\widehat{H}_{\text{nuc.}}$ are the kinetic and nuclear attraction operators, respectively, and $\tilde{D}_{kl}$ a density matrix element. Observe that the integrals in the first and third terms are computed once and for all before the simulation. With the reduction of the dimension of the basis the number of two-electron integrals is kept fairly small and they can thus be kept in memory. No time-consuming input/output to disk is therefore needed. Once the Hamiltonian is formulated, the usual self-consistent field iterations are performed, however, with the difference that the GSCRF problem is solved at the same time (vide supra). Since a good starting guess exists for the density matrix, the number of iterations is generally small.

The reason this procedure is an efficient approximation is due to the fundamental property of natural orbitals. They were introduced by Löwdin in connection with

configuration interaction (CI) calculations [113]. Their key property is that for a given dimension M of one-electron functions, they are the minimum to the absolute difference integral between a density described in that basis of dimension M and the density described in a complete basis [113,114]. The above procedure utilizes this property in that the most compact basis possible is obtained, which is able to describe the space spanned by the input densities with a prescribed accuracy. This property is also used in the construction of generally contracted atomic natural orbital (ANO) basis sets, which have been shown to be quite successful [115,116,117,118,119]. Three typical M/N are $33/104$ for Sr^{2+}, $42/204$ for *para*-benzoquinone and $54/276$ for trimethylamine-*N*-oxide [120,121,122].

At this stage, when the nature of the basis is known, we return to the question, how the MME needed to evaluate $\langle\psi_i|\widehat{V}_{\text{perm.}|c_j\rangle}$ and $\langle\psi_i|\widehat{V}_{\text{pol.}|c_j\rangle}$ is done in practice. We use a method that takes advantage of basic properties of Gaussian functions, which is also very similar to the distributed multipole analysis of Stone [123,124,125]. For an arbitrary pair of basis functions $\psi_i\psi_j(\mathbf{r})$, we use the orbital expansion

$$\psi_i\psi_j(\mathbf{r}) = \sum_{m,n} c_{mi}c_{nj}\theta_m\theta_n(\mathbf{r}) \tag{9-14}$$

where $\{\theta_m\}_{m=1,\ldots,N}$ is the ACBS and $\{c_{mi}\}$ the natural orbital coefficients. Two cases are treated: Basis functions θ_m and θ_n are centred either on the same atom or on different atoms. To start with the former case, the multipoles to assign to this atom centre, $\mathbf{r}_a$, for that specific pair of atomic basis functions are

$$q_a^{mn} = \langle\theta_m|\theta_n\rangle \tag{9-15}$$

$$\boldsymbol{\mu}_a^{mn} = \langle\theta_m|\boldsymbol{\mu} - \mathbf{r}_a|\theta_n\rangle \tag{9-16}$$

$$Q_a^{mn} = \langle\theta_m|Q - \mathbf{r}_a\mathbf{r}_a|\theta_n\rangle \tag{9-17}$$

In the latter case, the same integrals will give the multipoles, but the expansion centre is no longer obvious. For a pair of primitive Gaussians, the optimal centre is the centre for the product Gaussian. Since it would be far too costly to let each primitive pair of basis functions have a unique centre, a weighted average of all primitive centres is computed with the absolute value of the associated charge as weight. This construction is meant to give a compromise centre for which low-order multipoles are most important. Therefore, each term in Eq. (9-14) has a centre and a magnitude, hence the contributions to the different centres are collected and the MME is obtained. Stone has in a recent article studied how individual moments change with basis set [126]. His observations are that these do not seem to converge, while the electric potential that these multipoles define is more stable. See also the study by Söderhjelm et al. for further studies of MME [127]. Based on this and our experience with the MME defined in this way, we conclude that the MME can be used to simplify the evaluation of the electrostatic interaction, with an acceptable loss of accuracy for most, but certainly not all, systems.

The HF method is limited to electronic ground states and systems which are well described by single determinant wave functions. To overcome these limitations, QMSTAT was recently augmented with a quantum chemical method that can treat systems with a multiconfigurational wave function. The complete active space self-consistent field (CASSCF) method would be a good choice in this respect [128,129,130]. In that method an expansion of Slater determinants is achieved by a selection of so-called active orbitals. All expansion coefficients are optimized, i.e. both orbital and CI coefficients, with respect to the energy of a single root or to the energy of an average of states. The latter procedure, called state-average CASSCF (SA-CASSCF), is known to lead to more stable optimizations if excited states are involved. The SA-CASSCF wave function is for a particular state variational with respect to the CI coefficients, but not to the orbital coefficients. This makes the task of computing analytical gradients more difficult, but Stålring et al. have formulated and implemented the relevant equations [131]. Unfortunately, SA-CASSCF takes too much time for a hybrid approach to the statistical mechanical problem to be feasible. Some further approximation is needed for all but very small molecules. The most common way forward in the literature is to discard the hybrid approach [112,132,133,134,135,136]. Our choice instead is to construct a quantum chemical method that approximates the CASSCF method.

Once more the key to being able to approximate CASSCF is the similarity between the different calculations. Instead of repeating several very general calculations for a particular problem, we prepare a less general basis honed to the particular problem under study. The following procedure is used: A number of SA-CASSCF calculations are made for a set of slightly different Hamiltonians, in the same way as in the construction of the natural orbital basis in the HF procedure above. In contrast to the HF calculations, we are getting wave functions not only for the ground state, but also for higher states; if we are making calculations on spectroscopy, the relevant states in the electronic transitions should of course be included. Therefore, we obtain $N_\mathrm{S} \cdot N_\mathrm{P}$ states, where N_S is the number of relevant states and N_P the number of different CASSCF calculations. Many of these states are overlapping significantly with each other. We use this set of states to expand the wave function in QMSTAT, but to simplify the mathematical treatment, an orthogonal set of states that span the same space is preferred. The CAS state interaction (CASSI) method can make this construction [137,138]. The original purpose of CASSI was to evaluate matrix elements for CASSCF wave functions, such as transition dipole moments. A set of orthogonal states, $\{\Psi_i\}_i = 1, \ldots, {}_{N_\mathrm{S}} \cdot {}_{N_\mathrm{P}}$, are obtained with CASSI, which span the same space as the input CASSCF states and also are eigenfunctions to the Hamiltonian. To put it differently, a set of states that diagonalize both the overlap matrix and the Hamiltonian matrix are obtained. It is in terms of these eigenstates that the effective solute wave function is linearly expanded:

$$\Psi^{\mathrm{QMSTAT}} = \sum_i C_i \Psi_i \tag{9-18}$$

The coefficients C_i are determined through a variational procedure. The orthogonality of the basis states leads to the coefficients being obtained through a diagonalization of the effective Hamiltonian matrix. As described below, the eigenstates can be slightly modified to improve performance, but the linear ansatz is fundamental.

To obtain the Hamiltonian matrix the matrix elements $\langle \Psi_i | \widehat{V}_{\text{solv.}|\Psi_j\rangle}$ have to be computed. With the *one-electron transition density matrix*, $\mathbf{\Gamma}$, also calculated by CASSI, this involves the following summation:

$$\langle \Psi_i | \widehat{V}_{\text{solv.}} | \Psi_j \rangle = \sum_{k,l} \Gamma^{i,j}_{k,l} \langle \psi_k | \widehat{V}_{\text{solv.}} | \psi_l \rangle \tag{9-19}$$

where ψ_i is a basis function for the density matrix and $\Gamma^{i,j}_{k,l}$ is a transition density matrix element. Note here that ψ_i is a general notation for a basis function; in many cases it equals an atom-centred basis function, θ_i, but not always, as described further below. Straightforward substitution of Eq. (9-8) in Eq. (9-19) gives the expression for $\langle \Psi_i | \widehat{V}_{\text{nel.}} | \psi_j \rangle$. For the other two contributions to the solvent perturbation, each basis-set pair density has to be multicentre multipole expanded. In analogy with Eq. (9-14) the density which is expanded is

$$\Psi_i \Psi_j(\mathbf{r}) = \sum_{k,l} \Gamma^{i,j}_{k,l} \Psi_k \Psi_l(\mathbf{r}) \tag{9-20}$$

and each term is once more treated with the same procedure as described above for the HF wave functions. Observe also that the diagonalization of the Hamiltonian matrix gives rise to higher states, which are representations of solvated excited states if excited states are included in the preceding CASSCF calculations.

As noted above there is significant overlap between the input CASSCF states. This implies that numerical problems can occur in the construction of the orthogonal states and states need to be deleted. Compare this with ordinary HF calculations with large basis sets which sometimes delete orbitals on account of near-linear dependencies in the non-orthogonal ACBS. In mathematical terms the procedure is as follows: The overlap matrix for the CASSCF states is diagonalized; all eigenvectors that correspond to eigenvalues less than some threshold t_s are deleted and the eigenvector matrix $\mathbf{X}$ becomes rectangular; the subsequent diagonalization of $\mathbf{X}^\dagger \mathbf{H} \mathbf{X}$, where $\mathbf{H}$ is the Hamiltonian matrix for the CASSCF states, thus produces a smaller number of orthogonal CASSI states than input CASSCF states and with the near-linear dependencies removed. This procedure will reduce the range of the index-pair $(i,\ j)$ in Eq. (9-19) (and similar). Computational savings are thus obtained. Further savings are achieved by reducing the range of the index-pair (k, l) with the following procedure: An average density matrix is constructed with elements

$$D_{k,l} = \frac{1}{N} \sum_{i=1}^{N} \Gamma^{i,i}_{k,l} \tag{9-21}$$

Then the same procedure as in the construction of the natural orbital basis for the HF calculations is used, and the truncated set of natural orbitals that is obtained is used to expand the transition density matrix, and hence the index-pair (k, l) is contracted. In practice this means that instead of making one large transformation with the transition density matrix in Eq. (9-19), two smaller ones are done: first one from the ACBS to truncated orbital basis, then to state basis. For reasonable thresholds in the orbital construction, t_{d}, this will lead to a speed-up of the QMSTAT calculations. Details of the two procedures described above can be found in reference [139].

9.2.3. Statistical Mechanical Method

The approximate solution to the Schrödinger equation, defined by the effective Hamiltonian in Eq. (9-1), with either method described in the previous section, associates to every vector of molecule coordinates, $\mathbf{R}$, together with the solvent–solvent interaction potential, an energy $E(\mathbf{R})$. From basic classical statistical mechanics an *N-particle distribution function* (PDF) $n(\mathbf{R})$ is thus obtained:

$$n(\mathbf{R}) = N! \frac{\mathrm{e}^{-E(\mathbf{R})/kT}}{\int \mathrm{e}^{-E(\mathbf{R})/kT} \mathrm{d}\mathbf{R}} \tag{9-22}$$

where kT is the Boltzmann constant times the temperature. For weak interactions, i.e. interaction energies $\sim kT$, the equation above shows that the distribution will have finite width: It cannot be approximated by a δ-function. In the single structure energy minimum approximation, where the lowest energy structure is used to estimate averages, this is the fundamental approximation. Its merit is questionable, unless very strong interactions dominate the system. To take the finite width into account, or entropy in other words, a better solution to the statistical mechanical problem is required. In QMSTAT, the well-known Metropolis–Monte Carlo (MMC) algorithm is used, which mathematically is formalized by Hastings [140,141,142]. With an estimate of the PDF, Boltzmann averages can be computed for properties such as excitation energies, dipoles, angles and so on. The MMC algorithm converges to the exact solution to the statistical mechanical problem, although a statistical error always remains in practice. There are methods available to monitor the convergence of the MMC algorithm and the balance of the sampled space; they are described elsewhere [122,142,143].

To solve the statistical mechanical problem this way in QMSTAT requires a quantum chemical problem to be solved in each Monte Carlo step. This approach is sometimes called a hybrid approach: quantum chemistry and statistical mechanics are solved together. It is well known that consecutive configurations generated by the MMC algorithm are correlated. This is the reason why most MMC algorithms do not sample every configuration, rather with some frequency, generated configurations are added to the estimate of the PDF; the other steps are only the path between

sampled configurations. This observation has led to the formulation of an alternative method, which requires less quantum chemical computations. It is called the sequential method and has been extensively described by Coutinho, Canuto and co-workers and has been applied in several QM/MM studies by these and other researchers (see for example references [144,145,146,147,148]). By first constructing the PDF for the system under study, but with a fully classical force-field, then substituting the classical solute for the quantum chemical solute, the number of quantum chemical calculations can be reduced significantly since the generation of configurations between the sampled ones does not require any demanding quantum chemical equations to be solved. The advantage is obvious and the reduction of the number of quantum chemical computations may be absolutely necessary if the computational effort associated to the given quantum chemical method is high. The sequential method is, however, not an exact solution to the statistical mechanical problem for the combined system. Since the PDF is computed with one solute–solvent interaction, while the properties are computed with another solute–solvent interaction, it is formally necessary to re-weigh the probability density for each sampled configuration, which for a finite sample will worsen the quality of the statistics. How well the sequential method approximates the hybrid method depends on how well the fully classical force-field reproduces the forces of the combined quantum/classical system. The complicated couplings between the solute electronic degrees of freedom with the solvent in anions and diffuse excited states, discussed above, are two examples where fully classical force-fields, at this stage of development, are unreliable. The hybrid approach in QMSTAT hence means that we emphasize the statistical mechanical aspects and the coupling between solute and solvent in the solvation problem. That this is possible hinges on the compact quantum chemical methods.

Finally, some practical features of the simulation are noted. Since we use a non-periodic dielectric continuum to model long-ranged electrostatics, the explicitly described molecules have to be prevented from coming too close to the boundary where the energy becomes discontinuous. For the water molecules a short-range repulsive interaction is added between a given water molecule and its image-charges. This does not model any physical interaction. The quantum chemical region should satisfy the same condition, but since it should also be kept in the interior of the explicitly modelled water, we add a harmonic energy term which penalizes translations away from the cavity centre. The solute is rarely farther away from the centre than 1 Ä.

9.2.4. Parametrization and Simulation Protocol

The subsections above have presented the details of QMSTAT and described how they fit together. In this subsection the parametrization of the intermolecular potential is described and a typical simulation protocol is given.

Our approach to the parametrization is the same as in many other modern force-fields, i.e. we use microscopic ab initio quantum chemical calculations on monomers and dimers as reference instead of macroscopic experimental quantities [8]. For simulations with the state-based quantum chemical method, the CAS second-order

perturbation (CASPT2) interaction potential is the target [149,150,151]. The counterpoise corrected interaction potential for a solute–solvent dimer with CASPT2 contains all types of interactions, including the dispersion interaction, for both ground and excited states [152,153]. In principle, the parameters in $\widehat{V}_{\text{nel.}}$, higher-order repulsion, solute–solvent dispersion and possibly the parameters in the electric-field damping can be adjusted to fit the QMSTAT solute–solvent potentials to the CASPT2 potentials. This naïve way of making the parametrization has two problems: First, the different terms are not perfectly separated in the supermolecular potential, and thus several different set of parameters can be fitted to the limited CASPT2 data. Since each term has a physical content, it is from a strict methodological point of view preferable if the terms are fitted separately as far as possible. Second, the electrostatic interaction in CASPT2 differs slightly from the interaction in CASSCF. Since QMSTAT uses CASSCF states in its description of the density, this difference can contaminate the fitting procedure. This problem, however, is often a minor one since CASSCF densities tend to be good.

The parametrization procedure that we have opted for in the most recent works is as follows: (1) Compute the intermolecular dynamic correlation energy for the ground state with a second-order Møller–Plesset (MP2) expression that only contains the intermolecular part and which uses monomer orbitals. Fit the dispersion parameters to this potential. To aid in the distribution of the parameters, a version of the exchange-hole method by Becke and Johnson is sometimes used [154,155]. Becke and Johnson show that the molecular dispersion coefficient can be obtained fairly well by a relation that involves the static polarizability and the exchange-hole dipole moment:

$$\langle d_X^2 \rangle = \int \rho(r_1) d_X^2(r_1) \mathrm{d}r_1 \tag{9-23}$$

where

$$d_X^2(r_1) = \left(\frac{1}{\rho(r_1)} \sum_{ab} [\langle \psi_a | r | \psi_b \rangle \psi_a \Psi_b(r_1)] - r_1 \right)^2 \tag{9-24}$$

where ρ is the electron density and ψ_a is an occupied HF molecular orbital. The integral has to be numerically evaluated, where we use the quadrature of Lindh et al. [156]. To localize $\langle d_X^2 \rangle$ Johnson and Becke use a Hirschfeld partitioning. We use instead the localized basis, $\{\tilde{\theta}_i\}_i$, obtained in the Loprop method [157]. In Loprop, one-electron property integrals are transformed to an orthogonal and approximately localized basis, and thus molecular properties are distributed. In this particular application, Eq. (9-23) in this local basis is

$$\langle d_X^2 \rangle = \sum_{\alpha} \sum_{i,j \in \Omega_\alpha} D_{ij} \int \tilde{\theta}_i \tilde{\theta}_j(r_1) d_X^2(r_1) \mathrm{d}r_1 \tag{9-25}$$

where α runs over all molecular centres, and Ω_α is the set of basis functions assigned to centre α. To every centre a local exchange-hole value is obtained, and Loprop can

also compute localized polarizabilities, hence all values needed to compute localized dispersion coefficients according to the formula proposed by Becke and Johnson are available. The magnitude of the values may need to be adjusted to reproduce the total dispersion curve, but the relative values seem to work well in our limited number of applications where this method has been used. Further work should lead to an improved factor so that no second-order Møller–Plesset calculation is required. (2) Compute the supermolecular interaction potential with CASSCF. Fit the repulsive parameters to the CASSCF curve, which contains the electrostatic and repulsive interactions, but no (or only very little) of the dispersion interaction. In this step, the interaction potential of not only the ground state but also the relevant excited states, is considered. The damping is usually set to zero, unless this leads to too poor quality of the QMSTAT interaction potential. If the subsequent simulation runs into a polarization catastrophe, then damping is added and some reparametrization is done.

As observed in the section on how to obtain a less redundant basis set for the QMSTAT calculations, the geometry of the quantum chemical region is frozen. This is a limitation of the model, and only solutes for which no significant flexibilities exist can be handled ("significant" meaning that they exist and are of quantitative relevance for the properties under study). If the frozen geometry approximation is tenable, a geometry has to be chosen. The most obvious choice is the optimal gas-phase geometry. For many applications this has been found to be an approximation of sufficient quality. In some cases, however, the solvent effects on the geometry have been significant and sometimes even the purpose of the study. Then numerical free-energy gradients for selected degrees of freedom are computed with free-energy perturbation calculations. The simple method by Zwanzig has been used to compute free-energy differences [158]:

$$\Delta G = -RT \ln \langle \mathrm{e}^{-\Delta U/kT} \rangle_T \tag{9-26}$$

This equation is exact, but since the thermal average has to be estimated by a finite sample, statistical errors will grow along the magnitude of the perturbation ΔU. As shown by Lu et al. perturbation schemes with better performance can be formulated [159,160]. The final simulation and calculation of properties are done in the free-energy optimal geometry thus obtained.

9.3. EXAMPLES OF APPLICATIONS

QMSTAT has to date been applied in a number of studies since its original formulation [19,20,21,85,120,121,122,139,161,162,163,164,165,166]. These involve studies of ground state solvation, with geometry optimizations in a water solvent and solvation of ions; also, solvent shift distributions have been computed for a number of different one-photon absorption and fluorescence transitions. We will not review all these studies, instead three noteworthy applications of QMSTAT are highlighted below. We start with a study of the solvation of the monatomic ions Li^+, Na^+, F^- and Cl^-, with special focus on the coupling between repulsion and the electronic degrees

of freedom. Then the solvation of the quadrupolar *para*-benzoquinone is reviewed, where we emphasize a non-trivial asymmetry in the solvation. Finally, results from a simulation of the fluorescence of indole in aqueous solution and at a non-polar/polar interface are summarized.

9.3.1. The Polarization and Repulsion Are Coupled in Some Monatomic Ions

It was referred to above, in connection with the description of the non-electrostatic operator in QMSTAT, that there is a well-known effect on the polarizability of anions from the environment to the anion. Qualitatively speaking, the environment compresses the charge distribution of the otherwise diffuse anion, on account of the anti-symmetry restrictions between the ion and the environment. We model the hydration of four monatomic ions (Li^+, Na^+, F^- and Cl^-) with QMSTAT to, among other things, study how the polarization and the Pauli repulsion couple [85].

The HF version of QMSTAT is used. A compact basis set of natural orbitals is constructed for each ion. Since the polarizability converges very slowly with increasing basis set, already here some reduction of the polarizability is made [167,168]. Parametrizations are done as described in a previous subsection, followed by MMC simulations. An estimate of the particle distribution function to each ion, $n(\mathbf{R})$, is thus obtained. Observe that the hybrid approach to the statistical mechanical problem implies that the non-electrostatic operator is active in the determination of $n(\mathbf{R})$.

An analysis of the coupling is done. Four different energies are computed for every configuration with this aim in mind: (1) The total energy with both polarization and repulsion active, $E_{\mathrm{p}}^{\mathrm{r}}$. (2) The energy with the repulsion between water and ion removed, E_{p}; this is achieved by setting the parameters to this interaction to zero. (3) The energy with the polarization of the ion removed, E^{r}; this is achieved by only including the same number of natural orbitals in the basis as occupied orbitals for the given ion, hence no relaxation from the gas-phase electronic structure is possible. (4) The energy with both repulsion and polarization removed as above, E. If no coupling exists, such as in fully classical force-fields, the equation

$$E_{\mathrm{p}}^{\mathrm{r}} = E + (E_{\mathrm{p}} - E) + (E^{\mathrm{r}} - E) \tag{9-27}$$

should hold. Deviations from Eq. (9-27) for the actual energies is thus a quantitative measure of how strongly the polarization and repulsion couple in QMSTAT. In Figure 9-2, the distribution of the energy coupling term, that is the left-hand side minus the right-hand side of Eq. (9-27), is shown. In Figure 9-2(c) and (d), the distributions for the cations are shown. They are very close to zero, just slightly shifted to negative coupling energies. The fact that repulsion and polarization are as good as uncoupled for these systems is a result of their low polarizability. The slight negative shift we suggest follows from cooperation between electrostatics and repulsion. On account of their charge, the partially negative oxygen atom from the solvent will be close to the cation, hence the electrons on the cations are driven away from nearby solvent molecules by the electrostatic interaction. With the non-electrostatic

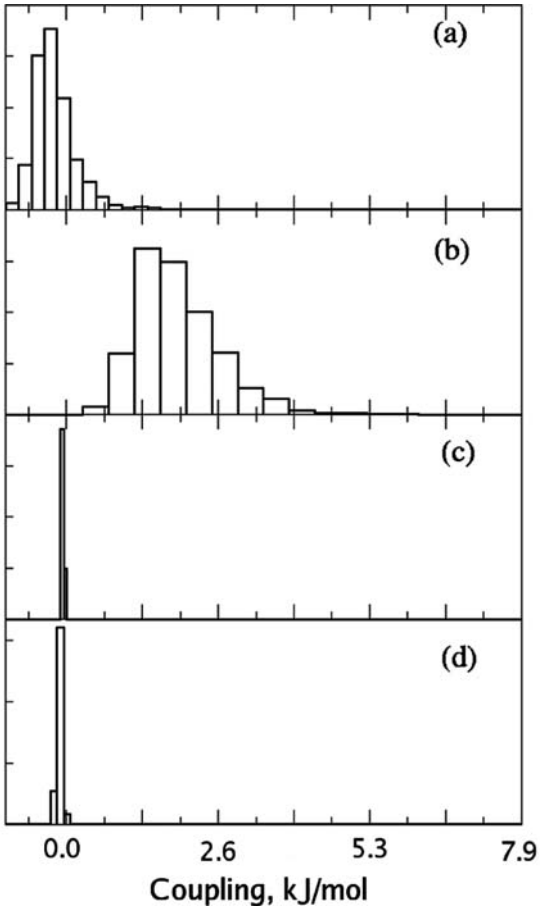

Figure 9-2. The distribution of the coupling term (left-hand side minus right-hand side of Eq. 9-27) for (**a**) F^-, (**b**) Cl^-, (**c**) Li^+ and (**d**) Na^+

repulsion active, the electrons are driven further in that direction. The anions have wider distributions, and the most polarizable ion, Cl^-, has the broadest distribution, see Figure 9-2(b). The configurations with positive couplings can be explained in the opposite way to the negative couplings for the cations above. The negative couplings for the anions, F^- in particular, imply that a more complex mechanism operates as well. Our proposal to explain this is based on the solvation structure. It is obvious that in a given configuration there are gaps in the solvation cage to an ion. If the polarizing field on the ion from the solvent is directed such that the polarized charge distribution points towards these gaps, then the polarization of the ion can lower the repulsion, compared to the situation when there is no relaxation. Hence, a negative coupling follows.

The magnitudes of the couplings show that for the two cations, it would involve no significant error to use Eq. (9-27). For the anions, we see that the coupling is larger, and for the chloride ion, it is of the order of the thermal energy at room temperature. But as stated above, we have not reached basis-set saturation with respect to the gas-phase polarizability, therefore the magnitudes are dependent on the basis set in the HF calculation. A more diffuse basis set would lead to a larger coupling. To underestimate the polarizability of the ion, and ignore the coupling, is a way to avoid some of the problems. However, since the repulsion is determined by the polarized effective wave function, the spherical symmetry of the repulsion, which is usually used in fully classical force-fields, is no longer exactly valid. This can have an influence on the hydration structure of polarizable ions. It has already been found in a previous simulation study that the polarizability alone lowers the symmetry of the solvation structure of monatomic ions [169]. Couplings between polarization and repulsion could also be of importance at interfaces. If the two media that make up the interface compress the electron differently, the polarizability becomes anisotropic. The polarization of ions at interfaces has attracted some interest recently [170,171,172].

9.3.2. Asymmetric Solvation from Many-Body Interactions

The solvation of *para*-benzoquinone (PBQ) in aqueous solution and its one-photon absorption spectrum are modelled with QMSTAT. The study reveals that the many-body nature of electronic polarization can have a complex influence on the solvation [139]. PBQ with four water molecules is schematically presented in Figure 9-3. We use the multiconfigurational quantum chemical method since excited states are of interest as well. The two lowest excited states are included together with the ground state. The excited states are near-degenerate, which is of importance for the spectrum; this aspect of the study is not reviewed here, though. A simulation with the ground state interacting with the solvent is done, and the spectrum and the solvation structure are analysed.

The analysis of the solvation structure to the ground state of PBQ reveals a noteworthy feature of the structure around the carbonyl oxygen atoms. If the solvent is closely coordinated to the oxygen atom on the one side of PBQ, it is more probable for the coordination on the other side of PBQ to be farther away. In mathematical terms, there is hence a negative correlation between the two sides of PBQ or, in other

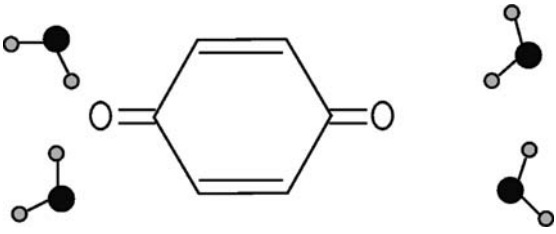

Figure 9-3. Para-benzoquinone and four water molecules distributed at the two carbonyl oxygen atoms

words, asymmetric solvation structures are more probable. In the original publication, this is shown by conditional distribution functions, $g(r_1|r_2 \in \mathcal{I}_i)$. Given that the distance between PBQ and the closest water molecule coordinated on one side, r_2, is within some interval $\mathcal{I}_i$, the distribution for the distance to the closest water molecule coordinated on the other side is obtained. If r_1 and r_2 are independent variables, then $g(r_1|r_2 \in \mathcal{I}_i) = g(r_1)$. However, this is not found to be the case. To provide an explanation based on simple properties of the molecules, two simplified models are formulated, which together with additional extended QMSTAT simulations give the following results [122]. The polarization of PBQ is the key to the asymmetry, or the correlation. If we qualitatively picture PBQ interacting with water as a polarizable, quadrupolar particle with one dipolar particle on the left-hand side and another dipolar particle on the right-hand side (with their dipoles $\boldsymbol{\mu}$ pointing directly at PBQ), then one term appears in the potential energy which involves the polarizability of PBQ, α:

$$U_{\text{pol.}} = -2|\boldsymbol{\mu}|^2\alpha\left(\frac{1}{r_1^3} - \frac{1}{r_2^3}\right)^2 \tag{9-28}$$

Obviously, when $r_1 = r_2$ the electric field from the dipoles perfectly cancel on PBQ, and no favourable polarization energy is obtained. For all other relative differences of r_1 and r_2, a stabilizing energy contribution is obtained. The statistical mechanical problem for the full potential energy of this simplified system is solved exactly with numerical integration for different polarizabilities on the central quadrupolar particle. A clear relation between magnitude of electronic polarizability and negative correlation (and thus asymmetry) is found. It should be observed that this follows from the many-body nature of the polarization and cannot be described by increasing the permanent moments to emulate the polarized state. Neither will a mean-field description of the solvent capture the additional contribution to the solvation from the asymmetry, since the average solvent configuration of course is symmetric.

9.3.3. Solute–Solvent Interactions in the L_a and L_b Excited States of Indole

We set up to study the fluorescence of indole in aqueous solution and also at the air–water interface [166]. Indole is a well-known chromophore, which is responsible for the photophysics of the amino acid tryptophan. Like many other medium-sized organic molecules, it has two low-lying excited states, known for historical reasons as L_a and L_b. Different interactions with the surrounding environment of these two states, as well as the ground state, lead to solvent (or more general environment) shifts to the one-photon spectrum. Most notably, the fluorescence spectrum of indole has long been known to be very sensitive to the polarity of the surrounding, a fact which is used by biophysical chemists to qualitatively monitor structure modifications of proteins [173,174,175,176,177,178,179]. The protein environment is a complex environment with many non-polar/polar interfaces. Since it is difficult to model proteins with high accuracy, we chose instead to make generalizations from the air–water interface simulations to the more complex protein environment.

Since QMSTAT is easily adapted to this interface (remove the dielectric boundary and allow indole to translate freely), we get the same accuracy as in the bulk simulations.

To explain the fluorescence behaviour in aqueous bulk, an L_a–L_b state inversion has been suggested. In gas phase the lowest excited state is L_b and is thus the state which emits light. But the L_a state is more polar, and hence in sufficiently polar media, L_a can become the state which emits light. There are other explanations in the literature, although the state-inversion one is the most used in the current literature. Our simulation of the aqueous bulk gives unequivocal support to the state-inversion explanation. Since QMSTAT is a state-based approach, with the wave function constructed as in Eq. (9-18), it is easy to assign the identity of the lowest excited state by a simple inspection of the expansion coefficients. The angle $\phi = \arctan|\frac{C_3}{C_2}|$ for the first and second excited states in the simulation will tell how L_a-like and L_b-like these states are, since the second state in the basis is the pure L_b state and the third state the pure L_a state (observe that $C_2^2 + C_3^2 \approx 1$). The distributions of ϕ for the first and second excited states are shown in Figure 9-4 for (a) the simulation where the ground state interacts with the solvent and (b) the simulation where the first excited state interacts with the solvent, where the geometry of indole is the optimal gas-phase geometry for the L_a state. It is seen from this figure that when the ground state interacts with the solvent, the reaction field on indole is not sufficient to cause a root flip, and the first excited state is best described as an L_b state. In contrast, when the first excited state in the given geometry interacts with the solvent, the first excited state has an identity much like an L_a state. Hence a root flip has occurred. In

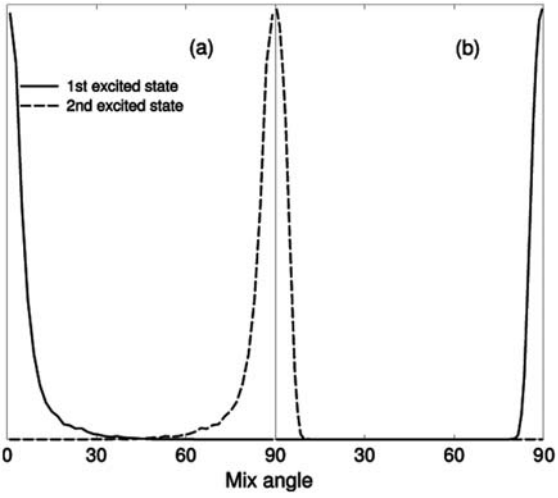

Figure 9-4. The distribution of the mix angle for the second and third state basis function for (**a**) the simulation with the ground state interacting with the solvent and (**b**) the simulation with the first excited state interacting with the solvent when indole is in the L_a optimal geometry

the simulation the first excited state interacts with the solvent, but in the L_b optimal geometry, it is found that the first excited state can be either L_a, L_b or a mixture (result not shown), in the ensemble of solute–solvent configurations. The conclusion is that even if the L_b state is occupied by the absorption of a photon, the solvent will eventually put the L_a state lower, and then the geometry changes and the L_a state becomes the lowest excited state. An inspection of the energies of the different states and how large their shifts are gives further support to this conclusion.

From the simulations at the air–water surface, the shift distributions given in Figure 9-5 are obtained for absorption and fluorescence. The orientation of indole relative to the surface is not completely optimized in the simulation, rather it is held partially restrained is some given way. With this approach, different types of orientations to the interface can be studied. We only report the results from the "wedge"-initialized simulations, with indole cutting into the surface with its benzene

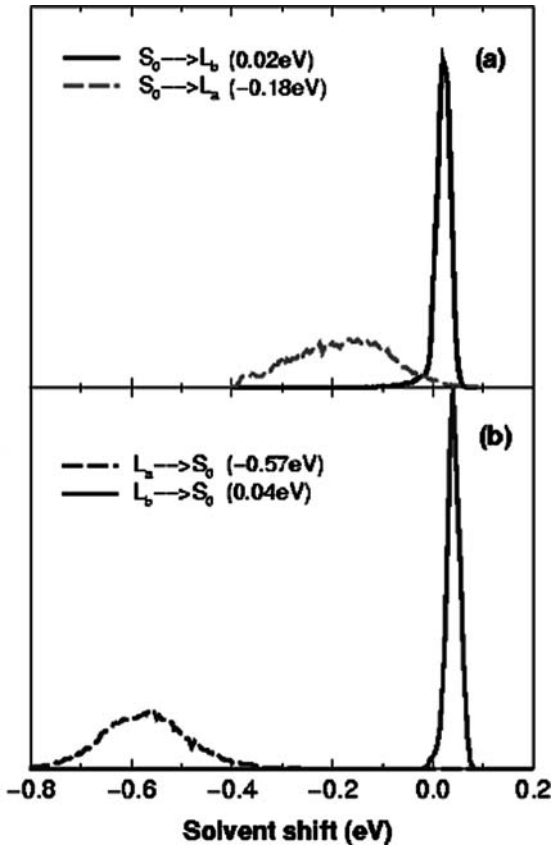

Figure 9-5. The solvent shift distributions for (**a**) the two absorption transitions and (**b**) the two fluorescence transitions in indole at the air–water interface

side pointing towards the air. To start with the absorption transitions, $S_0 \rightarrow L_b$ and $S_0 \rightarrow L_a$, they have the same qualitative behaviour as the transitions in bulk, that is, a tiny shift of $S_0 \rightarrow L_b$, on account of the similar interactions with the solvent of the two states, and a red-shift of $S_0 \rightarrow L_a$, on account of the stronger interactions the final state has with the solvent compared to the initial state. Quantitatively, the results for the $S_0 \rightarrow L_a$ transition are somewhat surprising: The shift for the same transition in aqueous bulk is -0.11 eV, which is smaller in magnitude than the -0.18 eV which is the shift in the interface simulation. Since, by definition, the shift is zero sufficiently far away from the water phase into the air, we can from these numbers conclude that the shift does not monotonously decrease as indole approaches the surface. For the fluorescence, the shift at the surface is more or less the same as in the bulk: -0.57 eV for the former environment, -0.58 eV for the latter. From an analysis of the electric potential over the molecule in the different environments and states, it is concluded that the interactions at the surface can be understood from two counter-acting effects: a *dielectric depletion* and an *interface-specific* effect. The former effect is expected and originates from the fact that there is less polar media present to respond to and interact with indole. It acts to decrease the shift. We identify the latter effect, which hence acts to increase the shift at the surface, to derive from stronger hydrogen bonds at the interface. In the bulk, there is a lot of water present to bind with, and hence the hydrogen bond formed between indole and water is not as strong as it can be, while at the surface there is a stronger bond formed since less water is present. Both the ground and the L_a state are stabilized by this, although the latter more, since it can form the strongest hydrogen bonds of the two states, as shown by supermolecular calculations of the indole–water dimer. As a consequence, this effect will act to increase the magnitude of the shift for both the $S_0 \rightarrow L_a$ and the $L_a \rightarrow S_0$ transitions. It should be noted that previous simulations studies, and more recently experiment, have also shown that water at hydrophobic surfaces forms stronger hydrogen bonds [180,181,182,183,184,185,186,181187].

As a final note, we point out two special advantages of QMSTAT for this study. First, to study the fluorescence, the solvent configurations have to be sampled with the solvent interacting with the excited state of indole. The sequential approach would require classical force-field parameters valid for excited states, which are more difficult to obtain. In QMSTAT, this is not a problem. Second, the nature of the excited state in this study is an issue. With QMSTAT, the solute–solvent interactions, the solvent configurations and the properties of the excited solute are coupled, and hence the nature of the excited state is not assumed, in any instance, but follows from the simulation.

9.4. SUMMARY

The discrete effective quantum chemical solvent model QMSTAT has been presented in detail, in its present formulation. The presentation emphasizes the connection between the quantum chemical model, the intermolecular interactions and the statistical mechanical description, which exists in any quantum chemical solvent model. In

QMSTAT the redundancy of some standard quantum chemical methods is reduced to obtain compact basis sets for both the HF method and a state-based multiconfigurational method similar to CASSCF. This is achieved by a few calculations, which precede the actual simulation; the subsequent simulation then proceeds with much less computational effort compared to what had been the case without such preparations. This enables QMSTAT to solve the statistical mechanical problem with the hybrid approach, which is exact in the limit of infinite sampling. Consequently, there is special focus on the statistical mechanical side of the solvation problem in QMSTAT, and in situations where the quantum chemical solution is strongly coupled to the statistical mechanical solution and vice versa, such as in the solvation of the monatomic ions and indole, described above, QMSTAT is expected to be a good choice. The use of a non-electrostatic perturbation to model the Pauli effects is also fairly unique in this context, although it has been used in other instances of molecular modelling. Early theory on solvochromism and simulations of simple systems has commented on the influence the modified repulsion between solute and solvent has upon an instantaneous transition in one-photon spectroscopy. QMSTAT is hence able to include some of these effects.

REFERENCES

1. Margenau H, Kestner NR (1969) Theory of Intermolecular Forces, Pergamon Press Ltd., 1st ed. Headington Hill Hall, Oxford
2. Buckingham AD, Utting BD (1970) Ann Rev Phys Chem 21:287–316
3. Pople JA (1982) Faraday Discuss Chem Soc 73:7–17
4. Israelachvili JN (1992) Intermolecular and surface forces 2nd ed. Academic Press, London
5. Jerziorski B, Moszynski R et al. (1994) Chem Rev 94:1887–1930
6. Woon DE (1994) J Chem Phys 100:2838–2850
7. Stone AJ (1996) The Theory of Intermolecular Forces, 1st edn. Oxford University Press, Oxford
8. Engkvist O, Åstrand P-O et al. (2000) Chem Rev 100:4087–4108
9. Chałasiński G, Szczęśniak MM (2000) Chem Rev 100:4227–4252
10. Coulson CA (1960) Rev Mod Phys 32:170–177
11. Pople JA (1965) J Chem Phys 43:S229–S230
12. Karplus M (1990) J Phys Chem 94:5435–5436
13. Ángyán JG (1992) J Math Chem 10:93–137
14. Tomasi J, Perisco M (1994) Chem Rev 94:2027–2094
15. Cramer CJ, Truhlar DG (1999) Chem Rev 99:2161–2200
16. Luque FJ, Curutchet C et al. (2003) Phys Chem Chem Phys 5:3827–3836
17. Tomasi J (2004) Theor Chem Acc 112:184–203
18. Tomasi J, Mennucci B et al. (2005) Chem Rev 105:2999–3093
19. Öhrn A, Karlström G (2007) Theor Chem Acc 117:441–449
20. Moriarty NW, Karlström G (1996) J Phys Chem 100:17791–17796
21. Öhrn A, Karlström G (2006) Mol Phys 104:3087–3099
22. Wallqvist A, Ahlström P et al. (1990) J Phys Chem 94:1649–1656
23. Stillinger FH, Rahman A (1974) J Chem Phys 60:1545–1557
24. Berendsen HJC, Grigera JR et al. (1987) J Phys Chem 91:6269–6271
25. Rullmann JAC, van Duijnen PT (1988) Mol Phys 63:451–475

26. Rick SW, Stuart SJ (2002) Rev Comp Chem 18:89–146
27. Tapia O (1991) J Mol Struct (THEOCHEM) 72:59–72
28. de Vries AH, van Duijnen PT et al. (1995) J Comp Chem 16:37–55
29. Jansen G, Colonna F et al. (1996) Int J Quant Chem 58:251–265
30. Böttcher CJF, van Belle OC et al. (1973) Theory of Electric Polarization, vol. 1, 2nd ed. Elsevier Scientific Publishing Company, Amsterdam
31. Friedman HL (1975) Mol Phys 29:1533–139
32. Wallqvist A (1993) Mol Sim 10:13–17
33. Petraglio G, Ceccarelli M et al. (2005) J Chem Phys 123:44103
34. Buckingham AD (1959) Quart Rev 13:183–214
35. Ahlrichs R (1976) Theor Chim Acta 41:7–15
36. Hall GG, Smith CM (1984) Int J Quant Chem 25:881–890
37. Hall GG, Smith CM (1986) Theor Chim Acta 69:71–81
38. Guillot B, Guissani Y (2001) J Chem Phys 114:6720–6733
39. Paricaud P, Předota M et al. (2005) J Chem Phys 122:244511
40. Piquemal JP, Cisneros GA et al. (2006) J Chem Phys 124:104101
41. Elking D, Darden T et al. (2007) J Comp Chem 28:1261–1274
42. Applequist J, Carl JR et al. (1972) J Am Chem Soc 94:2952–2960
43. Thole BT (1981) Chem Phys 59:341–350
44. van Duijnen PT, Swart M (1998) J Phys Chem A 102:2399–2407
45. Hellmann H (1935) J Chem Phys 3:61
46. Phillips JC, Kleinman L (1959) Phys Rev 116:287–294
47. Weeks JD, Rice SA (1968) J Chem Phys 49:2741–2755
48. Bonifacic V, Hunzinaga S (1974) J Chem Phys 60:2779–2786
49. Kahn LR, Baybutt P et al. (1976) J Chem Phys 65:3826–3853
50. Szasz L (1985) Pseudopotential theory of atoms and molecules, John Wiley & Sons, New York
51. Pelissier M, Komiha N et al. (1988) J Comp Chem 9:298–302
52. Andrae D, Häussermann U et al.(1990) Theor Chim Acta 77:123–141
53. Dolg M. Grotendorst J (2000) In: Modern Methods and Algorithms of Quantum Chemistry, NIC Series, Vol 3. John von Neumann Institute for Computing, Jülich, pp 507–540
54. Barandiarán Z, Seijo L (1988) J Chem Phys 89:5739–5746
55. Seijo L, Barandiarán Z et al. (1993) J Chem Phys 98:4041–4046
56. Seijo L, Barandiarán Z (1996) Int J Quant Chem 60:617–634
57. Seijo L, Barandiarán Z (2003) J Chem Phys 118:5335–5346
58. Nicolas G, Durand P (1980) J Chem Phys 72:453–463
59. Huzinaga S (1991) J Mol Struct (THEOCHEM) 234:51–73
60. Poteau R, Ortega I et al. (2001) J Phys Chem A 105:198–205
61. Abarenkov IV, Antonova IM (2004) Int J Quant Chem 100:649–660
62. Carissan Y, Bessac F et al. (2006) Int J Quant Chem 106:727–733
63. Schnitker J, Rossky PJ (1987) J Chem Phys 86:3462–3470
64. Wallqvist A, Thirumalai D et al. (1987) J Chem Phys 86:6404–6418
65. Vaidehi N, Wesolowski TA et al. (1992) J Chem Phys 97:4264–4271
66. Panas I (1993) Chem Phys Lett 201:255–260
67. Panas I (1993) Chem Phys Lett 206:312–317
68. Yoshida N, Kato S (2000) J Chem Phys 113:4974–4984
69. Hart EJ, Boag JW (1962) J Am Chem Soc 84:4090–4095
70. Car R, Parrinello M (1985) Phys Rev Lett 55:2471–2474
71. Kerdcharoen T, Liedl KR et al. (1996) Chem Phys 211:313–323

72. Murrell JN, Randić M et al. (1965) Proc Roy Soc A 284:566–581
73. Jeziorski B, Bulski M et al. (1976) Int J Quant Chem 10:281–297
74. Gresh N, Claverie P et al. (1986) Int J Quant Chem 29:101–118
75. Wallqvist A, Karlström G (1989) Chem Scr 29A:131–137
76. Wheatley RJ, Price SL (1990) Mol Phys 69:507–533
77. Jensen JH, Gordon MS (1996) Mol Phys 89:1313–1325
78. Gavezzotti A (2003) J Phys Chem B 107:2344–2353
79. Valderrama E, Wheatley RJ (2003) J Comp Chem 24:2075–2082
80. Gresh N, Piquemal JP et al. (2005) J Comp Chem 26:1113–1130
81. Söderhjelm P, Karlström G et al. (2006) J Chem Phys 124:244101
82. Mayer JE, Mayer MG (1933) Phys Rev 43:605–611
83. Pyper NC, Pike CG et al. (1992) Mol Phys 76:353–372
84. Giese TJ, York DM (2004) J Chem Phys 120:9903–9906
85. Öhrn A, Karlström G (2004) J Phys Chem B 108:8452–8459
86. Krishtal A, Senet P et al. (2006) J Chem Phys 125:034312
87. Heaton RJ, Madden PA et al. (2006) J Chem Phys 125:144104
88. Serr A, Netz RR (2006) Int J Quant Chem 106:2960–2974
89. Price WC, Sherman WF (1960) Proc Roy Soc A 255:5–21
90. Zipp A, Kauzmann W (1973) J Chem Phys 59:4215–4224
91. Nowak R, Bernstein ER (1987) J Chem Phys 87:2457–2465
92. Larrégaray P, Cavina A et al. (2005) Chem Phys 308:13–25
93. Bayliss NS, McRae EG (1954) J Phys Chem 58:1002–1006
94. Dobosavljević V, Henebry CW et al. (1988) J Chem Phys 88:5781–5789
95. Dobosavljević V, Henebry CW et al. (1989) J Chem Phys 91:2470–2478
96. Surján P, Ángyán JG (1994) Chem Phys Lett 225:258–264
97. Chalmet S, Ruiz-López M (2000) Chem Phys Lett 329:154–159
98. Tang KT, Toennies JP (1984) J Chem Phys 80:3726–3741
99. Brdarski S, Karlström G (1998) J Phys Chem A 102:8182–8192
100. London F (1942) J Phys Chem 46:305–316
101. London F (1930) Z Phys 60:245–279
102. London F (1930) Z Phys Chem B 11:222–251
103. Stone AJ, Tong C-S (1989) Chem Phys 137:121–135
104. Thole BT, van Duijnen PT (1980) Theor Chim Acta 55:307–318
105. Thole BT, van Duijnen PT (1982) Chem Phys 71:211–220
106. van Duijnen PT, de Vries AH (1996) Int J Quant Chem 60:1111–1132
107. Ángyán JG, Jansen G (1990) Chem Phys Lett 175:313–318
108. Li J, Cramer CJ et al. (2000) Int J Quant Chem 77:264–280
109. Szabo A, Ostlund NS (1989) Modern Quantum Chemistry 2nd edn. Dover Publications, Mineola
110. Hall GG (1951) Proc Roy Soc A 205:541–552
111. Roothaan CCJ (1951) Rev Mod Phys 23:69–89
112. Bernhardsson A, Lindh R et al. (1996) Chem Phys Lett 251:141–149
113. Löwdin P-O (1955) Phys Rev 97:1474–1489
114. Davidsson ER (1972) Rev Mod Phys 44:451–464
115. Almlöf J, Taylor PR (1987) J Chem Phys 86:4070–4077
116. Widmark P-O, Malmqvist P-Å et al. (1990) Theor Chim Acta 77:291–306
117. Widmark P-O, Persson BJ et al. (1991) Theor Chim Acta 79:419–432
118. Pierloot K, Dumez B et al. (1995) Theor Chim Acta 90:87–114
119. Roos BO, Veryazov V et al. (2004) Theor Chem Acc 111:345–351

120. Tofteberg T, Öhrn A et al. (2006) Chem Phys Lett 429:436–439
121. Öhrn A, Karlström G (2007) Chem Phys Chem 8:523–525
122. Öhrn A, Karlström G (2007) J Chem Theory Comput 3:1993–2001
123. Karlström G (1981) In: VanDuijnen PT, Nieuwpoort WC (ed) Proceeding of fifth seminar on Computational Methods in Quantum Chemistry, Laboratory of Chemical Physics, University of Groningen, Groningen, The Netherlands, p 353
124. Stone AJ (1981) Chem Phys Lett 83:233–239
125. Stone AJ, Alderton M (1985) Mol Phys 56:1047–1064
126. Stone AJ (2005) J Chem Theory Comput 1:1128–1132
127. Söderhjelm P, Krogh JW et al. (2007) J Comp Chem 28:1083–1090
128. Roos BO, Taylor PR et al. (1980) Chem Phys 48:157–173
129. Roos BO (1987) Adv Chem Phys 69:399–445
130. Roos BO, Andersson K (1992) Chem Phys Lett 192:5–13
131. Stålring J, Bernhardsson A et al. (2001) Mol Phys 99:103–114
132. Serrano-Andrés L, Roos BO (1996) J Am Chem Soc 118:185–195
133. Serrano-Andrés L, Fülscher MP et al. (1997) Int J Quant Chem 65:167–181
134. Sánchez ML, Martín ME et al. (2002) J Phys Chem B 106:4813–4817
135. Losa AM, Galván IF et al. (2006) J Phys Chem B 110:18064–18071
136. Borin AC, Serrano-Andrés L et al. (2006) Int J Quant Chem 106:2564–2577
137. Malmqvist PÅ (1986) Int J Quant Chem 30:479–494
138. Malmqvist PÅ, Roos BO (1989) Chem Phys Lett 155:189–194
139. Öhrn A, Aquilante F (2007) Phys Chem Chem Phys 9:470–480
140. Metropolis N, Rusenbluth AW et al. (1953) J Chem Phys 21:1087–1092
141. Hastings WK (1970) Biometrika 57:97–109
142. Robert CP, Casella G (2004) Monte Carlo statistical methods 2nd edn. Springer, New York
143. Brooks SP, Roberts GO (1998) Stat Comput 8:319–335
144. Coutinho K, Canuto S (1997) Adv Quant Chem 28:89–105
145. Coutinho K, Canuto S (2003) J Mol Struct (THEOCHEM) 632:235–246
146. Rivelino R, Cabral BJC et al. (2005) Chem Phys Lett 407:13–17
147. Grozema FC, van Duijnen PT (1998) J Phys Chem A 102:7984–7989
148. Kongsted J, Osted A et al. (2004) J Chem Phys 121:8435–8445
149. Andersson K, Malmqvist P-Å (1990) J Phys Chem 94:5483–5488
150. Andersson K, Malmqvist P-Å et al. (1992) J Chem Phys 96:1218
151. Roos BO, Andersson K et al. (1996) Adv Chem Phys 93:219–331
152. Boys SF, Bernardi F (1970) Mol Phys 19:553–566
153. van Duijneveldt FB, van Duijneveldt-van de Rijdt JGCM et al. (1994) Chem Rev 94:1873–1885
154. Becke AD, Johnson ER (2005) J Chem Phys 122:154104
155. Johnson ER, Becke AD (2005) J Chem Phys 123:024101
156. Lindh R, Malmqvist P-Å et al. (2001) Theor Chem Acc 106:178–187
157. Gagliardi L, Lindh R et al. (2004) J Chem Phys 121:4494–4500
158. Zwanzig RW (1954) J Chem Phys 22:1420–1426
159. Lu N, Singh JK et al. (2003) J Chem Phys 118:2977–2984
160. Lu N, Kofke DA et al. (2003) J Comp Chem 25:28–39
161. Moriarty NW Karlström G (1997) J Chem Phys 106:6470–6474
162. Moriarty NW, Karlström G (1997) Chem Phys Lett 279:372–376
163. Hermida-Ramón JM, Karlström G (2003) J Phys Chem A 107:5217–5222
164. Hermida-Ramón JM, Karlström G (2004) J Mol Struct (THEOCHEM) 712:167–173
165. Öhrn A, Karlström G (2006) J Phys Chem A 110:1934–1942

166. Öhrn A, Karlström G (2007) J Phys Chem A 111:10468–10477
167. Klopper W, Schütz M et al. (1995) J Chem Phys 103:1085–1098
168. Schütz M, Brdarski S et al. (1997) J Chem Phys 107:4597–4605
169. Carignano MA, Karlström G et al. (1997) J Phys Chem B 101:1142–1147
170. Jungwirth P, Tobias DJ (2002) J Phys Chem B 106:6361–6373
171. Hagberg D, Brdarski S et al. (2005) J Phys Chem B 109:4111–4117
172. Jungwirth P, Tobias DJ (2006) Chem Rev 106:1259–1281
173. Teale FWJ, Weber G (1957) Biochem J 65:476–482
174. van Duuren BL (1963) Chem Rev 63:325–354
175. Mataga N, Torihashi Y et al. (1964) Theor Chim Acta 2:158–167
176. Beechem JM, Brand L (1985) Annu Rev Biochem 54:43–71
177. Valeur B (2001) Molecular fluorescence, principles and applications Wiley-VCH, Weinheim
178. Jameson DM, Croney JC et al. (2003) Methods Enzymol 360:1–43
179. Royer CA (2006) Chem Rev 106:1769–1784
180. Lee CY, McCammon JA et al. (1984) J Chem Phys 80:4448–4455
181. Linse P (1987) J Chem Phys 86:4177–4187
182. Wallqvist A (1990) Chem Phys Lett 165:437–442
183. Du Q, Superfine R et al. (1993) Phys Rev Lett 70:2313–2316
184. Benjamin I (1996) Chem Rev 96:1449–1475
185. Liu P, Harder E et al. (2005) J Phys Chem B 109:2949–2955
186. Richmond GL (2001) Chem Rev 102:2693–2724
187. Benjamin I (2006) Chem Rev 106:1212–1233

CHAPTER 10

MOLECULAR DYNAMICS SIMULATION METHODS INCLUDING QUANTUM EFFECTS

THOMAS S. HOFER, BERNHARD R. RANDOLF, AND BERND M. RODE

Theoretical Chemistry Division, Institute of General, Inorganic and Theoretical Chemistry, University of Innsbruck, Innrain 52a, A-6020 Innsbruck, Austria, e-mail: Bernd.M.Rode@uibk.ac.at

Abstract: The progress of computational chemistry in the treatment of liquid systems is outlined, and the combination of the statistical methods (in particular molecular dynamics) with quantum mechanics as the main foundation of this progress is emphasised. The difficulties of experimental studies of liquid systems without having obtained sophisticated theoretical models describing the structural entities and the dynamical behaviour of these liquids demonstrate that chemistry research is in a transition phase, where theory and high-performance computing have not only become a valuable supplement, but an essential and almost indispensable component to secure a correct interpretation of measured data in solution chemistry

Keywords: Statistical simulations, Structure of liquids, Picosecond dynamics, Ab initio simulation methods, QM/MM simulations, QMCF MD simulations

10.1. INTRODUCTION

As most chemical and virtually all biochemical processes occur in liquid state, solvation of the reaction partners is one of the most prominent topics for the determination of chemical reactivity and reaction mechanisms and for the control of reaction conditions and resulting materials. Besides an exhaustive investigation by various experimental methods [1,2,3], theoretical approaches have gained an increasing importance in the treatment of solvation effects [4,5,6,7,8]. The reason for this is not only the need for sufficiently accurate models for a physically correct interpretation of the experimental data (Theory determines, what we observe!), but also the limitation of experimental methods in dealing with ultrafast reaction dynamics in the pico- or even subpicosecond regime. These processes have become more and more the domain of computational simulations and a critical evaluation of the accuracy of simulation methods covering experimentally inaccessible systems is of utmost importance, therefore.

On the other hand, even simulations by the relatively crude force field methods already reveal the striking influence of solvation phenomena, for example, when

S. Canuto (ed.), Solvation Effects on Molecules and Biomolecules, 247–278.
DOI 10.1007/978-1-4020-8270-2_10,

structure and dynamical transformations of simple oligopeptides are studied in vacuo and embedded in water: the strong differences become visible within picoseconds of the simulations, clearly proving the necessity of considering solvent effects in the determination of biopolymer structures. Therefore, it should also be obvious that crystal structures of such compounds cannot be expected to reflect the structures actually present in their biological environment.

When dealing with biological processes, ions constitute an essential foundation of numerous vital processes, particularly in the formation of electrical and osmotic equilibria controlling cell chemistry [9,10,11]. Numerous ions display strong toxic effects and their similarity or difference to the biologically important ions is the basis for understanding their noxious effects. Especially metal cations are important in this context, and these ions show enormous differences in their solvation effects, e.g. exchange rates varying within more than 20 orders of magnitude [3]. Most of the biologically important metal ions' solvent exchange rates correspond to extremely fast processes with mean lifetimes of solvated species below the nanosecond range and thus beyond most of the experimental capabilities and are, consequently, a real challenge for computational theoretical methods. Such ultrafast exchange processes cause a simultaneous presence of several solvated species with different compositions and different structures, and the interpretation of the reactivity of such ions has to consider this multispecies presence – and any experimental investigation which can only obtain a time-averaged result might not be adequate for this interpretation. However, the subtle energetic differences between these species require a very high methodical accuracy of the simulations. A comparison of results for solvated ions obtained by classical pair or even three-body-corrected potential simulations immediately reveals that even structural averages might not be correctly reflected by these approaches, and that polarisation and charge transfer effects have to be appropriately introduced in the methodology. Investigations in the past decade have clearly proven that only a quantum mechanical treatment of energy and forces can provide the required accuracy for this purpose [8,12].

Even with the best computational resources available to date a complete quantum mechanical treatment of a simulation box containing a solute and a sufficient number of solvent molecules representative of a realistic liquid state is still far from feasibility. The subsequent chapter on simulation methods will show, which compromises have been sought to overcome this problem, and demonstrate the enormous requirements of computer capacity and central processor (CP) time for simulations at the level including quantum mechanics. A first idea of this effort can be easily gained by the consideration of a medium-sized solvate consisting of a solute and only one complete solvation layer (which often is not sufficient to embrace all solvation effects). Assuming as example a simple anion such as phosphate, whose first hydration layer contains between 12 and 15 water molecules, one has to deal with a system of one third-row element, 16–19 second-row elements and 24–30 hydrogen atoms. This system has to be embedded then in another 500–1000 solvent molecules, for which the quantum effects could be neglected as long as a continuous transition of solvent molecules to and from the solvate itself is properly managed. To perform a

Monte Carlo (MC) simulation of the previously sketched solvate with a satisfactory statistical sampling implies the quantum mechanical energy calculation of this system in at least a few million different configurations. For a molecular dynamics (MD) simulation with timesteps short enough to properly describe also hydrogen movements ($\sim$0.2 fs), a 20 ps trajectory already requires 100,000 calculations, in this case not only of energies but also of the forces acting on all particles. In both cases one easily arrives at CP times of several months, even using all possibilities of parallelising the computations. The actual computation time then still depends on the level of accuracy employed in the quantum mechanical formalism. Simplified procedures such as semiempirical molecular orbital (MO) or common density functional methods [13,14,15] and even single-zeta ab initio Hartree–Fock (HF) calculations [16] have, unfortunately, proven not to be accurate enough to describe solvated ions in a proper way. On the other hand, correlated ab initio methods, even at the very simple perturbational MP/2 level, are boosting computing times to a still unaffordable extent.

At present, ab initio simulations have to be performed, therefore, with a modest but sufficient size of the quantum mechanical part of the system, and the basis set as well as the employed quantum mechanical level will always be a compromise between accuracy and computational effort. However, the continuous improvement of computer technology and theoretical concepts are shifting these limits year by year, and an optimistic outlook to the future of simulation work is fully justified, therefore.

The examples of applications given in the latter part of this chapter will show that even at the present state of the art and technology, many solvated ions could be treated with sufficient quality to obtain reliable results not only for structural details and species distributions, but also for the aforementioned ultrafast dynamical processes determining the chemical behaviour of such solvates. On the other hand, the latest improvements of the simulation methodology have opened a straightforward access to the treatment of other arbitrary solvated systems as computational capabilities increase. Therefore, simulation methods are not only becoming a valuable research field of their own, but also an essential supplement – if not prerequisite – for the interpretation of experimental investigations of solvates.

In the following, an overview of the methodical framework of molecular dynamics (MD) simulations will be given, which – in contrast to MC simulations – also deliver dynamical data including rovibrational spectra. Quality, capability and limitations of the methods will then be illustrated by a number of representative examples.

10.2. METHODOLOGIES FOR SIMULATING LIQUID SYSTEMS

Statistical simulation methods can be basically separated into two approaches. The Monte Carlo (MC) framework [17,18,19] utilises random structural variations of single structural units (atoms, molecules, groups, etc.) followed by an evaluation of energies to decide whether the resulting new arrangement of atoms is accepted or should be discarded. Sampling of molecular dynamics (MD) employs equations

of motion [18,19,20,21] – particles are propagated according to their respective positions, velocities and forces. Whereas only the total energy of the system is required in a Monte Carlo simulation, the forces acting on all particles have to be evaluated in the case of a molecular dynamics study. The evaluation of these methods is based on statistical mechanics [22].

Besides the requirement of accurate algorithms to integrate the equation of motions in MD simulations the accuracy of the forces plays a pivotal role. Methodologies to derive intermolecular forces can be divided into two main groups – molecular mechanics (MM) or quantum mechanics (QM).

10.2.1. Molecular Mechanics

Methods relying on parametrised potential functions for the description of energy hypersurfaces are commonly referred to as molecular mechanics (MM) or classical mechanics and these methods have a long tradition in computational chemistry. Entire data sets of balanced potential functions and their respective parameters are referred to as *force fields* [23,24,25]. The key advantage of MM methods is the low computational demand compared to quantum mechanical computations.

In general force fields are divided into bonding and non-bonding potential contributions. Bonding potentials, containing contributions such as intramolecular bonds, angles and torsions, are not required for the treatment of hydrated ions except for solute molecules such as water (in this case only bonding and angle contributions are required). Non-bonding interactions, consisting of Coulombic and non-Coulombic contributions, are mandatory for all kinds of pair interactions including ion–solvent interactions.

The representation of chemical systems on the basis of parametrised potential functions is by no means trivial and endless efforts have been devoted to balance and refine the employed parameters and functions yielding a considerable number of force fields along with various different parameter sets. These parameter sets are aimed at distinct classes of chemical systems, basically organic compounds, nucleic acids or proteins, whereas the treatment of compounds involving metal atoms is more difficult.

In many previous studies [8,12] potential functions have been newly constructed ensuring the compatibility with the parameters (e.g. partial charges) of the solvent potentials. The first step involves the scanning of the energy hypersurface of the respective ion–solvent interaction at an adequate ab initio level. Figure 10-1a illustrates the degrees of freedom in the scanning of ion–water interactions. Afterwards the obtained data set consisting of several thousand individual interaction points is fitted to a suitable analytical form representing the pair interaction energies (e.g. ion–oxygen and ion–hydrogen in the case of water). The analytical representation for ion–ligand interactions in general consists of a Coulomb term plus a set of r^{-n} terms with n ranging from 4 to 12 and eventually an exponential function improving the description of the non-Coulombic interactions. One of the most common representations is the 6–12 Lennard-Jones potential consisting only of two terms, r^{-6} and r^{-12}. Other suitable potential forms than those given in Eq. (10-1)

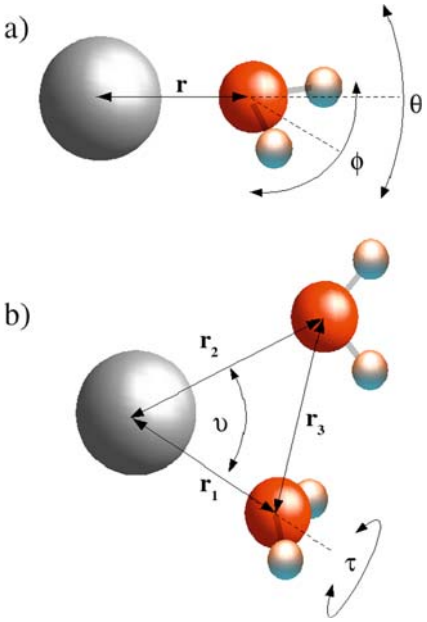

Figure 10-1. Scheme for the scan of an ion–water (**a**) two-body and (**b**) three-body hypersurface

could be utilised as well. The choice of the partial charges q_i and q_j as well as the exponents a to d is crucial – the parameters A–F are obtained from the fitting procedure:

$$V_{\mathrm{ij}}^{\mathrm{pair}} = \frac{q_i q_j}{r_{12}} + \frac{A}{r_{ij}^a} + \frac{B}{r_{ij}^b} + \frac{C}{r_{ij}^c} + \frac{D}{r_{ij}^d} + E \cdot \mathrm{e}^{F \cdot r_{ij}} \qquad \left(4 \le a, b, c, d \le 12\right) \tag{10-1}$$

Not every possible combinations results in an applicable potential: artificial minima in the function as well as a non-physical 'black hole' behaviour close to the nucleus have to be avoided by all means and thus all obtained potential functions have to be critically evaluated. Among the valid pair potentials those showing the lowest root mean square deviation are to be preferred. Despite this considerable effort, the accuracy of these functions is limited. Due to the fitting procedure these pair potentials resemble the energy hypersurface in an average way. Furthermore, polarisation and charge transfer as well as many-body effects are not considered in this simple pair approach. One method to account for these effects in an averaged way are polarisable interaction models [26,27,28] which vary potential parameters as for example the partial charges along the simulation. Another possibility is the implementation of hydrated ion models – atoms residing in the close vicinity of the ion are treated with different interaction potentials than those atoms located in the bulk. In general particles are not allowed to exchange between the different regions,

however, preventing the evaluation of short time dynamics such as mean residence times.

Another frequently used possibility is the construction of three-body potentials correcting the pair interaction potentials with respect to three-body terms. In analogy to the case of pair potentials a scan of the energy hypersurface has to be carried out by varying degrees of freedom (see Figure 10-1b for an ion–water–water scan). Naturally, the number of interaction points required for a representative sampling is considerably higher than in the case of pair interactions. In general tens of thousands of different configurations need to be calculated. The deviation between the energy resulting from the previously constructed pair potential and the interaction energy based on the three-body QM calculation is fitted to an adequate analytical representation. Again, the parameters A–E are obtained via the fitting procedure; r_{cut} is a suitable cutoff distance beyond which three-body effects become negligible:

$$V_{\mathrm{ijk}}^{\mathrm{3bd}} = \left(A \cdot \mathrm{e}^{-B\cdot(r_{ij}+r_{ik})} \cdot \mathrm{e}^{-C\cdot r_{jk}} - \frac{D}{r_{ij}^{k}} - \frac{D}{r_{ik}^{k}} - \frac{E}{r_{jk}^{k}} \right) \cdot \left(r_{\mathrm{cut}} - r_{ij}\right)^{2} \left(r_{\mathrm{cut}} - r_{ij}\right)^{2} \tag{10-2}$$

The construction of four-body correction potentials is even much more complex and as four-body terms have only small contributions to the total interaction energy are rarely performed. Therefore, only two-body potentials and eventually a three-body correction are utilised in the majority of classical simulations.

However, it has been shown that despite the tedious effort devoted to the construction of potential functions the results of classical simulations are error prone and often fail to predict even crude properties of hydrates such as coordination numbers and, therefore, related properties such as species distributions and geometries.

It has been shown that shell models are capable of improving the description, but other shortcomings like the lack of exchange of ligands between the different potential regions restrain the simulation. Polarisable models on the other hand take into account only polarisation effects, while the non-Coulombic contributions remain unchanged.

10.2.2. Quantum Mechanics

An alternative to the molecular mechanical approach is the quantum mechanics (QM) framework. Much of work has been devoted in the past decades to establish and improve QM methodologies ranging from simple semiempirical methods to high-level correlated ab initio methods [20,21,29]. The substantial advantage of quantum mechanical calculations is the inclusion of all *n*-body effects, including charge transfer and polarisation. Furthermore, bonds are automatically formed and broken as necessary along the simulation.

The main disadvantage of QM methods is the associated complexity of the theoretical framework: the electronic Schrödinger equation can only be solved in a

numerical way for many-electron systems. A variety of computational methods is available nowadays showing different levels of accuracy which are strongly correlated to an enormous computational demand. Non-experts are likely to get lost among the different possibilities and instead of selecting appropriate methods, execute computations in a black box manner implicitly assuming the results to be reliable. Although the use of high-performance computing clusters for quantum mechanical computations is quite common, the number of particles and, therefore, the treatable system size is still limited–depending on the level of accuracy–between a few to one hundred atoms. A full ab initio treatment of even a small simulation box with a few hundred molecules is not feasible today and compromises between accuracy and computational effort have to be sought.

Simple studies reduce the system size to one full layer of hydration and so-called polarisable continuum models (PCM) are utilised to model the influence of the surrounding solvent [30]. Mostly geometry optimisations are carried out and conclusions are drawn based on energetic and geometric properties of the optimised complex [31]. The computational effort is considerably lower than a treatment including explicit solvent and so is the quality of results. First, the optimised structures correspond to an environment at 0 K thus neglecting all effects of entropy which is known to be one of the most crucial parameters determining solution chemistry. Thus, the comparison of structures showing different energies and geometries is likely to be misleading–for example species distributions within the hydration shells of hydrated ions cannot be discussed only on the basis of energetic data. Furthermore, polarisation effects are not incorporated in a proper way by most PCM methods as surface effects of the electron density cannot be excluded. Considering the influence of the nearest neighbour atoms (in this example the second hydration shell) it is obvious that the distribution of the atoms and, therefore, the resulting potential is inhomogeneous, while PCM accounts for an homogeneous influence of the surrounding solvent. Thus, the inclusion of a complete second hydration layer will improve the overall description of the electron density, but results in a substantial increase of the computational effort as well as in a more complicated sampling of the energy hypersurface. Point charge embedding in combination with a PCM appears to be a substantial improvement but will also complicate the treatment of the hypersurface.

Car–Parrinello (CP) type simulations [32] achieve the necessary compromise between effort and accuracy by reducing the number of particles as well as the simulation time on the one hand and by the employment of simple generalised gradient approximation density functionals such as PBE [33,34] or BLYP [35] on the other hand. In the case of hydrated ions the reduction of the number of solvent molecules is in many cases chosen too low to properly hydrate the ion and to reflect the surrounding bulk liquid. The reduction of the simulation time is sometimes at the expense of a proper equilibration period.

Although CP MD are often referred to as ‘first principle’ or ab initio simulations, this notation is highly questionable. Recent discussions [36,37,38,39] of the underlying density functional theory have concluded that present implementations utilise too many approximations and exhibit severe physical shortcomings like self-interaction

or a wrong description of the kinetic energy, thus rather justifying the classification as semiempirical methods and that a substantial revision of DFT methods has to be carried out to truly claim the ab initio status for these methods.

Another frequently used approach to reduce the computational effort is the hybrid quantum mechanical/molecular mechanical (QM/MM) framework which will be discussed in more detail below.

10.2.3. The Quantum Mechanical/Molecular Mechanical Scheme

In the QM/MM approach [40,41,42,43,44], the chemically most relevant subregion is treated by quantum mechanics while the remaining part is described by molecular mechanics potential functions. While the treatment of the subregions is straightforward, the coupling between the different zones is challenging, especially when molecules are exchanged or bonds are cut by the QM/MM interface. In general, much larger elementary boxes than in CP studies can be employed and the theoretical level of the quantum mechanical treatment is not restricted to simple density functionals – basically every affordable ab initio level can be applied in the treatment of the QM region.

The evaluation of interactions between particles inside and outside the quantum mechanical region is usually achieved on the basis of molecular mechanics, i.e. by the application of parametrised potential functions. Thus, parameters for partial charges and non-Coulombic interactions are required for all QM particles although these species are treated by quantum mechanics. The construction of these functions is a time-consuming and tedious task requiring the evaluation of thousands of solute–solvent interaction points, which afterwards have to be fitted to an analytical representation in agreement with all other MM functions like the solvent–solvent interactions. As mentioned earlier the accuracy of these functions is in many cases insufficient for the treatment of polarisable compounds such as solvated ions [4,5,6,7,8]. Sometimes these insufficiencies can be partially compensated by the inclusion of correction potentials as discussed above, but the accuracy is still not always satisfactory.

Today QM/MM methodologies are well-established tools and their applications are versatile and flexible. This framework is utilised in a variety of computational studies, typical examples are investigations related to solution chemistry [8] as well as the treatment of active sites of biomolecules [45]. Although the quantum mechanical effort is very high, increased accuracy and the ability to form and break chemical bonds as needed are the key feature for the implementation of this method. A variety of approaches have been described to realise the coupling between the high- and low-level regions [40]. One of the most prominent approaches is the ONIOM method (Our-own *N*-layered Integrated molecular Orbital and Molecular mechanics) [46,47], which allows to divide the system into an arbitrary number of layers each treated at a different level of theory. Typically the level of accuracy is decreasing when moving from the inside regions to the outside ones.

It was realised from extended QM/MM MD simulations (including first plus second hydration shells of an individual ion) [7,48,49,50,51] that the non-Coulombic contribution of the solute–solvent potential is negligibly small at the increased size of the quantum mechanical region (approximately a radius of 5–6 Å) and can be omitted, therefore. However, point charges are still required for the evaluation of Coulombic interactions. Results of the extended QM/MM MD simulations have indicated that the assignment of fixed partial charges as typically done in force field studies might be inappropriate in the case of highly polarising ions. For example an assignment of a +3 charge to Al(III) results in artefacts near the QM/MM border [50]. Although the QM treatment accounts properly for polarisation effects this information is not available in the MM treatment. A distinct 'pressure' of the MM particles onto the QM region occurs. The derivation of partial charges by population analysis during the simulation based on the molecular orbitals not only accounts for all polarisation effects but also gives the opportunity to adapt the partial charges to all structural changes occurring as the simulation proceeds. For example in the case of Al(III) the effective charge ranges from +2.0 to +2.5 units depending on the respective population analysis scheme and the current geometry of the system.

Finally, the inclusion of MM data into the QM region appears desirable so that the quantum mechanical treatment is 'aware' of its surrounding, i.e. the bulk of a liquid in its momentaneous structure. These so-called electrostatic embedding techniques [40,52,53] have been frequently employed in various quantum mechanical studies. Partial charges of the MM atoms resembling the chemical surrounding can be included as a perturbation part of the Hamiltonian, thus allowing the molecular orbitals to adapt to the surrounding potentials – otherwise surface effects resulting from a virtual vacuum environment are likely to cause artefacts near the QM/MM border.

These three critical points, namely the neglect of non-Coulombic contributions for solute atoms, a fluctuating charge distribution of the QM particles and electrostatic embedding of MM partial charges, lead to the formulation of the quantum mechanical charge field (QMCF) ansatz [54] which has been applied in molecular dynamics studies of various hydrated systems, recently.

The details of the QMCF methodology will be outlined in the next section. The embedding of MM partial charges will be discussed in more detail as the application of this technique in connection with the periodic simulation environment is by no means straightforward.

10.2.4. The Quantum Mechanical Charge Field Framework

10.2.4.1. The charge field approach

Similar as in all hybrid QM/MM methods [41,42,43,44] the system is partitioned into two subregions, the QM region centred on the chemically most relevant region and the MM zone containing the remaining part of the system. While the treatment of interactions within the subregions is the standardised application of the respective theoretical level, the coupling between the regions is rather complex.

In order to renounce all non-Coulombic solute–solvent potentials during the QM/MM coupling it has to be ensured that the distance between the interacting species and thereby the distance to the QM border is sufficiently large: all non-Coulombic interactions are beyond the non-Coulombic cutoff distance (see particle A and B in Figure 10-2a). Therefore, the QM region should contain at least two full layers of ligands, for example first plus second hydration shells in the case of a hydrated ion or a composite system like $[Fe(CN)_6]^{3/4+}$ or PO_4^{3-} plus one full layer of water. Ligands close to the QM/MM intersection (Figure 10-2a particle C) do not fulfil this condition and, therefore the non-Coulombic potentials have to be applied in any case which is referred to as 'potential embedding'.

Consequently, the QM zone is split into two subregions in order to distinguish between the respective species (cf. Figure 10-2b). The inner region has been termed 'QM core', the outer zone 'QM layer'. The main difference between these regions is the application of non-Coulombic interaction potentials–particles located in the 'QM core' area are not subject to potential embedding. In many cases first shell ligands are allowed to be included in this region (particle B in Figure 10-2a) as the cutoffs for the non-Coulombic interaction potentials are sufficiently small (e.g. a few Ångström in the case of the BJH-CF2 water model [55,56]). The only data required to account for the QM/MM coupling are partial charges which may be assigned to the different species as fixed charges at the beginning of the simulation, or preferably on the basis of the electron density obtained from the quantum mechanical treatment by performing a population analysis in every step of the simulation. As the only interaction between 'QM core' and MM particles is represented by Coulombic charge contributions (plus any optional long-range corrections for the Coulombic cutoff such as Ewald summation or reaction field schemes) this feature is considered as the 'charge field approach' in the framework of the 'quantum mechanical charge field' ansatz [54].

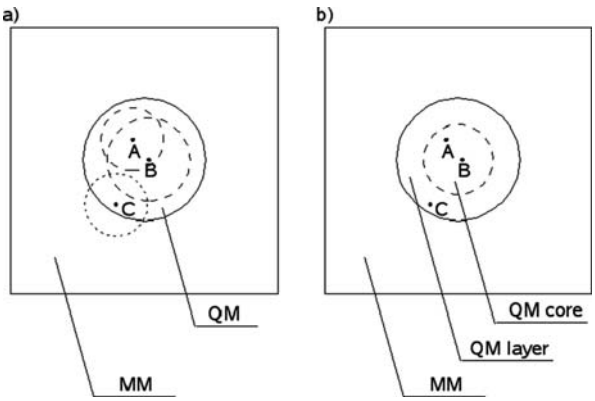

Figure 10-2. (**a**) The non-Coulombic interactions of particles A and B may be renounced due to the size of the QM region. Particle C is located too close to the QM/MM border, hence non-Coulombic potentials have to be applied. (**b**) Definition of the "QM core" and "QM layer" region

One crucial condition is that no solute species is leaving the 'core region', where no non-Coulombic potential data are supplied. Otherwise the particles would come too close to the QM/MM border and the charge field approximation will not be fulfilled anymore.

To evaluate the Coulombic interactions between QM (i.e. core and layer) and MM particles point charges have to be supplied and the respective energy and force contributions are calculated according to Coulomb's law. The simplest way is to assign predefined partial charges to all QM species. The assignment of too high charges like +3.0 unit charges in the case of Al(III) or +2.0 for Zn(II) resulted in an artificial behaviour in QM/MM transition region. Alternatively, partial charges can be derived on the basis of the electron density obtained from the QM calculation. This latter method accounts for all charge transfer, polarisation and many-body effects as well as for any change in geometry for example by rovibrational motion or ligand exchange reactions. Therefore, the latter method has been chosen as standard in the QMCF methodology.

10.2.4.2. Electrostatic embedding and the periodic box

The electrostatic embedding of MM partial charges as a perturbational potential in the Hamilton operator is a frequently used method to account for Coulombic interactions between QM atoms and MM point charges. As the respective potential contributions influence the quantum mechanical calculation and by that the molecular orbitals and the associated electron density, this approach is rated superior compared to a Coulombic interaction model utilising fixed partial charges.

The main objective of point charge embedding is the incorporation of an external field of partial charges (a charge field) into the quantum mechanical treatment in order to modify the molecular orbitals accordingly. Negative point charges repel the density while positive charges will result in an attraction. Figure 10-3b illustrates the difference of the total electron density in an Al(III) water complex including first plus second hydration shells with and without point charge embedding. Both hypersurfaces utilise the same threshold value, thus the total volumes are equivalent. In general the hypersurface of the calculation without embedded point charges (dark hypersurface) dominates, while the density with embedding (bright hypersurface) remains hidden except for distinct regions, demonstrating the influence of the external potential. For example MM partial charges of oxygen atoms with negative values located in the vicinity of QM hydrogen atoms result in a shift of the density away from the oxygen resulting in an improved description of hydrogen bonding – a subsequent population analysis thus yields higher partial charges of the respective hydrogen atoms. Thus, the description of the QM/MM coupling has been substantially improved.

The inclusion of point charges is achieved by adding the contributions of all MM point charges as a perturbational potential term $\hat{V}_{\mathrm{PC}}$ to the electronic Hamilton operator $\hat{H}^{\mathrm{el}}$:

$$\hat{H}^{\mathrm{el}}_{\mathrm{PC}} = \hat{H}^{\mathrm{el}} + \hat{V}_{\mathrm{PC}} \tag{10-3}$$

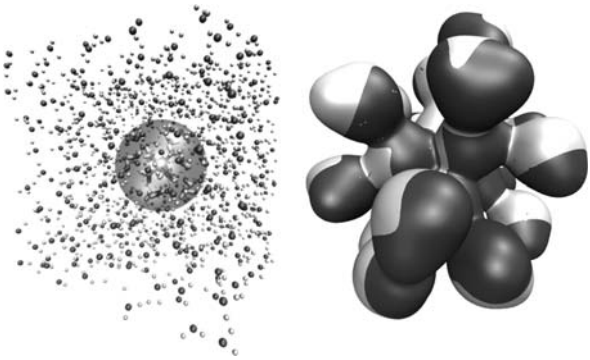

Figure 10-3. (**a**) The QM region (indicated by a sphere) surrounded by MM point charges. (**b**) Schematic electron density of an Al(III) water cluster with (*bright surface*) and without (*dark surface*) point charge embedding

$$\hat{H}_{PC}^{el} = -\frac{1}{2}\sum_{i=1}^{n}\hat{\nabla}^2 - \sum_{i=1}^{n}\sum_{J=1}^{N}\frac{q_J}{r_{iJ}} + \sum_{i=1}^{n-1}\sum_{j=i+1}^{N}\frac{1}{r_{ij}} - \sum_{i=1}^{n}\sum_{J=1}^{M}\frac{q_J}{r_{iJ}} \quad (10\text{-}4)$$

with M being the number of all MM point charges, n the number of electrons and N the number of QM nuclei. It can be deduced from Eq. (10-4) that the contributions of the nuclei–electron interactions and the electron–point charge interactions are similar: while in the first case the respective nuclear charge is employed in the latter case effective atomic charges are applied representing the electron population of the MM particles. Both contributions are included together with the kinetic energy operator in the *core* Hamiltonian $\hat{h}_{\mathrm{PC}}^{\mathrm{core}}$ which corresponds to the one-electron contributions:

$$\hat{h}_{PC}^{core} = -\frac{1}{2}\sum_{i=1}^{n}\hat{\nabla}^2 - \sum_{i=1}^{n}\sum_{J=1}^{N+M}\frac{q_J}{r_{iJ}} \quad (10\text{-}5)$$

As these contributions only involve the coordinates of one particular electron in the operator they are less demanding with respect to the computational effort and hence the embedding procedure does not significantly extend the computing time. A significant shortcoming is that common implementations do not distinguish the point charge energy contributions from the electron–nuclei energies and thus the respective amounts cannot be directly accessed from the computations.

The evaluation of forces is straightforward as well. The forces acting on the QM atom A are defined as the negative derivative of the energy expectation value $\langle E\rangle$ with respect to the nuclear geometry x_μ for all directions of space ($\mu = 1, 2, 3$ corresponding to the *x,y,z* axes):

$$F_{\mathrm{A}_\mu} = -\frac{\partial\langle E\rangle}{\partial x_{\mathrm{A}_\mu}} = -\frac{\partial\langle\Psi|\hat{H}_{\mathrm{PC}}^{\mathrm{el}}|\Psi\rangle}{\partial x_{\mathrm{A}_\mu}} = -\frac{\partial\langle\Psi|\cdots\sum_{i=1}^{n}\frac{q_1}{r_{i1}}\cdots|\Psi\rangle}{\partial x_{\mathrm{A}_\mu}} \quad (10\text{-}6)$$

The interaction between a particular point charge (e.g. point charge q_1) and the QM atom A can be deduced by separating the respective operator from the force expression:

$$F_{\mathrm{A}1_\mu} = -F_{1\mathrm{A}_\mu} = -\frac{\partial\langle\Psi|\sum_{i=1}^{n}\frac{q_1}{r_{i1}}|\Psi\rangle}{\partial x_{\mathrm{A}_\mu}} \tag{10-7}$$

To obtain the total force acting on an embedded particle (i.e. an MM particle) the sum of forces between the particular point charge and all QM atoms has to be evaluated as implemented in many quantum chemistry program packages:

$$F_{1_\mu} = -\sum_{J=1}^{N} F_{1J_\mu} = -\sum_{J=1}^{N}\frac{-\partial\langle\Psi|\sum_{i=1}^{n}\frac{q_1}{r_{i1}}|\Psi\rangle}{\partial x_{J_\mu}} \tag{10-8}$$

Thus, all force components resulting from the embedding technique can be obtained conveniently from the quantum mechanical calculation.

Despite the promising performance of this ansatz some shortcomings were recognised. Figure 10-4a demonstrates the influence of the simulation box on the distribution of the point charges. The QM region is not homogeneously surrounded by MM particles and thus, the box shape is likely to affect the QM calculation. Furthermore, no distinct cutoff can be applied for QM particles (see Figure 10-4b). The definition of an arbitrary cutoff region centered at a particle of choice (for instance the QM center or particle A) will automatically result in a wrong cutoff region for all other QM atoms. MM charges which would have been included are missing while others that should not be taken into account are incorporated in the QM treatment. These inconsistencies in the definition of distinct cutoff regions have some negative consequences. Important corrections for the neglect of long-range interactions like Ewald summation or reaction field methodologies cannot be applied because the MM point charges acting on a particular QM atom are not restrained by a distinct cutoff distance.

However, the treatment of forces in combination with embedding results in even more serious errors. Figure 10-4c displays the interaction of the QM atoms A and B with the partial charge 1. While the evaluation of forces is coherent for particle A, the interaction is wrong for atom B. According to the *minimum image convention* particle B should interact with the point charge 1', the periodic image of point charge 1, to ensure the correct treatment of the continuum structure with respect to the periodic boundary condition. This has a critical impact on the forces: the distance to particle 1' is lower than to particle 1, resulting in different values of the respective force. The second shortcoming namely the different orientation of the forces is the most serious error encountered in this embedding scheme, as it results in uncontrollable artefacts for all occurring interactions, and discontinuities of forces will occur whenever MM particles are imaged after moving through the simulation boundaries. Hence, the simulation will not correspond to an equilibrium state.

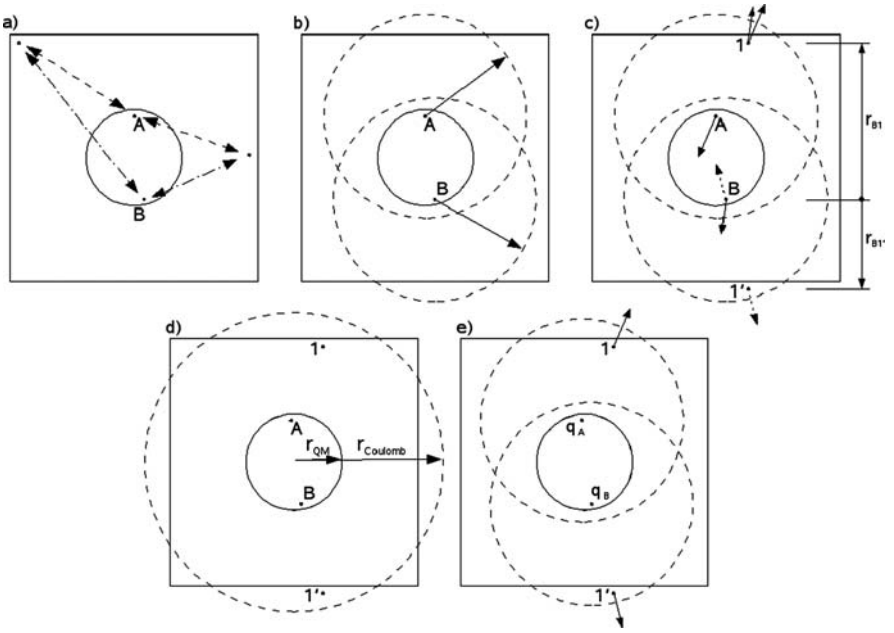

Figure 10-4. (**a**) Inconsistency in embedding due to the shape of the simulation box. (**b**) Desired regions for the application of long-range electrostatic corrections. (**c**) Violation of the minimum image convention for particle B. (**d**) Extended embedding region for separate treatment of QM forces. (**e**) Coulombic forces for separate treatment of MM forces

One pragmatic way to deal with this problem is to separate the treatment of the Coulombic interactions for QM and MM particles. As reaction field and Ewald summation methods cannot be applied due to the inconsistencies encountered in the definition of distinct cutoff regions, the inclusion of all point charges and their respective images – thereby significantly extending the embedding region beyond the box (see Figure 10-4d) – is a valid approach to correct the forces for the QM particles. The resulting excess of point charges can be compared to a simplistic form of a long-range correction – the larger the excess the better the correction. A suitable distance to ensure that all relevant MM charges of a respective QM atom are included is the size of the Coulombic cutoff, thus the radius criteria defining the cavity to include point charges is r_{QM} plus r_{Coulomb} (see Figure 10-4d). A too large point charge distance cutoff would include images of the QM atoms as MM point charges. Employing a sufficiently large simulation box compared to the size of the QM region and the Coulombic cutoff distance should prevent this situation, however. To further improve the description of the QM forces the entire system can be treated as cavity within a polarising field of a surrounding medium applying a polarisable continuum model.

To obtain the interaction of the MM particles a population analysis is carried out yielding charges for the QM atoms. The energy and force contributions are then

calculated according to Coulomb's law allowing the application of the minimum image convention as well as shifted cutoffs and associated long-range correction methods (see Figure 10-4e). Application of this scheme eliminates all inconsistencies encountered in the derivation of forces, although at the cost of a separate treatment of the Coulombic forces.

The application of the methodology outlined results in stable simulation trajectories, but due to the separate treatment of the Coulombic interaction for QM and MM atoms, a violation of the conservation of momentum occurs. In general the forces between a particular QM atom and an MM particle show different absolute values due to the different treatment of Coulombic forces:

$$|F_{1A}| \neq |F_{A1}| \tag{10-9}$$

and hence, the sum of forces over all N_{total} atoms is not conserved.

$$\sum_{i=1}^{N_{\text{total}}} F_i \neq 0 \tag{10-10}$$

After the execution of an MD timestep a rise of the total linear momentum occurs and the resulting configuration has to be considered a non-equilibrium state:

$$\left(\sum_{i=1}^{N_{\text{total}}} F_i\right) \cdot \Delta t = \Delta \left(\sum_{i=1}^{N_{\text{total}}} m_i \cdot v_i\right) \tag{10-11}$$

As the forces are in general not conserved the momentum rises along the simulation until artefacts occur (e.g. artificial diffusion effects) and the simulation has to be aborted. The amount of total momentum required to destabilise a simulation strongly depends on the system. While strong hydrates like Al(III)(aq.) are almost unaffected, weakly interacting systems like pure water or hydrated monovalent ions are very sensitive to these inconsistencies.

An alternative solution to this problem is to apply the force obtained by Coulomb's law to both the QM and the MM counterparts, but then the embedding of MM charges has to be discarded as otherwise the Coulombic contributions for the QM atoms would be treated twice. On the other hand the improved description of the electron density makes the embedding technique a desirable feature. Therefore, an embedding scheme has to be sought which on the one hand allows the inclusion of the point charges to improve the quantum mechanical description, but on the other hand does not show any inconsistencies in the derivation of forces or with respect to momentum conservation.

10.2.4.3. A general electrostatic embedding scheme for QM/MM simulations

To derive an embedding scheme compatible with an application in a periodic environment the properties of the embedding technique and the QM calculations have to be recalled. Partial charges are included in the Hamiltonian as outlined in the

previous section. Upon execution of the QM calculation the molecular orbitals are formed according to the external potential. However, as any derivation of forces violates basic conditions of the periodic environment, embedding of partial charges cannot be applied to molecular dynamics studies. One possibility to overcome this limitation is to include MM point charges during the energy calculation, thereby modifying the molecular orbitals, but to discard the embedding while computing the forces acting on the QM nuclei. The forces are derived utilising the improved MOs, thus retaining the advantage of the embedding technique to improve the quantum mechanical treatment and, thereby, the forces acting on the QM atoms and their respective partial charges. Naturally, the sum of forces equals zero for this subset of forces.

The derivation of consistent forces between QM and MM particles is performed by calculating QM charges for the respective atoms employing a suitable population analysis scheme and subsequent evaluation according to Coulomb's law. Utilising this approach all essential requirements of the periodic environment like the minimum image convention and the application of suitable cutoff techniques are retained. As the Coulombic forces are applied to both the QM and MM particles no violation of the conservation of momentum occurs. As a further important feature of this approach the long-range corrections like Ewald summation or reaction field methods compensating the cutoff applied to the Coulombic interactions can be easily applied without any special modifications.

The implementation of this methodology proved to eliminate the errors associated with the force inconsistency of the Coulombic charge interactions. One critical step in the application of this technique is the choice of a proper population analysis scheme. Simple test computations can indicate which of the many schemes is suitable for a specific problem.

The only drawback of this methodology is a problem in the energy data obtained from the quantum mechanical computation. As the initial computation of the energy and the associated molecular orbitals is performed including the embedded partial charges, the total energy contains electron-point charge and nuclei-point charge contributions. While the latter are usually given as distinct output in various program packages, the potential energy contribution to the one-electron energy is usually not separated into electron-nuclei and electron–point charge interactions, but as the main target of these computations are the internuclear forces, this shortcoming is less problematic. If, however, exact energies are mandatory an additional energy evaluation utilising the previously generated MOs as starting guess has to be performed without embedding of charges. The molecular orbitals of this final computation have to remain unmodified – even a single SCF step would modify the orbitals according to the vacuum surrounding the QM region. Most program packages can be forced to calculate energies without modification of the MOs by requesting only a single energy iteration. The thus obtained energy corresponds to the QM energy employing the starting orbitals without the contribution of the embedded point charges. Since even a single self-consistent field (SCF) cycle modifies the MOs this optional energy evaluation has to be carried out after the force calculation and the population analysis.

10.2.5. Implementation of Consistent Embedding in the QMCF MD Approach

The implementation of the previous considerations in the quantum mechanical charge field ansatz combines the outlined schemes of the charge field approach and the electrostatic embedding technique. According to the classification of the different regions (core, layer, MM region; see Figure 10-1b), different force expressions can be defined. The force acting on the particle J in the core region $F_{\mathrm{J}}^{\mathrm{core}}$ can be derived as

$$F_J^{\mathrm{core}} = F_J^{\mathrm{QM}} + \sum_{I=1}^{M} \frac{q_J^{\mathrm{QM}} \cdot q_I^{\mathrm{MM}}}{r_{IJ}^2} \cdot \left[1 + 2 \cdot \frac{\epsilon + 1}{2\epsilon - 1} \cdot \left(\frac{r_{IJ}}{r_c} \right)^3 \right] \quad (10\text{-}12)$$

The first contribution $F_{\mathrm{J}}^{\mathrm{QM}}$ correspond to the force component obtained from the quantum mechanical treatment (with embedding of partial charges enabled in the energy step as outlined in the previous section). The second part accounts for the Coulombic interactions between particle J and all MM atoms (M) according to their respective partial charges. While the partial charges of the MM particles are defined by the employed MM model, a population analysis is utilised to derive QM point charges as discussed above. The reaction field method was utilised in this example to correct the error associated with the cutoff of the Coulombic interactions which corresponds to the second part of the Coulombic expression. This method accounts for the influence of the surrounding medium beyond the cutoff distance r_c according to the respective dielectric constant ϵ. Alternatively, an Ewald summation schemes could be applied as well [57].

The force on a particle J located in the layer region is similar to that of the core region, however, an additional force contribution resulting from the non-Coulombic interactions F_{IJ}^{nC} between the layer and the MM atoms has to be taken into account:

$$F_J^{\mathrm{layer}} = F_J^{\mathrm{QM}} + \sum_{I=1}^{M} \left\{ \frac{q_J^{\mathrm{QM}} \cdot q_I^{\mathrm{MM}}}{r_{IJ}^2} \cdot \left[1 + 2 \cdot \frac{\epsilon + 1}{2\epsilon - 1} \cdot \left(\frac{r_{IJ}}{r_c} \right)^3 \right] + F_{IJ}^{nC} \right\} \quad (10\text{-}13)$$

Finally, the forces on a particle J located in the MM region are given by the following expression:

$$F_{\mathrm{J}}^{\mathrm{MM}} = \sum_{\substack{I=1 \\ I \neq J}}^{M} F_{\mathrm{IJ}}^{\mathrm{MM}} + \sum_{I=1}^{N_1+N_2} \frac{q_{\mathrm{I}}^{\mathrm{QM}} \cdot q_{\mathrm{J}}^{\mathrm{MM}}}{r_{\mathrm{IJ}}^2} \cdot \left[1 + 2 \cdot \frac{\epsilon + 1}{2\epsilon - 1} \cdot \left(\frac{r_{IJ}}{r_c} \right)^3 \right] + \sum_{I=1}^{N_2} F_{\mathrm{IJ}}^{\mathrm{nC}} \quad (10\text{-}14)$$

The first sum corresponds to the interaction of particle J with all (M – 1) MM atoms based on classical models. The associated force F_{IJ}^{MM} is in general composed

of Coulombic (including the long-range electrostatic corrections), non-Coulombic and intramolecular force field contributions. The second sum corresponds to the charge field interaction with all core (N_1) and layer (N_2) atoms. The respective force contributions are equivalent to the Coulombic forces applied to the QM atoms and hence, force consistency and momentum conservation of these contributions is achieved. Finally, the non-Coulombic forces between particle J and all layer atoms (N_2) have to be taken into account. Again, the equivalent force contributions as for the QM atoms are employed, ensuring no violation of the total linear momentum results from these coupling contributions.

The implementation of these force definitions in a molecular dynamics framework is straightforward: after the identification of QM and MM particles (for example based on the centre of mass of the respective molecules) the quantum mechanical treatment is carried out according to the general embedding methodology. After the derivation of QM energies, forces and partial charges, the MM and coupling contributions have to be evaluated and the derived forces are applied in the integration step of the MD framework. As solvent molecules are included entirely in either the QM or MM region, no bonds are cut by the QM/MM boundary.

A special treatment is necessary whenever particles are to be exchanged between the QM and MM region, however. In this case a smoothing procedure has to be applied to ensure a continuous transition of forces upon the migration of molecules between the QM and MM region. To ensure that no artefacts related to the molecular geometry occur during this smoothing procedure, the MM treatment of the molecules should account for intramolecular motions. Therefore, the application of flexible models for solvent molecules like the BJH-CF2 water model [55,56] appears to be mandatory in hybrid QM/MM simulations allowing the exchange of molecules between QM and MM regions.

A small smoothing layer at the QM/MM transition region is defined. The forces of all particles in this region are evaluated twice, first as a layer atom and once more as if the particle were already part of the MM region:

$$F_J^{\text{smooth}} = S(r) \cdot \left(F_J^{\text{layer}} - F_J^{\text{MM}} \right) + F_J^{\text{MM}} \tag{10-15}$$

To ensure a continuous transition between the QM and MM region a smoothing factor is derived for all particles of the respective molecule, based on the centre of mass, shifting the weight continuously from the QM to the MM force component.

The smoothing factor $S(r)$ is defined by a continuous function gradually increasing from zero to one:

$$\begin{aligned} S(r) &= 1, \text{for } \mathrm{r} \leq \mathrm{r}_1 \\ S(r) &= \frac{(\mathrm{r}_0^2 - \mathrm{r}^2)^2(\mathrm{r}_0^2 + 2\mathrm{r}^2 - 3\mathrm{r}_1^2)}{(\mathrm{r}_0^2 - \mathrm{r}_1^2)^3}, \text{for } \mathrm{r}_1 < \mathrm{r} \leq \mathrm{r}_0 \\ S(r) &= 0, \text{for } \mathrm{r} > \mathrm{r}_0 \end{aligned} \tag{10-16}$$

r is the distance of a given solvent molecule's centre of mass from the centre of the QM region, r_0 the radius of the layer region and r_1 the inner border of the smoothing region. A thickness of 0.2 Å is usually employed as this value was found to be the minimum distance to ensure smooth transitions of solvent molecules. This method is the simplest and least demanding smoothing procedure. The forces of the exchanging particles are continuously changed from the QM to the MM force, although this treatment results in a slight violation of momentum conservation. Considering the computational cost of a quantum mechanical simulation compared to a classical one, this deviation is too small to have a noticeable effect within a feasible simulation time. Too large smoothing areas (for example a thickness of 0.5 Å) have been found to result in a significant violation of momentum conservation [58], however. In order to renounce these slight inconsistencies more complex smoothing schemes have been derived which, however, require more than one force evaluation within one timestep. This appears to be too much effort as the quantum mechanical calculation time is dramatically boosted without a real improvement of accuracy, at least from the practical point of view.

The usual framework of MD simulations [18] like periodic boundary condition, minimal image convention, shifted-cutoffs, long-range force corrections (in this case by the reaction field method), thermostatisation and a sufficiently large number of solvent molecules is maintained and ensured that the system corresponds to liquid bulk. A significant number of particles has to be included in the QM region to uphold the charge field approach for the core species, which increases the computational effort significantly, but the continuous and rapid progress of computing facilities will allow the broad application of this methodology to ever larger systems in solution.

Besides the improved description of the electron density associated with the point charge embedding technique, the neglect of non-Coulombics due to the charge field approach has a significant impact on the applicability of the QMCF MD framework to chemical systems. The following examples demonstrate the practical aspects and flexibility of this methodology in the treatment of composite systems, which would require complex potential functions in conventional QM/MM methodologies.

10.3. RESULTS OF QMCF MD SIMULATIONS

The first test cases of the QMCF MD methodology focused on the re-evaluation of hydrated ions which had already been investigated by conventional QM/MM MD simulations. Although the data obtained from these investigations have been in good agreement with experimental studies, a further improvement in the description of these systems was expected upon application of the QMCF MD methodology, especially in the region close to the QM/MM border. The details of the simulation protocol as well as the basis sets for the quantum mechanical treatment were the same as applied in the QM/MM MD studies [50,51].

Due to the extended size of the quantum mechanical region required for an ab initio QMCF MD simulation the only presently feasible quantum mechanical treatment

is the single determinant level, and thus the Hartree–Fock level was applied in all simulations. Density functional theory is less appropriate in the case of hydrated ions as the methodically inherent unphysical self-interaction is expected to be large in the case of polarising systems like hydrated ions. On the other hand, compared to the considerably large solute–solvent interaction energies the influence of electron correlation can be considered minor. Simple test calculations of ionic clusters at different levels of theory have supported these conclusions [13,50,59,60,61,62,63,64], and QM/MM MD simulations employing different density functionals have shown significant deviations from experimental and ab initio data [13,14,15]. The shortcomings of DFT are visible in structural properties such as coordination numbers, and data related to dynamics such as mean ligand residence times (MRT) have been found to differ even more from experimental values and results of ab initio computations. For example, the mean residence time of a first shell water molecule in the pure solvent was found to be approximately four times larger than the experimental estimation [65] and a Hartree–Fock level simulation [66,67]. A re-calibration of the functionals leading to different parameter sets could improve the performance of DFT methods when applied to ionic systems, but that would only underline the semiempirical character of common DFT methods.

Conventional QM/MM MD simulations at MP/2 level [7,48,66], restricting the QM region to a one-shell treatment due to the substantial increase of the computational effort, have indicated that an extended quantum mechanical zone (i.e. first plus second hydration shells of an ion) at Hartree–Fock level is more important for the quality of results than the treatment of a smaller system (i.e. an ion with its first hydration shell only) at correlated level – the inclusion of many-body and polarisation effects extending beyond the first shell is more crucial than the partial correction of electron correlation.

Figure 10-5a and b depicts the ion–oxygen radial distribution functions (RDFs) of Al(III) and Zn(II) in aqueous solution obtained from a conventional QM/MM [50,51] and a QMCF MD simulation. In both cases the first and second hydration shells have been included in the QM region, in the QMCF studies the ion and its first hydration shell formed the ‘core region’. In general all important structural features like first and second shell distances and coordination numbers are very similar.

In the case of hydrated Al(III) the first shell consisting of six water molecules was shifted from 1.8 to 1.9 Å when changing from conventional QM/MM to QMCF treatment. The second shell distances coincide showing a value of 4.1 Å, the average second shell coordination number increases slightly from 12.2 to 12.5 when the QMCF scheme is applied. However, the third shell as well as the transition to the bulk reveals significant changes. In the case of the conventional QM/MM MD simulation the third shell forms a plateau whereas a distinct peak results when the QMCF framework is applied.

In the case of Zn(II) the first and second shells show similar shapes and the maxima are found at 2.1 and 4.4 Å, respectively. The average second shell coordination number decreased from 13.8 to 13.2 when changing from the QM/MM to the QMCF scheme, whereas the first shell coordination number remains at 6. The main structural

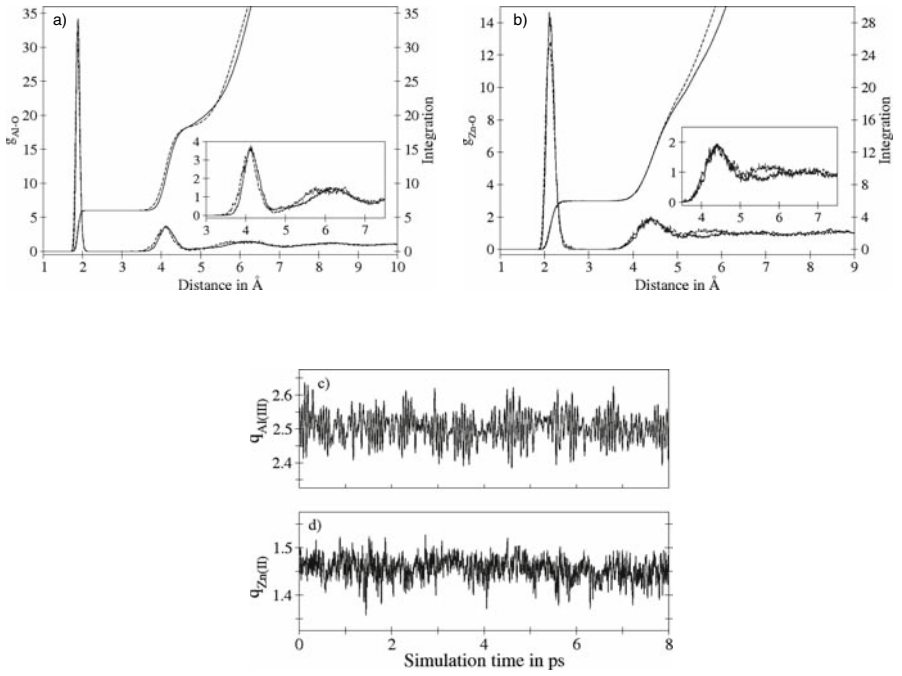

Figure 10-5. Ion–oxygen radial distribution functions obtained from a QMCF (*solid line*) and a QM/MM (*dashed line*) MD simulation of (**a**) Al(III) and (**b**) Zn(II) in aqueous solution. Fluctuation of the QM charge for (**c**) Al(III) and (**d**) Zn(II)

difference is found in the transition region between the second shell and the bulk. In the case of the QM/MM study the second shell is not separated from the bulk by a minimum – a broad peak is observed which does not correspond to a distinct third hydration layer. The QMCF framework yields a well-defined second shell peak with a minimum before the bulk region.

The findings of these two examples clearly demonstrate the improved performance of the QMCF ansatz. The depolarisation of the central species is not included in conventional QM/MM coupling and due to the fixed partial charges of the ionic species (+3 and +2 in the case of Al(III) and Zn(II), respectively) an overestimation of the Coulombic interactions between QM and MM atoms results, leading to 'pressure' artefacts near the QM/MM transition region. The application of quantum mechanically derived partial charges (in this case according to Mulliken [68] accounts for polarisation and charge-transfer effects of the ions as well their respective ligands, and these properties are thus accounted for in the coupling of the two regions. Figure 10-5c displays the fluctuation of the partial charges of Al(III) and Zn(II) over a time period of 8 ps. The effective charges oscillate between +2.35 to +2.65 in the case of Al(III) and between +1.35 and +1.55 in the case of Zn(II). The

remaining charge contribution resulting from the difference of the formal and actual charges is distributed to the solvent molecules in the QM region according to the actual geometry, leading to a fluctuating polarisation of the surrounding solvent. As shown by the radial distribution functions this treatment results in an elimination of 'pressure' artefacts at the QM/MM border which at the same time leads to an improved description of ligand exchange dynamics. The mean ligand residence time for second shell water molecules derived employing a direct evaluation of exchanges [69] decreased from 26 to 21 ps in the case of Al(III) and increased from 3.3 to 3.9 ps in the case of Zn(II) when changing from the conventional QM/MM to the QMCF treatment.

The transition artefacts found in conventional QM/MM MD studies are occurring due to the overestimation of Coulombic forces between the QM and MM particles resulting from too high partial charges assigned to the ions. Recent investigations of different smoothing methodologies have concluded that artefacts occur due to insufficiencies of the applied smoothing methodology [58]. However, it is evident that the smoothing procedure is not related to the occurrence of these 'pressure' artefacts.

The studies of Al(III) and Zn(II) have served as a methodical proof of the QMCF concept showing improvements of the accuracy resulting from the optimised QM/MM coupling, and at the same time eliminating the requirement of potential parameters (Coulombics and non-Coulombics) for the central species. QMCF simulations of other systems like Mn(II) and Cu(II) have led to the same conclusion [54].

The capability to renounce potentials for all species located in the QM 'core region' allows the convenient treatment of systems which display a non-spherical potential surface. The first examples in this context are Pd(II) and Pt(II) in aqueous solution. The hydration structure of these ions was believed to be similar to structures found in their crystals, namely square-planar. Recent experimental [70] and theoretical investigations [71] concluded that one or two additional ligands are present in axial positions at elongated bond distances, and hence the first shell structures should correspond to a (bi-)pyramidal configuration. Potential functions would have to account, additionally to the radial description, for an angular dependence to distinguish between axial and equatorial positions. Besides the problems related to the construction of a reliable representation to properly describe this energy hypersurface, the implementation in an actual simulation faces some obstacles. First, a plane (or its associated normal vector) needs to be defined during the simulation to identify axial and equatorial ligands based on the angle relative to this plane. This could be done arbitrarily or utilising the four nearest ligands. Marcos and coworkers solved this problem by utilising different potential models for the treatment of axial and equatorial ligands [71]. The second challenge is related to changes in the definition of the equatorial plane whenever the associated ligands are exchanged in the course of the simulation. Although the rate constant for these exchanges is considerably low and hence, their occurrence during the simulation is rather improbable, it is difficult to give an estimation to what extent the progressing simulation is influenced by this implicit constraint. As a consequence, the system could be

hindered to evolve towards configurations or transition states associated with these exchanges, which could then lead to a non-ergodic sampling of the configurational space.

A quantum mechanical description on the other hand does not face these problems as the different interactions with respect to any position are automatically taken into account. Based on the fact that the QM/MM coupling realised in the QMCF framework does not require any non-Coulombic potential data for the central species and Coulombic interactions are treated based on the fluctuating charge distribution within the QM region, the study of these systems is straightforward provided that the quantum mechanical region is sufficiently large. Thus, QMCF MD simulations of Pd(II) and Pt(II) were carried out starting with the ion and four water ligands in the 'core region', the 'layer' was defined to include the full second hydration shell.

Figure 10-6a displays the Pd(II)–oxygen and Pt(II)–oxygen RDFs obtained from the QMCF simulations. Equatorial and axial ligands within the first shell are clearly separated. The broad minimum between the peak originating from the axial ligands and the second shell suggests that these molecules are a distinct feature of the first shell. The average first shell coordination numbers deduced from the RDF's running integration are 5.7 and 5.6 for Pd(II) and Pt(II), respectively. These non-integer values indicate that in both cases a species distribution associated with exchange reactions of first shell ligands exists, which interchanges on the timescale of the simulation, i.e. the picosecond scale. The corresponding distance plots displayed in Figure 10-3d and e reveal that none of the equatorial ligands is involved in these exchanges within the simulation time and hence, only the axial ligands should be considered in the determination of the mean ligand residence times, which were evaluated according to the 'direct' method [69] as 2.8 and 3.2 ps for Pd(II) and Pt(II), respectively. These values do not agree with the rate constants for Pd(II) and Pt(II) determined by NMR measurements as 5.6×10^{2} and 3.9×10^{-4} s^{-1} [72]. As the geometries of the aquo-complexes were described as square-planar it can be concluded that these rate constants refer to the exchange of equatorial ligands only as the exchange of the axial ligands is much too fast to be detected by NMR methods. However, both experimentally determined rate constants (equatorial) and the (axial) mean residence times obtained from the simulations indicate that Pd(II) forms a weaker hydrate structure than the Pt(II) ion.

The occurrence of different species in a solution interchanging on the picosecond timescale is a serious challenge for experimental investigations. Any measurement carried out over a longer time interval will automatically average all occurring species and thereby bond lengths and coordination numbers. Figure 10-6b and c displays the coordination number distributions obtained from the different simulations. Five- and six-fold coordinations are dominating along the simulation trajectory. The fit of experimental diffraction patterns in most cases is carried out assuming a distinct coordination number, whereas in models accounting for multiple species it would be mandatory to obtain a reliable description of these systems. Simulation data can thus provide valuable information on how to construct such models.

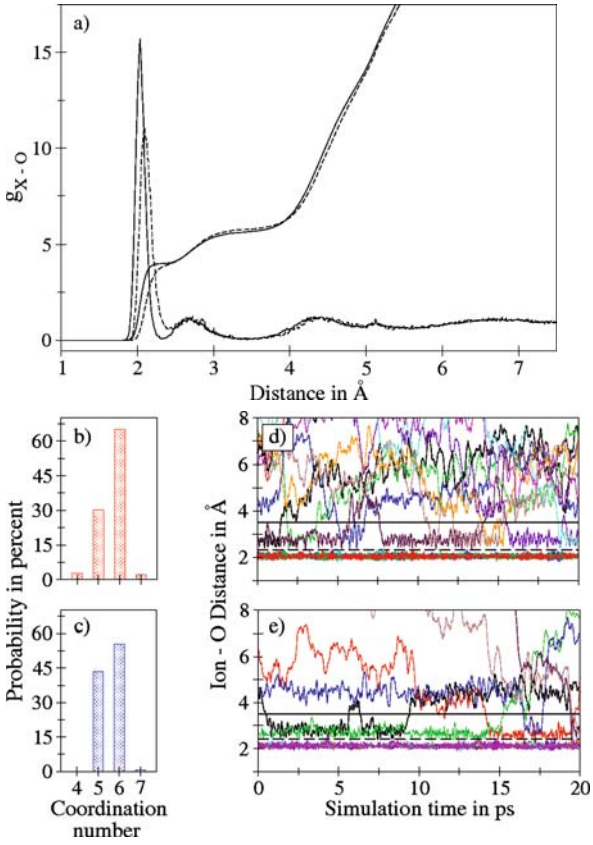

Figure 10-6. (**a**) Ion–oxygen radial distribution functions obtained from a QMCF MD simulation of Pd(II) (*solid line*) and Pt(II) (*dashed line*) in aqueous solution. Coordination number distribution within the first shell for (**b**) Pd(II) and (**c**) Pt(II) and associated exchange plots for (**d**) Pd(II) and (**e**) Pt(II)

As soon as the number of atoms of the solute species increases, the associated energy hypersurfaces become more complex due to the lower symmetry of the system. In the case of the mercury(I) dimer Hg_2^{2+} ligands coordinated to one of the mercury atoms are bound more strongly than ligands coordinating both Hg atoms at the same time. In analogy to the case of Pd(II) and Pt(II) potential functions have to account for the angle between the ion-ligand vector and a predefined axis, in this case the Hg(I)–Hg(I) bond. Again the advantages of the QMCF MD methodology for a convenient treatment of the system are evident.

In this simulation the ion formed the 'core region'. The centre of mass of the Hg_2^{2+} ion served as the centre of the quantum mechanical region, hence all water molecules up to a radius of 6.4 Å have been included in the layer region. Figure 10-7a shows a snapshot of the simulation showing the typical arrangement of the ligands bound

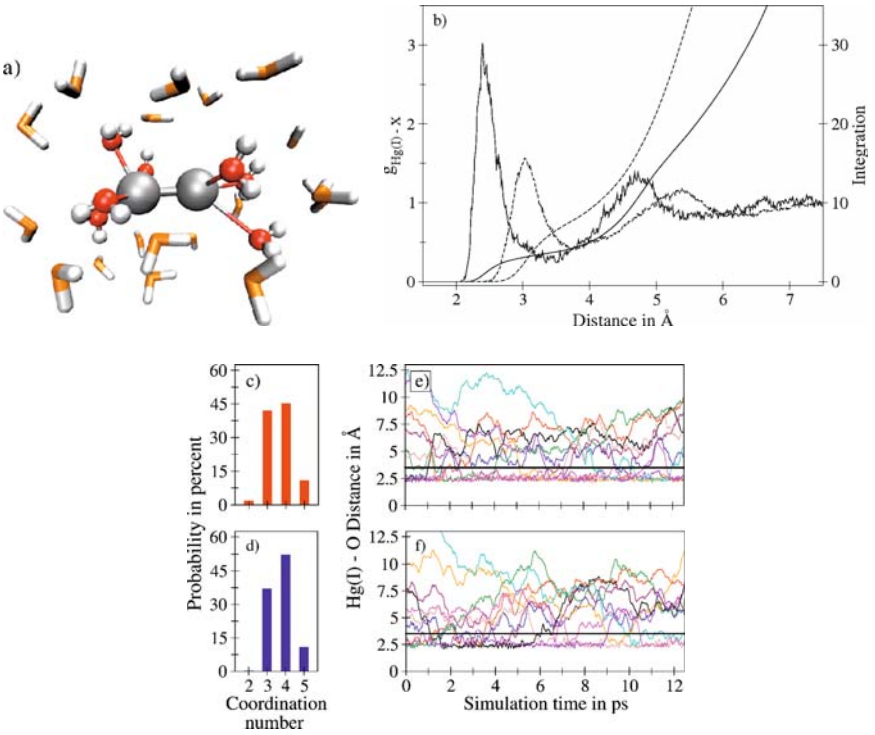

Figure 10-7. (**a**) Snapshot of a QMCF MD simulation of Hg_2^{2+} in aqueous solution. (**b**) Hg(I)–oxygen (*solid line*) and Hg(I)–hydrogen (*dashed line*) radial distribution functions. (**c, d**) Coordination number distribution within the first shell for both Hg(I) atoms and associated exchange plots (**e**, **f**)

to the Hg_2^{2+} ion. Water molecules bound to both Hg atoms at the same time are very rare and these configurations are very short-lived.

Figure 10-7b displays the Hg(I)–oxygen and Hg(I)–hydrogen radial distribution functions. Two well-defined peaks representing the first and second hydration shells are centred at 2.4 and 4.7 Å in the Hg(I)–O RDF and at 3.0 and 5.35 Å in the Hg(I)–H RDF, respectively. The mean Hg(I)–Hg(I) bond length was found to be 2.63 Å. This structural description is in good agreement with data obtained from diffraction experiments [73].

The average first shell coordination number of 3.7 indicates, together with the considerable high elevation of the minimum between first and second shells, that a considerable number of ligand exchange reactions took place within the simulation time. Figure 10-7c–f displays the coordination number distributions and the corresponding ligand distance plots for both atoms of the mercury dimer. Three- and four-coordinated species are dominating, five-coordination occurs during about 10% of the simulation time. The exchange plots clearly demonstrate the high exchange rate of ligands migrating from the first to the second shell and vice versa. No favoured

exchange mechanism can be detected and in some cases multiple ligands are involved in the exchange process. The mean ligand residence times of the first shell ligands were separately evaluated for the two Hg sites as 2.9 and 3.0 ps according to the direct method [69]; 3.0 ps is only slightly larger than the MRT in the pure solvent indicating the high lability of this hydrate. In addition to the structural and dynamical analysis, a simulation can provide energetic data as well. The hydration energy of the Hg_2^{2+} ion was calculated performing free energy calculations utilising every 50th configuration. The average value of −1137 kJ/mol perfectly agrees with the experimentally estimated value of −1148 kJ/mol [74]. This good agreement is another important indicator demonstrating the high quality of the QMCF framework.

Diatomic solute species composed of different elements such as the titanyl ion TiO^{2+} further increase the system's complexity. The properties of ligands coordinated to the Ti and O atoms are significantly different and the construction of a suitable and accurate representation of the ion–ligand energy hypersurface required for classical and conventional QM/MM MD studies is very difficult. A recent QMCF MD study of the TiO^{2+} system in aqueous solution [75] has demonstrated that the treatment of this solute is equally feasible as that of the previous examples. The Ti atom was selected as the centre of the QM region, the 'core' zone included the O atom of the TiO^{2+} (Ti–O distance 1.57 Å) as well as the five first shell ligands coordinated to the Ti atom. Figure 10-8b and c displays the Ti–oxygen and O_{oxo}–O radial distribution functions. Five ligands are coordinated to the Ti atom at a mean distance of 2.1 Å, whereas just a single water forms a hydrogen bond to the oxo-atom. One particular advantage of simulation methods is the possibility to investigate the properties of singled-out molecules or atoms. Thus, a separate analysis of the first shell water molecules revealed an elongated bond length of 2.3 Å for the water molecule in *trans*-position of the oxo-atom (see Figure 10-8a) which cannot be deduced merely from the overall Ti–O RDF, as the contribution of the ligand in *trans*-position is overlapping with the contributions of the four in-plane ligands. Whereas the Ti–water interaction was found to be strong and no exchange of these ligands occurred during

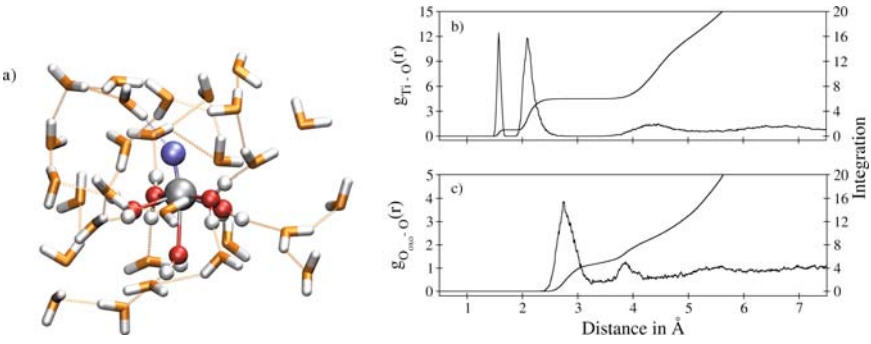

Figure 10-8. (**a**) Snapshot of a QMCF MD simulation of TiO^+ in aqueous solution. (**b**) Ti–O and (**c**) O_{oxo}–O radial distribution functions

the simulation time of 15 ps, the water molecule bound to the O atom via weak hydrogen bonding is mobile and exchanges on the picosecond scale (MRT: 3.6 ps).

The oxo-anions PO_4^{3-} and ClO_4^- serve as final examples. In this case the oxygen atoms form a tetrahedral arrangement around the central atom (see Figure 10-9a). These composite ions serve as the most refined example for the capabilities of the QMCF MD methodology. As the ion is entirely included in the 'core' region, the only contribution to the force between the atoms of the ions and the MM particles is achieved via the charge field interaction. Therefore, the central atom of the ions was chosen as the QM centre. The entire first hydration shell of the oxoions was included in the 'layer' region.

Figure 10-9b and d displays the O and H radial distribution functions of the central atoms P and Cl obtained by QMCF MD simulations (only the water oxygens are depicted). Whereas the well-defined first shell peaks in the case of phosphate indicate a strong interaction with the solvent, a broad peak with low intensity is obtained in the case of perchlorate. As the associated integration differs only slightly from the exponential increase corresponding to the ideal distribution, it can be deduced that the hydration shell of the perchlorate ion is highly disordered. In contrast to the well-defined minima between first and second shells of phosphate, only weak minima are visible in the case of perchlorate. The Cl–H RDF indicates that no second shell structure is formed at all. The mean ligand residence times for first shell ligands were determined as 3.9 ps for PO_4^{3-} and as 1.5 ps in the case of ClO_4^- utilising the 'direct' method [69]. Comparison of these values with the MRT of the pure solvent of 1.5 ps clearly demonstrates the 'structure breaking' properties of the perchlorate ion. The averaged radial distribution functions of the oxo-atoms lead to similar conclusions. While well-defined first and second shell structures are obtained in the case of phosphate, a disordered, weakly bound first shell structure is found in the case of perchlorate.

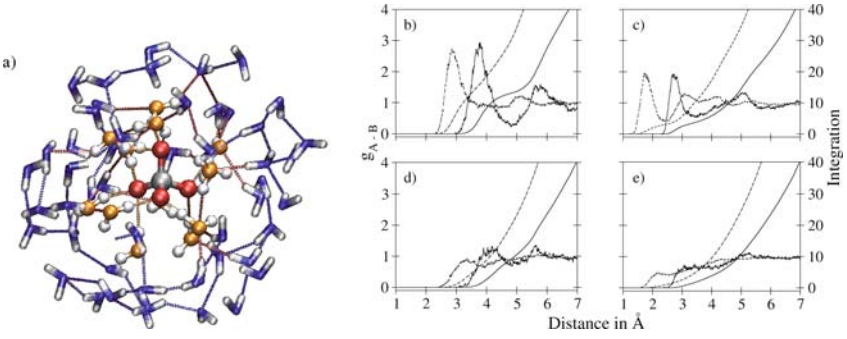

Figure 10-9. (**a**) Snapshot of a QMCF MD simulation of PO_4^{3-} in aqueous solution. (**b**) P–O (*solid line*) and P–H (*dashed line*) and (**c**) O_{oxo} –O (*solid line*) and O_{oxo} –H (*dashed line*) radial distribution function obtained from a QMCF MD simulation of PO_4^{3-} in aqueous solution. (**d**) Cl–O (*solid line*) and Cl–H (*dashed line*) and (**e**) O_{oxo} –O (*solid line*) and O_{oxo}–H (*dashed line*) radial distribution functions obtained from a QMCF MD simulation of ClO_4^- in aqueous solution

A recent QMCF MD and LAXS (large angle X-ray scattering) study [76] of the sulfate ion has once more demonstrated the reliability of this simulation technique for the description of composite solutes and an accuracy equivalent to best experimental methods. Precise predictions of vibrational spectra as well as the solvation energy of this anion [77] have clearly indicated the ability of the QMCF MD approach to investigate a variety of properties in a general and comprehensive way.

The simulations of these composite ions also demonstrate the enhanced capabilities of the QMCF MD approach allowing the straightforward treatment of composite systems without the need for solute–solvent potentials. With the electrostatic embedding technique and the quantum mechanical point charges representing the fluctuations of the electron density an increased accuracy compared to conventional QM/MM methodologies is achieved, too. The continuous increase of computational capacities as well as the improvement of ab initio methods will allow larger quantum mechanical regions and eventually the application of correlated ab initio methods in the QM region.

10.4. CONCLUSION AND OUTLOOK

The quantum mechanical charge field ansatz has emerged as a promising methodology for the study of complex species in solution, also for systems with low symmetry and/or composite compounds. The general electrostatic embedding scheme suitable for the periodic environment in combination with the application of fluctuating quantum mechanical point charges utilised in the evaluation of the Coulombic interactions between QM and MM particles guarantees a more accurate coupling between the two subregions than conventional QM schemes. The technique allowing to renounce solute–solvent non-Coulombic potential functions greatly enhances the applicability of ab initio MD simulations to a variety of chemical systems, provided that the QM region can be chosen sufficiently large to include at least one full layer of solvent molecules. Basically, every affordable system (with respect to size and necessary quantum mechanical level) can be selected as solute species. The combination of the QMCF approach with force field methods will allow the treatment of biomolecules and applications in material sciences related to surfaces and interface phenomena and appears a most promising methodology for various disciplines of chemistry, therefore.

ACKNOWLEDGEMENT

Financial support of this work by the Austrian Science Foundation (FWF Project No 18429) and the Hypo Tirol Bank is gratefully acknowledged.

REFERENCES

1. Ohtaki H, Radnai T (1993) Structure and dynamics of hydrated ions. Chem Rev 93(3):1157–1204
2. Neilson GW, Enderby JE (1989) The coordination of metal aquaions. In Advances in Inorganic Chemistry, vol 34, Academic Press, Inc, Orlando, p 195–218

3. Helm L, Merbach AE (2005) Inorganic and Bioinorganic solvent exchange mechanism. Chem Rev 105:1923
4. Detrich JH, Clementi E et al (1984) Monte Carlo liquid water simulation with four-body interactions included. Chem Phys Lett 112:426
5. Curtiss LA, Woods Halley J et al (1987) Nonaddidivity of *ab initio* pair potentials for molecular dynamics of multivalent transition metal ions in water. J Chem Phys 86(4):2319–2327
6. Elrod MJ, Saykelly RJ (1994) Many-Body effects in intermolecular forces. Chem Rev 94:1974
7. Rode BM, Schwenk CF, et al (2004 b) Structure and Dynamics of Hydrated Ions - New Insights through Quantum Mechanical Simulation. J Mol Liq 110:105
8. Rode BM, Schwenk CF et al (2005) The combination of quantum chemistry and statistical simulations: a most powerful tool to access structure and dynamics of liquid systems. Coord Chem Rev 249:2993
9. Sigel H (1974) Metal ions in biological systems, vol 1. M. Dekker, New York
10. Clapham DE (1995) Calcium signaling. Cell 80:259
11. da Silva JJRF, Williams RJP (1991) The biological chemistry of the elements, Clarendon Press - Oxford, New York
12. Rode BM, Hofer TS (2006) How to access structure and dynamics of solutions: the capabilities of Computational Methods. Pure & Appl Chem 78:525
13. Schwenk CF, Hofer TS et al (2004a) The structure breaking effect of hydrated Cs(I). J Phys Chem A 108:1509
14. Schwenk CF, Löffler HH et al (2001) Molecular dynamics simulations of Ca^{2+} in water: comparison of a classical simulation including three-body corrections and Born-Oppenheimer ab initio and density functional theory quantum mechanical/molecular mechanics simulations. J Chem Phys 115:10808
15. Schwenk CF, Rode BM (2003) Extended ab initio quantum mechanical/molecular mechanical molecular dynamics simulations of hydrated Cu^{2+}. J Chem Phys 119:9523
16. Kerdcharoen T, Liedl KR et al (1996) A QM/MM simulation method applied to the solution of Li^{+} in liquid ammonia. Chem Phys 211:313–323
17. Metropolis N, Rosenbluth AW et al (1953) Equation of state calculations by fast computing machines. J Chem Phys 21(6):1087–1092
18. Allen MP, Tildesley DJ (1990) Computer simulation of liquids, Oxford Science Publications, Oxford
19. Frenkel D, Smit B (2002) Understanding molecular simulation. Academic press, San Diego – London
20. Leach AR (2001) Molecular modelling, vol 2nd edn. Prentice-Hall, Essex
21. Jensen F (1999) Introduction to computational chemistry, Wiley, Chichester
22. McQuarrie (1976) Statistical mechanics, Harper & Row, New York
23. Pearlman DA, Case DA et al (1995) AMBER, a package of computer programs for applying molecular mechanics, normal mode analysis, molecular dynamics and free energy calculations to simulate the structural and energetic properties of molecules. Comp Phys Commun 91:1
24. MacKerell AD, Brooks B et al (1998) CHARMM: the energy function and its parameterization with an overview of the program in *The Encyclopedia of Computational Chemistry*, Wiley, Chichester
25. Brooks BR, Bruccoleri RE et al (1983) CHARMM: a program for macromolecular energy, minimization, and dynamics calculations. J Comp Chem 4:187
26. Brodholt J, Sampoli M et al (1995) Liquidvapor and liquidliquid phase equilibria of the Brodholt-SampoliVallauri polarizable water model. Mol Phys 86:149

27. Chialvo AA, Cummings PT (1996) Engineering a simple polarizable model for the molecular simulation of water applicable over wide ranges of state conditions. J Chem Phys 105:8274
28. Dang LX, Chang TM (1997) Molecular dynamics study of water clusters, liquid, and liquidvapor interface of water with many-body potentials. J Chem Phys 106:8149
29. Cramer CJ (2002) Essentials of computational chemistry, Wiley, West Sussex
30. Cramer CJ, Truhlar DG (1999) Implicit solvation models: equilibria, structure, spectra, and dynamics. Chem Rev 99:2161
31. Rotzinger FP (2005) Implicit solvation models: equilibria, structure, spectra, and dynamics. Chem Rev 105:2003
32. Car R, Parinello M (1985) Unified approach for molecular-dynamics and density functional theory. Phys Rev Lett 55(22):2471–2474
33. Perdew JP, Burke K et al (1996) Generalized gradient approximation made simple. Phys Rev Lett 77:3865
34. Perdew JP, Burke K et al (1997) Generalized gradient approximation made simple (Errata). Phys Rev Lett 78:1396
35. Becke AD (1988) Density-functional exchange-energy approximation with correct asymptotic behavior. Phys Rev A 38:3098
36. Becke AD (1993) Density-functional thermochemistry. III. The role of exact exchange. J Chem Phys 98:5648–5652
37. Kutzelnigg W (2006) Density Functional Theory (DFT) and ab-initio quantum chemistry (AIQC). Story of a difficult partnership. In: Maroulis G, Simos T (eds) Trends and perspectives in modern computational science, International Science Publishers (VSP), Leiden p 23
38. Bartlett RJ, Schweigert IV et al (2006) Ab initio DFT: getting the right answer for the right reason. J Mol Struct (Theochem) 764:33
39. Bartlett RJ, Lotrich VF et al (2005) Ab initio density functional theory: the best of both worlds? J Chem Phys 06:2205
40. Lin H, Truhlar DG (2007) QM/MM: what have we learned, where are we, and where do we go from here? Theor Chem Acc 117:185
41. Warshel A, Levitt M (1976) Theoretical studies of enzymic reactions: dielectric, electrostatic and steric stabilization of the carbenium ion in the reaction of lysozyme. J Mol Biol 103:227
42. Field MJ, Bash PA et al (1990) A combined quantum mechanical and molecular mechanical potential for molecular dynamics simulations. J Comput Chem 11(6):700–733
43. Gao J (1993) Potential of mean force for the isomerization of DMF in aqueous solution: a Monte Carlo QM/MM simulation study. J Am Chem Soc 115:2930–2935
44. Bakowies D, Thiel W (1996) Hybrid models for combined quantum mechanical and molecular mechanical approaches. J Phys Chem 100(25):10580–10594
45. Senn HM, Thiel W (2007) QM/MM studies of enzymes. Curr Opin Chem Biol 11:182
46. Dapprich S, Komàromi I et al (1999) A new ONIOM implementation in Gaussian98. Part I. The calculation of energies, gradients, vibrational frequencies and electronic field derivatives. J Mol Struct (Theochem) 461–462:1–21
47. Svensson M, Humbel S et al (1996) ONIOM: a multilayered integrated MO + MM method for geometry optimizations and single point energy predictions. A test for Diels-Alder Reactions and $Pt(P(t\text{-}Bu_3)_2) + H_2$ oxidative addition. J Phys Chem 100(50):19357–19363
48. Schwenk CF, Rode BM (2004a) Influence of electron correlation effects on the solvation of Cu(II). J Am Chem Soc 126:12786–12787
49. Kritayakornupong C, Plankensteiner K et al (2004) The Jahn-Teller effect of Ti(III) ion in aqueous solution: extended ab initio QM/MM molecular dynamics simulations. Chem Phys Chem 5: 1499–1506

50. Hofer TS, Randolf BR et al (2005b) Influence of polarization and many body quantum effects on the solvation shell of Al(III) in dilute aqueous solution?extended ab initio QM/MM MD simulations. Phys Chem Chem Phys 7:1382
51. Fatmi MQ, Hofer TS et al (2005) An extended ab initio QM/MM MD approach to structure and dynamics of Zn(II) in aqueous solution. J Chem Phys 123:4514
52. Laio A, VandeVondele J, et al (2002) A Hamiltonian electrostatic coupling scheme for hybrid CarParrinello molecular dynamics simulations. J Chem Phys 116:6941
53. Voloshina E, Gaston N et al (2007) Embedding procedure for ab initio correlation calculations in group II metals. J Chem Phys 126:134115
54. Rode BM, Hofer TS et al (2006) Ab initio quantum mechanical charge field molecular dynamics – a QM/MM MD procedure for accurate simulations of ions and complexes. Theor Chem Acc 115:77
55. Stillinger FH, Rahman A (1978) Revised central force potentials for water. J Chem Phys 68(2):666
56. Bopp P, Janscó G et al (1983) An improved Potential for non-rigid water molecules in the liquid phase. Chem Phys Lett 98(2):129
57. Nam K, Gao J et al (2005) An efficient linear-scaling ewald method for long-range electrostatic interactions in combined QM/MM calculations. J Chem Theor Comput 1:2
58. Heyden A, Lin H et al (2007) Adaptive partitioning in combined quantum mechanical and molecular mechanical calculations of potential energy functions for multiscale simulations. J Phys Chem B 111:2231
59. Hofer TS, Randolf BR et al (2005c) Structure-breaking effects of solvated Rb(I) in dilute aqueous solution – an ab initio QM/MM MD approach. J Comput Chem 26:949
60. Hofer TS, Rode BM (2004) The solvation structure of Pb(II) in dilute aqueous solution – an ab initio QM/MM MD approach. J Chem Phys 121:6406
61. Hofer TS, Rode BM et al (2005d) Structure and dynamics of solvated Ba(II) in dilute aqueous solution – an ab initio QM/MM MD approach. Chem Phys 312:81
62. Hofer TS, Pribil AB et al (2005a) Structure and dynamics of solvated Sn(II) in aqueous solution - an ab initio QM/MM MD approach. J Am Chem Soc 127:14231
63. Hofer TS, Scharnagl H et al (2006b) Structure and dynamics of La(III) in aqueous solution – an ab initio QM/MM MD approach. Chem Phys 327:31
64. Hofer TS, Randolf BR et al (2006a) Sr(II) in water: a labile hydrate with a highly mobile structure. J Phys Chem B 110:20409
65. Lock AJ, Woutersen S et al (2001) Femtochemistry and Femtobiology, World Scientific Publishing, Singapore
66. Xenides D, Randolf BR et al (2005) Structure and ultrafast dynamics of liquid water: a quantum mechanics/ molecular mechanics molecular dynamics simulations study. J Chem Phys 122:4506
67. Xenides D, Randolf BR et al (2006) Hydrogen bonding in liquid water: an ab initio QM/MM MD simulation study. J Mol Liquids 123:61
68. Mulliken RS (1962) Criteria for the construction of good self-consistent-field molecular orbital wave functions, and the significance of LCAO-MO population analysis. J Chem Phys 36:3428
69. Hofer TS, Tran HT, et al (2004) Characterisation of dynamics and reactivities of solvated ions by ab initio simulations. J Comput Chem 25:211–217
70. Purans J, Fourest B et al (2005) Understanding the hydration structure of square-planar aquaions: the $[Pd(H_2O)_4]^{2+}$ case. J Phys Chem B 109:11074
71. Martinez JM, Torrico F et al (2004) Understanding the hydration structure of square-planar aquaions: the $[Pd(H_2O)_4]^{2+}$ case. J Phys Chem A 108:15851
72. Helm L, Merbach AE (1999) Water exchange on metal ions: experiments and simulations. Coord Chem Rev 187:151

73. Rosdahl J, Persson I et al (2004) On the solvation of the mercury(I) ion. A structural, vibration spectroscopic and quantum chemical study. Inorg Chem A 357:2624
74. Yizhak M (1997) Ion properties, Marcel Dekker, Inc., New York
75. Fatmi MQ, Hofer TS et al (2007) Quantum mechanical charge field molecular dynamics simulation of the TiO^{2+} ion in aqueous solution. J Comput Chem 28:1704
76. Vchirawongkwin V, Persson I et al (2007) Structure and dynamics of sulfate ion in aqueous solution – an ab initio QMCF MD simulation and large angle X-ray scattering study. J Phys Chem B 111:4150
77. Vchirawongkwin V, Rode BM (2007) Solvation energy and vibrational spectrum of sulfate in water – an ab initio quantum mechanical simulation. Chem Phys Lett 443:152

CHAPTER 11

SOLVATION IN POLYMERS

HOSSEIN ESLAMI[1,2] AND FLORIAN MÜLLER-PLATHE[1]

[1] *Eduard-Zintl-Institut für Anorganische und Physikalische Chemie, Technische Universität Darmstadt, Petersenstrasse 20, Darmstadt D-64287, Germany*
e-mail: h.eslami@theo.chemie.tu-darmstadt.de
[2] *Department of Chemistry, College of Sciences, Persian Gulf University, Boushehr 75168, Iran*

Abstract: In this chapter the process of solvation in polymers is discussed. In the first few sections the statistical mechanics of solvation, Flory's theory of polymer solutions, and its comparison with classical solution methods for interpretation of experimental data are discussed. Sorption of gases in polymers and the methods of calculation of chemical potentials, and hence calculation of Henry's law constants and sorption isotherms of gases in polymers are discussed in details in Section 11.6. The solvation structures as well as the effect of solvent on equilibrium and dynamics of polymer-size change in solutions are described with the main emphasis on molecular dynamics simulation method to obtain understanding of solvation of nonpolar polymers in nonpolar solvents and that of polar polymers in polar solvents. Finally, the dynamics of solvation with a short review of the experimental, theoretical, and simulation methods are explained in this chapter

11.1. INTRODUCTION

The study of solvation effect is an interesting topic in polymer physical chemistry from theoretical, experimental, and practical points of view, and has triggered a numerous number of studies for many years. In this chapter two extreme cases, very dilute solutions of gases in polymers and (up to) the solution of polymers in solvents, are described in details. The equilibrium sorption of gases, vapors, and liquids in polymers is of essential importance in many areas of polymer technology. For example, solubilities of small molecules in polymers are required for the design and operation of polymer plants so that residual monomers, oligomers, and polymerization solvents can be removed from the polymer products. Gas solubilities also play important roles in such applications as designing polymer barrier materials for packaging applications, developing membranes for gas separations, foaming, and plasticization. On the other extreme, when a polymer is exposed to a solvent, the solvent molecules diffuse into the porous structure of the polymer. If the polymer is soluble in the solvent there is an attractive interaction between polymer and solvent and the net interaction between polymer segments is repulsive. Therefore, the coiled

S. Canuto (ed.), Solvation Effects on Molecules and Biomolecules, 279–320.
DOI 10.1007/978-1-4020-8270-2_11,

polymer chains start swelling, and eventually the process leads to saturation where the swelled polymer chains are in equilibrium with the solvent. In this case, understanding of such phenomena as polymer chain dynamics, its equilibrium structure in the presence of solvent, and the solvation structure is important.

Although experimental and theoretical works have been successful for studying phenomena of this type, however, for example the experimental methods cannot reveal the detailed solvation structures to describe the interaction between solvent and polymer. Theoretical methods are also either not completely atomistic or they assume a certain molecular behavior. Molecular simulation methods, on the other hand, can produce most atomistic information about the solvation process.

In this chapter we will mostly focus on the application of molecular dynamics simulation technique to understand solvation process in polymers. The organization of this chapter is as follow. In the first few sections the thermodynamics and statistical mechanics of solvation are introduced. In this regards, Flory's theory of polymer solutions has been compared with the classical solution methods for interpretation of experimental data. Very dilute solution of gases in polymers and the methods of calculation of chemical potentials, and hence calculation of Henry's law constants and sorption isotherms of gases in polymers are discussed in Section 11.6.1. The solution of polymers in solvents, solvent effect on equilibrium and dynamics of polymer-size change in solutions, and the solvation structures are described, with the main emphasis on molecular dynamics simulation method to obtain understanding of solvation of nonpolar polymers in nonpolar solvents and that of polar polymers in polar solvents, in Section 11.6.2. Finally, the dynamics of solvation with a short review of the experimental, theoretical, and simulation methods are explained in Section 11.7.

11.2. CLASSICAL THERMODYNAMICS OF SOLVATION

Generally the solvation process is defined as the process of transferring a solute molecule, *s*, from a fixed position in the ideal gas state into a fixed position in the condensed phase [1]. The process is usually performed at constant temperature, constant pressure, and constant composition of the liquid phase. If the solute is a simple spherical molecule, we need to keep its center fixed, but if it is a more complex molecule, we need to keep the center of mass of the molecule at a fixed position. Of course, in complex molecules the geometrical location of the center of mass might shift upon changing the conformation of the molecule. In such cases, the processes of solvation of a molecule at a specified conformation and an average solvation process over all possible conformations of the molecule must be distinguished. The solvation process may also happen at constant volume, instead of constant pressure. Defining the process of solvation, we now introduce the corresponding thermodynamic quantities such as solvation free energy, solvation entropy, and so on, each refers to the change in the corresponding thermodynamics state function in the solvation process. Considering two phases, gas and liquid, in equilibrium at the same temperature and the same pressure, according to classical solution theory we have the following relations for the chemical potential of solute, *s*, in each phase:

$$\mu_s^g = \mu_s^0 + k_B T \ln(P_s) \tag{11-1}$$

and

$$\mu_s^l = \mu_s^* + k_B T \ln(x_s) \tag{11-2}$$

where, T is the temperature, k_B is the Boltzmann constant, μ_s^0 and μ_s^* are the standard-state chemical potentials of s in the gas and liquid phases, respectively, P_s is the partial pressure of s in the gas phase, x_s is the mole fraction of s in the liquid phase and superscripts g and l indicate the gas and liquid phases, respectively.

At equilibrium $\mu_s^g = \mu_s^l$, therefore

$$\mu_s^* - \mu_s^0 = k_B T \ln\left(\frac{P_s}{x_s}\right) \tag{11-3}$$

This equation provides a very simple way of computing the difference in the standard-state chemical potentials (or as it will be seen in Section 11.3, the solvation free energy) from vapor pressure measurements.

11.3. STATISTICAL MECHANICS OF SOLVATION

The determination of solvation free energy of solutes in solvents is a problem of primary importance, since all thermodynamic quantities can be derived from the free energies. For a system of N particles located at $r_1, r_2, \ldots, r_N$, the statistical mechanical expression for the Helmholtz free energy, A, reads as [2]

$$A = -k_B T \ln(Q) = \frac{1}{N! \Lambda^{3N}} \int_0^\infty \cdots \int_0^\infty \exp\left(-U_N\left(r^N\right)/k_B T\right) \mathrm{d}r^N \tag{11-4}$$

where Q is the canonical partition function, $\Lambda = h/(2\pi m k_B T)^{1/2}$ is the de Broglie wavelength, U_N is the potential energy of the system, and r^N stands for the whole set of coordinates, $r_1, r_2, \ldots, r_N$. Assuming pairwise additivity of the potential energy between particles, we have

$$U_N = \sum_i^N \sum_{j>i}^N \boldsymbol{u}_{ij}(\boldsymbol{r}_{ij}) \tag{11-5}$$

where u_{ij} is the pair potential interacting between particles i and j and r_{ij} is the interparticle distance. The expression for the chemical potential is obtained by taking the logarithm of the ratios of partition functions for a system composed of N particles, with the solute density of ρ_s, and a system composed of $N+1$ particles, which is obtained by adding one solute particle to the previous N-particle system, i.e.,

$$\mu_s = A_{N+1} - A_N = k_B T \ln\left(\rho_s \Lambda^3\right) - k_B T \ln\left(\langle \exp(-\Delta U / k_B T)\rangle\right) \quad (11\text{-}6)$$

with

$$\Delta U = U_{N+1} - U_N \quad (11\text{-}7)$$

and the brackets indicate the ensemble average. Equation (11-6) can be simply arranged as the sum of contributions from pure solute chemical potential and a term related to the solute concentration, like Eqs. (11-1) or (11-2). Ben-Naim [1], however, used another more general form to interpret various contributions to the chemical potential as

$$\mu_s = \mu_s^{ex} + k_B T \ln\left(\rho_s \Lambda^3\right) \quad (11\text{-}8)$$

where μ_s^{ex} is called the excess chemical potential of solute. The second term on the right hand side of Eq. (11-8) is the chemical potential of the ideal gas. According to Eq. (11-8), the chemical potential of the solute is split into two terms; a term arising from putting the solute molecule at a fixed position in the solution, μ_s^{ex}, and a term arising from releasing the constraint, i.e., letting the solute molecule move freely, which results in the contribution $k_B T \ln\left(\rho_s \Lambda^3\right)$ to the chemical potential. On releasing the constraint of keeping the solute molecule at a fixed position, it will gain its translational kinetic energy and will wander throughout the entire volume of the system, and hence there is a translational contribution to the chemical potential.

Considering solute molecules at the density of ${\rho_s}^{ig}$ in the ideal gas phase in equilibrium with solute molecule in the liquid phase at a density of ${\rho_s}^{l}$ and considering the fact that at equilibrium the chemical potentials of solute in both phases are equal, we can write

$$\Delta G_{sol} = \mu_s^{ex,1} - \mu_s^{ex,ig} = \mu_s^{ex,1} = k_B T \ln\left(\frac{\rho_s^l}{\rho_s^g}\right) \quad (11\text{-}9)$$

where ΔG_{sol} stands for the free energy change due to solvation. Equation (11-9) is similar to Eq. (11-3), except the concentration scales in both phases are written in Eq. (11-9) in terms of solute density, and the standard-state chemical potentials in Eq. (11-3) are replaced by the excess chemical potentials in Eq. (11-9). On converting the mole-fraction scale in Eq. (11-3) to the concentration scale, the same expression for ΔG will be obtained. This means that solvation Gibbs free energy change is equal in magnitude with the standard-state Gibbs free energy change when the concentration scale is used. This equality holds just for the Gibbs free energy change of the two afore-cited processes.

Therefore, according to Eq. (11-9), the Gibbs free energy change of solvation is expressed as the change in chemical potential on transferring a solute molecule from a fixed position in the gas phase to a fixed position in the liquid phase. The free energy of solvation can be decomposed to several contributions including formation of cavity and contributions due to the van der Waals and electrostatic forces

[3,4,5,6]. The formation of a cavity to accommodate the solute molecules includes breaking down the cohesive forces between solvent molecules, therefore its corresponding free energy is positive. On the other hand the van der Waals forces between the solute and solvent molecules contribute favorably to solvation free energy. Usually, these two terms, cavitation and the van der Waals interactions, are referred to as nonelectrostatic contributions. The electrostatic contribution to the free energy measures the work needed to build up the charge distribution of the solute in solution and includes two components; the work necessary to create the solute's gas-phase charge distribution in solution and the work required to polarize the solute charge distribution by the solvent. It is worth considering that the electrostatic contribution includes not only the gain of the electrostatic interaction energy between the solute and solvent molecules, but also the work needed to generate the solvent reaction field induced by the solute charge distribution [3]. In the case of polar solvents such as water, the van der Waals contribution is moderate and cannot fully compensate the unfavorable effect of the cavitation term, whereas for nonpolar solvents, the cavitation work is smaller (in absolute terms) than the van der Waals contribution due to the weaker interactions between solvent molecules. For nonpolar solutes, in nonpolar solvents the nonelectrostatic term can be the main contribution to solvation. On the contrary, for most solutes of interest, in polar solvents such as water the electrostatic term makes the dominant contribution to the free energy of solvation, due to the strength of solute–solvent electrostatic interactions.

Having described the solvation free energy we now focus on the solvation enthalpy, which is defined as

$$\Delta H_{\text{sol}} = \Delta U_{\text{sol}} + P\Delta V_{\text{sol}} \tag{11-10}$$

where ΔH_{sol}, ΔU_{sol}, and ΔV_{sol} are the changes in enthalpy, internal energy, and volume on solvation. The solvation energy is defined as the difference in the average potential energy of solution and the average potential energy of the pure solvent. The potential energy of solution is composed of contributions from solute–solvent interactions and solvent–solvent interactions, i.e.,

$$\Delta U_{\text{sol}} = \Delta U_{\text{solvent-solvent}} + \Delta U \tag{11-11}$$

where ΔU indicates the solvent–solute interaction energy. The solvent–solvent interaction energy is called solvent reorganization energy, which expresses the change in the total intermolecular solvent interaction energy induced by introducing solute molecule. Supposing U_{N+1} as the potential energy of an (N+1)-molecule system, i.e., N solvent molecules and one solute molecule, the solvent–solvent reorganization energy is defined as

$$\Delta U_{\text{solvent-solvent}} = \langle U_N \rangle_{N+1} - \langle U_N \rangle_N \tag{11-12}$$

The solvent–solvent reorganization energy and the solvent–solute interaction energy can be calculated using simulation methods, employing the above-written formulas as

$$\Delta U_{\text{solvent-solvent}} = \frac{\langle U_N V \mathrm{e}^{-\Delta U/k_\mathrm{B}T}\rangle - \langle U_N\rangle\langle V \mathrm{e}^{-\Delta U/k_\mathrm{B}T}\rangle}{\langle V \mathrm{e}^{-\Delta U/k_\mathrm{B}T}\rangle} \tag{11-13}$$

and

$$\Delta U = \frac{\left\langle \Delta U V \mathrm{e}^{-\Delta U/k_\mathrm{B}T}\right\rangle}{\left\langle V \mathrm{e}^{-\Delta U/k_\mathrm{B}T}\right\rangle} \tag{11-14}$$

where the brackets indicate the averages in the isothermal–isobaric ensemble.

11.4. POLYMER SOLUTIONS

The classical Raoult's law connects the vapor pressure of the ith component, P_i, in a mixture to its vapor pressure at pure state, P_i^*, i.e.,

$$P_i = P_i^* x_i \tag{11-15}$$

where x_i is the mole fraction of the ith component in the liquid phase. In a binary solution consisting of a solvent and a polymer, with molecular weight of approximately thousand times higher than that of the solvent, the mole fraction of the solvent is close to unity. Therefore, according to the Raoult's law the partial pressure of the solvent is equal to its vapor pressure. However, experiment does not confirm the validity of Raoult's law for such a mixture. Moreover, experiment shows that the deviation from ideality is not strongly temperature dependent, which means that deviation in the entropy of mixing is higher than that of the heat of mixing from their corresponding values for ideal mixing.

Flory [7,8,9] proposed a lattice model to derive an approximation for the entropy of mixing of polymers with solvents. Considering a binary solution of solvent molecules and polymers, in such a system a molecule of one type can be exchanged with a molecule of the other type. The entropy of mixing is related to the number of possible arrangements in the solution. In polymer solutions a polymer molecule is, may be thousands of time, bigger in size than a solvent molecule. The long-chain polymer molecule is considered to consist of N chain segments, each of which equal in size to that of the solvent molecule. Therefore, N is the ratio of the molar volume of the polymer to that of the solvent. A solvent and a segment may replace one another in a liquid lattice. The total configurational entropy of this solution is calculable by counting the number of possible ways of arranging the polymer and solvent molecules as it is formulated by Flory [7,8,9], i.e.,

$$\Delta S = -k_\mathrm{B}\left(N_{\text{solvent}} \ln\left(\upsilon_{\text{solvent}}\right) + N_\mathrm{s} \ln\left(\upsilon_\mathrm{s}\right)\right) \tag{11-16}$$

where N is the number of molecules and υ is the volume fraction and is defined as

$$\upsilon_{\text{solvent}} = \frac{N_{\text{solvent}}}{N_{\text{solvent}} + N_{\text{s}}\boldsymbol{N}} \tag{11-17}$$

and

$$\upsilon_{\text{s}} = \frac{N_{\text{s}}\boldsymbol{N}}{N_{\text{solvent}} + N_{\text{s}}\boldsymbol{N}} \tag{11-18}$$

Later Hildebrand [10] obtained the same result assuming that free volume available to the molecules per unit volume of liquid is the same for the polymer as for the solvent. The heat of mixing is defined as the difference between the total interaction energy in the mixture compared with that of pure components. Based on their lattice theory model, Flory [7,8,9] and Huggins [11,12] obtained the following expression for the heat of mixing:

$$\Delta H_{\text{mix}} = k_{\text{B}} T N_{\text{solvent}} \upsilon_{\text{s}} \chi \tag{11-19}$$

where χ is a dimensionless quantity characterizing the interaction energy per solvent molecule divided by $k_{\text{B}}T$. This assumption shows that the difference in energy of a solute molecule immersed in the pure polymer compared to the one surrounded by molecules of its own, pure solvent, is $k_{\text{B}}T\chi$. The free energy of mixing is simply formulated in terms of Eqs. (11-16) and (11-19) as

$$\Delta G_{\text{mix}} = k_{\text{B}} T \left(N_{\text{solvent}} \ln\left(\upsilon_{\text{solvent}}\right) + N_{\text{s}} \ln\left(\upsilon_{\text{s}}\right) + \chi N_{\text{solvent}} \upsilon_{\text{s}}\right) \tag{11-20}$$

The chemical potential of the solvent, μ_{solvent}, and that of solute, μ_{s}, in the solution relative to their corresponding chemical potentials in the pure liquid is obtained by differentiating the above expression for the free energy of mixing as

$$\mu_{\text{solvent}} - \mu^0_{\text{solvent}} = k_{\text{B}} T \left(\ln(1 - \upsilon_{\text{s}}) + \left(1 - \frac{1}{\boldsymbol{N}}\right) \upsilon_{\text{s}} + \chi \upsilon_{\text{s}}^2\right) \tag{11-21}$$

and

$$\mu_{\text{s}} - \mu^0_{\text{s}} = k_{\text{B}} T \left(\ln(\upsilon_{\text{s}}) + (1 - \boldsymbol{N})(1 - \upsilon_{\text{s}}) + \chi \boldsymbol{N} \ (1 - \upsilon_{\text{s}})^2\right) \tag{11-22}$$

The mole-fraction scale is usually used when the sizes of the solute and solvent molecules are approximately equal, but the volume-fraction scale is used when the sizes are different. This will be explained in the following sections.

11.5. COMPARISON OF FLORY–HUGGINS AND CLASSICAL SOLUTION THEORIES

So far two models have been employed to rationalize the solvation process; the classical solution model, either the mole-fraction scale or any other concentration scale, and the Flory–Huggins model. The question is where to use which theoretical model to interpret the results of partitioning experiments, in which solute molecules distribute between two phases, α and β. If the two phases are at equilibrium at the same temperature and the same pressure, $\mu_s^{\alpha} = \mu_s^{\beta}$. After rearrangement and applying Eq. (11-8), we can write

$$\Delta G_s^{\beta} - \Delta G_s^{\alpha} = \mu_s^{ex,\beta} - \mu_s^{ex,\alpha} = k_B T \ln\left(\frac{\rho_s^{\alpha}}{\rho_s^{\beta}}\right) \tag{11-23}$$

where ρ_s^{α} and ρ_s^{β} are the solute densities in phase α and β, respectively. Equation (11-23) represents the difference in the solvation Gibbs free energy change in the two phases. When one of the phases is the ideal gas, Eq. (11-23) reduces to Eq. (11-9). When we deal with spherical molecules in spherical or near-spherical solvents, the classical mole-fraction scale approach is a better approximation in treating the data. It is shown [13,14,15] that the solubility of iodine in some near-spherical solvents of different sizes is better approximated by the mole-fraction scale approach than that of volume fraction or Flory–Huggins theory. On the other hand the solubility of some solutes in complex solvents can be better represented by Flory–Huggins method [16,17].

Suppose that we transfer solute *s* from a medium into other nonpolar media of long-chain *n*-alkanes with different chain lengths. The transfer free energy should be independent of chain length [18] because it should reflect only the chemical change seen by the solute molecule on transferring from the initial medium to the alkane medium. In other words, the solute should see the same nonpolar environment, independent of the chain length in alkane solvents. According to this, the theoretical model employed to analyze the experimental results should show the independency of the solvation free energy with respect to the chain length. The partition coefficient of benzene as the solute between *n*-alkanes with 8–16 carbon atoms and water at various temperatures, as determined by de Young and Dill [17], shows that Flory–Huggins theory better reveals the above-mentioned fact. de Young and Dill [17] tried to describe the partitioning data by introducing the mole-fraction ratios, $K_x = x_s^w/x_s^a$, the volume-fraction ratios, $K_V = \upsilon_s^w/\upsilon_s^a$, and the Flory–Huggins corrected volume-fraction relation, K_V^c, which is expressed as

$$\ln\left(K_V^c\right) = \ln\left(\frac{\upsilon_s^w}{\upsilon_s^a}\right) + \left(\frac{V_s}{V_w} - \frac{V_s}{V_a}\right) \tag{11-24}$$

where υ is the volume fraction, V is the molar volume, and subscripts or superscripts *s*, *w*, and *a* represent solute, water, and alkane, respectively. Figure 11-1 shows

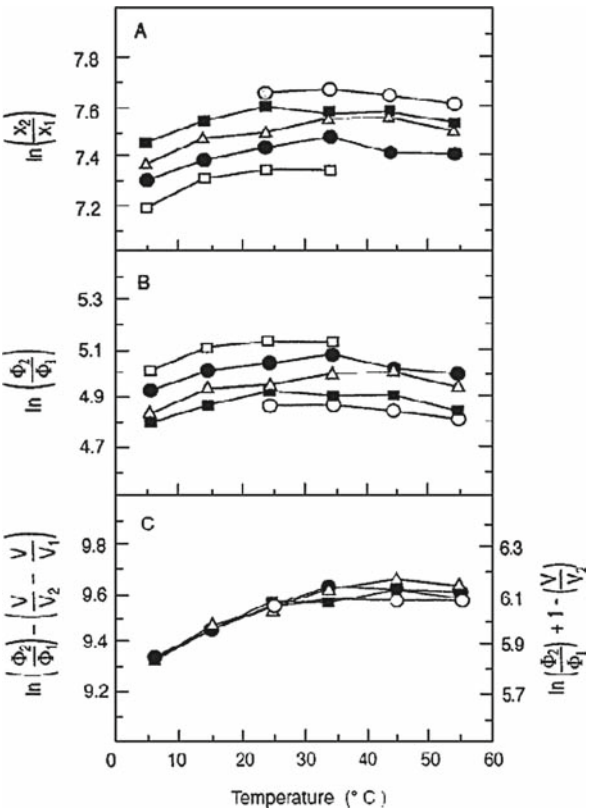

Figure 11-1. Temperature dependence of the partitioning of benzene (*s*) between water (*w*) and *n*-alkanes (*a*) of different chain lengths: octane (□), decane (●), dodecane (Δ), tetradecane (■), and hexadecane (◯). In (**C**), the left vertical scale pertains when Flory–Huggins theory is applied to both the *a* and *w* phases, whereas the right vertical scale pertains when Flory–Huggins theory is applied only to the a phase. The figure is taken from de Young and Dill [17] with permission

that the mole-fraction scale and the volume-fraction scale partition coefficients are dependent on the chain length of the solvent hydrocarbon, but the Flory–Huggins partition coefficient is independent of the chain length [17]. As explained in Section 11.4, Flory–Huggins theory uses the volume-fraction concentrations, whereas the classical approach uses the mole fraction or molar concentrations. This distinction is not important, as any concentration scale is convertible to any other. The important distinction is in the second term on the right hand side of Eq. (11-24). This term has been interpreted by Sharp et al. [19] as the size entropy since it depends on the ratios of sizes of solute and solvent molecules. Sharp et al. [19] claimed that this second term is of a very general applicability, since Flory–Huggins theory reduces to the classical thermodynamic theory when the sizes are identical.

11.5.1. Effect of Internal Degrees of Freedom

Chan and Dill [18,20] derived solution chemical potentials from general statistical mechanical theory and concluded that classical thermodynamic treatments generally assume separability of the translational and internal degrees of freedom. Under this assumption, it follows that there should be no size entropy of the Flory–Huggins type. They showed that when internal and translational degrees of freedom are coupled, as in the case of polymers or complex solutes, an entropy is involved which is called coupling entropy, instead of size entropy introduced by Sharp et al. [19]. To describe this coupling among degrees of freedom, Chan and Dill [20] chose a dimer as a simple nonspherical molecule and tried to transfer it from a pure dimer state to a lattice. The model is chosen because the results can be computed exactly [20,21] so that they cannot be dismissed as artifacts of approximations. In a solution with monomeric solvent a dimer has two possible orientations, therefore a total of only 2^N different orientations of N dimer are possible. But in a solution of dimers, the exact treatment of Fisher [21] shows that a total of κ^N, with κ=1.791623 (less than 2^N) is possible. This is due to the fact that in the condensed phase the orientations of different dimers are coupled. Therefore, each dimer is hindered and cannot rotate freely to adopt its possible two states. Thus each dimer gains an orientational entropy of $k_B \ln(2/\kappa)$ upon transferring to solution. Therefore, there is a conformational contribution of $k_B T \ln(2/\kappa)$ to the transfer free energy, which should be added to Eq. (11-24), in addition of the center of mass translation term $k_B T \ln(\rho)$.

11.5.2. Coupling of the Center of Mass of One Molecule to the Excluded Volume of Another (Polymer Solutions)

Chan and Dill [20] showed that the polymer coupling entropy is due to the excluded volume in the Flory–Huggins theory. In fact each polymer segment may interact with some other chain of the nearby chain and this diminishes the chance of the center of mass of this molecule occupying a given spatial position. There is a difference of $k_B T$ in the conformational entropy per monomer between the infinitely dilute and maximally condensed phases. This means that the center of mass translations are coupled to the excluded volume of the segment of a chain. The magnitude of this coupling is dependent on the concentration, because there is more coupling in the concentrated solutions. Figure 11-2 shows that for spheres, without any orientational entropy, only translational degrees of freedom contribute to the distribution of molecules. For rods, placement of the centers of mass is not independent of the orientations or configurations of the neighboring molecules. Figure 11-2a shows rod orientations or polymer conformations that are compatible, i.e., not in steric conflict, with the relative centers of mass. Figure 11-2b shows how the same center of mass positions are not viable when the orientations or internal conformations would cause two different parts of molecules to lie in the same region of space. This coupling of excluded volume with centers of mass is treated by Flory–Huggins theory. Chan and Dill [20] applied a general statistical mechanical treatment and a generalized Flory–Huggins theory to show that when solutes and solvents are complex enough that they can interfere

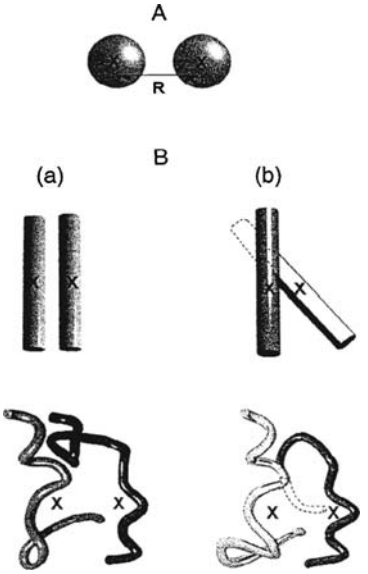

Figure 11-2. Steric interference. (**A**) To avoid steric violations in placing the centers of mass of two spheres in space, their separation must be greater than one sphere diameter. (**B**) For nonspherical molecules, steric violations are determined by a complex coupling of center of mass positions and orientations (for rods) or chain conformations (for polymers). (**a**) and (**b**) show two identical center of mass positions for two molecules. In (**a**) the relative orientations lead to no steric conflict, while the configurations in (**b**) are impossible because of steric violations. The figure is taken from Chan and Dill [18] with permission

with each other in solution there is an entropy of coupling translational freedom to excluded volume. Their results agree well with the exact lattice enumeration results [22] of configurations of a single chain and with the computer enumeration results [23]. The enumeration results also show that if a polymer is not longer than 6–8 monomer units, the Flory–Huggins theory is reasonably accurate. Their results also show that the Flory–Huggins theory approximates the coupling entropy for polymeric solvents or solutes, but not for other systems. According to Flory–Huggins theory, when polymer *a* is transferred from its pure liquid phase into a liquid solution with polymer *b*, if the chain length of *a* is greater than that of *b*, polymer *a* will experience less steric interference in solution with *b* and configurational entropy will favor the transfer. If the chain lengths are equal the configurational entropy will not drive the system either way, and if the chain length of *b* is greater than the chain length of *a* the configurational entropy will oppose the transfer of *a* from pure liquid *a* to a solution with *b*. The dependence on size-difference in the chemical potential approaches zero with diminishing concentration of *b*. For the case of transferring globular molecules, if either solution involves polymers, the Flory–Huggins theory should be approximately valid, but if both solutes are also globular but not spherical, Flory–Huggins theory is not appropriate enough and up to now there is no general

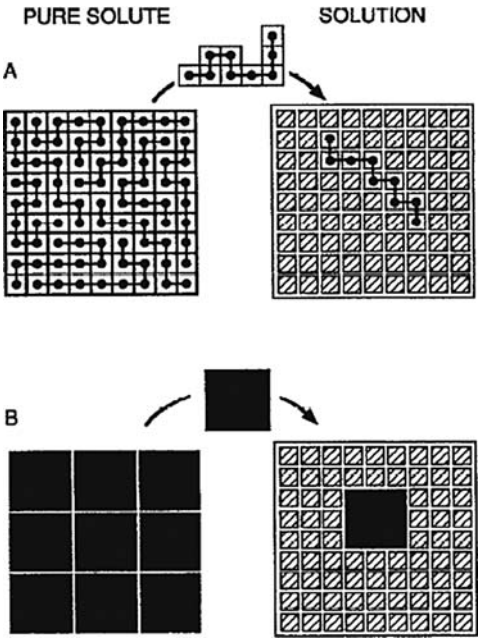

Figure 11-3. (**A**) Transfer of a flexible polymer and (**B**) transfer of a globular molecule of the same size from the condensed pure phase to a dilute solution. The figure is taken from Chan and Dill [20]

theory for treating such systems. Figure 11-3 compares the transfer of a polymer from its pure liquid state to a dilute solution with that of transfer of a more globular molecule, a large square, from its pure phase to dilute solution, to illustrate how polymer solutions differ from simpler solutions. The figures are shown so that both the polymer and the globular molecule have identical sizes. Upon transferring to the solution, the polymer gains conformational freedom, because it can adopt any sterically available conformation in the solution, but its conformations are constrained by the configurations of the neighboring chains in the pure state. In contrast, there is no internal entropy in the case of a globular molecule. Therefore it gains only the translational entropy, but not the rotational or configurational entropies.

11.5.3. Effect of Molecular Shape and Architecture

Krukowski et al. [24] studied the effect of molecular shape in details by performing exact enumerations on lattice models of different molecular shapes. They calculated the entropic component of the chemical potential, i.e.,

$$\mu^{(s)} = k_B T \ln \left(\frac{\partial S_{\text{config}}}{\partial N} \right)_{T,V} \tag{11-25}$$

for inserting different geometrical shapes into a pure medium of other such molecules. They adopted the mole-fraction scale, density scale, and Flory–Huggins entropic component of the chemical potentials to compare these three cases. Since in their theory, the Flory–Huggins internal partition function depends on the lattice coordination number, z (z=4 and 6 for the square and simple cubic lattices, respectively), they added a $k_B T \ln(q)$ term to the Flory–Huggins in order to compare all the treatments on an equal footing. As it is shown in Figure 11-4 at low densities, the chemical potentials are independent of the shape of the molecule, because at low densities there is enough space for the solute molecule to be inserted. At higher densities, it is easier to insert a globular molecule into a medium of the same molecules than inserting a more articulated molecule into a medium of similar molecules. Krukowski et al. [24] founded that articulated molecules are more accurately treated by the Flory–Huggins theory, while globular molecules are more accurately treated by the classical solution theory in comparison with arbitrary distribution of the centers of mass. Therefore, configurational freedom per polymer molecule diminishes with polymer concentration and Flory–Huggins theory applies well to these kinds of solutions. According to the explanations and formulations by Krukowski et al. [24], the mole-fraction scale and the Flory–Huggins entropic components of the chemical potential treat change in total entropy, including center of mass translational entropy and internal configurational entropy of all solutes in solution, while the density scale accounts only for the translational entropy of the added solute, which can be located at any viable position. Therefore, in Figure 11-4, deviations occur among the three treatments at high densities where translations, rotations, and steric packing

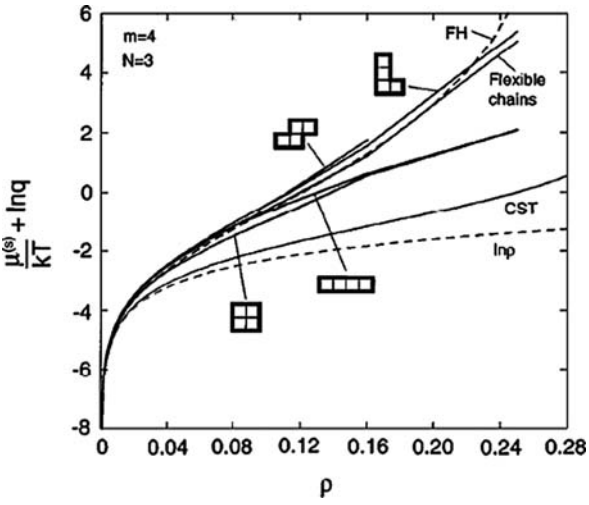

Figure 11-4. Comparison of exact chemical potentials with Flory–Huggins theory (FH), mole-fraction-based classical solution theory (CST), and density-based ($\ln(\rho)$) approximations. The figure is taken from Krukowski et al. [24] with permission

are coupled to each other. In the high-density regime, the more articulated shapes, like the crosses and angles, are better approximated by Flory–Huggins than the more globular shapes such as the squares.

11.6. SOLVATION IN POLYMERS

Solvation is an interesting topic in polymer physical chemistry both from theoretical and experimental points of view, and it has triggered numerous studies for many years. When a polymer is exposed to a solvent, the solvent molecules may diffuse into it. If the polymer is soluble in the solvent there is an attractive interaction between polymer and solvent and the net interaction between polymer segments is repulsive. Therefore, the coiled polymer chains start swelling, and eventually the process leads to saturation where the swollen polymer chains are in equilibrium with the solvent. The understanding of polymer chain dynamics and its equilibrium structure in the presence of solvent is important. One of the most important phenomena in the polymer solvation is the change in the overall size of the polymer chain upon solvation. In fact at equilibrium the average size of isolated polymer molecules in solution is a function of solvent quality and varies from expanded conformations in good solvents to random walk conformations in poor solvents.

Experimental as well as theoretical methods have been widely employed to study such phenomena as solubility, the conformational structures, size change, and so on. Although these methods have been very successful, however, for example the experimental methods cannot reveal the detailed solvation structures to describe the interaction between solvent and polymer. Either theoretical methods are also not completely atomistic or they assume a certain molecular behavior. Molecular simulation methods, on the other hand, can produce most atomistic information about the solvation process. In this section we will mostly focus on the application of molecular dynamics simulation technique to understand solvation process in polymers.

11.6.1. Sorption of Gases in Polymers

Knowledge of the solubilities of small molecules in polymers is essential for the design and operation of polymer plants so that residual monomers, oligomers, and polymerization solvents can be removed from the polymer products. Gas solubilities also play important roles in such applications as designing polymer barrier materials for packaging applications, developing membranes for gas separations, foaming, and plasticization. For gases in polymers, the solubility describes the concentration C of the gas inside a polymer at equilibrium with the gas at a partial pressure P and is often described phenomenologically by the dual-mode sorption theory [25,26]:

$$C = k_{\mathrm{H}} P + C_{\infty} \frac{bP}{1 + bP} \tag{11-26}$$

where k_{H} is Henry's law solubility coefficient, C_{∞} is the saturation concentration of the gas, and b is the affinity coefficient. This model assumes that there are two

distinct modes by which a glassy polymer can sorb gas molecules: Henry's law and a Langmuir mechanism which corresponds to the sorption of gases into specific sorption sites in the polymer. Henry's constant has the same physical meaning for glassy polymers as it does for rubbery polymers and liquids, whereas the Langmuir-type term is believed to account for gas sorption into interstitial spaces and microvoids, which are consequences of local heterogeneities and are intimately related to the slow relaxation processes associated with the glassy state of the polymer. Local equilibrium is assumed between the two modes. The dual-mode sorption equation, Eq. (11-26), provides a linear relationship against the pressure in the low-pressure region, i.e.,

$$C = (k_{\mathrm{H}} + C_{\infty} b)\, P = S_0 P \tag{11-27}$$

where S_0 is called the apparent solubility coefficient in the zero-pressure limit in glassy polymers.

Considering a real gas at temperature T and pressure P in equilibrium with a polymer phase and assuming that at equilibrium the concentration of the sorbed gas inside the polymer is C, we can write the following expression connecting the solubility coefficient to the excess chemical potentials:

$$\mu^{\mathrm{ex}}_{\text{gas in polymer}}(T,\, P) - \mu^{\mathrm{ex}}_{\text{gas}}(T,\, P) = -k_{\mathrm{B}} T \ln (S k_{\mathrm{B}} T) \tag{11-28}$$

where S is the solubility coefficient defined as C/P. Because of the fact that gas solubilities have been determined by means of different methods, they have been expressed in different units. The most frequently used unit is the volume of gas (in cm^3) reduced to the standard conditions dissolved in 1 cm^3 of polymer, i.e.,

$$S = \frac{V_{\mathrm{g}}(\mathrm{STP})}{V_{\mathrm{p}} P} \tag{11-29}$$

where V_{g} (STP) is the volume of the penetrant gas at STP conditions (T_0=273.15 K and P_0=1 atm), and V_{p} is the volume of polymer at temperature T and pressure P. Correspondingly, Eq. (11-28) is written as

$$\mu^{\mathrm{ex}}_{\text{gas in polymer}}(T,\, P) - \mu^{\mathrm{ex}}_{\text{gas}}(T,\, P) = -k_{\mathrm{B}} T \ln \left(\frac{S T P_0}{T_0} \right) \tag{11-30}$$

At relatively low pressures the second term on the left hand side of Eq. (11-30) is nearly zero and can be neglected.

Traditional approaches for the calculation of the phase equilibria and sorption of penetrant molecules in polymers are based on equation-of-state models [27,28,29], which take into account the *PVT* properties of both gas and polymer, and the activity coefficient models [30], which take into account the specific interactions between

polymer and penetrant molecules. Molecular simulations are the other attractive methods for this type of calculation. These methods do not invoke any approximations, and predictions are based on well-defined molecular characteristics. In the following sections we describe the application of molecular simulation methods in the case of sorption of gases in polymers.

11.6.1.1. Molecular simulation methods for calculation of phase equilibria

There are several methods for the calculation of phase coexistence points using molecular simulation, such as thermodynamic scaling method [31,32], histogram reweighting method [33,34], the Gibbs–Duhem integration method [35,36], NPT plus test-particle method [37,38], various extensions of it to other ensembles [39,40], and the Gibbs ensemble Monte Carlo method [41]. The last technique has been applied to coexistence properties of simple systems, such as fluids of spherical Lennard-Jones or Yukawa particles [42,43], as well as more complex systems, such as polyatomic hydrocarbons [44,45] and chain molecules [46]. There are also reports on the mixed methods in which the molecular simulation approaches have been utilized to calculate the chemical potentials in the condensed phase, and the results from equations-of-state predictions are used to calculate the phase coexistence point [47], or to calculate the interaction energy parameters of solvent and polymer, in combination with statistical mechanical theories for the study of phase equilibria of polymer–solvent mixtures [48].

Many computational studies of the permeation of small gas molecules through polymers have appeared, which were designed to analyze, on an atomic scale, diffusion mechanisms or to calculate the diffusion coefficient and the solubility parameters. Most of these studies have dealt with flexible polymer chains of relatively simple structure such as polyethylene, polypropylene, and poly-(isobutylene) [49,50,51,52,53]. There are, however, a few reports on polymers consisting of stiff chains. For example, Mooney and MacElroy [54] studied the diffusion of small molecules in semicrystalline aromatic polymers and Cuthbert et al. [55] have calculated the Henry's law constant for a number of small molecules in polystyrene and studied the effect of box size on the calculated Henry's law constants. Most of these reports are limited to the calculation of solubility coefficients at a single temperature and in the zero-pressure limit. However, there are few reports on the calculation of solubilities at higher pressures, for example the reports by de Pablo et al. [56] on the calculation of solubilities of alkanes in polyethylene, by Abu-Shargh [53] on the calculation of solubility of propene in polypropylene, and by Lim et al. [47] on the sorption of methane and carbon dioxide in amorphous polyetherimide. In the former two cases, the authors have used Gibbs ensemble Monte Carlo method [41,57] to do the calculations, and in the latter case, the authors have used an equation-of-state method to describe the gas phase.

11.6.1.2. Grand equilibrium method: application to the calculation of solubility of gases in polystyrene

In the Gibbs ensemble simulation method one specifies the thermodynamic variables temperature, global composition, and global pressure for the simulation of both phases in separate volumes. Practically, this set of thermodynamic variables is in many cases not convenient and simultaneous simulation of both phases has the disadvantage that fluctuations occurring in one phase influence the other one. Recently a new method, grand equilibrium method, has been developed by Vrabec and Hasse [58]. This method circumvents the afore-cited problems for the study of phase equilibria. The specified thermodynamic variables are temperature and composition and two independent simulations are performed for the two phases without the need to exchange particles in the condensed phase. According to this method for a mixture composed of several components, it is possible to do a simulation in the isothermal–isobaric (*NPT*) ensemble at constant temperature, a constant composition of the condensed phase, and at an arbitrary constant pressure, preferably close to the pressure at the phase coexistence point, to obtain the density of the condensed phase.

In the grand equilibrium method, a simulation of the condensed phase is done to calculate the excess chemical potentials, μ_i^{ex}, and the partial molar volumes, V_i, of all components. One may use the test-particle insertion method [59] to calculate the excess chemical potentials and the partial molar volumes as

$$\mu^{\mathrm{ex}} = -k_{\mathrm{B}}T \ln\left\langle \frac{PV}{Nk_{\mathrm{B}}T} \exp\left(-\Delta U/k_{\mathrm{B}}T\right)\right\rangle \tag{11-31}$$

and

$$V_i = \frac{\left\langle V^2 \exp\left(-\Delta U/k_{\mathrm{B}}T\right)\right\rangle}{\left\langle V \exp\left(-\Delta U/k_{\mathrm{B}}T\right)\right\rangle} - \langle V\rangle \tag{11-32}$$

where ΔU is the potential energy of interaction between the test particle and the host polymer, V is the volume, and N is the number of particles. Knowing the parameters V_i and μ_i^{ex} from this simulation, the desired excess chemical potentials as functions of pressure are obtained from a first-order Taylor series expansion, i.e.,

$$\mu_i^{\mathrm{ex}}(P) = \mu_i^{\mathrm{ex}}(P^*) + \frac{V_i}{kT}\left(P - P^*\right) \tag{11-33}$$

where P^* is the target pressure at which the *NPT* ensemble simulation is done. Once the $\mu_i^{ex}(P)$ is determined from Eq. (11-33) by one *NPT* ensemble simulation of the condensed phase, one vapor/gas simulation has to be performed in the pseudo-grand canonical ensemble (pseudo-μVT). In a common grand canonical ensemble [60] the parameters temperature, volume, and the chemical potential of all species are fixed, while in this pseudo-μVT ensemble simulation, the parameters T and V are fixed in the common way, but instead of fixing the chemical potentials, they are set as a function of the instantaneous pressure in the gas phase. This procedure ensures that

equilibrium between the condensed phase and the gas phase is imposed. In a common μVT ensemble simulation [60], the chemical potentials are set through insertion and deletion of particles by the comparison between the resulting potential energy change and the desired fixed chemical potential. Here, starting from a low-density state point, the gas-phase simulation is forced to change its state to the corresponding phase equilibrium state point.

Recently, we have applied this method for the calculation of solubilities of gases in polystyrene over a wide range of temperatures and pressures [61]. To calculate the excess chemical potential at infinite dilution, first molecular dynamics simulations are performed at a specified temperature and pressure of the polymer, without any gas molecules. After equilibration, several configurations are extracted at different times from the dynamic simulation and used to insert the test particles. A test molecule is repeatedly inserted into the selected configurations at random positions and in random orientations and the energy change due to insertions is calculated. The excess chemical potential is then calculated as the average of the Boltzmann factor of the test-particle insertions according to Eq. (11-33). This Boltzmann factor is interpreted as the acceptance probability in hypothetical Monte Carlo moves, which would insert a particle into a configuration.

The variation of the infinite dilution excess chemical potentials with time for CH_4 and C_3H_8 at 300 K over the whole 3.9 ns of simulation are shown in Figure 11-5. The fluctuations for C_3H_8 are larger than that of CH_4. This is reasonable, because of the larger size of C_3H_8 compared to CH_4. In fact, a trial insertion will be "successful" if the particle enters a cavity, which is bigger than the particle. The number of smaller cavities in a configuration is much larger than the number of bigger ones; therefore, the number of small cavities is more likely to remain essentially unchanged between two polymer configurations than the number of bigger ones. If the cavity

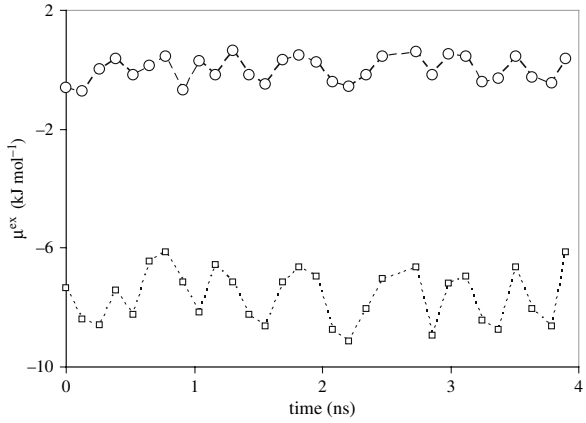

Figure 11-5. The excess chemical potential at infinite dilution for methane (◯) and propane (□) in polystyrene at 300 K and 1.0 atm calculated at 130 ps intervals. The figure is taken from Eslami and Müller-Plathe [61]

size is big enough, such cavities may altogether disappear and reappear between two configurations. In a glassy polymer it takes a relatively long time for disappearance and reappearance of big cavities. In this case calculation of free energies for bigger molecules is less reliable. Calculating the excess chemical potentials over a 3.9 ns run for CO_2 in PS we have calculated its solubility coefficients in the zero-pressure limit, S_0, according to Eq. (11-28). The results are indicated in Figure 11-6 and are compared with experimental measurements [62,63,64,65,66,67,68,69] compiled by Paterson et al. [70]. As it is seen in Figure 11-6, our calculated values of S_0 are higher than the corresponding experimental values. Similar differences between experimentally and computed solubility coefficient values have been observed in previous studies [47,71]. As found earlier by Knopp and Suter [72] there is an error of (2–4) $k_B T$ commonly found in the calculation of Helmholtz energies by molecular simulations. Moreover, the main contribution to the solubility comes from single holes in the simulated polymer structure, which might not be present in similar proportion in real polymers [73].

We can also compare the calculated solubility ratios with the corresponding values from experimental measurements. The ratios of solubility coefficients in the zero-pressure limit to that of Ar are compared with the corresponding experimental quantities in Table 11-1. As it is clear from Table 11-1, the calculated ratios are within the experimentally obtained values. This confirms that the calculated values

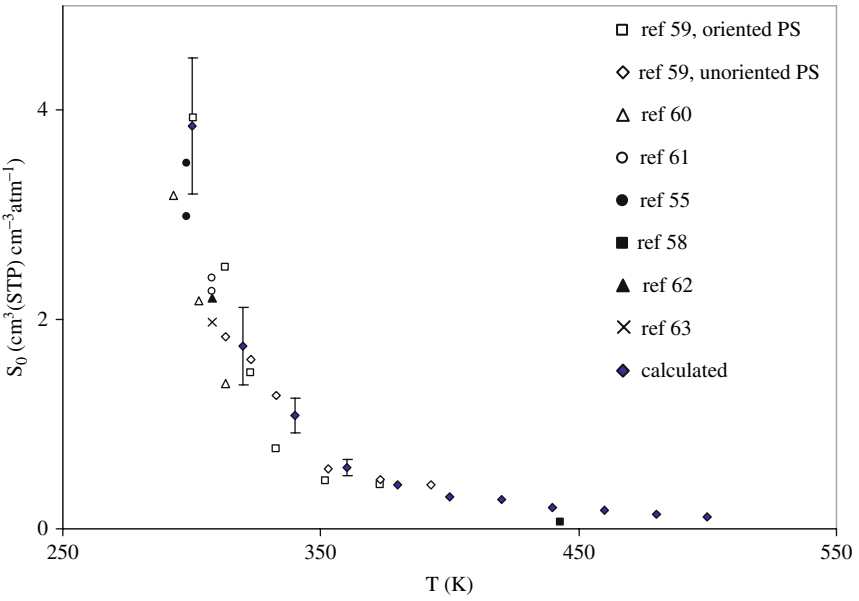

Figure 11-6. Temperature dependence of S_0 for CO_2 sorbed in polystyrene compared with experimental measurements. The figure is taken from Eslami and Müller-Plathe [61]

Table 11-1. Comparison of the calculated and experimental ratios of solubility coefficients of gases in atactic polystyrene with respect to Ar at 300 K and zero-pressure limit. The sources of experimental data are (a) Vieth et al. [63] (b) Odani et al. [74] (c) Sada et al. [66] (d) Vieth et al. [62] (e) Barrie et al. [146] and (f) Yavorsky [147]. The table is taken from Eslami and Müller-Plathe [61]

Gas	$S_0/(S_0)_{Ar}$		Reference
	Calculated	Experimental	
N_2	0.46	0.50	a, b
CO_2	10.0	10.0	c
CH_4	2.91	2.85	d
C_3H_8	62.4	43.6–101.2	e, f

of the solubility coefficient are higher with respect to the experimental measurements nearly by the same factor.

To compute the sorption isotherms many simulation boxes of polystyrene and gas molecules at the specified composition are generated and molecular dynamics simulation at constant temperature and at a constant pressure close to the experimental coexistence point is done. The grand canonical ensemble molecular dynamics method [60] is used to insert gas molecules in the simulation box. Here, a fractional molecule is inserted and grown to a full molecule with the passage of time. A fractional molecule is a molecule whose potential energy of interaction to the rest of the system is scaled somehow by a fractional number, ranging between zero and one. When the fractional molecule grows to a full molecule it will be added as an indistinguishable penetrant molecule to the system and then the next fractional molecule will be inserted, until reaching the desired concentration of the gas in polystyrene. Having an equilibrated mixture of polystyrene with gas molecules at a fixed temperature and pressure, Widom's test-particle method [59] is applied to compute the excess chemical potential and the partial molar volume of the sorbed gas, as described above. Then a pseudo-grand canonical ensemble molecular dynamics simulation in the gas phase is performed to calculate the phase coexistence point. Setting the values of chemical potential, temperature, and volume as independent thermodynamic variables, one of the penetrant molecules in the box is chosen as the fractional molecule. Depending on the variation of the fractional number with time, the penetrant molecules are exchanged with the material reservoir until reaching the equilibrium state consistent with the pre-fixed values of temperature, volume, and chemical potential. More details for performing grand canonical ensemble molecular dynamics simulation is described elsewhere [60]. The computed sorption isotherm for carbon dioxide, as a typical example, is plotted in Figure 11-7. From the results in Figure 11-7 it is clear that our calculated solubilities tend to show higher slopes at low pressures in accordance with our calculations in the zero-pressure limit. Consequently, we predict higher solubility isotherms compared to the experimental solubility isotherms.

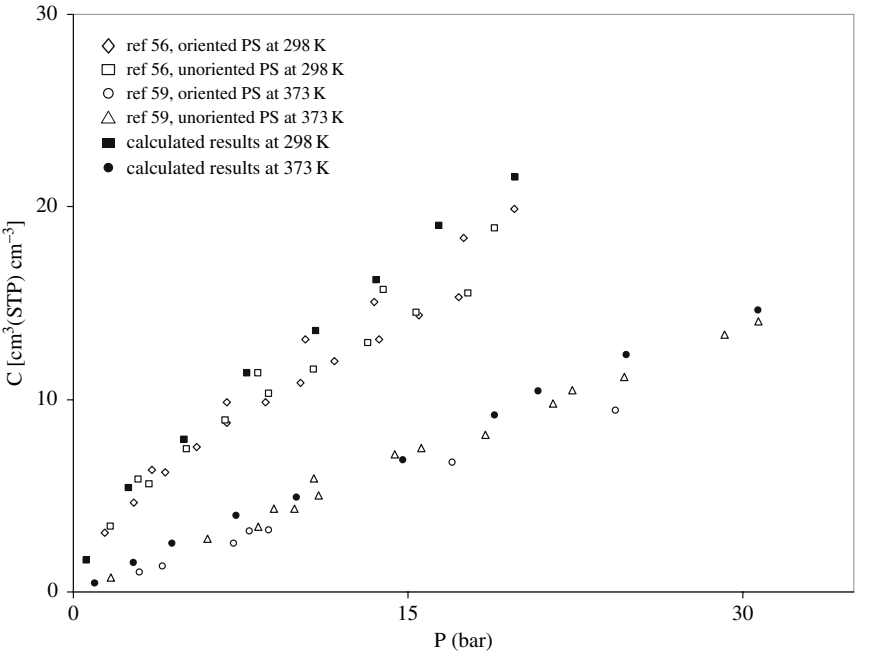

Figure 11-7. Sorption isotherms for CO_2 in polystyrene at 298 K. The figure is taken from Eslami and Müller-Plathe [61]

Considering the inconsistencies between experimental measurements [29,65,74], as evident in Figures 11-6 and 11-7, our predictions are more or less within the uncertainty range of experimental measurements. For CO_2 at 373 K, our calculated Henry's law constant is in close agreement with experiment [65], see Figure 11-6, therefore, the calculated solubility isotherm in Figure 11-7 is also close to the experiment [65].

11.6.2. Concentrated Solutions of Polymers in Solvents

We now consider the second alternative, the concentrated solutions of polymers in solvents, where the concentration of solvent can be changed over a wide range. Here the polymer molecules will evenly distribute among the solvent molecules and a new set of interactions between solvent and solute molecules sets up, which results in a solvation structure. There are many interaction configurations, called solvation structures. Specification of solvation structures is very important in such disciplines as bioscience [75], pharmacy [76], and lavation [77]. The polymer solvation structure has been the subject of studies in recent years. In the concept of polymer solvation, since the overall size of polymer also changes in solution, therefore, the solvation

structure refers to such phenomena as the interaction configurations between polymer and solvent molecules, the overall size of polymer chain, local conformation of both polymer and solvent, and even the distribution of bond lengths and bond angles, which will be described in the following sections.

11.6.2.1. Solvation structure: mixtures of nonpolar polymers with nonpolar solvents

Molecular simulation methods provide an acceptable picture of the solvent structure around a solute. For small spherical solutes, the solvent structure can be represented by the radial distribution function (RDF), $g(r)$, defined as

$$g(r) = \frac{\langle N(r, r + \mathrm{d}r)\rangle}{4\pi\rho r^2\,\mathrm{d}r} \tag{11-34}$$

where N stands for the number of solvent molecules found when sampling in the spherical layer located between the distances r and $r + \mathrm{d}r$ from the solute and ρ is the number density of the solvent. The solvation of polystyrene (PS) in benzene [78], as an example of a nonpolar solute dissolved in a nonpolar solvent, and that of poly(vinyl alcohol) (PVA) in water, ethanol, and water–ethanol mixtures [79], as an example of a polar solute dissolved in a polar solvent, have been studied in details. In the former case it is noticed that the calculated center of mass radial distribution function for benzene–benzene does not change qualitatively with the PS content, see Figure 11-8. In Figure 11-8 the difference in absolute peak heights only reflects different benzene number densities. The solvation of phenyl groups of PS, described by the mixed benzene–phenyl RDF, is qualitatively very similar to the benzene–benzene

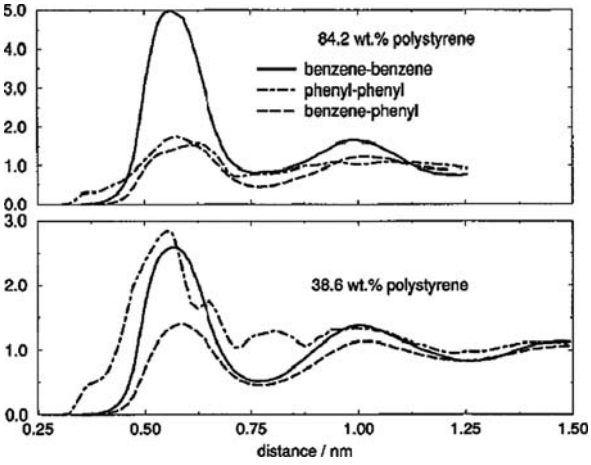

Figure 11-8. Center of mass radial distribution functions for aromatic groups (benzene and/or phenyl) for two benzene–polystyrene mixtures. The normalization is chosen so that all radial distribution functions approach 1 at infinity. The figure is taken from Müller-Plathe [78]

RDF (Figure 11-8). The small shoulder at around 0.4 nm and the minimum following the first peak at around 0.75 nm, in Figure 11-8, are attributed to connectivity of the PS chain enforcing distances on pairs of phenyl groups.

The composition of the immediate surroundings of a benzene molecule or a phenyl group for different PS–benzene solutions is analyzed [78] by integrating the first peak of RDFs. According to the results [78], tabulated in Table 11-2, the total number of nearest neighbors of a benzene molecule is around 12.5 and is practically independent of polymer concentration. As the polymer concentration increases, neighboring benzene molecules are simply replaced by phenyl groups. In contrast, the total number of nearest neighbors of a phenyl group decreases almost uniformly from 11.9 neighbors (38.6 wt%) to 10.8 neighbors (pure PS). This means, that the connectivity of PS causes aromatic rings to pack less tightly than they would in a liquid. Also the results [78] in Table 11-2 reveal that there is some preference for phenyl groups or benzene molecules to be surrounded by like groups or molecules. For example, at a concentration of 55.7 wt% PS, a phenyl group has, on average, 4.6 benzene molecules in its first solvation shell and 7.6 other phenyl groups. At this composition, the number of phenyl groups and benzene molecules is almost equal, so one would expect a 1:1 ratio of both species, if solvation were purely statistical. Because of the connectivity, a phenyl group will always have a small number of other phenyls in its first solvation shell and the remaining coordination sites can then be filled statistically. The number of predetermined phenyl neighbors of a phenyl group varies from 3.09 to 1.97 for mixtures of 38.6 to 84.2 wt% PS, respectively.

Table 11-2. Composition of nearest neighbor solvent shells of benzene molecules and phenyl groups, respectively.[a] The table is taken from Müller-Plathe [78]

Wt% polystyrene	No. of benzene molecules	No. of phenyl groups	Total no. of neighbors (benzene + phenyl)	Benzene/phenyl ratio (in solvation shell)	Benzene/phenyl ratio (overall)
(a) Nearest neighbors of benzene					
0	12.6	0	12.6	∞	∞
38.6	9.7	2.8	12.5	3.42	2.12
55.7	8.4	4.4	12.7	1.92	1.06
72.7	5.9	6.5	12.4	0.91	0.5
84.2	4.8	7.5	12.3	0.64	0.25
(b) Nearest neighbors of phenyl					
38.6	6.0	5.9	11.9	1.01	2.12
55.7	4.6	7.6	12.2	0.61	1.06
72.7	3.3	8.5	11.7	0.38	0.5
84.2	1.9	9.5	11.3	0.20	0.25
100	0	10.8	10.8	0	0

[a]Numbers are calculated by integrating the first peak of the appropriate center of mass radial distribution function that is from 0 to 0.75 nm.

Therefore it was concluded that if there are effects other than connectivity that cause nonstatistical solvation, they must be very small [78].

Although the results discussed so far in this section show that there is no considerable solvation effect in the case of PS in benzene, a similar recent study by Ji and Yang [80] on the detailed structures and mechanism of solvation of polyethylene (PE) in biphenyl, solution of a nonpolar polymer in a nonpolar solvent, shows considerable accumulation of biphenyl in the solvation shell of PE. They observed three set of interaction configurations between PE and biphenyl, in which the orientation of biphenyl molecules with respect to chain alignment is different [80]. Moreover, we may address to the solvation of poly(oxyethylene) (POE) in benzene studied by Tasaki [81], as an example of a system composed of a polar polymer solute in a nonpolar solvent. Tasaki [81] analyzed the RDF functions for POE oxygen atom and the nearby benzene carbon atom and that of POE methylene carbon atom and the nearby benzene carbon atoms and showed that the first one displayed a peak at 0.55 nm, while the second one showed a broad peak ranging between 0.4 and 0.65 nm, with the center locating around 0.5 nm. They observed the same trend for RDF of other benzene carbon atoms and reported that the orientational preference of benzene molecule in the solvation shell with respect to OE unit in POE is a perpendicular orientation. Their observation is in agreement with NMR high-field shift of POE methylene hydrogen atom in benzene. Also their comparison on the RDF of POE methylene carbon and the nearby benzene carbon atom with that of bulk benzene showed the same trend. Therefore, based on their reports there is a very small perturbation of the solvent structure by POE.

The mutual orientation of aromatic rings can also be depicted by the cosine of the angle between the plane normals $\mathbf{u}_3$ of two rings [78]. Since the rotation of one ring by 180° leads to an indistinguishable situation from the original orientation, one can also calculate $|\mathbf{u}_{3,i}\mathbf{u}_{3,j}|$. This product is 1 for two coplanar rings, 0 for a T-shaped arrangement, and 1/2 for a random distribution of orientations. The orientational distribution functions (ODFs) as a function of the average distance between the pair of rings calculated by Müller-Plathe [78] is shown in Figure 11-9. It is seen that for all ODFs at a close distance, <0.5 nm, rings are predominantly coplanar. Of course, there are only very few pairs at this distance, as is evident from the RDFs. We generally observe that orientational correlation is quickly lost with distance, little structure being visible beyond 0.9 nm, i.e., before the second peak in the radial distribution function (Figure 11-9). Around the typical nearest neighbor distance of 0.5 nm, we find minima (below 1/2) which confirms the dominance of perpendicular arrangements in the first solvent shell. For the benzene–benzene and benzene–phenyl ODFs, there is a clear tendency for this minimum to decrease with polymer content. This means that the T-shaped packing of benzene molecules and of benzene molecules around a phenyl group becomes more favored as the polymer content increases. The phenyl–phenyl ODFs are different from the other two, in that

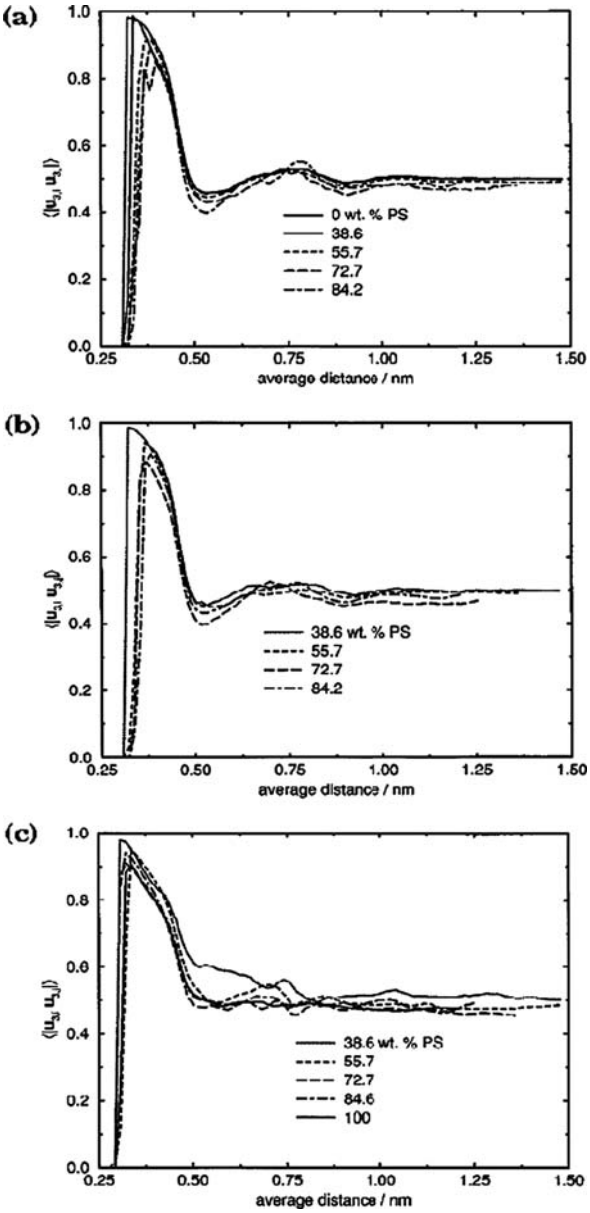

Figure 11-9. Orientation distribution functions describing the mutual orientation of the plane normals of aromatic rings: (**a**) benzene–benzene; (**b**) benzene–phenyl; (**c**) phenyl–phenyl. The figure is taken from Müller-Plathe [78]

there are no minima in the range of the first solvent shell. This indicates that, already at this distance, phenyl groups are randomly oriented.

11.6.2.2. Solvation structure: mixtures of polar polymers with polar solvents

The following results in the case of solvation of poly(vinyl alcohol) (PVA) in water, ethanol, and water–ethanol mixtures show that the situation in the case of solvation of polar polymers in polar solvents is different from the above case of the solvation of nonpolar polymers in nonpolar solvents. Shown in Figure 11-10 is the distribution of solvent oxygen and carbon atoms around the PVA oxygen (OPVA) calculated by Müller-Plathe and van Gunsteren [79]. In all solvents the first peak in the RDF is at

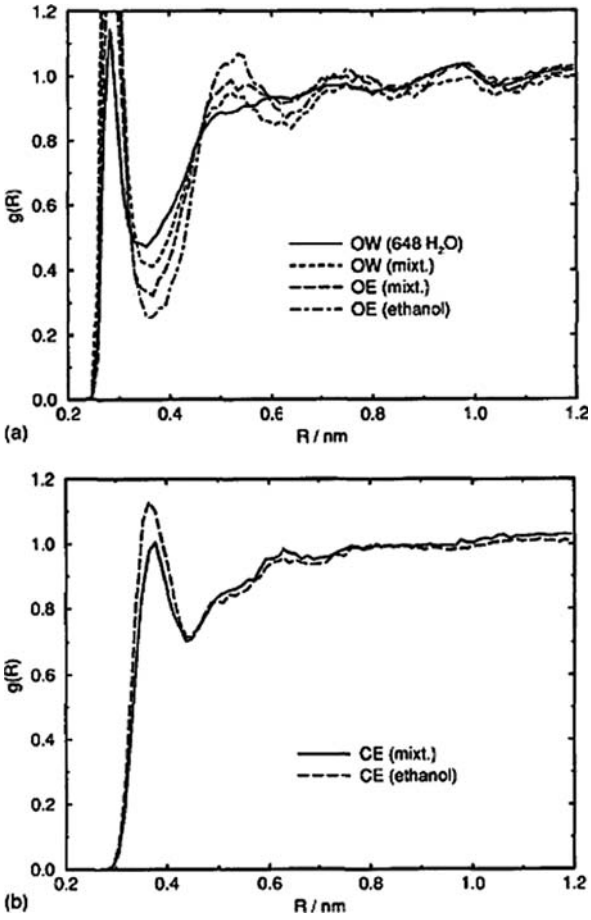

Figure 11-10 Solvation of the oxygen atoms of poly(vinyl alcohol). (**a**) Partial radial distribution functions of PVA oxygen with solvent oxygen and (**b**) solvent carbon atoms. The figure is taken from Müller-Plathe and van Gunsteren [79]

around 0.3 nm indicating hydrogen bonding of the first solvation shell to a solvent oxygen atom. Integrating over the first peak in Figure 11-10a to $r = 0.35$ nm shows that an OPVA has on average 2.5 water oxygens (OW) in its first solvation shell if the solvent is pure water, 1.0 OW and 0.7 ethanol oxygen (OE) if the solvent contains equal amounts of water and ethanol, and 1.10 OE for pure ethanol as a solvent. This is already a qualitative indication that the hydroxyl groups of PVA are more efficiently solvated by water than by the bulkier ethanol. The valley following the first peak in Figure 11-10a is deeper for ethanol than for water and it also deepens with the ethanol content. This is a consequence of the relative molecular size. If an ethanol molecule is hydrogen-bonded to a PVA hydroxyl group, its aliphatic groups will prevent further oxygens (of water or other ethanol molecules) from approaching the PVA causing an area of oxygen depletion at around 0.35 nm. Figure 11-10b shows clearly that this region coincides with the first peak in the OPVA and ethanol carbon (CE) RDF. The second peak of the RDF, Figure 11-10a, at 0.5–0.6 nm shows the same pattern as the minimum between first and second peaks. It is more pronounced for OE than for OW and it increases with ethanol content. For pure water, the peak is absent since the small water molecules can sit at nearly any distance from the hydroxyl oxygen which smears out this peak, whereas the exclusion of second-shell OE by first-shell CE leads to enrichment of OE immediately beyond the exclusion zone. There is a small third peak in the RDF, Figure 11-10a, at 0.65–0.85 nm for all solvents. The small maximum before 1.0 nm and the small minimum thereafter are residual artifacts of the spherical cut-off at this distance. The solvation situation around the PVA carbon atoms also shows that both PVA carbon atoms, connected to the OPVA and the adjacent carbon atom, are solvated very similarly.

11.6.2.3. Hydrogen bonding in polar polymer–solvent mixtures

In this section we study the competitive solvation of PVA in ethanol–water mixture. For this propose the concept of local atomic fractions, defined as follow, has been used by Müller-Plathe and van Gunsteren [79]

$$x_{AB}(r) = \frac{n_{AB}(r)}{\sum_{A} n_{AB}(r)} \tag{11-35}$$

where $x_{AB}(r)$ is the local atomic fraction of solvent atom A around a solute atom of type B and A runs over all non-H solvent atom types (OW, OE, and CE). Normalizing $x_{AB}(r)$ by $x_{AB}(\infty)$, one arrives at a quantity which is 1 if the composition within the radius r is the same as in the bulk, but which is greater (less) than 1 if the solvent sphere contains more (less) of A than the bulk solvent. Figure 11-11a shows the normalized local atomic fractions around OPVA. The preference for water as the closest neighbor is clearly evident. Across the range of the first peak in the RDFs, see Figure 11-11, there is an excess of both OW and OE at the expense of CE. However, there is always more water than ethanol. The OE fraction drops slightly below its bulk value between 0.38 and 0.48 nm due to the exclusion by CE. The

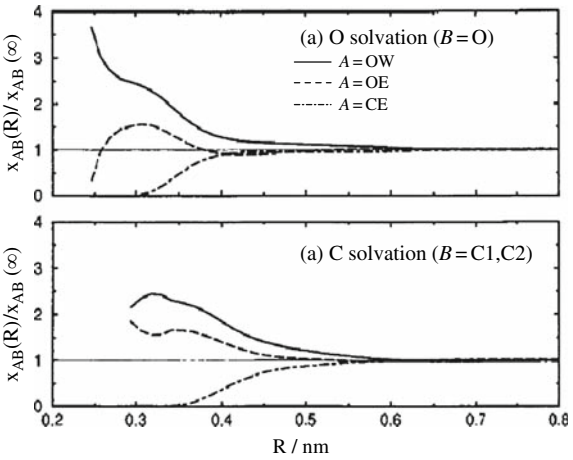

Figure 11-11. Solvent competition for solvation of PVA. (**a**) O atoms and (**b**) carbon atoms in water, water–ethanol, and ethanol. The figure is taken from Müller-Plathe and van Gunsteren [79]

excess of OW, on the other hand, persists out to 0.6 nm, possibly due to a secondary shell of water molecules hydrogen-bonded to the first. The solvation of the PVA carbons shows the same global pattern, Figure 11-11b, an excess of OW and OE and a deficiency of CE at short distances which, however, decay smoothly to the bulk values. It is interesting to note that the environment of PVA carbons is also mainly polar. Since there is no strong interaction in the force field between the aliphatic groups of PVA and the polar parts of the solvent, this means that the polar groups of the solvents are attracted by the hydroxyl groups of PVA. The hydrophobic areas of the PVA backbone are probably too small and too close to the hydroxyl groups to show separate hydrophobic solvation (a preferred hydrophobic environment). This confirms the picture of PVA being an entirely hydrophilic polymer.

Another criterion to analyze the solvation of PVA are hydrogen bonds formed by the PVA hydroxyl groups. The hydrogen bonds of a PVA OH group can be classified (i) into internal (intramolecular) or external (to solvent) and (ii) according to whether the O acts as hydrogen donor or acceptor. This gives rise to the five hydrogen bond types listed in Table 11-3. One notes that there appears to be a systematic decrease in the total number of hydrogen bonds of the PVA 15-mer from 22 in aqueous solution to 16 in ethanol. This is caused by a decrease of the external hydrogen bonds; the number of internal ones (H→O) varies unsystematically. The smaller number of external hydrogen bonds is caused by the larger space requirement of ethanol as compared to water which prevents further ethanol molecules from approaching the PVA closely, as was already evident from the RDFs (Figure 11-11a). There are 8.7 hydrogen bonds to water and only 5.4 to ethanol. It is interesting to note that water has a preference for acting as a hydrogen donor rather than an acceptor ((H→OW)/(HW→O) = 5/11). This means that the hydroxyl group can have more incoming (approximately 2) hydrogen bonds but only one outgoing. In particular,

Table 11-3. Hydrogen bonds of the 15-mer poly(vinyl alcohol) hydroxyl groups. The first line for each system gives the average number of hydrogen bonds of a given type at any time point, the second line gives in parentheses their average life times (ps)[a]. The table is taken from Müller-Plathe [78]

Solvent	H→O	H→OW	H→OE	HW→O	HE→O	Ext.[b]	Total[b]
432 H_20	4.8	5.9		11.7		17.6	22.4
	(11.6)	(1.7)		(2.1)			
648 H_20	6.1	5.0		11.0		16.0	22.1
	(13.0)	(1.7)		(3.3)			
162 H_20/162 EtOH	4.4	3.3	2.8	5.4	2.6	14.1	18.5
	(21.6)	(3.4)	(3.0)	(4.3)	(2.9)		
216 EtOH	6.5		5.1		4.6	9.7	16.2
	(34.4)		(4.1)		(3.3)		

[a]Atom types (columns headings): H and O denote PVA hydroxyl hydrogen and oxygen, respectively; HW and OW denote water hydrogen and oxygen; HE and OE denote ethanol hydroxyl hydrogen and oxygen. The arrows point from donated hydrogen to acceptor.
[b]Ext. and total denote the number of external (to solvent) hydrogen bonds and the total number of hydrogen bonds (intramolecular plus external) of the PVA 15-mer.

if the H is already donated in an intramolecular H bond there can still be two incoming H bonds from water molecules. In the case of ethanol, the effect is much less pronounced and, if anything, the trend is reversed. Here, the size of the ethanol molecules prevents more than one ethanol molecule occupying H donor positions around a PVA hydroxyl. From Table 11-3 one calculates that there are 1.07 external H bonds per hydroxyl group in water, 0.94 in the mixture, and 0.65 in ethanol.

11.6.3. Solvent Effect on Polymer Size in the Solution

One of the most important phenomena in the polymer solvation is the change in the overall size of the polymer chain upon solvation. In fact at equilibrium the average size of isolated polymer molecules in solution is a function of solvent quality and varies from expanded conformations in good solvents to random walk conformations in poor solvents. This is referred to as collapse transition and was first predicted by Stockmayer [82] more than 45 years ago. The phenomenon was observed by Nishio et al. [83] and Swislow et al. [84] more than 25 years ago and is still a subject of much experimental, computational, and theoretical research today. So far many investigators have tried to study the chain size with solvation using a variety of methods.

Experimentally the overall size of the polymer chain can be studied by light scattering and neutron scattering. A great deal of theoretical work is present in the literature which tries to predict the properties of mixtures in terms of their components. The analytical model by Rouse–Zimm [85,86] is one of the earliest works to derive fundamental properties of polymer solutions. Advances were made subsequently in dilute and concentrated solutions using perturbation theory [87], self-consistent field theory [88], and scaling theory [89].

Monte Carlo as well as molecular dynamics simulations have also been applied widely to understand how polymers behave in solution. Most of the existing simulations are based on the Monte Carlo studies of lattice models [90,91], but the time-dependent properties cannot be studied in stochastic Monte Carlo approach. Therefore, there has been a gradual growth in the use of molecular dynamics simulation. The pioneering works on the molecular dynamics simulations of polymer chains in the solution are the works, by Bishop et al. [92], which used a polymer chain consisting repulsive spheres connecting by springs in a solvent of repulsive spheres. Later Rapaport [93] used a hard-sphere model for both chains and solvents. Although in both studies it has been concluded that the mean-square radius of gyration and end-to-end distance of the chain are equal both in the pure state and in the presence of solvent, the system size was too small to explore the solvent effect.

In 1981 Bruns and Bansal [94] used a Lennard–Jones (LJ) model of polymer and solvent and analyzed the structural properties of the chain. In contrast to previous reports [92,93], a significant solvent effect was observed by Bruns and Bansal [94]. The study of solvent effect on the static properties of polymer was succeeded by Khalatur et al. [95] on the static properties of a 16-bead polymer chain in a solvent. All potentials used were of LJ type. There are many other reports in the literature to understand the equilibrium size and shape of polymer as a function of solvent quality [96,97,98]. Most of these studies are exploratory rather than quantitative, probably due to the computational expense, since the large relaxation times of the polymer chains as well as the large system sizes imply powerful computer resources. However, with the availability of high-performance computers, the problem has been addressed in earnest [99].

In the previous report on the solvation of PVA in water–ethanol mixtures [79], the spatial extension of PVA chain is also studied. This is done by calculating the radius of gyration, R_g, or the end-to-end distance (in this case the distance between the terminal methyl group carbon atoms) of the polymer. The results shown in Figures 11-12 and 11-13 show the time development of R_g and the end-to-end distance for PVA 15-mer in three different solvents [79]. The initial chain conformation which is the same random coil for all systems is too compact and R_g takes several hundred picoseconds to converge to its final value. In Figure 11-12, this is clearly visible for the solvent mixture and pure ethanol. (The final chain conformation of the 432 water solvent was taken as the initial conformation for the 648 water solvent. Hence, for water, there is no equilibration phase visible in Figure 11-12.) The expansion of the chain in the solvent mixture appears to go through an intermediate step which exists for about a nanosecond before the final expansion takes place. The end-to-end distances converge to their final range much quicker than R_g, probably because their relative fluctuations are larger. As a result, no plateau similar to that found in the R_g for the solvent mixture is observed for the end-to-end distance. The ratio of end-to-end distance and R_g already tells that the 15-mer is too short to exhibit polymer chain statistics.

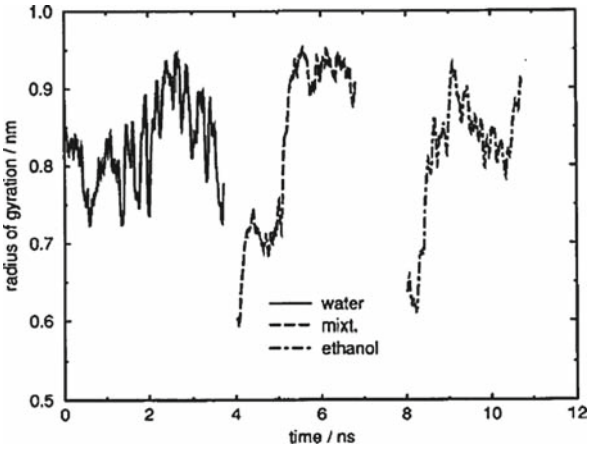

Figure 11-12. Time evolution of the radius of gyration of the poly(vinyl alcohol) 15-mer in solution. The water curve is that of the 648-water system. The curves for the water/ethanol mixture and pure ethanol are offset in x direction by 4 and 8 ns, respectively. The figure is taken from Müller-Plathe and van Gunsteren [79]

11.6.4. The Solvent Effect on Dynamics of Polymer Collapse

Equilibrium properties of the collapse transition and the relationship between polymer size and solvent quality are studied widely, and are addressed in the previous section, but up to now less is known about the collapse dynamics. There has been a

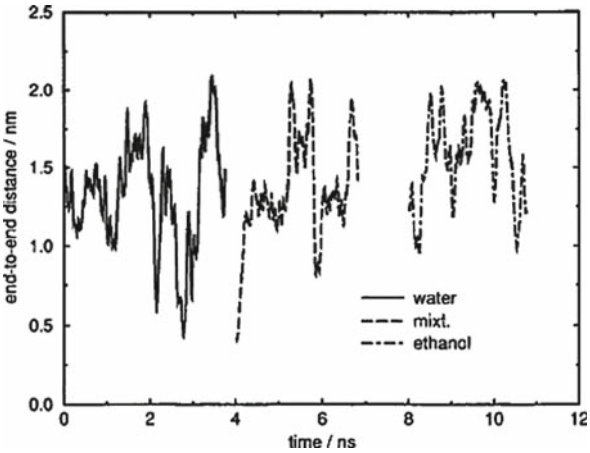

Figure 11-13. Time evolution of the end-to-end distance of the poly(vinyl alcohol) 15-mer in solution. The water curve is that of the 648-water system. The curves for the water/ethanol mixture and pure ethanol are offset in x direction by 4 and 8 ns, respectively. The figure is taken from Müller-Plathe and van Gunsteren [79]

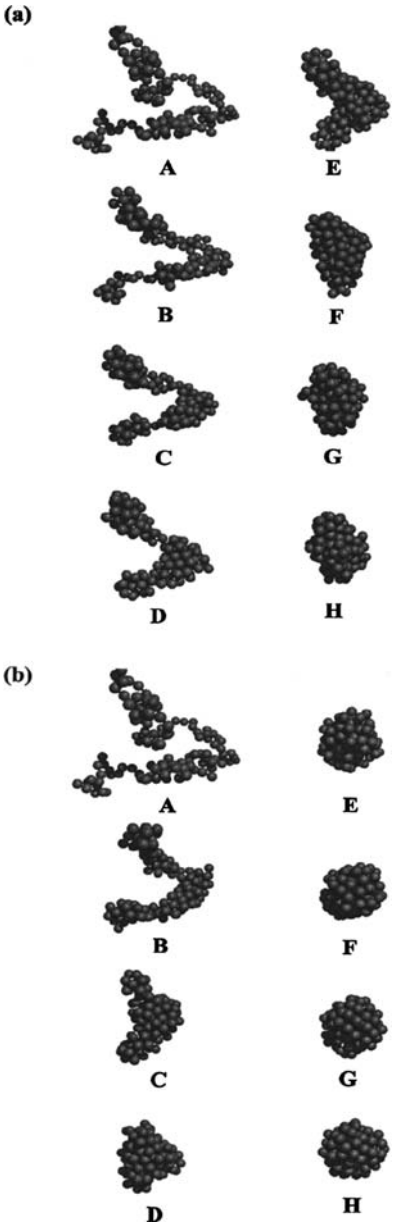

Figure 11-14. Snapshots of a collapsing N=128 chain in MD simulations with quenching depth, ε_{LJ}/k_BT, of (**a**) 1.00 and (**b**) 0.1. The time interval between snapshots is 10 τ_{MD} and the sequence is A to H. The surrounding solvent molecules are omitted for clarity. The figure is taken from Chang and Yethiraj [106] with permission

number of theoretical attempts to describe the dynamics of the collapse transition. A phenomenological theory is proposed by de Gennes [100], in which a two-stage collapse is proposed. According to this model, following the abrupt change in solvent quality, a single flexible chain crumples on a minimal scale along the backbone, forming blobs or collections of collapsed monomers. Then the blobs swell laterally and the chain contracts longitudinally to form a sausage-like conformation. The collapse proceeds with a lateral expansion of the sausage accompanied by a longitudinal shortening until the final stage of a compact globule is reached. A refined version of the theory was presented by Grosberg et al. [101], who proposed a different two-stage mechanism. A review of the recent works in this field is given by Polson and Zuckermann [102].

Experimental observations of the collapse transition in synthetic polymers are difficult due to the strong coupling of the interchain collapse with the interchain aggregation on changing solvent quality. Recently the study of collapse dynamics in dilute solutions of noninteracting polymers in case where the aggregation time is significantly larger than the collapse time is done by Zhu and Napper [103], by Nakata and Nakagawa [104], and by Kayaman et al. [105], using dynamic light scattering.

Much of the recent understanding of the collapse dynamics comes from computer simulation studies. Chang and Yethiraj [106] studied the effect of solvent on the collapse dynamics, performing MD simulation on a bead-spring model of polymer. They considered the effect of the solvent as the second component in an explicit fashion. Initial configurations are generated for a polymer in a good solvent. The system is then quenched by a sudden decrease in temperature. The polymer molecule is collapsed to a globule. Their studies [106] show that the collapse is more rapid for short chains and more rapid for deeper quenches. The snapshots of collapsing 128 chains in MD simulation of Chang and Yethiraj [106] are given in Figure 11-14. In a similar study by Polson and Gallant [107] on equilibrium properties and dynamics of collapse, MD simulation of a single homopolymer chain in an explicit monomeric LJ solvent is used. They [107] concluded that a faster collapse transition occurs with increasing monomer hydrophobicity. Their results also show that increasing the solvent density leads to an overall decrease of the size of polymer and that increasing the chain length increases the collapse time.

11.7. TIME-DEPENDENT SOLVATION RESPONSE

An excited solute molecule can lose its energy by exchanging energy with the surrounding solvent molecules or by inducing its surrounding molecules, solvent molecules, to rearrange so that they provide a significant stabilizing influence. It is the latter case which is important in the concept of solvation and we are going to explain it in detail in the following sections. However, an interested reader to the former case, called vibrational relaxation, is referred to a nice review by Elsaessar and Kaiser [108] on vibrational and vibronic relation of large polyatomic molecules in liquids.

When the solute molecule in a solution is excited electronically, it will eventually fluoresce back down to its ground electronic state. Naturally, the fastest fluorescence corresponds to the solute molecule, emitting light of roughly the same characteristics as had just been absorbed. However, if something about solvent–solute changes with the evolution of time, the time profile of the subsequent fluorescence will reveal the dynamics. In fact the solvent–solute system changes its energy as the solvation process proceeds, which is called solvation dynamics.

11.7.1. Experimental Methods

Time-resolved fluorescence has been a useful tool to study solvation dynamics since the original work by Bakshiev et al. [109]. Usually, an ultrafast laser pulse excites solute molecules. The charge distribution in the excited state usually differs substantially from the ground state. If the solvent molecules are polar enough, they will rapidly reorient depending on the magnitude of solute–solvent interactions. Therefore, a dynamic equilibrium corresponding to the new excited-state charge distribution of the solute is established. The process is shown schematically in Figure 11-15.

The relaxation time for this new dynamic equilibrium varies from femtoseconds to picoseconds. The fast reorientation of solvent molecules causes a fast solvatochromic shift in the fluorescence band of the organic chromophores. Solvation dynamics is measured in terms of $\langle \delta\nu\,(0)\,\delta\nu\,(t)\rangle$, where the fluctuating frequency $\nu(t)$ is the difference in solvation energies between the two electronic states involved, i.e., $\nu(t)=\Delta E(t)/h$ [110]. In time-resolved emission spectroscopy the time dependence of the excited-state distribution is monitored via the frequency shift of the emission

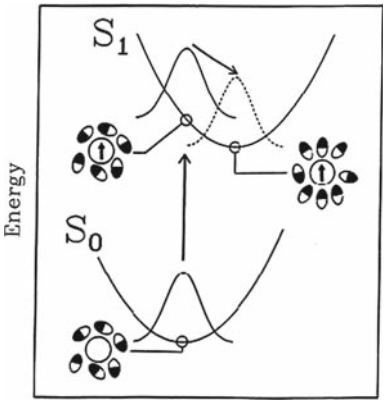

Figure 11-15. Electronic excitation of a solute with zero dipole moment in its ground state, S_0, but a large dipole in its excited electronic state, S_1. Since the electronic transition is faster than nuclear motions the initial arrangement of solvent molecules in the exited state is the same as in the ground state. Then the solvent molecules reorganize in order to lower the solvation energy in the excited state. The figure is taken from Stratt and Maroncelli [110] with permission

spectrum after excitation [111]. The temporal features of the solvation are captured in terms of the normalized response function:

$$C_\nu(t) = \frac{\nu(t) - \nu(\infty)}{\nu(0) - \nu(\infty)} \tag{11-36}$$

where $C_\nu(t)$ is the normalized spectral response function, $\nu(0)$, $\nu(t)$, $\nu(\infty)$, are the optical frequencies that correspond to the maxima of the emission spectra at times zero, t, and infinity, respectively. Within the framework of linear response theory [112] the response of the system to the solute perturbation obeys the same dynamics as the fluctuations of the energy gap experienced by an unperturbed solute in equilibrium with its solvent environment. Thus measurement of $C_\nu(t)$ is equivalent to measurement of solvation dynamics. In fact many types of intermolecular interactions, including dispersion forces, dipole–dipole or higher-order multipolar interactions, and hydrogen bonding may be involved in the process of solvation. Practically, one can choose solutes whose electronic transitions are primarily sensitive to only one type of interaction and thereby study the dynamics of this particular interaction. For example, tetrazine [113], benzophenone anion [114], a number of aromatic amines [115], and coumarin-153 have been chosen to probe the dynamics of dispersion-type interactions, hydrogen bonding, and dipolar interactions, respectively.

In the case of polymer solutions there are reports in the literature on the solvation dynamics of solvent in polar solvent–polymer solutions. For example, the water molecules in the first hydration shell of the polymers form hydrogen bonds with it. Dielectric relaxation methods have been applied by Shinyashiki et al. [116,117] to study polymer–water interactions. Studies of these kinds show that the dielectric relaxation time of water is 2–3 orders of magnitude higher than that of pure water [116,117]. The slower relaxation component of polymer-bound water has implications in charge transport in polymer–water systems [118]. In fact the solvation dynamics of water have been studied in many environments such as in DNA by [119], in reverse micelles by Willard [120], in sol–gel matrix by Pal et al. [121], and in proteins by Pal [122]. It is observed that while solvation dynamics occurs in around a 1-ps time scale in bulk water [123], in many confined media the solvation dynamics of water exhibits a component in the 100–1000 ps time scale, as is reported by Faeder and Ladanyi [124] and by Michael and Benjamin [125]. Though solvation dynamics of water molecules in different confined environments have been extensively studied, reports on the aqueous solutions of polymers are scarce. Hydrophilic and hydrophobic interactions strongly influence conformation of water-soluble polymers in aqueous solutions. Water molecules present in the hydration layer of polymers are restricted and the study of dynamics in aqueous polymer solutions is of fundamental importance to understand the behavior of biological macromolecules. Maeda et al. [126] used Raman spectroscopy and Desbrieres et al. [127] used quasi-elastic light scattering to study the behavior of aqueous polymer solutions. Argaman and Huppert [128] have studied solvation dynamics in neat liquid polyethers, $CH_3(OCH_2CH_2)_nOCH_3$ (n = 2–4). Apart from the major ultrafast subpicosecond components, they detected two relatively long components in the 10 and 100 ps

time scales, which they attributed to the motion of the polyethers. The solvation dynamics of water in an aqueous solution of poly(vinylpyrrolidone) (PVP) using 2,6-*p*-toluidinonaphthalene sulfonate (TNS) as a probe is studied by Sen [129]. In aqueous solution of PVP they found a biexponential solvation dynamics with a major component of 60 ps and a slower component of 800 ps. The retardation of the solvation dynamics in the dilute polymer solution compared to that in the bulk water is attributed to the restricted movement of water molecules in the vicinity of the polymer chains.

11.7.2. Theoretical Studies

There are many theoretical studies of nonpolar solvation dynamics in the literature, among which we may address the theory developed by Saven and Skinner [130] and by Stephens et al. [131], in which the dynamics of the fluctuating energy gap is generated by a Green's function for the relative solvent–solute motion. An alternative theoretical model is based on the time-dependent density functional theory [132,133], in which the slow component of the solvation time correlation function is directly related to the coupling between the solute motion and the solvent collective modes. In this theory the solvation time correlation function is expressed in terms of the wave vector and time-dependent solvent dynamics and solute self-dynamics structure factors and wave vector-dependent vertex, which couples the solute fluctuating transition frequency to the solvent collective modes. This coupling vertex is written in terms of the solute–solvent direct correlation function. The theory has been applied to analyze the slow decay of the solvation time correlation function in a dense LJ fluid [134].

A mode coupling theory is recently developed [135] which goes beyond the time-dependent density functional theory method. In this theory a projection operator formalism is used to derive an expression for the coupling vertex projecting the fluctuating transition frequency onto the subspace spanned by the product of the solvent self-density and solvent collective density modes. The theory has been applied to the case of nonpolar solvation dynamics of dense Lennard-Jones fluid. Also it has been extended to the case of solvation dynamics of the LJ fluid in the supercritical state [135].

There are also a number of theories taking into account dipolar solvation dynamics. These theories use the solvent's dielectric response function as the dynamical input and also include effects due to the molecular nature of the solvent. The most sophisticated of these theories, by Raineri et al. [136] and by Friedman [137], uses fully atomistic representations for both solute and solvent and recent comparisons have shown it to be capable of quantitatively reproducing both the static and dynamic aspects of solvation of C153 [110]. In these cases the theoretical nature of solvation dynamics is fully understood. However, it must be remembered that much of the success of these theories rests on using the dynamical content of the complicated function, dielectric response function, determined from experiment. Although there

has been some recent progress in formulating ab initio theories of solvent's dielectric response function for idealized model solvents [138], we are a long way from being able to model realistic solvents. Thus, the quantitatively successful theories to date are ones which relate two complex phenomena, solvation dynamics and dielectric relaxation, rather than providing an ab initio theory of either one [110]. This last point has been explained by Stratt and Maroncelli [110] in the case of solvation dynamics in nonpolar solvents like benzene or dioxane, as an example. While these solvents are nondipolar, they nevertheless are still enough polar, as attested to by their position in solvatochromically based polarity scales. Experiments with C153 have uncovered substantial time-dependent solvation in these solvents which is in all ways analogous to that found in dipolar solvents [139]. While the energetics of solvation can be accurately modeled by fully atomistic representations of such solvents, the dynamical input, solvent's dielectric response function, needed to model solvation dynamics is not available [110].

11.7.3. Computer Simulations and the Mechanisms of Solvation

Computer simulation methods play an important role in understanding the solvation dynamics. Since the time resolution is much easier to achieve in computer simulation, the ultrafast component of solvation in coumarine-153 (C153) was discovered in simulations well before it was observed experimentally. In the simulation methods, usually after equilibrating the system composed of a single solute molecule in a bath of solvent molecules, one can monitor the temporal behavior of fluctuations in an equilibrium simulation to calculate the correlation function. Also one may introduce an instantaneous change in the solute–solvent interaction potential and follow the dynamics. The former method is more directly tied to theoretical treatments of solvation dynamics, while the latter one more corresponds to the time-resolved fluorescence experiments. In the computer simulation studies it is important to be sure that the linear response behavior is observed. In simulations of some systems, significant deviation from the linear response regime has been reported [140]. This is due to the significant changes in the solute–solvent interaction energy in the two solute states considered. Nevertheless in many cases, even when the solvent is very polar, linear response is valid.

Early simulation studies on solvation dynamics mostly focused on the behavior of small atomic or diatomic solutes in small molecule solvents [141,142]. One of the most popular solvation probes is coumarin C153 (its scheme is given in Figure 11-16). Due to the fact that transition from ground to excited state in C153 is associated with a large molecular dipole moment increase, this has a measurable effect on polar solvents and leads to time-dependent emission spectra, shown in Figure 11-16.

Nowadays, however, molecular dynamics has been applied to study the dynamics of solvation of C153 as the solute in some polar solvents such as 1,4-dioxane and fluoroform. Cinacchi et al. [143] used an all-atom chemically detailed model of both

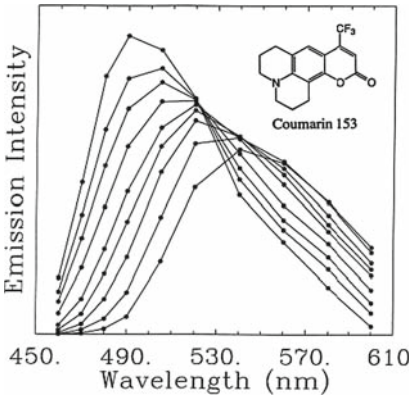

Figure 11-16. Time-resolved emission spectra of C153 at 296 K in formamide showing the continuous red shift with time characteristic of solvation dynamics. The times represented are 0, 0.05, 0.1, 0.2, 0.5, 1, 2, 5, and 50 ps in order of decreasing peak intensity. The figure is taken from Stratt and Maroncelli [110] with permission

solvent and solute (in the case of solute they applied a different set of atomic charges in the ground and excited states) in their molecular dynamics study to simulate the dynamics of solvation. They defined the solvatochromic shift in terms of the difference between solvent–solute electrostatic interactions. Their calculated solvation response function is fitted by a combination of two exponentials. One feature of the simulation results, not observed in fluorescence experiments, is the oscillations that are evident in the former case, which are usually too small to be observed experimentally. These oscillations are related to libration motions of the solvent. It is worth considering that the force field used to reproduce time-dependent properties, such as solvation response function, must be fully atomistic. Applying a united atom model for solvent produces results substantially different from experiment, which may be due to less accurate description of the dynamics arising from a solvent molecule in the cage formed by its nearest neighbors. The effect of the accuracy of force-field model is shown in the simulation of solvation dynamics of C153 in supercritical fluoroform, by Ingrosso and Ladanyi [144]. They did their calculations with a two- and five-site model of fluoroform and concluded that the five-site model generates results much closer to experiment.

To our knowledge, there is no computer simulation study on the solvation dynamics of polymers in solvents. However, one close study by Olender and Nitzan [145] is the use of molecular dynamics simulation to understand solvation dynamics of a classical charge in a series of ethers of increasing molecular weight, $CH_3(CH_2OCH_2)_nH$ with $n = 1$, 2, and 4. They argued that the linear response theory did not provide a good representation of the solvation in their studied polyethers. Their results also showed that with increasing molecular size, the short-time solvation dynamics is dominated by intramolecular segmental motions.

11.8. SUMMARY

In this chapter the process of solvation in polymers is discussed with the main emphasis on the application of molecular dynamics simulation at the atomistic level. We have studied a wide range of concentrations, namely from a very dilute solution of penetrant gases in polymers to very concentrated solutions of polymers in solvents. In the former case, a new molecular dynamics simulation method has been applied to calculate the solubility coefficients of gases in polymers. It is shown that one needs to perform two separate simulations, one simulation in the NPT ensemble of the polymer phase and one simulation in pseudo-μVT ensemble of the gas phase, instead of doing simultaneous simulations of both phases which is usually done in Gibbs ensemble Monte Carlo simulation method. There is no need to exchange particles between two phases. The excess chemical potentials in the polymer phase are calculated using Widom's test-particle insertion method. A correct trend is calculated for the solubility coefficients of gases with temperature. Although the calculated solubility coefficients are higher than the experimental ones, as it is often found for solubility coefficients calculated using molecular simulation methods, the ratio of solubility coefficients (selectivity) are quite close to the corresponding experimental data. The overall accuracy of the calculated sorption isotherms depends on the initial slope, S_0, calculated using test-particle method.

In the case of polymer solutions, we have reported molecular dynamics simulations of a realistic nonpolar polymer–solvent mixture over a wide range of composition. It has been demonstrated that molecular dynamics simulations are capable of describing correctly the structural and dynamical properties of such systems. It is seen that in this case no considerable solvation effect is observed and the components are distributed statistically. The situation, however, is shown to be different in the case of polar polymer–polar solvent mixtures (PVA in water and ethanol). The comparison between PVA solutions in water and in ethanol shows a clear preference for an aqueous environment, due to the smaller size of water molecules that allows the OH groups of PVA to simultaneously form more hydrogen bonds to water than to ethanol. The solvent effect on the static and dynamics of chain collapse is studied. It is shown that average radius of gyration and the end-to-end distance depend on the quality of the solvent and the collapse rate depends on the chain length and the quench strength. Finally a short review on the experimental, theoretical, and computer simulation methods to study the solvation dynamics is given.

ACKNOWLEDGMENT

H. Eslami thanks Alexander von Humboldt Foundation for supporting his stay in TUD via AvH research fellowship.

REFERENCES

1. Ben-Naim A (1987) Solvation thermodynamics, Plenum, New York
2. McQuarrie DA (1976) Statistical mechanics, Harper Collins, New York
3. Orozco M, Luque FJ (2000) Chem Rev 100:4187

4. Huron MJ, Claverie P (1972) J Phys Chem 76:2123
5. Huron MJ, Claverie P (1974) J Phys Chem 78:1853
6. Huron MJ, Claverie P (1974) J Phys Chem 78:862
7. Flory PJ (1942) J Chem Phys 10:51
8. Flory PJ (1945) J Chem Phys 13:458
9. Flory PJ (1953) Principles of polymer chemistry, Cornell University Press, Ithaca, NY
10. Hildebrand JH (1947) J Chem Phys 15:225
11. Huggins ML (1942) J Am Chem Soc 64:1712
12. Huggins ML (1942) J Phys Chem 46:151
13. Shinoda K, Hildebrand JH (1957) J Phys Chem 61:789
14. Shinoda K, Hildebrand JH (1958) J Phys Chem 62:292
15. Hildebrand JH, Scott RL (1962) Regular solutions, Englewood Cliff, Prentice-Hall, NJ
16. de Young LR, Dill, KA (1988) Biochemistry 27:5281
17. de Young LR, Dill KA (1990) J Phys Chem 94:801
18. Chan HS, Dill KA (1997) Annu Rev Biophys Biomol Struct 26:425
19. Sharp KA, Nichollas A, Friedman R, Honig B (1991) Biochemistry 30:9686
20. Chan HS, Dill KA (1994) J Chem Phys 101:7007
21. Fisher ME (1961) Phys Rev 124:1664
22. Chan HS, Dill KA (1990) J Chem Phys 92:3118
23. Chan HS, Dill KA (1989) Macromolecules 22:4559
24. Krukowski AE, Chan HS, Dill KA (1995) J Chem Phys 103:10675
25. Stannett VT, Koros WJ, Paul DR, Lonsdale HK, Baker RW (1978) Adv Polym Sci 32:69
26. Frederickson GH, Helfand E (1985) Macromolecules 18:2201
27. Lacombe RH, Sanchez IC (1976) J Phys Chem 80:2568
28. Sanchez IC, Rodgers PA (1990) Pure Appl Chem 62:2107
29. von Solms N, Michelsen ML, Kontogeorgis GM (2005) Ind Eng Chem Res 44:3330.
30. Ozkan IA, Teja AS (2005) Fluid Phase Equilib 228–229:487
31. Valleau JP (1991) J Comput Phys 96:193
32. Valleau JP, Graham IS (1990) J Phys Chem 94:7894
33. McDonald IR, Singer K (1967) Discuss Faraday Soc 43:40
34. Potoff JJ, Panagiotopoulos AZ (1998) J Chem Phys 109:10914
35. Kofke DA (1993) Mol Phys 78:1331
36. Kofke DA (1993) J Chem Phys 98:4149
37. Boda D, Liszi J, Szalai I (1995) Chem Phys Lett 235:140
38. Boda D, Winkelmann J, Liszi J, Szalai I (1996) Mol Phys 87:601
39. Moller D, Fischer J (1990) Mol Phys 69:463
40. Boda D, Kristof T, Liszi J, Szalai I (2001) Mol Phys 99:2011
41. Panagiotopoulos AZ (1987) Mol Phys 61:813
42. Panagiotopoulos AZ, Quirke N, Stapleton M, Tildesley DJ (1998) Mol Phys 63:527
43. Rudisill EN, Cummings PT (1989) Mol Phys 68:629
44. de Pablo JJ, Prausnitz JM (1989) Fluid Phase Equil 53:177
45. de Pablo JJ, Bonnin M, Prausnitz JM (1992) Fluid Phase Equil 73:187
46. de Pablo JJ (1995) Fluid Phase Equil 104:195
47. Lim SY, Tsotsis TT, Sahimi MJ (2003) Chem Phys 119:496
48. Jang JG, Bae YC (2002) J Chem Phys 116:3484
49. Müller-Plathe F (1991) Macromolecules 24:6475
50. Krishna Pant PV, Boyd RH (1993) Macromolecules 26:679
51. Tamai Y, Tanaka H, Nakanishi K (1995) Macromolecules 28:2544
52. Pricl S, Fermeglia M (2003) Chem Eng Comm 190:1267

53. Abu-Shargh BF (2004) Polymer 45:6383
54. Mooney DA, MacElroy JMD (1999) J Chem Phys 110:11087
55. Cuthbert TR, Wagner NJ, Paulaitis ME (1997) Macromolecules 30:3058
56. de Pablo JJ, Laso M, Suter UW (1993) Macromolecules 26:6180
57. Vrabec J, Fischer J (1995) Mol Phys 85:781
58. Vrabec J, Hasse H (2002) Mol Phys 100:3375
59. Widom BJ (1963) J Chem Phys 39:2808
60. Eslami H, Müller-Plathe F (2007) J Comput Chem 28:1763
61. Eslami H, Müller-Plathe F (2007) Macromolecules 40:6413
62. Vieth WR, Frangoulis CS, Rionda JA (1966a) J Colloid Interface Sci 22:454
63. Vieth WR, Tam PM, Michaels AS (1966b) J Colloid Interface Sci 22:360
64. Newitt DM, Weale KE (1948) J Chem Soc 1541
65. Carfagna C, Nicodemo L, Nicolais L, Campanile G (1986) J Polym Sci Part B: Polym Phys 24:1805
66. Sada E, Humazawa H, Yakushiji H, Bamba Y, Sakata K, Wang ST (1987) Ind Eng Chem Res 26:433
67. Puleo AC, Muruganandam N, Paul DR (1989) J Polym Sci Part B: Polym Phys 27:2385
68. Raymond PC, Paul DR (1990) J Polym Sci Part B: Polym Phys 28:2079
69. Toi K, Paul DR (1982) Macromolecules 15:1104
70. Paterson R, Yampoi'skii Y, Fogg PGT (1999) J Phys Chem Ref Data 28:1255
71. Kucukpinar E, Doruker P (2003) Polymer 44:3607
72. Knopp B, Suter UW (1997) Macromolecules 30:6114
73. Müller-Plathe F, Rogers SC, van Gunsteren WF (1993) J Chem Phys 98:9895
74. Odani H, Taira K, Nemoto N, Kurata M (1979) Bull Inst Chem Res 57:226
75. Szenczi A, Kardos J, Medgyesi GA, Zavodszky N (2006) Biologicals 34:5
76. Mura P, Piccioli F, Gabbiani C, Camalli M, Messori L (2005) Inorg Chem 44:4897
77. Heuft JM, Meijer EJ (2005) J Chem Phys 123:94506
78. Müller-Plathe F (1996) Macromolecules 29:4782
79. Müller-Plathe F, van Gunsteren WF (1997) Polymer 38:2259
80. Ji Q, Yang X (2006) J Phys Chem B 110:22719
81. Tasaki K (1996) Macromolecules 29:8922
82. Stockmayer WH (1960) Macromol Chem Phys 35:54
83. Nishio I, Sun ST, Swislow G, Tanaka T (1979) Nature 281:208
84. Swislow G, Sun ST, Nishio I, Tanaka T (1980) Phys Rev Lett 44:796
85. Rouse PE (1953) J Chem Phys 21:1272
86. Zimm BH (1956) J Chem Phys 24:269
87. Yamakawa H (1971) Modern theory of polymer solutions, Harper & Row, New York
88. Muthukumar M, Edwards F (1982) J Chem Phys 76:2720
89. de Gennes PG (1979) Scaling concepts in polymer physics, Cornell University Press, Ithaca, NY
90. Binder K (1988) Colloid Polymer Sci 266:871
91. Kremer K, Binder K (1988) Comput Phys Rep 7:29
92. Bishop M, Kalos MH, Frisch HL (1979) J Chem Phys 70:1299
93. Rapaport DC (1979) J Chem Phys 71:3299
94. Bruns W, Bansal R (1981) J Chem Phys 74:2064
95. Khalatur PG, Papulov Yu G, Pavlov AS (1986) Mol Phys 58:887
96. Smit B, van der Put A, Peters CJ, de Swaan Arons J, Michels JPJ (1988) J Chem Phys 88:3372
97. Smit B, Cox KR, Michels JPJ (1989) Mol Phys 66:97
98. Luque J, Santamaria J, Freire JJ (1989) J Chem Phys 91:584
99. Dünweg B, Kremer K (1993) J Chem Phys 99:6983
100. de Gennes G (1985) J Phys Lett 46:L639
101. Grosberg AY, Nechaev SK, Shakhnovich EI (1988) J Phys Lett 49:2095

102. Polson JM, Zuckermann MJ (2002) J Chem Phys 116:7244
103. Zhu PW, Napper DH (1997) J Chem Phys 106:6492
104. Nakata M, Nakagawa T (1999) J Chem Phys 110:2703
105. Kayaman N, Gürel EE, Baysal BM, Karasz FE (1999) Macromolecules 32:8399
106. Chang R, Yethiraj A (2001) J Chem Phys 114:7688
107. Polson JM, Gallant JP (2006) J Chem Phys 124:184905
108. Elsaessar T, Kaiser W (1991) Annu Rev Phys Chem 42:83
109. Bakshiev NG, Mazurenko YT, Pieterskaya I (1996) Opt Spectrosc 21:307
110. Stratt RM, Maroncelli M (1996) J Phys Chem 100:12981
111. Bingemann D, Ernsting NP (1995) J Chem Phys 102:2691
112. Chandler D (1987) Introduction to modern statistical mechanics, Oxford University, Oxford, UK.
113. Ma J, Bout DV, Berg M (1995) J Chem Phys 103:9146
114. Lin Y, Jonah CD (1994) In: Simon JD (ed) Ultrafast dynamics of chemical systems, Kluwer, Dordrecht, p 137
115. Chapman CF, Fee RS, Maroncelli M (1995) J Phys Chem 99:4811
116. Shinyashiki N, Matsumura Y, Mashimo S, Yagihara S (1996) J Chem Phys 104:6877
117. Shinyashiki N, Yagihara S, Arita I, Mashimo S (1998) J Phys Chem B 102:3249
118. Ratner M, Shriver DF (1988) Chem Rev 88:109
119. Brauns EB, Madaras ML, Coleman RS, Murphy CJ, Berg MA (1999) J Am Chem Soc 121:11644
120. Willard DM, Levinger NE (2000) J Phys Chem B 104:11075
121. Pal SK, Mandal D, Sukul D, Sen S, Bhattacharyya K (2001) J Phys Chem B 105:1438
122. Pal SK, Sukul D, Mandal D, Sen S, Bhattacharyya K (2000) J Phys Chem B 104:2613
123. Jarzeba W, Walker GC, Johnson AE, Kahlow MA, Barbara PF (1998) J Phys Chem 92:7039
124. Faeder J, Ladanyi BM (2000) J Phys Chem B 104:1033
125. Michael D, Benjamin I (2001) J Chem Phys 114:2817
126. Maeda Y, Tsukida N, Kitano H, Terada T, Yamanaka J (1993) J Phys Chem 97:13903
127. Desbrieres J, Borsali R, Rinaudo M, Milas M (1993) Macromolecules 26:2592
128. Argaman R, Huppert D (1998) J Phys Chem A:6215
129. Sen S, Sukul D, Dutta P, Bhattacharyya K (2002) J Phys Chem B 106:3763
130. Saven JG, Skinner JL (1993) J Chem Phys 99:4391
131. Stephens MD, Saven JG, Skinner JL (1997) J Chem Phys 106:2129
132. Bagchi B (1994) J Chem Phys 100:6658
133. Bagchi B, Riswas R (1999) Adv Chem Phys 109:207
134. Yamaguchi T, Kimura Y, Nakahara M (2002) J Phys Chem B 106:9126
135. Egorov SA (2003) J Chem Phys 118:10643
136. Raineri FO, Resat H, Perng BC, Hirata F, Friedman HL (1994) J Chem Phys 100:1477
137. Friedman HL, Raineri FO, Hirata F, Perng BC (1995) J Stat Phys 78:239
138. Bagchi B, Chandra A (1993) Chem Phys 173:133
139. Reynolds L, Gardecki JA, Frankland SJV, Horng ML, Maroncelli M (1996) J Phys Chem 100:1037
140. Phelps DK, Weaver MJ, Ladanyi BM (1993) Chem Phys 176:575
141. Maroncelli M, Fleming GR (1988) J Chem Phys 89:5044
142. Bader JS, Chandler D (1989) Chem Phys Lett 157:501
143. Cinacchi G, Ingroso F, Tani A (2006) J Phys Chem B 110:13633
144. Ingrosso F, Ladanyi B (2006) J Phys Chem B 110:10120
145. Olender R, Nitzan A (1995) J Chem Phys 102:7180
146. Barrie JA, Williams MJL, Munday K (1980) Polym Eng Sci 20:21
147. Yavorsky JA (1984) Ph.D. Dissertation, Department of Chemistry and Geology, Clemson University.

CHAPTER 12

HYDROGEN BONDS AND SOLVENT EFFECTS IN SOIL PROCESSES: A THEORETICAL VIEW

DANIEL TUNEGA[1,2], ADELIA J. A. AQUINO[1,2], GEORG HABERHAUER[3], MARTIN H. GERZABEK[2], AND HANS LISCHKA[1]

[1]*Institute for Theoretical Chemistry, University of Vienna, Währingerstrasse 17, A-1090 Vienna, Austria, e-mail: daniel.tunega@univie.ac.at*

[2]*Institute of Soil Research, University of Natural Resources and Applied Life Sciences, Vienna, Peter-Jordan-Strasse 82, A-1190 Vienna, Austria*

[3]*Austrian Research Centers Seibersdorf, A-2444 Seibersdorf, Austria*

Abstract: The importance of hydrogen bonds and solvent effects in soil and environmental chemistry is demonstrated in this chapter. Humic substances as one of the major soil constituents are modeled by means of representative functional groups. Their capability to form hydrogen bonds is demonstrated on interactions with selected sets of polar molecules, anions and acidic pesticides, particularly 2,4-dichlorophenoxyacetic. It was shown that anionic species form complexes of similar strength as corresponding neutral molecules if solvent effects are taken into account. Of all functional groups carboxyl showed the highest chemical activity in the formation of complexes. The calculations demonstrate that the solvent effect substantially lowers the complex formation energies, especially in case of charged systems.

The soil minerals kaolinite and goethite studied in this work possess very active surfaces, which are formed from hydroxyl groups. These OH groups are very flexible and able to act as a proton donor or acceptor for hydrogen bond formation. Polar molecules (e.g., H_2O, acetic acid) form strongly bound complexes via multiple hydrogen bonds. It was shown that strong sorbent sites exist on irregular clay mineral surfaces formed on the corner and edges of clay mineral particles

Keywords: Functional groups, Soil minerals, Solvent effect, Hydrogen bonds, DFT

12.1. INTRODUCTION

Hydrogen bonding is a key structural feature in many chemical areas ranging from inorganic to biological chemistry [1,2,3,4,5]. Hydrogen bonds constitute the major bonding factor in water and in aqueous solutions [6]. They have also been ascribed the capability of sustaining the stabilization of supramolecular structures, such as DNA or tertiary structures of proteins [7]. Another important subject is environmental pollution since it is one of the major problems of our civilization. In many

S. Canuto (ed.), Solvation Effects on Molecules and Biomolecules, 321–347.
DOI 10.1007/978-1-4020-8270-2_12,

processes of the environmental pollution hydrogen bonds play a dominant role. Produced chemical pollutants represent serious risks for the quality of air, water sources and soils. The knowledge of the transport, fixation, accumulation and distribution of pollutants in the ecosystem is very important for the assessment of soil contamination and for the application of protective remediation methods. The fate of pollutants is directly connected with the adsorption processes occurring in soils that has impact on solute transport, microbial degradation, plant uptake through roots and, thus, the transfer of pollutants into other compartments of the ecosystem and the food chain.

Soils are complex entities containing large portions of organic and inorganic (mineral) constituents. The soil organic material (SOM) is considered as a heterogeneous entity for which humic substances (HS) [8] are generated by the biochemical transformation of plant and animal residue and represent a major fraction of the dissolved and particulate organic matter in natural ecosystems. HS are large macromolecules with variable size, structure and chemical compositions. Their reactivity depends on their functional group chemistry and microstructure, which are in turn influenced by the composition of the surrounding media. HS represent important organic components actively participating in sorption processes [9]. They act as traps for pollutants mainly via surface functional groups or binding in cavity-like sorption sites [8]. It was also shown that inorganic soil constituents, e.g., soil minerals (clays, oxides), have a significant impact on the sorption properties of various species (e.g., Parker and Rae [10], Dixon and Schulze [11]). Thus, for the improvement of the present understanding it is necessary to consider a manifold of different chemical interfaces, the clay minerals and pedogenic oxides being the most active inorganic components of soils participating in sorption processes [12].

A comprehensive modeling of the just-described complex soil system at a molecular level is not possible. Therefore, it was the goal of our work during the recent years to develop and investigate microscopic sub-scenarios where (i) individual interactions of characteristic chemical groups representing the activity of SOM with organic substances, primarily certain classes of pesticides, and (ii) adsorption properties of various clay mineral surfaces were investigated. The combining theme characterizing the attractive interactions between individual molecular species is the hydrogen bond. It is the purpose of this chapter to present a survey of the variety of hydrogen-bonded systems occurring in soil adsorption processes and to describe the possibilities for accurate quantum chemical calculations. Special attention is devoted to the class of the phenoxyacetic acid (PAA) derivatives, which represent a broad spectrum of herbicides extensively used in agriculture. Their behavior in soils (solubility, adsorption–desorption, chemical resistance and biodegradation) is governed by their chemical structure. In the PAA derivatives mainly the polar carboxyl group is responsible for their relatively high chemical activity and dominates in interactions with clay mineral surfaces.

Computational modeling of hydrogen bonding scenarios represents a complex problem. Electronic structure calculations based on quantum mechanical methods provide undoubtedly the most fundamental and reliable framework for reliable

calculations of molecular systems. Nevertheless, computations using quantum chemical methods can be carried out only for relatively small systems and are not routinely applicable to complex macromolecular surroundings encountered in soil systems.

Hydrogen bonds have been studied in detail by a huge number of experimental and theoretical investigations. A recent overview on computational studies on hydrogen bonds can be found in the work by Rozas [13]. The major purpose of the quantum chemical calculations was the study of the basic bonding properties of hydrogen bonds aiming at precise data for interaction energies, structural parameters (interatomic distances and angles, total atomic charge, dipole moments) and vibrational spectra. Most of these studies were focused on the investigation of isolated complexes. Environmental effects were not taken into account. Nevertheless, the environment plays an important role in the determination of properties and reactivity of substances in condensed phase. The complexity of chemical phenomena in solution has made it necessary to develop a variety of models and computational techniques to describe molecules in solution. These techniques differ in the level of detail used to describe the chemical system, the physical rules underlying the process of interest, and the mathematical formalism used to implement these rules. The final goal of all these models is the understanding of the behavior of molecules in a variety of environmental systems. One straightforward option would be to include solvent molecules explicitly as a cluster around the solute. In this case the whole cluster would be treated by quantum chemical methods. The applicability of this approach, however, is limited by the size of the cluster, considering the drastically increasing amount of computational effort with the size of the system. Mixed quantum mechanical–molecular mechanical (QM-MM) or completely classical models (force field or molecular mechanics methods) lead to drastic speedups of the calculations and can be used for extended molecular dynamics and Monte Carlo simulations [14,15,16,17,18,19]. However, it is not easy to determine reliable force field parameters describing the whole range of hydrogen bonds (weak to strong) in sufficient accuracy. An efficient combination of QM and MM approaches have been developed by Coutinho, Canuto and co-workers [20,21] in the form of sequential MC-QM method (s-MC-QM). Another interesting concept for solvent effects has been proposed by introducing the averaged solvent electrostatic potential (ASEP) [22,23]. A combination of ASEP and the above-mentioned s-MC-QM approach has been published recently [24]. An alternative to taking into account the solvent molecules explicitly are methods based on polarizable continuum models (PCM) [25,26,27,28], the conductor-like screening model (COSMO) [29,30] or the solvent model (SM) [31,32]. In these approaches the solute is treated by quantum mechanical methods and a modeling of the solute cavity by atom-centered overlapping spheres. The advantage of these methods lies in much less time-consuming calculations than corresponding quantum chemical approaches using explicit solvent molecules.

In our studies, solvent effects were included in three different ways: (i) by explicit inclusion of water molecules, (ii) by using a continuum solvation model and (iii) by the combination of models (i) and (ii). The first approach is called microsolvation,

the second is denominated as global solvation. The advantage of the microsolvation model is its capacity to describe explicitly specific local interactions as hydrogen bonds, an aspect which is missing in the global solvation approach. The microsolvation model is size-limited and long-range effects of a polar solvent are absent while in the global solvation approach they are included. Model (iii) combines the advantages of models (i) and (ii). Such calculations are also referred to as "liquid" phase calculations here.

12.2. SIMULATON METHODS

The quantum chemical calculations are based on density functional theory (DFT) methods in various forms. DFT methods show a good computational efficiency allowing the treatment of sufficiently large molecular systems and giving reasonable accuracy. For the investigation of adsorption processes on clay mineral surfaces two approaches were used. The first one is a cluster approach where a certain section is cut from the crystal surface. Dangling bonds are saturated with hydrogen atoms and the positions of atoms not directly involved in the adsorption processes are frozen at the values of the periodic system in order to avoid artificial restructurings of the cluster. In many cases these clusters together with the adsorbents are embedded into a polarizable continuum using PCM model [25,26,27,28] or COSMO [29,30] methods.

The second approach is the use of methods employing translational periodicity. Large periodic simulation cells (supercells) are used for the description of aperiodic cases in an effort to minimize artificial periodic effects. The periodic approach is used here for the study of surface properties of solids where simulated models possess two-dimensional translational periodicity. DFT methods in combination with the Car–Parinello type molecular dynamics (MD) were used as a very efficient tool for the study of systems up to the size of several hundred atoms. Within this size of model systems it is reasonable to run short MD simulations up to tens of picoseconds. Even though this time scale represents relatively short dynamic simulations, valuable statistically averaged properties can be achieved, e.g., structures or energetic stabilities. Moreover, these time lengths are satisfactory for obtaining, e.g., radial distribution functions or power spectra (corresponding to phonon spectra).

In case of molecular and cluster calculations, programs Turbomole [33] and Gaussian [34] were applied. Both programs offer very good possibilities to treat larger systems by using methods to reduce the amount of work for the calculation of the time-consuming two-electron integrals (e.g., resolution of the identity (RI) method in TURBOMOLE [35] and layer techniques ONIOM in Gaussian [36]) for embedding the critical part of the system in an environment for which cheaper methods can be used. Mostly the B3LYP hybrid functional [37] was used in our calculations; in some cases we used pure DFT functionals like BLYP [38,39,40]. The RI method was used for calculations with pure DFT functionals. In special cases, calculations based on the Møller–Plesset perturbation theory to second order (MP2) [41] were carried out for comparison reasons. The split valence polarization (SVP) [42] and the modified SVP+sp are the basis sets used practically in all molecular

calculations. In several cases the TZVP [43] and TZVP+sp (similar augmentation as in case of SVP+sp) basis sets were used for controlling the accuracy of the SVP+sp results. The SVP+sp basis was constructed by augmenting the SVP basis with a set of s and p functions on atoms that participated in the hydrogen bonding. The exponents of these additional basis functions were obtained by dividing the smallest respective exponent of the SVP basis set by a factor of three. As has been shown in the work by Tunega et al. [44] the basis set superposition error (BSSE) is reduced substantially using the SVP+sp basis set. The counterpoise method [45] was used to correct the BSSE.

The program VASP [46] was used in calculations on periodic models. In the VASP calculations, the local density approximation (LDA) [47] and the generalized gradient approximation (GGA) [48] are used for the description of the electron exchange–correlation interaction. The calculations were performed in a plane-wave basis set by means of the projector-augmented wave (PAW) method [49,50]. In case of large computational cells the Brillouin-zone sampling was restricted to the Γ point, otherwise *k*-point testing according Monkorst–Pack scheme [51] was always performed prior to a particular calculation. The plane-wave cutoff energy in the range of 350–400 eV was used in cases of static structural relaxations which correspond to great precision in the calculation. In MD simulations, the plane-wave cutoff energy was lowered to 200 eV to allow relatively long run in a reasonable real time. The finite-temperature MD simulations were usually performed at 300 K using a canonical ensemble with Nosé thermostat procedure [52]. The velocity-Verlet algorithm [53] with a time step Δt=1 fs was chosen in all MD calculations. The simulation times depend on the complexity of models and ranged from 2 to 20 ps. Thermal equilibration was always performed prior to MD run used for statistical analysis. In all calculations computational box volumes and shapes were kept constant.

12.3. ORGANIC FUNCTIONAL GROUPS AS MODELS FOR HUMIC SUBSTANCES

The selection of the molecular systems investigated in this study was based on our interest in the properties of organic soil constituents such as humic substances and pesticides. HS contain several relevant functional groups in an otherwise indefinable structure. These groups are mainly carboxyl, carbonyl, alcoholic and phenolic units, which play a major role in binding of polar molecules from a polar solvent environment. In this context we decided to investigate the hydrogen bond effect in different media in binary complexes, having acetic acid or acetate as one of the constituents. This choice was based considering the major role that carboxyl group plays as functional group of HS. The second component of these binary complexes contained as characteristic features carbonyl, amino and hydroxyl groups. The deprotonated form of carboxylic acid was also considered since interactions with acetate in natural soil environments occur, as well.

The fate of the terrestrial and aquatic pollution due to pesticide deliverances is of great ecological concern in our days. 2,4-dichlorophenoxyacetic acid (2,4-D) is presently amongst the most employed herbicides [54], almost ubiquitous in agriculture [55]. It belongs to the class of phenoxyacetic acids having an acidic carboxyl group (pK_a=2.9) [56,57]. This is the reason why it is quite mobile in aqueous systems and exists in its anionic form over a wide pH range in natural waters. Acetic acid often appears in soils and is a good general model for interactions with various functional groups. Therefore, we undertook two sets of investigations. In the first one the interaction of acetic acid and acetate with a set of selected functional groups (see below) was studied. In the second set the interaction of 2,4-D and its deprotonated form, respectively, with different model organic compounds was selected in order to mimic the interactions of HS in soils.

12.3.1. Binary Complexes with Acetic Acid and Acetate

Two series of six different dimers were investigated [58]. The first series was formed by acetic acid (HAc) as one component and HAc, acetaldehyde (AcH), methanol (MeOH), phenol (PhOH), ammonia (NH_3) and acetamide ($AcNH_2$) as the other one. The second series was composed of the acetate anion (Ac^-) as one component in interaction with the molecules from the first set.

The calculations were performed at the DFT/BLYP level of theory and the SVP+sp basis set in gas phase and in solution. Three different solvents water, DMSO and *n*-heptane with relative dielectric constants ε_r = 78.39, 46.70 and 1.92, respectively, were used in the PCM approach. Full geometry optimizations were performed in all calculations and interaction energies were BSSE corrected. Enthalpies and Gibbs free energies were computed for the gas-phase structures within the standard harmonic oscillator/rigid rotator/ideal gas approximation at T = 298.15 K. The Gibbs free energies of formations of complexes in solution (ΔG^{sol}) were calculated using earlier approaches [59,60] according to the equation:

$$\Delta G^{sol} = \Delta G^{gas} + \Delta\Delta G_{solv} + RT \ln(1/22.4) \qquad (12\text{-}1)$$

where ΔG^{gas} is the Gibbs free energy of formation in the gas phase, $\Delta\Delta G_{solv}$ is the difference in free energy of solvation (ΔG_{solv}) of the complex and respective components. The last term is a correction to the change of reference state from ideal gas to solution [61].

All of the selected neutral molecules form cyclic structures with acetic acid in the gas phase establishing two hydrogen bonds, showing that the OH group and the carbonyl oxygen atom of the carboxyl group of HAc participate in the hydrogen bond formation. The strongest hydrogen bonds for neutral complexes are formed in the acetic acid dimer with H···O distances of 1.625 Å. The calculated formation enthalpy ΔH^{gas} of –14.7 kcal/mol (Table 12-1) is in good agreement with experimental gas-phase formation enthalpies ranging between –14.2 and –15.3 kcal/mol [62,63,64,65], and with other calculations [66,67,68]. The other molecules form weaker complexes in the gas phase with two non-equivalent hydrogen bonds

Table 12-1. Interaction enthalpies and Gibbs free interaction energies for gas phase and liquid phases using the BLYP/SVP+sp approach. Energies are in kcal/mol

System	Gas		Heptane	DMSO	Water
	ΔH^{gas}	ΔG^{gas}	ΔG^{sol}	ΔG^{sol}	ΔG^{sol}
HAc−HAc	−14.7	−1.9	−1.8	1.4	7.5
HAc−AcH	−6.2	3.5	2.7	4.8	8.3
HAc−MeOH	−8.0	1.8	1.6	4.3	6.7
HAc−PhOH	−6.9	3.1	3.0	6.2	11.2
HAc−NH_3	−8.7	0.6	−0.7	0.2	2.4
HAc−$AcNH_2$	−12.8	−3.2	−3.1	1.9	5.9
Ac^-−HAc	−25.5	−15.5	−9.7	−1.2	3.1
Ac^-−AcH	−10.7	−2.4	2.6	9.8	6.9
Ac^-−MeOH	−16.6	−7.8	−3.5	2.6	6.6
Ac^-−PhOH	−26.5	−16.5	−9.3	1.3	3.6
Ac^-−NH_3	−8.0	−0.8	1.8	6.3	6.5
Ac^-−$AcNH_2$	−22.0	−12.0	−4.8	5.1	9.6

(stronger and weaker one) with distances between 1.6 and 2.5 Å (Figure 12-1). The interaction energies (Table 12-1) correspond to the H···O distances in the complexes. For the charged complexes only one hydrogen bond is formed and the acetate anion acts as a very strong Brønsted base for protons from the partners in the dimers. In cases of $AcNH_2$, HAc, PhOH and MeOH, the formed hydrogen bond is stronger than in neutral complexes that is also reflected in calculated formation enthalpies shown in Table 12-1. Thermal contributions to ΔH amount to about 1–2 kcal/mol, which is of the order of 10–20%. However, the entropic contribution is substantial. For example, $T\Delta S$ for the formation of the acetic acid dimer in the gas phase amounts to –12.8 kcal/mol. This is in good agreement with the experimental value of about –10.7 kcal/mol [64,65]. This large loss of entropy is observed for all complexes and has the origin in the transformation of translational and rotational degrees of freedom of the monomers into vibrational ones in the complex. The unfavorable $T\Delta S$ factor is the cause for all neutral complexes in the gas phase (except the HAc dimer and HAc–$AcNH_2$) to be unstable according to calculated ΔG values.

The effects of the three solvents heptane, DMSO and water on formed hydrogen bonds are illustrated in Figure 12-1. It is observed that increasing strength of the solvent stabilizes the strong hydrogen bonds (they become shorter than in the gas phase). On the other hand, the weaker hydrogen bond in the neutral complexes starts to open with increasing strength of the solvent. This phenomenon leads to a decrease in the interaction energy but opens a possibility for improved solvation of both interacting subsystems since the solvent-accessible surface increases. As expected, the largest changes in hydrogen bond lengths are observed for the strongest solvent, water. In conclusion, for the neutral complexes it is observed that the polar solvent environment has a stabilization effect on the strong hydrogen bonds while the weak hydrogen bonds can even be broken under the effect of the solvent. An analogous

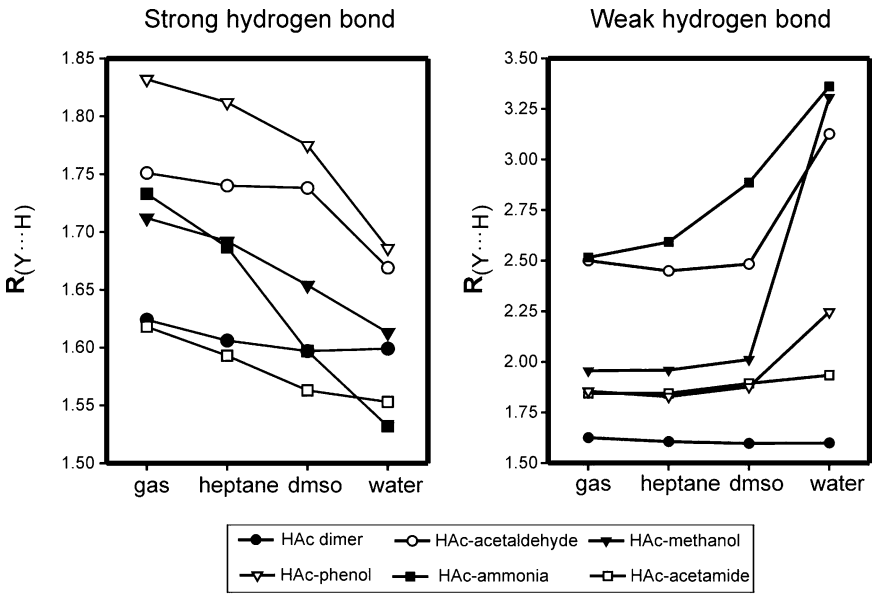

Figure 12-1. The dependence of the Y···H distance of the strong and weak hydrogen bonds in the HAc complexes on different solvent medium

behavior was observed for formamide dimers in different solvents by Sneddon et al. [69] using molecular mechanics simulations. On the other hand, for charged complexes containing the acetate anion, the structure of the hydrogen bonds does not change much from gas to water environment, and the solvent dependence of the hydrogen bond distances show smaller changes than for neutral ones. The interaction energies for the neutral and charged complexes in different solvents are collected in Table 12-1. It is observed that these energies decrease considerably in absolute value when the polarity of the solvent increases. The largest changes are observed for the acetic acid dimer and acetic acid–acetamide complex in agreement with calculations by Nakabayashi et al. [68] for the cyclic acetic acid dimer. Table 12-1 shows that the ΔG values of formation calculated according to Eq. 12-1 are positive except for the acetic acid dimer, the acetic acid–acetamide and acetic acid–ammonia complexes in heptane. This means that only these systems in these specific environments are thermodynamically stable. Our calculated ΔG value for acetic acid dimer in heptane (–1.8 kcal/mol) is comparable with the experimental value in chloroform of about –2.4 kcal/mol [70]. The interaction energies computed for the charged complexes (Table 12-1) also decrease with the increase of the solvent polarity, a behavior which can be explained similar to the neutral complexes. The reason for the destabilization of the complexes in strongly polar solvents can be found in the balance between the solvation energies of the separated molecules and the complexes. The separated molecules have large solvation energy since they are either charged or possess large

dipole moments. The solvation energy of the complexes is always smaller than the sum of solvation energies of individual components (in absolute value). As a consequence, the solvent energy contribution to ΔG of formation in solution is positive. An explanation of this effect was found in the decrease of the attractive part and an increase of the non-attractive part of the solvent-accessible surface area of the bimolecular complexes for polar solvents in comparison with individual components since the attractive surface area is "locked" in the formed hydrogen bonds between molecules in complexes. This destabilizing effect of $\Delta\Delta G_{solv}$ is a general one for the formation of bimolecular hydrogen-bonded complexes in polar solvents.

12.3.2. Binary Complexes of 2,4-Dichlorophenoxyacetic Acid (2,4-D)

The sorption activity of functional groups existing in humic substances with respect to the pesticide 2,4-D were investigated by means of a set of molecular model species (MS) – acetic acid (HAc), methanol (MeOH), acetaldehyde (AcH), methylamine ($MeNH_2$) and protonated methylamine ($MeNH_3^+$) [71]. Two sets of adsorption complexes were studied – with the neutral form of 2,4-D and with its deprotonated form (2,4-D^-), respectively. All calculations were performed at the B3LYP/SVP+sp level of the theory. In comparison to the reaction schemes for the binary acetic acid complexes of the previous subsection an extended solvation approach including microsolvation with two waters was used. The reaction energies, ΔE, ΔH and ΔG, were computed according to following reaction scheme:

$$\begin{aligned} &MS\cdots xH_2O + 2,4\text{-}D\cdots xH_2O \rightarrow MS\cdots 2,4\text{-}D + (H_2O)_{2x} \text{ and} \\ &MS\cdots xH_2O + 2,4\text{-}D^-\cdots xH_2O \rightarrow MS\cdots 2,4\text{-}D^- + (H_2O)_{2x} \end{aligned} \tag{12-2}$$

In (a) the gas-phase reaction $x = 0$ and PCM is not used, (b) in the global solvation reaction $x = 0$ and PCM is used, (c) in the microsolvation reaction $x = 2$ and PCM is not used and (d) in the combined approach $x = 2$ and PCM is used. Results of calculated reaction energies are collected in Table 12-2.

Neutral complexes of 2,4-D with AcH, MeOH and HAc (see structures a, b and e in Figure 12-2) are in the form of similar cyclic structures with two types of hydrogen bonds (stronger and weaker) as observed for the complexes of HAc in Section 3.1. It is evident that the hydrogen bond is the driving mechanism in the formation of all complexes. The OH group of 2,4-D forms a strong hydrogen bond acting as proton donor, while its carbonyl group, C=O, acts as proton acceptor forming much weaker hydrogen bonds in the complexes with AcH, MeOH and $MeNH_2$. For the complex with protonated methylamine (Figure 12-2d), the stronger hydrogen bond comes from the interaction between the carbonyl group of 2,4-D and the hydrogen atom from the NH_3^+ group of the protonated amine. A weak hydrogen bond appears in this complex coming from the interaction between the chlorine atom of the 2,4-D ring and another hydrogen atom of the NH_3^+ group of the amine. The complex 2,4-D···2 H_2O (Figure 12-2f) has also a cyclic form with three relatively strong hydrogen bonds.

Table 12-2. Computed complex formation energies (in kcal/mol) for 2,4-D and 2,4-D$^-$

MS	MS···xH$_2$O + 2,4-D···xH$_2$O→ MS···2,4-D + (H$_2$O)$_{2x}$											
	Gas phase (g) x=0, no PCM			Global solvation (gs) x = 0, PCM			Microsolvation (ms) x = 2, no PCM			ms+gs (mgs) x = 2, PCM		
	ΔE_g	ΔH_g	ΔG_g	ΔE_{gs}	ΔH_{gs}	ΔG_{gs}	ΔE_{ms}	ΔH_{ms}	ΔG_{ms}	ΔE_{mgs}	ΔH_{mgs}	ΔG_{mgs}
AcH	−11.4	−8.6	1.2	−2.6	0.2	10.0	−2.2	−1.8	−1.5	−4.1	−3.7	−3.4
MeOH	−12.5	−9.4	0.2	−4.2	−1.1	4.1	−3.9	−3.6	−4.3	−8.9	−8.6	−9.3
$MeNH_2$	−13.9	−11.1	−2.0	−7.3	−4.5	4.6	−3.1	−3.1	−3.8	−4.7	−4.7	−5.4
$MeNH_3^+$	−33.2	−29.6	−18.9	−4.9	−1.3	9.4	−2.8	−2.2	0.9	−0.6	−0.1	3.0
HAc	−18.0	−15.1	−4.0	−1.6	1.3	12.4	−0.8	−0.8	−1.5	−0.2	−0.2	−0.9
	MS···xH$_2$O + 2,4-D$^-$···xH$_2$O → MS···2,4-D$^-$ + (H$_2$O)$_{2x}$											
AcH	−11.5	−9.4	−1.3	1.4	3.5	11.6	5.7	5.3	5.1	−1.1	−1.5	−1.7
MeOH	−15.3	−13.0	−4.4	−1.6	0.7	9.3	1.2	0.8	0.1	−7.4	−7.8	−8.5
$MeNH_2$	−8.2	−6.1	1.6	2.1	4.2	11.9	10.5	10.2	9.2	4.1	3.8	2.8
$MeNH_3^+$	−116.0	−115.8	−106.6	−0.6	−0.5	8.8	−88.3	−89.2	−86.5	3.1	2.2	4.9
HAc	−21.2	−19.6	−8.6	−2.4	−0.8	10.2	3.9	2.5	2.8	−2.3	−3.7	−3.4
	$Ca^{2+}(H_2O)_6$ + 2,4-D$^-$···2 H_2O + Ac^-···2 H_2O → 2,4-D$^-$···$Ca^{2+}(H_2O)_2$···Ac^- + 2$(H_2O)_4$											
–	–	–	–	–	–	–	−220.9	−221.0	−216.3	−11.5	−11.6	−6.6

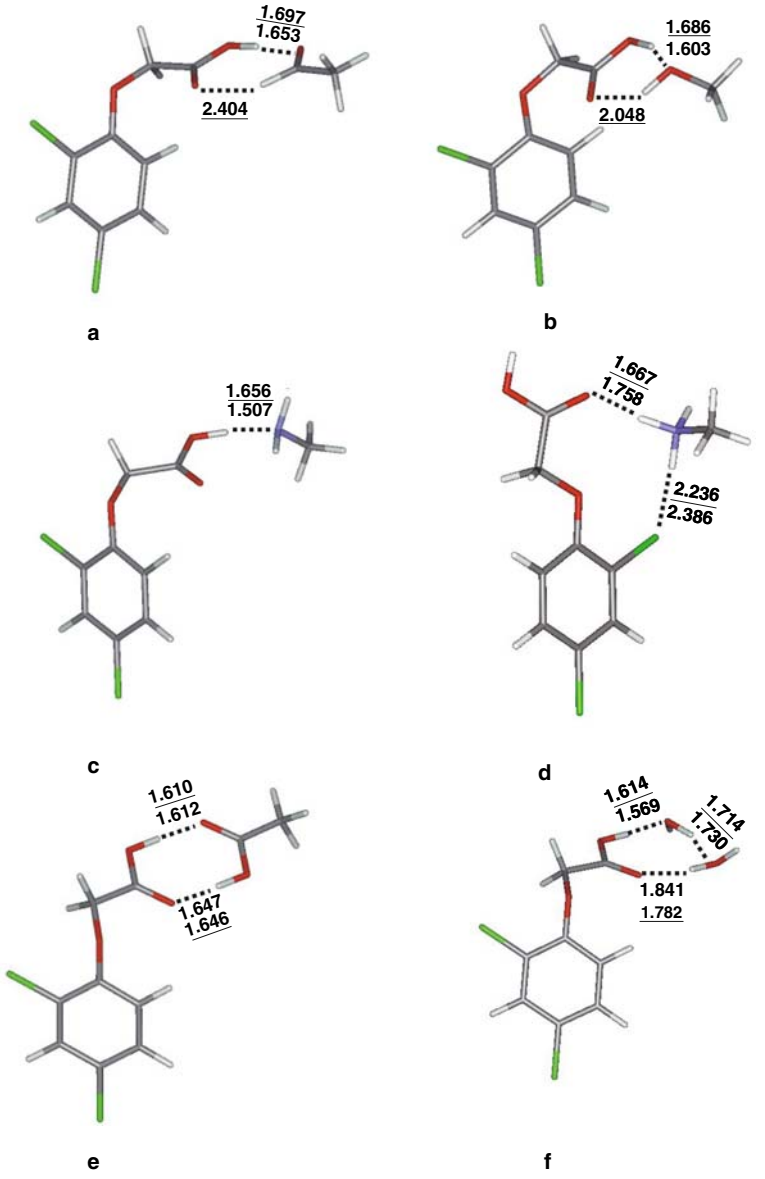

Figure 12-2. B3LYP/SVP+sp optimized structures of 2,4-D hydrogen-bonded complexes. (**a**) 2,4-D···Me-CHO; (**b**) 2,4-D···Me-OH; (**c**) 2,4-D···Me-NH_2; (**d**) 2,4-D···Me-NH_3^+; (**e**) 2,4-D···HAc; (**f**) 2,4-D···$(H_2O)_2$. Inserted numbers are hydrogen bond distances for the solvent and the gas phase (*underlined*)

The negatively charged structure 2,4-D$^-$ is only a proton acceptor and the formation of the second hydrogen bond is not found in most of the charged complexes. The hydrogen bonds formed in the negatively charged complexes are of different lengths and consequently of different strengths, depending on the proton donor capability of each MS. For example, the strongest hydrogen bond was observed for the acetic acid complex with the H···O distance of 1.419 Å and corresponding complex formation energy of –21.2 kcal/mol in the gas phase. The global solvent effect had the same impact on the hydrogen bond structures as was described in the previous section. Strong hydrogen bonds become even stronger while weak hydrogen bond was opened under the global solvent effect.

Table 12-2 collects the formation energies, enthalpies and Gibbs free energies calculated under the four different solvation conditions described above. Comparison of the calculated formation energies with our previous results for the interaction energies of acetic acid and similar MS (Table 12-1) shows that 2,4-D forms more strongly bound complexes than acetic acid in the gas phase with an energy difference of about 2–4 kcal/mol. Thermal and entropic contributions for the gas phase and global solvation are similar as in the case of HAc and Ac$^-$ interactions described in the previous section. Especially the entropy loss is large that is typical for the association reactions like A + B → C. This approach makes all complex formation reactions using only global solvation unfavorable, since all respective ΔG_{gs} values of Table 12-2 are positive. In order to assess the validity of the simple association scheme, the microsolvation approach with explicit insertion of H_2O molecules was used as the next step and the results are shown in Table 12-2 as well. Similar to the global solvation approach, a considerable decrease (in absolute value) of the interaction energies in comparison to the gas-phase approach is already observed in case of microsolvation. However, in contrast to the gas phase and global solvation, comparison of the ΔH and ΔG values shows that the entropy loss is much smaller in the microsolvation reactions. $T\Delta S$ for the formation reaction of the complex between 2,4-D and acetic acid, for instance, is –0.7 kcal/mol as compared with –11.1 kcal/mol for the complex formation obtained for the gas-phase reaction. The reason for this difference is that the microsolvation reaction scheme (Eq. 12-2) does not represent a pure association but a replacement of solvent waters from the reactants. It is clear that this scheme is still quite simple and that a final verification could be achieved only by MD or Monte Carlo (MC) investigations preferably at a complete ab initio or QM/MM level. The combined microsolvation and global solvation approach (ms+gs) shows that the influence of the global solvent effect is not so important anymore as compared to the pure global solvation. An extreme importance of global solvation is found for cases where the reaction schemes are not charge-balanced as is the case of the interaction of protonated methylamine with 2,4-D$^-$ (see Table 12-2). Results of the ms+gs calculation showed that all complex formation reactions in solvent are favorable except the cases of $MeNH_3^+$ with neutral and anionic 2,4-D and $MeNH_2$ with the 2,4-D$^-$ anion, respectively.

12.4. HYDROGEN-BONDED INTERACTIONS IN SOIL MINERALS AND THEIR SURFACES

Various chemical and physical processes (e.g., sorption, mineral dissolution) in soils appear at mineral–water interfaces. In particular, soil minerals significantly contribute to sorption of various pollutants (e.g., heavy metal cations, pesticides), which represent a high ecological risk. The speciation of surface sites has been studied intensively during the last 30 years by various experimental methods. However, experimental investigations usually give only an overall picture about adsorption processes and practically no details about the mechanism of these processes. In many cases, the dominant mechanism for adsorption of various species is the formation of hydrogen bonds. In this part we present a characterization of surface adsorption sites of two soil minerals (kaolinite and goethite) by means of quantum chemical density functional theory-based simulations. Models of surface sites are investigated in their interactions with water molecules, and structural, energetic and dynamic properties of these sites are evaluated. The chemical activities of these sites are estimated on the basis of calculated interaction energies for several molecules.

12.4.1. Hydrogen-Bonded Interactions of Surfaces of the Isolated Kaolinite Layer

Cluster and periodic model approaches were used in the study of interactions of water, acetic acid (HAc) with the (001) surfaces (octahedral, K(O), and tetrahedral, K(T)) of the kaolinite layer [72,73]. The model of the isolated kaolinite layer is given in Figure 12-3. In both approaches the formation of several relatively strong hydrogen bonds between surface hydroxyl groups on the octahedral site and adsorbed species was found. Table 12-3 collects structural parameters for formed hydrogen bond complex of the isolated H_2O molecule on the octahedral surface of the kaolinite layer, collected from three types of calculations. All three approaches used give relatively similar results. The water molecule forms three hydrogen bonds, in two of them water is a proton acceptor, while in the third, the strongest one, water is a proton donor to one of the surface OH groups. A similar hydrogen-bonded scheme was observed for HAc. The carbonyl group forms three relatively strong hydrogen bonds with the surface OH groups while the hydroxyl of the –COOH group forms very strong hydrogen bond (less than 1.5 Å) with the one oxygen of the surface OH group. On the other hand, only weak hydrogen bonds with O···H distances > 2.0 Å were observed for the tetrahedral side of the kaolinite layer and surface oxygen atoms are found to be weak attractors for water H atoms.

In a subsequent study both surfaces of the kaolinite layer were covered by monomolecular layers of water [74] and the structure and dynamics of both systems were investigated using ab initio MD. Figure 12-4 represents snapshots from the MD simulations. The arrangement and the structure of the water layer differ significantly on both surfaces. On the octahedral side the water layer stays in a relatively stable configuration due to formation of strong hydrogen bonds with the surface OH groups. This interaction significantly influences the layout of the water molecules

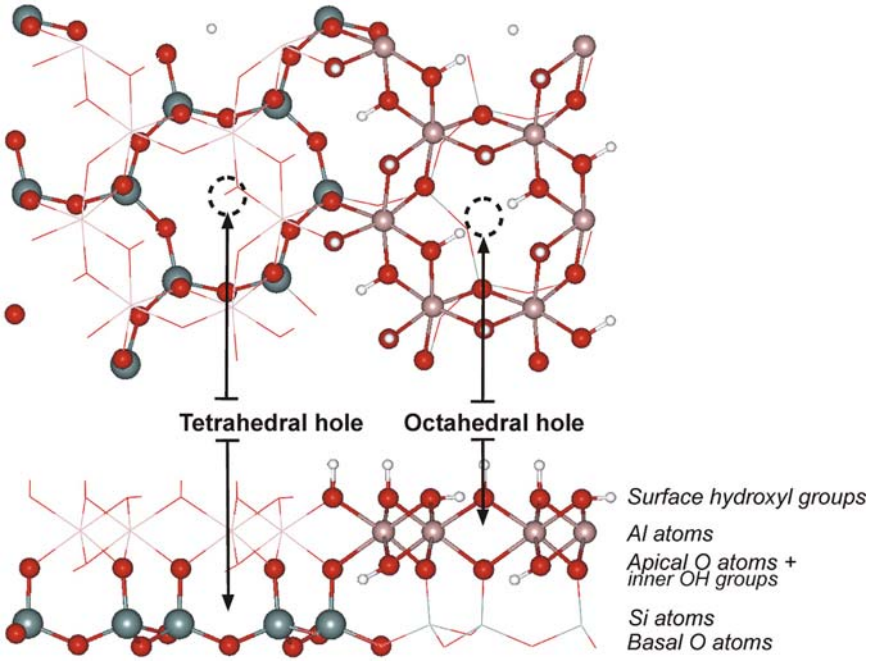

Figure 12-3. The structural model of the isolated kaolinte layer

in this case. On the other hand, the water molecules on the tetrahedral surface have a tendency to aggregate forming hydrogen bonds among themselves and only temporarily weak hydrogen bonds with the basal oxygen atoms of the tetrahedral surface are formed. Finally, ab initio MD was used in the simulation of the water layer confined between two kaolinite surfaces (snapshot of the MD is given in Figure 12-5). This MD confirms the results from the simulation of the monomolecular water layer. The tetrahedral surface interacts weakly with water molecules while the octahedral surface forms relatively strong hydrogen bonds with water molecules. Results of all studies led to the general conclusion that the octahedral and tetrahedral surfaces are of different chemical nature. The octahedral surface is much more chemically active than the tetrahedral one and is able to strongly bind polar molecules. The octahedral surface can be considered as hydrophilic while the tetrahedral as hydrophobic.

The observed structural differences between the octahedral and tetrahedral surfaces are also reflected in calculated interaction energies. The first row of Table 12-4 shows interaction energies obtained from static relaxations. The interaction energy for the octahedral surface is much higher (in absolute value) than for the tetrahedral surface. It has to be noted that these interaction energies are not corrected by thermal contributions. We computed thermal factors from molecular dynamics simulations. The energy of adsorption for one water molecule was calculated according to

Table 12-3. Comparison of calculated structural parameters for the kaolinite(O)−H_2O system obtained from geometry optimizations of a cluster model (ONIOM(B3LYP/SVP:PM3 method) and the periodic DFT(PW91) approach) (static relaxation and MD simulation) [73]. Bond lengths and interatomic distances are in Å, angles are in degrees. Superscript "w" stands for water, subscripts distinguish O and H atoms of three different surface OH groups

Structural parameter	Cluster model	Static relaxation	MD
$H_1{}^w$–O^w	0.997	1.048	1.039
$H_2{}^w$–O^w	0.965	0.987	0.989
$H_1{}^w$–O^w–$H_2{}^w$	105.8	110.4	109.8
$H_1{}^w\cdots O_1$	1.628	1.528	1.590
$O^w\cdots H_2$	1.886	1.712	1.817
$O^w\cdots H_3$	1.957	1.732	1.816
O_1–H_1	0.987	0.995	0.997
O_2–H_2	0.973	0.997	0.998
O_3–H_3	0.970	0.998	1.000
$O^w\cdots O_1$	2.615	2.572	2.610
$O^w\cdots O_2$	2.917	2.699	2.778
$O^w\cdots O_3$	2.815	2.709	2.775
$O_1\cdots H_1{}^w$–O^w	169.7	173.5	167.4
O_2–$H_2\cdots O^w$	171.2	169.6	163.8
O_3–$H_3\cdots O^w$	159.7	165.3	162.2

$$\Delta U_{\mathrm{H}} = (\langle U(N)\rangle - (\langle U(0)\rangle - N \cdot \langle U(\mathrm{H_2O})\rangle))/N \tag{12-3}$$

N is the number of water molecules, $\langle U(N)\rangle$ is the averaged potential energy with N water molecules on the surface, $\langle U(0)\rangle$ is the averaged potential energy of a dry surface and $\langle U(H_2O)\rangle$ is the averaged potential energy of water molecule. Table 12-4 collects the calculated hydration energies for systems with one water molecule and with the water layer above both surfaces. Results for the single water molecule document a decrease of the interaction energy (in absolute value) for both surfaces due to the thermal motion but the clear energetic difference between both surfaces is preserved. The calculated hydration energies for the monomolecular water layer resulted in an increase of the interaction energies in absolute value for both surfaces, more for the tetrahedral one. The strong increase for the tetrahedral surface is due to interaction among water molecules and not between the surface and water molecules. An increase of the hydration energy is also observed for the octahedral surface but this increase is not as big as in case of the tetrahedral surface. Our calculated interaction energies are in reasonably good agreement with results computed by Wang et al. [75] using a classical MD based on the CLAYFF force field [76] for minerals gibbsite (similar surface as the octahedral kaolinite surface) and talc (similar surface as the tetrahedral kaolinite surface). For the tetrahedral surface our value of –8.3±0.4 kcal/mol agrees well with the result of –8.8±0.3 kcal/mol for the talc surface calculated by Wang et al. [75]. Also the result of –13.5±0.3 kcal/mol for gibbsite

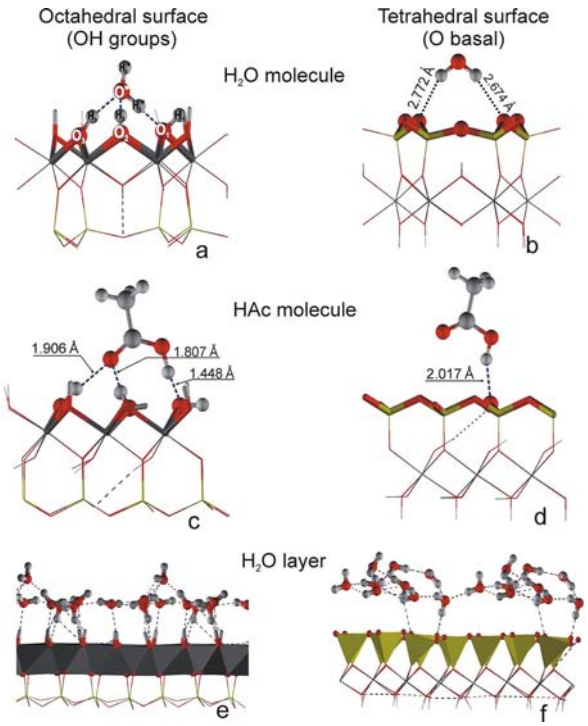

Figure 12-4. Models for the surface interactions of kaolinite. In case (**a**) atomic symbols correspond to those used in Table 12-3. Numbers in cases (**b**), (**c**) and (**d**) give hydrogen bond distances obtained in the cluster calculations at the ONIOM(B3LYP/SVP:PM3) level [73]

by Wang et al. [75] is close to our MD result of –12.1±2.2 kcal/mol for the octahedral surface. The computed hydration energies are also in relatively good agreement with the experimental hydration enthalpy of –10.6 kcal/mol of kaolinite [77].

12.4.2. Interactions of 2,4-D with the Octahedral Kaolinite Surface

Full optimizations and ab initio MD simulations of the adsorption of 2,4-D on the octahedral surface of the kaolinite layer were performed in the study by Tunega et al. [78]. Figure 12-6 displays the optimized adsorbed structure of 2,4-D on the kaolinite layer. The polar carboxyl group forms hydrogen bonds very similar to those described for acetic acid before [72,73]. The MD simulation provides a dynamical picture of the 2,4-D adsorption. During the 4 ps dynamics several proton H_1 jumps between the two oxygen atoms occurred, similarly as found in the MD study of HAc adsorption [73]. A comparison of both results showed a higher frequency of the proton jumps for 2,4-D that correlates with easier deprotonation of this molecule and its lower pK_a value than for HAc. The analysis of the optimized geometry and

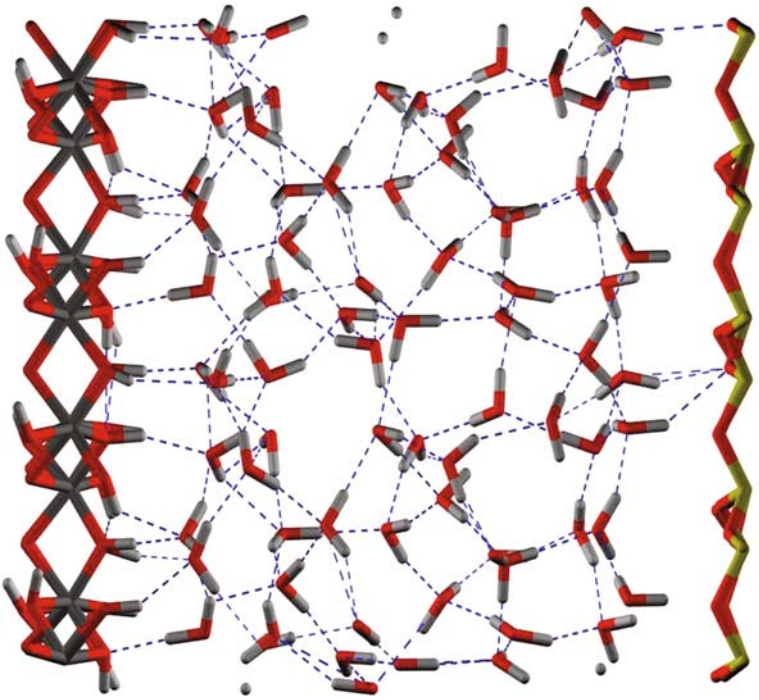

Figure 12-5. MD snapshot of the water layer confined between two kaolinite surfaces

the molecular dynamics showed that the chlorine atoms of 2,4-D also take part in the formation of weak hydrogen bonds with surface hydroxyl groups. We suppose that also the benzene ring contributes partly to the interactions via dispersion forces between the π bonds of the benzene ring and the surface OH groups. These observed additional interactions explain why 2,4-D has larger sorption energy (–28.0 kcal/mol) than acetic acid (–20.8 kcal/mol, [72]). The computed interaction energy is also significantly larger (in absolute value) than the energy of –14.7 kcal/mol calculated

Table 12-4. Computed interaction energies (in kcal/mol) of a single water molecule and a monomolecular water layer, respectively, with the two different (001) kaolinite surfaces

Water	Method	Tetrahedral surface	Octahedral surface
Single	Relaxation	−4.1	−13.1
Single	MD	−0.8±0.5	−8.3±3.2
Layer	MD	−8.3±0.4	−12.1±2.2
Layer	MD[a]	−8.8±0.3	−13.5±0.3

[a]Results for talc and gibbsite taken from the work by Kalinichev et al. [91]

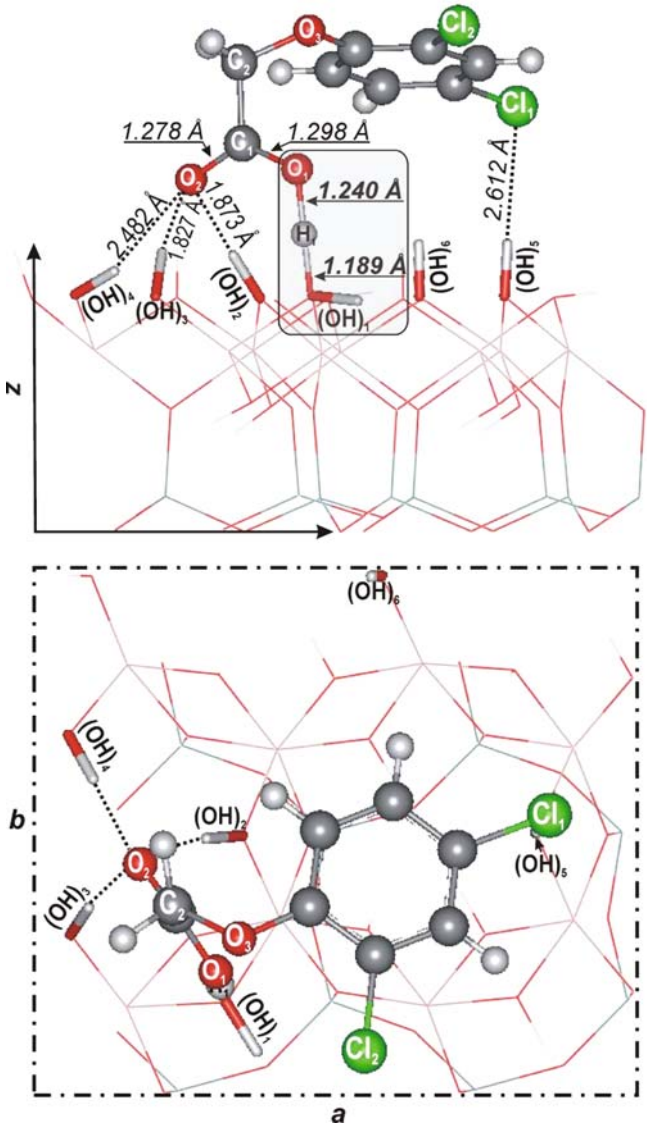

Figure 12-6. Two views of the optimized structure of 2,4-D interacting with the octahedral surface of the kaolinite layer

for the water molecule [72]. This fact suggests a significantly higher affinity of 2,4-D to the octahedral surface of kaolinite and its preferential sorption in comparison with water. The observed sorption of the neutral form of 2,4-D onto clay minerals (including kaolinite) at low pH (∼ 3) [79,80] or soils with high clay content [81] at low pH is in agreement with this finding.

12.4.3. Interaction of Broken Clay Surfaces with Water and Model Organic Molecules

Broken surfaces are of great interest since they are expected to have significantly higher chemical activity than regular ones. Defect sites arise when polar covalent bonds between oxygen atoms and central cations of the octahedral/tetrahedral sheets are cut. They can be represented schematically by the structures $\equiv TOH_2$, $\equiv TOH$ and $\equiv TO$ groups (T is either a tetrahedral or octahedral central cation). The actual occurrence of these species will mainly depend on pH conditions [82,83,84,85,86]. In general, sites on broken surfaces are amphoteric, being able to act as proton donor or as proton acceptor in the hydrogen bond formation.

In the present study three basic cluster models were constructed for the tetrahedral part of the broken surfaces: two one-site models, $(RO)_3SiO$ and $((RO)_3AlOH)^-$ ($R = CH_3$), and one two-site model (two terminal surface hydroxyl groups are available), $Si_2AlO_5H_3(OH)_2$, were constructed. Details on the cluster models can be found in the work by Aquino et al. [87]. Interactions with HAc and *N*-methylacetamide (NMA) have been studied. In case of the physical defect structures ($\equiv SiOH$ and $Si_2AlO_5H_3(OH)_2$) standard hydrogen bonds of moderate strength with H···O distances between ~1.68 and 1.96 Å are formed. Chemical defect structures (e.g., the negatively charged $\equiv SiO^-$) have significantly larger activity. Typical H···O distances are about 1.45 Å that is characteristic for strong hydrogen bonds. It is interesting to note that the $\equiv AlOH_2$ site has a higher chemical activity than $\equiv AlOH^-$. In cases of one-site models with Al ($\equiv AlOH_2$ and $\equiv AlOH^-$), HAc forms stronger hydrogen bonds than in case of the neutral cluster $\equiv SiOH$ with O···H distances about 1.41 Å. Calculated interaction energies (Table 12-5) vary significantly with the type of defect. As expected, for chemical defect structures (e.g., $\equiv SiO^-$) they are significantly larger in absolute value than those for the physical defects. Actual values depend on the total charge of the complex. In some cases proton transfer has been observed during geometry optimization (see Table 12-5). The structure and strength of NMA complexes depend on the NMA configuration and on the type of functional group (=N–H or C=O) involved in the hydrogen bond formation. Stronger hydrogen bonds are formed if the C=O group acts in hydrogen bonds as a proton acceptor (O···H distances are between 1.5 and 1.7 Å). The =N–H group is a weak proton donor with H···O distances about 2 Å. *cis*-NMA forms more stable complexes than *trans*-NMA (except the interaction with $\equiv AlOH^-$ model) because *cis* configuration is able to form hydrogen bonds with both functional groups. In all but one case the interactions with the surface groups are such that the CN bond length decreases that indicates an increase of the CN double bond character. Thus, the preference for planarity of the peptide group will be enhanced in this way in comparison to free NMA. On the other hand, if the nitrogen atom interacts with its lone pair with a surface defect, the CN bond length is decreased and the preference for planarity of the peptide group is reduced. These examples demonstrate that the planarity of the peptide bond can be substantially influenced by different interaction types with clay surfaces. In case of two-site models, calculated interaction energies for HAc and NMA are similar (Table 12-5). Hydrogen bond lengths are similar to those formed for

Table 12-5. Formation energies, ΔE_g (in gas) and ΔE_s (in solution), calculated at the BLYP/SVP+sp level. Energies are in kcal/mol

Complex	Note	ΔE_g	ΔE_s
≡SiOH···HAc	C=O acceptor, C-OH donor	−10.6	−8.3
≡SiO^-···Hac	Proton transfer to≡SiO^-	−41.9	−17.0
≡$AlOH_2$···Hac	C=O acceptor, C-OH donor	−25.6	−13.0
≡$AlOH^-$···HAc	C-OH donor	−20.7	−8.6
≡$AlOH_2$···Ac^-	Proton transfer to Ac^-	−49.9	−19.8
≡SiOH···*trans*-NMA	=N-H donor to ≡SiOH	−3.8	−4.8
≡SiOH···*trans*-NMA	C=O acceptor	−7.8	−8.6
≡SiOH···*cis*-NMA	=N-H donor, C=O acceptor	−11.6	−8.3
≡SiO^-···*trans*-NMA	=N-H donor	−35.2	−8.5
≡$AlOH_2$···*trans*-NMA	C=O acceptor	−15.2	−10.0
≡$AlOH_2$···*cis*-NMA	C=O acceptor, =N-H donor	−22.8	−11.1
≡$AlOH^-$···*cis*-NMA	=N-H donor	−12.1	−2.1
≡$AlOH^-$···*trans*-NMA	=N-H donor	−17.6	−4.1
$Si_2AlO_5H_3(OH)_2$···HAc	C=O acceptor, C-OH donor	−11.4	−5.6
$Si_2AlO_5H_3(OH)_2$···Ac^-	COO^- donor two OH	−36.1	−7.9
$Si_2AlO_5H_3(OH)_2$···*trans*-NMA	C=O acceptor to two OH	−10.2	−0.7
$Si_2AlO_5H_3(OH)_2$···*cis*-NMA	=N-H donor, C=O acceptor	−11.1	−1.6
≡SiOH···2 H_2O	1. H_2O donor, 2. H_2O acceptor	−14.1	−9.0

the neutral one–site ≡SiOH model. Figure 12-7 illustrates four complexes calculated for the two-site models.

The inclusion of solvation effects does not change the structural situation significantly. In case of complexes where two hydrogen bonds are formed, one is typically somewhat shortened and the other slightly stretched. Similar effects have been observed in our previous investigations (see Sections 3.1 and 3.2 and Aquino et al. [58,71]). Formation energies are strongly reduced in absolute value by solvation effects, especially those of charged complexes. This has also been observed previously [58,71] and has been traced back to a reduction of the solvent-accessible surface on complex formation.

12.4.4. Hydrogen Bond Interactions of Goethite Surface

Goethite (α-FeOOH) is an iron oxo-hydroxide representing an important constituent of soils. Goethite plays a significant role in environmental processes since it has a strong affinity to a variety of chemicals being able to sorb large amounts of heavy metal cations, anions, oxyanions [88] as well as organic pollutants such as polycyclic aromatic hydrocarbons [89]. Details about the goethite structure can be found, e.g., in the work by Hazemann et al. [90]. One of the most abundant surfaces, (110) contains more than one type of hydroxyl groups due to cutting through Fe–O bonds and their subsequent saturation with hydrogen atoms. Three different OH sites exist on this

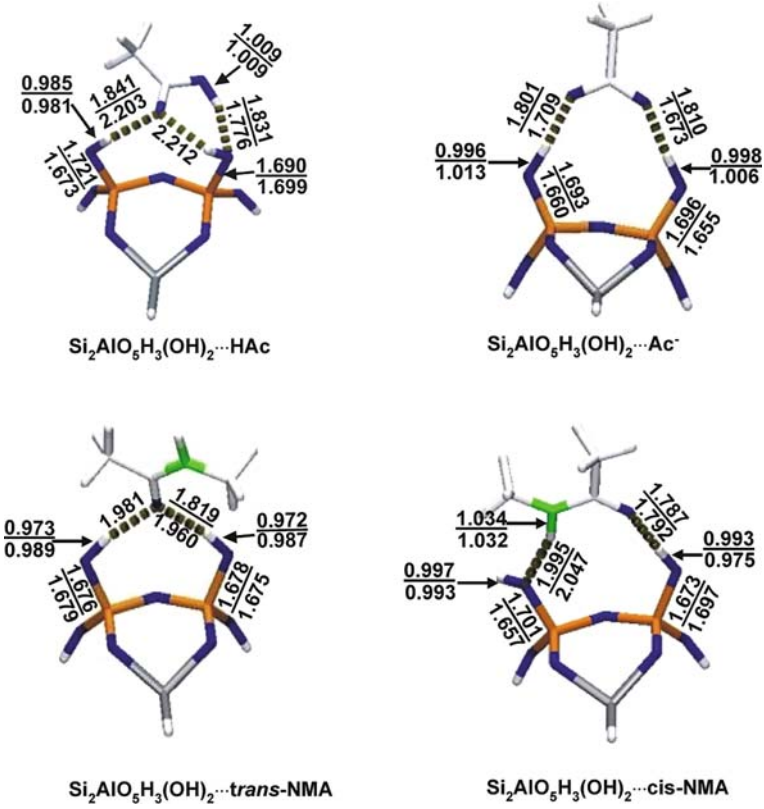

Figure 12-7. Structural models of two-site complexes of broken clay surfaces. Geometrical parameters were obtained at the BLYP/SVP+sp level for the gas phase and in solution (*underlined numbers*)

surface: (a) hydroxo – OH group is bound to one Fe atom, (b) μ-hydroxo – OH is bound to two Fe atoms and (c) μ_3-hydroxo – OH group is bound to three iron atoms. The arrangements of these OH types form different interaction sites for hydrogen bonds.

Our investigations of the goethite surface have started with a study of interactions of different hydroxo groups of molecular clusters containing four, six and eight iron atoms. More details about the construction of clusters and cluster complexes can be found in the works by Aquino et al. [71]. In this section we will present results for the cluster containing six Fe atoms (denoted as Fe_6OH) and all three types of the surface OH groups. Water, HAc, Ac^-, 2,4-D and 2,4-D^- are selected as adsorption partners.

Figure 12-8 represents adsorption structures of H_2O, HAc, Ac^-, 2,4-D and 2,4-D^-, respectively. The calculations showed that hydroxo and μ-hydroxo OH groups are flexible and can act either as a proton donor and/or proton acceptor, similar to the

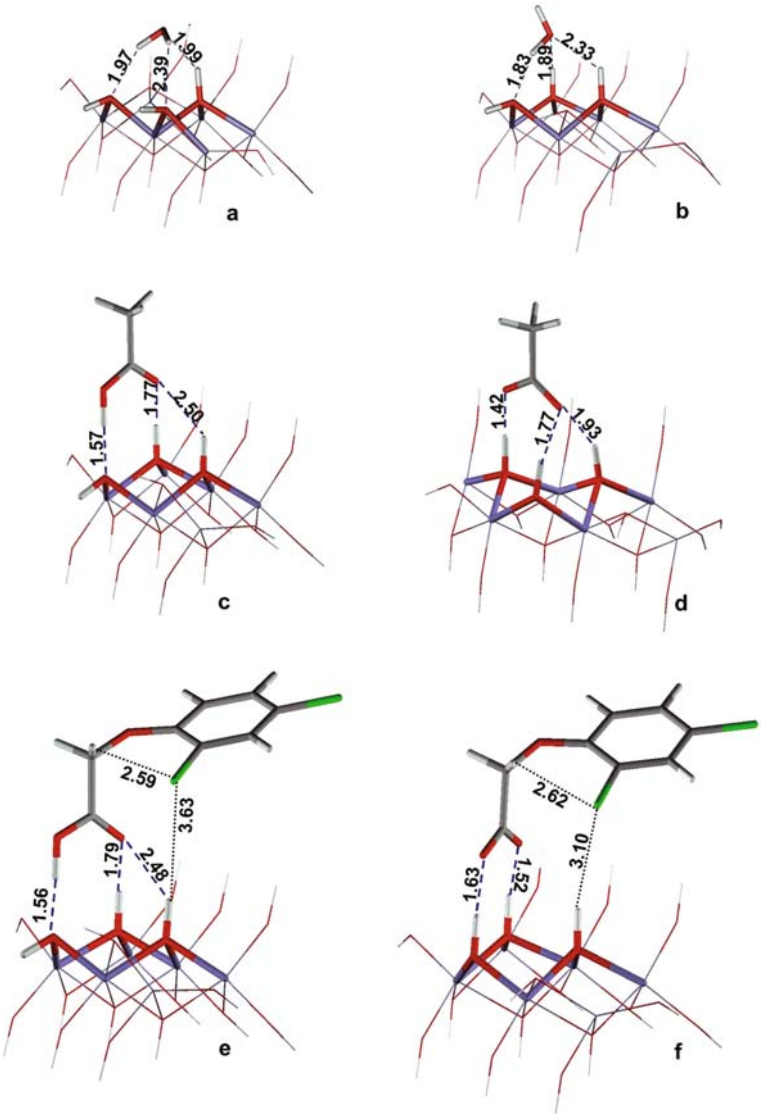

Figure 12-8. Optimized structures of the surface complexes formed between the surface cluster model of goethite (Fe_6OH) and water (a, b), acetic acid (c), acetate (d), 2,4-D (e), and 2, 4-D^-(f)

case of the kaolinite surface OH groups. On the other hand, the μ_3-hydroxo group is relatively rigid (the oxygen atom is fully saturated by four bonds) and acts exclusively as a proton donor in the hydrogen bonds. From Figure 12-8 it can be seen that surface OH groups are involved in the formation of usually three hydrogen bonds with the interacting species. In all cases (except Ac^-), two of them are stronger (see

Table 12-6. Interaction energies, ΔE, of H_2O, HAc, Ac^-, 2,4-D, 2,4-D^- adsorbed on a goethite cluster using the closed shell B3LYP approach and two basis sets. Energies are given in kcal/mol

System	Figure	ΔE (SVP)	ΔE (SVP+sp)
$Fe_6OH\cdots H_2O$[a]	12-8a	−20.1	−16.5
$Fe_6OH\cdots H_2O$[a]	12-8b	−17.5	−13.2
$Fe_6OH\cdots$Hac	12-8c	−23.7	−25.0
$Fe_6OH\cdots Ac^-$	12-8d	−58.3	−50.6
$Fe_6OH\cdots$2,4-D	12-8e	−23.9	−25.9
$Fe_6OH\cdots$2,4-D^-	12-8f	−37.4	−31.3

[a]Two different orientations of the H_2O molecule (for more details see Aquino et al. [71]).

hydrogen bond lengths given in Figure 12-8). Calculated interaction energies for different sites are collected in Table 12-6. They amount to ca. –20 kcal/mol for the adsorption of a water molecule, a value which is in line with the number and type of hydrogen bonds formed. Larger interaction energies were observed for the neutral acetic acid and 2,4-D. The deprotonated, anionic form of acetic acid and 2,4-D display even stronger interactions between –30 and –50 kcal/mol (B3LYP/SVP+sp results). The complexes of the 2,4-D^- anion differ from those of the acetate anion since chlorine atoms are also involved in weak interactions with the surface OH groups (Figure 12-8). The flexibility of the goethite surface OH groups is similar to that observed for the kaolinite surface OH groups [72,73] while their chemical activity is even larger. For example, calculated interaction energy for the H_2O molecule is about –8 kcal/mol for kaolinite (cluster model and B3LYP/SVP+sp method, [72]) and about –15 kcal/mol for goethite (Table 12-6). It means that the goethite surface OH groups are more active in hydrogen bond formation than kaolinite OH groups.

12.5. CONCLUSIONS

In this contribution we presented several examples for the important role hydrogen bonds and solvent effect play in soil and environmental chemistry. The structurally very complex humic substances were modeled by means of representative functional groups. The capability of forming hydrogen bonds was demonstrated for interactions of these groups with selected set of polar molecules, e.g., H_2O, acetic acid and its respective anion, Ac^-. In order to investigate the capability of humic functional groups to fix acidic pesticides in soils, the interactions of neutral and ionic forms of 2,4-D with a selected set of molecules were investigated as well. Calculations showed that the anionic forms (Ac^- and 2,4-D^-) form complexes of similar strength as corresponding neutral molecules if solvent effects are taken into account. It was shown that solvent effect substantially lowers the complex formation energies, especially in case of charged systems. The results obtained for the 2,4-D complexes showed the importance of the explicit inclusion of solvent molecules (microsolvation) interacting

with the molecules involved in the complex formation. Using this approach with the combination of the global solvation approach (polarizable continuum representing solvent) complex formation reactions are better described than applying purely the global solvation approach and the associative type of reactions.

The presented results showed how the surfaces of the kaolinite and goethite minerals interact with the polar water molecules. The octahedral surface of the kaolinite formed from surface hydroxyl groups is hydrophilic while the tetrahedral surface is hydrophobic. The kaolinite surface OH groups are very flexible and are able to act as proton donor or acceptor in interactions with polar molecules capable to form hydrogen bonds. A similar behavior was also observed for the surface OH groups of goethite except for the μ_3-OH type, which is only a proton donor. Computed interaction energies demonstrate strong hydration interactions with the octahedral kaolinite surface but only weak hydration of the tetrahedral surface. The goethite (110) surface is even more hydrophilic than the octahedral kaolinite surface when comparing the computed interaction energies. We conclude that the kaolinite and goethite surface hydroxyl groups have amphoteric character and can behave in particular circumstances as solid acid and/or solid base, respectively, depending on the conjugate partner. Interactions of 2,4-D molecule with kaolinite and goethite surfaces are similar and calculated gas-phase complex formation energies are larger (in absolute value) than those with our investigated set of organic functional groups. This reflects the fact that the –COOH group is able to form multiple hydrogen bonds with the surface OH groups. It was also shown that strong sorbent sites can exist on irregular clay mineral surfaces formed on the corner and edges of clay mineral particles.

In conclusion, we have achieved a detailed picture of the activity and the form of interactions with polar and charged species of organic functional groups representing reactive sites of humic substances and of two important soil minerals, kaolinite and goethite.

ACKNOWLEDGMENTS

This work was supported by the Austrian Sciences Fund (project P17967-N11) and by the German Research Foundation, the priority program SPP 1315 (project GE 1676/1-1). We are grateful for the technical support and computer time at the Linux-PC clusters Schrödinger I–III of the computer centre of the University of Vienna.

REFERENCES

1. Hamilton WC, Ibers JA (1968) Hydrogen bonding in solids, Benjamin, New York
2. Jeffrey GA, Saenger W (1991) Hydrogen bonding in biological structures, Springer-Verlag, Berlin
3. Jeffrey GA (1997) An introduction to hydrogen bonding, Oxford University Press, Oxford
4. Scheiner (1997) Hydrogen bonding. A theoretical perspective, Oxford University Press, Oxford
5. Steiner T (2002) Angew Chem Int Ed 41:48

6. Maréchal Y (2007) The hydrogen bond and the water molecule. The physics and chemistry of water, aqueous and bio media, Elsevier, Amsterdam
7. Baldwin B (2006) Peptide solvation and H-bonds, Elsevier Academic, San Diego
8. Ghabbour EA, Davis G (2000) Humic substances – versatile components of plants, soils and water, Royal Society of Chemistry, Cambridge, UK
9. Kile DE, Wershaw RL, Chiou CT (1999) Environ Sci Technol 33:2053
10. Parker A, Rae JE (1998) Environmental interactions of clays, Springer-Verlag, Berlin
11. Dixon JB, Schulze DG (2002) Soil mineralogy with environmental applications, Soil Science Society of America, Madison
12. Kahle M, Kleber M, Jahn R (2003) J Plant Nutr Soil Sci 166:737
13. Rozas I (2007) Phys Chem Chem Phys 9:2782
14. Hermans J, Berendsen HJC, van Gunsteren WF, Postma JPM (1984) Biopolymers 23:1513
15. Jorgensen WL, Ravimohan C (1985) J Chem Phys 83:3050
16. van Gunsteren WF, Berendsen HJC (1990) Angewandte Chemie 29:992
17. Kollman P (1993) Chem Rev 93:2395
18. Orozco M, Luque FJ (2000) Chem Rev 100:4187
19. Cramer CJ (2002) Essentials of computational chemistry. In: Theories and Models, Wiley, New York
20. Coutinho K, Canuto S (2000) J Chem Phys 112:9874
21. Coutinho K, Saavedra N, Serrano A, Canuto S (2001) J Mol Struct (Theochem) 539:171
22. Sánchez ML, Aguilar MA, Olivares del Valle FJ (1997) J Comput Chem 18:313
23. Sánchez Mendoza ML, Aguilar MA, Olivares del Valle FJ (1998) J Mol Struct (Theochem) 26:181
24. Coutinho K, Georg HC, Fonseca TL, Ludwig V, Canuto S (2007) Chem Phys Lett 437:148
25. Miertus S, Scrocco E, Tomasi J (1981) Chem Phys 55:117
26. Miertus S, Tomasi J (1982) Chem Phys 65:239
27. Cossi M, Barone V, Camini R, Tomasi J (1996) Chem Phys Lett 255:327
28. Tomasi J, Mennucci B, Cammi R (2005) Chem Rev 105:2999
29. Klamt A, Schüürmann G (1993) J Chem Soc Perkin Trans 2:799
30. Truong TN, Stefanovich EV (1995) J Chem Phys 103:3709
31. Cramer CJ, Truhlar DG (1991) J Am Chem Soc 113:8305
32. Cramer CJ, Truhlar DG (1992) Science 256:213
33. Ahlrichs R, Bär M, Häser M, Horn H, Kölmel C (1989) Chem Phys Lett 162:165
34. Frisch MJ, Trucks GW, Schlegel HB, Scuseria GE, Robb MA, Cheeseman JR, Montgomery Jr JA, Vreven T, Kudin KN, Burant JC; Millam JM, Iyengar SS, Tomasi J, Barone V, Mennucci B, Cossi M, Scalmani G, Rega N, Petersson GA, Nakatsuji H, Hada M; Ehara M, Toyota K, Fukuda R, Hasegawa J, Ishida M, Nakajima T, Honda Y; Kitao O, Nakai H, Klene M, Li X, Knox JE, Hratchian HP; Cross JB, Bakken V, Adamo C, Jaramillo J; Gomperts R, Stratmann RE, Yazyev O, Austin AJ, Cammi R, Pomelli C, Ochterski JW, Ayala PY, Morokuma K, Voth GA, Salvador P, Dannenberg JJ, Zakrzewski VG; Dapprich S, Daniels AD, Strain MC, Farkas O, Malick DK, Rabuck AD, Raghavachari K, Foresman JB, Ortiz JV, Cui Q, Baboul AG, Clifford S, Cioslowski J, Stefanov BB, Liu G, Liashenko A, Piskorz P, Komaromi I, Martin RL, Fox DJ, Keith T, Al-Laham MA, Peng CY, Nanayakkara A, Challacombe M, Gill PMW, Johnson B, Chen W, Wong MW, Gonzalez C, Pople JA (2003) Gaussian 03, Revision B.02. Gaussian Inc., Pittsburgh, PA
35. von Arnim M, Ahlrichs R (1998) J Comp Chem 19:1746
36. Maseras F, Morokuma K (1995) J Comp Chem 16:1170
37. Becke AD (1993) J Chem Phys 98:5648
38. Becke AD (1988) Phys Rev A 38:3098
39. Lee C, Yang W, Parr RG (1988) Phys Rev B 37:785
40. Miehlich B, Savin A, Stoll H, Preuss H (1989) Chem Phys Lett 157:200

41. Head-Gordon M, Pople JA, Frisch MJ (1988) Chem Phys Lett 153:503
42. Schäfer A, Horn H, Ahlrichs R (1992) J Chem Phys 97:2571
43. Schäfer A, Huber C, Ahlrichs R (1994) J Chem Phys 100:5829
44. Tunega D, Haberhauer G, Gerzabek MH, Lischka H (2000) J Phys Chem 104:6824
45. Boys SF, Bernardi F (1970) Mol Phys 19:553
46. Kresse G, Furthmüller J (1996) Phys Re B 54:11169
47. Perdew JP, Zunger A (1981) Phys Rev B 23:548
48. Perdew JP, Wang Y (1992) Phys Rev B 45:13244
49. Blöchl PE (1994) Phys Rev B 50:17953
50. Kresse G, Joubert D (1999) Phys Rev B 59:1758
51. Monkhorst HJ, Pack JD (1976) Phys Rev B 13:5188
52. Nosé S (1984) J Chem Phys 81:511
53. Ferrario M, Ryckaert JP (1985) Mol Phys 54:587
54. Munro IC, Carlo GL, Orr JC, Sund KG, Wilson RM, Kennepohl E, Lynch BS, Jablinske M, Lee NL (1992) J Am College Toxicol 11:559
55. Donald DB, Gurprasad NP, Quinnett-Abbott L, Cash K (2001) Environ Toxicol Chem 20:279
56. Buckingham J (1988) Dictionary of organic compounds, 5th edn, Suppl 2. Chapman & Hall, New York
57. McBride MB (1994) Environmental chemistry of soils, Oxford University Press, New York
58. Aquino AJA, Tunega D, Haberhauer G, Gerzabek MH, Lischka H (2002) J Phys Chem A 106:1862
59. Aquino AJA, Tunega D, Harberhauer G, Gerzabek M, Lischka H (2000) Phys Chem Chem Phys 2:2845
60. Aquino AJA, Tunega D, Harberhauer G, Gerzabek M, Lischka H (2001) Phys Chem Chem Phys 3:1979
61. Cieplak P, Kollman PA (1988) J Am Chem Soc 110:3734
62. Mathews DM, Sheets BN (1969) J Chem Soc A – Inorg Phys Theor 15:2203
63. Chao J, Zwolinski J (1978) J Phys Chem Ref Data 7:363
64. Frurip DJ, Curtiss LA, Blander M (1980) J Am Chem Soc 102:2610
65. Winkler A, Behl JB, Hess PJ (1994) Chem Phys 100:2717
66. Colominas C, Teixido J, Cemeli J, Luque FJ, Orozco M (1998) J Phys Chem B 102:2269
67. Dannenberg JJ, Paraskevas LR, Sharma V (2000) J Phys Chem A 104:6617
68. Nakabayashi T, Sato H, Hirata F, Nishi N (2001) J Phys Chem A 105:245
69. Sneddon SF, Tobias DJ, Brooks CL III (1989) J Mol Biol 209:817
70. Fujii Y, Yamada H, Mizuta MJ (1988) Phys Chem 92:6768
71. Aquino AJA, Tunega D, Haberhauer G, Gerzabek MH, Lischka H (2007) Eur J Soil Sci: 58:889
72. Tunega D, Haberhauer G, Gerzabek MH, Lischka H (2002a) Langmuir 18:139
73. Tunega D, Benco L, Haberhauer G, Gerzabek MH, Lischka H (2002b) J Phys Chem B 106:11515
74. Tunega D, Gerzabek MH, Lischka H (2004a) J Phys Chem B 108:5930
75. Wang J, Kalinichev AG, Kirkpatrick RJ (2006) Geochim Cosmochim Acta 70:562
76. Cygan RT, Liang J-J, Kalinichev AG (2004) J Phys Chem B 108:1255
77. Constanzo PM, Giese RF, Lipsicas M (1984) Clays Clay Miner 32:419
78. Tunega D, Haberhauer G, Gerzabek MH, Lischka H (2004b) Soil Sci 169:44
79. Clausen L, Fabricius I, Madsen L (2001) J Environ Qual 30:846
80. Vasudevan D, Cooper EM, van Exem OL (2002) Environ Sci Technol 36:501
81. Spadotto CA, Hornsby AG (2003) J Environ Qual 32:949
82. Sposito G (1984) The surface chemistry of soils, Oxford Univ Press, New York
83. Ward DB, Brady PB (1998) Clays Clay Miner 46:453
84. Huertas FJ, Chou L, Wollast R (1998) Geochim Cosmochim Acta 62:417

85. Huertas FJ, Chou L, Wollast R (1999) Geochim Cosmochim Acta 63:3261
86. Benyahya L, Garnier JM (1999) Environ Sci Technol 33:1398
87. Aquino AJA, Tunega D, Haberhauer G, Gerzabek MH, Lischka H (2003) J Comput Chem 24:1853
88. Hayes KF, Roe AL, Brown GEB Jr, Hodgson KO, Leckie JO, Parks GA (1987) Science 238:783
89. Kanel SR, Neppolian B, Jung HY, Choi H (2004) Environ Eng Sci 21:741
90. Hazemann JL, Bérar JF, Manceau A (1991) Mater Sci Forum 79:821
91. Wang J, Kalinichev AG, Kirkpatrick RJ (2006) Geochim Cosmochim Acta 70:562

CHAPTER 13

LINEAR RESPONSE THEORY IN CONNECTION TO DENSITY FUNCTIONAL THEORY/MOLECULAR DYNAMICS AND COUPLED CLUSTER/MOLECULAR DYNAMICS METHODS

KESTUTIS AIDAS[1], JACOB KONGSTED[2], AND KURT V. MIKKELSEN[1]

[1] *Department of Chemistry, H. C. Ørsted Institute, University of Copenhagen, Universitetsparken 5, DK-2100 Copenhagen Ø, Denmark, e-mail: kmi@theory.ki.ku.dk*

[2] *Department of Theoretical Chemistry, Chemical Center, University of Lund, P.O. Box 124, S-221 00 Lund, Sweden*

Keywords:

13.1. INTRODUCTION

Presently we are concerned with computational methods for calculating molecular properties of molecules interacting with a solvent, proteins, polymers or carbon nanotubes.We describe, using response methods, how to derive theoretical methods for calculating molecular properties of molecules interacting with a structured environment. Generally, in our opinion, modern response theory represents a solid theoretical approach for the determination of time-dependent electromagnetic properties of molecules in vacuum [1,2,3,4,5,6,7]. In the context of dielectric medium approaches, the procedures for performing calculations using modern response theory for solvated molecular systems have been described within the last couple of decades [8,9,10,11,12]. Dielectric medium models are generally not able to describe correctly the interactions between the solvent and the solute when the interactions are dominated by structural environments. Interactions between molecules and structural environments are typically encountered when one investigates phenomena in biochemistry, chemistry, material science, nano-science and physics.

Our present focus is on density functional theory and coupled cluster methods for describing molecular systems interacting with a structured environment, and we focus on the derivation of linear response properties and compare the expressions that we obtain for the two different electronic structure methods. Based on linear response

S. Canuto (ed.), Solvation Effects on Molecules and Biomolecules, 349–380.
DOI 10.1007/978-1-4020-8270-2_13,

functions we are able to calculate molecular properties of molecules interacting with structural environments and the molecular properties considered in this context are

- frequency-dependent polarizabilities,
- excitation and deexcitation energies,
- circular dichroism and optical rotation,
- transition moments,
- NMR shielding constants, and
- magnetizabilities.

The model that we utilize for describing the interactions between molecules and structured environments is given by the combined quantum mechanical/molecular mechanical (QM/MM) method [13,14,15,16,17,18,19,20,21,22,23,24,25,26,27,28,29,30,31,32,33,34,35,36,37,38,39,40,41,42,43,44,45,46,47,48,49]. The QM/MM methods are based on the following division of a large system: (i) a smaller part of the large system is treated quantum mechanically and the molecules belonging to this part of the system are denoted the QM system. The QM system is the system of primary interest and is the system that we wish to investigate and to determine molecular properties for. (ii) The major part of the large system is treated by classical mechanics and this system is denoted the MM system. The MM system is normally obtained from classical simulations based on interaction potentials including electrostatic, induction, repulsive and dispersion interactions. The interactions between the QM and the MM systems are included in the many-body quantum mechanical Hamiltonian and this provides methods for calculating quantum mechanically the molecular properties of the QM system interacting with the MM system, the structured environment.

The QM/MM model and the interaction Hamiltonian can be improved by increasing either the QM level or the parametrization of the MM force field. Here we focus on quantum mechanical methods based on correlated coupled cluster and density functional theory. In terms of interaction potentials we utilize pair potentials for taking care of the couplings in the MM system and for the couplings between the classical and quantum mechanical systems. Furthermore, we include in both the MM/MM and QM/MM couplings an explicit term accounting for the (many-body) polarization of the MM system. Generally, the advantages of the presented method are (i) the use of a highly correlated wave function approach, (ii) an explicit account of polarization effects in the MM environment and (iii) the use of response theory [50,51] to calculate molecular properties. Overall, this procedure in conjunction with the response theory formalism enables us to calculate dynamical molecular properties (as well as excitation energies and transition properties) without the restrictions dictated by the finite field (FF) or few-state methods. In this presentation, we will focus on the calculation of optical molecular properties represented by the investigations of the linear molecular properties of acetone.

This presentation is structured in the following way. The first section outlines the procedure for the quantum mechanics and classical mechanics approach. The following two sections contain an overview of how to establish a density functional theory and molecular mechanics method along with the theoretical background for

extending this method to include response theory. Sections 5 and 6 cover the coupled cluster-molecular mechanics method and the coupled cluster-molecular mechanics response theory. Section 7 contains results covering linear response properties of solvated acetone and in the final section we conclude.

13.2. THE COMBINED QUANTUM MECHANICS AND MOLECULAR MECHANICS MODEL

This section provides the fundamental equations for the quantum mechanical and molecular mechanical approach for determining the energies of molecules interacting with a structured environment. We can illustrate the QM/MM procedure as indicated in Figure 13-1 for a system where one part is described by quantum mechanics (QM) and the other part is described by classical mechanics or molecular mechanics (MM). The electrons and the nuclei of the QM system are treated separately at positions $\mathbf{r}_j$ and $\mathbf{R}_m$, respectively. We represent the particles in the MM part by effective charges positioned at the atomic sites, $\mathbf{R}_s$, and induced dipole moments located at ($\mathbf{R}_a$).

The total energy for the system is given by the following terms [14,15,16,25]

$$E = E_{\mathrm{QM}} + E_{\mathrm{QM/MM}} + E_{\mathrm{MM}} \tag{13-1}$$

where E_{QM} is the usual quantum mechanical energy described by the Born–Oppenheimer many-body vacuum Hamiltonian, $\hat{H}_{\mathrm{QM}}$ which in first quantization and atomic units is given by

$$\begin{aligned} H = &-\frac{1}{2}\sum_{i=1}^{N}\nabla_i^2 - \sum_{i=1}^{N}\sum_{m=1}^{M}\frac{Z_m}{|\mathbf{r}_i - \mathbf{R}_m|} + \frac{1}{2}\sum_{i,j(i\neq j)}^{N}\frac{1}{|\mathbf{r}_i - \mathbf{r}_j|} \\ &+ \frac{1}{2}\sum_{m,n(m\neq n)}^{M}\frac{Z_m Z_n}{|\mathbf{R}_m - \mathbf{R}_n|} \end{aligned} \tag{13-2}$$

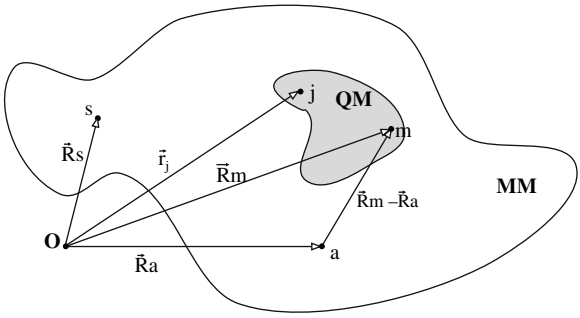

Figure 13-1. An illustration of the QM/MM concept. The vector $\mathbf{r}_j$ ($\mathbf{R}_m$) describes an electron (a nucleus) in the QM part. The vectors $\mathbf{R}_a$ and $\mathbf{R}_s$ point to the positions of the induced dipole moment and the effective point charge, respectively, in the MM part

where the nuclear charge of the mth nucleus is given by Z_m. The kinetic energy of the electrons is given by the first term in Eq. (13-2) and the interactions between the electrons and the nuclei are represented by the second term. The repulsion energies arising from the electron–electron and the nuclear repulsion energy are given by the third and fourth terms, respectively.

We will mostly use second quantization and thereby represent the molecular electronic Hamiltonian in Eq. (13-2) as

$$\hat{H} = \sum_{pq} h_{pq} \hat{E}_{pq} + \frac{1}{2} \sum_{pqrs} g_{pqrs} \hat{e}_{pqrs} + h_{\text{nuc}} \tag{13-3}$$

where the integrals are given by

$$h_{pq} = \int \phi_p^*(\mathbf{r}) \left(-\frac{1}{2} \nabla^2 - \sum_{m=1}^{M} \frac{Z_m}{|\mathbf{r} - \mathbf{R}_m|} \right) \phi_q(\mathbf{r}) \mathrm{d}\mathbf{r} \tag{13-4}$$

$$g_{pqrs} = \int \int \frac{\phi_p^*(\mathbf{r_1}) \phi_r^*(\mathbf{r_2}) \phi_q(\mathbf{r_1}) \phi_s(\mathbf{r_2})}{|\mathbf{r}_1 - \mathbf{r}_2|} \mathrm{d}\mathbf{r_1} \mathrm{d}\mathbf{r_2} \tag{13-5}$$

We have utilized the fermion creation and annihilation operators denoted $\hat{a}_{p\sigma}^{\dagger}$, and $\hat{a}_{p\sigma}$, respectively. These operators act on the electron in the pth orbital with the projected spin σ. The set $\{|\phi_p(\mathbf{r})\rangle\}$ represents the molecular orbitals and the last term, h_{nuc}, in Eq. (13-3) is the nuclear repulsion energy. We use the following definitions of the one-electron excitation operator

$$\hat{E}_{pq} = \sum_{\sigma} \hat{a}_{p\sigma}^{\dagger} \hat{a}_{q\sigma} \tag{13-6}$$

and the two-electron excitation operator

$$\hat{e}_{pqrs} = \sum_{\sigma\tau} \hat{a}_{p\sigma}^{\dagger} \hat{a}_{r\tau}^{\dagger} \hat{a}_{s\tau} \hat{a}_{q\sigma} \tag{13-7}$$

The interactions between the quantum mechanical and the classical subsystems are given by the term $E_{\text{QM/MM}}$, in Eq. (13-1). The last term in Eq. (13-1), E_{MM}, provides the energy of the classically treated part of the total system and is represented by molecular mechanics.

The interactions between the quantum mechanical and classical subsystems are given by the following interaction operator

$$\hat{H}_{\text{QM/MM}} = \hat{H}^{\text{el}} + \hat{H}^{\text{vdw}} + \hat{H}^{\text{pol}} \tag{13-8}$$

where the term $\hat{H}^{\text{el}}$ covers electrostatic interactions and is given by

$$\hat{H}^{\mathrm{el}} = -\sum_{s=1}^{S} \hat{N}_s + E_{S,N}^{\mathrm{el,nuc}} \tag{13-9}$$

where the electronic contribution is written in terms of

$$\hat{N}_s = \sum_{pq} \langle \phi_p | \frac{q_s}{|\mathbf{r} - \mathbf{R_s}|} | \phi_q \rangle \hat{E}_{pq} \tag{13-10}$$

The electrostatic interactions between the partial charges in the classical subsystem and the electrons and the nuclei in the QM system are described by this term. We let the term $E_{S,N}^{\mathrm{el,nuc}}$ denote the interactions between the MM partial charges and the QM nuclei and the index s runs over all the sites in the MM system. Typically, the sites in the MM system are located at the MM atoms having the partial charge q_s and positioned according to the position vector $\mathbf{R}_s$.

The interaction energy related to the induced dipole moments (μ_a^{ind}), where the index a refers to the polarizable site of each MM molecule, is given as

$$\begin{aligned} E[\mu_a^{\mathrm{ind}}] = &-\sum_{a=1}^{A} \mu_a^{\mathrm{ind}} \left(\mathbf{E}^s(\mathbf{R}_a) + \langle \hat{\mathbf{R}}\mathbf{r}_a \rangle + \mathbf{E}^n(\mathbf{R}_a) \right) \\ &- \frac{1}{2} \sum_{a,a'(a \neq a')}^{A} \mu_a^{\mathrm{ind}} \mathbf{T}_{aa'} \mu_{a'}^{\mathrm{ind}} \end{aligned} \tag{13-11}$$

where $T_{aa'}$ is the dipole interaction tensor,

$$\mathbf{T}_{aa'} = \frac{1}{|\mathbf{R}_a - \mathbf{R}_{a'}|^3} \left[\frac{3(\mathbf{R}_a - \mathbf{R}_{a'})(\mathbf{R}_a - \mathbf{R}_{a'})^{\mathrm{T}}}{|\mathbf{R}_a - \mathbf{R}_{a'}|^2} - \mathbf{1} \right] \tag{13-12}$$

and we let $\mathbf{E}^n(\mathbf{R}_a)$ denote the electric field due to the QM nuclei at the centre a of each MM molecule. The electric field due to the partial charges situated at the other MM molecules is given by $\mathbf{E}^s(\mathbf{R}_a)$ and the QM electronic electric field operator is written as

$$\hat{\mathbf{R}}\mathbf{r}_a = \sum_{pq} \langle \phi_p | \frac{\mathbf{r} - \mathbf{R_a}}{|\mathbf{r} - \mathbf{R_a}|^3} | \phi_q \rangle \hat{E}_{pq} \tag{13-13}$$

where the expectation value of this operator over the electronic wave function determines the electric field at position $\mathbf{R}_a$.

For each MM molecule we calculate the induced dipole moment, μ_a^{ind}, as

$$\mu_a^{\mathrm{ind}} = \alpha_a \mathbf{E}_a^{\mathrm{total}} \tag{13-14}$$

where the electric field is given by

$$\mathbf{E}_a^{\mathrm{total}}(\mathbf{R}_a) = \langle \hat{\mathbf{R}}\mathbf{r}_a \rangle + \mathbf{E}^n(\mathbf{R}_a) + \mathbf{E}^s(\mathbf{R}_a) + \mathbf{E}^{\mathrm{ind}}(\mathbf{R}_a) \tag{13-15}$$

and α^a is the polarizability tensor at each MM molecule. The individual components in the expression for $\mathbf{E}_a^{\mathrm{total}}$ are the electric field strengths due to

- the electrons in the quantum mechanical subsystem $\hat{\mathbf{R}}\mathbf{r}_a$,
- the nuclei in the quantum mechanical subsystem $\mathbf{E}^n(\mathbf{R}_a)$,
- the charges in the classical subsystem $\mathbf{E}^s(\mathbf{R}_a)$ and
- the induced dipole moments within the classical subsystem $\mathbf{E}^{\mathrm{ind}}(\mathbf{R}_a)$.

The self-energy, E_{self}, due to the classical induced dipole moments [52] is given by

$$\begin{aligned} E_{\mathrm{self}} &= \sum_{\mathrm{a}=1}^{A} \int_0^{\mu_a^{\mathrm{ind}}} \mathrm{E}_{\mathrm{a}}^{\mathrm{total}'} \mathrm{d}\mu_a^{\mathrm{ind}'} = \sum_{\mathrm{a}=1}^{A} \int_0^{\mu_a^{\mathrm{ind}}} \mu_{\mathrm{a}}^{\mathrm{ind}'} \alpha_a^{-1} \mathrm{d}\mu_a^{\mathrm{ind}'} \\ &= \frac{1}{2} \sum_{\mathrm{a}=1}^{A} \mu_a^{\mathrm{ind}} \alpha_a^{-1} \mu_a^{\mathrm{ind}} \\ &= \frac{1}{2} \sum_{\mathrm{a}=1}^{A} \mu_{\mathrm{a}}^{\mathrm{ind}} \left(\mathrm{E}^s(\mathbf{R}_{\mathrm{a}}) + \langle \hat{\mathbf{R}}\mathbf{r}_{\mathrm{a}} \rangle + \mathrm{E}^n(\mathbf{R}_{\mathrm{a}}) \right) + \frac{1}{2} \sum_{a,a'(a \neq a')}^{A} \mu_a^{\mathrm{ind}} \mathrm{T}_{\mathrm{aa}'} \mu_{\mathrm{a}'}^{\mathrm{ind}} \end{aligned} \tag{13-16}$$

Finally, we obtain by addition of the energy contributions in Eq. (13-11) and Eq. 13-16)

$$E[\mu_a^{\mathrm{ind}}] + E_{\mathrm{self}} = -\frac{1}{2} \sum_{a=1}^{A} \mu_a^{\mathrm{ind}} \left(\langle \hat{\mathbf{R}}\mathbf{r}_a \rangle + \mathbf{E}^n(\mathbf{R}_a) \right) - \frac{1}{2} \sum_{a=1}^{A} \mu_a^{\mathrm{ind}} \mathbf{E}^s(\mathbf{R}_a). \tag{13-17}$$

The second term in Eq. (13-17) concerns particles and induced moments located in the MM system. The polarization energy for the QM system interacting with the MM polarization sites is given by the first term in Eq. (13-17) and it is related to the interaction operator, $\hat{H}^{\mathrm{pol}}$, as

$$\hat{H}^{\mathrm{pol}} = -\frac{1}{2} \sum_{a=1}^{A} \mu_a^{\mathrm{ind}} \cdot (\hat{\mathbf{R}}\mathbf{r}_a + \mathbf{E}^n(\mathbf{R}_a)) \tag{13-18}$$

where μ_a^{ind} and also $\hat{H}^{\mathrm{pol}}$ depend on the electronic wave function as it enters in the determination of the electronic electric field.

For the van der Waals interaction one is able to select a large number of different types of intermolecular potentials as seen in Ref. [53]. Presently we have selected the 6–12 Lennard–Jones potential and we model the van der Waals contributions as

$$\hat{H}^{\mathrm{vdw}} = \sum_{a=1}^{A} \sum_{m:\mathrm{centre}} \left[\frac{A_{ma}}{|\mathbf{R}_m - \mathbf{R}_a|^{12}} - \frac{B_{ma}}{|\mathbf{R}_m - \mathbf{R}_a|^{6}} \right] \tag{13-19}$$

and the a and m denote the MM and QM sites, respectively.

In a mean field and linear approximation, the induced dipole moments are related to the wave function through Eq. (13-14) and we introduce the polarizability and the electric fields in place of the induced moments by inserting this equation once into Eq. (13-18). Taking the expectation value of Eq. (13-8) we obtain the following expression for the QM/MM energy [24,54]

$$\begin{aligned} E_{\mathrm{QM/MM}} &= E^{\mathrm{vdw}} + E^{\mathrm{el}} + E^{\mathrm{pol}} \\ &= E^{\mathrm{vdw}} + E^{\mathrm{el,nuc}}_{S,N} - \sum_{s=1}^{S} \langle \hat{N}_s \rangle \\ &\quad - \frac{1}{2} \sum_{a=1}^{A} \langle \mathbf{R}\hat{\mathbf{r}}_a \rangle^{\mathrm{T}} \alpha_a \left\{ \langle \mathbf{R}\hat{\mathbf{r}}_a \rangle + \mathbf{O}^{\mathrm{ns}}_a(\mathbf{R}_a) \right\} + O^{\mathrm{ns}}_{\mathrm{ind}} \end{aligned} \tag{13-20}$$

where the vector $\mathbf{O}^{\mathrm{ns}}_a(\mathbf{R}_a)$ and the energy term $O^{\mathrm{ns}}_{\mathrm{ind}}$ are defined as

$$\mathbf{O}^{\mathrm{ns}}_a(\mathbf{R}_a) = 2\mathbf{E}^n(\mathbf{R}_a) + \mathbf{E}^s(\mathbf{R}_a) + \mathbf{E}^{\mathrm{ind}}(\mathbf{R}_a) \tag{13-21}$$

and

$$O^{\mathrm{ns}}_{\mathrm{ind}} = -\frac{1}{2} \sum_{a=1}^{A} \left[\left(\mathbf{E}^n(\mathbf{R}_a) \right)^{\mathrm{T}} \alpha_a \left\{ \mathbf{E}^n(\mathbf{R}_a) + \mathbf{E}^s(\mathbf{R}_a) + \mathbf{E}^{\mathrm{ind}}(\mathbf{R}_a) \right\} \right] \tag{13-22}$$

For the optimization of the QM system this is the important energy contribution along with the usual vacuum-type expression $\langle \hat{H}_{\mathrm{QM}} \rangle$ and the term in Eq. (13-23), (discussed below) which depends on the induced dipole moments.

We write the total energy for the classical system in two terms: (i) an intramolecular term, E^{intra}_{MM}, and (ii) an intermolecular contribution, $E_{\mathrm{MM/MM}}$. The intermolecular MM energy is written as

$$E_{\mathrm{MM/MM}}[|\Psi\rangle] = \frac{1}{2} \sum_{s,s'(s \neq s')}^{S} \frac{q_s q_{s'}}{|\mathbf{R}_s - \mathbf{R}_{s'}|} - \frac{1}{2} \sum_{a=1}^{A} \mu^{\mathrm{ind}}_a \mathbf{E}^s(\mathbf{R}_a) + E^{\mathrm{vdw}}_{\mathrm{MM/MM}} \tag{13-23}$$

where the term $E^{\mathrm{vdw}}_{\mathrm{MM/MM}}$ is the van der Waals MM/MM energy and the second term is the MM part of the energy in Eq. (13-17). Since the total energy of the MM system depends on the wave function of the QM system we illustrate the dependence of $E_{\mathrm{MM/MM}}$ on the QM system through the induced dipole moments by writing $E_{\mathrm{MM/MM}}$ as a functional of the wave function, $|\Psi\rangle$.

13.3. COMBINED DENSITY FUNCTIONAL THEORY AND MOLECULAR MECHANICS MODEL

This section contains the background for the combination of density functional theory and molecular mechanics. Following the basic philosophy of quantum mechanics/molecular mechanics approaches we partition the total system into at least two parts which can be treated simultaneously. The quantum mechanical subsystem is described using DFT and the classical subsystem is given by molecular mechanics. Based on the QM/MM approach we have that the total energy of the system is

$$E_{\mathrm{tot}}[\rho] = E_{\mathrm{DFT}}[\rho] + E_{\mathrm{DFT/MM}}[\rho] + E_{\mathrm{MM}}[\rho] \tag{13-24}$$

where the first term is the energy of the subsystem treated using DFT

$$E_{\mathrm{DFT}}[\rho] = \int h(\mathbf{r})\rho(\mathbf{r})\mathrm{d}\mathbf{r} + \frac{1}{2}\iint \frac{\rho(\mathbf{r})\rho(\mathbf{r}')}{|\mathbf{r}-\mathbf{r}'|}\mathrm{d}\mathbf{r}\mathrm{d}\mathbf{r}' + E_{\mathrm{xc}}[\rho] + U_{\mathrm{NN}} \tag{13-25}$$

where we denote $\rho(\mathbf{r})$ the electronic density. The vectors $\mathbf{r}$ and $\mathbf{r}'$ are the position vectors for the electrons. The four contributions in Eq. (13-25) represent the one-electron kinetic and nuclear-attraction operators (the first term), the Hartree and exchange energy contributions (the second and third terms, respectively) and the last term U_{NN} is the inter-nuclear repulsion energy. For the DFT/MM energy functional we have the following expression [55,56,57]

$$\begin{aligned} E_{\mathrm{DFT/MM}}[\rho] &= E^{\mathrm{vdw}} + E^{\mathrm{el}} + E^{\mathrm{pol}} \\ &= E^{\mathrm{vdw}} + E_{S,N}^{\mathrm{el,nuc}} - \sum_{s}\int \rho(\mathbf{r})N_s(\mathbf{r})\mathrm{d}\mathbf{r} \\ &\quad - \frac{1}{2}\sum_{a}\left(\int \rho(\mathbf{r})\mathbf{R}\mathbf{r}_a(\mathbf{r})\mathrm{d}\mathbf{r}\right)\alpha_a \\ &\quad \times \left[\int \rho(\mathbf{r})\mathbf{R}\mathbf{r}_a(\mathbf{r})\mathrm{d}\mathbf{r} + \mathbf{O}_a^{\mathrm{ns}}\right] + O_{\mathrm{ind}}^{\mathrm{ns}} \end{aligned} \tag{13-26}$$

where the Coulomb interactions between the electrons and a MM nucleus (the sum over s is again the sum over charge sites in the MM system) is represented by the operator $N_s(\mathbf{r})$. The term $E_{S,N}^{\mathrm{el,nuc}}$ takes care of the Coulomb interactions between the nuclei in the MM and QM subsystems. The QM electric field operator at site a in the MM system is represented by $\mathbf{R}\mathbf{r}_a(\mathbf{r})$ and α_a is the polarizability tensor at the same site. The van der Waals contribution is denoted by the term E^{vdw} and it is given by a 6–12 Lennard–Jones potential. The other terms, the vector $\mathbf{O}_a^{\mathrm{ns}}(\mathbf{R}_a)$ and the energy term $O_{\mathrm{ind}}^{\mathrm{ns}}$, have been defined in Section 2. The electric field arising from the MM charges at the polarizable site a is given by $\mathbf{E}^s(\mathbf{R}_a)$. The electric field due to the QM

nuclei is described by the vector $\mathbf{E}^n(\mathbf{R}_a)$. The electric field due to the induced dipole moments, $\mathbf{E}^{\text{ind}}(\mathbf{R}_a)$, is determined as

$$\mathbf{E}^{\text{ind}}(\mathbf{R}_a) = \sum_{a' \neq a} \mathbf{T}_{aa'} \mu_{a'}^{\text{ind}} \tag{13-27}$$

where $\mathbf{T}_{aa'}$ is the dipole tensor given in Eq. (13-12). As discussed in Section 2, we decompose the energy of the MM subsystem into an intramolecular term, $E_{\text{MM}}^{\text{intra}}$ (independent of the density), and an intermolecular contribution, $E_{\text{MM/MM}}$ (dependent on the density), and the latter we write as [55]

$$E_{\text{MM/MM}}[\rho] = \frac{1}{2} \sum_{s,s'(s \neq s')}^{S} \frac{q_s q_{s'}}{|\mathbf{R}_s - \mathbf{R}_{s'}|} - \frac{1}{2} \sum_{a=1}^{A} \mu_a^{\text{ind}} \mathbf{E}^s(\mathbf{R}_a) + E_{\text{MM/MM}}^{\text{vdw}} \tag{13-28}$$

The expression contains the van der Waals MM/MM energy given by $E_{\text{MM/MM}}^{\text{vdw}}$ and the polarization term is the second term in Eq. (13-28) which depends explicitly on the induced dipole moments determined as

$$\mu_a^{\text{ind}} = \alpha_a \left(\int \rho(\mathbf{r}) \mathbf{R}\mathbf{r}_a(\mathbf{r}) \mathrm{d}\mathbf{r} + \mathbf{E}^n(\mathbf{R}_a) + \mathbf{E}^s(\mathbf{R}_a) + \mathbf{E}^{\text{ind}}(\mathbf{R}_a) \right) \tag{13-29}$$

Our next step is to minimize the energy of the total system with respect to the density and thereby we are able to define an effective Kohn–Sham (KS) operator. In first quantization, the KS operator is divided into a vacuum and a coupling contribution

$$f^{\text{KS}}(\mathbf{r}) = f_o^{\text{KS}}(\mathbf{r}) + v_{\text{DFT/MM}}(\mathbf{r}) \tag{13-30}$$

The vacuum contribution is given as

$$f_o^{\text{KS}}(\mathbf{r}) = h(\mathbf{r}) + j(\mathbf{r}) + v_{\text{xc}}(\mathbf{r}) \tag{13-31}$$

where

$$j(\mathbf{r}) = \int \frac{\rho(\mathbf{r}')}{|\mathbf{r} - \mathbf{r}'|} \mathrm{d}\mathbf{r}' \tag{13-32}$$

is the Hartree term and

$$v_{\text{xc}}(\mathbf{r}) = \frac{\delta E_{\text{xc}}}{\delta \rho(\mathbf{r})} \tag{13-33}$$

is the exchange term. We determine the DFT/MM contribution to be [57]

$$v_{\mathrm{DFT/MM}}(\mathbf{r}) = -\sum_s N_s(\mathbf{r}) - \sum_a \left[\int \rho(\mathbf{r}')\mathbf{R}\mathbf{r}_a(\mathbf{r}')\mathrm{d}\mathbf{r}' + \frac{1}{2}\mathbf{E}_a^{\mathrm{ns}} \right]^{\mathrm{T}} \alpha_a \mathbf{R}\mathbf{r}_a(\mathbf{r}) \tag{13-34}$$

where

$$\mathbf{E}_a^{\mathrm{ns}} = 2\mathbf{E}^n(\mathbf{R}_a) + 2\mathbf{E}^s(\mathbf{R}_a) + \mathbf{E}^{\mathrm{ind}}(\mathbf{R}_a) \tag{13-35}$$

Accordingly, the modifications to the KS operator are twofold: (i) a static contribution through the static multipole moments (here charges) of the solvent molecules and (ii) a dynamical contribution which depends linearly on the electronic polarizability of the environment and also depends on the electronic density of the QM region. Due to the latter fact we need within each SCF iteration to update the DFT/MM part of the KS operator with the set of induced dipole moments determined from Eq. (13-29). We emphasize that it is the dynamical contribution that gives rise to polarization of the MM subsystem by the QM subsystem.

It is advantageous when considering response theory to utilize a second quantization representation of the DFT/MM method and we have for the DFT/MM potential in Eq. (13-34)

$$\hat{v}_{\mathrm{DFT/MM}} = \sum_{pq} \left(-\sum_s n_{pq}^s - \sum_a \left[\langle \hat{\mathbf{R}}\mathbf{r}_a \rangle + \frac{1}{2}\mathbf{E}_a^{\mathrm{ns}} \right]^{\mathrm{T}} \alpha_a \mathbf{t}_{pq}^a \right) \hat{E}_{pq} \tag{13-36}$$

which has been written in terms of the Coulomb (n_{pq}^s) and electric field (t_{pq}^a) integrals.

13.4. RESPONSE FUNCTIONS FOR THE DENSITY FUNCTIONAL THEORY/MOLECULAR MECHANICS METHOD

This section considers how to derive the response functions for the density functional theory molecular mechanics method and the derivation of these response functions is similar to the procedure of obtaining density functional theory response functions for molecules in vacuum [58]. For the method and the derivation, we utilize the adiabatic approximation and thereby we assume that $v_{\mathrm{xc}}[\rho](\mathbf{r}, \mathbf{t}) = v_{\mathrm{xc}}[\rho](\mathbf{r})$.

Our starting point involves the determination of the expectation value of a time-independent operator $\hat{A}$. In the case of a time-dependent perturbation given by the operator $\hat{V}(t)$, the expectation value of $\hat{A}$ is time dependent. We expand the expression for the time-dependent expectation value in orders of the perturbation and find

$$\langle t|\hat{A}|t\rangle = \langle t|\hat{A}|t\rangle^{(0)} + \langle t|\hat{A}|t\rangle^{(1)} + \langle t|\hat{A}|t\rangle^{(2)} + \cdots \tag{13-37}$$

Furthermore, if we denote $\hat{V}^{\omega}$ as the Fourier transformation of $\hat{V}(t)$

$$\hat{V}(t) = \int \hat{V}^{\omega} \exp(-\mathrm{i}\omega t)\mathrm{d}\omega \tag{13-38}$$

we have that the Fourier representations of the time-dependent terms in Eq. (13-37) are given by

$$\langle t|\hat{A}|t\rangle^{(1)} = \int \langle\langle \hat{A}; \hat{V}^{\omega}\rangle\rangle_{\omega} \exp(-\mathrm{i}\omega t)\mathrm{d}\omega \tag{13-39}$$

$$\langle t|\hat{A}|t\rangle^{(2)} = \frac{1}{2}\int\int \langle\langle \hat{A}; \hat{V}^{\omega_1}, \hat{V}^{\omega_2}\rangle\rangle_{\omega_1,\omega_2} \exp(-\mathrm{i}(\omega_1+\omega_2)t)\mathrm{d}\omega_1\mathrm{d}\omega_2 \tag{13-40}$$

The expressions in Eqs. (13-39) and (13-40) define the linear and quadratic response functions implicitly.

For the Kohn–Sham reference determinant we have that it is a solution to the time-dependent Schrödinger equation,

$$(\hat{H} + \hat{V}(t))|t\rangle = \mathrm{i}\frac{\mathrm{d}}{\mathrm{d}t}|t\rangle \tag{13-41}$$

where

$$\hat{H} = \sum_i f^{\mathrm{KS}}(\mathbf{r}_i, t) \tag{13-42}$$

and for the reference Kohn–Sham determinant we utilize the anti-Hermitian operator $\hat{\kappa}(t)$ for an exponential parametrization of the time evolution. The anti-Hermitian operator $\hat{\kappa}(t)$ is given by

$$\hat{\kappa}(t) = \sum_{rs} \kappa_{rs}(t)\hat{E}_{rs} = \sum_{rs} \kappa_{rs}(t) \sum_{\sigma} a^{\dagger}_{r\sigma} a_{s\sigma} \tag{13-43}$$

Denoting $|0\rangle$ as the unperturbed Kohn–Sham determinant, we have the following representation for the reference Kohn–Sham determinant

$$|t\rangle = \exp[-\hat{\kappa}(t)]|0\rangle \tag{13-44}$$

Our next step requires a representation of the time dependence of the electron density $\hat{\rho}(\mathbf{r}) = \sum_{pq} \phi^{*}_{p}(\mathbf{r})\phi_q(\mathbf{r})\hat{E}_{pq}$

$$\rho(\mathbf{r}, t) = \langle t|\hat{\rho}(\mathbf{r})|t\rangle = \langle 0|\exp[\hat{\kappa}(t)]\hat{\rho}(\mathbf{r})\exp[-\hat{\kappa}(t)]|0\rangle \tag{13-45}$$

and we rewrite the time-dependent electron density through a Baker–Campbell–Hausdorff expansion and we find the following expression in terms of the variation parameters $\hat{\kappa}(t)$

$$\begin{aligned}\rho(\mathbf{r},t) = \rho(\mathbf{r},0) &+ \langle 0|[\hat{\kappa}(t),\hat{\rho}(\mathbf{r})]|0\rangle \\ &+ \frac{1}{2}\langle 0|[\hat{\kappa}(t),[\hat{\kappa}(t),\hat{\rho}(\mathbf{r})]]|0\rangle + O(\hat{\kappa}(t)^3)\end{aligned} \tag{13-46}$$

As the perturbation is applied onto the molecular system we represent the $\hat{\kappa}(t)$ parameters through the perturbation orders

$$\hat{\kappa}(t) = \hat{\kappa}^{(1)}(t) + \hat{\kappa}^{(2)}(t) + \cdots \tag{13-47}$$

with the Fourier transformations

$$\begin{aligned}\hat{\kappa}^{(1)}(t) &= \int \hat{\kappa}^{\omega} \exp(-\mathrm{i}\omega t)\mathrm{d}\omega \\ \hat{\kappa}^{(2)}(t) &= \frac{1}{2}\int\int \hat{\kappa}^{\omega_1\omega_2} \exp(-\mathrm{i}(\omega_1+\omega_2)t)\mathrm{d}\omega_1\mathrm{d}\omega_2\end{aligned} \tag{13-48}$$

We write the perturbed density matrices to second order as

$$D^{(0)}_{pq} = \langle 0|\hat{E}_{pq}|0\rangle \tag{13-49}$$

$$D^{(1)}_{pq} = \langle 0|[\hat{\kappa}^{(1)},\hat{E}_{pq}]|0\rangle \tag{13-50}$$

$$D^{(2)}_{pq} = \langle 0|[\hat{\kappa}^{(2)},\hat{E}_{pq}]|0\rangle + \frac{1}{2}\langle 0|[\hat{\kappa}^{(1)},[\hat{\kappa}^{(1)},\hat{E}_{pq}]]|0\rangle \tag{13-51}$$

where we have used the expansions in Eqs. (13-46) and (13-47). We determine the nth-order correction to the density as

$$\rho^{(n)}(\mathbf{r},t) = \sum_{pq} \phi^*_p(\mathbf{r})\phi_q(\mathbf{r})D^{(n)}_{pq} \tag{13-52}$$

The Kohn–Sham Hamiltonian is expanded similarly and we obtain

$$\begin{aligned}\hat{H} &= \sum_n \hat{H}^{(n)} = \sum_{pq} f^{(n)}\hat{E}_{pq} \\ &= \sum_{pq}\left(\delta_{0n}h_{pq} + j^{(n)}_{pq} + v^{(n)}_{\mathrm{QM/MM},pq} + v^{(n)}_{\mathrm{xc},pq}\right)\hat{E}_{pq}\end{aligned} \tag{13-53}$$

using the following elements:

- h_{pq} that contains the kinetic energy and nuclear-attraction integrals,
- $j_{pq}^{(n)}$ that denotes the electron-repulsion nth-order Coulomb interaction integrals,
- the integral over the exchange–correlation potential, $v_{\mathrm{xc},pq}^{(n)}$, and
- the nth-order contributions from the environment which are given by the integrals $v_{\mathrm{QM/MM},pq}^{(n)}$.

We derive the response functions using the Ehrenfest theorem for a time-independent one-electron operator $\hat{Q}$

$$\left\langle 0\right| \left[\hat{Q}, \exp\left[\hat{\kappa}(t)\right] \left(\hat{H}(t) + V(t) - \mathrm{i}\frac{\mathrm{d}}{\mathrm{d}t} \right) \exp\left[-\hat{\kappa}(t)\right] \right] \left| 0\right\rangle = 0 \tag{13-54}$$

and we obtain an algebraic equation for the first-order parameters

$$\langle 0|[\hat{\mathbf{q}}, [\hat{\kappa}^{\omega}, \hat{H}^{0}] + \hat{H}^{\omega}]|0\rangle + \omega\langle 0|[\hat{\mathbf{q}}, \hat{\kappa}^{\omega}]|0\rangle = -\langle 0|[\hat{\mathbf{q}}, \hat{V}^{\omega}]|0\rangle \tag{13-55}$$

which is done by

- collecting the excitation operators, $\hat{E}_{pq}$, in Eq. (13-43) in the column vector $\hat{\mathbf{q}}$,
- expanding Eq. (13-54) to first order and
- transforming to the frequency domain.

The Fourier transformation of the first-order perturbed Kohn–Sham Hamiltonian is given by

$$\hat{H}^{\omega} = \sum_{pq} f^{\omega} \hat{E}_{pq} = \sum_{pq} \left(j_{pq}^{\omega} + v_{\mathrm{QM/MM},pq}^{\omega} + v_{\mathrm{xc},pq}^{\omega} \right) \hat{E}_{pq} \tag{13-56}$$

The matrix elements are of the same physical origin as in Eq. (13-53). We rewrite Eq. (13-55) as

$$(\underline{\underline{\mathbf{E}}} - \omega \underline{\underline{\mathbf{S}}})\, \kappa^{\omega} = \mathrm{V}^{\omega} \tag{13-57}$$

where we have used that

$$\hat{\kappa}^{\omega} = \hat{\mathbf{q}}^{\dagger} \boldsymbol{\kappa}^{\omega} \tag{13-58}$$

We define the following terms

- $\underline{\underline{\mathbf{E}}}$ is

$$\underline{\underline{\mathbf{E}}}\boldsymbol{\kappa}^{\omega} = -\langle 0|[\hat{\mathbf{q}}, [\hat{\kappa}^{\omega}, \hat{H}^{0}] + \hat{H}^{\omega}]|0\rangle \tag{13-59}$$

- $\underline{\underline{\mathbf{S}}}$ is

$$\underline{\underline{\mathbf{S}}} = \langle 0|[\hat{\mathbf{q}}, \hat{\mathbf{q}}^\dagger]|0\rangle \tag{13-60}$$

- and $\mathbf{V}^\omega$ is

$$\mathbf{V}^\omega = \langle 0|[\hat{\mathbf{q}}, \hat{V}^\omega]|0\rangle \tag{13-61}$$

At this point we are able to obtain from the solution of κ^ω in Eq. (13-57) the linear response function as

$$\langle\langle \hat{A}; \hat{V}\rangle\rangle_\omega = \langle 0|[\hat{\kappa}^\omega, \hat{A}]|0\rangle = -\mathbf{A}^\dagger \kappa^\omega = -\mathbf{A}^\dagger \left(\underline{\underline{\mathbf{E}}} - \omega \underline{\underline{\mathbf{S}}}\right)^{-1} \mathbf{V}^\omega \tag{13-62}$$

where $\mathbf{A}$ is defined as

$$\mathbf{A} = \langle 0|[\hat{\mathbf{q}}, \hat{A}]|0\rangle \tag{13-63}$$

The explicit QM/MM contributions to the linear response function enter the $\underline{\underline{\mathbf{E}}}$ matrix and in the following we investigate how the QM/MM contributions modify the expressions. We have that

$$\underline{\underline{\mathbf{E}}}^{\mathrm{QM/MM}} \boldsymbol{\kappa}^\omega = -\langle 0|[\hat{\mathbf{q}}, [\hat{\kappa}^\omega, \hat{v}^0_{\mathrm{QM/MM}}] + \hat{v}^\omega_{\mathrm{QM/MM}}]|0\rangle \tag{13-64}$$

As a start, we consider the commutator between $\hat{\kappa}^\omega = \sum_{mn} \kappa^\omega_{mn} \hat{E}_{mn}$ and a general one-electron operator $\hat{A} = \sum_{pq} A_{pq} \hat{E}_{pq}$ and we have

$$\begin{aligned} [\hat{\kappa}^\omega, \hat{A}] &= \sum_{pq} \sum_{m} \left(\kappa^\omega_{pm} A_{mq} - \kappa^\omega_{mq} A_{pm}\right) \hat{E}_{pq} \\ &\equiv \sum_{pq} A(\kappa^\omega)_{pq} \hat{E}_{pq} = \hat{A}(\kappa^\omega) \end{aligned} \tag{13-65}$$

in terms of one-index-transformed integrals [59].

We are able to apply successively the relation in Eq. (13-66) and thereby we determine the higher-order index transformed integrals, e.g.,

$$\begin{aligned} [\hat{\kappa}^{\omega_1}, [\hat{\kappa}^{\omega_2}, [\ldots [\hat{\kappa}^{\omega_n}, \hat{A}]\ldots]] &= \sum_{pq} A(\kappa^{\omega_n}, ..., \kappa^{\omega_2}, \kappa^{\omega_1})_{pq} \hat{E}_{pq} \\ &= \hat{A}(\kappa^{\omega_n}, \ldots, \kappa^{\omega_2}, \kappa^{\omega_1}). \end{aligned} \tag{13-66}$$

Finally, we have the QM/MM contribution for the linear transformed $\underline{\underline{\mathbf{E}}}$ matrix

$$\underline{\underline{\mathbf{E}}}^{\mathrm{QM/MM}}\boldsymbol{\kappa}^{\omega} = -\langle 0|[\hat{\mathbf{q}}, \hat{Q}_1^{\omega} + \hat{Q}_2^{\omega}]|0\rangle \tag{13-67}$$

where we have defined the following terms

$$\hat{Q}_1^{\omega} = [\hat{K}, {}^{\omega}\hat{\mathrm{v}}^0_{\mathrm{QM/MM}}] = \hat{\mathrm{v}}^0_{\mathrm{QM/MM}}(K^{\omega}) \tag{13-68}$$

$$\begin{aligned}\hat{Q}_2^{\omega} &= \hat{\mathrm{v}}^{\omega}_{\mathrm{QM/MM}} \\ &= -\sum_a \sum_{rs} D^{\omega}_{rs}\mathbf{t}^a_{rs}\boldsymbol{\alpha}_a\hat{\mathbf{R}}\mathbf{r}_a \\ &= -\sum_a \langle 0|[\hat{\kappa}^{\omega}, \hat{\mathbf{R}}\mathbf{r}_a]|0\rangle\boldsymbol{\alpha}_a\hat{\mathbf{R}}\mathbf{r}_a \\ &= -\sum_a \langle 0|\hat{\mathbf{R}}\mathbf{r}_a(\kappa^{\omega})|0\rangle\boldsymbol{\alpha}_a\hat{\mathbf{R}}\mathbf{r}_a\end{aligned} \tag{13-69}$$

We note that the two operators $\hat{Q}_1^{\omega}$ and $\hat{Q}_2^{\omega}$ contain the QM/MM contributions to the linear response equations due to

- a *frozen* environment (e.g., optimized with respect to the ground state density) and
- the induced polarization in the environment as a consequence of the time-dependent perturbation, respectively.

13.5. THE COMBINED COUPLED CLUSTER/MOLECULAR MECHANICS METHOD

Using a cluster operator, $\hat{T}$, and an exponential ansatz [60,61], the coupled cluster wave function is written as

$$|\mathrm{CC}\rangle = \exp(\hat{T})|\mathrm{HF}\rangle \tag{13-70}$$

where the cluster operator is defined by

$$\hat{T} = \hat{T}_1 + \hat{T}_2 + \hat{T}_3 + \cdots + \hat{T}_n = \sum_{i=1}^{n}\sum_{\mu_i} t_{\mu_i}\hat{\tau}_{\mu_i} \tag{13-71}$$

and the i-electron excitation operators and the excitation amplitudes are denoted $\hat{\tau}_{\mu_i}$ and t_{μ_i}, respectively. Finally, the reference wave function is given by the Hartree–Fock state $|HF\rangle$.

The determination of a coupled cluster wave function does not follow the conventional variational procedure but a non-variational procedure where the excitation amplitudes are determined by a projection technique. We have that the coupled cluster energy for a molecule in vacuum is given by

$$E_{\mathrm{CC}} = \langle \mathrm{HF}|\exp(-\hat{T})\hat{H}\exp(\hat{T})|\mathrm{HF}\rangle \tag{13-72}$$

and we have a set of amplitude equations that we obtain by projecting onto the set of excited Slater determinants

$$e_{\mu_i} = \langle \mu_i | \exp(-\hat{T}) \hat{H} \exp(\hat{T}) | \mathrm{HF} \rangle = 0 \tag{13-73}$$

We have defined the following states $\langle \mu_i | = \langle \mathrm{HF} | \hat{\tau}^{\dagger}_{\mu_i}$ and we have that $\langle \mu_i | \nu_j \rangle = \delta_{\mu,\nu} \delta_{i,j}$. For the calculation of molecular properties it is advantageous to introduce a variational Lagrangian as [51,52,53,54,55,56,57,58,59,60,61,62,63,64]

$$L_{\mathrm{CC}}(\boldsymbol{t}, \bar{\mathbf{t}}) = E_{\mathrm{CC}}(\boldsymbol{t}) + \sum_{i,\mu_i} \bar{t}_{\mu_i} e_{\mu_i} = E_{\mathrm{CC}}(\boldsymbol{t}) + \bar{\boldsymbol{t}} \boldsymbol{e}(\boldsymbol{t}) \tag{13-74}$$

where we have used the following vectors:

- the Lagrangian multipliers are contained within the vector $\bar{\boldsymbol{t}}$ and
- the vector ***e(t)*** contains the amplitude equations (Eq. (13-74)).

By requiring that the Lagrangian is simultaneously stationary with respect to $\boldsymbol{t}$ and $\bar{\boldsymbol{t}}$ we obtain

$$\frac{\partial L_{\mathrm{CC}}(\boldsymbol{t}, \bar{\boldsymbol{t}})}{\partial \bar{t}_{\mu_i}} = e_{\mu_i}(\bar{\boldsymbol{t}}) = \langle \mu_i | \exp(-\hat{T}) \hat{H} \exp(\hat{T}) | \mathrm{HF} \rangle = 0 \tag{13-75}$$

$$\begin{aligned} \frac{\partial L_{\mathrm{CC}}(\boldsymbol{t}, \bar{\boldsymbol{t}})}{\partial t_{\nu_j}} &= \frac{\partial E_{\mathrm{CC}}(\boldsymbol{t})}{\partial t_{\nu_j}} + \sum_{i,\mu_i} \bar{t}_{\mu_i} \frac{\partial e_{\mu_i}(\boldsymbol{t})}{\partial t_{\nu_j}} \\ &= \eta_{\nu_j} + \sum_{i,\mu_i} \bar{t}_{\mu_i} A_{\mu_i \nu_j} \\ &= \langle \Lambda | [\hat{H}, \hat{\tau}_{\nu_j}] | \mathrm{CC} \rangle = 0 \end{aligned} \tag{13-76}$$

where we have defined the following terms:

- the state $\langle \Lambda |$

$$\langle \Lambda | = (\langle \mathrm{HF} | + \sum_{i,\mu_i} \bar{t}_{\mu_i} \langle \mu_i |) \exp(-\hat{T}) \tag{13-77}$$

- and the vector η containing the elements

$$\eta_{\nu_j} = \langle \mathrm{HF} | \left[\hat{H}, \hat{\tau}_{\nu_j} \right] | \mathrm{CC} \rangle \tag{13-78}$$

- as well as the coupled cluster Jacobian

$$A_{\mu_i \nu_j} = \langle \mu_i | \exp(-\hat{T}) \left[\hat{H}, \hat{\tau}_{\nu_j} \right] | \mathrm{CC} \rangle \tag{13-79}$$

Presently, we are able to determine the coupled cluster energy based on the variational Lagrangian and expectation values for real operators

$$\langle \hat{X} \rangle = \langle \Lambda | \hat{X} | \mathrm{CC} \rangle. \tag{13-80}$$

For the optimization of the coupled cluster wave function in the presence of the classical subsystem we write the CC/MM Lagrangian as [24]

$$\begin{aligned} L_{\mathrm{CC/MM}}(\boldsymbol{t}, \bar{\boldsymbol{t}}) = \langle \Lambda | \hat{H}_{\mathrm{QM}} | \mathrm{CC} \rangle - \sum_{s=1}^{S} \langle \hat{N}_s \rangle \\ - \frac{1}{2} \sum_{a=1}^{A} \langle \hat{\mathbf{R}}\hat{\mathbf{r}}_{\mathbf{a}} \rangle^T \alpha_a \left[\langle \hat{\mathbf{R}}\hat{\mathbf{r}}_{\mathbf{a}} \rangle + \mathbf{O}_a^{\mathrm{ns}}(\mathbf{R}_a) \right] \\ + E^{\mathrm{vdw}} + E_{S,N}^{\mathrm{el,nuc}} + O_{\mathrm{ind}}^{\mathrm{ns}} + E_{\mathrm{MM}}(\boldsymbol{t}, \bar{\boldsymbol{t}}) \end{aligned} \tag{13-81}$$

and this Lagrangian is nonlinear in both the $\boldsymbol{t}$ and $\bar{\boldsymbol{t}}$ parameters.

To obtain an optimized coupled cluster state, we require that the Lagrangian, $L_{\mathrm{CC}}/\mathrm{MM}(\boldsymbol{t}, \bar{\boldsymbol{t}})$, is stationary with respect to both the $\boldsymbol{t}$ and $\bar{\boldsymbol{t}}$ parameters. It is advantageous to define the following one-electron interaction operator, $\hat{T}^g$, as

$$\hat{T}^g = -\sum_{s=1}^{S} \hat{N}_s - \sum_{a=1}^{A} \left[\langle \Lambda | \hat{\mathbf{R}}\hat{\mathbf{r}}_{\mathbf{a}} | CC \rangle + \frac{1}{2} \mathbf{E}_a^{\mathrm{ns}}(\mathbf{R}_a) \right]^{\mathrm{T}} \alpha_a \hat{\mathbf{R}}\hat{\mathbf{r}}_{\mathbf{a}} \tag{13-82}$$

where

$$\mathbf{E}_a^{\mathrm{ns}}(\mathbf{R}_a) = 2\mathbf{E}^n(\mathbf{R}_a) + 2\mathbf{E}^s(\mathbf{R}_a) + \mathbf{E}^{\mathrm{ind}}(\mathbf{R}_a) \tag{13-83}$$

This gives rather compact expressions for the optimization conditions for the CC/MM wave function

$$\frac{\partial L_{\mathrm{CC/MM}}(\boldsymbol{t}, \bar{\boldsymbol{t}})}{\partial \bar{t}_{\mu_i}} = \left\langle \mu_i \right| \exp(-\hat{T}) \left[\hat{H}_{\mathrm{QM}} + \hat{T}^g \right] \exp(\hat{T}) \left| \mathrm{HF} \right\rangle = 0 \tag{13-84}$$

and

$$\frac{\partial L_{\mathrm{CC/MM}}(\boldsymbol{t}, \bar{\boldsymbol{t}})}{\partial t_{v_i}} = \langle \Lambda | [\hat{H}_{\mathrm{QM}} + \hat{T}^g, \hat{\tau}_{v_i}] | \mathrm{CC} \rangle = 0 \tag{13-85}$$

The effective one-electron operator $\hat{T}^g$ depends on both the $\boldsymbol{t}$ and $\bar{\boldsymbol{t}}$ parameters. Therefore we have the situation that the two equations Eq. (13-85) and Eq. (13-86) are

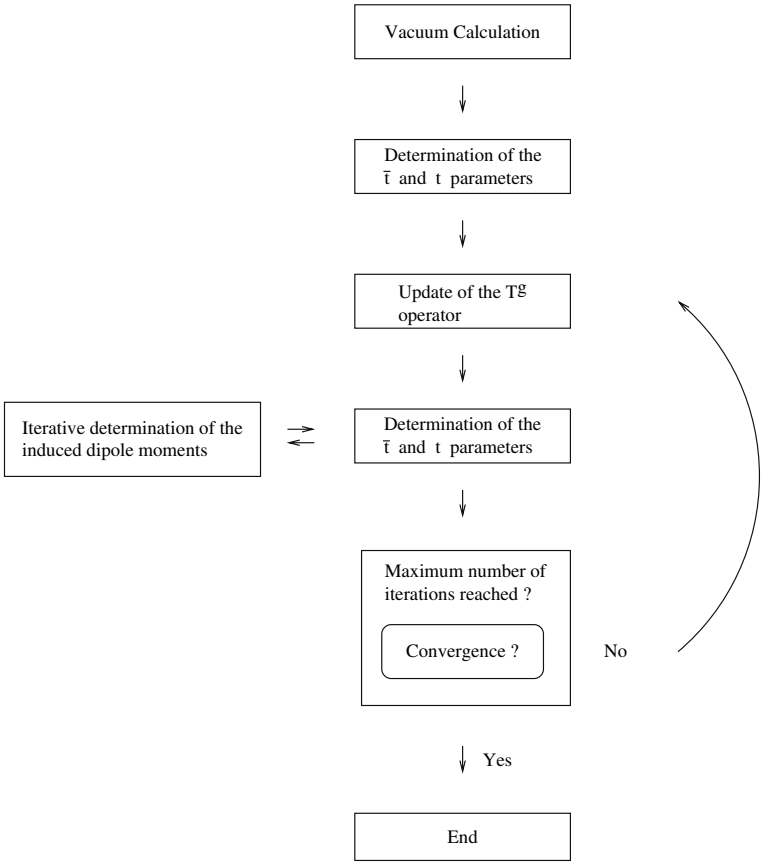

Figure 13-2. A figure presenting the procedure of the CC/MM wave function optimization

coupled, and this coupling represents an additional complication compared to the corresponding optimization conditions for a molecule in vacuum. The procedure for solving the coupled equations is illustrated in Figure 13-2. We are able to form the $\hat{T}^g$ operator based on a set of t and $\bar{t}$ parameters along with the necessary integrals. Next we solve the t equations and thereafter the $\bar{t}$ equations as in the vacuum case but with modified one-electron integrals. Having done this, we obtain a new set of t and $\bar{t}$ parameters which makes it possible to update the operator $\hat{T}^g$. We continue with this procedure until convergence is obtained, and for each iteration we update the induced dipole moments, μ_a^{ind}, calculated using Eq. (13-14). The induced dipole moments depend on the induced electric field and therefore this equation has to be solved iteratively.

13.6. COUPLED CLUSTER/MOLECULAR MECHANICS RESPONSE THEORY

In this section we outline the coupled cluster-molecular mechanics response method, the CC/MM response method. Ref. [51] considers CC response functions for molecular systems in vacuum and for further details we refer to this article. The identification of response functions is closely connected to time-dependent perturbation theory [51,65,66,67,68,69,70]. Our starting point is the quasienergy and we identify the response functions as simple derivatives of the quasienergy. For a molecular system in vacuum where $\hat{H}_{\mathrm{QM}}$ is the vacuum Hamiltonian for the unperturbed molecule and $\hat{V}^t$ is a time-dependent perturbation we have the following time-dependent Hamiltonian, $\hat{H}$,

$$\hat{H} = \hat{H}_{\mathrm{QM}} + \hat{V}^t \tag{13-86}$$

and we write $\hat{V}^t$ as a Fourier expansion

$$\begin{aligned} \hat{V}^t &= \sum_{k=-N}^{N} \exp(-\mathrm{i}\omega_k t)\hat{V}^{\omega_k} \\ &= \sum_{k=-N}^{N} \exp(-\mathrm{i}\omega_k t) \sum_{y} \epsilon_y(\omega_k)\hat{Y} \end{aligned} \tag{13-87}$$

Here we require that $\epsilon_y(\omega_k) = \epsilon_k(-\omega_k)^*$ and that the operators $\hat{Y}$ are Hermitian.

Presently, we assume that we have a time-dependent wave function, $|\tilde{O}(t)\rangle$, and that it is normalized to unity. Furthermore, we require that $|\tilde{O}(t)\rangle$ reduces to the time-independent wave function, $|O\rangle$, in the limit of no perturbation. The time-independent wave function, $|O\rangle$, is the solution to the time-independent Schrödinger equation and $|O\rangle$ is normalized. Therefore, for an exact state we write the time-dependent wave function as [50,51]

$$|\bar{O}(t)\rangle = \exp(-\mathrm{i}F(t))|\tilde{O}(t)\rangle \tag{13-88}$$

and F(t) is a real function of time. We have the following time evolution of the system

$$\hat{H}|\bar{O}(t)\rangle = \mathrm{i}\frac{\partial}{\partial t}|\bar{O}(t)\rangle \tag{13-89}$$

Our next step is to insert the ansatz (Eq. (13-89)) into the time-dependent Schrödinger equation where we let a dot indicate a time derivative and $\partial_t = \frac{\partial}{\partial t}$

$$\exp(-\mathrm{i}F(t))\left[\hat{H} - \mathrm{i}\partial_t - \dot{F}(t)\right]|\tilde{O}(t)\rangle = 0 \tag{13-90}$$

In the phase-isolated form we have

$$\left[\hat{H} - \mathrm{i}\partial_t - \dot{F}(t)\right]|\tilde{O}(t)\rangle = 0 \tag{13-91}$$

and we obtain an equation for $\dot{F}(t)$ by projecting Eq. (13-92) onto the time-dependent phase-isolated wave function,

$$\dot{F}(t) = \left\langle \tilde{O}(t) \left| \left[\hat{H} - \mathrm{i}\partial_t\right] \right| \tilde{O}(t) \right\rangle \tag{13-92}$$

and in the absence of the perturbation we find

$$\dot{F}(t) = E_0 \tag{13-93}$$

and $\dot{F}(t)$ reduces to the stationary energy. The time-dependent quasienergy [51] is given as

$$Q(t) \equiv \dot{F}(t) = \left\langle \tilde{O}(t) \right| \left[\hat{H} - \mathrm{i}\partial_t\right] |\tilde{O}(t)\rangle \tag{13-94}$$

Following Refs. [51,68] we may identify the response functions as derivatives of the time-averaged quasienergy:

$$\langle \hat{X} \rangle = \frac{\mathrm{d}\{Q(t)\}_T}{\mathrm{d}\epsilon_x(0)} \tag{13-95}$$

$$\langle\langle X, Y \rangle\rangle_{\omega_{k_1}} = \frac{\mathrm{d}^2\{Q(t)\}_T}{\mathrm{d}\epsilon_x(\omega_0)\mathrm{d}\epsilon_y(\omega_{k_1})} \tag{13-96}$$

$$\langle\langle X, Y, Z \rangle\rangle_{\omega_{k_1},\omega_{k_2}} = \frac{\mathrm{d}^3\{Q(t)\}_T}{\mathrm{d}\epsilon_x(\omega_0)\mathrm{d}\epsilon_y(\omega_{k_1})\mathrm{d}\epsilon_z(\omega_{k_2})} \tag{13-97}$$

$$\langle\langle X, Y, Z \ldots \rangle\rangle_{\omega_{k_1},\omega_{k_2}\ldots} = \frac{\mathrm{d}^{n+1}\{Q(t)\}_T}{\mathrm{d}\epsilon_x(\omega_0)\mathrm{d}\epsilon_y(\omega_{k_1})\mathrm{d}\epsilon_z(\omega_{k_2})\ldots} \tag{13-98}$$

where

$$\omega_0 = -\sum_{i=1}^{n} \omega_{k_i} \tag{13-99}$$

Turning now to the specific case of a coupled cluster wave function we write the time-dependent CC wave function as

$$|\overline{\mathrm{CC}}(t)\rangle = \exp(-\mathrm{i}F(t))|\widetilde{\mathrm{CC}}(t)\rangle = \exp(-\mathrm{i}F(t))\exp(\hat{T}(t))|\mathrm{HF}\rangle \quad (13\text{-}100)$$

where the cluster operator is now time dependent

$$\hat{T}(t) = \sum_{i=1}^{n} \hat{T}_i(t) = \sum_{i,\mu_i} \hat{\tau}_{\mu_i} t_{\mu_i}(t) \quad (13\text{-}101)$$

and the time dependence enters through the amplitudes, $t_{\mu_i}(t)$. The operator $\hat{\tau}_{\mu_i}$ is the time-independent i-fold electronic excitation operator and we assume that

$$\langle \mathrm{HF}|\hat{\tau}_{\mu_i} = 0 \quad (13\text{-}102)$$

Next we insert the time-dependent CC wave function (Eq. (13-101)) into the time-dependent Schrödinger equation

$$\left(\hat{H} - \mathrm{i}\frac{\partial}{\partial t}\right)|\overline{\mathrm{CC}}(t)\rangle = 0 \quad (13\text{-}103)$$

and we obtain

$$\exp(-\hat{T}(t))\hat{H}\exp(\hat{T}(t))|\mathrm{HF}\rangle = \left(\dot{F}(t) + \mathrm{i}\sum_{\mathrm{i},\mu} \hat{\tau}_{\mu_i}\dot{t}(t)_{\mu_i}\right)|\mathrm{HF}\rangle \quad (13\text{-}104)$$

Projection of Eq. (13-105) onto the state $\langle \mathrm{HF}|$ gives an equation for the time-dependent CC quasienergy [51], $Q(t)$,

$$Q(t) = \dot{F}(t) = \langle \mathrm{HF}|\hat{H}\exp(\hat{T}(t))|\mathrm{HF}\rangle = \langle \mathrm{HF}|\hat{H}|\widetilde{\mathrm{CC}}(t)\rangle \quad (13\text{-}105)$$

Thereafter, we construct a CC quasienergy Lagrangian, $L_{\mathrm{CC(t)}}$ [51,71]

$$\begin{aligned} L_{\mathrm{CC}}(t) &= Q(t) + \sum_{\mu_i,i} \bar{t}_{\mu_i}(t)(e_{\mu_i}(t) - \mathrm{i}\partial t_{\mu_i}(t)/\partial t) \\ &= \langle\widetilde{\Lambda}|\left(\hat{H} - \mathrm{i}\frac{\partial}{\partial t}\right)|\widetilde{\mathrm{CC}}\rangle \end{aligned} \quad (13\text{-}106)$$

where the Lagrangian multipliers are given by the time-dependent parameters $\bar{t}_{\mu_i}(t)$ and furthermore, we have defined the auxiliary function $\langle\widetilde{\Lambda}|$ as

$$\langle\widetilde{\Lambda}| = (\langle \mathrm{HF}| + \sum_{i,\mu_i} \bar{t}_{\mu_i}(t)\langle\mu_i|)\exp(-\hat{T}(t)) \quad (13\text{-}107)$$

Furthermore, for the time-dependent case we have the following CC amplitude equation (Eq. (13-74))

$$e_{\mu_i}(t) - \mathrm{i}\partial t_{\mu_i}(t)/\partial t = \langle \mu_i | \exp(-\hat{T}(t))\hat{H}\exp(\hat{T}(t))|\mathrm{HF}\rangle - \mathrm{i}\partial t_{\mu_i}(t)/\partial t \tag{13-108}$$

We obtain by expanding the Lagrangian in orders of the perturbation along with the time-averaged procedure [51] the response functions as derivatives of the time-averaged CC quasienergy $\{L(t)\}_T$. Finally, we obtain the response equations from the stationary condition. In particular, the linear response function is given by

$$\langle\langle \hat{X}, \hat{Y}\rangle\rangle_{\omega_y} = \frac{1}{2}C^{\pm\omega}\frac{\mathrm{d}^2\{L_{\mathrm{CC}}(t)\}_T}{\mathrm{d}\epsilon_x(\omega_x)\mathrm{d}\epsilon_y(\omega_y)} \tag{13-109}$$

where the derivatives are taken at zero field strength. The operator $C^{\pm\omega}$ is defined as

$$C^{\pm\omega} f^{XY}(\omega_x, \omega_y) = f^{XY}(\omega_x, \omega_y) + \left(f^{XY}(-\omega_x, -\omega_y)\right)^* \tag{13-110}$$

and the sum of the frequencies equals zero.

We obtain the modifications to the response equations due to the coupling between the quantum mechanical and classical mechanical subsystems by constructing the corresponding time-dependent CC/MM energy functional [24]

$$\begin{aligned} L_{\mathrm{CC/MM}}(t) =& Q(t) + \sum_{\mu,i}\bar{t}_{\mu_i}(t)(e_{\mu_i}(t) - \mathrm{i}\partial t_{\mu_i}(t)/\partial t) \\ & - \sum_{s=1}^{S}\langle\widetilde{\Lambda}|\hat{N}_s|\widetilde{\mathrm{CC}}\rangle - \frac{1}{2}\sum_{a=1}^{A}\langle\widetilde{\Lambda}|\mathbf{R}\hat{\mathbf{r}}_a|\widetilde{\mathrm{CC}}\rangle\alpha_a \\ & \times\left\{\langle\widetilde{\Lambda}|\mathbf{R}\hat{\mathbf{r}}_a|\widetilde{\mathrm{CC}}\rangle + \mathbf{O}_a^{\mathrm{ns}}(\mathbf{R_a})\right\} \\ & + E^{\mathrm{vdw}} + E_{S,N}^{\mathrm{el,nuc}} + O_{\mathrm{ind}}^{\mathrm{ns}} + E_{\mathrm{MM}} \end{aligned} \tag{13-111}$$

where basically we have added the interaction terms to the vacuum Lagrangian. In Table 13-1 we present the explicit expressions for the matrices and vectors that are used in the linear CC/MM response method.

We determine the modifications to the response equations due to the interaction terms by

- expanding the CC/MM Lagrangians in order of the perturbation,
- collecting orders of the expanded CC/MM Lagrangians,
- performing the time average and
- performing the differentiation of the time-averaged quasienergy.

Thereby, we get the expression for the linear response function

$$\langle\langle \hat{X}, \hat{Y} \rangle\rangle_{\omega_y} = \frac{1}{2} C^{\pm\omega} P\left(X(\omega_x), Y(\omega_y)\right) \left[\boldsymbol{\eta}^X \boldsymbol{t}^Y(\omega_y) + \frac{1}{2} \mathbf{F} \boldsymbol{t}^X(\omega_x) \boldsymbol{t}^Y(\omega_y) - \frac{1}{2} \bar{\boldsymbol{t}}^X(\omega_x) \bar{\boldsymbol{t}}^Y(\omega_y) \mathbf{J} \right] \tag{13-112}$$

In these expressions we have used the definitions of the vectors and matrices given in Table 13-1 and furthermore introduced the symmetrizer defined as (for linear response)

$$P\left(X(\omega_x), Y(\omega_y)\right) g^{XY}(\omega_x, \omega_y) = g^{XY}(\omega_x, \omega_y) + g^{YX}(\omega_y, \omega_x) \tag{13-113}$$

The effective one-electron operators introduced in Table describe the CC/MM interactions when determining the response equations and are defined as

$$\hat{T}^g = -\sum_{s=1}^{S} \hat{N}_s - \sum_{a=1}^{A} \left[\langle \Lambda | \mathbf{R}\hat{\mathbf{r}}_\mathbf{a} | \mathrm{CC} \rangle + \frac{1}{2} \mathbf{E}_a^{\mathrm{ns}}(\mathbf{R}_a) \right]^{\mathrm{T}} \alpha_a \mathbf{R}\hat{\mathbf{r}}_\mathbf{a} \tag{13-114}$$

where the vector $\mathbf{E}^{\mathrm{ns}_a}(\mathbf{R}_a)$ is defined as

Table 13-1. Matrices and vectors for linear and quadratic response functions

Quantity	Derivative expression[a]	Vacuum contribution	Solvent contribution[b]
$A_{\mu_i \nu_j}$	$\dfrac{\partial^2 \{L^{(2)}_{\mathrm{CC/MM}}\}_T}{\partial \bar{t}^{(1)}_{\mu_i}(\omega_x) \partial t^{(1)}_{\nu_j}(\omega_y)}$	$\langle \bar{\mu}_i \vert \left[\hat{H_{\mathrm{QM}}}, \hat{\tau}_{\nu_j} \right] \vert \mathrm{CC} \rangle$	$\langle \bar{\mu}_i \vert \left[\hat{T}^g, \hat{\tau}_{\nu_j} \right] \vert \mathrm{CC} \rangle + \langle \bar{\mu}_i \vert \hat{T}^{g\nu_j} \vert \mathrm{CC} \rangle$
$F_{\mu_i \nu_j}$	$\dfrac{\partial^2 \{L^{(2)}_{\mathrm{CC/MM}}\}_T}{\partial \bar{t}^{(1)}_{\mu_i}(\omega_x) \partial t^{(1)}_{\nu_j}(\omega_y)}$	$\langle \Lambda \vert \left[\left[\hat{H}_{\mathrm{QM}}, \hat{\tau}_{\mu_i} \right], \hat{\tau}_{\nu_j} \right] \vert \mathrm{CC} \rangle$	$\langle \Lambda \vert \left[\left[\hat{T}^g, \hat{\tau}_{\mu_i} \right] \hat{\tau}_{\nu_j} \right] \vert \mathrm{CC} \rangle$ $+ \frac{1}{2} P^{\mu_i \nu_j} \langle \Lambda \vert \left[\hat{T}^{g\mu_i}, \hat{\tau}_{\nu_j} \right] \vert \mathrm{CC} \rangle$
$\xi^Y_{\mu_i}$	$\dfrac{\partial^2 \{L^{(2)}_{\mathrm{CC/MM}}\}_T}{\partial \epsilon_y(\omega_y) \partial \bar{t}^{(1)}_{\mu_i}(\omega_y)}$	$\langle \bar{\mu}_i \vert \hat{Y} \vert \mathrm{CC} \rangle$	
$\eta^Y_{\mu_i}$	$\dfrac{\partial^2 \{L^{(2)}_{\mathrm{CC/MM}}\}_T}{\partial \epsilon_y(\omega_y) \partial t^{(1)}_{\mu_i}(\omega_y)}$	$\langle \Lambda \vert \left[\hat{Y}, \hat{\tau}_{\nu_i} \right] \vert \mathrm{CC} \rangle$	
$J_{\mu_i \nu_j}$	$\dfrac{\partial^2 \{L^{(2)}_{\mathrm{CC/MM}}\}_T}{\partial \bar{t}^{(1)}_{\mu_i}(\omega_x) \partial \bar{t}^{(1)}_{\nu_j}(\omega_y)}$		$\frac{1}{2} P^{\mu_i \nu_j} \langle \bar{\mu}_i \vert {}^{\nu} \hat{T}^g \vert \mathrm{CC} \rangle$

[a]The sum of the frequencies in the derivative expressions is zero. All vectors and matrices are defined for zero field strength.

[b]For the definitions of the effective operators $\hat{T}^{g\nu_j}$, ${}^{\nu_j}\hat{T}^g$ and $\hat{T}^{g\nu_j\sigma_k}$ see text.

$$\mathbf{E}_a^{\mathrm{ns}}(\mathbf{R}_a) = 2\mathbf{E}^n(\mathbf{R}_a) + 2\mathbf{E}^s(\mathbf{R}_a) + \mathbf{E}^{\mathrm{ind}}(\mathbf{R}_a) \tag{13-115}$$

and

$$\hat{T}^{g\nu_j} = -\sum_{a=1}^{A} \left\langle \Lambda \left| \left[\mathbf{R}\hat{\mathbf{r}}_a, \hat{\tau}_{\nu_j} \right] \right| \mathrm{CC} \right\rangle \alpha^a \mathbf{R}\hat{\mathbf{r}}_a \tag{13-116}$$

$$\hat{T}^{g\nu_j\sigma_k} = -\sum_{a=1}^{A} \left\langle \Lambda \left| \left[\left[\mathbf{R}\hat{\mathbf{r}}_a, \hat{\tau}_{\nu_j} \right], \hat{\tau}_{\sigma_k} \right] \right| \mathrm{CC} \right\rangle \alpha^a \mathbf{R}\hat{\mathbf{r}}_a \tag{13-117}$$

$$\hat{T}^{g\nu_j\sigma_k\delta_k} = -\sum_{a=1}^{A} \left\langle \Lambda \left| \left[\left[\left[\mathbf{R}\hat{\mathbf{r}}_a, \hat{\tau}_{\nu_j} \right], \hat{\tau}_{\sigma_k} \right], \hat{\tau}_{\delta_k} \right] \right| \mathrm{CC} \right\rangle \alpha^a \mathbf{R}\hat{\mathbf{r}}_a \tag{13-118}$$

$${}^{\nu_j}\hat{T}^g = -\sum_{a=1}^{A} \left\langle \bar{\nu}_j | \mathbf{R}\hat{\mathbf{r}}_a | \mathrm{CC} \right\rangle \alpha^a \mathbf{R}\hat{\mathbf{r}}_a \tag{13-119}$$

$${}^{\nu_j}\hat{T}^{g\sigma_k} = -\sum_{a=1}^{A} \left\langle \bar{\nu}_j \left| \left[\mathbf{R}\hat{\mathbf{r}}_a, \hat{\tau}_{\sigma_k} \right] \right| \mathrm{CC} \right\rangle \alpha^a \mathbf{R}\hat{\mathbf{r}}_a \tag{13-120}$$

We note that the perturbation-dependent quantities have no direct solvent contributions while the **J** matrix have no vacuum part.

Based on the above description we note that all the interaction contributions are described using effective one-electron operators and we only need linear transformations of trial vectors in connection to the interaction contributions to the **A**, **F** and **J** matrices defined in Table 13-1. The following transformations are needed ${}^{\mathrm{solvent}}\rho = {}^{\mathrm{solvent}}\mathbf{A}\mathbf{t}^C$, ${}^{\mathrm{solvent}}\sigma = \bar{\mathbf{t}}^B\,{}^{\mathrm{solvent}}\mathbf{A}$, $\boldsymbol{\zeta} = \bar{\mathbf{t}}^B\mathbf{J}$ and ${}^{\mathrm{solvent}}\gamma = {}^{\mathrm{solvent}}\mathbf{F}\mathbf{t}^C$ where the two vectors t^C and $\bar{\mathbf{t}}^B$ denote a right and a left trial vectors, respectively. For the transformations of the Jacobian we obtain

$$\begin{aligned} {}^{\mathrm{solvent}}\rho_{\mu_i} &= \sum_{\nu_j, j} \langle \mu_i | \exp(-\hat{T}) \left[\hat{T}^g, \hat{\tau}_{\nu_j} \right] | \mathrm{CC} \rangle t_{\nu_j}^C \\ &\quad + \sum_{\nu_j, j} \langle \mu_i | \exp(-\hat{T}) \hat{T}^{g\nu_j} | \mathrm{CC} \rangle t_{\nu_j}^C \\ &= \langle \mu_i | \exp(-\hat{T}) \left[\hat{T}^g, \hat{C} \right] | \mathrm{CC} \rangle + \langle \mu_{\mathrm{i}} | \exp(-\hat{T}) \hat{T}^{gC} | \mathrm{CC} \rangle \end{aligned} \tag{13-121}$$

where $\hat{C} = \sum_{\nu_j, j} \hat{\tau}_{\nu_j} t^C_{\nu_j}$ and

$$\hat{T}^{gC} = -\sum_{a=1}^{A} \langle \Lambda | [\hat{\mathbf{Rr}}_a, \hat{C}]] | \mathrm{CC} \rangle \alpha^a \hat{\mathbf{Rr}}_a = -\sum_{a=1}^{A} \sum_{j,\nu_j} \eta^{\hat{\mathbf{Rr}}_a}_{\nu_j} t^C_{\nu_j} \alpha^a \hat{\mathbf{Rr}}_a \tag{13-122}$$

In these expressions we have used the definition of the η^X vector given in Table 13-1. We note that

- the first term in Eq. (13-122) is calculated in the same manner as a standard one-electron Hamiltonian contribution [72] and
- the last contribution is equivalent to the calculation of a ξ^X vector with an operator constructed by taking the sum of dot products of $\eta^{\hat{\mathbf{Rr}}_\mathbf{a}}$ vectors and the **C** trial vector and multiplying this number and the polarizability on the $\hat{\mathbf{Rr}}_\mathbf{a}$ operator.

For the left transformation of the Jacobian matrix we have

$$\begin{aligned}
{}^{\text{solvent}}\sigma_{\nu_j} &= \sum_{\mu_i, i} \bar{t}^B_{\mu_i} \langle \mu_i | \exp(-\hat{T}) \left[\hat{T}^g, \hat{\tau}_{\nu_j} \right] | \mathrm{CC} \rangle \\
&\quad + \sum_{\mu_i, i} \bar{t}^B_{\mu_i} \langle \mu_i | \exp(-\hat{T}) \hat{T}^{g\nu_j} | \mathrm{CC} \rangle \\
&= \langle \mathrm{HF} | \sum_{\mu_i, i} \bar{t}^B_{\mu_i} \hat{\tau}^\dagger_{\mu_i} \exp(-\hat{T}) \left[\hat{T}^g, \hat{\tau}_{\nu_j} \right] | \mathrm{CC} \rangle \\
&\quad + \langle \mathrm{HF} | \sum_{\mu_i, i} \bar{t}^B_{\mu_i} \hat{\tau}^\dagger_{\mu_i} \exp(-\hat{T}) \hat{T}^{g\nu_j} | \mathrm{CC} \rangle \\
&= \langle \bar{B} | \left[\hat{T}^g, \hat{\tau}_{\nu_j} \right] | \mathrm{CC} \rangle + \langle \bar{B} | \hat{T}^{g\nu_j} | \mathrm{CC} \rangle
\end{aligned} \tag{13-123}$$

where $\langle \bar{B}| = \left(\langle \mathrm{HF}| \sum_{\mu_i, i} \bar{t}^B_{\mu_i} \hat{\tau}^\dagger_{\mu_i} \right) \exp(-\hat{T})$. We observe that the first term in Eq. (13-124) is calculated in the same manner as a standard one-electron Hamiltonian contribution [73] and that the last term in Eq.(13-124) is given as

$$\begin{aligned}
\langle \bar{B} | \hat{T}^{g\nu_j} | \mathrm{CC} \rangle &= -\sum_{a=1}^{A} \langle \Lambda | \left[\hat{\mathbf{Rr}}_\mathbf{a}, \hat{\tau}_{\nu_j} \right] | \mathrm{CC} \rangle \alpha_a \langle \bar{B} | \hat{\mathbf{Rr}}_\mathbf{a} | \mathrm{CC} \rangle \\
&= -\sum_{a=1}^{A} \eta^{\hat{Rr}_a}_{\nu_j} \alpha_a \sum_{\mu_i, i} \bar{t}^B_{\mu_i} \xi^{\hat{Rr}_a}_{\mu_i}
\end{aligned} \tag{13-124}$$

The $\xi^{\hat{Rr}_a}_{\mu_i}$ vector elements can be evaluated using the vacuum CC linear response code. Thereby, the operator $-\sum_a \sum_{\mu_i, i} \bar{t}^B_{\mu_i} \xi^{\hat{\mathbf{Rr}}_\mathbf{a}}_{\mu_i} \alpha_a \hat{\mathbf{Rr}}_\mathbf{a}$ may be constructed. Finally, performing a η-transformation of this operator we arrive at the result of equation Eq. (13-125).

13.7. LINEAR RESPONSE CALCULATIONS ON SOLVATED ACETONE

In the following we utilize the response methodology presented above to the calculation of the lowest $n \rightarrow \pi^*$ electronic excitation energy of acetone in aqueous solution. The $n \rightarrow \pi^*$ electronic excitation energies for acetone in vacuum and in water have been measured to be $\sim 36200\,\mathrm{cm}^{-1}$ (4.488 eV) and $\sim 37760\,\mathrm{cm}^{-1}$ (4.682 eV), respectively. This gives a solvent shift in the excitation energy of 1500–1600 cm^{-1} [74,75,76]. The solvent-induced shift for the $n \rightarrow \pi^*$ electronic excitation has been investigated by a large number of research groups utilizing different solvent models: a supermolecule approach [77], a reference interaction site self-consistent field (RISM-SCF) [78], a dielectric continuum model [79,80,107], CPMD [81,82,83,84] and MD [85,86,112] or MC [87,88,89,90,91,109,110,111] simulations in conjunction with QM/MM or supermolecule calculations. High-level coupled cluster calculations of acetone in vacuum have also been presented [86,92].

This section contains a brief comparison between two different density functional theory/molecular mechanics approaches and two wave function/molecular mechanics methods. Our focus is on the solvent-induced shift of the $n \rightarrow \pi^*$ electronic excitation in acetone when solvated by water. We utilize the Hartree–Fock/MM, DFT/MM and CC/MM methods that have been implemented in the Dalton program package [93] and for the coupled cluster approach we use the coupled cluster singles and doubles (CCSD) [94] implementation whereas the DFT calculations are performed using B3LYP and CAM-B3LYP functionals [95,96]. We use the aug-cc-pVDZ [97,108] basis set as the one-electron basis set for the QM/MM response calculations because this basis has been shown to provide converged results for excitation energy of acetone [86]. We obtain the molecular configurations from molecular dynamics simulations, and by using the MidasCpp program package [98] we translate/rotate the configurations in such a way that the acetone molecule is placed in the xz-plane with the oxygen atom in the origin and the C_2 axis aligned with the molecular z-axis. The final configurations form the structural input to the Dalton QM/MM calculations.

For the MD simulations we have used the MOLSIM [99] program package and the simulations have been performed using periodic boundary conditions and time steps of 2 fs for a cubic box containing 511 rigid water molecules and 1 rigid acetone molecule at the temperature of 298.15 K. We used the experimental liquid density for water [100] ($\rho_{298.15} = 997.0470\,\mathrm{kg/m}^3$) for determining the size of the cubic box. The evaluation of the intermolecular interactions was truncated at a spherical cut-off distance given by half the box length, and long-range interactions were described through a reaction field approach [101,102]. We used a time period of 400 ps and 1.2 ns for the equilibration and the production run, respectively, and we dumped for every 1 ps a configuration giving us a total of 1200 configurations for the quantum-classical calculations. For the intermolecular potentials we calculated at the B3LYP/aug-cc-pVTZ level the atomic partial point charges using Gaussian 03 [103] with the CHelpG procedure [104] and we constrained the dipole moment to the

ab initio value. For both water and acetone we use a potential accounting explicitly for polarization effects. For acetone we have assigned a dipole polarizability tensor calculated at the B3LYP/aug-cc-pVTZ level to the carbonyl carbon site, whereas for water we use the SPCpol water model [52] which includes a polarizability at the water oxygen site. The intermolecular interactions related to dispersion and repulsion are modelled by a 6–12 type Lennard–Jones potential

$$V_{\mathrm{LJ}} = \sum_{ij} 4\epsilon_{ij} \left[\left(\frac{\sigma_{ij}}{R_{ij}} \right)^{12} - \left(\frac{\sigma_{ij}}{R_{ij}} \right)^{6} \right] \tag{13-125}$$

where i and j belong to different molecules. The parameters ϵ_{ij} and σ_{ij} are determined using the Lorentz–Berthelot mixing rules,

- $\epsilon_{ij} = \left(\epsilon_i \epsilon_j\right)^{1/2}$ and
- $\sigma_{ij} = \left(\sigma_i + \sigma_j\right)/2$,

where ϵ_i and σ_i are atomic parameters [105,106].

We determine the excitation energy as a statistically averaged vertical excitation energy and we obtain the shift as the difference between this excitation energy and the vertical excitation energy in a vacuum calculation. We present the results for the QM/MM-MD calculations in Table 13-2. The Hartree–Fock/SPCpol calculations lead, compared to the three other QM/MM methods, to an overestimation of the excitation energies and the same occurs for the solvent-induced shift. The excitation energies calculated using a Hartree–Fock description are more than 0.5 eV too large compared to the three other methods and the solvent-induced shift is about $1000\,\mathrm{cm}^{-1}$ larger than the shifts calculated by the other three methods. For the two DFT methods and the CCSD method, we obtain excitation energies both in vacuum and solution that are rather similar and the excitation energies differ by less than 0.15 eV. The two DFT/MM-MD simulations give solvent-induced shifts of the excitation energies of 1438 and $1482\,\mathrm{cm}^{-1}$ for B3LYP/SPCpol and

Table 13-2. Vertical electronic $n \rightarrow \pi^*$ transition energy of acetone in gas phase, E_{gas}, and aqueous solution, E_{wat}, in units of eV. Excitation energy in aqueous solution was obtained from the combined QM/MM calculations treating acetone molecule at the quantum mechanical level of theory as indicated in the first column and using the polarizable potential for water molecules as a statistical average over 1200 molecular configurations extracted from classical MD simulation. The solvent shift in excitation energy, ΔE (in cm^{-1}), is evaluated as a difference between excitation energies in water and in vacuum

	E_{gas}	E_{wat}	ΔE
HF	5.080	5.371 ± 0.003	2348 ± 24
B3LYP	4.409	4.588 ± 0.002	1438 ± 20
CAM-B3LYP	4.473	4.656 ± 0.002	1482 ± 20
CCSD	4.550	4.719 ± 0.003	1369 ± 22
Exp.	4.488	4.682	1560

CAM-B3LYP/SCPpol, respectively. The CCSD/SPCpol calculations result in a solvent-induced shift of 1369 cm^{-1}. Therefore, we conclude that both DFT functionals are capable to predict solvent-induced shifts in the $n \rightarrow \pi^*$ excitation in acetone of the CCSD quality. For the absolute magnitudes of the $n \rightarrow \pi^*$ excitation energy, especially the CAM-B3LYP method is seen to perform well compared to CCSD. We find the HF model not to be able to describe this transition reliably.

As we compare with the experimental results for the shift in the electronic excitation energy (1500–1600 cm^{-1}), it is clear that for the three most reliable methods we obtain a slight underestimation of the solvent-induced shifts in excitation energy. However, the agreement between experimental and DFT- or CCSD- based solvent shifts is overall good. The remaining discrepancies could potentially be attributed to the possible imperfections in the force field parameters used for acetone and water in the QM/MM calculations and, especially, in the MD simulations.

13.8. CONCLUSION

We have presented methods that enable investigations of molecules surrounded by a structured environment and this could be a solvent, aerosols, a biological system, a dielectric film on a metallic surface, nano-particles and membranes. We have given a review of the theoretical background for the self-consistent polarization QM/MM model within DFT or wave function approaches such as Hartree–Fock and coupled cluster electronic structure theories. For the energy and response equations, we have covered the necessary mathematical derivations of the contributions arising from the coupling to the classical environment. The QM/MM methods are promising not only for studying ground state solvent effects, but also for considering excited and ionized states, calculating frequency-dependent linear and nonlinear polarizabilities, NMR parameters, magnetizabilities transition moments and vertical excitation energies. The QM/MM response methods enable us to investigate frequency-dependent molecular properties when investigating a molecule coupled to a structured environment and we achieve this by treating the quantum mechanical subsystem on a quantum mechanical level and the structured environment as a classical subsystem described as a molecular mechanics force field. Most importantly, we ensure that the interactions between the two subsystems are included directly in the optimization of the quantum mechanical wave function.

We have illustrated that the derived equations have a structure where energies and molecular properties can be obtained by a simple addition of QM/MM contributions to the conventional vacuum expressions. The actual implementations of these methods have been performed within the framework of the Dalton program and we have implemented QM/MM response methods that enable calculations of frequency-dependent electric and/or magnetic molecular properties up to and including quadratic response. We consider the QM/MM models, using B3LYP, CAM-B3LYP or CCSD as the quantum mechanical electronic structure model, as rather cost-effective methods for calculating molecular properties of large molecular samples.

In order to illustrate the applicabilities and accuracies of the QM/MM-MD methods we have undertaken a study of the vertical electronic $n \rightarrow \pi^*$ transition energies for acetone in aqueous solution. Based on the configurations obtained from molecular dynamics simulations, the calculations were carried out using (i) wave functions approaches such as HF/MM and CC/MM and (ii) DFT approaches such as B3LYP/MM and CAM-B3LYP/MM. From these comparisons and our previous work (17) we conclude that DFT/MM is an promising alternative to high-level CC/MM calculations in terms of accuracy. On the other hand HF/MM calculations are not sufficiently accurate for describing solvent-induced shifts in molecular properties.Having a hierarchy of QM/MM models both in terms of the description of the quantum mechanical subsystem and the classical subsystem enables systematic investigations of the importance of these specific intermolecular interactions on various molecular properties.Therefore, we have presented the theoretical framework that enables investigations of important aspects of solvation, which are not directly accessible from experimental observations.

ACKNOWLEDGEMENTS

The authors are grateful to Prof. Trygve Helgaker (University of Oslo, Norway) and Dr. Pawel Salek (KTH, Sweden) for letting us use their implementation of CAM-B3LYP in Dalton. The authors thank the Danish Center for Scientific Computing (DCSC) for computational resources. K.V.M. thanks Forskningsrådet for Natur og Univers (FNU) and the EU network NANOQUANT for support. J.K. acknowledges support from the Villum Kann Rasmussen Foundation.

REFERENCES

1. Olsen J, Jørgensen P (1985) J Chem Phys 82:3235
2. Bishop DM, (1994) Adv Quant Chem 25:1
3. Hammond BL, Rice JE (1992) J Chem Phys 97:1138
4. Karna SP, Talapatra GB, Wijekoon WMKP, Prasad PN (1992) Phys Rev A 45:2763
5. Sekino H, Bartlett RJ (1993) J Chem Phys 98:3022
6. Jonsson D, Norman P, Luo Y, Ågren H (1996) J Chem Phys 105:581
7. Jonsson D, Norman P, Ågren H (1996) J Chem Phys 105:6401
8. Christiansen O, Mikkelsen KV (1999) J Chem Phys 110:8348
9. Jonsson D, Norman P, Ågren H, Luo Y, Sylvester-Hvid KO, Mikkelsen KV (1998) J Chem Phys 109:6351
10. Sylvester-Hvid KO, Mikkelsen KV, Jonsson D, Norman P, Ågren H (1998) J Chem Phys 109:5576
11. Mikkelsen KV, Jørgensen P, Jensen HJAa (1994) J Chem Phys 100:6597
12. Mikkelsen KV, Sylvester-Hvid KO (1996) J Phys Chem 100:9116
13. Noell JO, Morokuma K (1975) Chem Phys Lett 36:465
14. Warshel A, Levitt M, (1976) J Mol Biol 103:227
15. Singh UC, Kollman PA (1986) J Comput Chem 7:718
16. Field MJ, Bash PA, Karplus M (1990) J Comput Chem 11:700
17. Muller RP, Warshel A (1995) J Phys Chem 99:17516
18. Luzhkov V, Warshel A (1991) J Am Chem Soc 113:4491

19. Thompson MA, (1996) J Phys Chem 100:14492
20. Warshel A, (1978) Chem Phys Lett 55:454
21. Thole BT, van Duijnen PTh (1982) Chemical Phys 71:211
22. DeVries AH, van Duijnen PTh, Juffer AH, Rullmann JAC, Dijkman JP, Merenga H, Thole BT (1995) J Comput Chem 16:37
23. van Duijnen PTh, DeVries AH (1996) Int J Quant Chem 60:1111
24. Kongsted J, Osted A, Mikkelsen KV, Christiansen O (2002) Mol Phys 100:1813
25. Gao J, Xia X (1992) Science 258:631
26. Gao J (1992) J Phys Chem 96:6432
27. Gao J, Freindorf M (1997) J Phys Chem A 101:3182
28. Martín ME, Sánchez ML, del Valle FJO, Aguilar MA (2000) J Chem Phys 113:6308
29. Cui Q, Karplus M (2000) J Chem Phys 112:1133
30. Cui Q, Karplus M (2000) J Phys Chem B 104:3721
31. Poulsen TD, Kongsted J, Osted A, Ogilby PR, Mikkelsen KV (2001) J Chem Phys 115:2393
32. Sánchez ML, Aguilar MA, del Valle FJO (1997) J Comput Chem 18:313
33. Sánchez ML, Aguilar MA, del Valle FJO (1998) J Mol Struct (Theochem) 426:181
34. Martín ME, Sánchez ML, Aguilar MA, del Valle FJO (2001) J Mol Struct (Theochem) 537:213
35. Martín ME, Aguilar MA, Chalmet S, Ruiz-López M (2001) Chem Phys Lett 344:107
36. Kawashima Y, Dupuis M, Hirao K (2002) J Chem Phys 117:248
37. Dupuis M, Kawashima Y, Hirao K (2002) J Chem Phys 117:1256
38. Dupuis M, Aida M, Kawashima Y, Hirao K (2002) J Chem Phys 117:1242
39. Stanton RV, Hartsough DS, Merz KM (1993) J Phys Chem 97:11868
40. Tuñón I, Martins-Costa MTC, Millot C, Ruiz-López MF, Rivail JL (1996) J Comput Chem 17:19
41. Jensen L, van Duijnen PTh, Snijders JG (2003) J Chem Phys 118:514
42. Sauer J, Sierka M (2000) J Comput Chem 21(16):1470
43. Brandle M, Sauer J, Dovesi R, Harrison NM (1998) J Chem Phys 109:10379
44. Sierka M, Sauer J (2000) J Chem Phys 112:6983
45. Day PN, Jensen JH, Gordon MS, Webb SP, Stevens WJ, Krauss M, Garmer D, Basch H, Cohen D (1996) J Chem Phys 105:1968
46. Svensson M, Humbel S, Froese RDJ, Matsubara T, Sieber S, Morokuma K (1996) J Phys Chem 100:19357
47. Ten-no S, Hirata F, Kato S (1993) Chem Phys Lett 214:391
48. Chalmet S, Ruiz-López MF (2000) Chem Phys Lett 329:154
49. Moriarty NW, Karlström G (1997) J Chem Phys 106:6470
50. Olsen J, Jørgensen P (1985) J Chem Phys 82:3235
51. Christiansen O, Jørgensen P, Hättig C (1998) Int J Quant Chem 68:1
52. Ahlström P, Wallqvist A, Engström S, Jönsson B (1989) Mol Phys 68:563
53. Engkvist O, Åstrand PO, Karlström G (2000) Chem Rev 100:4087
54. Kongsted J, Osted A, Mikkelsen KV, Christiansen O (2003) J Phys Chem A 107:2578
55. Kongsted J, Osted A, Mikkelsen KV, Christiansen O (2003) J Phys Chem A 107:2578
56. Kongsted J, Osted A, Mikkelsen KV, Christiansen O (2002) Mol Phys 100:1813
57. Nielsen CB, Christiansen O, Mikkelsen KV, Kongsted J (2007) J Chem Phys 126:154112
58. Salek P, Vahtras O, Helgaker T, Ågren H (2002) J Chem Phys 117:9630
59. Helgaker T, Jørgensen P, Olsen J (2000) Molecular electronic structure theory, Wiley, New York
60. Čížek J (1966) J Chem Phys 45:4256
61. Lee TJ, Scuseria GE (1995) Quantum mechanical electronic structure calculations with chemical accuracy, Kluwer Academic, Dordrecht
62. Arponen J (1983) Ann Phys 151:311

63. Helgaker T, Jørgensen P (1989) Theor Chim Acta 75:111
64. Koch H, Jensen HJAa, Jørgensen P, Helgaker T, Scuseria GE, Schaefer HF (1990) J Chem Phys 92:4924
65. Langhoff PW, Epstein ST, Karplus M (1972) Rev Mod Phys 44:602
66. Olsen J, Jørgensen P (1995) In: David R Yarkony (eds) Modern electronic structure theory, vol 2, chapter 13, World Scientific, Singapore, pp 857–990
67. Bishop DM (1994) Adv Quant Chem 25:2
68. Sasagane K, Aiga F, Itoh R (1993) J Chem Phys 99:3738
69. Oddershede J (1987) Adv Chem Phys 69:201
70. Hättig C, Heß BA (1995) Chem Phys Lett 233:359
71. Christiansen O, Koch H, Jørgensen P (1995) J Chem Phys 103:7429
72. Christiansen O, Koch H, Halkier A, Jørgensen P, Helgaker T, Sánchez de Meras A (1996) J Chem Phys 105:6921
73. Christiansen O, Halkier A, Koch H, Jørgensen P, Helgaker T (1998) J Chem Phys 108:2801
74. Hayes WP, Timmons CJ (1965) Spectrochimica Acta 21:529
75. Bayliss NS, Wills-Johnson G (1968) Spectrochimica Acta A 24:551
76. Bayliss NS, McRae EG (1954) J Phys Chem 58:1006
77. Liao DW, Mebel AM, Chen YT, Lin SH (1997) J Phys Chem A 101:9925
78. Ten-no S, Hirata F, Kato S (1994) J Chem Phys 100:7443
79. Cossi M, Barone V (2000) J Chem Phys 112:2427
80. Serrano-Andrés L, Fülscher MP, Karlström G (1997) Int J Quantum Chem 65:167
81. Crescenzi O, Pavone M, De Angelis F, Barone V (2005) J Phys Chem B 109:445
82. Röhrig UF, Frank I, Hutter J, Laio A, VandeVondele J, Rothlisberger U (2003) Chem Phys Chem 4:1177
83. Bernasconi L, Sprik M, Hutter J (2003) J Chem Phys 119:12417
84. Sulpizi MM, Röhrig UF, Hutter J, Rothlisberger U (2005) Int J Quantum Chem 101:671
85. Aquilante F, Cossi M, Crescenzi O, Scalmani G, Barone V (2003) Mol Phys 101:1945
86. Aidas K, Kongsted J, Osted A, Mikkelsen KV, Christiansen O (2005) J Phys Chem A 109:8001
87. Grozema FC, van Duijnen PTh (1998) J Phys Chem A 102:7984
88. Coutinho K, Canuto S (2003) J Mol Struc (Theochem) 632:235
89. Coutinho K, Saavedra N, Canuto S (1999) J Mol Struct (Theochem) 466:69
90. Gao J (1994) J Am Chem Soc 116:9324
91. Öhrn A, Karlström G (2007) Theor Chem Acc 117:441
92. Gwaltney SR, Bartlett RJ (1995) Chem Phys Lett 241:26
93. "DALTON, a molecular electronic structure program", Release 2.0 (2005) see http://www.kjemi.uio.no/software/dalton/dalton.html
94. Purvis GD, Bartlett RJ (1982) J Chem Phys 76:1910
95. Yanai T, Tew DP, Handy NC (2004) Chem Phys Lett 393:51
96. Peach MJG, Helgaker T, Sałek P, Keal TW, Lutnæs OB, Tozer DJ, Handy NC (2006) Phys Chem Chem Phys 8:558
97. Kendall RA, Dunning TH, Harrison RJ (1992) J Chem Phys 96:6796
98. Christiansen O (2004) "MidasCpp, molecular interactions, dynamics and simulation in C++"
99. Linse P (2001) Molsim is an integrated md/mc/bd simulation program belonging to the molsim package. Version 3.3.0, Dec 05
100. Tanaka M, Girard G, Davis R, Peuto A, Bignell N, (2001) Metrologia 38:301
101. Nymand TM, Linse P (2000) J Chem Phys 112:6386
102. Nymand TM, Linse P (2000) J Chem Phys 112:6152

103. Frisch MJ, Trucks GW, Schlegel HB, Scuseria GE, Robb MA, Cheeseman JR, Montgomery Jr JA, Vreven T, Kudin KN, Burant JC, Millam JM, Iyengar SS, Tomasi J, Barone V, Mennucci B, Cossi M, Scalmani G, Rega N, Petersson GA, Nakatsuji H, Hada M, Ehara M, Toyota K, Fukuda R, Hasegawa J, Ishida M, Nakajima T, Honda Y, Kitao O, Nakai H, Klene M, Li X, Knox JE, Hratchian HP, Cross JB, Bakken V, Adamo C, Jaramillo J, Gomperts R, Stratmann RE, Yazyev O, Austin AJ, Cammi R, Pomelli C, Ochterski JW, Ayala PY, Morokuma K, Voth GA, Salvador P, Dannenberg JJ, Zakrzewski VG, Dapprich S, Daniels AD, Strain MC, Farkas O, Malick DK, Rabuck AD, Raghavachari K, Foresman JB, Ortiz JV, Cui Q, Baboul AG, Clifford S, Cioslowski J, Stefanov BB, Liu G, Liashenko A, Piskorz P, Komaromi I, Martin RL, Fox DJ, Keith T, Al-Laham MA, Peng CY, Nanayakkara A, Challacombe M, Gill PMW, Johnson B, Chen W, Wong MW, Gonzalez C, Pople JA, (2004) Gaussian 03, Revision B.05, Gaussian, Inc., Wallingford, CT
104. Breneman CM, Wiberg KB (1990) J Comp Chem 11:361
105. Allen MP, Tildesley DJ (1987) Computer simulation of liquids, Clarendon Press; Oxford
106. Jorgensen WL, Briggs JM, Contreras ML (1990) J Phys Chem 94:1683
107. Christiansen O, Mikkelsen KV (1999) J Chem Phys 110:1365
108. Woon DE, Dunning TH (1994) J Chem Phys 100:2975
109. Coutinho K, George HC, Fonseca TL, Ludwig V, Canuto S (2007) Chem Phys Lett 437:148
110. Fonseca TL, Coutinho K, Canuto S (2007) J Chem Phys 126, Art. No. 034508
111. George HC, Coutinho K, Canuto S (2006) Chem Phys Lett 429:119
112. Pavone M, Brancato G, Morelli G, Barone V (2006) Chem Phys Chem 7:148

CHAPTER 14

COMBINED QM/MM METHODS FOR THE SIMULATION OF CONDENSED PHASE PROCESSES USING AN APPROXIMATE DFT APPROACH

MARCUS ELSTNER[1] AND QIANG CUI[2]

[1] *Department of Physical and Theoretical Chemistry, TU Braunschweig, Hans-Sommer-Straβe 10, D-38106 Braunschweig, Germany, e-mail: m.elstner@tu-bs.de*

[2] *Department of Chemistry and Theoretical Chemistry Institute, University of Wisconsin, Madison, 1101 University Ave, Madison, WI 53706, USA, e-mail: cui@chem.wisc.edu*

Abstract: The realistic simulation of chemical processes occurring in solution and in the active sites of biomolecules is a major challenge for theoretical chemistry since the requirement for a high (chemical) accuracy collides with the large system sizes and long timescales involved. In the last years much effort has been invested into the development of theoretical approaches that allow (i) the treatment of systems of large size with sufficient accuracy and (ii) the simulation of longer timescales. In this chapter, we discuss several choices to construct molecular models and the corresponding theoretical methods. This concerns in particular the recent development of multi-scale methods, where the approximate quantum mechanical (QM) method SCC-DFTB is coupled with molecular mechanics (MM) force fields and continuum electrostatic methods (CM) into combined QM/MM and QM/MM/CM approaches. Chemical events occurring on long timescales are approached by using either direct molecular dynamics simulations, minimum energy pathways based on geometry optimizations or free energy methods, where the potential of mean force along selected coordinate(s) is calculated. Various possible system setups and simulation methods are discussed for the investigation of the structure and energetics of polypeptides in the gas phase and solution as well as proton-transfer reactions in complex environments

14.1. INTRODUCTION

The starting point of every computer simulation in biology, chemistry or physics is the choice of an appropriate structural and computational model. Depending on the question of interest, simulations can consider only a part of the real-world system, although progress in computational methods allows one to treat increasingly realistic models.

The treatment of active site models of biomolecules in the gas phase or within a continuum description of the environment, as often used in the past, may lead to

S. Canuto (ed.), Solvation Effects on Molecules and Biomolecules, 381–405.
DOI 10.1007/978-1-4020-8270-2_14,

useful insights in many cases. In general, however, a more accurate representation of the environment is required. This is due to the heterogeneous and long-range nature of the electrostatic forces emerging from the protein environment and/or solvent, which have been shown to be a major factor governing the biological function, e.g., the efficiency of catalytic processes (see e.g. [1]). Furthermore, reactions may be coupled to conformational transitions in the environment, therefore, modeling may have to go beyond a static and/or continuum representation of the surrounding.

Combinations of quantum mechanical (QM) methods for the description of the active site with a molecular mechanics (MM) treatment of the environment in the so-called QM/MM methods became the method of choice within the last decade, although already proposed in 1976 by Levitt and Warshel [2]. These methods allow for a realistic description of condensed phase systems since they represent the microscopic environment with a QM treatment of the active site; recent comprehensive reviews of these approaches can be found in Refs. [3,4,5,6,7].

There exists a large variety of QM/MM implementations. First of all, they differ in the QM approach chosen for the active site. While early approaches often used semi-empirical (SE) methods like MNDO, AM1 or PM3 for the QM region, nowadays density functional theory (DFT) or even ab initio approaches are applied more frequently due to increased computational resources. The MM region is usually treated using standard force field parameters for biological structures like AMBER [8] or CHARMM [9] (implemented in various software packages), i.e., a simple point charge representation is used and the polarization of the environment is neglected.

Many QM/MM simulations differ in the setup of the system, introducing further approximations. Often, the active site and the surrounding protein matrix are treated within the QM/MM scheme, neglecting the larger environment, i.e., the bulk water solution and/or membrane. In this case, constraints at the protein surface have to be introduced in order to keep the protein close to the crystal structure. These constraints may be given by harmonic forces or by using a stochastic boundary potential [10]. Solvent effects can be approximately captured by using the charge scaling procedure [11]. More elaborate models use periodic boundary conditions and treat the membrane and water explicitly within the MM framework, however, in this approach several other problems can arise: (i) the setup and equilibration is very demanding with respect to human and computer resources, (ii) the long relaxation times of the bulk water, i.e., the collective response of the bulk water with respect to changes in the active site may take a very long time to sample and (iii) the calculation of minimum energy pathways becomes more complicated, since water molecules or residue side chains not relevant to the reaction of interest may flip in orientation and introduce spurious energy jumps in the energy profile. Therefore, QM/MM methods have been combined with continuum methods, in order to capture solvent effects outside the QM/MM region in a more efficient way.

The second challenge for computational chemistry concerns the timescale accessible in the simulations. Biological reactions occur on a variety of timescales, ranging from the ultra-fast photochemical reactions occurring within several hundred femtoseconds up to the millisecond or even second timescale reactions found in catalysis

or protein folding. Direct molecular dynamics simulations with DFT methods can be performed up to several tens of picoseconds, while SE methods can readily approach the nanosecond regime. The latter is sufficient to describe reactions with effective free energy barriers of a few kcal/mol, such as the transitions between different conformations of the alanine dipeptide (see discussions below). The barriers for most chemical reactions, however, are much higher and cannot be overcome during a direct MD simulation. One way of dealing with this problem is to employ reaction path techniques, i.e., to calculate the path of minimal energy between a given reactant and product. This approach neglects the effect of thermal fluctuations, which has been shown to be a dramatic simplification in general [12,13]. One possible solution is to estimate the entropic contributions by using a normal mode analysis for the QM region along the reaction path and MD simulations of the MM part by keeping the QM part fixed [14]. Of course, these methods only work when a minimum energy path constitutes a good zero-order approximation. Otherwise, free energy techniques like free energy perturbation or umbrella sampling have to be applied [15], which require the definition of a reaction coordinate and MD simulations in the nanosecond timescale, which is not yet accessible to DFT methods. This is the reason that SE methods became more popular again in recent years, although they show an overall lower accuracy compared to DFT methods, thus their application to new systems generally requires careful testing.

In the last years, we have developed an approximate SE scheme based on DFT, called self-consistent charge density functional tight binding (SCC-DFTB) [16], and implemented it into several QM/MM schemes [17,18,19,20,21], recently also including an implicit solvent model [22]. We have applied the methodology in combination with direct molecular dynamics simulations, reaction path search algorithms and free energy sampling methods to various biological problems as discussed below [22,23,24,25].

14.2. SCC-DFTB

The derivation of the SCC-DFTB [16] model starts by an expansion of the DFT total energy functional up to second order around a given reference density $\rho_0(\rho_0' = \rho_0(\mathbf{r}'), \int' = \int \mathrm{d}\mathbf{r}')$:

$$\begin{aligned} E = &\sum_i^{\mathrm{occ}} \langle \phi_i | \hat{H}^0 | \phi_i \rangle + \frac{1}{2} \int \int' \left(\frac{1}{|\mathbf{r} - \mathbf{r}'|} + \left. \frac{\delta^2 E_{\mathrm{xc}}}{\delta\rho\, \delta\rho'} \right|_{\rho_0} \right) \delta\rho\, \delta\rho' \\ &- \frac{1}{2} \int \int' \frac{\rho_0' \rho_0}{|\mathbf{r} - \mathbf{r}'|} + E_{\mathrm{xc}}[\rho_0] - \int V_{\mathrm{xc}}[\rho_0] \rho_0 + E_{\mathrm{cc}} \end{aligned} \tag{14-1}$$

The specific choice of ρ_0 as a superposition of the densities of neutral atoms,

$$\rho_0 = \sum_\alpha \rho_0^\alpha, \tag{14-2}$$

is of central importance in the SCC-DFTB method, since it allows efficient approximations of the energy terms in Eq. (14-1):

- The effective Kohn–Sham Hamilton $\hat{H}^0 = \hat{H}[\rho_0]$ contains only the "neutral", zero-order charge density, which is the key for a transferable computational scheme. The Kohn–Sham states ϕ_i are expanded in a (minimal) atomic orbital (AO) basis, η_μ,

$$\phi_i = \sum_\mu c_\mu^i \eta_\mu, \tag{14-3}$$

  which allows to write the matrix elements as follows:

$$< \phi_i | \hat{H}^0 | \phi_i > = \sum_{\mu\nu} c_\mu^i c_\nu^i < \eta_\mu | \hat{H}^0 | \eta_\nu > = \sum_{\mu\nu} c_\mu^i c_\nu^i H_{\mu\nu}^0 \tag{14-4}$$

  The dependence of the AO matrix elements $H_{\mu\nu}^0$ on the "neutral" charge density only allows (after further approximations like the neglect of three-center and crystal field terms [26]) to calculate and store the matrix elements into parameter tables, which are read in before a calculation of a molecular system is started. Since no integrals have to be calculated during the program runtime and the Hamilton matrix is represented in a minimal basis, a speedup of roughly three orders of magnitude is achieved compared to full DFT (GGA) methods with medium-sized basis sets. The basis functions η_μ are confined atomic orbitals, calculated by solving the atomic Kohn–Sham equations in the presence of an additional harmonic potential [27]. This makes the basis functions more compact, which is appropriate for most molecular applications, where the atomic wave-functions would be too diffuse. Since $H_{\mu\nu}^0$ contains only the densities of the neutral atoms, the effect of the charge transfer between the atoms in a real system is taken care of by the second-order terms as described below.
- Also the last four terms in Eq. (14-1) depend on the reference density only. These terms are grouped together into a single energy contribution, called the repulsive energy term E_{rep}. E_{rep} can be approximated as a sum of pair potentials, which are fitted with respect to DFT calculations (for more details, see e.g. [24,26]).
- The second-order terms contain the contributions arising from the charge density fluctuations $\delta\rho = \rho - \rho_0$, which describe the deviation of the ground state density ρ from the reference density [28]. This term is represented by a sum of atomic contributions

$$\delta\rho = \sum_\alpha \delta\rho^\alpha, \tag{14-5}$$

  and a monopole approximation of the atomic contributions allows for an efficient approximation of the second energy derivative in the second term of Eq. (14-1) by a function $\gamma_{\alpha\beta}$.

With these three approximations, the SCC-DFTB total energy finally reads:

$$E = \sum_{i}^{\text{occ}} \sum_{\mu\nu} c_\mu^i c_\nu^i H_{\mu\nu}^0 + E_{\text{rep}}[\rho_0] + \frac{1}{2} \sum_{\alpha\beta} \Delta q_\alpha \Delta q_\beta \gamma_{\alpha\beta} \tag{14-6}$$

14.2.1. Performance of SCC-DFTB

To evaluate the performance of an approximate method is a quite involved process. First of all, there are the standard tests of small molecules, for which molecular properties like heats of formations, geometries, vibrational frequencies, dipole moments, etc., are compared with experimental values or high-level calculations. SCC-DFTB performs excellently for geometries and quite well for reaction energies, while especially for heats of formations of these molecules other semi-empirical methods turned out to be superior [16,29,30,31].

A particular interesting property is the proton affinity, which is crucial for an appropriate description of proton-transfer reactions and which semi-empirical methods have problems to predict well in general [32]. In the case of SCC-DFTB, the problem has been traced back to the second-order expansion of the DFT total energy. For charged systems, where the charge is localized, this approximation breaks down. It has been shown that for these cases the total energy Eq. (14-1) has to be expanded up to the third order in the density fluctuations [24,28,33]. This is in particular crucial for the calculation of deprotonation energies, where the inclusion of third-order terms leads to significant improvement.

Further, a good performance for small molecules does not guarantee a good description of larger molecules. For example, the structures and relative energies of secondary structural elements pose significant problems for semi-empirical models like AM1 and PM3, but are well described at the SCC-DFTB level [34,35].

However, since SCC-DFTB is derived from DFT, it inherits the DFT failures and shortcomings. On the one hand, there is the deficiency of DFT for the description of van der Waals bonded complexes. Here, we extended SCC-DFTB by an explicit treatment of attractive dispersion forces [36], an extension called hereafter SCC-DFTB-D, which has been added to DFT methods in the same way later on as well [37,38]. We have shown that this term is crucial not only for the interaction of DNA bases [36,39,40] or DNA intercalators [41,42], but also, for example, for the structure and stability of water on a graphite surface [43] and certain peptide configurations [21,23,44].

Similarly, SCC-DFTB inherits the failure of DFT-GGA to describe charge transfer excited states within the linear response formalism; for a detailed discussion, see, for example, Refs. [24,45,46].

14.3. METHODS TO TREAT ENVIRONMENTAL EFFECTS

The quantum mechanical treatment is always limited to a small subsystem due to the high computational cost. Semi-empirical (SE) methods can treat much larger systems than ab initio or DFT approaches, however, they are still not able to include a part

of the environment of sufficient size in order to capture the solvent (environmental) effects on the solute.

In biological systems or water, the interactions of a solute with its environment consist of the short-ranged van der Waals forces and electrostatic interactions. In particular the latter ones pose a severe computational bottleneck due to their heterogeneous and long-range nature. Further, in order to account for changes in the electrostatic interactions during a chemical reaction, a proper treatment of solvent relaxation has to be considered. Here, two effects can be distinguished: first, the response of the electronic degrees of freedom to the solvent (and changes therein), which is described by the electronic polarization. More involved are the ionic degrees of freedom, i.e., the structural rearrangement of the environment due to the changes of the solute, which occur on timescales that often exceed the simulation times accessible in a molecular dynamics run.

To effectively represent the coupling between the environment and the quantum region, quantum mechanical methods have been coupled to empirical force field methods in the QM/MM methods. Although introduced as early as in 1977 [2], it was not until the early 1990s that QM/MM methods became widely used in the study of biological systems (a recent comprehensive review can be found in Ref. [7]). Several QM/MM implementations with SCC-DFTB as the QM part have been realized up to now, incorporating it into various empirical force field packages [17,18,19,20,21]. But even for QM/MM approaches using SE methods as QM, the collective reorganization in the environment can become a computational bottleneck. Therefore, much effort is invested into developing so-called "multi-scale" methods, which combine QM/MM with continuum electrostatic methods (CM) for an integrated treatment of large systems. The DFTB QM/MM coupling to CHARMM has been combined with a continuum approach [22,47], the generalized solvent boundary potential developed by B. Roux and coworkers [48] originally for classical simulations. The SCC-DFTB/MM methodology [23,24] as well as the SCC-DFTB/MM/CM methodology [22,49] has been reviewed recently. Briefly, similar to the standard stochastic boundary simulations, GSBP partitions the system into inner and outer regions and the effects of the outer region on the inner, reaction region are represented implicitly within the total effective potential (potential of mean force) [48],

$$W_{\mathrm{GSBP}} = U^{(\mathrm{ii})} + U^{(\mathrm{io})}_{\mathrm{int}} + U^{(\mathrm{io})}_{\mathrm{LJ}} + \Delta W_{\mathrm{np}} + \Delta W^{(\mathrm{io})}_{\mathrm{elec}} + \Delta W^{(\mathrm{ii})}_{\mathrm{elec}}, \tag{14-7}$$

where $U^{(\mathrm{ii})}$ is the complete inner–inner potential energy, $U^{(\mathrm{io})}_{\mathrm{int}}$ and $U^{(\mathrm{io})}_{\mathrm{LJ}}$ are the inner–outer internal (bonds, angles and dihedrals) and Lennard-Jones potential energies, respectively, and ΔW_{np} is the non-polar confining potential. The last two terms in Eq. (14-7) are the core of GSBP, representing the long-range electrostatic interaction between the outer and inner regions. The contribution from distant protein charges (screened by the bulk solvent) in the outer region, $\Delta W^{(\mathrm{io})}_{\mathrm{elec}}$, is represented in terms of the corresponding electrostatic potential in the inner region, $\phi^{(\mathrm{o})}_{\mathrm{s}}(\mathbf{r}_\alpha)$,

$$\Delta W^{(\mathrm{io})}_{\mathrm{elec}} = \sum_{\alpha \in \mathrm{inner}} q_\alpha \phi^{(\mathrm{o})}_{\mathrm{s}}(\mathbf{r}_\alpha) \tag{14-8}$$

The dielectric effect on the interactions among inner region atoms is represented through a reaction field term,

$$\Delta W_{\text{elec}}^{(\text{ii})} = \frac{1}{2} \sum_{mn} Q_m M_{mn} Q_n \tag{14-9}$$

where **M** and Q are the generalized reaction field matrix and generalized multipole moments, respectively, in a basis set expansion [48].

The advantage of the GSBP method lies in its ability to include these contributions explicitly while sampling configurational space of the reaction region during a simulation at minimal additional cost. The static field potential, $\phi_{\text{s}}^{(\text{o})}(\mathbf{r})$, and the generalized reaction field matrix **M** are computed only once based on Poisson–Boltzmann calculations and stored for subsequent simulations. The only quantities that need to be updated during the simulation are the generalized multipole moments, Q_n,

$$Q_n = \sum_{\alpha \in \text{inner}} q_\alpha b_n(\mathbf{r}_\alpha) \tag{14-10}$$

where $b_n(\mathbf{r}_\alpha)$ is the nth basis function at nuclear position $\mathbf{r}_\alpha$.

As described in Ref. [50], the implementation of GSBP into a combined QM/MM framework is straightforward and involves the QM-QM and QM-MM reaction field, and the QM-static field terms. For the GSBP combined with SCC-DFTB, these terms take on a simple form because $\rho^{\text{QM}}(\mathbf{r})$ is expressed in terms of Mulliken charges [16]. Although the formulation of GSBP is self-consistent, the validity of the approach depends on many factors especially the size of the inner region and the choice of the dielectric "constant" for the outer region. Therefore, for any specific application, the simulation protocol has to be carefully tested using relevant benchmarks such as $\text{p}K_\text{a}$ of key residues.

14.4. SMALL POLYPEPTIDES IN AQUEOUS SOLUTION

In order to understand the formation, structure and stability of protein secondary structural elements, small peptides have been studied extensively by many groups in the gas phase and aqueous solution. Early peptide studies were based on geometry optimization and molecular dynamics (MD) simulations using empirical force fields (molecular mechanics: MM). The assessment of the quality of empirical force field methods, however, is a very difficult task. Clearly, the MM methods neglect the effects of charge transfer and polarization due to the use of simple point charge models. However, it is not clear a priori how much this affects their performance in specific applications. The point charges in conjunction with the van der Waals parameters are determined to reproduce condensed phase properties, therefore, MM cannot be expected to reproduce properties of small molecules (peptides) in the gas phase, for which QM methods could provide accurate benchmark data (The situation is different for polarizable force fields, which are expected to describe gas-phase structures as well [51].). Since the peptide geometries are determined by the interplay

of non-bonding and bonding interactions, the accuracy of the bonding interactions cannot be accessed independently. This is a problem in particular for the backbone Φ and Ψ dihedral angles, which are the main degrees of freedom for the peptide conformations and critical parameters for an accurate description of peptide/protein conformations [20].

On the other hand, the application of QM methods at the DFT or ab initio level to understand the dynamics, structure and stability of polypeptides is not straightforward as well. First of all, most interesting problems are not feasible due to overwhelming computational effort. Only small systems (10–50 atoms) on short timescales (10–50 ps) are accessible. These timescales are not sufficient to sample the conformational space since even for small polypetides at least nanosecond simulations are required. Second, explicit solvent molecules have to be included in the simulation, which very quickly exceeds the computational limits, a problem that can be overcome with QM/MM implementations. Third, since these molecules form intramolecular hydrogen bonds, the choice of the basis set is a critical issue due to the appearance of the basis set superposition error (BSSE), which can introduce quite significant errors. Fourth, the structure and energetics of these molecules is determined by a subtle balance of bonding and non-bonding (electrostatic, hydrogen bonding and van der Waals) interactions. DFT and ab initio methods describe the bonding and hydrogen-bonding interactions quite well, while van der Waals interactions are problematic, especially at the DFT-GGA level of theory. DFT-GGA methods using the popular BLYP, B3LYP or PBE (and others) functionals do not account properly for the attractive part (dispersion) of the van der Waals interactions. We therefore proposed to supplement DFT-GGA calculations with an empirical dispersion term as implemented in SCC-DFTB-D [36].

An alternative computational strategy to study peptides in solution is therefore to benchmark a fast QM or polarizable MM model [51] with respect to accurate QM data in the gas phase, and to apply this model for the study of peptides in solution. SCC-DFTB has been shown to reasonably reproduce higher level calculations with respect to relative energies, structures [23,34,35] and vibrational properties of different conformers of small polypeptides [44,52]. Since the combination of different amino acid residues allows for an overwhelming variety of structures with very different properties, structures with repeated residues like *N*-acetyl *L*-alanine$_n$ *N*-methylamide (Ace-Lala$_n$-NME) constitute a good starting point for systematic studies, which will be discussed in the following.

14.4.1. Ace-Lala-NME

Ace-Lala-NME has six stable conformers in the gas phase as described by quantum mechanical methods, the three lowest in energy forming internal hydrogen bonds while higher energy structures do not. Figure 14-1 shows the lowest energy conformer C_7^{eq} in the gas phase. Interestingly, ab initio and DFT approaches vary by 1–2 kcal/mol with respect to the relative stability of the six conformers [35], and different DFT functionals like PBE [53] and B3LYP [35] differ in this range for

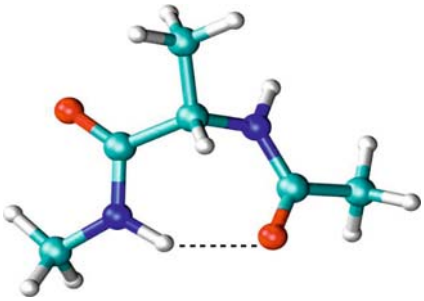

Figure 14-1. The lowest energy conformation C_7^{eq} of the alanine dipeptide model in gas phase

certain conformers as well. Although 1 kcal/mol accuracy is very difficult to achieve with quantum chemical methods and usually would be considered a satisfactory accuracy, errors in this order of magnitude would lead to very different populations of these conformers when performing MD simulations. Since small basis sets lead to BSSE errors of 2–3 kcal/mol for weakly hydrogen-bonded systems, the basis set convergence adds an additional error; to account for this using large basis sets would make the direct molecular dynamics simulation with DFT methods even much more impossible. These errors may accumulate for larger systems (e.g., longer polypeptides), therefore, the results from DFT calculations using medium-sized basis sets should be interpreted with some care. For longer peptides, the conformations differ not only in the number of hydrogen bonds but also in the degree of overall compactness. For more compact structures the BSSE and dispersion interactions become more prominent. For example, in Ace-Lala$_2$-NME the relative energies with B3LYP and MP2 are very different [35]. To analyze this difference in more detail is difficult [54], since BSSE is more severe for ab initio methods than for DFT, i.e., ab initio methods would favor more compact structures than DFT due to BSSE, while DFT describes these compact structures to be less favorable due to the missing dispersion interactions. Therefore, it is difficult to decide which factor contributes more to the discrepancy, the BSSE or missing dispersion. More elaborate methods and extended basis sets have to be used to achieve a sufficient precision. However, due to the high computational cost these methods cannot even be used for geometry optimization, therefore, SCC-DFTB with empirical dispersion corrections has been applied to perform the structural pre-screening using MD simulations [55,56].

On the other hand, SCC-DFTB does not suffer from BSSE and dispersion interactions can be approximately captured using the empirical correction introduced in SCC-DFTB-D. This may allow for a balanced description of various peptide conformations, even for large structures. Compared to the best ab initio results of Beachy et al. [51], SCC-DFTB seems to perform quite well, in particular geometries are described relatively accurately [23,35,39,57], which has been confirmed for DNA structures as well [36,41,42]. Of course, the approximate nature of SCC-DFTB should always be kept in mind, i.e., SCC-DFTB will not always give accuracy

comparable to DFT or ab initio methods. It depends on the specific application, whether a qualitative or (semi-)quantitative accuracy is achieved and, more importantly, is sufficient for the question in hand.

To simulate the effects of solvation, quantum chemistry traditionally uses implicit solvation methods, modeling the effect of the polarizable environments on the electronic structure of the solute. This works very well for rigid molecules. Here, it allows to calculate solvation free energies or other properties very efficiently, which depend on the electrostatic solvent response only (e.g., electronic excited states). In cases where the interaction of solute and solvent has to be considered in molecular detail, this approximation may be insufficient, in particular, when the solvent interaction changes the molecular structure. This is definitely the case for peptides, where solvation may change the conformations completely due to the formation of hydrogen bonds with water molecules, stabilizing conformers not stable in the gas phase. This effect, which depends on the detailed hydrogen bonds formed between solvent and peptide, cannot be captured by continuum models. For an at least approximate modeling of peptide structures, a first solvation shell of water molecules (Figure 14-2) has to be treated approximately, before augmenting with an implicit solvent model [58]. This procedure allows to calculate spectroscopic properties using optimized geometries and normal mode analysis. However, it relies on an insightful placement of water molecules, which is possible only for small peptides and few water molecules. Even then, this static approximation gives only very limited insights. Dynamically, every conformational state (like α, β, etc., conformations) occupies an extended volume in the configurational space, i.e., a range of dihedral Φ and Ψ angles can be attributed to this state. These states may differ in entropy significantly, which is completely neglected in the static picture. Further, the possible conformations of the solvent molecules for every state have to be sampled (averaged), which can have different impacts on the properties of the molecule due to the electrostatic interactions. Therefore including more water molecules in, for example, a QM/MM simulation makes the use of optimized geometries obscure. The internal structure

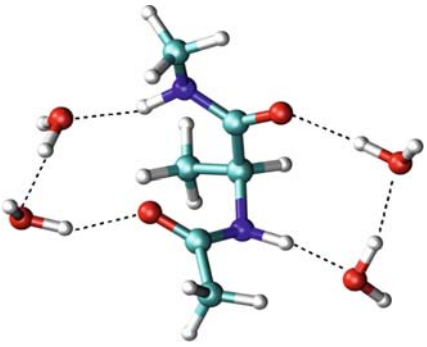

Figure 14-2. The alanine dipeptide model surrounded by four water molecules from the first solvation shell

of the solvent can overrule the geometrical and energetic properties of the solute [17], making optimized geometries nearly meaningless. Further, the solvent structure around hydrophobic and hydrophilic regions of the peptide is the key to understand the hydrophobic forces, which have a strong impact on structure and energetics of the peptide. These arise from the differences in the structure (and hindered conformation flexibility) of the water cage around the solute, which are only captured well in a molecular representation of the solvent.

The sampling of the phase space of small peptides like Ace-Lala-NME with molecular dynamics requires typically simulations over few nanoseconds. These timescales are not yet within reach with DFT or ab initio approaches, while easily accessible using semi-empirical methods like SCC-DFTB. A typical setup involves a QM region consisting of the peptide, surrounded by a cubic box filled with water molecules described with MM and periodic boundary conditions [20]. The simulations show broad regions associated with main peptide conformations. Interestingly, the distribution of the dihedral angles in the Ramachandran plot resembles the distribution of these angles as extracted from alanine (or glycine) residues in proteins as found in protein structure databases. Further, none of the force fields at that time could reproduce these results [20]: the force fields differed significantly in terms of relative intensities of the conformers, between themselves and in comparison to the SCC-DFTB description. New parametrizations seem to overcome these problems, leading to a quite good agreement with the crystal data [59,60].

The energy differences and barriers between the different conformers are in the order of 1–3 kcal/mol. In this case, few nanoseconds suffice to converge the statistics, however, for longer peptides even SCC-DFTB will be not efficient enough. To overcome this problem, either faster methods like polarizable force field methods or more elaborate sampling techniques have to be applied. An interesting techniques is the replica exchange molecular dynamics [19] methodology, where MD simulations are performed at different temperatures, which allows for a much more efficient sampling. An alternative are free energy methods [15], which can be applied if a reaction coordinate can be defined describing the structural transition between two conformers. Along this reaction coordinate, the structural transition can be driven and free energy differences can be evaluated from the MD simulation, as discussed in more detail below.

14.4.2. Helix Formation in Ace-Lala$_n$-NME Peptides with n = 4–20

Interestingly, for these molecules the most common α-helical structural motive is not stable in the gas phase. It converts into a 3_{10} helix for small polypeptides with $n<8$ upon geometry optimization with DFT methods. Only for $n \geq 8$, α conformations start to form in the middle of the helix. However, these helices are energetically less stable than the pure 3_{10} helices [34].

The situation changes dramatically in solution. QM/MM simulations of these two helices in solution modeled by water droplets showed that the larger helix dipole of the α-helix leads to a stronger Coulomb interaction with the solvent [17], which leads

to transition from the 3_{10} to the α-helical conformation within 10 ps [18]. Therefore, the aqueous solvent with a high dielectric constant stabilizes the α-helical conformation significantly.

On the other hand, dispersion interactions play an important role for the relative stabilities of these conformers. Using SCC-DFTB–D instead of SCC-DFTB for optimization of the helical structures in gas phase yields stable conformations beginning with peptide lengths of $n \geq 4$. Further, for the optimized structures α_R becomes energetically more stable for peptides with nine alanine residues and more [21,23], which is in agreement with their appearance in structural databases for this size. Although it is well known that DNA structures are stabilized to a large degree by van der Waals stacking interactions between adjacent base pair steps, the result for peptides was somewhat surprising, since it was believed that the stability is mainly due to hydrogen-bonding interactions.

A particular interesting observation was made when treating an entire protein with SCC-DFTB and only the surrounding water molecules with an empirical potential, applying periodic boundary conditions [21]. Of course, even SCC-DFTB would be much too costly to perform MD simulations for a protein-like Crambin with more than 600 atoms. This becomes only possible when applying a linear scaling algorithm for SCC-DFTB. These methods make use of the local nature of the density matrix in real space, which allows to compute the big system part by part and then joining the density matrices of the subsystems into the total density matrix of the entire system. This in combination with parallelization of the algorithm allows for long MD simulations.

Crambin has two α-helical regions, which are rapidly converted into 3_{10} conformations during the dynamics [21]. Although these helical conformations would be stable in a high dielectric environment like water, they were found to be unstable in the lower dielectric of a protein environment using SCC-DFTB as the QM method. Using the van der Waals augmented SCC-DFTB-D method as described above, the structure of Crambin remained close to the crystal structure, which shows the two α-helices. Therefore, the stability of peptide conformations is governed by a subtle balance of the intrinsic stability of the peptide and the interaction with the polar environment. van der Waals forces seem to be of major importance for the intrinsic stability of the peptides. It can therefore be concluded that neither HF nor DFT (GGA) methods are able to reliably describe polypeptide or protein structures, unless weak van der Waals interactions are explicitly included or better DFT functionals are developed. The comparison with a high-resolution crystal structure showed the QM/MM simulation could reproduce geometrical details better than several molecular mechanics force fields, which are found to produce systematic deviations for the main-chain bond angles and critical dihedral angles. Further, the atomic charges fluctuate around their main values, and a significant charge transfer has been found between the terminal residues, which may have an effect on the conformational stability.

14.5. STUDY OF NON-NATURAL PEPTIDES: β AND α/β -PEPTIDES

An interesting recent set of applications of SCC-DFTB involve non-natural biomolecules [61, 62] such as β- and α/β-peptides, which are oligomers of β- or of α- and β-amino acid residues, respectively. These non-natural peptides have attracted a tremendous amount of interest in recent years due to their potential in biomedical and materials applications [63,64]. For example, they have the advantage that there is no mechanism in the body for their degradation and therefore can be used as antimicrobial materials [65,66,67,68,69,70] and gene delivery agents [71], and are possible candidates for lung surfactant mimics. However, due to the limited amount of quantitative structural and dynamical information [68,72,73,74,75,76,77,78,79,80,81,82], the sequence–structure–property relationships in these systems are not well understood. For example, β^3-residues that bear a side-chain branch point adjacent to the backbone, such as β^3-Val, have been suggested [83,84] to promote helix formation although the idea has been challenged [85].

Computational studies can potentially provide key insights into such sequence–structural relation issues, yet this is not straightforward for non-natural peptides because there are only very limited amount of experimental data for establishing reliable molecular models. Therefore, we have initiated a "bottom-up" approach for simulating β- and α/β-peptides that starts from atomic-level models and systematically propagates to larger and coarser length scales. In particular, we use QM/MM simulations as the reference to facilitate the development of a reliable MM force field for peptides that contain β-amino acids. In the future where larger-scale simulations (e.g., for the study of phase behaviors) are needed, the all-atom MM simulations can be used to parametrize an effective coarse-grained model. The reason to use a QM/MM model is that a QM model, in contrast to a MM model, can be directly calibrated against high-level ab initio calculations in the gas phase, which makes QM/MM simulations a uniquely meaningful reference. Considering computational efficiency, the QM/MM calculations are carried out at the SCC-DFTB/CHARMM level; to make sure that this is appropriate, we first benchmarked SCC-DFTB in the gas phase against high-level DFT and ab initio calculations. Then, the SCC-DFTB/CHARMM results were used to guide the development of an all-atom MM model for several β amino acids. In the following, we briefly discuss the gas-phase benchmark results, which are followed by short discussions of the SCC-DFTB/CHARMM results in the condensed phase.

14.5.1. Gas-Phase Benchmark

As benchmark in the gas phase, we have studied the structure, energy and dipole moment of various conformers in a number of β-dipeptides (β^3-GLY and β^3-ALA) and β-heptapeptides. Systematic conformational searches were carried out for the dipeptides; for the heptapeptides, the conformers of interest include the 14-helix and two different 10/12 mixed helical structures [63]. As reference, the structures were fully optimized at the B3LYP/6-31+G** level, and energies were evaluated at the

Table 14-1. Rms differences in optimized dihedral angles in various β-peptides compared to the standard SCC-DFTB results[a]

Model	SCC-dispersion[c]	B3LYP	LMP2[f]
Dipeptide	8.8	13.4[d]	9.9
Heptapeptide[b]	6.7	9.0[e]	

[a]All dihedral angles rms differences are in degrees;
[b]Only the 10/12 mixed helices are included; for the 14-helix, see text;
[c]SCC-DFTB with the empirical dispersion interaction [86];
[d]B3LYP/6-31+G**;
[e]B3LYP/6-31G*;
[f]LMP2/6-31G**.

LMP2/6-311G** level. At the SCC-DFTB level, the effects of an empirical dispersion correction [86] have also been tested.

For the dipeptides, there is overall very good agreement between SCC-DFTB, B3LYP and LMP2 structure and relative energies (Tables 14-1 and 14-2). Dispersion has, in general, little effect on the SCC-DFTB results, although including the dispersion causes certain conformers to disappear as local minima, often in agreement with the LMP2 result. The RMS errors of the various SCC-DFTB models relative to the LMP2 results are 1.2–1.3 kcal/mol, only slightly larger than the value of 0.9 kcal/mol for B3LYP (Table 14-2). For dipole moments, the SCC-DFTB results deviate from the B3LYP/6-31+G** values by ∼15% and the RMS error is 0.9 Debye.

For the three heptapeptides studied, the findings are overall similar to that for the dipeptides, which show that the standard SCC-DFTB parametrization gives rather reliable structures (RMSD of backbone atoms is normally less than 0.2 Å) and relative energetics (RMS error on the order of 2–3 kcal/mol) for various conformers as compared to B3LYP and LMP2 calculations. In some cases, dispersion forces change the geometry or energetics of the heptapeptides studied here. For example,

Table 14-2. Rms differences in relative energetics for various β-peptides compared to LMP2/6-311G** single point energies[a]

Model	SCC[d]	SCC-dispersion[e]	B3LYP[f]
Dipeptide[b]	1.2	1.3	0.9
Heptapeptide[b]	3.3	4.5	2.2
Heptapeptide[c]	2.0	–	2.6

[a]All energies are in kcal/mol;
[b]With the standard SCC-DFTB-optimized structures; for the heptapeptides, only the 10/12 mixed helices and the fully optimized 14-helices are included;
[c]With B3LYP/6-31G*- optimized structures;
[d]The standard parametrization of SCC-DFTB [87];
[e]SCC-DFTB with the empirical dispersion interaction [86];
[f]B3LYP/6-31+G**.

for the β-substituted hepta–alanine, with dispersion included in the SCC-DFTB, 14-membered-ring hydrogen bonds are formed except at the C-terminus; the average dihedral angles for the four middle residues are $\phi = -160.5^\circ$, $\theta = 61.0^\circ$, $\psi = -127.8^\circ$, very close to the values in an ideal 14-helix [63]. Without dispersion, the two hydrogen bonds close to the C-terminus are completely lost, which leads to a structure with a RMSD value larger than 1.1 Å relative to the ideal 14-helix (Figure 14-3).

Therefore, it seems that the standard SCC-DFTB can describe the intrinsic structural–energy relation of β-peptides to a satisfactory degree, although the effect of dispersion should be monitored carefully.

14.5.2. Solution Results

As benchmark in solution, we have studied a series of α/β-peptides that include a cyclic β-amino acid, trans-2-amino-cyclo-pentane-carboxylic acid (ACPC); these peptides are close to those studied experimentally in the Gellman group. Here we briefly discuss the simulation results for an octapeptide (with the sequence ACPC-A-ACPC-A-ACPC-A-ACPC-A, see Figure 14-4) in methanol solution, where the peptide is treated using SCC-DFTB and methanol using the MEOH model in the CHARMM 22 all-atom force field [88]; calculations show that this methanol model describes the bulk property rather well. The issue of interest is the relative stability of the 14/15 and 11-helical structures. NOE data in methanol suggest that both conformers appear with likely similar stability [82]. Motivated by this observation, the potential of mean force (PMF) associated with the conversion between the two helical forms is calculated using umbrella sampling [89]. The reaction coordinate is

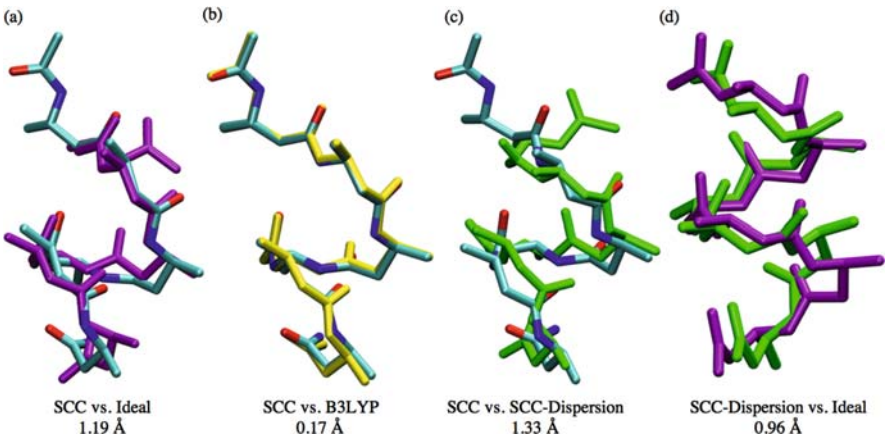

Figure 14-3. Comparison of different structures of model **E** from different calculations (the number below each superposition is the backbone RMSD): (**a**) SCC-DFTB-optimized structure (CPK color) vs ideal 14-helix (*purple*); (**b**) SCC-DFTB-optimized structure (CPK color) vs B3LYP/6-31G* -optimized structure (*yellow*); (**c**) SCC-DFTB-optimized structure (CPK color) vs SCC-DFTB+dispersion optimized structure (*green*); (**d**) SCC-DFTB+dispersion optimized structure (*green*) vs ideal 14-helix (*purple*)

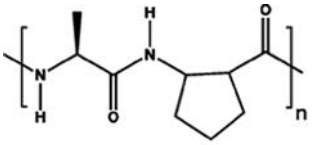

Figure 14-4. The α/β mixed peptide models studied here in methanol solution ($n = 4$)

chosen to be the end-to-end distance between the amide nitrogen in the first residue and the carbonyl carbon in the last residue, and the sampled range is between 10.6 and 18.0 Å; the amount of simulations include approximately 4 ns.

Figure 14-5a depicts the potential of mean force for the conversion between the 14/15 helix and the 11-helix. The SCC-DFTB/MM simulations show that the 11-helix is more stable than the 14/15 helix by about 3 kcal/mol. If we consider that the gas-phase calculations discussed above suggest that SCC-DFTB tends to underestimate the stability of shorter and wider helices (e.g., the stability of 14-helix is underestimated compared to 10/12 mixed helices for heptapeptides), the PMF result implies that the two helical forms are even closer in free energy (14/15 helix is shorter and wider than the 11-helix) than 3 kcal/mol, which is qualitatively consistent with the experimental NOE data [82]. There is an interesting difference in the stability of the backbone hydrogen-bonding interactions between the two helical forms (Figure 14-5b). Although the occupancy of the backbone hydrogen bonds is rather high (~ 0.7) for the 11-helix, the value is substantially lower (< 0.4) for the 14/15 helix, implying a very dynamical structure for the latter.

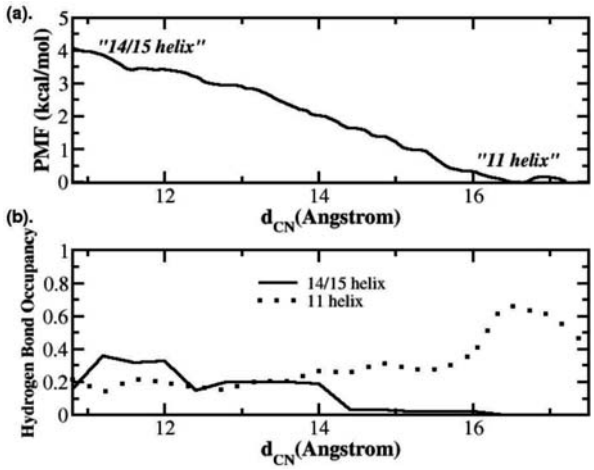

Figure 14-5. SCC-DFTB/MM simulations for octapeptide (ACPC-A-ACPC-A-ACPC-A-ACPC-A) in methanol solution. (**a**) PMF for the conversion between the 14/15 helix and 11-helix of octapeptide; (**b**)hydrogen-bonding occupancy analysis (*solid line*: 14/15 helix; *dashed line*: 11-helix)

14.6. STUDYING PROTON-TRANSFER REACTIONS IN COMPLEX ENVIRONMENTS

Proton-transfer reactions play an important role in biological processes such as enzyme catalysis or bio-energetics. Especially in the latter case, protons are transported over long distances to create proton gradients across the cell membrane. Large free energy barriers ($\geq$ 10 kcal/mol) determine the long timescales (ns–ms) of these chemical reactions, which cannot be studied using direct molecular dynamics simulations of nanoseconds. Instead, either reaction path techniques or methods to compute free energy differences have to be applied, which will be discussed in the following.

14.6.1. Minimum Energy Pathways (MEPs)

Bacteriorhodopsin (bR) is a transmembrane protein located in the cell membrane of purple bacteria and contains in its ground state an all-*trans* retinal chromophore that absorbs at 570 nm. After illumination, the chromophore isomerizes, and a proton is pumped in five consecutive steps from the cytoplasm to the extracellular side of the membrane. The resulting pH gradient is then used to synthesize ATP. In the first proton-transfer step, the proton located at the retinal chromophore Schiff base is transferred to a nearby aspartate residue (Figure 14-6). Our studies on this first proton-transfer step in bacteriorhodopsin (bR) after photoisomerization [90,91,92]

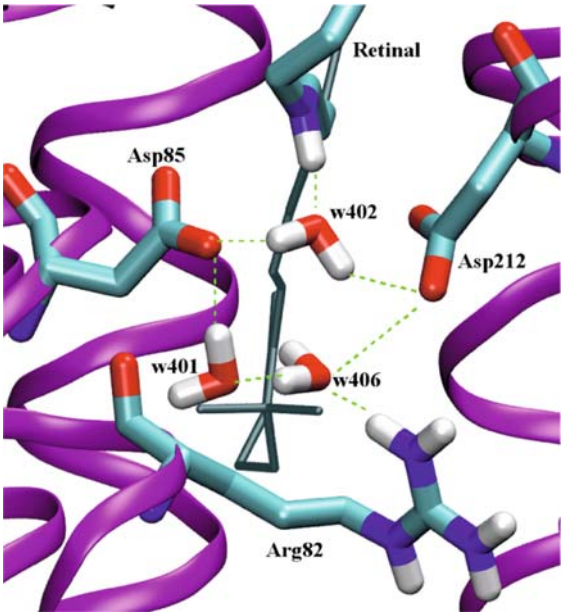

Figure 14-6. The bR retinal binding pocket showing the NH group at the retinal chromophore, the two aspartates 85 and 212 and the three water molecules forming a strong hydrogen-bonded network

is a good example that illustrates the approximations involved in many similar studies. First of all, the active site (retinal chromophore, two aspartates, one threonine side chain and water molecules) is described by a quantum method (in this case SCC-DFTB), the remainder of the protein by an empirical force field method (CHARMM), while no solvent effects are taken into account, i.e., the protein is treated in vacuo. This is acceptable here because the active site is deeply buried in the center of the protein and solvation effects on the active site are expected to be small. A simple way to test this is to use the charge scaling procedure [11], where the force field charges are modified according to Poisson–Boltzmann calculations for the protein embedded in a dielectric environment. This leads to an effective downscaling of the force field charges, especially for those charges exposed to the solvent. In the case of the first protein transfer step in the bR photocycle, the effect of charge scaling was negligible.

Second, the calculation of minimum *energy* pathways (MEPs) could be justified by the fact that the protein environment does not change significantly during the proton transfer and entropic effects have been shown to be marginal. The reason for that is a very rigid binding pocket, where the proton donor and acceptor are tightly bound by an extended hydrogen-bonding network (Figure 14-6). Although the first proton-transfer step seems to be a simple reaction, where a proton is transferred from a donor to a nearby acceptor, a detailed analysis showed that many protein degrees are involved, i.e., it would be difficult to define a proper reaction coordinate. Calculating the energy change along a certain geometrical coordinate by "coordinate driving" can fail dramatically [92]. More elaborate approaches like the conjugate peak refinement (CPR) [93] algorithm, which allow for an optimization of the MEP with taking the multitude of degrees of freedom into account, are more appropriate. CPR starts by interpolation of an initial and final structure to construct the first search direction. This is a severe bias, inherent also in other reaction path approaches, that can be overcome by introducing different initial conditions.

The MEPs have been determined for the first proton-transfer step, i.e., the proton transfer from the retinal chromophore to the nearby aspartate (Asp85) [91]. Several pathways have been studied by using different initial and final configurations and by introducing various intermediate states. When only the initial and final states are specified, a direct transfer mechanism is found where the proton from the chromophore goes directly to the aspartate. Other mechanisms could be found by introducing side-chain residues as proton-transfer intermediates ("relay groups"), i.e., adding structures to the pathway where the proton is located on specific side chains. For the main reaction mechanisms identified, the reaction is isoenergetic and the barriers is between 11 and 13 kcal/mol, which are consistent with experimental findings [91]. The good agreement with experiment is surprising at first sight, but can be rationalized as follows: first, the MEPs are meaningful in this example due to the negligible influence of conformational entropy changes, as discussed above. Since DFT-GGA (all the above calculations are based on DFT-GGA or SCC-DFTB) is known to underestimate proton-transfer barriers (see, e.g., [94]), one may expect an underestimation of the barrier height by 2–4 kcal/mol. However, zero-point

vibrational energies have been neglected in our calculations, which have been shown to lower the effective proton-transfer barriers to the same order of magnitude [3]. Therefore, the agreement with experimental results is due in part to error cancellation. Further improving the calculations by including zero-point vibrational energy (and potentially tunneling) would require to calculate the potential energy at at least the MP2 level of theory, which is much more demanding computationally.

Further analysis revealed the detailed contribution of the protein environment to this proton-transfer reaction. For example, the calculations unraveled the role of the protein environment on the stabilization of the end states and the origin of the proton-transfer barrier. Further, the relevant chromophore conformations consistent with a productive photocycle have been determined, which has been difficult to resolve experimentally. In particular, the electrostatic interaction of the chromophore with the protein sensitively calibrates the key energetic properties. The reaction would be grossly exergonic in the gas phase, and only the interaction with several key residues and water molecules makes the reaction nearly isoenergetic. The reaction barrier results from interaction with the remainder of the protein [90]. Since the reaction is isoenergetic, the question arises as to how the reverse process, the reprotonation of the chromophore, is prevented. Possible mechanisms for that are structural changes in the active site after proton transfer, such as changes in the distance of the proton acceptor to a threonine (Thr89) and relocation of water molecules. Both processes change the proton affinity of the proton acceptor, thereby lowering the energy of the product state and making the reverse reaction more unlikely [92].

14.6.2. Free Energy Simulations Using Multi-scale Approaches

The first proton-transfer step in bR is an example where unsolvated protein models and minimum energy pathway methods can be applied, i.e., a deeply buried active site which is tightly bound, leading to negligible effects from solvation and entropy. In many other systems, however, the proton transfer (or other chemical reactions) is coupled to significant structural response of the protein and/or the solvent, where alternative methods have to be used. One way to do this is to use umbrella sampling techniques, where the reaction coordinate can assume a complicated form for long-range proton-transfer processes [47]. With these techniques, much more complex situations can be studied [22]. A particularly excitinng direction is to study proton translocation across the membrane, where a proper and efficient treatment of the heterogeneous protein/solvent/membrane environment is particularly important, such as in aquaporin [47] and cytochrome *c* oxidase.

A useful example that illustrates the difference between MEP and PMF results is the long-range proton transfer in carbonic anhydrase II (CAII), which is a zinc-enzyme that catalyzes the interconversion of CO_2 and HCO_3^- [95]. The rate-limiting step of the catalytic cycle is a proton transfer between a zinc-bound water/hydroxide and the neutral/protonated His64 residue close to the protein/solvent interface. Since this proton transfer spans at least 8–10 Å depending on the orientation of the His64 sidechain (“in” vs “out”, both observed in the x-ray study [96]), the transfer is

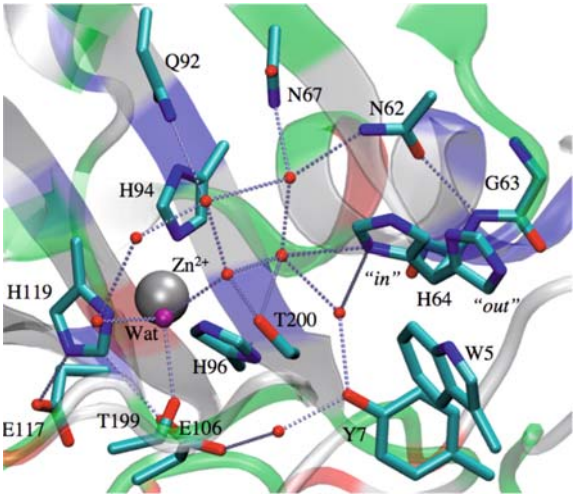

Figure 14-7. The active site of CAII rendered from the crystal structure (PDB ID: 2CBA [96]). All dotted lines correspond to hydrogen-bonding interactions with distances $\leq$3.5 Å. E117 and E106 are in close proximity to H119, and E106 also interacts with T199 through the presumed hydroxyl proton of T199 (not shown for clarity). H64 is resolved to partially occupy both the "in" and "out" rotameric states

believed to be mediated by the water molecules in the active site (see Figure 14-7). As discussed extensively in the literature, there are multiple water wires of different lengths in the active site that connect the donor/acceptor groups (zinc-bound water, His64). A question of interest is whether specific length of water wire dominates the proton transfer or all wires have comparable contributions. It is worth pointing out here that since the active site of CAII is rather polar, a proper treatment of electrostatics in the QM/MM simulations is important even for qualitative properties such as the distribution of water in the active site and the propensity of His64 to adopt different orientations; for more detailed discussions, see Refs. [50, 97]. In all the calculations discussed below, the SCC-DFTB/MM-GSBP protocol is used, which has been validated by comparing to both periodic simulations using the Ewald summation [97] and microscopic pK_a simulations [98].

As the first approach, a large number of MEPs have been collected starting from different snapshots collected from equilibrium MD simulations at the SCC-DFTB/MM level. Since essentially a positive charge is transferred over a long distance in the proton transfer, it was not surprising that the MEP energetics were found to depend on the origin of the starting structure, which reflects the fact that the active-site residues/solvent respond significantly to the proton transfer. For example, when the starting structure came from a CHOH (zinc-bound water, neutral His64) equilibrium simulation, the proton transfer from the zinc-water to His64 is largely *endothermic* (on average by as much as $\sim$13 kcal/mol). By contrast, when the starting structure came from a COHH (zinc-bound hydroxide, protonated His64) simulation, the same proton-transfer reaction was found largely *exothermic*. As an attempt to

capture the "intrinsic barrier" for the proton-transfer reaction, which is known to be close to thermoneutral experimentally [99], we generated configurations from equilibrium MD simulations in which protons along a specific type of water wire were restrained to be of equal distance from nearby heavy atoms (e.g., oxygen in water or $N\epsilon$ in His64). In this way, the charge distribution associated with the reactive components is midway between the CHOH and COHH states, thus the active-site configuration was expected to facilitate a thermoneutral proton-transfer process as confirmed by MEP calculations using such generated configurations as the starting structure. Interestingly, the barriers in such "TS-reorganized" MEPs showed a steep dependence on the length of the water wire; it was small ($\sim$6.8$\pm$2.2 kcal/mol) with short wires but substantially higher than the experimental value ($\sim$10 kcal/mol) with longer water wires (e.g., 17.4$\pm$2.0 kcal/mol for four-water wires).

This steep wire-length dependence is in striking contrast with the more rigorous PMF calculations [100,101]. In the PMF calculations, a collective coordinate [102] is used to monitor the progress of the proton transfer without enforcing specific sequence of events involving individual protons along the wire; the use of a collective coordinate is important because this allows averaging over different water wire configurations, which is proper since the lifetime of various water wires is on the picosecond timescale [50,97], much faster than the timescale of the proton transfer (μs) [99]. In the PMF calculations, the wire-length dependence is examined by comparing results with different His64 orientations ("in" and "out", which is about 8 and 11 Å from the zinc, respectively); both configurations are associated with multiple lengths of water wires but different relative populations (clearly, longer water wires have higher population for the "out" configuration). The two sets of PMF calculations produced barriers of very similar values, which suggests that the length of the water wire (or orientation of the acceptor group) is unlikely an important factor in determining the proton-transfer rate. Physically speaking, this makes sense for the following reason. The pK_a of both the donor and acceptor groups in CAII are shown experimentally to be around 7.0 [95], thus the dominant energetic component is related to the proton exchange between water in the wire and the donor/acceptor group; with either the conventional Grotthius mechanism [103,104] (zinc-bound water first transfers a proton to the next water, generating a hydronium) or the "proton-hole" mechanism we proposed recently [100] (which involves transfer of a water proton to His64 first, generating a hydroxide), the energetics change is approximately 7 pK_a unit, which is close to the experimentally observed barrier of $\sim$10 kcal/mol. In other words, once either a hydronium or a hydroxide is generated, the species can move without a major barrier (consistent with the high mobility of hydronium and hydroxide in solution [105]) over a variable distance and therefore the dependence on the length of the water wire is not expected to be large (for more complete discussions, see Refs. [100,101]).

Further analysis of the configurations sampled in the MEP simulations suggested that the MEP results artificially favored the concerted proton transfers, which correlate to significant distance dependence. As discussed above, to generate the "TS-reorganized" configurations all transferring protons along the wire are

constrained to be half-way between the neighboring heavy atoms; therefore, such sampled protein/solvent configurations would favor a concerted over step-wise proton transfers. Although *all* atoms in the inner region are allowed to move in the MEP searches, the local nature of MEPs does not allow collective reorganization of the active-site residues/solvent molecules, thus the "memory" of the sampling procedure is not erased.

In short, this example clearly illustrates that care must be exercised when using MEP to probe the mechanism of chemical reactions in biomolecules, especially when collective rearrangements in the environment are expected (e.g., reactions involving charge transport).

14.7. CONCLUSIONS

Solvation plays a crucial role for the structure, dynamics and function of small molecules as well as for proteins and nucleic acids. When modeling solvation effects, especially for biomolecules, one often has to deal with large molecular systems and long timescales. Indeed, a proper account for solvation generally requires the inclusion of many solvent molecules, which leads to expanded system size and long simulation timescales required for capturing collective solvent response.

For studying chemical reactions in the condensed phase, for example, a QM/MM setup with a QM description for a small region (active site) and a MM description for the remainder of the system (including the biomolecule and solvent) would be, in principle, appropriate. In practice, periodic boundary conditions can be applied, as they have been shown to be fruitful in many applications, some of which were also reviewed here. However, the periodic boundary approach becomes impractical for many problems of interest. For very large biomolecules containing more than several 10,000 atoms (e.g., the ribosome), the computational cost is overwhelming. Even for smaller systems, the slow protein/solvent response to electronic structural changes associated with the chemical reaction demands long sampling times, which renders simulations difficult to converge.

Therefore, a more practical approach is to represent the most relevant part of the protein and solvent environment at an atomistic level, which is then surrounded by a continuum description. In this contribution, we have discussed two examples for such a protocol: (i) for the simulation of peptides, a first solvation shell can be included in the QM description before adding implicit solvation, which works particularly well for predicting vibrational properties. For more reliable description of the peptide dynamics, however, more advanced techniques that involve extended QM/MM simulations, either for a direct simulation of the system or for parametrizing empirical force fields, are required. (ii) For the simulation of proton-transfer processes, in cases where the active site is shielded from the solvent by the protein, solvation of the protein can be approximated with a charge scaling procedure; in those cases, minimum energy path (MEP) calculations can be fruitful for mechanistic analysis. In cases where the active site is more solvent accessible, the augmentation of QM/MM approaches with implicit solvation models (e.g., in the generalized solvent boundary

potential framework) is advisable; moreover, since solvent can reorganize significantly during the proton transfer, it is important to perform proper sampling and MEP can be misleading for those systems.

The methods discussed here merely represent the beginning of increasingly complex computational architectures, where more than one QM method may be combined with other QM methods, MM methods, continuum electrostatic approaches and coarse-grained models in a coherent "multi-scale" framework. With such developments, increasingly complex chemical and biological systems can be analyzed computationally in a routine and realistic fashion.

REFERENCES

1. Warshel A, Sharma PK, Liu MKH, Olsson M (2006) Chem Rev 106:3210
2. Warshel A, Levitt M (1976) J Mol Biol
3. Gao J, Truhlar DG (2002) Annu Rev Phys Chem 53:467
4. Shurki A, Warshel A (2003) Adv Protein Chem 66:249
5. Field MJ (2002) J Comput Chem 23:48
6. Friesner RA, Guallar V (2005) Annu Rev Phys Chem 56:389
7. Senn HM, Thiel W (2007) Curr Opin Chem Biol 11:182
8. Cornell WD, Cieplak P, Bayly CI, Gould IR, Merz KM, Ferguson DM, Spellmeyer DC, Fox T, Caldwell JW, Kollman PA (1995) J Am Chem Soc 117:5179
9. MacKerell AD Jr, Bashford D, Bellot M, Dunbrack RL Jr, Evanseck JD, Field MJ, Fischer S, Gao J, Guo H, Ha S et al (1998) J Phys Chem B 102:3586
10. Brooks CL III, Karplus M (1989) J Mol Biol 208:159
11. Dinner AR, Lopez X, Karplus M (2003) Theor Chem Acc 109:118
12. Zhang Y, Kua J, McCammon J (2003) J Phys Chem B 107:4459
13. Klahn M, Braun-Sand S, Rosta E, Warshel A (2005) J Phys Chem B 109:15645
14. Zhang YK, Liu HY, Yang WT (2000) J Chem Phys 112:3483
15. Kollman P (1993) Chem Rev 93:2395
16. Elstner M, Porezag D, Jungnickel G, Elstner J, Haugk M, Frauenheim T, Suhai S, Seifert G (1998) Phys Rev B 58:7260
17. Han W, Elstner M, Jalkanen KJ, Frauenheim T, Suhai S (2000) Int J Quant Chem 78:459
18. Cui Q, Elstner M, Kaxiras E, Frauenheim T, Karplus M (2001) J Phys Chem B 105:569
19. Seabra GDM, Walker RC, Elstner M, Case DA, Roitberg AE (2007) J Phys Chem A 111:5655
20. Hu H, Elstner M, Hermans J (2003) Proteins: Struct Funct Genet 50:451
21. Liu H, Elstner M, Kaxiras E, Frauenheim T, Hermans J, Yang W (2001) Proteins: Struct Funct Genet 44:484
22. Riccardi D, Schaefer P, Yang Y, Yu H, Ghosh N, Prat-Resina X, Konig P, Li G, Xu D, Guo H et al (2006) J Phys Chem B 110:6458
23. Elstner M, Frauenheim T, Suhai S (2003) J Mol Struct: THEOCHEM 632:29
24. Elstner M (2006) Theor Chem Acc 116:316
25. Cui Q (2006) Theor Chem Acc 116:51
26. Seifert G (2007) J Phys Chem A 111:5609
27. Porezag D, Frauenheim T, Köhler T, Seifert G, Kaschner R (1995) Phys Rev B 51:12947
28. Elstner M (2007) J Phys Chem A 111:5614
29. Kruger T, Elstner M, Schiffels P, Frauenheim T (2005) J Chem Phys 122:114110
30. Otte N, Scholten M, Thiel W (2007) J Phys Chem A 111:5751

31. Sattelmeyer KW, Tirado-Rives J, Jorgensen WL (2006) J Phys Chem A 110:13551
32. Range K, Riccardi D, Elstner M, Cui Q, York D (2005) Phys Chem Chem Phys 7:3070
33. Yang Y, Yu H, York D, Cui Q, Elstner M (2007) J Phys Chem B in print
34. Elstner M, Jalkanen KJ, Knapp-Mohammady M, Frauenheim Th, Suhai S (2000) Chem Phys 256:15
35. Elstner M, Jalkanen KJ, Knapp-Mohammadi M, Frauenheim Th, Suhai S (2001) Chem Phys 263:203
36. Elstner M, Hobza P, Frauenheim T, Suhai S, Kaxiras E (2001) J Chem Phys 114:5149
37. Wu Q, Wang W (2002) J Chem Phys 116:515
38. Grimme S (2004) J Comput Chem 25:1463; cited By (since 1996):119
39. Kubar T, Jurecka P, Cyerny J, Ryezac J, Otyepka M, Valdes H, Hobza P (2007) J Phys Chem A 111:5642
40. Kabelac M, Valdes H, Sherer EC, Cramer CJ, Hobza P (2007) Phys Chem Chem Phys 9:5000
41. Reha D, Kabelac M, Ryjacek F, Sponer J, Sponer JE, Elstner M, Suhai S, Hobza P (2003) J Am Chem Soc 125:5581
42. Kumar A, Elstner M, Suhai S (2003) Int J Quantum Chem 95:44
43. Lin CS, Zhang RQ, Lee ST, Elstner M, Frauenheim T, Wan LJ (2005) J Phys Chem B 109:14183
44. Jalkanen KJ, Elstner M, Suhai S (2004) J Mol Struct: THEOCHEM 675:61
45. Wanko M, Garavelli M, Bernardi F, Niehaus TA, Frauenheim T, Elstner M (2004) J Chem Phys 120:1674
46. Dreuw A, Head-Gordon M (2005) Chem Rev 105:4009
47. Konig PH, Ghosh N, Hoffmann M, Elstner M, Tajkhorshid E, Frauenheim T, Cui Q (2006) J Phys Chem A 110:548
48. Im W, Berneche S, Roux B (2001) J Chem Phys 114:2924
49. Cui Q (2006) Theor Chem Acc 116:51
50. Schaefer P, Riccardi D, Cui Q (2005) J Chem Phys 123:014905
51. Beachy MD, Chasman D, Murphy RB, Halgren TA, Friesner RA (1997) J Am Chem Soc 119:5908
52. Bohr HG, Jalkanen KJ, Elstner M, Frimand K, Suhai S (1999) Chem Phys 246:13
53. Kaschner R, Hohl D (1998) J Phys Chem A 102:5111
54. Holroyd LF, vanMourik T (2007) Chem Phys Letters 442:42
55. Valdes H, Reha D, Hobza P (2006) J Phys Chem B 110:6385
56. Schwabe T, Grimme S (2007) Phys Chem Chem Phys 9:3397
57. Liu H, Elstner M, Kaxiras E, Frauenheim T, Hermans J, Yang W (2001) Proteins 44:484
58. Han WG, Jalkanen KJ, Elstner M, Suhai S (1998) J Phys Chem B 102:2587
59. MacKerell AD Jr, Feig M, Brooks CL III (2004) J Am Chem Soc 126:698
60. Hornak V, Abel R, Okur A, Strockbine B, Roitberg A, Simmerling C (2006) Proteins: Struct Funct Genet 65:712
61. Zhu X, Yethiraj A, Cui Q (2007) J Comput Theor Chem 3:1538
62. Zhu X, Gellman S, Yethiraj A, Cui Q (2008) J Phys Chem B 112:5439
63. Cheng RP, Gellman SH, DeGrado WF (2001) Chem Rev 101:3219
64. Schmitt MA, Weisblum B, Gellman SH (2007) J Am Chem Soc 129:417
65. Porter EA, Wang XF, Lee HS, Weisblum B, Gellman SH (2000) Nature 404:565
66. Porter EA, Weisblum B, Gellman SH (2002) J Am Chem Soc 124:7324
67. Raguse TL, Porter EA, Weisblum B, Gellman SH (2002) J Am Chem Soc 124:12774
68. Hamuro Y, Schneider JP, DeGrado WF (1999) J Am Chem Soc 121:12200
69. Liu DH, DeGrado WF (2001) J Am Chem Soc 123:7553
70. Schmitt MA, Weisblum B, Gellman SH (2004) J Am Chem Soc 126:6848
71. Eldred SE, Pancost MR, Otte KM, Rozema D, Stahl SS, Gellman SH (2005) Bioconjug Chem 16:694

72. Appella DH, Christianson LA, Karle IL, Powell DR, Gellman SH (1996) J Am Chem Soc 118:13071
73. Appella DH, Christianson LA, Klein DA, Richards MR, Powell DR, Gellman SH (1999) J Am Chem Soc 121:7574
74. Appella DH, Christianson LA, Karle IL, Powell DR, Gellman SH (1999) J Am Chem Soc 121:6206
75. Seebach D, Overhand M, Küuhnle FNM, Martinoni B, Oberer L, Hommel U, Widmer H (1996) Helv Chim Acta 79:913
76. Seebach D, Ciceri PE, Overhand M, Jaun B, Rigo D, Oberer L, Hommel U, Amstutz R, Widmer H (1996) Helv Chim Acta 79:2043
77. Seebach D, Gademann K, Schreiber JV, Matthews JL, Hintermann T, Jaun B, Oberer L, Hommel U, Widmer H (1997) Helv Chim Acta 80:2033
78. Arvidsson PI, Rueping M, Seebach D (2001) Chem Commun 649–650
79. Cheng RP, DeGrado WF (2001) J Am Chem Soc 123:5162
80. Cheng RP, DeGrado WF (2002) J Am Chem Soc 124:11564
81. Hayen A, Schmitt MA, Ngassa FN, Thomasson KA, Gellman SH (2004) Angew Chem Int Ed 43:505
82. Schmitt MA, Choi SH, Guzei IA, Gellman SH (2005) J Am Chem Soc 127:13130
83. Raguse TL, Lai JR, Gellman SH (2002) Helv Chim Acta 85:4154
84. Hart SA, Bahadoor ABF, Matthews EE, Qiu XYJ, Schepartz A (2003) J Am Chem Soc 125:4022
85. Glättli A, Seebach D, van Gunsteren WF (2004) Helv Chim Acta 87:2487
86. Elstner M, Hobza P, Frauenheim T, Suhai S, Kaxiras E (2001) J Chem Phys 114:5149
87. Elstner M, Porezag D, Jungnickel G, Elsner J, Haugk M, Frauenheim T, Suhai S, Seifert G (1998) Phys Rev B 58:7260
88. MacKerell AD Jr (1998) J Phys Chem B 102:3586
89. Torrie GM, Valleau JP (1977) J Comput Phys 23:187
90. Bondar A, Fischer S, Smith JC, Elstner M, Suhai S (2004) J Am Chem Soc 126:14668
91. Bondar A, Elstner M, Suhai S, Smith JC, Fischer S (2004) Structure 12:1281
92. Bondar A, Suhai S, Fischer S, Smith JC, Elstner M (2007) J Struct Biol 157
93. Fischer S, Karplus M (1992) Chem Phys Lett 194:252
94. Sadhukhan S, Munoz D, Adamo C, Scuseria GE (1999) Chem Phys Lett 306:83
95. Silverman DN, Lindskog S (1988) Acc Chem Res 21:30
96. Håkansson K, Carlsson M, Svensson LA, Liljas A (1992) J Mol Biol 227:1192
97. Riccardi D, Schaefer P, Yang Y, Yu H, Ghosh N, Prat-Resina X, Konig P, Li G, Xu D, Guo H et al (2006) J Phys Chem B 110:6458
98. Riccardi D, Cui Q (2007) J Phys Chem A 111:5703
99. Silverman DN (1995) Methods Enzymol 249:479
100. Riccardi D, König P, Prat-Resina X, Yu H, Elstner M, Frauenheim T, Cui Q (2006) J Am Chem Soc 128:16302
101. Riccardi D, Koenig P, Guo H, Cui Q (2008) Biochem 47:2369
102. Koenig P, Ghosh N, Hoffman M, Elstner M, Tajkhorshid E, Frauenheim T, Cui Q (2006) J Phys Chem A 110:548
103. de Grotthuss CJT (1806) Ann Chim 58:54
104. Mohammed OF, Pines D, Dreyer J, Pines E, Nibbering ETJ (2005) Science 310:83
105. Voth GA (2006) Acc Chem Res 39:143

CHAPTER 15

SOLVATION OF HYDROGEN BONDED SYSTEMS: CH···O, OH···O, AND COOPERATIVITY

STEVE SCHEINER

Department of Chemistry & Biochemistry, Utah State University, Logan, UT 84322-0300, USA, e-mail: scheiner@cc.usu.edu

Abstract: The effect of solvation upon hydrogen bonds is assessed by a number of computational techniques. The SCRF approach and its more refined variants, which treat the solvent as a polarizable continuum, are compared with results obtained via treatment of discrete interactions with individual solvent molecules. The effect of solvation upon CH··O H-bonds is very much like its influence upon conventional OH··O bonds. Results obtained with a continuum model of solvent are not altered much by explicit inclusion of a first hydration sphere. The H-bond energy arising from the $C^{\alpha}H$ group of amino acids is fairly substantial and can even exceed the NH··O H-bond energy in certain conformations of a polypeptide. On the other hand, both H-bonds rapidly weaken when placed in an aqueous environment. Chains composed of CH··O bonds show a comparable degree of cooperativity as do OH··O bonds. When placed in a polarizable medium, the cooperativity lessens along with the strength of the individual H-bonds. The functional side chains of certain amino acids, such as histidine, can form H-bonds simultaneously at a number of sites. Multiple H-bonds follow the usual patterns of positive and negative cooperativity found within one-dimensional H-bonded chains. The calculated solvation energy of the pertinent molecule in polarizable medium is considerably smaller than the combined interaction energy of the molecule and its surrounding water molecules. However, this difference is much smaller when each H-bond energy is computed not in vacuo, but rather within a polarizable medium

15.1. INTRODUCTION

The earliest applications of quantum chemistry were targeted toward molecules in the gas phase. This was in part due to an interest in such an environment which allows researchers to focus on the intrinsic properties of the molecule of interest. But also, since much of practical chemistry takes place in solution of some sort, this environment presents an important avenue of inquiry as well. However, such solvated systems were typically out of reach of quantum calculations. For one thing, the inclusion of a number of solvent molecules into the calculations would commonly take the system beyond the capabilities of computers at the time. Secondly, solvent

S. Canuto (ed.), Solvation Effects on Molecules and Biomolecules, 407–432.
DOI 10.1007/978-1-4020-8270-2_15,

systems are anything but static, as the solvent molecules move very quickly from one site to another, and rotate as well.

Over the course of time, ways were devised to treat such complex solvated systems. One direction involved dynamics calculations which followed the motions of the molecules over the course of brief timeframes. The motions were guided by empirical force fields that were devised to approximate the interactions between the various molecules. Another avenue of attack employed the strategy of averaging these motions in a way that also incorporated the mutual polarizations of the solute and its surrounding solvent. The primary means of including solvation into quantum calculations in the early years was thus via some variant of the Onsager ideas [1] of immersing the system within a polarizable continuum, with a dielectric constant ε. The charge distribution of the solute induces a so-called reaction field within the medium, which then acts back upon the solute. These changes are computed in a self-consistent manner, leading to their designation as the self-consistent reaction field (SCRF) approach. The most primitive of such methods is the original implementation of the Onsager formalism [1,2,3] wherein the only component of the charge distribution considered is the dipole moment, and the cavity is restricted to a simple spherical shape, even if the solute itself is far from spherical. Despite its approximate nature, this approach found a great deal of use over the years.

Over the last decade or two, this technique has been refined in a number of ways. Good reviews of this field have been published in the last few years, [4,5,6] to which the reader is enthusiastically referred to for some historical perspective, as well as more detail about the methods and their improvements.

It is one thing to consider the solvation of a relatively nonpolar system, such as an inert gas atom or a hydrocarbon. In such a case, there will be only very weak specific interactions with the solvent molecules, so a polarizable continuum model seems at first blush to be a very reasonable approximation. However, if the solute is a polar system, which can form very specific, highly directional, and relatively strong hydrogen bonds with the solvent molecules, this sort of treatment would appear more problematic. Nevertheless, past work has shown evidence that the approach can have some real successes. A 1997 study of tautomerism of triazolopyrimidines [7] calculated equilibria that were in good agreement with the ^{15}N NMR spectroscopy data. Likewise, the equilibrium between neutral and zwitterionic forms of the amino acid glycine was handled well [8]. Indeed, a series of calculations have demonstrated that this treatment can work well for solvated radicals [8,9,10,11] of various sorts. And even much larger systems, such as a protein like ubiquitin [12], have recently been shown to be within reach of this approach.

A good deal of work over the last decade or two has brought to light the fact that a CH group can function as a proton donor in a hydrogen bond [13,14,15,16,17,18,19,20,21,22,23,24,25,26,27,28]. This work continues to this day, with unabated vigor [29,30,31,32,33,34,35,36,37,38,39,40,41,42]. Our own group has been active in this field as well, considering the fundamental properties of these CH··O interactions [43,44,45,46,47], including spectroscopic properties [48], and their implications for biological systems [49]. The focus of the present chapter

concerns a comparison of CH··O H-bonds with their more conventional NH··O and OH··O cousins. In particular, we focus upon how the two sorts of H-bonds differ with respect to their response to solvation. And in the latter respect, a good deal of attention is paid to inclusion of specific interactions with discrete solvent molecules as a counterpoint to a broad polarizable continuum treatment.

The review begins with a very brief summary of some early results achieved with an overly simplified solvation approach. The next section describes a number of variants of a more sophisticated continuum technique, and how the results differ. Attention then shifts to larger, biologically important systems such as amino acids, their functional side chains, and thence to dipeptides. The last major section deals with the phenomenon of H-bond cooperativity and how this property might differ for CH··O as compared to OH··O H-bonds. In a number of places, there is some discussion as to how one might introduce specific interactions with a small number of discrete solvent molecules, within the general framework of the continuum approach.

15.1.1. Early Applications of Rudimentary SCRF

As indicated above, the early considerations of solvent effects took a simplified approach, wherein the cavity in which the solute was placed was taken as spherical, and the dipole of the solute was considered to the exclusion of higher multipoles. As one example, this group [50] applied this method to a series of HX molecules (X = F, Cl, Br) that formed a H-bond with each of a set of amines. HBr is the strongest of the HX acids considered, and the various degrees of methylation of amines led to a progression of basicity from NH_3 to NMe_3. The "pull" on the proton from X to N was quantified in terms of a normalized proton affinity difference (NPAD) between the two subunits. All the HX··amine pairs were found to be neutral pairs, but the degree of proton transfer from X to N grew modestly as either the acidity of HX or basicity of the amine was enhanced. On the other hand, when immersed in a dielectric medium, the amount of proton transfer was magnified. The sensitivity of the degree of proton transfer to dielectric constant of the medium was fairly small for HF, larger for HCl, and quite large for HBr. Indeed, a number of the H-bonded complexes suffered enough of a proton transfer that they would be better characterized as $^{-}X\cdots HN^{+}$ ion pairs within polarizable medium. The better stabilization of the ion pair than a neutral pair is easily predictable, based upon the much higher dipole of the former. An interesting finding to emerge from that work was how different the three HX acids behave with regard to their sensitivity to the polarizability of the medium.

Another early effort in this direction [51] considered the competition for the bridging proton within the H-bond connecting a formate $HCOO^{-}$ anion and an imine base of the sort $HN{=}CH_2$. In the gas phase, it was found that the neutral pair $HCOOH\cdot\cdot NHCH_2$ was preferred over an ion pair. However, again as in the aforementioned XH··amine complexes, the ion pair is progressively more favored as the dielectric constant of the medium rises. More specifically, in an in vacuo situation, the neutral pair in which the proton resides on the carboxylate rather than the imine

is preferred by about 20 kcal/mol. Raising the dielectric constant from unity first equalizes the energies of the neutral and ion pair states, but further growth of ε results in preferential stabilization of the $HCOO^{-}\cdot{}^{+}HNHCH_2$ ion pair, i.e., proton transfer from carboxylate to imine. An interesting conclusion of this study was the sensitivity of the proton transfer energetics to the precise orientation of the H-bond within the $HCOOH\cdot\cdot NHCH_2$ complex. In fact, the angular aspects of the H-bond were found to couple with the medium's polarizability so as to either facilitate or mitigate against the transformation from neutral to ion pair.

15.2. SOLVATION OF CH··O AND OH··O H-BONDS

Over the last years, the basic concepts embedded within the SCRF formalism have undergone some significant improvements, and there are several commonly used variants on this idea. To exemplify the different methods and how their results differ, one recent work from this group [52] considered the sensitivity of results to the particular variant chosen. Due to its dependence upon only the dipole moment of the solute, the older approach is referred to herein as the "dipole" variant. The dipole method is also crude in the sense that the solute is placed in a spherical cavity within the solute medium, not a very realistic shape in most cases. The polarizable continuum method (PCM) [53,54,55] embeds the solute in a cavity that more accurately mimics the shape of the molecule, created by a series of overlapping spheres. The reaction field is represented by an apparent surface charge approach. The standard PCM approach utilizes an integral equation formulation (IEF) [56,57]. A variant of this method is the conductor-polarized continuum model (CPCM) [58] wherein the apparent charges distributed on the cavity surface are such that the total electrostatic potential cancels on the surface. The self-consistent isodensity PCM procedure [59] determines the cavity self-consistently from an isodensity surface. The UAHF (United Atom model for Hartree–Fock/6-31 G*) definition [60] was used for the construction of the solute cavity.

This particular set of calculations focused on CH··O sorts of H-bonds, and compared the data with the more conventional OH··O H-bond found in the classical water dimer. The CH··O interactions were constructed by pairing CH_4 and its fluorosubstituted derivatives with OH_2 as proton acceptor. The solvation energies computed for F_3CH by each of several different methods are reported in the first four rows of Table 15-1 for three different solvents, each with its own characteristic dielectric constant ε. The next four rows refer to HOH, followed by the $F_3CH\cdot\cdot OH_2$ complex. Moving from left to right in Table 15-1 corresponds to progressively more polar solvent, beginning with CCl_4 with a dielectric constant of 2.2, to water with ε=78.4. Intermediate between these two extremes lies ether, with a dielectric constant of 4.3. In nearly all cases, the solvation energy rises (becomes more negative) as the dielectric constant of the solvent increases. The values obtained with the most primitive Dipole method tend to be smaller in magnitude than those corresponding to the other procedures, in some cases much smaller (by a factor of 2 or 3). The PCM, CPCM,

Table 15-1. Solvation energies (kcal/mol) computed for $F_3CH{\cdot\cdot}OH_2$ and its individual subunits at the B3LYP/6-31+G** level

Species	Method	$\varepsilon = 2.2$	$\varepsilon = 4.3$	$\varepsilon = 78.4$
F_3CH	Dipole	–0.34	–0.53	–0.78
	PCM	–0.61	–1.25	–2.52
	CPCM	–0.75	–1.41	–2.54
	SCI-PCM	–1.09	–1.73	–2.61
HOH	Dipole	–0.95	–1.48	–2.14
	PCM	–1.73	–3.67	–7.70
	CPCM	–2.17	–4.17	–7.77
	SCI-PCM	–2.35	–3.70	–5.45
$F_3CH{\cdot\cdot}OH_2$	Dipole	–1.47	–4.05	–3.40
	PCM	–2.05	–4.05	–8.06
	CPCM	–2.42	–4.47	–8.12
	SCI-PCM	–2.71	–4.47	–6.02
Contribution of solvation energy to binding energy[a]				
$F_3CH{\cdot\cdot}OH_2$	Dipole	–0.18	–2.04	–0.48
	PCM	0.29	0.87	2.16
	CPCM	0.50	1.11	2.19
	SCI-PCM	0.73	0.97	2.05

[a]Computed as difference between complex and sum of subunits.

and SCIPCM methods yield generally similar solvation energies, albeit with some residual variation from one method to the next.

Perhaps more important than the solvation energies of any of the individual species are the *differences* between the complex on one hand, and the sum of its constituents on the other. These differences correspond to the effect of each solvent upon the interaction energy, that is the correction that must be added to the gas-phase H-bond energy. As listed in the bottom section of Table 15-1, these quantities are positive for the three PCM methods, indicating that the interaction energy is smaller (less negative) in solvent compared to vacuum. Indeed, the deviations between these three methods with regard to the all-important ΔE_{solv} are considerably smaller than the variations in the solvation energies of the individual species. These ΔE_{solv} values are roughly 0.5, 1.0, and 2.1 kcal/mol, in CCl_4, ether, and water, respectively. In striking contrast, the more primitive Dipole approach predicts the opposite result that interaction energies in solvent are more negative than in vacuo, as denoted by the negative values in the Dipole row of ΔE_{solv}.

Gas-phase interaction energies are reported in the second column of Table 15-2 for the CH··O H-bond contained in $F_3CH{\cdot\cdot}OH_2$, where the trends may be compared with the classical H-bond of the water dimer. The two interaction energies do not differ much, with the latter being stronger by some 23–33%, with values supplied both at

Table 15-2. Interaction energies (kcal/mol) computed for the complexes combining F_3CH and HOH as proton donors to OH_2 with the 6-31+G** basis set

System	Gas phase[a]	Method	ε = 2.2		ε = 4.3		ε = 78.4	
			DFT	HF	DFT	HF	DFT	HF
$F_3CH\cdot\cdot OH_2$	–4.16	Dipole	–4.35	–4.56	–6.20	–4.98	–4.64	–5.57
	(–3.88)	PCM	–3.88	–3.46	–3.30	–2.76	–2.00	–1.28
		CPCM	–3.66	–3.22	–3.05	–2.49	–1.98	–1.25
		SCIPCM	–3.44	–2.92	–3.19	–2.25	–2.11	–1.28
$HOH\cdot\cdot OH_2$	–5.54	Dipole	–6.05	–4.94	–6.43	–5.10	–6.99	–5.34
	(–4.78)	PCM	–5.27	–4.37	–4.65	–3.64	–3.13	–1.97
		CPCM	–5.05	–4.13	–4.40	–3.37	–3.10	–1.94
		SCIPCM	–5.02	–3.96	–4.63	–3.39	–4.05	–2.58

[a]HF value in parentheses.

the B3LYP and HF levels. The data reported in the ensuing columns represent the interaction energies within the indicated solvents. The interaction energies computed for each system with the PCM, CPCM, and SCIPCM methods all tend to be quite similar to one another, regardless of which solvent is considered. There is a tendency for the PCM method to yield the most negative interaction energy and SCIPCM the least negative, but again, the differences between these three methods are fairly small. The primitive Dipole approximation, on the other hand, is frequently quite at odds with the results of the other methods. Taking the $F_3CH\cdot\cdot OH_2$ system in aqueous solvent as an example, the DFT interaction energies of the former three methods lie in the range between –2.0 and –2.1 kcal/mol, while the dipole value is more than double the magnitude, at –4.6 kcal/mol. Due to the agreement between the PCM, CPCM, and SCIPCM methods, and the fact that CPCM data tend to fall approximately midway between the extremes of the other two, most of the following narrative and analysis make use of the CPCM results.

The trends in the computed interaction, i.e., H-bond, energies may be visualized in Figure 15-1 which plots the correlated B3LYP value of ΔE vs the Onsager function $F_o = (\varepsilon-1)/(\varepsilon+2)$ that relates ε to the permanent electric moment and polarizability of each solvent molecule [1,2]. Note that F_o is equal to zero for the gas phase wherein ε=1, and climbs to an asymptote of unity as the solvent becomes progressively more polar and ε approaches ∞. The high value of ε for water leads to a F_o of 0.96, rather close to the theoretical limit of 1.0. This figure includes data not only for $F_3CH\cdot\cdot OH_2$, but also for other degrees of fluorosubstitution of the methane. In all cases, the rise in polarity of the solvent leads to a less negative value of ΔE, i.e., a weakening of the H-bond. This rise is very nearly a linear function of F_o and also reasonably regular in the sense that the energetic ordering of the various H-bonds remains the same, regardless of the solvent. As the solvent becomes more polar, the spacing between the energies of the systems is reduced by a certain amount. For example, $F_3CH\cdot\cdot OH_2$ is more strongly bound than $F_2CH_2\cdot\cdot H_2O$ by 1.30 kcal/mol in the gas phase, but this

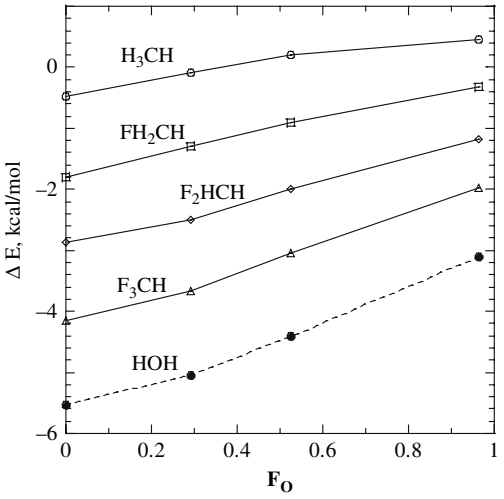

Figure 15-1. B3LYP interaction energies computed for each labeled proton donor with water as acceptor. Onsager function F_o is equal to $(\varepsilon-1)/(\varepsilon+2)$ where ε refers to dielectric constant of the medium

advantage is diminished to 0.81 kcal/mol in water. It is important to note that the conventional OH··O H-bond of the water dimer behaves in very much a parallel fashion to the four CH··O bonds illustrated in Figure 15-1, weakening at a similar rate as ε increases.

The continuum model suffers from the obvious deficiency that it ignores specific interactions with solvent molecules. Any deficit of this approach ought to be particularly noticeable in the case of aqueous solvation, and the strong H-bonding interactions of neighboring water molecules. A first approximation to elucidate the magnitude of the errors introduced by this omission might be the inclusion of a first hydration shell around all pertinent entities. And indeed, this approach has witnessed some real success in recent years [4,5,6,8,9,10,11,61]. The $F_3CH\cdot\cdot OH_2$ complex was hence surrounded by a first sphere of explicit water molecules. There are five peripheral atoms in $F_3CH\cdot\cdot OH_2$, three F and two H, and one solvating water was permitted to interact with each. Of course, the F atoms of F_3CH served as proton acceptors to these solvating molecules, and the H atoms of OH_2 as donors, as illustrated in Figure 15-2. As in the case of the complexes themselves, all H-bonds were held to be linear ($\theta_{OH\cdot\cdot X}$=180°). Following geometry optimization, the solvated complex was then placed in the larger cavity of the SCRF water dielectric continuum that contains not only the $F_3CH\cdot\cdot OH_2$ complex, but also the five explicit solvent molecules. In the next step, each of the two constituent subunits of $F_3CH\cdot\cdot OH_2$ was permitted to interact with the appropriate number of explicit water molecules, as pictured in the upper part of Figure 15-2, and was likewise placed within the dielectric medium. The H-bond energy of this complex was then calculated as the difference in energy between the solvated complex and the sum of the two hydrated subunits.

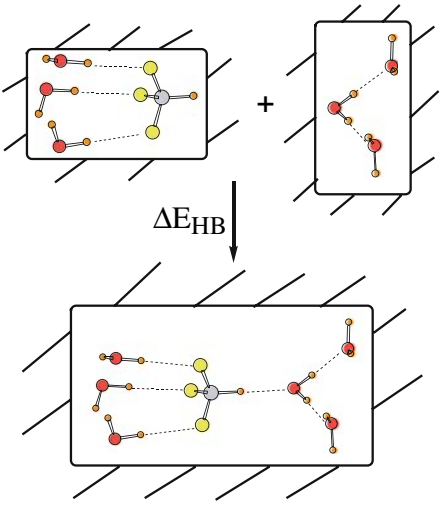

Figure 15-2. Geometries of partially solvated F_3CH and OH_2, and their complex $F_3CH\cdots OH_2$, all embedded in a dielectric continuum

In order to insure a fair comparison with the OH··O bond in the water dimer, the $HOH\cdot\cdot OH_2$ complex was also surrounded by five waters, three around the proton donor and two around the acceptor. (One of the molecules solvating the donor molecule was situated around its peripheral H, the other two donated protons to this molecule's lone pairs.)

The H-bond energies of the $F_3CH\cdot\cdot OH_2$ and $HOH\cdot\cdot OH_2$ complexes, computed in this manner, were –3.2 and –4.8 kcal/mol, respectively. These values are surprisingly similar to the H-bond energies, –2.0 and –3.1 kcal/mol, obtained above in aqueous solvent modeled as a dielectric continuum, with no explicit solvent molecules at all. Also of some importance, the pure continuum result that $HOH\cdot\cdot OH_2$ is more tightly bound than $F_3CH\cdot\cdot OH_2$ in aqueous solvent by 1.1 kcal/mol is changed only slightly, to 1.6 kcal/mol, upon explicit introduction of the first hydration sphere. In this case at least, while the continuum model is certainly not absolutely accurate in a quantitative sense, it does appear to provide very reasonable approximations to the environments it is meant to reproduce.

15.3. BIOLOGICALLY IMPORTANT H-BONDS

The CH··O H-bonds of the foregoing section placed the CH group on a fluorosubstituted methane. Of some interest is this same CH group within the context of a system that might occur in a protein, particularly as detailed calculations had provided some support for the notion that a CH··O sort of H-bond might be especially important as an element in protein structure and stability.

15.3.1. Amino Acids

In particular, a series of various amino acids [62] were paired up with a water molecule. The latter was positioned such that it could accept a proton from the $C^{\alpha}H$ group that is common to all amino acids. Calculations at a correlated MP2 level, with a moderate sized 6-31+G** basis set indicated the strength of the ensuing $C^{\alpha}H{\cdot\cdot}O$ H-bond to be surprisingly large, in excess of 2 kcal/mol, even after correction for basis set superposition error. This quantity is roughly half of that of the strength of a conventional H-bond, such as the $OH{\cdot\cdot}O$ interaction in the water dimer, at the same level of theory. Another somewhat surprising finding was that the interaction energy in the pairing of the amino acid with water had very low sensitivity to the identity of the particular amino acid. For example, the latter property was computed to be 2.1 kcal/mol for alanine and 2.0 for valine. Serine, with its hydroxyl group, was very close to this amount at 2.3 kcal/mol, and Cys's SH yielded a value of 1.9. It is reiterated that the H-bond being examined here does not involve the side chain directly, but rather the $C^{\alpha}H$ group in each case. The quantum calculations of this specific interaction had also revealed that the $C^{\alpha}H$ covalent bond is contracted by some 1–3 mÅ by the interaction, which also shifted the stretching frequency of this bond to the blue by 20–50 cm^{-1}.

The first entry of Table 15-3 reports the interaction energy computed for the H-bond between the $C^{\alpha}H$ group of alanine and a water molecule, at the MP2/6-31 + G** level, in vacuo, i.e., without any medium present at all. The entry immediately below indicates that this same H-bond energy rises slightly from 2.9 to 3.6 kcal/mol when the methyl group of Ala is replaced by the CH_2OH group of serine. When the entire dimer, consisting of amino acid (AA) plus one explicit water molecule positioned so as to interact with the $C^{\alpha}H$, is immersed in a continuum of dielectric constant 78 so as to simulate an aqueous environment, the interaction is no longer attractive, as noted in the second column of Table 15-3. Specifically, the solvation energy of the amino acid–water pair is *less* stabilizing than is the sum of this same quantity for the amino acid and water molecule, each computed separately. One may thus conclude that there is indeed an interaction between the $C^{\alpha}H$ group and a water molecule acceptor that is far from negligible, at least in the gas phase. On the other hand, this attraction is reduced, perhaps to the point of vanishing altogether if the dimer is immersed in aqueous solvent.

Table 15-3. $C^{\alpha}H{\cdot\cdot}O$ H-bond energy (kcal/mol) as computed in different ways

	AA + 1 water		AA–MeAA[a]	
	QM	QM+CPCM	CPCM	CPCM-reopt
Ala	2.9	Not attractive	3.7	4.2
Ser	3.6	Not attractive	4.1	4.8

[a]Comparison of CPCM solvation energies of AA and methylated AA.

As above, a major doubt about this solvation model stems from the fact that the continuum approach does not treat any individual H-bond explicitly. Another major consideration in this case is that any H-bond involving the $C^{\alpha}H$ group would clearly be weaker than the numerous and more conventional OH··O or NH··O bonds in which an amino acid is engaged. Might this weaker CH··O interaction be hidden in the "wash" of a surrounding polarizable medium?

It is not a trivial task to design a set of calculations which will unambiguously and clearly assess the strength of a particular H-bond, when the method as such does not address individual bonds. In other words, a quantum chemical calculation can simply add the water molecule to the amino acid, in the position of interest, as described above. But a continuum approach places the entire molecule inside a cavity hollowed out of the dielectric material, so in principle handles all possible H-bonds collectively, some of which would be much stronger than the CH··O interaction of interest. And moreover, the dielectric does not explicitly deal with all the aspects of a H-bond, such as charge transfer.

One strategy to deal with this issue might be to consider a pair of molecules, one with and one without the possibility of the pertinent $C^{\alpha}H$··O interaction. The situation for the amino acid alanine is illustrated in Figure 15-3a which explicitly indicates the $C^{\alpha}H$ group. By replacing this H atom by a methyl group, as illustrated in Figure 15-3b, the $C^{\alpha}H$ is no longer available to form a H-bond, while the remainder of the amino acid is essentially unaffected. Immersion of both of these systems in a dielectric continuum permits the same sorts of interactions to occur between the medium and each of the groups, most importantly COOH and NH_2, leaving the only substantive difference as the $C^{\alpha}H$ group in Figure 15-3a replaced by a methyl group in Figure 15-3b.

When Ala and Me-Ala, both fully optimized in vacuo, were placed into the polarizable medium, with dielectric constant 78 to simulate water, the total solvation energies were computed to be –14.45 and –10.80 kcal/mol, respectively. One can take

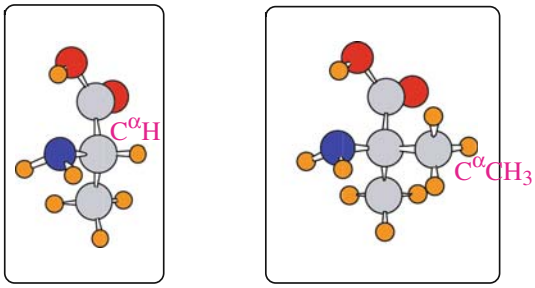

Figure 15-3. (**a**) Alanine and (**b**) methylalanine both fully optimized. Rectangular outline represents cavity carved out of dielectric medium in which the two molecules are embedded. Actual cavity is more closely akin to shape of each molecule

the greater stabilization of the former, by 3.65 kcal/mol, to represent an approximation of the amount contributed by the $C^{\alpha}H$ group, since this group is not present in the latter molecule. This quantity is reported in the third column of Table 15-3, where it is obviously somewhat larger in magnitude than the energy computed directly for the specific $C^{\alpha}H{\cdot\cdot}O$ H-bond by quantum mechanical means. This overestimate of the $C^{\alpha}H{\cdot\cdot}O$ contribution can be seen in the next row of Table 15-3 to extend also to the serine residue. The final column of Table 15-3 indicates that a reoptimization of the geometries of all species concerned within the framework of the aqueous dielectric exaggerates the overestimate by another 0.5–0.7 kcal/mol. On the positive side, this rather crude means of estimating the contribution of one particular H-bond to the full panoply of solvation effects is surprisingly close to the full quantum mechanical value, at least the in vacuo estimate. The overestimation is even more severe when compared to the case of the Ala–water complex when immersed in an aqueous dielectric continuum, wherein the interaction is in fact nonattractive. The exaggeration of the bond strength cannot be attributed directly to the dipole moment, as the values for Ala and Me-Ala are very close, 7.27 and 7.17 D, respectively. One may thus conclude that the stabilizing effect of the $CH{\cdot\cdot}O$ H-bond that is formed by the $C^{\alpha}H$ group of amino acids is simulated by the replacement of the H-bond itself by a dielectric continuum model to only a very modest level of accuracy.

15.3.2. Dipeptide

The preceding section has dealt with each amino acid without connection to another, in which the $C^{\alpha}H$ is flanked by COOH and NH_2 groups. Of perhaps greater relevance to a polypeptide chain would be surrounding the $C^{\alpha}H$ by full peptide groups. Calculations have been carried out of the relevant $HCONHC^{\alpha}H_2CONH_2$ dipeptide system [63] which was paired with a formamide $HCONH_2$ proton acceptor. The dipeptide is prone to one of two conformations which represent minima on the potential energy surface. The C7 and C5 conformers are named in this manner so as to indicate the number of atoms in the H-bonded cycle. For each conformation, the O atom of the formamide was brought up first to the NH group of the dipeptide, and then to the $C^{\alpha}H$; geometry optimizations led to estimates of the H-bond energy. The results, reported in Table 15-4, indicate that the strength of the $C^{\alpha}H{\cdot\cdot}O$ bond amounts to some 2–4 kcal/mol, depending upon the precise level of theory. There is a tendency for this interaction to be somewhat stronger in the C5 conformer, similar to the structure adopted by the β-sheet of proteins. The strength of the $NH{\cdot\cdot}O$ bond, on the other hand, is highly sensitive to dipeptide conformation, being three to five times stronger for C7 as compared to C5. This weakness leads to the even more surprising conclusion that the $NH{\cdot\cdot}O$ H-bond is weaker than its $C^{\alpha}H{\cdot\cdot}O$ correlate in the C5 geometry.

The weakness of the nominally strong $NH{\cdot\cdot}O$ bond when placed within the context of the C5 conformer is indeed startling. The preceding result pertains to the in vacuo situation, so it was deemed important to examine its sensitivity to solvation phenomena. If the $NH{\cdot\cdot}O$ H-bond is so much weaker in the C5 structure, then one

Table 15-4. Intermolecular H-bond energies between dipeptide and formamide[a]

	NH··O	$C^{\alpha}H$··O
C7		
MP2/6-31+G**	–7.4	–2.8
B3LYP/6-31+G**	–7.2	–2.4
HF/6-31+G**	–7.2	–2.2
HF/6-31 G*	–7.0	–2.0
C5		
MP2/6-31+G**	–2.5	–3.8
B3LYP/6-31+G**	–1.6	–2.9
HF/6-31+G**	–1.5	–2.8
HF/6-31 G*	–1.3	–2.5

[a]Including counterpoise correction.

might expect the solvation energy of C5 to be correspondingly smaller than for C7. However, this supposition was shown to be faulty: the solvation energies of the two structures are identical to within 4%, when immersed within an aqueous polarizable continuum. This finding provides another indication that the neglect of specific H-bonds by the continuum model can lead to important deficiencies. In fact, the anomalous weakness of the NH··O H-bond in the C5 dipeptide has been traced to the proximity of the carbonyl O to the proton-donating NH group [64]. This O atom perturbs the electrostatic potential in the vicinity of the NH, making this group less attractive to an oncoming proton acceptor.

Turning now to an assessment of the H-bond energies within a dielectric medium, via explicit inclusion of both the dipeptide and the formamide, relevant data are reported in Table 15-5 for the more stable C7 conformer. A dielectric constant of

Table 15-5. Interaction energies (kcal/mol) computed at the B3LYP/6-31+G** level for the C7 dipeptide, using various dielectric constants

ε	NH··O	$C^{\alpha}H$··O
ΔE[a]		
1	–7.5	–2.6
4.3	–2.0	+1.8
78	+1.5	+1.3
ΔE_{unopt}[b]		
1	–7.5	–2.6
4.3	–1.9	+2.0
78	+1.6	+4.1

[a]Geometry optimized in solvent; no counterpoise correction.
[b]Gas-phase geometry, no counterpoise correction.

4.3 is commonly considered most appropriate to the interior of a protein, while 78 refers explicitly to water. The data displayed in Table 15-5 indicate how quickly the interaction energy is reduced as the medium becomes more polarizable. Indeed, even when ε is as small as 4.3, the $C^{\alpha}H{\cdot\cdot}O$ interaction energy becomes positive, indicating loss of its attractive nature. Both the NH··O and $C^{\alpha}H{\cdot\cdot}O$ bonds lose their binding character in water, according to this formalism.

15.4. COOPERATIVITY

One of the most interesting and often overlooked aspects of hydrogen bonding is cooperativity. By that is meant the concept [65,66] that the total interaction energy in a trimer of the sort AH··BH··CH is typically somewhat different than the sum of H-bond energies in AH··BH and BH··CH, when evaluated separately. When the full trimer system is more strongly bound than the sum of dimers, this sort of cooperativity is commonly referred to as positive, in contrast to the negative cooperativity that is associated with a weakened interaction in the full trimer.

There are several contributing causes to cooperativity, but the simplest and most obvious rationale is that when a pair of molecules pair up as in AH··BH, the electron distributions of each monomer are perturbed. In this example, the BH proton usually acquires a more positive charge as electron density is drawn out of BH and deposited on AH. The higher positive charge of the latter H makes BH a stronger proton donor when CH is added to the growing chain, than would be the case were BH not involved in a prior H-bond with AH. Negative cooperativity is often observed when a single molecule acts as double donor. Taking a group of water molecules as an example, the transfer of electron density from the second to the first molecule of $HOH{\cdots}OH_2$ would reduce the partial positive charge of the first H. Addition of a third molecule to the left of this chain, as in $H_2O{\cdot\cdot}HOH{\cdots}OH_2$, would therefore result in a weaker H-bond than if it were simply appended to a single water molecule.

15.4.1. One-Dimensional Chains

Cooperativity, in both its positive and negative manifestations, is easily assessed in quantum chemical calculations that include all links in a chain explicitly. And indeed, numerous calculations over the years [67,68,69,70,71,72,73,74,75,76, 77,78,79,80] have supported the notion that a series of conventional H-bonds, as might occur in a chain of water molecules depicted in Figure 15-4a, exhibits positive cooperativity. The most prominent manifestation of this feature is that the total binding energy of the five molecules shown, comprising four separate H-bonds, is significantly greater than four times the H-bond energy of a water dimer. What was considered more interesting was whether such positive cooperativity would be characteristic also of the less common CH··O interactions [81,82,83,84]. This issue was considered [85] by assembling chains of H_2CO molecules which are held together by such bonds, as in Figure 15-4b. By replacing the nonparticipating H atom of each H_2CO molecule by F, it was possible to examine how the electron-withdrawing

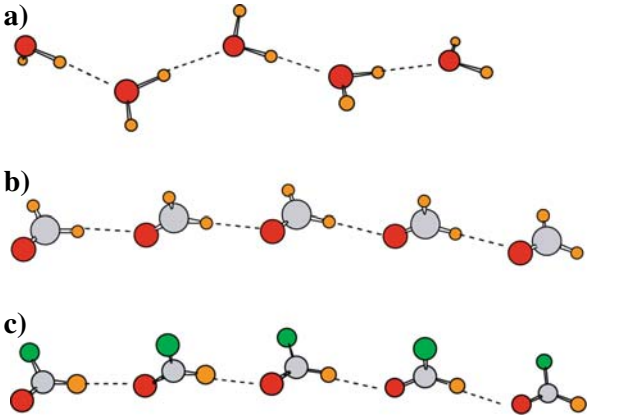

Figure 15-4. Pentameric chains of (**a**) HOH, (**b**) H_2CO, and (**c**) HFCO molecules

nature of the latter atom might affect both the H-bond strength per se, and also the cooperativity in Figure 15-4c.

The strengths of the H-bonds in each chain can be evaluated in a number of different ways. There are "end" bonds which correspond to the energy required to break off one of the terminal molecules:

$$\Delta E_{\text{end}}(n) = E(n) - [E(n-1) - E(1)] \tag{15-1}$$

where $E(m)$ refers to the energy of a chain of m molecules. The breaking of the chain somewhere other than at its end is grouped into the "mid" category:

$$\Delta E_{\text{mid}}(n) = E(n) = [E(n-m) - E(m)] \tag{15-2}$$

where $m>1$. In the case of the tetramer, this midpoint breakage would result in a pair of dimers, while the pentamer would separate into a dimer and a trimer. The final column of Table 15-6 contains a "mean" H-bond energy of the entire n-mer, evaluated as the energy required to break this chain into n individual monomers, divided by *n–1*, the number of H-bonds present:

$$\Delta E_{\text{mean}}(n) = [E(n) - nE(1)]/(n-1) \tag{15-3}$$

This quantity can be derived by pulling the complex apart, one unit at a time, from the end. In other words, $\Delta E_{\text{mean}}(n)$ represents the average of the ΔE_{end} quantities for chains of length *n, n–1, n–2*, etc.:

$$\Delta E_{\text{mean}}(n) = [\Delta E_{\text{end}}(n) + \Delta E_{\text{end}}(n-1) + \cdots + \Delta E_{\text{end}}(2)]/(n-1) \tag{15-4}$$

so it can also be considered as the average end binding energies of the n-mer, and all those smaller than it.

Table 15-6. Energetics (kcal/mol) of H-bonds in chains of length n, calculated at MP2/6-31+G** level, corrected for basis set superposition error

n	End	Mid	Mean
(a) HOH			
2	4.48	–	4.48
3	5.54	–	4.99
4	5.99	7.11	5.27
5	6.21	7.76	5.46
∞	7.43		6.09
(b) H_2CO			
2	1.74	–	1.74
3	1.89	–	1.82
4	1.96	2.13	1.88
5	1.99	2.25	1.91
∞	2.17		2.02
(c) HFCO			
2	2.13	–	2.13
3	2.60	–	2.35
4	2.77	3.23	2.47
5	2.83	3.46	2.55
∞	3.35		2.82

On the grounds of positive cooperativity, it is not surprising to note that the H-bond energy of any of the three systems increases as the chain grows longer, whether ΔE_{end} or ΔE_{mid}. The behavior of the end and mean H-bond energies are both illustrated in Figure 15-5 as a function of (the reciprocal of) the length of the chain. Solid lines refer to the end bonds, broken lines to the means.

As noted in a number of prior works [75,83,86], H-bond energies, and certain other properties, grow very nearly linearly in relation to the reciprocal of the number of monomers in the chain. It thus becomes possible to obtain a valuable estimate of the H-bond energies when extrapolated to chains of infinite length. These values are reported in the indicated rows of Table 15-6. For example, the H-bond energy of the dimer of H_2CO is 1.74 kcal/mol, and grows to 2.17 kcal/mol in the infinite chain, an enhancement of 25%. These percentage increases are 57 and 66% for the HFCO and HOH chains, respectively. It would thus appear that the energetics of cooperativity, even on a percentage basis, are larger for those systems which have stronger H-bonds to begin with. The cooperativity of the HFCO chain is surprisingly large in the sense that its 57% increase is nearly as large as the 66% rise in the water chain, even though the H-bond energy of the HFCO dimer (2.13 kcal/mol) is less than half the magnitude of the 4.48 kcal/mol of the water dimer.

The measure of cooperativity mentioned above focuses on a single H-bond, say the terminal one, and monitors the change in its properties as the chain elongates. Another measure of cooperativity might focus on a given chain length, say a pentamer,

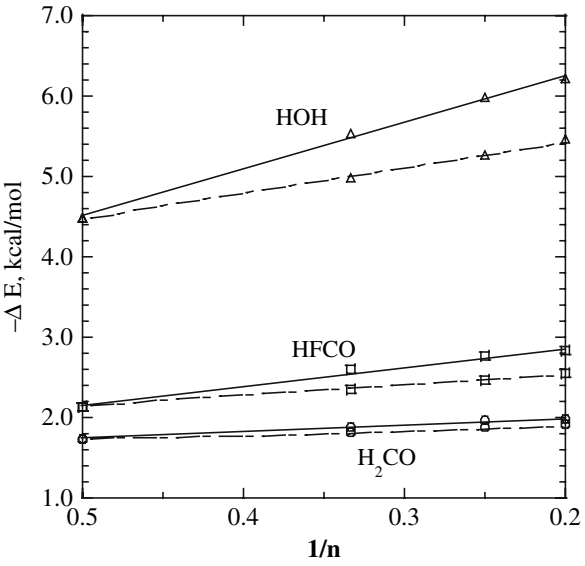

Figure 15-5. MP2/6-31+G** H-bond energies, corrected by counterpoise, computed for chains of *n* monomer subunits. *Solid lines* represent energetics of end H-bonds; mean values derived by breaking the entire chain into monomers are indicated by *broken lines*

and compare the properties of a terminal H-bond, wherein only one of the two participating molecules is interacting directly with others in the chain, with a H-bond occurring in the interior of the chain, in which case both of the partner molecules form H-bonds with other molecules. One may note from Table 15-6 that the energies of the latter type of H-bonds (labeled "mid") are consistently greater than those of the end bonds. This finding is true for CH··O and OH··O bonds alike, consistent with prior work that indicated that H-bond energies are larger within the confines of a chain of amides than on its ends [76]. Taking the pentamers as reference point, the mid H-bonds are stronger than the ends by 13, 22, and 25% for the H_2CO, HFCO, and HOH systems, respectively. Thus, in either means of measuring this quantity, the HFCO systems manifest a cooperativity disproportionately large, when compared with its H-bond energy.

An interesting aspect of cooperativity, and one that has seldom been probed, is how this property is affected by solvation. In order to examine this question, the various H-bonded chains were next immersed in various solvents, each represented by a continuum with the dielectric constant ε characteristic of that solvent. Table 15-7 reports the average H-bond energy (computed as the energy required to break the *n*-mer apart into *n* separate monomers, divided by the number of H-bonds in the chain) for dielectric constants varying from unity (vacuum) up to 78 to represent aqueous solution.

Table 15-7. Energetics (kcal/mol) of "mean" H-bonds in chains of length n, calculated at B3LYP/6-31+G** level, corrected for basis set superposition error, evaluated in solvents with different dielectric constants ε, by CPCM procedure

n	ε = 1 vacuum	ε = 2 CCl_4	ε = 4 ether	ε = 78 water
(a) HOH				
2	4.75	5.03	4.35	2.99
3	5.34	5.48	4.69	3.18
4	5.68	5.74	4.90	3.32
5	5.92	5.94	5.05	3.41
(b) H_2CO				
2	1.65	1.23	0.83	0.21
3	1.75	1.30	0.87	0.21
4	1.81	1.33	0.88	0.20
5	1.86	1.36	0.90	0.20
(c) HFCO				
2	2.08	1.64	1.02	–0.02
3	2.32	1.77	1.11	0.02
4	2.46	1.85	1.15	0.02
5	2.55	1.90	1.18	0.03

Scanning the data from left to right indicates the H-bonds generally weaken as the dielectric constant increases. This pattern is consistent with the idea that separated monomers are more stabilized by interaction with a dielectric continuum than are the H-bonded chains. (There is an interesting exception to this rule for the water chains, which are more tightly bound for ε=2 than in vacuum, but the H-bonds then weaken as ε progresses to higher values.) Placement in solvent retains the general principle of cooperativity, in the sense that the H-bonds strengthen as each chain grows longer.

However, there is a clear lessening of the cooperative effect as the solvent becomes more polar. Taking the H_2CO chains as an example, the mean H-bond energy in the pentamer is greater than that in the dimer by 0.21 kcal/mol in vacuo, whereas this difference diminishes to 0.13 in CCl_4, 0.07 for ε=4, and vanishes entirely in water. A similar reduction in cooperativity is observed in the other CH··O bonded chains involving HFCO. Where the water chains differ is that they retain their energetic cooperativity, even when ε has climbed to 78. Even at this high value of ε, the mean H-bond energy of the water pentamer is 14% higher than that in the monomer.

In summary, the CH··O H-bond mirrors the cooperativity of the more conventional H-bonds, although there are some significant differences as well. Either sort of interaction grows stronger as the number of monomers in the chain increases. The degree of cooperativity is roughly proportional to the strength of the H-bond. Thus, one sees a sharper growth of H-bond strength accompanying chain elongation in the order $(H_2CO)_n < (HFCO)_n < (H_2O)_n$. It is estimated that the mean H-bond

energy in an infinite chain of H_2CO molecules is 25% greater than the same quantity in a dimer, while the long water chain exhibits a 66% enhancement over $(H_2O)_2$. Although containing substantially weaker individual H-bonds than those in water chains, $(HFCO)_n$ manifests an energetic cooperativity that is nearly as large as the OH··O congeners. H-bonds that occur in the interiors of each chain are stronger than terminal H-bonds. The magnification in strength, within the context of the pentamer, is 13, 22, and 25% for the H_2CO, HFCO, and HOH systems, respectively, another indication that the cooperativity is directly related to intrinsic H-bond energy, and that in $(HFCO)_n$ is disproportionately large. Placement of the chains in the context of a dielectric continuum indicates a weakening H-bond, as well as a diminishing degree of cooperativity, with growing dielectric constant. All evidence of cooperativity vanishes for the CH··O chains when ε reaches 78, whereas the OH··O H-bonds strengthen with greater n even at this high value of ε.

15.4.2. Clusters

The preceding discussion of cooperativity had invoked a linear chain of molecules, each link thereof serving as both single proton donor and single acceptor simultaneously. On the other hand, there are a number of different species, some of real biological relevance, which are capable of forming a multiplicity of H-bonds all at the same time. Imidazole (Im) is such a case, and its importance lies in its role as the functional group of the histidine residue of proteins. Figure 15-6 illustrates the primary locations at which water molecules are anticipated to attach to Im. The numerical values in the figure refer to the H-bond energy of that particular water, each computed for a dimeric system containing only the Im plus the pertinent water molecule [87]. The classical H-bond energies of the NH··O and OH··N types amount to 6.0 and 6.7 kcal/mol, respectively, a result that is typical of these sorts of H-bonds. But it is worth noting that the CH··O bonds are far from negligible, contributing more than 2 kcal/mol. Considering that there are three such bonds, their total of 7.0 kcal/mol represents an important contribution to the full solvation. Also important are the water molecules that sit right up above and below the aromatic ring.

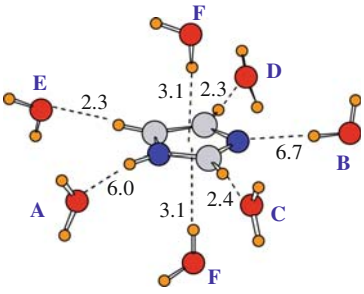

Figure 15-6. Hydration sites around the imidazole molecule. Numbers indicate calculated H-bond energy (kcal/mol) for each individual site [87]

Each of these OH··π bonds contributes another 3.1 kcal/mol to the total 25.9 kcal/mol arising from a summation of all seven interactions.

One important issue, though, is the possibility that the sum of specific interaction energies in the first column of Table 15-8 ignores the potential effects of cooperativity. This issue was addressed [88] in a series of calculations wherein imidazole was combined with two molecules of water at a time. For example, the first row of Table 15-8 indicates that when water molecules were placed on the two imidazole N atoms simultaneously, one as proton acceptor and another as donor (labeled sites A and B, respectively, in Figure 15-6), the total interaction energy was enhanced by 0.4 kcal/mol, representing a slight increase of 3% as compared to the simple summing of the two H-bond energies computed in the presence of one water molecule at a time. Since the imidazole molecule serves in the dual capacity of proton donor and acceptor, it is not surprising that this cooperativity is positive. The remaining rows of Table 15-8 report the comparable results for other pairs of hydration sites. It is clear that negative cooperativity is observed when the central imidazole acts as double proton donor or double acceptor. Sites A and C, for example, both refer to proton acceptor waters, and the total interaction energy is considerably less (12%) than would be predicted from simple summation of individual H-bond energies, computed separately for each dimer. Likewise when sites A and D are combined, both proton acceptors, an even bigger drop of 19% is observed. Site F, hovering over the aromatic ring, is a proton donor by nature, even if it is the π-cloud of imidazole and not a lone pair that accepts the proton. It is therefore sensible to note positive cooperativity when combined with proton acceptor site A, in contrast to negative cooperativity with donor site B. The large negative cooperativity in the last row of Table 15-8, at least on a percentage basis, corresponds to a combination of donor and acceptor, so is puzzling and represents a topic for further exploration.

Given the fact that the cooperativity, both positive and negative, amounts to only small amounts, and coupled with the compensatory effects of positive vs negative

Table 15-8. Energetic cooperativity (kcal/mol) of hydration sites of imidazole

Sites[a]	Simple sum[b]	Explicit calculation[c]	Percentage change
A+B	12.7	13.1	+3.1
A+C	8.4	7.4	–12.0
A+D	8.3	6.7	–19.3
B+C	9.1	9.0	–1.6
B+E	9.0	9.0	0.0
F+A	8.6	9.2	+7.2
F+B	9.3	8.9	–4.1
F+C	5.0	5.0	0.0
F+D	4.9	3.9	–21.0

[a]Sites labeled in Figure 15-6.
[b]Addition of specific H-bond energies computed for dimer.
[c]Total interaction energy for Im+ 2 H_2O.

cooperativity, the addition of the individual H-bond energies for the seven principal hydration sites of imidazole probably represents a reasonably accurate estimate of the full hydration energy that would be computed with all water molecules present simultaneously. One may wonder then how the 25.9 kcal/mol that arises from the above seven specific interactions compares with the solvation energy computed by simply placing the imidazole molecule into a polarizable continuum, with dielectric constant 78 so as to mimic water as a solvent. As indicated in the first row of Table 15-9, the total solvation energy arising from this sort of calculation is only 11.0 kcal/mol, which represents less than half of the estimate from specific interactions. Further entries in Table 15-9 refer to analogous quantities for other molecules. These molecules were chosen as models of the functional components of the aromatic amino acids. Just as imidazole represents the functional segment of the His residue, benzene, phenol, and indole correspond respectively to Phe, Tyr, and Trp. The last row in Table 15-9 refers to a protonated imidazole cation, so as to provide a point of comparison to charged species. It is clear that in all cases, the polarizable continuum model predicts only a fraction of the total interaction energy computed via specific interactions.

In that respect, then, the polarizable continuum estimate of hydration energy of these entities is considerably smaller than the quantum mechanical interaction energy of the molecule plus the appropriate number of first-shell water molecules. In this vein, then, it would be highly inaccurate to equate the interaction energy of a molecule such as imidazole with the molecules in its first solvation shell to the entire solvation energy when computed by a continuum approach.

However, the preceding individual H-bond energies were all computed in the gas phase. In a parallel approach to solvation, it is of interest to examine how the solvent surroundings affect each of the individual, discrete H-bonds. The influence of the solvent surroundings upon the individual H-bonds at sites A–F in Figure 15-6 was computed [88] for a variety of different dielectric constants. The H-bond energies are plotted in Figure 15-7 as a function of the Onsager function $F_o = (\varepsilon-1)/(\varepsilon+2)$, consistent with the original formulation. The right extremity of each curve corresponds to the water solvent, wherein ε=78 and $F_o = 0.96$.

It is immediately clear that the interaction energy in each case is very nearly a linear function of the F_o function, which simplifies interpolation. Perhaps more importantly, there is an obvious trend for the weakening of the H-bond energy as the

Table 15-9. Energetics (kcal/mol) of hydration

	Sum of specifics[a]	Polarizable continuum[b]
Imidazole	25.9	11.0
Benzene	10.8	1.8
Phenol	20.8	7.6
Indole	25.7	6.2
ImH^+	78.3	63.2

[a] Addition of specific H-bond energies computed from in vacuo dimer.
[b] Immersion of molecule in polarizable medium, with ε=78.

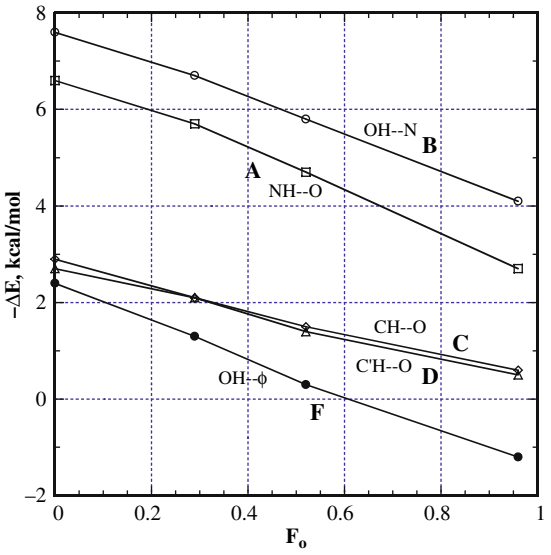

Figure 15-7. Interaction energies (kcal/mol) between imidazole and water molecule, at each of various sites defined in Figure 15-4, within context of solvent. Horizontal axis F_o is defined as $(\varepsilon-1)/(\varepsilon+2)$ where ε represents dielectric constant of medium

medium becomes more polarizable. Indeed, the F site, placing water directly above the imidazole plane, is not attractive at all in aqueous solvent. The various CH··O H-bond energies drop from 2–3 kcal/mol in vacuo down to less than 1 kcal/mol in water. And the conventional H-bonds in sites A and B diminish from the 6–8 kcal/mol range to 3–4 kcal/mol.

Summing the seven H-bond energies determined in water, i.e., the rightmost values in Figure 15-7 (taking the F site as nonbinding), leads to a total interaction energy of some 9 kcal/mol. Unlike the sum of gas-phase H-bond energies, this quantity is fairly similar to the value of 11.0 kcal/mol reported in the first row of Table 15-9, which represented the full solvation energy of imidazole in water, computed in terms of an isolated imidazole molecule within a polarizable medium, with no explicit H-bonds present at all. In other words, the sum of first-shell H-bond energies, each computed in a pairwise fashion for the solute plus one solvent molecule, may reasonably estimate the solvation energy calculated by placing the solute alone inside the polarizable continuum.

One last issue concerns how the cooperativity between different sites is affected by immersion of the system within a polarizable continuum. This question is addressed by Figure 15-8, which represents the interaction energy between imidazole and a pair of water molecules. The solid lines represent this quantity over a range of dielectric constants, computed for the full imidazole + 2 H_2O system, for various pairs of sites. The broken curves correspond to the same pair of sites, except that the binding energy is computed without cooperativity, i.e., as a simple sum of the individual H-bond energies from Figure 15-7. The positive cooperativity of the

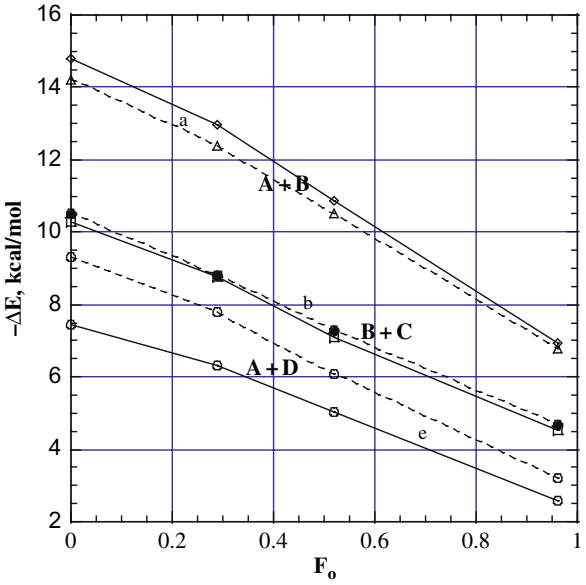

Figure 15-8. Interaction energies (kcal/mol) between imidazole and pairs of water molecules, at each of various sites defined in Figure 15-4, within context of solvent. $F_o = (\varepsilon-1)/(\varepsilon+2)$. Broken lines refer to simple addition of individual H-bond energies computed for imidazole + one water, with data taken from Figure 15-5

A+B donor/acceptor sites is indicated by the greater values for the solid than for the broken curves in the upper part of Figure 15-8. The double acceptor A+D sites exhibit opposite behavior, wherein the lower values for the solid curve correspond to negative cooperativity. As one looks from left to right in Figure 15-8, the spacings between the broken and solid curves diminish. This pattern reflects a diminishing cooperativity, be it positive or negative, as the solvent polarity grows stronger.

ACKNOWLEDGMENT

I am grateful to the many talented researchers with whom I have had the good fortune to work; their names are contained within the pertinent references. The NIH has funded a good deal of this work over the years.

REFERENCES

1. Onsager L (1936) Electric moments of molecules in liquids. J Am Chem Soc 58:1486–1493
2. Wong MW, Frisch MJ, Wiberg KB (1991a) Solvent effects. 1. The mediation of electrostatic effects by solvents. J Am Chem Soc 113:4776–4782
3. Wong MW, Wiberg KB, Frisch M (1991b) Hartree–Fock second derivatives and electric field properties in a solvent reaction field: Theory and application. J Chem Phys 95:8991–8998

4. Cramer CJ, Truhlar DG (1999) Implicit solvation models: Equilibria, structure, spectra, and dynamics. Chem Rev 99:2161–2200
5. Tomasi J, Cammi R, Mennucci B, Cappellia C, Corni S (2002) Molecular properties in solution described with a continuum solvation model. Phys Chem Chem Phys 4:5697–5712
6. Tomasi J, Mennucci B, Cammi R (2005) Quantum mechanical continuum solvation models. Chem Rev 105:2999–3093
7. Koch A, Thomas S, Kleinpeter E (1997) Ab initio study, semiempirical calculation and NMR spectroscopy of keto-enol tautomerism of triazolopyrimidines. J Mol Struct (Theochem) 401:1–14
8. Rega N, Cossi M, Barone V (1997) Intrinsic and environmental effects in the structure and magnetic properties of glycine radical in aqueous solution. J Am Chem Soc 119:12962–12967
9. Improta R, Scalmani G, Barone V (2001) Quantum mechanical prediction of the magnetic titration curve of a nitroxide 'spin probe'. Chem Phys Lett 336:349–356
10. Saracino GAA, Tedeschi A, D'Errico G, Improta R, Franco L, Ruzzi M, Corvaia C, Barone V (2002) Solvent polarity and pH effects on the magnetic properties of ionizable nitroxide radicals: A combined computational and experimental study of 2,2,5,5-tetramethyl-3-carboxypyrrolidine and 2,2,6,6-tetramethyl-4-carboxypiperidine nitroxides. J Phys Chem A 106:10700–10706
11. Improta R, Barone V (2004) Interplay of electronic, environmental, and vibrational effects in determining the hyperfine coupling constants of organic free radicals. Chem Rev 104:1231–1253
12. Komeiji Y, Ishida T, Fedorov DG, Kitaura K (2007) Change in a protein's electronic structure induced by an explicit solvent: An ab initio fragment molecular orbital study of ubiquitin. J Comput Chem 28:1750–1762
13. Hobza P, Sandorfy C (1984) Quantum chemical and statistical thermodynamic investigations of anesthetic activity. 3. The interaction between CH_4, CH_3Cl, CH_2Cl_2, $CHCl_3$, CCl_4, and an O-H$\cdots$O hydrogen bond. Can J Chem 62:606–609
14. Seiler P, Weisman GR, Glendening ED, Weinhold F, Johnson VB, Dunitz JD (1987) Observation of an eclipsed Csp3-CH_3 bond in a tricyclic orthoamide; Experimental and theoretical evidence for C-H$\cdots$O hydrogen bonds. Angew Chem Int Ed Engl 26:1175–1177
15. Wiberg KB, Waldron RF, Schulte G, Saunders M (1991) Lactones. 1. X-ray crystallographic studies of nonanolactone and tridecanoloactone: Nature of CH$\cdots$O nonbonded interactions. J Am Chem Soc 113:971–977
16. Feller D, Feyereisen MW (1993) Ab initio study of hydrogen bonding in the phenol–water system. J Comput Chem 14:1027–1035
17. Turi L, Dannenberg JJ (1993) Molecular orbital study of acetic acid aggregation. 1. Monomers and dimers. J Phys Chem 97:12197–12204
18. Koch U, Popelier PLA (1995) Characterization of C-H-O hydrogen bonds on the basis of the charge density. J Phys Chem 99:9747–9754
19. Alkorta I, Maluendes S (1995) Theoretical study of CH$\cdots$O hydrogen bonds in H_2O-CH_3F, H_2O-CH_2F_2, and H_2O-CHF_3. J Phys Chem 99:6457–6460
20. Novoa JJ, Mota F (1997) Substituent effects in intermolecular C(sp3)-H$\cdots$O(sp3) contacts: How strong can a C(sp3)-H$\cdots$O(sp3) hydrogen bond be? Chem Phys Lett 266:23–30
21. Hobza P, Spirko V, Havlas Z, Buchhold K, Reimann B, Barth H-D, Brutschy B (1999) Anti-hydrogen bond between chloroform and fluorobenzene. Chem Phys Lett 299:180–186
22. Cubero E, Orozco M, Hobza P, Luque FJ (1999) Hydrogen bond versus anti-hydrogen bond: A comparative analysis based on the electron density topology. J Phys Chem A 103:6394–6401
23. Vargas R, Garza J, Dixon DA, Hay BP (2000) How strong is the C^{α}-H$\cdots$O=C hydrogen bond? J Am Chem Soc 122:4750–4755
24. Alkorta I, Rozas I, Elguero J (2000) Effects of fluorine substitution on hydrogen bond interactions. J Fluor Chem 101:233–238

25. Hobza P, Havlas Z (2000) Blue-shifting hydrogen bonds. Chem Rev 100:4253–4264
26. Grabowski SJ (2001) A new measure of hydrogen bonding strength – ab initio and atoms in molecules studies. Chem Phys Lett 338:361–366
27. Wetmore SD, Schofield R, Smith DM, Radom L (2001) A theoretical investigation of the effects of electronegative substitution on the strength of C-H···N hydrogen bonds. J Phys Chem A 105: 8718–8726
28. van der Veken B, Herrebout WA, Szostak R, Shchepkin DN, Havlas Z, Hobza P (2001) The nature of improper, blue-shifting hydrogen bonding verified experimentally. J Am Chem Soc 123: 12290–12293
29. Saar BG, O'Donoghue GP, Steeves AH, John W Thoman J (2006) Evidence for a blue-shifting intramolecular hydrogen bond in the vibrational overtone spectrum of 1 H-nonafluorobutane. Chem Phys Lett 417:159–163
30. Yang Y, Zhang W, Gao X (2006) Blue-shifted and red-shifted hydrogen bonds: Theoretical study of the $CH_3CHO\cdots HNO$ complexes. Int J Quantum Chem 106:1199–1207
31. Spirko V, Hobza P (2006) Theoretical investigations into the blue-shifting hydrogen bond in benzene complexes. Chem Phys Chem 7:640–643
32. Shishkin OV, Palamarchuk GV, Gorb L, Leszczynski J (2006) Intramolecular hydrogen bonds in canonical 2'-deoxyribonucleotides: An atoms in molecules study. J Phys Chem B 110:4413–4422
33. McDowell SAC (2006) Blue and red shifts in $F_3C–H\cdots B$ (B = FH, ClH, OH_2, SH_2 and Cl^-) complexes predicted by a perturbative model. Chem Phys Lett 424:239–242
34. Karpfen A, Kryachko ES (2006) On blue shifts of C–H stretching modes of dimethyl ether in hydrogen- and halogen-bonded complexes. Chem Phys Lett 431:428–433
35. Kryachko ES, Karpfen A (2006) Theoretical force-field model for blue-shifted hydrogen bonds with fluoromethanes. Chem Phys 329:313–328
36. Tamasi G, Botta F, Cini R (2006) DFT-molecular modeling analysis of C–H···N and C–H···S hydrogen bond type interactions in selected platinum–purine/pyrimidine complexes. J Mol Struct (Theochem) 766:61–72
37. Quinn JR, Zimmerman SC, Del Bene JE, Shavitt I (2007) Does the A**.**T or G**.**C base-pair possess enhanced stability? Quantifying the effects of CH··O interactions and secondary interactions on base-pair stability using a phenomenological analysis and ab initio calculations. J Am Chem Soc 129: 934–941
38. Jablonski M, Sadlej AJ (2007) Blue-shifting intramolecular C-H···O interactions. J Phys Chem A 111:3423–3431
39. Vener MV, Egorova AN, Fomin DP, Tsirelson VG (2007) QTAIM study of the closed-shell interactions in peptide secondary structures: A cluster treatment of oligo- and polyalanines. Chem Phys Lett 440:279–285
40. Pluháková K, Hobza P (2007) On the nature of the surprisingly small (red) shift in the halothane···acetone complex. Chem Phys Chem 8:1352–1356
41. Hippler M (2007) Quantum chemical study and infrared spectroscopy of hydrogen-bonded $CHCl_3$–NH_3 in the gas phase. J Chem Phys 127:084306
42. Wang Z-X, Wu C, Lei H, Duan Y (2007) Accurate ab initio study on the hydrogen-bond pairs in protein secondary structures. J Chem Theory Comput 3:1527–1537
43. Gu Y, Kar T, Scheiner S (1999) Fundamental properties of the CH···O interaction: Is it a true hydrogen bond? J Am Chem Soc 121:9411–9422
44. Gu Y, Kar T, Scheiner S (2000a) Comparison of the CH···N and CH···O interactions involving substituted alkanes. J Mol Struct 552:17–31
45. Scheiner S, Grabowski SJ, Kar T (2001a) Influence of hybridization and substitution upon the properties of the CH··O hydrogen bond. J Phys Chem A 105:10607–10612

46. Scheiner S, Kar T (2002) Red versus blue-shifting hydrogen bonds: Are there fundamental distinctions? J Phys Chem A 106:1784–1789
47. Kryachko E, Scheiner S (2004) CH··F hydrogen bonds. Dimers of fluoromethanes. J Phys Chem A 108:2527–2535
48. Gu Y, Kar T, Scheiner S (2000b) Evaluation of the H-bonding properties of CH· · · O interactions based upon NMR spectra. J Mol Struct (Theochem) 500:441–452
49. Scheiner S (2006) Contributions of NH··O and CH··O H-bonds to the stability of β-sheets in proteins. J Phys Chem B 110:18670–18679
50. Kurnig IJ, Scheiner S (1987) Ab initio investigation of the structure of hydrogen halide – amine complexes in the gas phase and in a polarizable medium. Int J Quantum Chem QBS 14:47–56
51. Scheiner S, Duan X (1991) Effect of intermolecular orientation upon proton transfer within a polarizable medium. Biophys J 60:874–883
52. Scheiner S, Kar T (2005) Effect of solvent upon CH··O hydrogen bonds with implications for protein folding. J Phys Chem B 109:3681–3689
53. Miertus S, Scrocco E, Tomasi J (1981) Electrostatic interaction of a solute with a continuum. A direct utilization of ab initio molecular potentials for the prevision of solvent effects. Chem Phys 55: 117–129
54. Miertus S, Tomasi J (1982) Approximate evaluations of the electrostatic free energy and internal energy changes in solution processes. Chem Phys 65:239–245
55. Mennucci B, Tomasi J (1997) Continuum solvation models: A new approach to the problem of solute's charge distribution and cavity boundaries. J Chem Phys 106:5151–5198
56. Cancès E, Menucci B, Tomasi J (1997) A new integral equation formalism for the polarizable continuum model: Theoretical background and applications to isotropic and anisotropic dielectrics. J Chem Phys 107:3032–3041
57. Cossi M, Barone V, Mennucci B, Tomasi J (1998) Ab initio study of ionic solutions by a polarizable continuum dielectric model. Chem Phys Lett 286:253–260
58. Barone V, Cossi M (1998) Quantum calculation of molecular energies and energy gradients in solution by a conductor solvent model. J Phys Chem A 102:1995–2001
59. Foresman JB, Keith TA, Wiberg KB, Snoonian J, Frisch MJ (1996) Solvent effects. 5. Influence of cavity shape, truncation of electrostatics, and electron correlation on ab initio reaction field calculations. J Phys Chem 100:16098–16104
60. Barone V, Cossi M, Tomasi J (1997) A new definition of cavities for the computation of solvation free energies by the polarizable continuum model. J Chem Phys 107:3210–3221
61. Rega N, Cossi M, Barone V (1998) Structure and magnetic properties of glycine radical in aqueous solution at different pH values. J Am Chem Soc 120:5723–5732
62. Scheiner S, Kar T, Gu Y (2001b) Strength of the $C^{\alpha}H$··O hydrogen bond of amino acid residues. J Biol Chem 276:9832–9837
63. Scheiner S (2005) Relative strengths of NH··O and CH··O hydrogen bonds between polypeptide chain segments. J Phys Chem B 109:16132–16141
64. Scheiner S, Kar T (2007) Underlying source of the relation between polypeptide conformation and strength of NH··O hydrogen bonds. J Mol Struct 844–845:166–172
65. Jeffrey GA (1997) An introduction to hydrogen bonding. In: Truhlar DG (ed) Topics in physical chemistry, Oxford University Press, New York, p 303
66. Scheiner S (1997) Hydrogen bonding: A theoretical perspective, Oxford University Press, New York, p 375
67. Kurnig IJ, Szczesniak MM, Scheiner S (1986) Ab initio study of structure and cooperativity in H3N· · · HF· · · HF and H3P· · · HF· · · HF. J Phys Chem 90:4253–4258

68. Latajka Z, Scheiner S (1988) Structure, energetics and vibrational spectra of H-bonded systems. Dimers and trimers of HF and HCl. Chem Phys 122:413–430
69. Chalasinski G, Cybulski SM, Szczesniak MM, Scheiner S (1989) Nonadditive effects in HF and HCl trimers. J Chem Phys 91:7048–7056
70. Chalasinski G, Szczesniak MM, Cieplak P, Scheiner S (1991) Ab initio study of intermolecular potential of H_2O trimer. J Chem Phys 94:2873–2883
71. DuPré DB, Yappert MC (2002) Cooperative hydrogen- and πH-bonded interactions involving water and the ethylenic double bond. J Phys Chem A 106:567–574
72. Chen C, Liu M-H, Wu L-S (2003) Local analysis and comparative study of the hydrogen bonds in the linear (HCN)n and (HNC)n clusters. J Mol Struct (Theochem) 630:187–204
73. Suh SB, Kim JC, Choi YC, Yun S, Kim KS (2003) Nature of one-dimensional short hydrogen bonding: Bond distances, bond energies, and solvent effects. J Am Chem Soc 126:2186–2193
74. Hinton JF, Harpool RD (1977) An ab initio investigation of $(formamide)_n$ and formamide-$(water)_n$ systems. Tentative models for the liquid state and dilute aqueous solution. J Am Chem Soc 99: 349–353
75. Sheridan RP, Lee RH, Peters N, Allen LC (1979) Hydrogen-bond cooperativity in protein secondary structure. Biopolymers 18:2451–2458
76. Kobko N, Dannenberg JJ (2003b) Cooperativity in amide hydrogen bonding chains. Relation between energy, position, and H-bond chain length in peptide and protein folding models. J Phys Chem A 107:10389–10395
77. Ireta J, Neugebauer J, Scheffler M, Rojo A, Galvan M (2003) Density functional theory study of the cooperativity of hydrogen bonds in finite and infinite α-helices. J Phys Chem B 107:1432–1437
78. Wieczorek R, Dannenberg JJ (2003b) Hydrogen bond cooperativity, vibrational coupling, and dependence of helix stability on changes in amino acid sequence in small 3_{10}-helical peptides. A density functional theory study. J Am Chem Soc 125:14065–14071
79. Wieczorek R, Dannenberg JJ (2003a) H-bonding cooperativity and energetics of α-helix formation of five 17-amino acid peptides. J Am Chem Soc 125:8124–8129
80. Kobko N, Dannenberg JJ (2003a) Cooperativity in amide hydrogen bonding chains. A comparison between vibrational coupling through hydrogen bonds. Implications for peptide vibrational spectra. J Am Chem Soc 107:6688–6697
81. Masella M, Flament J-P (1999) A theoretical study of five water/ammonia/formaldehyde cyclic trimers: Influence of cooperative effects. J Chem Phys 110:7245–7255
82. Alkorta I, Elguero J (2003) Interaction of protein backbone with nucleic acid bases. J Phys Chem B 107:5306–5310
83. Parra RD, Bulusu S, Zeng XC (2003) Cooperative effects in one-dimensional chains of three-center hydrogen bonding interactions. J Chem Phys 118:3499–3509
84. Rivelino R, Chaudhuri P, Canuto S (2003) Quantifying multiple-body interaction terms in H-bonded HCN chains with many-body perturbation/coupled-cluster theories. J Chem Phys 118: 10593–10601
85. Kar T, Scheiner S (2004) Comparison of cooperativity in CH··O and OH··O hydrogen bonds. J Phys Chem A 108:9161–9168
86. Scheiner S, Nagle JF (1983) Ab initio molecular orbital estimates of charge partitioning between Bjerrum and ionic defects in ice. J Phys Chem 87:4267–4272
87. Scheiner S, Kar T, Pattanayak J (2002) Comparison of various types of hydrogen bonds involving aromatic amino acids. J Am Chem Soc 124:13257–13264
88. Kar T, Scheiner S (2006) Cooperativity of conventional and unconventional hydrogen bonds involving imidazole. Int J Quantum Chem 106:843–851

CHAPTER 16

SOLVATION IN SUPERCRITICAL FLUIDS

ANA C. FURLAN[1], FRANK W. FÁVERO[1], JAVIER RODRIGUEZ[2], DANIEL LARIA[2], AND MUNIR S. SKAF[1]

[1]*Institute of Chemistry, State University of Campinas, UNICAMP, Campinas, SP 13084-832, Brazil, e-mail: skaf@iqm.unicamp.br*

[2]*Department of Physics, Comisión Nacional de Energía Atómica, CNEA, Av. Libertador 8250, 1429, Buenos Aires, Argentina*

16.1. INTRODUCTION

Supercritical fluids (SCFs) comprise an important class of solvents and reaction media which have found many applications in basic and applied chemical sciences. SCFs, especially supercritical carbon dioxide, play a key role as one of the most important environmentally benign solvents in the so-called "green" chemistry applications. In the context of practical applications, SCFs are becoming increasingly viable in economic terms as an alternative to conventional organic solvents for purification, fractionation, and extraction of valuable organic compounds from a wide range of natural matrices* [1,2,3,4]. Academic and commercial extraction units are available for selective extraction of organic substances based on supercritical carbon dioxide (SC-CO_2). Two of the most successful and profitable large-scale SCF-based extraction processes are the extraction of caffeine from coffee beans and tea leaves and nicotine from tobacco. In the case of coffee beans, at the end of the extraction process one is left on one hand with whole taste- and aroma-preserved decaffeinated coffee, much appreciated by an important segment of the consumers market, and, on the other hand with high-purity caffeine which is a valuable commodity for pharmaceutical and food industries.

The potential for supercritical fluid extraction and purification of substances of high aggregated economic value is enormous in Brazil due the overwhelming biodiversity of its forests, comprising from 55,000 to 350,000 of known species of plants in the world [5]. Studies of the economic viability of SCF extraction of several

*References 2–4 are excellent reviews on fundamental and applied aspects of supercritical fluids in chemistry and physics.

S. Canuto (ed.), Solvation Effects on Molecules and Biomolecules, 433–453.
DOI 10.1007/978-1-4020-8270-2_16,

compounds of interest to pharmaceutical and food industries from Brazilian plants are being carried out [6]. In spite of that, there is still no industrial scale unit to produce extracts by SCF extraction in South America.

SC-CO_2 is also becoming increasingly important as reaction media [7] for a great variety of fundamental chemical reactions ranging from catalysis to polymerization, [8,9] to synthesis and growth of inorganic materials [1,2], to nanoparticle production and preparation processes [1,2,10,11], and to biotechnological applications such as activation and deactivation of enzymes [12], biomass conversion, and biocatalysis [1,2,13].

Another very important "green" chemistry solvent is supercritical water (SCW) [14]. Water under supercritical conditions is an extremely powerful oxidizing and cleansing agent that has been proven remarkably promising as a soil decontaminant by efficiently degrading persistent organic toxic wastes that are difficult to eliminate from polluted soils, and in the treatment of several types of industrial wastes such as textile and cellulose wastewater [2].

From a more fundamental point of view, the ability of SCFs to act as a highly selective solvent resides in the fact that their density can be markedly changed from dilute stem- to liquid-like values by small variations of the applied pressure [1]. Therefore, solute–solvent interactions and solubility for different types of solute can be effectively tuned by small adjustments in the solvent thermodynamic conditions [4]. In addition, vapor-like diffusion rates and high penetrability into solid matrices, inherent to SCFs, are also important attributes of these solvents. In this context, there has been a long-standing interest in understanding (i) the intermolecular structure and dynamics of SCF, (ii) solvation properties of many types of solutes, and (iii) solvent effects on chemical reactions taking place in supercritical environments. The most ubiquitous structural feature of SCFs is the existence of large structural inhomogeneities, especially near the critical point, which are well known in statistical mechanics as critical fluctuations [1,4]. Away from criticality but not far from the critical point, solvent molecules can also agglomerate or cluster around attractive solutes in a supercritical solution leading to a local density augmentation effect that is key to processes such as supercritical solvation and solubility, solute diffusion, solvent effects on solute vibrational relaxation and energy transfer, solvatochromic effects, and chemical reactions in these environments [4]. Effects associated with local solvent density augmentation often preclude reliable interpretations of experimental measurements of physicochemical properties based solely on bulk quantities such as pressure, solvent density, and temperature. Therefore, considerable efforts from both experimental and computational approaches have been devoted to investigate molecular details of solvation and density augmentation effects in supercritical fluids covering a wide range of thermodynamic conditions [15,16,17,18,19,20,21,22,23].

In this chapter, we will review some of the work that we have been doing in recent years in the context of solvation and dynamical properties in polar and non-polar supercritical solutions using molecular dynamics computer simulations. First we will discuss solvation of alkaloids in SC-CO_2 and provide detailed molecular views of the main structural features of the local density augmentation around simple alkaloids

and solute translational and reorientational dynamics under different pressure and temperature conditions [24], and also describe the effects of the presence of small fractions of ethanol as co-solvent on solvation structures and dynamics [25]. In the second half of this chapter, we will focus on properties of polar fluids such as water and ammonia under supercritical conditions. We will start with the dielectric behavior of supercritical water (SCW) [26] and review comparisons between simulations and experimental data, some of which remain controversial to this date. Next, we will concentrate on solvation dynamics in SCW using a model chromophore that captures the essential elements of a photo-excitable dye typically used in time-resolved Stokes shift fluorescence experiments, and conclude by reviewing equilibrium structural and dynamical aspects of excess electrons solvated in supercritical water [27] and supercritical ammonia [28] as function of solvent density and comparisons with experimentally measured optical absorption spectra of these systems.

16.2. NON-POLAR SCF

16.2.1. Solvation of Alkaloids in SC-CO_2

Several features are responsible for the popularity of CO_2 as the supercritical fluid of choice for many applications. First of all, with the critical point at mere 31.1°C and 78.2 bar, supercritical conditions can be easily attained and thermally unstable solutes would be safely manipulated at such temperatures. Second, CO_2 is also abundant, non-toxic and easily recoverable, and, therefore, inexpensive and environmentally benign. Nevertheless, polar molecules in general have limited solubility in SC-CO_2 because CO_2 lacks a dipolar moment. For gross extraction purposes, this problem is overcome by simply adding a highly polar co-solvent such as ethanol or water. Other applications, however, may require considerable improvement of CO_2 solubility of more complex molecular systems. To this end, different strategies have been adopted in order to design CO_2-philic surfactants, polymers, and, more recently, room-temperature ionic liquids [29,30]. The most common ones involve fluorination and addition of carbonyl groups and branched alkyl chains.

The basic idea behind the addition of CO_2-philic functionality to these complex molecules is to enhance the overall interaction with CO_2. Therefore, it is fundamental to understand at the molecular level how CO_2 molecules organize themselves around a solute. In this context, important insights have been reached by combining molecular dynamics (MD) simulation studies and spectroscopy measurements to investigate solvation of simple solute molecules in SC-CO_2. Anderton and Kauffman have used fluorescence spectroscopy of organic dyes (diphenylpolyenes) to investigate rotation dynamics in supercritical fluids [31]. Maroncelli and co-workers, more recently, have extended steady-state emission and fluorescence anisotropy techniques to quantitatively determine the local solvent density enhancement and its effect on the dynamics of the fluorescence probe in SC-CO_2 [20,21,32,33]. Using MD simulations, Maroncelli also introduced effective means of determining density augmentation which are in close agreement with experimental measurements [20,21,32].

In our studies, we have used Maroncelli's ideas to investigate solvation of three purine alkaloids in SC-CO_2, in addition to a few other molecules with potential pharmaceutical applications and that can be efficiently solvated in SC-CO_2. The purine alkaloids that we have studied are caffeine (1,3,7-trimethylxanthine), theophylline (1,3-dimethylxanthine), and theobromine (3,7-dimethylxanthine) (Figure 16-1). Caffeine is an alkaloid found in common beverages such as coffee, tea, and cocoa, which may present physiological effects on mammals, including cardiac stimulation and arterial dilation [34]. Theophylline and theobromine are two other alkaloids of pharmaceutical value that are closely related to caffeine in terms of chemical structure and physiological effects. In contrast to caffeine, little is known about their supercritical extraction [35]. In a series of recent studies, Mohamed and collaborators have reported experimental results for the supercritical extraction of purine alkaloids and fats from commercially important food products using CO_2, ethane, and their mixtures [35,36]. Detailed information on the extractability of caffeine, theophylline, and theobromine from herbal maté tea leaves (*Ilex paraguariensis*), as well as their individual solubilities in supercritical CO_2, has been reported for various conditions of temperature and pressure [35]. These works, along with the earlier papers by Johannsen and Brunner [37] and by Li et al. [38] reveal important features about the solubility properties of methylxanthines in supercritical CO_2. However, little is known about their solvation properties in molecular terms. In the first of such studies, we have reported results from molecular dynamics (MD) computer simulations aimed at investigating in molecular details the characteristics of the solvation of caffeine, theophylline, and theobromine in CO_2 under different supercritical conditions.

In our simulations, we have used the EPM2 potential of Harris and Yung [39] for CO_2, which reproduces remarkably well the liquid–vapor coexistence curve, as well as some thermodynamic, structural, and dynamical properties of the real fluid. The molecular geometry and atomic charges for the alkaloids were determined from ab initio quantum chemical calculations performed at the RHF/6-311 G(d, f) level with the Merz–Kollman charge protocol [40]. The full interaction potential is comprised by sums of Lennard-Jones and Coulombic terms between all pair of atoms belonging to different molecules. The solutes' Lennard-Jones parameters were extracted from the OPLS all-atom force field of Jörgensen and collaborators [41]. Simulations were performed on systems consisting of a single solute surrounded by a collection of 300

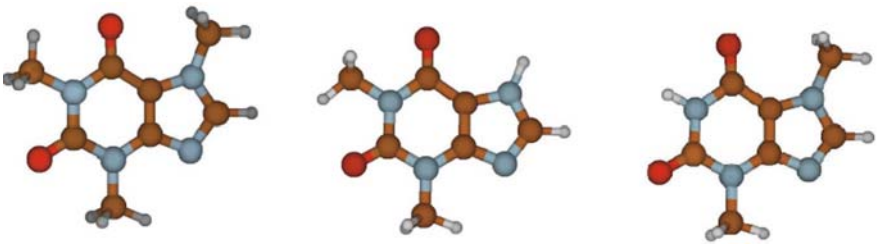

Figure 16-1. Molecular structures of caffeine (*left*), theophylline (*center*), and theobromine (*right*)

CO_2 molecules at an average temperature of 313 K and bulk density ranging from $0.25\rho_c$ to $2.0\rho_c$, with $\rho_c \approx 0.468$ g/cm^3 the critical density of CO_2. The thermodynamic states were chosen in correspondence to experimental conditions [35].

In order to determine the distribution of solvent molecules around the surface of a solute of arbitrary shape, Maroncelli introduced the solvation shell distribution function formally expressed as [21]

$$g_{ss}(r) = \left\langle \exp\left\{ \frac{-u(s, \vec{\Omega})}{k_B T} \right\} \right\rangle_{s(\vec{\Omega}, r)},$$

where u is the solute–solvent interaction energy and the subscript $s(\vec{\Omega}, r)$ means that the average is taken over all combinations of center-of-mass distance r and relative solute–solvent orientation $\vec{\Omega}$ that are consistent with a given value of s [21]. The $g_{ss}(r)$ distribution is a physically very sensible indicator of the relative probability of finding a solvent molecule within the first solvation shell of a solute of *arbitrary shape*. As defined, $g_{ss}(r)$ is the probability of finding a solvent molecule, regardless of its relative orientation, at a distance r away from the nearest solute atom relative to a random distribution of solvent molecules. Thus, $g_{ss}(r)$ measures the change in solvent density relative to the bulk at a distance r from the surface of a solute of arbitrary shape. Figure 16-2 compares schematically the solvation shell in terms of the usual radial pair distribution function, $g(r)$, and $g_{ss}(r)$.

Results for $g_{ss}(r)$ computed for caffeine at various CO_2 supercritical states are shown in Figure 16-3. The distributions present a single peak near 3.3 Å which increases with decreasing density, indicating an enhanced attraction of solvent molecules by the solute in dilute steam-like environments. At the highest density considered (0.94 g/cm^3), one notices the development of a well-defined second peak typical of dense fluids. In dense liquid solutions, the average local solvent density near the solute is not markedly different from the bulk density because of the strongly repulsive, packing forces that determine the microscopic structure of the solvent. In contrast, less densely packed supercritical fluids exhibit large structural fluctuations, which allow for a molecular agglomeration around the solute, often leading to large increments in the local solvent density in the vicinity of attractive solutes, as seen in Figure 16-3. Such substantial differences between local and bulk densities may

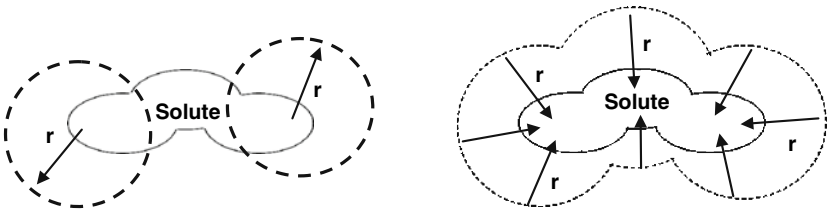

Figure 16-2. Schematic representations of the solvation shell described in terms of the $g(r)$ (*left*) and $g_{ss}(r)$ (*right*) functions

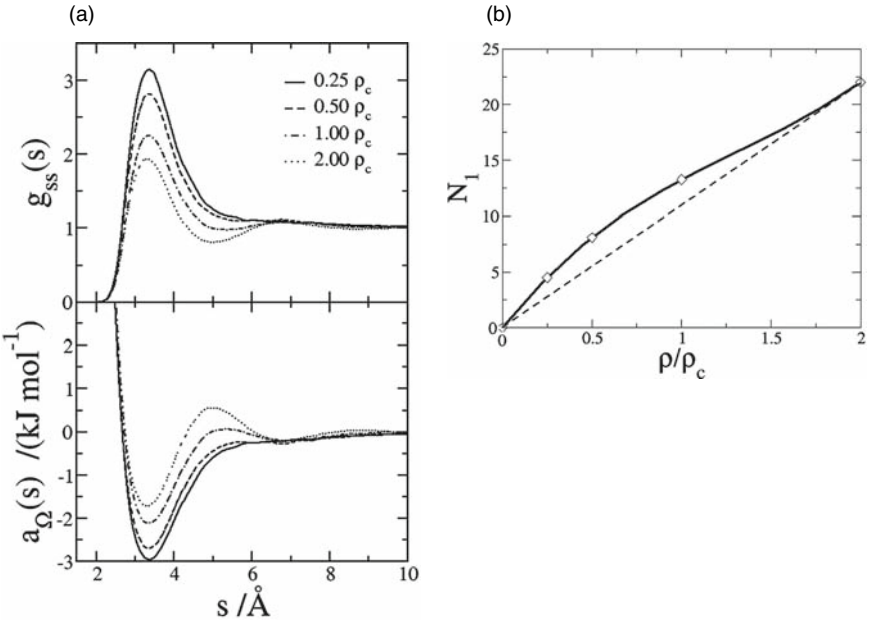

Figure 16-3. (**a**) Solvation shell (*top*) and free-energy (*bottom*) functions for caffeine–CO_2 systems at 313 K and different densities. (**b**) Non-spherical first shell coordination number as function of solvent density. The *dashed line* represents ideal behavior. From Ref [25]

undermine accurate theoretical treatments of the solvation properties in supercritical ambients and often preclude the interpretation of experimental data in terms of bulk thermodynamic arguments. The lower panel of Figure 16-3a shows the function $a_\Omega(r) = -k_B T \ln g_{ss}(r)$ which is a measure of the solvation free-energy profile since $g_{ss}(r)$ stands for the solute-solvent potential of mean force [21]. The depth of the first well of $a_\Omega(r)$ is a relative measure of the free-energy benefit of a solvent particle for being in the first solvation shell around the solute [21,22]. This benefit is greater for more dilute solvent regimes where solute–solvent interactions prevail over solvent–solvent ones. Figure 16-3b depicts the average number N_1 of molecules contained within the (non-spherical) solvation shell of caffeine as a function of bulk density. The dashed line connects the dilute-gas regime and a high-density reference state ($2\rho_c$) that represents the dense liquid behavior. The straight line reflects the expected increase in the first shell coordination number in the absence of a density augmentation effect. It is shown that the enhancement of the solvent population in the solvation shell with respect to the bulk passes through a maximum for densities between $0.5\rho_c$ and $1.0\rho_c$. Maroncelli has performed beautiful fluorescence experiments to measure local enhancements.

For large polyatomic solutes, the solvent may pack differently depending on the region of the molecule. Investigating how solvent molecules organize around the solute may contribute with important molecular insights to the understanding of

solvation in supercritical fluids. Details of the solvent distribution around caffeine in SC-CO_2 can be seen from the color density maps shown in Figure 16-4. The scale is relative to the respective bulk density.

Three cross-sections for the caffeine system are shown for the lowest and highest densities considered. At $2\rho_c$ the average solvent distribution is considerably more homogeneous, with mild concentration enhancement and depletion (light blue) around the solute molecule. At low bulk density, the solvent packing is highly non-uniform, with a local density around the carbonyl oxygens and above and below the plane of the rings, which can be as high as six times the bulk density. Such an inhomogeneity gradually decreases with increasing bulk density. Similar behavior is also observed for theophylline and theobromine. The major difference between caffeine and the dimethylxanthines is the substantial increase in the local density near the carbonyls that is allowed by the absence of the third methyl group in different positions for theophylline and theobromine (Figure 16-1), thus permitting further approximation of the solvent molecules in the neighborhood of the oxygen atoms. The solvent density contour maps around each solute indicate an inhomogeneous distribution of CO_2 molecules in the close vicinity of the alkaloids with a strong density enhancement above and below the rings and around the carbonyl oxygens. Such a feature stems

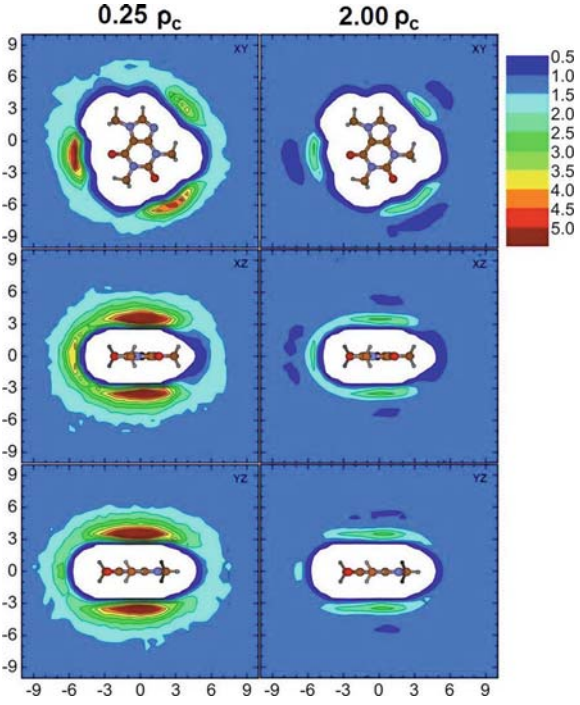

Figure 16-4. Solvent density maps for caffeine in CO_2 at $0.25\rho_c$ and $2.0\rho_c$ and 313 K. The color scale is relative to the corresponding bulk density and the grid spans a 10×10 Å^2 area

from multipolar interactions between the solute and the solvent molecules. The domination contribution in this case is the interaction between the carbonyl local dipole and the quadrupole moment of CO_2. The main symmetry axis of CO_2 and the solute C=O groups are preferentially oriented in a T-shape fashion. Interestingly, it has been established in the literature that the favorable interactions between CO_2 and carbonyl groups are responsible for the relatively high solubility of certain molecules and polymers in supercritical CO_2 [42,43].

16.2.2. Effects from Adding a Co-solvent

One of the drawbacks of pure CO_2 as supercritical solvent is the low solubility of polar compounds which is attributed to lack of a strong permanent dipole moment in CO_2. In order to improve solvation and extraction power, a highly polar or associative liquid is added to SC-CO_2 in small quantities as co-solvent. Ethanol is the co-solvent of choice for a number of reasons, including its superior mixibility (compared to water, for instance) with CO_2 and its wide acceptance in pharmaceutical and food-related supercritical extractions.

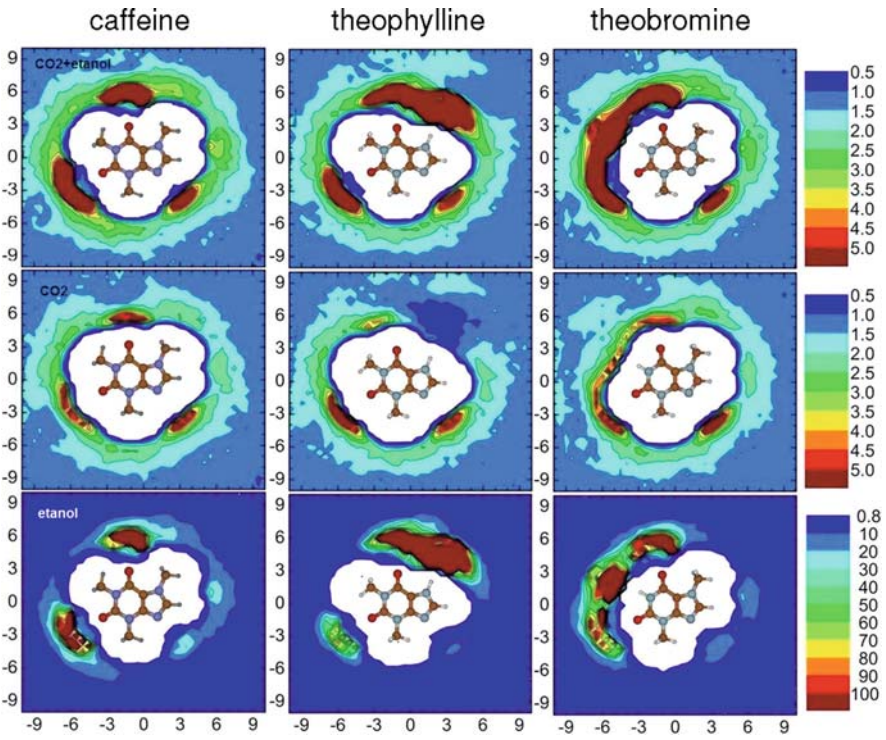

Figure 16-5. Solvent density maps for CO_2+5%ethanol at $0.25\rho_c$ and 313 K

In our studies [25], we have investigated solvation structures and dynamics of different types of alkaloids in SC-CO_2 systems containing a small fraction (5% in mole) of ethanol. Simulation results show the existence of a strong preferential solvation of the purine alkaloids (caffeine, theophylline, and theobromine) by ethanol driven by specific hydrogen bond interaction between the solute and solvent molecules. Both translation and reorientation dynamics are significantly slowed down in the presence of ethanol, as expected. The solvent density maps computed at low solvent density ($0.25\rho_c$) and 313 K depicted in Figure 16-5 shows nicely the distribution of solvent molecules around the solutes. The top panels indicate solvent distributions similar to that observed in pure CO_2, with strong density enhancement around the carbonyl and above and below the molecular plane. The middle and bottom panels depict density maps for CO_2 and ethanol individual contributions to the total solvent density distribution, respectively. The results show that some CO_2 has been displaced by ethanol, especially around the carbonyl oxygens and around the NH groups in theophylline and theobromine. However, the overall number of CO_2 molecules in the first solvation layer is little affected, going from nearly 4.5 in pure CO_2 to approximately 6.0 in CO_2 + 5% ethanol. Figure 16-5 also shows a remarkable build up of ethanol around the solute. Whereas the local density of CO_2 can be as high as five to six times the density far away from the solute, that of ethanol can reach values 100 times higher than the bulk density of ethanol in the system. Nearly 3 of the 15 ethanol molecules present in the system are in close contact with the solute at these thermodynamic conditions, demonstrating strong preferential solvation by ethanol.

16.3. POLAR SCFs

We now turn attention to a completely different kind of supercritical fluid: supercritical water (SCW). Supercritical states of water provide environments with special properties where many reactive processes with important technological applications take place. Two key aspects combine to make chemical reactivity under these conditions so peculiar: the solvent high compressibility, which allows for large density variations with relatively minor changes in the applied pressure and the drastic reduction of bulk polarity, clearly manifested in the drop of the macroscopic dielectric constant from $\varepsilon \sim 80$ at room temperature to approximately 6 at near-critical conditions. From a microscopic perspective, the unique features of supercritical fluids as reaction media are associated with density inhomogeneities present in these systems [1,4].

In the following subsections we will review simulation studies we have performed aiming at investigating the dielectric behavior of SCW and solvation dynamics of excess electrons, making a close connection to recent pulse radiolysis and time-dependent fluorescence experiments.

16.3.1. Dielectric Behavior SC-Water

A few years ago, microwave spectroscopy measurements have been reported for SCW at several different densities ranging from ρ = 1.0 down to 0.1 g/cm^3, which

indicated a very intriguing dynamical behavior of water molecules under supercritical conditions at sufficiently low densities [44,45]. By fitting the measured frequency-dependent dielectric permittivity with a single Debye dispersion relation, it has been found that the dielectric relaxation time τ_D presents a non-monotonic density dependence, with an unexpected branch for $\rho < 0.4\,g/cm^3$ showing a sharp increase of τ_D with decreasing density [44,45]. This interesting feature could lead to distinctive dynamical solvent effects on molecular or ionic probes in solution. The slowing down of the main dielectric relaxation channel with decreasing density for dilute regimes (far from criticality, where dynamical slowing down are well known to take place) is a counterintuitive behavior that demanded analysis from a theoretical perspective given that lowering the density one would expect less association between molecules and, therefore, faster dipole reorientation relaxation rates.

Largely motivated by these experiments, we carried out MD simulations using the SPC/E model for water for several thermodynamic states above the critical temperature of model (T_c = 640 K) with densities ranging from 0.05 up to 1.0 g/cm^3, as indicated in Table 16-1 [26].

Table 16-1 shows results for the dielectric constant $\varepsilon(0)$, Kirkwood g-factor g_K, and the static dipole cross-correlation parameter $g^0 = \langle |\mathbf{M}(0)|^2 \rangle / (N\mu^2) - 1$ where $\mathbf{M}(t) = \sum_{i=1}^{N} \mu_i(t)$ is the system's collective dipole at time t, for a selected set of thermodynamic states. The experimental values for $\varepsilon(0)$ are shown within parentheses. The overall trend of these quantities with density and temperature is consistent with the expectation of a higher degree of dipolar correlation at higher densities and/or lower temperatures. At liquid-like densities (states 10–12), where polarizability effects are known to be important, the simulated model underestimates $\varepsilon(0)$, a feature common to most non-polarizable water models. Given the error bars and differences in thermodynamic states, our estimates for $\varepsilon(0)$ for states 10–12 are

Table 16-1. State parameters and static dielectric properties for SPC/E water [26]

State	ρ (g/cm^3)	T (K)	$\epsilon(0)$[a]	g_K	g^0
1	0.05	1500	1.2	1.01	0.07
2	0.05	1000	1.3	1.00	0.08
3	0.05	720	1.4 (1.2)	1.04	0.15
4	0.1	1000	1.7 (1.5)	1.02	0.17
5	0.1	720	2.0 (1.6)	1.07	0.28
6	0.2	650	3.7 (3.0)	1.18	0.56
7	0.4	650	8.2 (7.2)	1.48	1.09
8	0.6	650	13.8 (13.4)	1.71	1.47
9	0.7	650	16.3 (17.0)	1.74	1.53
10[b]	0.9	450	29.5 (39.4)	1.72	1.54
11[b]	1.0	340	48.0 (66.3)	1.92	1.85
12[b]	1.0	315	53.0 (73.3)	1.97	1.92

[a]The errors $\varepsilon(0)$ are roughly 8%. Experimental values are in parenthesis
[b]Do not correspond to a supercritical state.

consistent with other simulations on the SPC/E model. As the density decreases, polarizability-induced effects become less important and one finds a better agreement with the experimental measurements. A closer inspection of Table 16-1 reveals that in the dilute regime ($\rho < 0.4$ g/cm^3), our simulations actually overestimate $\varepsilon(0)$ because of the enhanced dipole moment (2.35 D) of SPC/E water compared to the gas phase value (1.85 D). Nevertheless, our results for the static dielectric properties for the supercritical states are generally in good agreement with the experimental data and are also consistent with MD results for the fully polarizable model of Bursulaya and Kim [46].

The analysis of the dynamics and dielectric relaxation is made by means of the collective dipole time–correlation function $\Phi(t) = \langle \mathbf{M}(t).\mathbf{M}(0)\rangle \big/ \langle |\mathbf{M}(0)|^2 \rangle$, from which one can obtain the far-infrared spectrum by a Fourier–Laplace transformation and the main dielectric relaxation time by fitting $\Phi(t)$ by exponential or multi-exponentials in the long-time rotational-diffusion regime. Results for $\Phi(t)$ and the corresponding frequency-dependent absorption coefficient, $A'' = \Omega \int \Phi(t) \cos(\omega t) \mathrm{d}t$ are shown in Figure 16-6 for several simulated states. The main spectra capture essentially the microwave region whereas the insert shows the far-infrared spectral region.

The decay of $\Phi(t)$ can be divided into well-separated regimes with distinct timescales: a fast initial Gaussian and librational decays, followed by a slower relaxation associated with rotational-diffusion motions. The high-frequency or fast relaxation channels are dictated by the molecule's inertial characteristics and the short-range structural properties of the system, while rotational-diffusion relaxation normally depends on long-range structural features [14]. With the exception of the very diluted and hot states (state 1 and 2), the long-time behavior of the dipolar correlations can be well described by single exponential functions, leading to Lorentzian bands in the dielectric loss frequency spectra $A''(\omega)$ (Figure 16-6, right). The relative

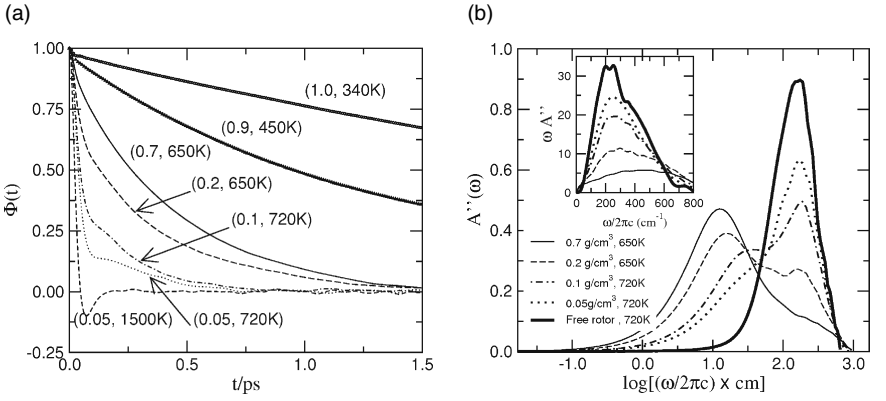

Figure 16-6. Left: collective dipole time correlation for SCW states. *Right*: corresponding frequency-dependent absorption coefficients [26]

importance of the distinct relaxation channels processes depends on the thermodynamic state considered: at normal liquid densities, rotational-diffusion motions dominate the collective relaxation, whereas fast inertial rotations are responsible for most of the relaxation in steam-like states. The difference between inertial and rotational-diffusion timescales tends to diminish as the density is lowered. These features are also manifested in the dielectric loss spectra $A''(\omega)$. Going from state 9 (650 K, 0.7 g/cm^3) to state 6 (650 K, 0.2 g/cm^3) the low-frequency, Debye band gradually decreases in intensity and shifts from 12 to 16 cm^{-1}, while the high-frequency band becomes more intense and moves toward lower frequencies. This trend continues as the density is further lowered down to the ideal, vanishing torque limit of the free rotor, where only a dispersion band due to fast inertial rotations remains. The high-frequency librational behavior is better depicted in the insert. The librational band shifts toward lower frequencies at low densities due to a less interconnected hydrogen bond network and, hence, smaller restoring torques under these conditions. The behavior of the Debye band, on the other hand, seems to be consistent with the diminution of long-range structural correlations expected at lower densities and higher temperatures. The limiting behavior seems to be that of the free rotor.

A comparison between experimental and simulated main Debye relaxation time is presented in Figure 16-7. Simulation and experimental results show excellent agreement for not so dilute systems ($\rho > 0.4$ g/cm^3). However, below this density the experimental Debye time increases with decreasing density, whereas simulation results for this quantity keep decreasing and approaching the limiting behavior of a collection of free rotors. The extent of the loss of dynamic correlation between

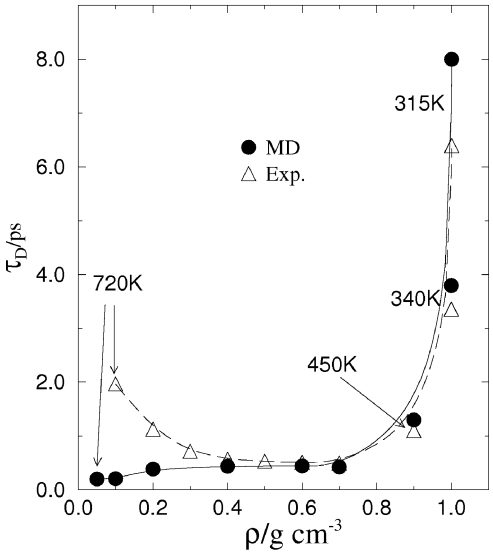

Figure 16-7. Experimental and simulated Debye times for SCW [26]

water molecules in hot diluted supercritical environments has been further analyzed in terms of the single-particle correlation functions for dipole reorientation using stochastic collision and diffusion models. Such analysis indicates that there is consistency with the free-rotor limit and, therefore, further theoretical and experimental studies must be conducted in order to resolve this discrepancy.

Very recently, detailed further analyses of the translation and reorientation dynamics of SCW have been reported showing consistency with our results in the limit of very low-density supercritical states for water [47]. The dynamical behavior of SCW in this study is also compared to that of supercritical benzene showing that the density dependence of the self-diffusion coefficient and rotational dynamics of SCW is smaller than that of supercritical benzene because SCW is capable of maintaining stronger degrees of structural correlations and orientational anisotropy than benzene, which tends to lose intermolecular correlations at a much faster rate upon decreasing density [47].

16.3.2. Excess Electrons in Polar SCFs – Equilibrium Aspects

Excess electrons dissolved in liquids and amorphous materials constitute pristine spectroscopic probes for steady-state and time-dependent optical spectroscopies because of its large optical cross-section and the sufficiently long lifetime of the first excited state [48]. Spectroscopic signals from solvated electrons yield valuable information regarding the structure and ultra-fast dynamical response of the system. The solvated electron is also the prototype system for mixed quantum-classical simulations and has been extensively used in the investigation of a variety of new physical phenomena in condensed phases and finite clusters [49]. At supercritical temperatures, large displacements in chemical equilibria and solvation-induced modifications in the reaction rates by several orders of magnitude are not uncommon, a fact that reveals the importance of the reactant complex–solvent coupling as a key factor determining the channels that drive the dynamics of the reactive processes [1,4].

Given the inherently quantum nature of the electron, its solvation normally exhibits well-differentiated characteristics from what is usually encountered in cases of simpler, classical, anionic solutes. Most notable is the existence of the electronic localization phenomenon, reflected in the dramatic drop that appears in the electronic drift mobility. The transition from delocalized to localized states is usually described in terms of the spatial confinement of the electronic density within a solvent cavity, whose average shape fluctuations can normally be inferred from the analysis of the position and line shape of the electron absorption band. Supercritical environments are particularly appropriate to investigate density effects on the electronic localization, since supercritical fluids allow sweeping the whole fluid density range without worrying about the occurrence of liquid–gas phase transitions in the host fluid, as already mentioned. There is a long-standing interest in investigating the localization–delocalization transition of excess electrons in supercritical water and other fluids [50,51]. There are several indirect experimental evidence of this phenomenon in the literature [52,53], but no accurate molecular level description of the phenomena.

In this context, we recently examined electronic solvation in supercritical states of water and ammonia using Feynman path integral molecular dynamics techniques [27,28]. Our simulation experiments found that at temperatures slightly above the critical one ($T_c = 647$ K), the localization transition in water, expressed in terms of the spatial extent of the electron, takes place in a density range roughly between one- and two-tenths of the triple point density. This value is substantially higher than that previously estimated from mobility measurements at nearly critical conditions. We also found that, similarly to what is found at ambient temperatures, the broad absorption spectrum at supercritical conditions comprises transitions from an s-ground state into three p-like excited states, exhibiting a considerable redshift as one moves to lower densities, somewhat larger than that found in experiments. For the case of the electronic solvation in ammonia [28], we observe several differences from the aqueous systems [27]. First, compared to what is found in water, changes in temperature and density seem to promote less dramatic disruptions in the intermolecular spatial correlations of ammonia. Second, the differences in the critical temperatures of both fluids lead to more important quantum thermal effects on the electron solvation for the case of ammonia. Our results show that the solvation properties of excess electrons result from a complex interplay between a variety of phenomena, including: (i) packing effects and specific intermolecular connectivity of the host fluid, (ii) thermal quantum fluctuations, and (iii) the specific characteristics of the coupling between the electron and the solvent response.

Our simulations are based on well-established mixed quantum-classical methods in which the electron is described by a fully quantum-statistical mechanical approach whereas the solvent degrees of freedom are treated classically. Details of the method are described elsewhere [27,28]. The extent of the electron localization in different supercritical environments can be conveniently probed by analyzing the behavior of the correlation length $R(\beta\hbar/2)$ of the electron, represented as polymer of pseudoparticles in the Feynman path integral representation of quantum mechanics. Using the simulation trajectories, R is computed from the mean squared displacement along the "polymer" path, $R^2(t - t') = \left\langle |\mathbf{r}(t) - \mathbf{r}(t')|^2 \right\rangle$, where $\boldsymbol{r}(t)$ represents the electron position at imaginary time t and $1/\beta$ is Boltzmann constant times the temperature.

Solvated electrons in water and ammonia in the vicinity of their corresponding triple points are known to be localized and characterized by length scales R of similar order of the size of a solvent molecule, i.e., intermediate between 3 and 4 Å. In contrast, for the particular case of low-density SCW ($\rho_w < 0.1$ g/cm^3), the correlation function $R(t)$ looks similar to that corresponding to a Gaussian, non-interacting bead polymer, with the longest correlation length comparable to λ_{DB}, the electron de Broglie thermal wavelength. In Figure 16-8 we present results for R in SCW and supercritical ammonia (SCA), at $T^* = T/T_c = 1.10$ for each fluid. To facilitate comparison between results from the two fluids, we have scaled all temperatures and densities by the corresponding critical ($T^*=T/T_c$) and triple point ($\rho^*=\rho/\rho_t$) values, respectively. The sharp drop to practically half of its ideal, i.e., non-interacting, ρ=0, value within a narrow density interval along with a change in the slope of the curve reveal that the onset of the electronic localization in SCA takes place at $\rho_a^* \sim 0.25$ and

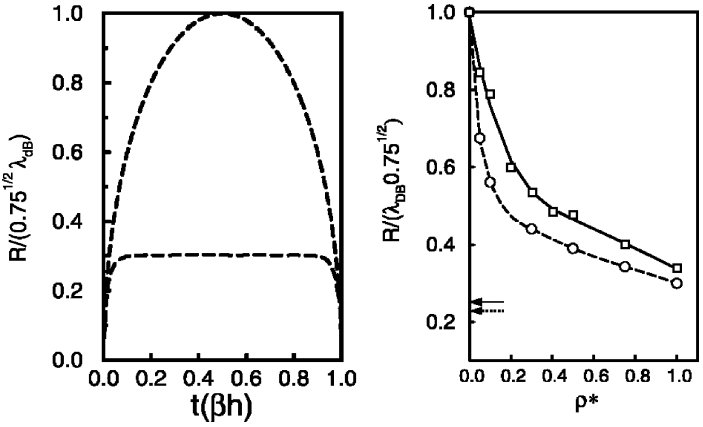

Figure 16-8. Left: two limiting behavior of the electron correlation length: free (*upper curve*) and localized (*lower*). *Right*: electron correlation lengths in SCW (*circles*) and SCA (*squares*) as function of the reduced density. The horizontal arrows indicate the correlation lengths for solvated electrons at the corresponding triple points of the two fluids. Change in slope indicates the onset of localization [28]

for SCW at $\rho_w{}^* \sim 0.15$. This difference in the transition point is due to the fact that polarization fluctuations in the latter fluid are more effective in promoting electronic localization.

Analysis of the radial pair distribution function for the electron centroid and solvent center-of-mass computed at different densities reveals some very interesting features. At high densities, the essentially localized electron is surrounded by the solvent resembling the solvation of a classical anion such as Cl^- or Br^-. At low densities, however, the electron is sufficiently extended (delocalized) such that its wavefunction tunnels through several neighboring water or ammonia molecules (Figure 16-9).

Using a plane wave representation for the electron wavefunction with 16^3 grid points and approximately 800 independent electronic and molecular configurations from the path integral molecular dynamics trajectories, we have also computed the density of states for the electron under different supercritical conditions of the solvents and the corresponding steady-state optical absorption spectra. The latter were computed within the dipolar approximation from the following expression within the Frank–Condon approximation:

$$I(E) \propto (1 - e^{-\beta E})E \left\langle \sum_{i>0, \varepsilon_i < 0} |\langle \psi_0 | \hat{\mu} | \psi_i \rangle|^2 \delta(\varepsilon_i - \varepsilon_0 - E) \right\rangle$$

where ε_i and ψ_i represent the ith electronic eigenenergy and eigenfunction, respectively, $\hat{\boldsymbol{\mu}}$ is the dipole moment operator, and the sum extends over all bound states. Results for the density of states reveal that the distribution of bound states at supercritical conditions includes four states: a ground s-like state and three, nondegenerate, somewhat more delocalized excited states, with p-like characteristics.

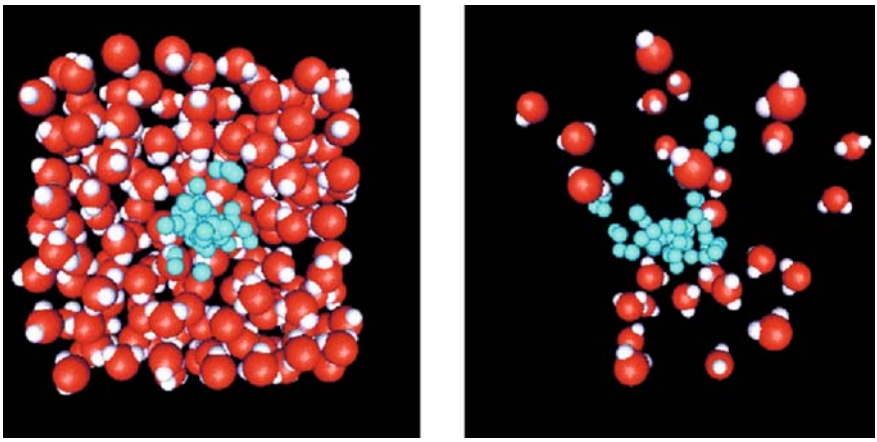

Figure 16-9. Snapshots of molecular configurations for the solvated electron polymer at two supercritical densities of water at 645 K. *Left*: 1.0 g/cm^3; *Right*: 0.05 g/cm^3

Similar results have also been reported for the distributions of the delocalized LUMO (identified as possible precursor states for solvated electrons) and the LUMO+1 Kohn–Sham orbitals of supercritical water in a recent ab initio molecular dynamics simulation study [54]. The computed ground state absorption spectra at four supercritical densities and at room temperature are shown in Figure 16-10. The position of the maximum at 298 K is slightly blue-shifted compared to experimental data, as noted elsewhere. Similar to the density of states, temperature alone does not lead to significant changes in the absorption band. Hamiltonians that include many-body polarizability effects yield better estimates of the room-temperature spectra but also fail to reproduce experimental spectra in hot water. At lower densities (0.5 g/cm^3), however, where interaction-induced effects are less important, the maxima of our simulated spectra are in reasonable agreement with the experimental data at similar thermodynamic conditions (see inset), being 0.2–0.3 eV below the two experimental values at the lowest density for which the spectrum has been calculated (0.1 g cm^3). The analysis of the spectrum at even lower densities, where all energy gaps become comparable to $k_B T$, requires transitions from different excited states (non-adiabatic dynamics) and such calculation has not been yet undertaken for these systems to the best of our knowledge.

The density dependence of the spectral red shifts for both SCW and SCA at intermediate to low densities is somewhat more pronounced than that experimentally measured. Unlike some reported experimental data, there are apparently no noticeable changes in the density dependence of the spectral band maximum as the localization transition is crossed. At any rate, the overall quality of agreement is comparable to that found at room temperature, which reveals a remarkable performance of the adopted model in view of the simplicity of the interaction potentials, the fact that there are no adjustable parameters, and the wide variety of supercritical

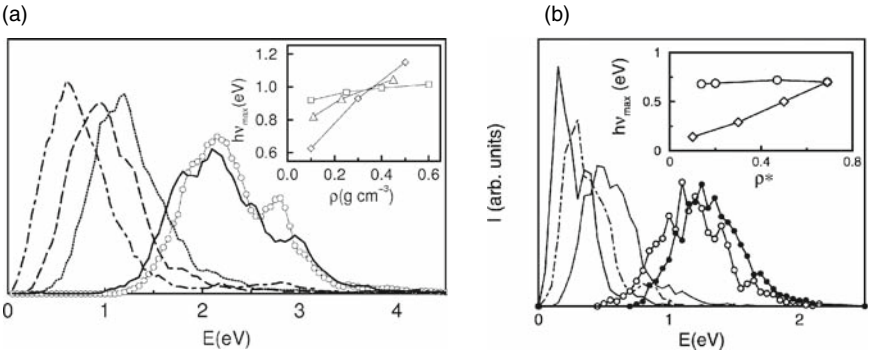

Figure 16-10. Left: optical absorption spectra for the solvated electron for different densities in SCW at 645 K. *Solid line*, 1.0 g/cm^3; *dotted line*, 0.5 g/cm^3; *dashed line*, 0.3 g/cm^3; *dot-dashed line*, 0.1 g/cm^3. Empty circles are for ambient conditions. *Right*: same for SCA at T^*=1.1 (reduced density are as marked). Filled circle are for the triple point of ammonia. The insert shows the density dependence of the absorption maxima in the low-density interval investigated. SCW: diamonds, our work; squares and triangles are from experiments. SCA: diamonds: our work; *circles*: experimental data. *Left* and *right* figures are from Ref. [27] and [28], respectively

conditions examined. Better agreement with experiments will certainly require refinements in the pseudopotential.

16.3.3. Excess Electrons in Polar SCFs – Solvation Dynamics

Solvation dynamics refers to the solvent reorganization or relaxation that accompanies the external excitation of a probe solute, usually a fluorescent organic dye or simply an excess solvated electron [55]. Experimentally, the process of solvent reorganization can be time monitored by the time evolution of the fluorescence emission in time-dependent ultra-fast Stokes shift spectroscopy.

The basic physical picture is schematically represented in Figure 16-11. Ground (S_0) and first excited (S_1) states of the solute have different charges or charge distributions. Upon solute excitation by a short-pulsed external laser, the solvent undergoes structural rearrangements in order to relax around the charge distribution of solute state S_1. Individual solute probes may fluoresce at different times from the excitation and, therefore, will emit at different wavelengths (red shifting) depending on the degree of reorganization of the solvent in its close vicinity.

A time-resolved fluorescence measurement collects the emission spectra at regular time intervals after the excitation, defined at $t=0$, from which one constructs the normalized solvation dynamics response function, $S(t) = [h\nu(t)-h\nu(\infty)]/[h\nu(0)-h\nu(\infty)]$ [55]. In our simulations, hundreds of uncorrelated equilibrium molecular configurations with the electron in its ground state Ψ_0 were selected as initial configurations ($t=0$). From each of these initial configurations, the electronic state is adiabatically promoted to the first excited state Ψ_1, the system is then propagated in

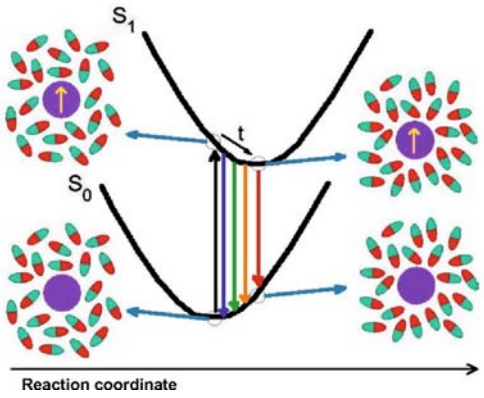

Figure 16-11. Representation of time-resolved spectroscopy

time over the S_1 adiabatic surface potential, and the instantaneous electron energy gap $\Delta E(t) = \varepsilon_1(t) - \varepsilon_0(t)$ is computed at each timestep of the simulation as the solvent reorganizes itself around the excited electron. An ensemble of non-equilibrium time history of $\Delta E(t)$ is thus obtained from which we compute the solvation dynamics response function $S_E(t) = \langle \Delta E(t) - \Delta E(\infty) \rangle_{neq} \big/ \langle \Delta E(0) - \Delta E(\infty) \rangle_{neq}$ [30].

Results for $S_E(t)$ at the ammonia supercritical states discussed above are shown in Figure 16-12. The high-density curve exhibits a clear bimodal character that is typical of solvation responses of dense liquids: a Gaussian-type initial decay accounting for a sizable fraction (~40–50%) of the total decay, followed by a much slower,

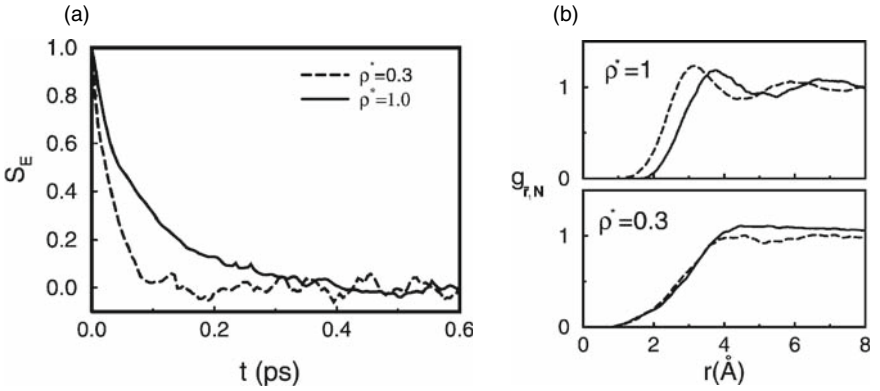

Figure 16-12. Left: normalized non-equilibrium response function for the electron energy gap in SCA at different densities and 450 K. *Right*: equilibrium spatial correlations between the center of the first excited state $\mathbf{r}_1$ and the nitrogen site of ammonia for the supercritical states. *Solid* and *dashed lines* correspond to adiabatic trajectories with forces taken from the ground and first excited electronic states, respectively. Adapted from Ref. [28]

diffusive tail that accounts for the manifold of slow processes, mainly rotational and spatial diffusive motions, that drive the long-time response of the solvent. This bimodal character is much less prominent at lower densities and the response practically vanishes after a sharp decay lasting ∼100 fs. Gaussian fits for this portion of the $S_E(t)$ response yield a relaxation rate of 25–30 fs^{-1} which is associated with the ballistic inertial reorientational motions of ammonia.

The near absence of diffusional contributions at low-density supercritical states is an important feature that seems to be unique to these environments. In order to investigate the differences in the mechanisms through which these systems relax, we present in Figure 16-12 (right panel) results for the two limiting, $t = 0$ and $t = \infty$, equilibrium spatial correlations between the center of the excited electronic distribution, $\bar{\mathbf{r}}_1 = \langle \Psi_1 | \mathbf{r} | \Psi_1 \rangle$, and the solvent's nitrogen site. Although, at high densities, one expects considerable rearrangements in the solvent spatial distribution around the solute due to the gross symmetry changes in the electronic wavefunction, the $t = 0$ distribution can be practically superimposed to that corresponding to $t = \infty$, by simply operating a negative, 0.5 Å shift in the radial coordinate (upper panel). On the other hand, at low densities, the changes in the two limiting distributions are much less pronounced, and are to be found at long range. Given the observed differences in the spatial correlations, we are led to believe that the slow portions of the relaxations at high densities can be ascribed to the approaching of the solvent molecules toward the center of the electronic charge. Finally, and more importantly, the shift toward smaller distances in the excited $g_{\bar{\mathbf{r}}_1 N}(r)$ function indicates that the localization mechanism for excited electrons in SCA is mainly driven by the polarization fluctuations that prevail in these environments, with only minor contributions from short-ranged, excluded volume effects, arising from electron–solvent exchange forces. Analysis of the non-equilibrium adiabatic evolution of the quantum mechanical electron spatial extent during the first 1.0 ps from the excitation provides further support to this interpretation [28].

16.4. CONCLUDING REMARKS

In this chapter, we have reviewed some of our own work on solvation properties in supercritical fluids using molecular dynamics computer simulations. We have presented the main aspects associated with the solvation structures of purine alkaloids in CO_2 under different supercritical conditions and in the presence of ethanol as co-solvent, highlighting the phenomena of solvent density augmentation in the immediate neighborhood of the solute and the effects from the strong preferential solvation by the polar co-solvent. We have also presented a summary of our results for the structure and dynamics of supercritical water and ammonia, focusing on the dielectric behavior of supercritical water as functions of density and temperature and the behavior of excess solvated electrons in aqueous and non-aqueous associative environments.

For CO_2 systems, we believe that the three most promising venues for further theoretical investigations are (1) to gain better understanding of the intermolecular

interactions between CO_2 and group contributions of important solute types, such as surfactant, polymers, and room-temperature ionic liquids and to correlate these interactions with new and improved methods for computing solvation free energies in such environments [56]; (2) to devise and apply new computer simulations methods for studying reactive properties in supercritical fluids; and (3) to further investigate interfacial systems containing SC-CO_2, with goals set to better understand the role of these systems in the synthesis of nanomaterials.

As for supercritical water and related systems, we believe that much effort is still needed to understand the formation and stability of molecular clusters and dilute conditions and their role in the fundamental solvation characteristics of these solvents. Very little is known today regarding the underlying molecular mechanisms associated with the role of supercritical water as both reaction media and reactant, especially in connection with quantum mechanical charge transfer and bond breaking effects. The latter is extremely important to our understanding, and, therefore, control, of supercritical water as a "green chemistry" reaction environment for practical applications.

REFERENCES

1. Noyori R (1999) Chem Rev 99(2): Special Issue (for recent accounts on chemical applications and fundamental aspects of supercritical fluids)
2. Erkey C, Kiran E (2006) J Supercrit Fluids 38(2): Special Issue (for reviews on the many applications of supercritical fluids in chemistry and chemical engineering)
3. Hutchinson KW, Foster NR (eds) (1995) Innovations in supercritical fluids science and technology, ACS Symposium Series 608, American Chemical Society, Washington (for recent advances in technological processes involving supercritical fluids)
4. Eckert CA, Knutson BL, Debenedetti PG (1996) Nature 383:313
5. Nodari RO, Guerra MP (1999) Biodiversidade: aspectos biológicos, geográficos, legais e éticos. In: J. Simões et al. (eds) Farmacognosia: da planta ao medicamento (in Portuguese), Universidade UFRGS, Porto Alegre, Brazil
6. Rosa PTV, Meireles MAA (2005) J Food Eng 67:235
7. Savage PE, Gopalan S, Mizan TI, Martino CJ, Brock EE (1995) AICHE J 41:1723
8. Cooper AI (2000) J Mater Chem 10:207
9. Yeo SD, Kiran E (2005) J Supercrit Fluids 34:287
10. Jung J, Perrut M (2001) J Supercrit Fluids 20:179
11. Hakuta Y, Hayashi H, Arai K (2003) Curr Opt Solid State Mat Sci 7:341
12. Klibanov AM (2001) Nature 409:241
13. Kamat SV, Beckman EJ, Russel AJ (1995) Crit Rev Biotech 15:41
14. Weingartner H and Franck EU (2005) Angew Chem Int Ed 44:2672
15. Eckert CA, Liotta CL, Bush D, Brown JS, Hallett JP (2004) J Phys Chem B 108:18108
16. Tucker SC, Maddox MW (1998) J Phys Chem B 102:2437
17. Stephens MD, Saven JG, Skinner JL (1997) J Chem Phys 106:2129
18. Elles CG, Crim FF (2006) Annu Rev Phys Chem 57:273
19. Marcus Y (2005) J Phys Org Chem 18:373
20. Patel N, Biswas R, Maroncelli M (2002) J Phys Chem B 106:7096
21. Song W, Biswas R, Maroncelli M (2000) J Phys Chem A 104:6924

22. Rocha SRP, Johnston KP, Westacott RE, Rossky PJ (2001) J Phys Chem B 105:12092
23. Rocha SRP, Johnston KP, Rossky PJ (2002) J Phys Chem B 106:13250
24. Fávero FW, Skaf MS (2005) J Supercrit Fluids 34:237
25. Fávero FW (2007) PhD Thesis, Institute of Chemistry, State University of Campinas
26. Skaf MS, Laria D (2000) J Chem Phys 113:3499
27. Laria D, Skaf MS (2002) J Phys Chem A 106:8066
28. Rodriguez J, Skaf MS, Laria D (2003) J Chem Phys 119:6044
29. Muldoon MJ, Aki SNVK, Anderson JL, Dixon JK, Brennecke JF (2007) J Phys Chem B 111:9001
30. Keskin S, Kayrak-Talay D, Akman U, Hortacsu O (2007) J Supercrit Fluids 43:150
31. Anderton RM, Kauffman JF (1995) J Phys Chem 99:13759
32. Song W, Maroncelli M (2003) Chem Phys Lett 378:410
33. Li HP, Arzhantsev S, Maroncelli M (2007) J Phys Chem B 111:3208
34. James J (1991) Caffeine and health, Academic Press, San Diego, CA
35. Saldaña MDA, Mohamed RS, Baer MG, Mazzafera P (1999) J Agric Food Chem 47:3804
36. Mohamed RS, Saldaña MDA, Mazzafera P, Zetzl C, Brunner G (2002) Ind Eng Chem Res 41:6751
37. Johannsen M, Brunner G (1994) Fluid Phase Equilib 95:215
38. Li S, Varadarajan GS, Stanley H (1991) Fluid Phase Equilib 68:263
39. Harris JG, Yung KH (1995) J Phys Chem 99:12021
40. Frisch MJ et al. (1998) Gaussian 98, Revision A. 7, Gaussian, Inc., Pittsburgh, PA
41. Kaminski GA, Friesner RA, Tirado-Rives J, Jörgensen WL (2001) J Phys Chem B 105:6474
42. Beckman EJ (2004) Chem Commun 17:1885
43. Sarbu T, Styranec T, Beckman EJ (2000) Nature 405:165
44. Okada K, Yao M, Hiejima Y, Kohno H, Kajihara Y (1997) J Chem Phys 107:9302
45. Okada K, Yao M, Hiejima Y, Kohno H, Kajihara Y (1999) J Chem Phys 110:3026
46. Bursulaya BD, Kim HJ (1999) J Chem Phys 110:9656
47. Yoshida K, Matsubayasi N, Nakahara M (2007) J Chem Phys 127:174509
48. Rossky PJ, Simon JD (1994) Nature 370:263
49. Turi L, Sheu S-W, Rossky PJ (2005) Science 309:914
50. Gaathon A, Czapski G, Jortner J (1972) J Chem Phys 58:2648
51. Jortner J, Gaathon A (1977) Can J Chem 55:1801
52. Cline JA, Jonah CD, Bartels DM (2000) In The solvated electron in supercritical water: spectra, yields, and reactions, Proceedings of the 1st International Symposium in Supercritical Water-cooled Reactors, Design, and Technology, Tokyo, Nov 6–9
53. Dimitrijevic NM, Takahashi K, Bartels DM, Jonah CD (2001) J Phys Chem A 105:7236
54. Boero M, Terakura K, Ikeshoji T, Leiw CC, Parrinello M (2001) J Chem Phys 115:2219
55. Ladanyi BM, Skaf MS (1993) Annu Rev Phys Chem 44:335
56. Su Z, Maroncelli M (2006) J Chem Phys 124:164506

CHAPTER 17

A QUANTUM CHEMICAL APPROACH TO FREE ENERGY CALCULATION FOR CHEMICAL REACTIONS IN CONDENSED SYSTEM: COMBINATION OF A QUANTUM CHEMICAL METHOD WITH A THEORY OF STATISTICAL MECHANICS

HIDEAKI TAKAHASHI[1], NOBUYUKI MATUBAYASI[2], AND MASAYOSHI NAKANO[3]

[1] *Division of Chemical Engineering, Department of Materials Engineering Science, Graduate School of Engineering Science, Osaka University, Toyonaka, Osaka 560-8531, Japan, email: takahasi@cheng.es.osaka-u.ac.jp*

[2] *Institute for Chemical Research, Kyoto University, Uji, Kyoto 611-0011, Japan, e-mail: nobuyuki@scl.kyoto-u.ac.jp*

[3] *Department of Materials Engineering Science, Graduate School of Engineering Science, Osaka University, Toyonaka, Osaka 560-8531, Japan*

Abstract: A recent development to compute free energy changes associated with chemical processes in condensed phase has been reviewed. The methodology is based on the hybrid quantum mechanical/molecular mechanical (QM/MM) approach combined with the novel theory of solutions, where the electronic structure calculation in the QM subsystem is conducted by the Kohn–Sham density functional theory (KS-DFT) utilizing the real-space grids to represent the one-electron orbitals, while the distribution functions for MM molecules needed to compute the free energy change of interest are constructed in terms of the QM/MM interaction energies. The following sections are devoted to the overview of the existing methodologies for the free energy calculation for chemical event and to the detailed description of the real-space-based DFT as well as the theory of solutions. Next we present a theory to combine the quantum mechanics with the statistical mechanics, where an emphasis will be placed on the treatment of the many-body interaction inherent with the quantum mechanical object. Finally, the several applications of the methodology to the solution system are presented to demonstrate the accuracy and efficiency of the method

17.1. INTRODUCTION

It is a subject of great interest and significance in computational and theoretical chemistry to determine possible pathways of chemical reactions in condensed matter such as biological molecules, solutions, or materials [1]. The quantity that governs

S. Canuto (ed.), Solvation Effects on Molecules and Biomolecules, 455–505.
DOI 10.1007/978-1-4020-8270-2_17,

the reaction path in many-particle system is, of course, the free energy change associated with the process. Hence, it is of primary importance to compute free energy change for the chemical event in large systems. In the enzymatic reaction, for instance, it is well known that the whole molecular structure of the protein immersed in water fluctuates, which may play a decisive role for the protein to exhibit its elaborate function. Hence, analyzing the property at the global energy minimum of the structure is obviously insufficient to understand how the aggregate of amino acid polymers regulates the enzymatic activity. Thus, the statistical mechanical treatment is essential for the study of the function of the protein. It can be readily recognized, however, that the free energy calculation is a heavily demanding task even under the state-of-the-art computational environment. The theoretical description of the chemical reaction essentially necessitates the use of the quantum chemical method [2,3] that is notorious for its large computational cost. Furthermore, the free energy calculation employing the method of the molecular simulations requires a large number of configuration samplings for its convergence. Thus, the major difficulty we encounter to solve the problem locates in the quantum chemical calculation combined with the method of statistical mechanics. The present article will address the issue of the development of an efficient methodology to compute free energy change associated with a chemical event in a large system. In the following we will make a review for the methodology related to quantum chemistry and statistical mechanics as well.

The quantum chemical approach [2] based on the molecular orbitals theory has been successfully applied to various systems. However, they have been limited mainly to the reactions of relatively small molecules in the gas phase. The difficulty in the quantum chemical method arises from the fact that the computational cost increases drastically as the number N of electrons in the system increases. Even at the low level of theory that neglects the electron correlation, it scales in order N^3–N^4. Indeed, it becomes practically infeasible for large system to include subsequent complicated procedure to account for the electron correlations. The recent development in the Kohn–Sham density functional theory (KS-DFT) [4] substantially alleviated such a difficulty by projecting the non-local exchange and correlation potential onto a local potential by a functional of the local electron density or its gradient. It allows one to compute the complicated exchange–correlation energy of electrons in comparable accuracy to the sophisticated molecular orbitals theory within a reasonable computational cost. A lot of theoretical works are being devoted to refine the exchange–correlation functionals. So far the method has been extensively applied to various systems and the efficiency has been well established though it suffers from many inherent deficiencies. Despite the success in DFT, the scope of its application is still limited to relatively small-sized systems.

In addition to the development in the methodology to compute electronic structures, there have been several attempts to handle the simulation of a chemical event in a system with a large number of degrees of freedom. The Car–Parrinello (CP) approach [5], often referred to as first-principles molecular dynamics (FPMD) method, opened the way to the molecular dynamics simulations based on the first-principles electronic structure calculations. The point of the method is to circumvent the explicit

diagonalization of the effective Hamiltonian in DFT by propagating the one-electron orbitals in the imaginary time. The CP approach is much less costly as compared with the conventional FPMD where the electronic state is strictly converged to the ground state based on the Born–Oppenheimer approximation at each MD step. However, the execution of CPMD for a system containing only a few hundreds of atoms requires massively parallel computers. The CP approach is particularly efficient for the reaction where whole of the system undergoes serious changes in the electronic structure. Within the hybrid quantum mechanical/molecular mechanical (QM/MM) approach [6], only the active site of the system is described quantum chemically while the electronically static environment is represented by classical force fields. The QM/MM method takes advantage of the fact that only the small part of the system takes part in the chemical reaction in most cases. The QM/MM simulations have been extensively applied to the reactions in solutions or biological systems. The order-*N* approach [7] provides a framework to compute electronic state where the computational cost scales linearly with respect to the number *N* of electrons contained in the system. Such method was first initiated by Yang [8] who proposed to divide the whole system into overlapping subsystems and the electronic structures of the constituent domains are solved locally. Then, the domains are connected by a common chemical potential introduced to ensure the norm conservation for the density matrix. The underlying key concept for this approach, often referred to as "divide and conquer", is clearly based on the "near-sightedness principle" postulated by Prodan and Kohn [9] and it constitutes the common framework of other order-*N* approaches. Substantial efforts are being made to establish an efficient algorithm. However, so far, we have no method of choice which can be used in practical applications with satisfying reliability.

To achieve our purpose, it is also desirable to obtain statistical mechanical properties within a modest computational cost by sampling the molecular configurations effectively. The free energy perturbation (FEP) [10] method, that is based on the Kirkwood charging formula, introduces a number of intermediate points on an arbitrary path connecting the initial and the final states of the event of interest. Then, the free energy change is obtained by integrating the free energy difference between the adjacent points along the path. The FEP approach is numerically exact, however, it requires a sufficient number of samplings in configuration space to achieve convergence at each intermediate point with no physical importance. As a consequence, FEP involves a huge number of configuration samplings along the reaction path. The solution theory, on the other hand, describes the free energy change in terms of the spatial distribution functions. In principle, the free energy change associated with a chemical reaction can be obtained by the solvation free energies of the reactant and the product. The solvation free energy can be exactly expressed in terms of the spatial distribution function of the solvent around the solute by virtue of the fact that one-to-one correspondence is rigorously established between the set of interaction potentials and the resultant distribution functions. Note that the solvent distribution is fully specified on the six-dimensional coordinate even when the rigid model is assumed for the molecule. In practice, the method of the reference interaction site

model (RISM) [11,12] is often utilized, where the distribution expressed in the full coordinate is reduced to a set of radial distribution functions between the interaction sites placed on the molecules. Then, the free energy can be obtained by solving a set of integral equations for the site–site radial distribution functions, for which PY or HNC approximations [13] are employed. Recently N. M. developed a novel approach, referred to as theory of energy representation [14,15,16], where the distribution functions of the solute–solvent interaction energy play a fundamental role to describe the solvation free energy. He demonstrated that a solution theory based on the energy distribution functions can also be rigorously constructed in parallel to that based on the spatial distributions. Within the framework of the theory of energy representation, each solvent molecule is treated as a whole, and the concept of the interaction site is no longer needed. Hence, the solvation free energy can be exactly expressed in terms of the one-dimensional distribution functions for any pair of solute and solvent. The details for the methodology will be given in Section 17.3.

In the preceding two paragraphs, we have briefly reviewed the independent approaches related to the quantum chemistry and the statistical mechanics. What we have to do to accomplish the free energy calculation in a condensed phase is to combine the method of quantum chemistry with that of statistical mechanics. Obviously the combination of the CP approach with the FEP procedure is most time consuming and will be almost intractable under an ordinary computational environment. The most popular approach in the quantum chemistry to incorporate the effect of the solvent is to combine the SCF procedure in the quantum chemistry with the polarizable continuum model (PCM) [17]. Since PCM is not based on the molecular theory, it suffers from the lack of the ability to describe the short-range interactions such as hydrogen bonds. However, it has been widely utilized in the quantum chemical calculations due mainly to the usefulness in practical applications. In the method of RISM-SCF [18]. on the other hand, SCF calculation is coupled with the solution of the RISM integral equations for the solvent and it allows us to construct the electronic structure of the solute as well as its solvation free energy with the sound description of the solvent as an aggregate of molecules. The major drawback of the method is that the electron density of the solute, which is spatially diffuse in nature, is reduced to a set of point charges for the construction of the site–site radial distributions. It is, then, anticipated that serious overestimation in the free energy takes place at the anionic sites of the solute. In our recent development [19], we combined the QM/MM approach with the method of the energy representation (QM/MM-ER). As noted above, the theory of energy representation is free from the concept of the interaction site; it is amenable to the combination with the quantum mechanical object in which the electron density is continuously distributed over the space. Thus, the QM solute can be represented without the loss of information content in the free energy calculations. However, a device has to be made to take into consideration the many-body interaction of the QM object since the standard version of the energy representation assumes that the solute–solvent interaction is pairwise. In Section 17.4 we provide the details of the QM/MM-ER method, where the focus will be placed on the formulation of the many-body effects in the solute–solvent interactions.

This review is organized as follows. In Section 17.2, the methodology of Kohn–Sham DFT with real-space grids [20,21] and its efficiency in the parallel computation are discussed. The theory of energy representation is formulated in Section 17.3, where the FEP and RISM theories are also introduced to make comparisons. In Section 17.4, a rigorous formulation to couple the QM/MM approach with the theory of energy representation is given. Section 17.5 is devoted to the demonstration of the QM/MM-ER simulation to examine the accuracy and efficiency of the method by computing the solvation free energy and the free energy change associated with a chemical process in aqueous solution.

17.2. REAL-SPACE GRID QM/MM APPROACH

17.2.1. Kohn–Sham Density Functional Theory

The heart of the density functional method is to express the electronic properties of an N-electron system by formulating a functional of its total electron density $n(\mathbf{r})$. Here, we briefly review the DFT in the electronic structure calculation. The first model based on the electron density was given by Thomas [22] and Fermi [23] who proposed an approximate functional for the total energy, although it has a critical drawback that it cannot realize chemical bonds due to the failure in expressing the kinetic energy. Later, their approach had been validated by the theorem given by Hohenberg and Kohn [24] who proved that one-to-one correspondence is established between an external potential and the resulting electron density. This was the milestone that triggered the subsequent extensive growth in DFT. A year later, Kohn and Sham [4] developed a framework of a practical theory to compute total energy and density by introducing one-electron orbitals in the analogous way taken by Slater [25]. The point of their approach is to construct the density $n(\mathbf{r})$ of a fully interacting N-electron system by that of the non-interacting *reference* system. One can, then, obtain the *exact* total energy provided that the true exchange and correlation functional is known. The existence of the universal functional $E_{\mathrm{xc}}[n]$ for the electron correlation is guaranteed by the HK theorem, however, only the approximate form can be available. Owing to the efforts by many quantum chemists or physicists devoted to the development of the functional, Kohn–Sham DFT can now afford almost comparable accuracy to the sophisticated molecular orbitals theories with much less computational costs.

The Kohn–Sham equations for one-electron orbitals $\{\psi_i\}$ is in the form as

$$\left[-\frac{1}{2}\nabla_i^2 + v_{\mathrm{eff}}(\mathbf{r})\right]\psi_i(\mathbf{r}) = \varepsilon_i\psi_i(\mathbf{r}), \tag{17-1}$$

where $v_{\mathrm{eff}}(\mathbf{r})$ is the effective potential for an electron and the atomic unit is adopted. Further, $v_{\mathrm{eff}}(\mathbf{r})$ in Eq. (17-1) is decomposed as

$$v_{\mathrm{eff}}(\mathbf{r}) = v_{\mathrm{ps}}(\mathbf{r}) + v_{\mathrm{H}}(\mathbf{r}) + v_{\mathrm{xc}}(\mathbf{r}), \tag{17-2}$$

where the first, second, and third terms are, respectively, sum of the atomic pseudopotential, Hartree potential, and exchange–correlation potential. The accuracy of the Kohn–Sham DFT is obviously dependent on the choice of the functional $v_{\mathrm{xc}}(\mathbf{r})$ in Eq. (17-2).

$v_{\mathrm{xc}}(\mathbf{r})$ is given by the functional derivative of $E_{\mathrm{xc}}[n]$ with respect to $n(\mathbf{r})$. In the local density approximation (LDA) [3], it can be written in terms of the exchange–correlation energy $\varepsilon_{\mathrm{xc}}(n(\mathbf{r}))$ felt by an electron in a homogeneous electron gas of the given $n(\mathbf{r})$ thus,

$$\begin{aligned} v_{\mathrm{xc}}(\mathbf{r}) &= \frac{\delta E_{\mathrm{xc}}[n]}{\delta n(\mathbf{r})} \\ &= \frac{\delta}{\delta n(\mathbf{r})} \int \mathrm{d}\mathbf{r} n(\mathbf{r}) \varepsilon_{\mathrm{xc}}(n(\mathbf{r})) \\ &= \varepsilon_{\mathrm{xc}}(n(\mathbf{r})) + n(\mathbf{r}) \frac{\delta \varepsilon_{\mathrm{xc}}(n(\mathbf{r}))}{\delta n(\mathbf{r})}. \end{aligned} \tag{17-3}$$

$E_{\mathrm{xc}}[n]$ in Eq. (17-3) is, further, decomposed into the contributions from the exchange and correlation energies,

$$E_{\mathrm{xc}}[n] = E_{\mathrm{x}}[n] + E_{\mathrm{c}}[n]. \tag{17-4}$$

The explicit form for $E_{\mathrm{x}}[n]$ was originally given by Dirac [26] as an approximation to the Hartree–Fock exchange energy,

$$E_{\mathrm{x}}^{\mathrm{LDA}}[n] = -\frac{3}{2}\left(\frac{3}{4\pi}\right)^{1/3} \sum_{\sigma} \int d\mathbf{r} n_{\sigma}(\mathbf{r})^{4/3} \tag{17-5}$$

where σ represents the up or down spin orientation. The most prevailing form for $E_{\mathrm{c}}[n]$ is formulated by Lee, Yang, and Parr (LYP) [27] who utilized the Colle and Salvetti [28] formula that expresses the correlation energy by a functional of the Hartree–Fock second-order density matrix. In the LYP approach, they successfully converted the formula given by Colle and Salvetti into a purely density functional form.

In the present work, we employ the Kleinman and Bylander [29] separable form for the norm-conserving pseudopotential $v_{\mathrm{ps}}(\mathbf{r})$ in Eq. (17-2):

$$v_{\mathrm{ps}}(\mathbf{r}) = \sum_{a} V_{\mathrm{loc}}^{a}(|\mathbf{r} - \mathbf{R}_a|) + \sum_{a,l,m} \frac{\left|\phi_{l,m}^{a} \Delta V_l^a\right\rangle \left\langle \phi_{l,m}^{a} \Delta V_l^a\right|}{\left\langle \phi_{l,m}^{a}\right| \Delta V_l^a \left|\phi_{l,m}^{a}\right\rangle}, \tag{17-6}$$

where $\mathbf{R}_a$, $\phi_{l,m}^{a}$, and ΔV_l^a are, respectively, the position vector of atom a, atomic pseudo-wavefunction of the angular momentum quantum number l and m, and the difference between the l-dependent pseudopotential V_l^a and the local pseudopotential V_{loc}^{a}. It should be noted for later reference that the use of the pseudopotential substantially alleviates the rapid behavior of the wavefunctions for valence electrons at atomic core regions.

17.2.2. Kohn–Sham DFT with Real-Space Grids

To solve the Kohn–Sham equations in Eq. (17-1), the one-electron orbitals ψ_i must be represented by a set of basis functions. In the field of quantum chemistry, atomic-orbital basis has been commonly used on the basis of the linear combination of the atomic orbitals (LCAO) approach [2]. The use of the Gaussian-type orbitals instead of the Slater-type orbitals makes the four-centered two-electron integrals easy, due to the fact that a product of the two Gaussian functions that have two different centers also becomes a Gaussian centered at another point. In practice, a basis function in LCAO is constituted from a linear combination of primitive Gaussian functions with fixed coefficients to mimic the behavior of a Slater-type function. A huge amount of two-electron integrals with respect to primitive basis functions are to be computed and stored in preparation for the self-consistent field (SCF) calculation. A critical drawback in the LCAO approach is that the Hamiltonian matrix has non-zero elements in the non-diagonal part, which inevitably leads to the increase in the amount of the data communications when a parallel algorithm is applied. Another prevailing method to expand the wavefunctions is to employ the set of plane waves, the eigenfunctions of the kinetic energy operator. Since a finite sum of the plane waves with discrete eigenvalues exhibits a periodicity, it is often utilized in the first-principles calculations of crystals. The matrix element for the kinetic energy operator appearing in Eq. (17-1) is readily computed in the momentum space, however, the exchange–correlation term $v_{\mathrm{xc}}(\mathbf{r})$ can be evaluated only after the total electron density is obtained in the real space. It is, therefore, required to transform all the one-electron wavefunction to the real-space representation from the momentum space to complete the operation of the effective Hamiltonian. In order to expedite the transformations of the wave functions between the real- and momentum-space representation, the fast-Fourier transformation (FFT) is utilized. Indeed, the procedure for the FFTs is the most time-consuming part in the whole calculation. Though the plane wave expansion method is useful for the single-CPU calculation, it is never suitable for parallel computing since the FFT spoils parallel efficiency especially when the distributed memory architectures are employed.

A recent development in the real-space formalism has been established by Chelikowsky and coworkers [30,31,32]. Since most of the operators in Eq. (17-2) are local in the real-space representation, it is quite natural to express the one-electron orbitals by a set of probability amplitudes on the discrete grid points that are uniformly distributed over a real-space cell. In the parallel implementation, we distribute the values such as wavefunctions or operators to the processors by dividing the cell into subspaces. In the case that the Hamiltonian matrix has non-zero elements only in the vicinity of its diagonal part, the data communications among the processors can be suppressed minimally by enabling the high-performance computing on the massively parallel computer. Figure 17-1 is a schematic illustration that shows how to divide the real-space cell in the case of the 4-CPU parallel computation. The division of the real space is designed so that the amount of the data communication among the CPUs becomes minimum. As shown in the figure, each CPU is required

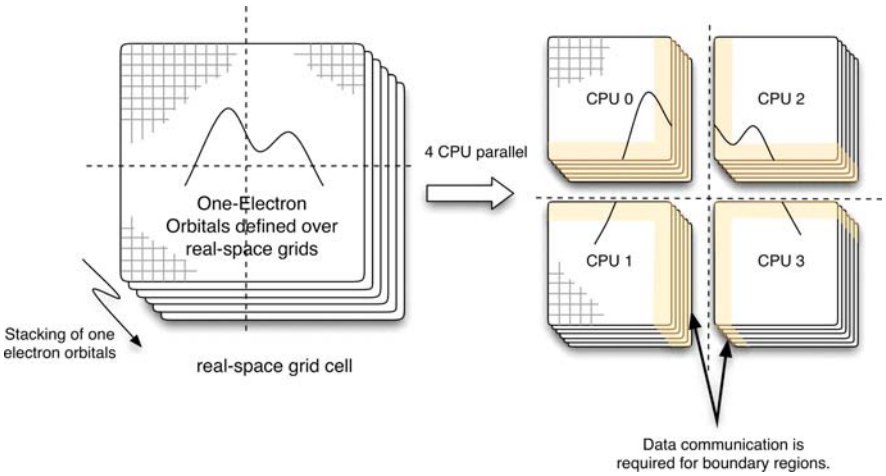

Figure 17-1. Schematic illustration to show how to divide the real-space QM cell in the case of the 4-CPU parallel computation

only to maintain the one-electron wavefunctions at its own subspace except for the boundary regions (the shaded region), which enables one to reduce the amount of the data communication and also the memory space used. Furthermore, real-space grid approach has several advantages: (1) local augmentation of the basis can be implemented straightforwardly by placing the double grids near the atomic core regions, (2) arbitrary boundary conditions (periodic or non-periodic) are available, and (3) overlap matrix of the real-space basis is unity and the molecular integration can be performed easily. The following paragraphs are devoted to the details for the implementation of the real-space grid approach focusing on the parallel efficiency in particular.

Within the real-space method, the kinetic energy operator is expressed by the finite-difference scheme. Here, we derive the matrix elements for the kinetic energy operator of one dimension in the first-order finite difference. By the Taylor expansion of a wavefunction $\psi(l)$ at the grid point l we obtain the equations,

$$\begin{aligned}\psi(l+1) &= \psi(l) + \frac{1}{1!}\psi'(l)\cdot h + \frac{1}{2!}\psi''(l)\cdot h^2 + \mathrm{O}(h^3),\\ \psi(l-1) &= \psi(l) - \frac{1}{1!}\psi'(l)\cdot h + \frac{1}{2!}\psi''(l)\cdot h^2 + \mathrm{O}(h^3),\end{aligned} \tag{17-7}$$

where h is the grid spacing. Adding the upper and lower equations in Eq. (17-7), the second-order derivative of the wavefunction at the grid l can be derived, thus,

$$\psi''(l) = \frac{1}{h^2}\{\psi(l+1) - 2\psi(l) + \psi(l-1)\} + \mathrm{O}(h^4). \tag{17-8}$$

Higher order finite-difference scheme can be formulated with the similar manner. The approximate matrix form of the kinetic energy operator in the first-order finite-difference expression becomes in the form as

$$-\frac{1}{2}\nabla^2 = -\frac{1}{2h^2}\begin{pmatrix} 2 & -1 & & & O \\ -1 & 2 & -1 & & \\ & -1 & 2 & -1 & \\ & & \ddots & \ddots & \ddots \\ O & & & -1 & 2 \end{pmatrix}. \tag{17-9}$$

It is noteworthy that the matrix is very sparse and it is profitable for parallelization since the non-locality of the operator is confined within the small region of the real space. The general form of the kinetic energy operator in three dimension by the higher order finite difference scheme is represented as

$$\begin{aligned} -\frac{1}{2}\nabla^2\psi(x_l, y_m, z_n) = -\frac{1}{2h^2}\Bigg[& \sum_{k_1=-L}^{L} C_{k_1}\psi(x_l + k_1 h, y_m, z_n) \\ & + \sum_{k_2=-L}^{L} C_{k_2}\psi(x_l, y_m + k_2 h, z_n) \\ & + \sum_{k_3=-L}^{L} C_{k_3}\psi(x_l, y_m, z_n + k_3 h)\Bigg], \end{aligned} \tag{17-10}$$

where the number L denotes the order of the expansion and C_{k_1}, C_{k_2}, and C_{k_3} are the expansion coefficients for which a table is given by Chelikowsky [31] for L = 1–6.

The classical electronic potential $v_{\mathrm{H}}(\mathbf{r})$ in Eq. (17-2), referred to as Hartree potential, is defined by

$$v_{\mathrm{H}}(\mathbf{r}) = \int \frac{n(\mathbf{r}')}{|\mathbf{r} - \mathbf{r}'|}\mathrm{d}\mathbf{r}'. \tag{17-11}$$

In the periodic system Eq. (17-11) can be easily evaluated by transforming the electron density to the reciprocal space by utilizing the fast Fourier transformations (FFT). In the non-periodic system, on the other hand, $v_{\mathrm{H}}(\mathbf{r})$ can be determined by the direct summation of the classical electron repulsions for all the pair of electron densities on the grid points. However, it is computationally very demanding because it requires twofold loop for all the grid point in the real-space cell. Furthermore, in the parallel implementation, each CPU must be provided with the densities on all grid points in the cell. It means that a large amount of data must be communicated among the processors at every SCF step. Barnett and Landman [33] proposed a method that utilizes the FFT even for non-periodic system. Unfortunately, the use of FFT spoils the parallel efficiency on a cluster consisting of independent computers combined

through networking as described above. For the high parallel performance we take the approach to solve the following Poisson equation for $v_{\mathrm{H}}(\mathbf{r})$,

$$\nabla^2 v_{\mathrm{H}}(\mathbf{r}) = -4\pi n(\mathbf{r}), \tag{17-12}$$

for which the conjugated gradient (CG) procedure with an approximate boundary condition is employed. The Laplacian operator in Eq. (17-12) can also be expressed by the finite-difference method as represented in Eq. (17-10). This implies that the values that must be communicated to solve the Poisson equation are common to those used in the computation of the kinetic energy operator. It should also be noted that the CG algorithm can achieve a rapid convergence of the Hartree potential without any particular choice of the initial guess for the potential. As a boundary condition for Eq. (17-12), we use the expression,

$$v_{\mathrm{H}}^{\mathrm{BD}}(\mathbf{r}) = \sum_a \frac{Q_a}{|\mathbf{r} - \mathbf{R}_a|}, \tag{17-13}$$

where Q_a is the fractional charges alloted to the ath atom of position $\mathbf{R}_a$. Equation (17-13) becomes a better approximation for Hartree potential when the boundary is far enough from the atomic core regions. Q_a is determined by the multicenter numerical integration scheme proposed by Becke [34] and updated at every SCF step.

The second term in Eq. (17-6) is the pseudopotential that is introduced to realize the smooth behavior of the one-electron wavefunctions. It includes the non-local part and the overlap integrals between the Kohn–Sham orbitals, and the atomic pseudopotentials must be communicated between adjacent subdomains, however, it can also be incorporated easily in the parallel computation without serious loss of efficiency. This is due to the fact that the non-local pseudopotential is confined only within a small region of space near the atomic core. To improve the description of the rapid behavior of the non-local pseudopotential in the vicinity of the atomic core, we employ the time-saving double-grid method developed by Ono and Hirose [35]. The feature of the method is to neglect the explicit computation of the Kohn–Sham orbitals on dense-grid points and they are estimated by Lagrange interpolations of the original coarse-grid points instead. The interpolation can be done successfully by the benefit of the smooth behavior of the wavefunctions on the pseudopotentials. The contribution of the dense-grid points is implicitly involved in the weight factors defined at coarse-grid points. It is worthy to note that there is no need to recompute the weight factors on coarse-grid points during the SCF procedure. The accuracy of the real-space grid approach reinforced by the time-saving double-grid method has been well established by applying the method to various systems. The detailed explanation of the double-grid method is presented in Ono and Hirose [35]. The computational accuracy is almost comparable to that of the sophisticated Gaussian basis sets such as Dunning's correlation-consistent basis set with polarization augmented by diffuse functions (aug-cc-pVDZ) [36].

We discuss here the treatment of the exchange–correlation functional $E_{\mathrm{xc}}[n]$ in the real-space approach. The evaluation of the LDA exchange potential or energy given by Eq. (17-3) or Eq. (17-5) is obviously straightforward. In a more sophisticated approach, the LDA exchange energy is corrected by a functional of the gradient of the electron spin density $\nabla n_\sigma(\mathbf{r})$, which is referred to as the generalized gradient approximation (GGA). Applying Becke's gradient correction [37] to Eq. (17-5), the exchange energy functional is expressed by

$$E_{\mathrm{X}}^{\mathrm{Becke}}[n] = E_{\mathrm{X}}^{\mathrm{LDA}}[n] - \beta \sum_{\sigma} \int n_\sigma^{4/3} \frac{x_\sigma^2}{(1 + 6\beta x_\sigma \sin \mathrm{h}^{-1} x_\sigma)} \mathrm{d}\mathbf{r}, \quad (17\text{-}14)$$

where the parameter β is set at 0.0042 and the term x_σ is the dimensionless ratio defined as

$$x_\sigma = \frac{|\nabla n_\sigma(\mathbf{r})|}{n_\sigma(\mathbf{r})^{4/3}}. \quad (17\text{-}15)$$

x_σ becomes negligible at the zero gradient limit and is regarded as an inhomogeneity parameter. The evaluation of the LDA potential in Eq. (17-3) under a parallel architecture requires no communication because the operator given by the derivative of Eq. (17-5) is fully local in the real space. The GGA term in Eq. (17-14) includes the gradient of the spin density, however, it is expressed also by the finite-difference approach as well as the kinetic energy or the Hartree potential. Hence, the data to be communicated in the GGA are common to those used for the Hartree energy operator and, hence no additional data throughput is required. The same is true for the correlation energy E_{c} formulated by Lee, Yang, and Parr (LYP). Thus, the parallelization of the exchange–correlation potential is straightforward even at the GGA level.

As has been suggested by the discussion so far, it is essential for the parallel computation in the real-space method to divide the Hamiltonian or wavefunctions spatially in order to make use of the locality of the operators [38]. The parallel efficiency was examined by carrying out the DFT calculation for the active site of HIV-1 PR with model substrate, which contains 98 valence electrons; 80 grid points have been used for each axis of the real-space cell. The parallel computing has been performed on a distributed memory architecture consisting of 8 CPUs (Pentium 4/3.2 GHz) connected by a Giga-bit switch. The data communications among CPUs have been commanded by the MPI (message passing interface). We measured the time spent for 1 SCF step by using an MPI function (MPI_WTIME) to compare the efficiency with respect to the number of CPUs employed. We also performed a single-CPU calculation and found that it takes 29.0 s for an SCF step. To evaluate the parallel performance of the present approach, we define the speedup S and the parallel efficiency P as

$$S = \frac{\text{time for 1 CPU}}{\text{time for } n \text{ CPUs}}, \quad (17\text{-}16)$$

$$P = \frac{S}{\text{number of CPUs}} \times 100. \tag{17-17}$$

Figure 17-2 summarizes the speedup and the parallel efficiency with respect to the number of CPUs employed. For the 2-CPU and 4-CPU calculations, the speedup is excellent and the efficiencies P have reached to 90.0% and 88.5%, respectively. However, the efficiency P is decreased to 80.5% when 8 CPUs are employed, which is mainly attributed to the increase in the communication relative to the net computational cost. The amount of the communication at the boundary scales in the square of the cell size, while the net computational cost scales in the cube of it. Therefore, the parallel efficiency in the 8-CPU calculation may be recovered when one computes a larger system. Anyway, the efficiency $P = 80$–90% is quite satisfying as a quantum chemical calculation where a huge number of operations is required for data of large size. Obviously, such high efficiency is mainly due to the choice of the real-space grids as a basis function that makes the most operators in the effective Hamiltonian local. The present approach is readily extended to an architecture with a larger number of CPUs and the parallel efficiency will not be spoiled seriously as far as the balance is kept appropriately between the net computational cost and the amount of communication. It should be stressed here that the free energy change plays a key role in the study of the biological system and the free energy calculation generally requires a lot of molecular configurations for ensemble averages along the process of interest. Therefore, development to expedite the computation itself is essential in addition to the invention of the methodologies for the large-scale electronic

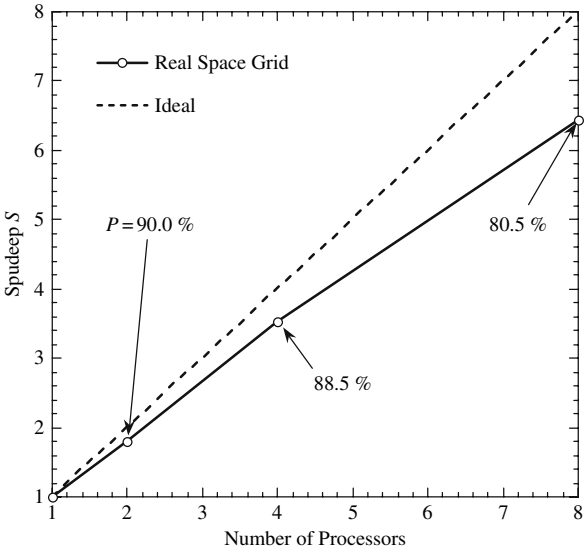

Figure 17-2. Speedup S and parallel efficiency P as functions of number of processors

structure or the free energy calculation. The present demonstration has revealed that the grid-based approach in combination with the KS-DFT is amenable to the parallel computation and gives high efficiency on a common architecture organized by the standard parallel interface.

17.2.3. Hybrid Quantum Mechanical/Molecular Mechanical (QM/MM) Approach

It is often the case that only a small part of the condensed system takes part in a chemical process such as the reactions in solution or in enzyme. The QM/MM approach is the promising computational technique to solve such problems [6,39], where only the chemically active site is described by quantum mechanics and the remaining environment serves as an electrostatic field to the Hamiltonian of the QM region. The efficiency of the approach has been well established through a variety of calculations. In this subsection, we propose a QM/MM approach based on the DFT that utilizes the real-space grid method in an attempt to realize the high-performance computing in large systems.

In the QM/MM method, total energy E of the whole system is decomposed into three terms,

$$E = E_{\mathrm{QM}} + E_{\mathrm{QM/MM}} + E_{\mathrm{MM}} \tag{17-18}$$

where E_{QM} is the electronic energy of the QM subsystem, E_{MM} is the energy of the MM subsystem represented by classical models, and $E_{\mathrm{QM/MM}}$ is the interaction energy between the QM and MM subsystems. In the framework of the DFT, E_{QM} can be obtained by solving the Kohn–Sham equations in Eq. (17-1) containing the electrostatic field $v_{\mathrm{pc}}(\mathbf{r})$:

$$\left[-\frac{1}{2}\nabla_i^2 + v_{\mathrm{eff}}(\mathbf{r}) + v_{\mathrm{pc}}(\mathbf{r})\right]\psi_i(\mathbf{r}) = \varepsilon_i\psi_i(\mathbf{r}). \tag{17-19}$$

$v_{\mathrm{pc}}(\mathbf{r})$: is the potential formed by point charges in the MM subsystem and is expressed as,

$$v_{\mathrm{pc}}(\mathbf{r}) = \sum_k \frac{q_k}{|\mathbf{r} - \mathbf{s}_k|}, \tag{17-20}$$

where the suffix k runs over the MM sites of coordinate $\mathbf{s}_k$ with charge q_{k}. Once the eigenfunctions ψ_i are obtained, the energy E_{QM} can be computed as

$$E_{\mathrm{QM}} = \sum_i \langle\psi_i| -\frac{1}{2}\nabla_i^2 + \hat{v}_{\mathrm{eff}}|\psi_i\rangle - \frac{1}{2}\int \frac{n(\mathbf{r}_1)n(\mathbf{r}_2)}{|\mathbf{r}_1 - \mathbf{r}_2|}\mathrm{d}\mathbf{r}_1\mathrm{d}\mathbf{r}_2 + E_{\mathrm{xc}}[n] - \int n(\mathbf{r})v_{\mathrm{xc}}(n(\mathbf{r}))\mathrm{d}\mathbf{r} + \sum_{a<b}\frac{Z_aZ_b}{R_{ab}}. \tag{17-21}$$

Note that the first term of r.h.s. in Eq. (17-21) does not contain the electrostatic field $\nu_{\rm pc}(\mathbf{r})$. The last term in Eq. (17-21) represents the sum of the nuclear repulsion energies. The interaction energy $E_{\rm QM/MM}$ is expressed by the sum of the electrostatic $E_{\rm ELS}$ and the van der Waals interaction $E_{\rm vdW}$ as

$$\begin{aligned} E_{\rm QM/MM} &= E_{\rm ELS} + E_{\rm vdW} \\ &= \sum_i \langle \psi_i | \hat{v}_{\rm pc} | \psi_i \rangle + \sum_a \sum_k \frac{Z_a q_k}{|\mathbf{R}_a - \mathbf{s}_k|} + E_{\rm vdW}, \end{aligned} \tag{17-22}$$

where the first term in $E_{\rm ELS}$ is the interaction between one-electron wavefunctions and the electrostatic field, and the second term is the nuclear-site interaction. $E_{\rm vdW}$ in Eq. (17-22) is, further, approximated by the equation of Lennard-Jones (LJ) with empirical parameters (ε,σ) as

$$E_{\rm vdW} = \sum_{k,l} 4\varepsilon_{kl} \left(\left(\frac{\sigma_{kl}}{r_{kl}} \right)^{12} - \left(\frac{\sigma_{kl}}{r_{kl}} \right)^{6} \right). \tag{17-23}$$

The derivatives of these energies with respect to the coordinates of the QM and MM atoms are easily formulated. The remaining term $E_{\rm MM}$ in Eq. (17-18) is composed from two-body electrostatic and LJ interactions and can be computed by utilizing the parameter set of potential field such as Amber, Charmm, or OPLS.

In the implementation of the QM/MM approach with the real-space method, the QM cell that contains the real-space grids is embedded in the MM cell. One should take care for the evaluation of the potential $\nu_{\rm pc}(\mathbf{r})$ defined as Eq. (17-20). When a point charge in MM region goes inside the QM cell, it makes a singularity in the effective Kohn–Sham Hamiltonian, which may give rise to a numerical instability. To circumvent the problem, we replace a point charge distribution

$$P(\mathbf{r}) = \sum_i q_i \delta(\mathbf{r} - \mathbf{r}_i) \tag{17-24}$$

by a summation of the Gaussian charge distributions $P'(\mathbf{r})$,

$$P'(\mathbf{r}) = \sum_i q_i \left(\frac{\alpha}{\pi} \right)^{3/2} \exp(-\alpha |\mathbf{r} - \mathbf{s}_i|^2), \tag{17-25}$$

where exponent α specifies the width of the Gaussian function. Accordingly, the potential $\nu_{\rm pc}(\mathbf{r})$ becomes,

$$\nu_{\rm pc}(\mathbf{r}) = \sum_i \frac{q_i}{|\mathbf{r} - \mathbf{s}_i|} \mathrm{erf}(\sqrt{\alpha} |\mathbf{r} - \mathbf{s}_i|) \,. \tag{17-26}$$

Equation (17-26) ensures the modest behavior of the potential near the center of the charge and the numerical instability is substantially alleviated [40,41].

17.3. THEORY OF SOLUTIONS IN THE ENERGY REPRESENTATION

The evaluation of the free energy is essential to quantitatively treat a chemical process in condensed phase. In this section, we review methods of free-energy calculation within the context of classical statistical mechanics. We start with the standard free-energy perturbation and thermodynamic integration methods. We then introduce the method of distribution functions in solution. The method of energy representation is described in its classical form in this section, and is combined with the QM/MM methodology in the next section.

17.3.1. Free-Energy Perturbation and Thermodynamic Integration Methods

The most fundamental quantity to describe a process in solution is the free energy (change). Indeed, it governs the equilibrium and rate constants of the process. The free-energy change corresponding to the insertion process of a solute in solution is the chemical potential (solvation free energy). Once the chemical potentials are known for the species present in the initial and final states of a process of interest, the free energy change for the process can be readily evaluated. Therefore, it is of primary importance in statistical mechanics of solutions to establish a scheme to determine the chemical potential (solvation free energy) of a solute in solution.

Let H_0 and H_1 be respectively the Hamiltonians at the initial and final states of a process in solution. When the solvation process is concerned, the initial and final states are typically the pure solvent and solution systems of interest. The corresponding free-energy change ΔF is given by

$$\exp(-\beta \Delta F) = \frac{\int d\Gamma \exp(-\beta H_1)}{\int d\Gamma \exp(-\beta H_0)}, \tag{17-27}$$

where β is the inverse of the Boltzmann constant k_B, T is the temperature, and Γ is the (collective) coordinate for the phase space. When the classical statistical mechanics is adopted and the Hamiltonian change between the initial and final states does not involve the kinetic part, Eq. (17-27) reduces to

$$\exp(-\beta \Delta F) = \frac{\int d\mathbf{X} \exp(-\beta U_1)}{\int d\mathbf{X} \exp(-\beta U_0)}, \tag{17-28}$$

where $\mathbf{X}$ is the (collective) coordinate for the configuration and U_0 and U_1 are the potential energies of the system at the initial and final states, respectively. Equation (17-28) is the starting point of our development. It should be noted that Eq. (17-28) cannot be used when a quantum fluid is to be treated.

When U_1–U_0 is denoted by ΔU, Eq. (17-28) is rewritten as

$$\exp(-\beta \Delta F) = \langle \exp(-\beta \Delta U) \rangle_0, \tag{17-29}$$

where $< ... >_0$ is the ensemble average taken for the initial state whose configuration is sampled according to the potential energy U_0. Equation (17-29) shows that the free-energy change ΔF can be calculated, in principle, by performing only the simulation for the initial state and averaging the Boltzmann factor of the relevant energy change ΔU. Indeed, Eq. (17-29) is the basis of the particle insertion method for evaluating the solvation free energy (chemical potential) of a solute in solution [13,42,43]. In the particle insertion method, the pure solvent is simulated and the solute molecule of interest is inserted randomly into the pure solvent. The chemical potential is then obtained from

$$\exp(-\beta\Delta F) = \int \mathrm{d}(\Delta U)\exp(-\beta\Delta U) f(\Delta U), \tag{17-30}$$

where $f(\Delta U)$ is the probability distribution function of ΔU in the pure solvent system. The particle insertion method is convenient and fast since only the pure solvent configurations need to be prepared and the free energy is calculated from a one-step insertion process of the solute. As is well documented, however, the particle insertion method is applicable only for a small and weakly interacting solute, see Figure 17-3. When the solute is large, it almost always overlaps with solvent molecules upon insertion and $f(\Delta U)$ is well sampled only toward large (repulsive) value of ΔU. The Boltzmann factor $\exp(-\beta\Delta U)$ increases steeply, on the other hand, toward small (attractive) ΔU. The small ΔU region, which is often ill sampled, makes a significant contribution in Eq. (17-30). Thus, Eq. (17-30) is not computationally useful and the particle insertion method cannot be used for most of "interesting" systems. Actually, the calculation of the average of the exponential of the energy change is often prohibitive unless the energy change is small in magnitude.

The standard and often used methods to circumvent the difficulty associated with the form of Eq. (17-30) are the free-energy perturbation and thermodynamic integration methods [13,42,43]. These methods are generally applicable to free-energy

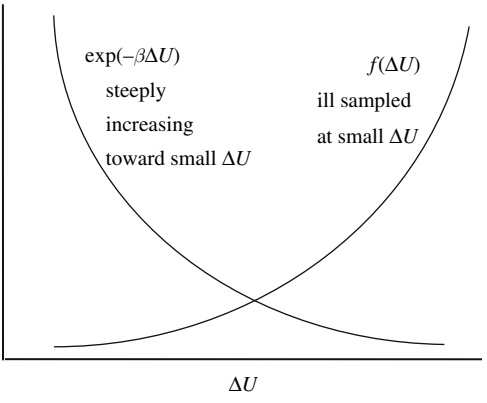

Figure 17-3. A schematic distribution of ΔU value in the particle insertion method

evaluation. In the present review, we restrict our development to the solvation process; the initial state is the pure solvent and the final state is the solution system of interest.

The free-energy perturbation method utilizes the intermediate states connecting the initial and final states of the process of interest. Let V_i ($i = 0, \ldots, N$) be a sequence of potential energies where the initial and final onesV_0 and V_N are taken to the potential functions U_0 and U_1 for the initial and final states, respectively. For an arbitrary (set of) V_i, Eq. (17-28) can be expressed as

$$\exp(-\beta\Delta F) = \prod_{i=0}^{N-1} \langle \exp(-\beta(V_{i+1} - V_i)) \rangle_i, \tag{17-31}$$

where $< ... >_i$ is the ensemble average taken with respect to the potential function V_i. Equation (17-31) shows that ΔF is given as the sum of the free-energy change accompanying the energy change from V_i to V_{i+1} ($i = 0, \ldots, N$–1). The states corresponding to V_i ($i = 1, \ldots, N$–1) are called intermediate states. The free energy is a state function and does not depend on the choice of the intermediate states in principle. From the computational viewpoint, the point is to "select" the set of V_i so that the change from V_i to V_{i+1} is "small" in magnitude. When V_i and V_{i+1} are "similar" and the energy change is small, the difficulty encountered in the particle insertion method can be circumvented and the calculation of the free-energy change becomes feasible. The drawback is that a number of intermediate states need to be prepared and that the computational cost is enhanced accordingly.

In the thermodynamic integration method, the intermediate states are introduced with respect to the coupling parameter $\lambda(0 \leq \lambda \leq 1)$ The potential function at the coupling parameter of λ is denoted by U_λ and satisfies $U_\lambda = U_0$ and $U_\lambda = U_1$ at the initial and final states ($\lambda = 0$ and 1), respectively. The intermediate states correspond to $0 < \lambda < 1$. The form of averaging-the-exponential is then avoided by rewriting Eq. (17-28) as

$$\Delta F = \int_0^1 d\lambda \left\langle \frac{\partial U_\lambda}{\partial \lambda} \right\rangle_\lambda, \tag{17-32}$$

where $< ... >_\lambda$ is the ensemble average when the potential energy is U_λ. As is the case of the free-energy perturbation method, ΔF value calculated by Eq. (17-32) is independent of the choice of the intermediate states in principle. The integrand of Eq. (17-32) is a preferable average from the computational viewpoint. The exponential average is not involved any more. In practice, the integral of Eq. (17-32) is replaced by a discretized sum and a finite number of intermediate states are to be treated explicitly. Since a systematic error is introduced by the discretization, a large number of intermediate states need to be prepared and the computational demand increases correspondingly.

In both the free-energy perturbation and thermodynamic integration methods, the key to the computational accuracy and efficiency is the choice of the intermediate

states as a function of the coupling parameter λ. Note that the intermediate states adopted in the free-energy perturbation method can be considered as a finite subset of the intermediate states introduced continuously over $0 < \lambda < 1$. A straightforward implementation of the intermediate states is possible by varying the system potential energy linearly. When the solvation is concerned and the solute–solvent interaction is expressed as the sum of Lennard-Jones and Coulombic terms, the linear variation is realized by the intermediate solute–solvent interaction given by

$$\lambda \sum_{i,j} \left(4\varepsilon_{ij} \left\{ \left(\frac{\sigma_{ij}}{r_{ij}} \right)^{12} - \left(\frac{\sigma_{ij}}{r_{ij}} \right)^{6} \right\} + \frac{q_i q_j}{r_{ij}} \right), \tag{17-33}$$

where i and j refer to solute and solvent interaction sites, respectively. The first term in the sum expresses the Lennard-Jones interaction at the distance r_{ij} between the solute and solvent sites, and ε_{ij} and σ_{ij} are the energy and length parameters, respectively. The second term in the sum corresponds to the Coulombic interaction, and q_i and q_j are the charges on the solute and solvent sites, respectively. The linear scaling of the solute–solvent interaction with Eq. (17-33) is often ill behaved numerically around $\lambda = 0$. This is related to the appearance of $r = 0$ singularity at $\lambda = 0$. To alleviate the problem, a non-linear scaling, which is obtained by replacing λ with λ^n ($n \geq 2$) in Eq. (17-33), can be used [44,45]. The calculation becomes more stable near $\lambda = 0$. The $r = 0$ singularity is still present in the non-linear scaling, however, and careful analysis is necessary to determine the λ values actually sampled. Another choice of the intermediate states is provided by

$$4\lambda\varepsilon \left(\left(\frac{\sigma^2}{r^2 + (1-\lambda)\,\delta} \right)^{6} - \left(\frac{\sigma^2}{r^2 + (1-\lambda)\,\delta} \right)^{3} \right), \tag{17-34}$$

or similar expressions for the Lennard-Jones part [44,46]. The $r = 0$ singularity is then absent and the free-energy calculation on the basis of Eq. (17-34) is numerically stable.

Although the free-energy perturbation and thermodynamic integration methods are exact under a given set of potential functions in principle, they are not free from systematic errors in practice. The systematic error most often encountered in the free-energy perturbation method is the non-coincidence of the free-energy changes ΔF calculated from the forward variation of the coupling parameter λ from 0 to 1 and the backward variation from 1 to 0. The common practice is to average the ΔF from the forward and backward calculations. It is pointed out, however, that the simple averaging is itself a source of systematic error [47]. To achieve the accuracy, the use of Bennett's weighting function is recommended [47,48]. In the thermodynamic integration method, a systematic error is inevitable when the integral over λ in Eq. (17-32) is discretized. A careful examination of discretization is necessary, especially when the integrand of Eq. (17-32) exhibits a non-monotonic dependence on λ and/or varies steeply over some range of λ.

17.3.2. Distribution Functions in Solution

A molecular picture of solutions is established through distribution (correlation) functions. Correspondingly, a molecular description of the solvation free energy can be implemented by formulating a functional which expresses the solvation free energy in terms of only distribution functions in the solution and pure solvent systems of interest. An approximate functional needs to be constructed in practice, however, since the exact functional involves an infinite series of many-body distribution functions [49]. The theories introduced in Sections 17.3.4 and 17.3.5 are formulated to provide the solvation free energy with simple distribution functions in closed form. In this section, a general description of distribution functions is provided.

The system of our interest is a dilute solution containing a single solute molecule. Even when the solute concentration is finite, our development is valid by viewing one of the solute molecules as the "solute" and the others as part of mixed solvent. To describe completely the configuration of a solvent molecule relative to the solute, the position and orientation need to be specified simultaneously. The complete set of the position and orientation is called the full coordinate and is denoted collectively by **x**. If the solute and/or solvent are flexible, the intramolecular degrees of freedom are also incorporated into **x**. In the full coordinate representation, the instantaneous distribution $\hat{\rho}^f$ is introduced as

$$\hat{\rho}^f(\mathbf{x}) = \sum_i \delta(\mathbf{x} - \mathbf{x}_i), \tag{17-35}$$

where $\mathbf{x}_i$ is the full coordinate of the ith solvent molecule and the sum is taken over all the solvent molecules. The superscript f is attached to emphasize that Eq. (17-35) is in the full coordinate representation. The distribution functions are generated from the averages of products of $\hat{\rho}^f$ in the system of interest.

When the distribution function is generated from $\hat{\rho}^f$, a multidimensional description is inevitable. Indeed, the full coordinate **x** is six-dimensional (five for linear molecule) for rigid species and involves more for flexible species. To implement the full coordinate representation, the expansion in terms of spherical harmonics can be employed [13]. However, the calculation of multidimensional distribution functions is often slow in molecular simulation and the numerical realization is not straightforward. When the coordinate has too "fine" information content, the corresponding distribution function needs additional methodology for handling. Too much information is not desirable both from the computational viewpoint (large memory and slow convergence) and the conceptual viewpoint (unclear perception in mind).

It is then useful to reduce the information content by introducing a "projected" coordinate. With projection, some information of **x** is retained, while the others are disregarded. When the projection is implemented with respect to a function $P(\mathbf{x})$, the corresponding distribution functions are generated from the instantaneous distribution given by

$$\sum_i \delta(p - P(\mathbf{x}_i)), \tag{17-36}$$

where p is the value of $P(\mathbf{x})$ and serves as the coordinate for the distribution function.

A typical choice of $P(\mathbf{x})$ is the radial distance between the atomic sites (interaction sites) of the molecule. When a pair of atomic sites in the solute and solvent molecules is picked up, the histogram of its radial distance is averaged with an appropriate normalization to give the site–site radial distribution function. For example, when the solute and solvent is both H_2O (when one of the molecule in pure water is viewed as the "solute" and the others as the "solvent"), the O–O, O–H, and H–H radial distribution functions are generated by the projections onto O–O, O–H, and H–H distances, respectively. It should be noted that the radial distribution functions do not represent a simultaneous distribution of a set of site–site radial distances. In the case of water, the O–O radial distribution function specifies only the O–O distance and the other distance information such as those for O–H and H–H is disregarded. Similarly, the O–H radial distribution function does not contain explicit information about the O–O and H–H distances. In Figure 17-4, we show the O–O and O–H radial distribution functions of water at 1 g/cm^3 and 25°C. It is seen from the O–O radial distribution function that the neighboring water molecules stay in the distance of ∼2.8 Å. The O–H radial distribution function shows that the intermolecular hydrogen-bonding distance is ∼2 Å. The second peak of the O–O radial distribution function is characteristic of water. Usually, the second peak appears at about twice the distance of the first peak. In water, the second-peak position is ∼1.6 times of the first-peak position. This provides a view that the ice-like structure remains even in liquid water.

Another useful distribution function is for the interaction pair energy. An example is shown in Figure 17-5 for water at 1 g/cm^3 and 25°C. The peak at ∼–6 kcal/mol corresponds to the intermolecular hydrogen bonding of water in the liquid state. In the high-energy regime, the distribution function vanishes. This reflects the excluded volume effect and is consistent with the fact that radial distribution functions vanish at short distances.

Of course, the choice of the projecting function $P(\mathbf{x})$ of Eq. (17-36) is not unique. The choice depends on the purpose. For example, when the angle of the hydrogen

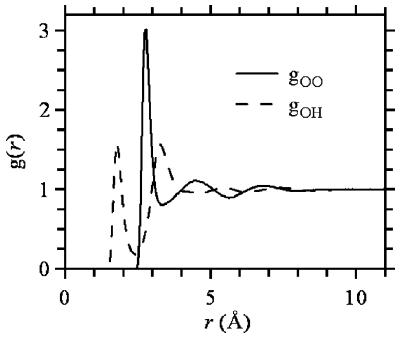

Figure 17-4. The O-O radial distribution function g_{OO} and the O-H radial distribution function g_{OH} as functions of the distance r of water at 1 g/cm^3 and 25°C

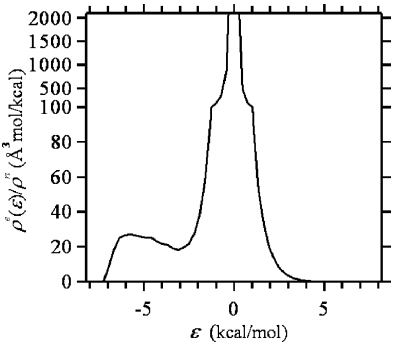

Figure 17-5. The distribution function for the pair energy of water at 1 g/cm^3 and 25°C as a function of the energy value ε. The distribution function $\rho^e(\varepsilon)$ is normalized by the bulk (number) density ρ^n. Note that the graduation of the ordinate is changed at 100 Å^3 mol/kcal

bonding is of interest, it is most useful to adopt the hydrogen-bonding angle itself as $P(\mathbf{x})$. In general, no *a priori* criterion is present for preferable projection. The desirable form of projection can be based only upon the target quantity to be investigated.

17.3.3. Density-Functional Theory

The solvation free energy can be evaluated using the Kirkwood charging formula [13,42,43]. It introduces a set of intermediate states connecting the initial and final states of the gradual insertion process of the solute; the initial and final states correspond to the pure solvent system without the solute and the solution system of interest, respectively. The free energy perturbation and thermodynamic integration methods are based on the Kirkwood charging formula, and in principle provide the "exact" solvation free energy under a given set of potential functions. These methods are, however, expensive in computation and practical only to small molecules. For the purpose of analyzing the solvation free energy on the molecular level, furthermore, it is necessary to express the solvation free energy only in terms of distribution functions in the solution and pure solvent systems of interest. Within the framework of the Kirkwood charging formula, the intermediate states are actually arbitrary and are employed for the convenience of formulation and computation. They are not of physical significance since the free energy is a state function.

A molecular description of the solvation free energy can be implemented by formulating a functional which expresses the solvation free energy in terms of distribution functions in the solution and pure solvent systems. The exact functional is not useful, however, since it is an infinite series of many-body distribution functions [49]. In practice, an approximate but accurate functional needs to be constructed which is expressed with few-body distribution functions in closed form. When such a functional is formulated and the distribution functions constituting the approximate functional are readily obtained by computer simulation, the solvation free energy can

be determined and analyzed with reasonable computational load in terms of exact microscopic information of the systems of interest.

It is a statistical-mechanical theory of solutions to express the solvation free energy as a functional of distribution functions. Traditionally, the theory of solutions is formulated with a diagrammatic approach [13], in which an approximation is provided in a two-step procedure. In the first step, the free energy and/or distribution function is expanded with respect to the solute–solvent interaction potential function or its related function as an infinite, perturbation series. In the second step, a renormalization scheme is applied; a set of functions are defined through partial summation of the series and are employed for substitution to make the infinite series more tractable. An approximation is typically introduced by neglecting diagrams of ill character.

We adopt an alternative route to the distribution function theory. The approach is based on the density-functional theory. In this approach, the change of variables is conducted through Legendre transform from the solute–solvent interaction potential function to the solute–solvent distribution function or the solvent density around the solute. The (solvation) free energy is then expressed approximately by expanding the corresponding Legendre-transformed function with respect to the distribution function to some low order.

The target quantity of the development is the solvation free energy. The solvation free energy $\Delta\mu$ is the free energy change corresponding to the gradual insertion process of the solute molecule. In $\Delta\mu$, only the contribution from the potential energy is involved and the ideal (kinetic) contribution is excluded. When the intramolecular energy of the solute is $\Psi(\psi)$ and the total solvent–solvent interaction energy is $U(\mathbf{X})$, $\Delta\mu$ is expressed as

$$\exp\left(-\beta\Delta\mu\right) = \frac{\int \mathrm{d}\psi \mathrm{d}\mathbf{X} \exp\left(-\beta\left\{\Psi\left(\psi\right) + \sum_i v\left(\psi, \mathbf{x}_i\right) + U\left(\mathbf{X}\right)\right\}\right)}{\int \mathrm{d}\psi \mathrm{d}\mathbf{X} \exp\left(-\beta\left\{\Psi\left(\psi\right) + U\left(\mathbf{X}\right)\right\}\right)}, \tag{17-37}$$

where $\mathbf{X}$ represents the solvent configuration collectively and β is the inverse of the product of the Boltzmann constant and the temperature. A restriction of attention to a certain set of solute intramolecular state can be made simply by the corresponding alteration of the domain of integration over ψ.

The starting point of the density-functional treatment is the Kirkwood charging formula. When the solute–solvent interaction potential of interest is $v(\mathbf{x})$, the intermediate states are described as $u_\lambda(\mathbf{x})$, where λ is the coupling parameter to identify the state. When $\lambda = 0$, the system is the pure solvent system and $u_0(\mathbf{x}) = 0$ (no solute–solvent interaction). When $\lambda = 1$, the solute interacts with the solvent at full coupling and $u_\lambda(\mathbf{x}) = v(\mathbf{x})$. The form of $u_\lambda(\mathbf{x})$ at $0 < \lambda < 1$ is arbitrary. The Kirkwood charging formula is an integration over the coupling parameter and is expressed as

$$\Delta\mu = \int_0^1 \mathrm{d}\lambda \int \mathrm{d}\mathbf{x} \frac{\partial u_\lambda\left(\mathbf{x}\right)}{\partial\lambda} \rho^f\left(\mathbf{x}; u_\lambda\right), \tag{17-38}$$

where $\rho^f(\mathbf{x};u_\lambda)$ is the ensemble average of Eq. (17-35) in the presence of the solute–solvent interaction u_λ. The superscript f means that the function is represented over the full coordinate $\mathbf{x}$. The partial integration then provides

$$\begin{aligned}\Delta\mu &= \int \mathrm{d}\mathbf{x} v(\mathbf{x}) \rho^f(\mathbf{x};v) - \int_0^1 \mathrm{d}\lambda \int \mathrm{d}\mathbf{x} u_\lambda(\mathbf{x}) \frac{\partial \rho^f(\mathbf{x};u_\lambda)}{\partial\lambda} \\ &\equiv \int \mathrm{d}\mathbf{x} v(\mathbf{x}) \rho^f(\mathbf{x}) - F^f\left[\rho^f(\mathbf{x})\right],\end{aligned} \tag{17-39}$$

where the density-functional F^f is defined in the second equation. $\Delta\mu$ and F^f are related to each other with Legendre transform since the map is proved to be one-to-one from the solute–solvent interaction potential to the distribution function [13]. An approximation can be devised by introducing the indirect part ω^f of the potential of mean force as

$$\rho^f{}_\lambda(\mathbf{x}) = \rho^f{}_0(\mathbf{x}) \exp\left(-\beta\left(u\left(\mathbf{x};\rho^f{}_\lambda\right) + \omega^f\left(\mathbf{x};\rho^f{}_\lambda\right)\right)\right). \tag{17-40}$$

Actually, the dependence is now written in terms of the distribution function $\rho^f{}_\lambda$, instead of the potential. This is possible due to the property of one-to-one correspondence. When the solvent–solvent correlation is absent (low-density limit), ω^f is zero. In other words, all the "complicated" solvent–solvent correlations are put into ω. Equations (17-39) and (17-40) lead exactly to

$$\begin{aligned}F^f\left[\rho^f(\mathbf{x})\right] = k_\mathrm{B}T \int \mathrm{d}\mathbf{x} \Bigg[&\left(\rho^f(\mathbf{x}) - \rho^f{}_0(\mathbf{x})\right) - \rho^f(\mathbf{x}) \log\left(\frac{\rho^f(\mathbf{x})}{\rho^f{}_0(\mathbf{x})}\right) \\ &-\beta\left(\rho^f(\mathbf{x}) - \rho_0(\mathbf{x})\right) \int_0^1 \mathrm{d}\lambda \omega^f\left(\mathbf{x};\rho^f{}_\lambda\right) \Bigg]\end{aligned} \tag{17-41}$$

when u_λ is taken so that $\rho^f{}_\lambda$ varies linearly against λ. Equation (17-41) is exact, and an approximation is introduced to the λ integral of ω^f. When ω^f is taken to vary linearly with λ, the HNC (hypernetted-chain) approximation is obtained. When $\exp(-\beta\omega^f)$–1 is set to be linear, it is the PY (Percus–Yevick) approximation.

The above is the brief introduction to the density-functional theory of solutions. The mathematical development is quite straightforward. The numerical implementation is difficult, however, in the full coordinate representation. As noted in Section 17.3.2, the full coordinate is multidimensional; the solute–solvent distribution is a function over high-dimensional configuration space and cannot be implemented in practice. To overcome the problem of dimensionality, it is necessary to introduce a projected coordinate. In Section 17.3.5, we introduce the energy representation and formulate the density-functional theory in the energy representation.

17.3.4. Radial Distribution Functions and Reference Interaction Site Model

The method of reference interaction site model (RISM) is based on the site–site radial distribution functions. It introduces the "direct correlation functions" as the inverses of the correlation matrices of the site–site distance and formulates an approximate set of integral equation for the site–site radial distribution functions by adopting "closure" relationships between the radial distribution functions and direct correlation functions [11,12,13,50,51]. Compared to the molecular simulation method, the method of integral equation is much faster. The speed is achieved by restricting the attention only to the radial distribution functions and adopting approximate closures. Furthermore, the solvation free energy is expressed in closed form for some types of closure relationships [50,53]. In this case, no reference to the intermediate states of the solute-insertion process is required and the solvation free energy can be evaluated directly from the radial distribution functions obtained from the integral equation. When a closed-form functional for the solvation free energy is given in terms of distribution functions, the functional not only provides an efficient route of computation, but also sets a basis for the molecular understanding with respect to the distribution functions.

A drawback is present, of course, in any approximate method of solutions. Under a given set of potential functions, the molecular simulation gives the exact distribution functions when it is done long enough. In contrast, since the closure relationship is approximate, the radial distribution function obtained from the integral equation method is approximate. The solvation free energy calculated from the integral equation theory has two sources of errors. One is due to the approximate nature of the potential functions (force field), and the other comes from the approximation involved in the integral equation.

The drawbacks characteristic of RISM and its variants are related to the fact that they do not treat the whole molecule as a single unit and view a molecule as a collection of interaction sites. The method is thus applicable only when the potential function is of site–site form. As a consequence, the electronic distribution cannot be treated in the cloud-like form as implemented in quantum theories, but needs to be contracted into a set of point charges. In addition, the integral equation is ill behaved unless all of the interaction sites carry the repulsive core explicitly. For example, many of the potential functions of H_2O do not assign a repulsive core at the H-site. This is simply because the repulsive core for the O-site is large enough that other molecules cannot come too close to the H-site. The repulsive core of the H-site is buried in the O-site core and is not necessary to be treated explicitly at the level of potential functions. In RISM, however, a core parameter needs to be assigned to the H-site, too. The core parameter actually dictates the resulting solvation free energy sensitively and acts as an adjustable parameter in the method. Another, related problem is the so-called "problem of auxiliary site". The solution to the RISM integral equations exhibits unphysical dependence on the presence of auxiliary sites which simply label points in a molecule and make no contribution to the intermolecular interaction. This type of difficulty is absent when the whole molecule is treated as a

single unit. The difficulty arises when a molecule is treated as a collection of sites. In RISM, the correlation between a pair of sites is described at the two-body level for both the intramolecular and intermolecular ones. Since the sites in a molecule are tightly bound with one another, a partial incorporation of the intramolecular correlation is not desirable. This point is exemplified when the density is low. The RISM integral equations are not exact in the limit of zero solvent density and are not useful to evaluate the solvation free energy in a low-density fluid. It is well known in this instance, too, that the low-density limit is given exactly when the whole molecule is treated as a single unit [13]. Finally, since the molecular structure is an input in the RISM approach, an additional scheme needs to be devised to deal with flexible molecules.

In the commonly used RISM approach, the solvation free energy is often expressed in closed form in terms of radial distribution functions. An improvement of the approach may then be possible through combination with the molecular simulation; the radial distribution functions are exact under the used set of potential functions when they are calculated from the molecular simulation, instead of the integral equation. This line of approach was developed by Kast and Truong [52,53,54]. The computational efficiency is achieved compared to the free-energy perturbation and thermodynamic integration methods, while a particular care is mentioned to handle the ill-conditioned correlation matrices in the range of small reciprocal vector (large distance).

The above drawbacks of RISM and its variants are well documented since their first formulations [11,12]. They are all related to the point that a molecule is treated as a collection of sites. In the method of energy representation introduced next, each of the solute and solvent molecules is taken to be a single unit as a whole, and those drawbacks vanish.

17.3.5. Method of Energy Representation

In the method of energy representation, the projecting function $P(\mathbf{x})$ of Eq. (17-36) is taken to be the solute–solvent pair interaction energy. Figure 17-5 is an example of the distribution function in the energy representation. To introduce the energy representation, it is necessary to specify the solute–solvent interaction potential v of interest. Of course, v is a function of the solute configuration ψ and the solvent configuration $\mathbf{x}$. The instantaneous distribution $\hat{\rho}^e$ is defined as

$$\hat{\rho}^e(\varepsilon) = \sum_i \delta(v(\psi, \mathbf{x}_i) - \varepsilon), \tag{17-42}$$

where the sum is taken over the solvent molecules and a superscript e is attached to emphasize that a function is represented over the energy coordinate. The distribution functions in the energy representation are generated from the averages of products of $\hat{\rho}^e$ in the system of interest.

In the energy representation, the density-functional theory can be formulated by restricting the set of solute–solvent interaction potentials $u_\lambda(\psi,\mathbf{x})$ to those which are

constant over an equienergy surface of $v(\psi,\mathbf{x})$. In this case, when the value of $v(\psi,\mathbf{x})$ is denoted as ε, the intermediate states can be written as $u_\lambda(\varepsilon)$. At the end points, $u_0(\varepsilon) = 0$ and $u_1(\varepsilon) = \varepsilon$ since $v(\psi,\mathbf{x})$ itself is the potential function in the solution system of interest. It is then possible to show that the Kirkwood charging formula is given by

$$\Delta\mu = \int_0^1 \mathrm{d}\lambda \int \mathrm{d}\varepsilon \frac{\partial u_\lambda(\varepsilon)}{\partial\lambda} \rho^e(\varepsilon; u_\lambda), \tag{17-43}$$

where $\rho^e(\varepsilon;u_\lambda)$ is the ensemble average of Eq. (17-42) in the presence of the solute–solvent interaction u_λ. The superscript e is attached to mean the representation over the energy coordinate ε. The Legendre transform is also possible as

$$\begin{aligned}\Delta\mu &= \int \mathrm{d}\varepsilon u_1(\varepsilon)\rho^e(\varepsilon; v) - \int_0^1 \mathrm{d}\lambda \int \mathrm{d}\varepsilon u_\lambda(\varepsilon) \frac{\partial\rho^e(\varepsilon; u_\lambda)}{\partial\lambda} \\ &\equiv \int \mathrm{d}\varepsilon\varepsilon\rho^e(\varepsilon) - F^e\left[\rho^e(\varepsilon)\right]\end{aligned} \tag{17-44}$$

and the indirect part ω^e of the potential of mean force in the energy representation can be introduced correspondingly simply by rewriting $\mathbf{x}$ of Eq. (17-40) with ε as

$$\rho^e{}_\lambda(\varepsilon) = \rho^e{}_0(\varepsilon)\exp\left(-\beta\left(u\left(\varepsilon;\rho^e{}_\lambda\right) + \omega^e\left(\varepsilon;\rho^e{}_\lambda\right)\right)\right). \tag{17-45}$$

The density-functional is then expressed exactly as

$$\begin{aligned}F^e\left[\rho^e(\varepsilon)\right] = k_\mathrm{B}T \int \mathrm{d}\varepsilon \Bigg[&\left(\rho^e(\varepsilon) - \rho^e{}_0(\varepsilon)\right) - \rho^e(\varepsilon)\log\left(\frac{\rho^e(\varepsilon)}{\rho^e{}_0(\varepsilon)}\right) \\ &-\beta\left(\rho^e(\varepsilon) - \rho^e{}_0(\varepsilon)\right)\int_0^1 \mathrm{d}\lambda\omega^e\left(\varepsilon;\rho^e{}_\lambda\right)\Bigg]\end{aligned} \tag{17-46}$$

when u_λ is taken so that $\rho^e{}_\lambda$ varies linearly against λ. Note the parallelism of Eqs. (17-43, 17-44, 17-45, 17-46) to Eqs. (17-38, 17-39, 17-40, 17-41). In Eqs. (17-45) and (17-46), u and ω is written to depend on the distribution function $\rho^e{}_\lambda$, instead of the potential u_λ, by virtue of the property of one-to-one correspondence [14]. In the energy representation, the HNC-type and PY-type approximations are obtained by assuming the linear dependencies of ω^e and $\exp(-\beta\omega^e)$–1 on λ, respectively. Although Eq. (17-41) is hard to implement due to the high dimensionality of $\mathbf{x}$, Eq. (17-46) is straightforward to handle since ε is one-dimensional.

In the currently used version of the method of energy representation [15,16,19], the solvation free energy $\Delta\mu$ is approximately expressed in terms of distribution functions constructed from $\hat{\rho}^e$ in the solution and pure solvent systems. In our treatments, the solution system refers to the system in which the solute molecule interacts with the solvent under the solute–solvent interaction v of interest at full coupling. In the solution, the average distribution ρ^e of the v value is relevant in the approximate construction of $\Delta\mu$ and is given by

$$\rho^e(\varepsilon) = \left\langle \hat{\rho}^e(\varepsilon) \right\rangle, \tag{17-47}$$

where $\langle \cdots \rangle$ represents the ensemble average in the solution system of interest. On the other hand, the pure solvent system denotes the system in which no interaction is physically present between the solute and solvent molecules. At an instantaneous configuration of the pure solvent system, $\hat{\rho}^e$ is constructed by placing the solute molecule in the system as a test particle. The average distribution ρ_0^e and the correlation matrix χ_0^e then appear in the approximate functional for $\Delta\mu$ and are expressed, respectively, as

$$\rho_0^e(\varepsilon) = \left\langle \hat{\rho}^e(\varepsilon) \right\rangle_0 \tag{17-48}$$

and

$$\chi_0^e(\varepsilon, \eta) = \left\langle \hat{\rho}^e(\varepsilon)\, \hat{\rho}^e(\eta) \right\rangle_0 - \left\langle \hat{\rho}^e(\varepsilon) \right\rangle_0 \left\langle \hat{\rho}^e(\eta) \right\rangle_0, \tag{17-49}$$

where $\langle \cdots \rangle_0$ represents the ensemble average in the pure solvent system. In this case, the solute and solvent degrees of freedom are uncoupled from each other in the probability distribution.

An approximate functional for $\Delta\mu$ is derived in Matubayasi et al. [15,16] and Takahashi et al. [19]. The functional is constructed by adopting the Percus–Yevick-type approximation in the unfavorable region of the solute–solvent interaction and the hypernetted-chain-type approximation in the favorable region. $\Delta\mu$ is then given by a set of equations listed as

$$w^e(\varepsilon) = -k_{\mathrm{B}}T \log\left(\frac{\rho^e(\varepsilon)}{\rho_0^e(\varepsilon)}\right) - \varepsilon, \tag{17-50}$$

$$w_0^e(\varepsilon) = -k_{\mathrm{B}}T \int \mathrm{d}\eta \left(\frac{\delta(\varepsilon - \eta)}{\rho_0^e(\varepsilon)} - \left(\chi_0^e\right)^{-1}(\varepsilon, \eta)\right)\left(\rho^e(\eta) - \rho_0^e(\eta)\right), \tag{17-51}$$

$$\begin{aligned}\Delta\mu = &\int \mathrm{d}\varepsilon\, \varepsilon \rho^e(\varepsilon) - k_{\mathrm{B}}T \int \mathrm{d}\varepsilon \Big[\left(\rho^e(\varepsilon) - \rho_0^e(\varepsilon)\right) - \rho^e(\varepsilon) \log\left(\frac{\rho^e(\varepsilon)}{\rho_0^e(\varepsilon)}\right) \\ &- \left\{\alpha(\varepsilon) F(\varepsilon) + (1 - \alpha(\varepsilon)) F_0(\varepsilon)\right\}\left(\rho^e(\varepsilon) - \rho_0^e(\varepsilon)\right)\Big],\end{aligned} \tag{17-52}$$

$$F(\varepsilon) = \begin{cases} \beta w^e(\varepsilon) + 1 + \dfrac{\beta w^e(\varepsilon)}{\exp(-\beta w^e(\varepsilon)) - 1} & (\text{when } w^e(\varepsilon) \le 0) \\ \dfrac{1}{2}\beta w^e(\varepsilon) & (\text{when } w^e(\varepsilon) \ge 0) \end{cases}, \tag{17-53}$$

$$F_0(\varepsilon) = \begin{cases} -\log\left(1 - \beta w_0^e(\varepsilon)\right) + 1 + \dfrac{\log\left(1 - \beta w_0^e(\varepsilon)\right)}{\beta w_0^e(\varepsilon)} & (\text{when } w_0^e(\varepsilon) \le 0) \\ \dfrac{1}{2}\beta w_0^e(\varepsilon) & (\text{when } w_0^e(\varepsilon) \ge 0) \end{cases}, \tag{17-54}$$

$$\alpha(\varepsilon) = \begin{cases} 1 & \left(\text{when } \rho^e(\varepsilon) \ge \rho_0^e(\varepsilon)\right) \\ 1 - \left(\dfrac{\rho^e(\varepsilon) - \rho_0^e(\varepsilon)}{\rho^e(\varepsilon) + \rho_0^e(\varepsilon)}\right)^2 & \left((\text{when } \rho^e(\varepsilon) \le \rho_0^e(\varepsilon)\right). \end{cases} \tag{17-55}$$

When Eqs. (17-50), (17-51), (17-52), (17-53), (17-54) and (17-55) are used to evaluate the solvation free energy, the inputs are the three energy distribution functions ρ^e, ρ_0^e, χ_0^e given by Eqs. (17-47), (17-48) and (17-49), respectively. ρ^e is obtained from a simulation of the solution system of interest, and ρ_0^e and χ_0^e are constructed with a simulation of the pure solvent system. The approximate scheme provided by Eqs. (17-47), (17-48), (17-49), (17-50), (17-51), (17-52), (17-53), (17-54), and (17-55) does not require simulations at the intermediate states of solute insertion. It should be noted that when the solute molecule is inserted into the pure solvent system, it often overlaps with solvent molecules. The overlapping configurations contribute to ρ_0^e and χ_0^e at large energy coordinates and account for the excluded volume effect in the solvation free energy.

In Figure 17-6, the approximate values of the solvation free energy $\Delta\mu$ for typical solute molecules in solvent water are compared to the corresponding exact values obtained from the free-energy perturbation method. The (solvent) density of 1.0 g/cm^3 and the temperature of 25°C is an ambient state, and the densities of 1.0, 0.6, and 0.2 g/cm^3 at 400°C correspond to high-, medium-, and low-density supercritical states. The good agreement is observed between the approximate and exact values. The agreement is particularly notable at the medium- and low-density states of 0.6 and 0.2 g/cm^3 and 400°C. When the solute is ionic, the density at the state of 0.2 g/cm^3 and 400°C is not yet low in the sense, for example, that the hydration number at that state is comparable to the numbers at ambient states [55,56]. Even in this case, our approximate procedure is effective in determining the solvation free energy. The solvation free energies of water at 1.0 g/cm^3 and 400°C and of methanol and ethanol at 0.6 g/cm^3 and 400°C are rather small in magnitude. These behaviors are caused by the balance between the favorable and unfavorable contributions of

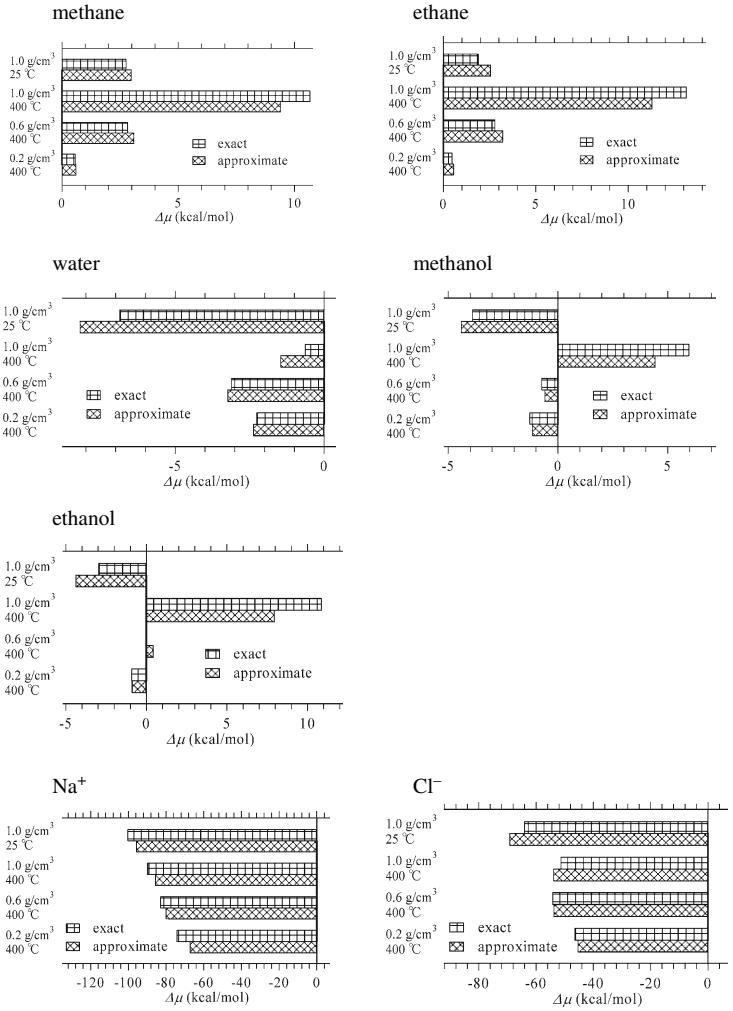

Figure 17-6. Comparison of the solvation free energy $\Delta\mu$ for typical solute molecules in solvent water. The thermodynamic state is specified by the solvent density and temperature

the solute–solvent interactions, and are well reproduced by our approximate method. Therefore, the single functional given by Eqs. (17-50), (17-51), (17-52), (17-53), (17-54), and (17-55) provides an accurate and efficient route to the solvation free energy for various types of solutes over a wide range of thermodynamic conditions.

By virtue of Eq. (17-37), the average sum of the solute–solvent interaction energy in the solution system of interest is smaller than or equal to $\Delta\mu$. This means that the density-functional F^e is always non-positive for any solute–solvent distribution function. Actually, the density functional is a measure of the "difference" between

ρ^e in solution and $\rho^e{}_0$ in the pure solvent. It is zero only when $\rho^e = \rho^e{}_0$. The density-functional is expected to be more negative when ρ^e and $\rho^e{}_0$ appear more differently. The first term of Eq. (17-44) is the average sum of the solute–solvent interaction energy in solution. It is more negative when ρ^e is more populated in the low-energy region of ε. A typical behavior is, on the other hand, that ρ_0 reduces monotonically toward the low-energy tail. Thus, the first term of Eq. (17-44) is more negative when ρ^e and $\rho^e{}_0$ are more different. This shows that the first and second terms of Eq. (17-44) fluctuate to the same direction through the variation of ρ^e. It is then expected that $\Delta\mu$ of Eq. (17-44) converges faster in molecular simulation than its components expressed as the first and second terms of Eq. (17-44). Indeed, usual experience is that when (an approximate form of) Eq. (17-46) is employed, the solvation free energy $\Delta\mu$ converges faster than the average sum $<u>$ of the solute–solvent interaction energy in solution. Table 17-1 lists illustrative examples of $\Delta\mu$ and $< u>$ for benzene and phenol solvated in water and *n*-octanol at 25°C and 1 atm.

As seen in Eq. (17-42), each of the solute and solvent molecules is taken as a single unit in the energy representation. The molecule is treated as a whole, while the coordinate for the distribution functions is one-dimensional. No explicit reference is made to the detail of the molecular structure by focusing on the interaction energy. The following advantages then emerge in the method of energy representation.

Firstly, the method is straightforwardly applicable to molecules with intramolecular flexibility. The implementation is indifferent whether the molecule is rigid or flexible. The information of structural fluctuation of the molecule is adsorbed when the energy coordinate is introduced by Eq. (17-42). For large molecules constituting protein, micellar, and membrane systems, it is not allowed to neglect the molecular flexibility. In the method of energy representation, an additional and/or separate scheme is not necessary to be formulated for large, flexible species.

Secondly, the treatment of inhomogeneous system and clusters is straightforward. So far, the formulation does not assume the system homogeneity and the thermodynamic limit. The application to inhomogeneous and/or finite systems is then possible without modification. The binding of a molecule to such nanoscale structures as protein, micelle, and membrane can be viewed as a solvation in an inhomogeneous and finite, mixed solvent [57]. The method of energy representation can thus be a

Table 17-1. Average and standard error for $\Delta\mu$ and $<u>$ of benzene and phenol in water and *n*-octanol calculated from 100-ps MD run of the solution system and 50-ps MD run of the pure solvent system. $\Delta\mu$ and $<u>$ are expressed in units of kcal/mol

System	Solvation free energy $\Delta\mu$	Average sum $<u>$ of the solute–solvent interaction
Benzene in water	0.6 ± 0.2	-15.4 ± 0.4
Phenol in water	-4.9 ± 0.4	-26.6 ± 0.9
Benzene in *n*-octanol	-5.3 ± 0.2	-13.1 ± 0.3
Phenol in *n*-octanol	-8.4 ± 0.3	-25.0 ± 0.6

useful approach to intermolecular correlation and association important in biological and interface sciences.

Thirdly, an accurate treatment is possible for supercritical fluid. In supercritical fluid, the solvent density and temperature can be varied over wide range and the solvent effect may act as a key to control a chemical process. It is well known that supercritical fluid can be described accurately when the whole molecule is treated as a single unit [13]. A multidimensional representation is necessary, however, in the usual coordinate space. By introducing the energy as the coordinate for distribution functions, the whole molecule can be taken as a single unit with keeping the description one-dimensional. The approximate functional given by Eqs. (17-47), (17-48), (17-49), (17-50), (17-51), (17-52), (17-53), (17-54), and (17-55) incorporates the intermolecular correlation at the two-body level. The solvation free energy obtained is then exact to second order in the solvent density. Since the method is exact in the low-density regime, a formulation of a good approximation in the high-density regime leads to an accurate description over a wide range of solvent density.

Finally, the combination with the QM/MM methodology can be performed. In QM/MM calculation, the many-body effect is introduced for the solute–solvent interaction and is beyond the applicability of conventional theories of solutions. In the method of energy representation, the fluctuation of the electronic state in response to the environment is viewed as a fluctuation of intramolecular coordinates of the QM solute. The evaluation becomes feasible for the free energy for the many-body effect of the electronic fluctuation. In addition, Eq. (17-42) makes no reference to the functional form of the potential function. It refers only to the value of the potential energy, and there is no need for deterioration or modification of the electronic-state calculation. Thus, the treatment is possible for an arbitrary distribution of charges. The contraction to a set of point charges is not necessary, and the effect of the diffuse (cloud-like) nature of electronic distribution can now be determined. The detail of the combination with the QM/MM methodology is given in Section 17.4.

17.4. COMBINATION OF THE QM/MM METHOD WITH THE THEORY OF SOLUTIONS

In Sections 17.2 and 17.3, we have reviewed the QM/MM approach based on the real-space grids [40,41,58,59,60,61,62] and the novel theory of solutions [14,15,16], respectively. As has been suggested, the theory of energy representation is readily applicable to a solute that is quantum chemically described. The present section is devoted to the details of the methodology, referred to as QM/MM-ER, developed by combining the QM/MM approach with the theory of energy representation [19]. The point of the method is to divide the total solvation free energy into the contributions due to the pairwise additive interaction between the solute and the solvent and the residual contribution due to the electron density fluctuation. A focus will be placed on the treatment of the many-body interaction inherent in the quantum chemical object.

17.4.1. Division of the Total Solvation Free Energy

In the formulation of Eq. (17-42), the solute–solvent interaction was assumed to be pairwise additive. When the QM/MM method is employed as introduced in Section 17.2.3, the electron density of the QM solute is determined through the interaction with a number of solvent molecules. The instantaneous electrostatic interaction between the point charges and the wavefunctions in the potential E_{ELS} is expressed as

$$\begin{aligned}\sum_i \langle \psi_i | \, \hat{v}_{\mathrm{pc}} \, | \psi_i \rangle &= \int n(\mathbf{r}) v_{\mathrm{pc}}(\mathbf{r}) \mathrm{d}\mathbf{r} \\ &= \sum_k \upsilon \, (n, \mathbf{x}_k),\end{aligned} \tag{17-56}$$

where $\mathbf{x}_k$ specifies the position of the kth interaction site in the MM system. From the last equality in Eq. (17-56), it seems that the solute–solvent interaction is pairwise additive in the QM/MM approach. However, electron density $n(\mathbf{r})$ is obtained by solving Eq. (17-19) that includes the external potential formed by the MM molecules of which coordinates are expressed collectively as $\mathbf{X}$. Therefore, $n(\mathbf{r})$ depends on $\mathbf{X}$ and the interaction energy of Eq. (17-56) inevitably involves many-body effect (*not* pairwise additive).

With the solute–solvent interaction of Eq. (17-56), it is possible to introduce the energy coordinate ε as the value of $\upsilon \, (n, \mathbf{x}_k)$. The one-to-one correspondence between the solute–solvent interaction and the distribution function is then valid in the energy representation with a form similar to the one presented in the Appendix of Matubayasi and Nakahara [16] for the solute with structural flexibility. An approximate functional for the excess chemical potential can thus be developed similarly. Our strategy to couple the QM/MM calculation with the method of energy representation is to evaluate the major part of the excess chemical potential by freezing the electron density at its average obtained by a QM/MM simulation and compute separately the remaining minor contribution due to the many-body effect that gives rise to the electron density fluctuation. The formulation is as follows.

We define the distortion energy E_{dist} as the difference between the energy of Eq. (17-21) and that of the isolated QM molecule E_0, thus,

$$E_{\mathrm{dist}} = E_{\mathrm{QM}} - E_0 \tag{17-57}$$

Note that the sum of Eqs. (17-56), (17-57), van der Waals energy E_{vdW} and the isolated solute energy E_0 is equivalent to $E_{\mathrm{QM}} + E_{\mathrm{QM/MM}}$ in Eq. (17-18). Then the excess chemical potential $\Delta\mu$ of the QM solute can be exactly given by

$$\exp(-\beta\Delta\mu) = \frac{\int \mathrm{d}\mathbf{X} \exp\left\{-\beta\left[E_{\mathrm{dist}} + E_{\mathrm{QM/MM}}(n, \mathbf{X}) + E_{\mathrm{MM}}(\mathbf{X})\right]\right\}}{\int \mathrm{d}\mathbf{X} \exp(-\beta E_{\mathrm{MM}}(\mathbf{X}))}, \tag{17-58}$$

where β is the inverse of the Boltzmann constant k_B multiplied by T and E_{MM} is the energy of MM solvent. Here, we introduce an arbitrarily chosen standard energy $\bar{E}$ and electron density $\tilde{n}(\mathbf{r})$ fixed at an arbitrary distribution. Then, $\Delta\mu - \bar{E}$ can be decomposed into the solvation free energy $\Delta\bar{\mu}$ for the QM solute with the fixed density $\tilde{n}(\mathbf{r})$ and the free energy change $\delta\mu$ corresponding to the density fluctuation around the distribution of $\tilde{n}(\mathbf{r})$, thus,

$$\Delta\mu = \Delta\bar{\mu} + \bar{E} + \delta\mu, \tag{17-59}$$

where

$$\exp(-\beta\Delta\bar{\mu}) = \frac{\int d\mathbf{X} \exp\left\{-\beta\left[E_{QM/MM}(\tilde{n}, \mathbf{X}) + E_{MM}(\mathbf{X})\right]\right\}}{\int d\mathbf{X} \exp(-\beta E_{MM}(\mathbf{X}))}, \tag{17-60}$$

$$\begin{aligned}\exp[-\beta(\delta\mu)] &= \frac{\int d\mathbf{X} \exp\left\{-\beta\left[E_{dist} + E_{QM/MM}(n, \mathbf{X}) + E_{MM}(\mathbf{X})\right]\right\}}{\int d\mathbf{X} \exp\left\{-\beta\left[\bar{E} + E_{QM/MM}(\tilde{n}, \mathbf{X}) + E_{MM}(\mathbf{X})\right]\right\}} \\ &= \frac{\int d\mathbf{X} \exp\left\{-\beta\left[\left(E_{dist} - \bar{E}\right) + E_{QM/MM}(n, \mathbf{X}) + E_{MM}(\mathbf{X})\right]\right\}}{\int d\mathbf{X} \exp\left\{-\beta\left[E_{QM/MM}(\tilde{n}, \mathbf{X}) + E_{MM}(\mathbf{X})\right]\right\}}.\end{aligned} \tag{17-61}$$

It is easy to see that Eqs. (17-59), (17-60), and (17-61) are equivalent to Eq. (17-58). It must be noted that Eq. (17-60) expresses the solvation free energy of a molecule with a pairwise additive potential, hence the theory of energy representation described in Section 17.3.4 can be applied without any further approximations. An appropriate choice of $\bar{E}$ and $\tilde{n}(\mathbf{r})$ will make the contribution $\bar{E} + \Delta\bar{\mu}$ major in the total excess chemical potential. The free energy change expressed by Eq. (17-61) directly depends on the choice of the standard energy $\bar{E}$ and involves many-body effects since the solute–solvent interaction is described by $E_{QM/MM}(n, \mathbf{X})$ at the final state

In order to determine the optimal value of $\bar{E}$, we introduce a variable ϕ defined by

$$\phi = E_{dist} - \bar{E} \tag{17-62}$$

and consider its distributions under the solute–solvent interaction of $E_{QM/MM}(\tilde{n}, \mathbf{X})$ and $E_{QM/MM}(n, \mathbf{X})$, respectively. Then, $\delta\mu$ corresponding to the density fluctuation can be evaluated by

$$\begin{aligned}\delta\mu &= \Delta\bar{E} + \delta\tilde{\mu} + k_B T \int d\phi P(\phi) \ln\left(\frac{P(\phi)}{P_0(\phi)}\right) \\ \delta\tilde{\mu} &= \int d\phi P(\phi)\delta v(\phi) \\ \Delta\bar{E} &= \int d\phi\phi P(\phi).\end{aligned} \tag{17-63}$$

In Eq. (17-63), $\delta\nu(\phi)$ is the conditioned free energy change where $\phi = E_{\text{dist}} - \bar{E}$ is imposed and $\delta\tilde{\mu}$ can be computed by using an approximate functional introduced in the next subsection. As a result, the total excess chemical potential $\Delta\mu$ in Eq. (17-59) can be rewritten as

$$\Delta\mu = \Delta\bar{\mu} + \bar{E} + \Delta\bar{E} + \delta\tilde{\mu} + k_{\text{B}}T \int \mathrm{d}\phi P(\phi) \ln\left(\frac{P(\phi)}{P_0(\phi)}\right). \tag{17-64}$$

The summation of the second and third terms of Eq. (17-64) can be simplified as follows. Since the standard energy $\bar{E}$ is independent of ϕ, a relation

$$\begin{aligned} \bar{E} + \Delta\bar{E} &= \bar{E} + \int \mathrm{d}\phi (E_{\text{dist}} - \bar{E}) P(\phi) \\ &= \int \mathrm{d}\phi E_{\text{dist}} P(\phi) \end{aligned} \tag{17-65}$$

holds exactly and the change of integral variable of Eq. (17-65) leads to

$$\bar{E} + \Delta\bar{E} = \int \mathrm{d}(E_{\text{dist}}) E_{\text{dist}} P'(E_{\text{dist}}), \tag{17-66}$$

where $P'(E_{\text{dist}})$ represents the probability distribution of E_{dist} in the solution under the interaction of $E_{\text{QM/MM}}(n, \mathbf{X})$. Thus, it has been proved for any choice of $\bar{E}$ that $\bar{E} + \Delta\bar{E}$ is the ensemble average of the distortion energy E_{dist} of the QM solute. An appropriate choice of $\bar{E}$ is to take

$$\bar{E} = \langle E_{\text{dist}} \rangle = \frac{\int \mathrm{d}\mathbf{X} E_{\text{dist}} \exp\left\{-\beta\left[E_{\text{dist}} + E_{\text{QM/MM}}(n, \mathbf{X}) + E_{\text{MM}}(\mathbf{X})\right]\right\}}{\int \mathrm{d}\mathbf{X} \exp\left\{-\beta\left[E_{\text{dist}} + E_{\text{QM/MM}}(n, \mathbf{X}) + E_{\text{MM}}(\mathbf{X})\right]\right\}}, \tag{17-67}$$

so that $\Delta\bar{E}$ in Eq. (17-66) becomes zero.

Another quantity to be determined is the frozen electron density distribution $\tilde{n}(\mathbf{r})$ that appears in Eq. (17-60). Of course, the optimal distribution $\tilde{n}(\mathbf{r})$ is the one that minimizes the contribution of the density fluctuation to the free energy change expressed by Eq. (17-61). Here, we propose to take the ensemble average of the instantaneous distribution $n(\mathbf{r})$ that fluctuates according to the solvent molecular motion as a most natural and practical choice of $\tilde{n}(\mathbf{r})$, thus,

$$\tilde{n}(\mathbf{r}) = \frac{\int \mathrm{d}\mathbf{X} n(\mathbf{r}) \exp\left\{-\beta\left[E_{\text{dist}} + E_{\text{QM/MM}}(n, \mathbf{X}) + E_{\text{MM}}(\mathbf{X})\right]\right\}}{\int \mathrm{d}\mathbf{X} \exp\left\{-\beta\left[E_{\text{dist}} + E_{\text{QM/MM}}(n, \mathbf{X}) + E_{\text{MM}}(\mathbf{X})\right]\right\}}. \tag{17-68}$$

Taking the average in the form of Eq. (17-68) is quite advantageous since it can be obtained in the same ensemble for the computation of $\bar{E}$ as seen in Eq. (17-67). That is, $\bar{E}$ and $\tilde{n}(\mathbf{r})$ can be determined through a single QM/MM simulation, which leads to substantial reduction of computational time.

17.4.2. Contribution of the Many-Body Effect

Here, we present a scheme to compute $\delta\mu$ introduced by Eq. (17-61). We first rewrite Eq. (17-61) as

$$\exp\left[-\beta\left(\delta\mu\right)\right] = \frac{\int \mathrm{d}\mathbf{X} \exp\left(-\beta\left\{\left[E_{\mathrm{dist}}\left(\Psi\right) - \bar{E}\right] + E_{\mathrm{QM/MM}}\left(n, \mathbf{X}\right) - E_{\mathrm{QM/MM}}\left(\tilde{n}, \mathbf{X}\right)\right\}\right) \times \exp\left\{-\beta\left[E_{\mathrm{QM/MM}}\left(\tilde{n}, \mathbf{X}\right) + E_{\mathrm{MM}}\left(\mathbf{X}\right)\right]\right\}}{\int \mathrm{d}\mathbf{X} \exp\left\{-\beta\left[E_{\mathrm{QM/MM}}\left(\tilde{n}, \mathbf{X}\right) + E_{\mathrm{MM}}\left(\mathbf{X}\right)\right]\right\}}$$
$$= \frac{\int \mathrm{d}\mathbf{X} \exp\left(-\beta\left\{\left[E_{\mathrm{dist}}\left(\Psi\right) - \bar{E}\right] + \sum_i \left[\upsilon\left(n, \mathbf{x}_i\right) - \upsilon\left(\tilde{n}, \mathbf{x}_i\right)\right]\right\}\right) \times \exp\left\{-\beta\left[E_{\mathrm{QM/MM}}\left(\tilde{n}, \mathbf{X}\right) + E_{\mathrm{MM}}\left(\mathbf{X}\right)\right]\right\}}{\int \mathrm{d}\mathbf{X} \exp\left\{-\beta\left[E_{\mathrm{QM/MM}}\left(\tilde{n}, \mathbf{X}\right) + E_{\mathrm{MM}}\left(\mathbf{X}\right)\right]\right\}}. \tag{17-69}$$

According to Eq. (17-69), the "pure solvent" refers in the computation of $\delta\mu$ to the pairwise additive potential system with the solute–solvent interaction $E_{\mathrm{QM/MM}}\left(\tilde{n}, \mathbf{X}\right)$. On the other hand, the "solution" system involves the solute–solvent interaction $E_{\mathrm{QM/MM}}\left(n, \mathbf{X}\right)$ with the QM energy term of $E_{\mathrm{dist}}\left(n\right) - \bar{E}$. From Eq. (17-69), the energy coordinate to formulate $\delta\mu$ in the energy representation is associated with the instantaneous distribution $\hat{\rho}\left(\zeta\right)$ through

$$\hat{\rho}\left(\zeta\right) = \sum_i \delta\left(\zeta - \left[\upsilon\left(n, \mathbf{x}_i\right) - \upsilon\left(\tilde{n}, \mathbf{x}_i\right)\right]\right). \tag{17-70}$$

The development presented in Section 17.3 is not applicable to Eq. (17-69), however, due to the term of $E_{\mathrm{dist}}\left(n\right) - \bar{E}$. To deal with this term, we resort to the scheme given in Matubayasi and Nakahara [16].

The point of the scheme is to consider the probability distribution function for the variable ϕ defined by Eq. (17-62). In the solution system, the probability distribution $P(\phi)$ is given by

$$P(\phi) = \frac{\int \mathrm{d}\mathbf{X}\delta\left(\phi - \left[E_{\mathrm{dist}}\left(n\right) - \bar{E}\right]\right) \times \exp\left(-\beta\left\{\left[E_{\mathrm{dist}}\left(n\right) - \bar{E}\right] + E_{\mathrm{QM/MM}}\left(n, \mathbf{X}\right) + E_{\mathrm{MM}}\left(\mathbf{X}\right)\right\}\right)}{\int \mathrm{d}\mathbf{X} \exp\left(-\beta\left\{\left[E_{\mathrm{dist}}\left(n\right) - \bar{E}\right] + E_{\mathrm{QM/MM}}\left(n, \mathbf{X}\right) + E_{\mathrm{MM}}\left(\mathbf{X}\right)\right\}\right)}. \tag{17-71}$$

Similarly, the probability distribution function $P_0\left(\phi\right)$ in the pure solvent system is written as

$$P_0\left(\phi\right) = \frac{\int \mathrm{d}\mathbf{X}\delta\left(\phi - \left[E_{\mathrm{dist}}\left(n\right) - \bar{E}\right]\right) \times \exp\left\{-\beta\left[E_{\mathrm{QM/MM}}\left(\tilde{n}, \mathbf{X}\right) + E_{\mathrm{MM}}\left(\mathbf{X}\right)\right]\right\}}{\int \mathrm{d}\mathbf{X} \exp\left\{-\beta\left[E_{\mathrm{QM/MM}}\left(\tilde{n}, \mathbf{X}\right) + E_{\mathrm{MM}}\left(\mathbf{X}\right)\right]\right\}}. \tag{17-72}$$

It should be noted that electron density n appearing in Eq. (17-72) is determined by solving Eq. (17-19) under a given solvent configuration $\mathbf{X}$, which is sampled

according to the solute–solvent interaction $E_{\mathrm{QM/MM}}(\tilde{n}, \mathbf{X})$. It is then possible to show that

$$P(\phi) = P_0(\phi) \exp\{-\beta[\phi + \delta\nu(\phi) - \delta\nu]\}, \tag{17-73}$$

where $\delta\nu(\phi)$ is given by

$$\exp[-\beta\delta\nu(\phi)] = \frac{\int \mathrm{d}\mathbf{X}\delta\left(\phi - \left[E_{\mathrm{dist}}(n) - \bar{E}\right]\right) \exp\left(-\beta\left\{E_{\mathrm{QM/MM}}(n, \mathbf{X}) + E_{\mathrm{MM}}(\mathbf{X})\right\}\right)}{\int \mathrm{d}\mathbf{X}\delta\left(\phi - \left[E_{\mathrm{dist}}(n) - \bar{E}\right]\right) \exp\left(-\beta\left\{E_{\mathrm{QM/MM}}(\tilde{n}, \mathbf{X}) + E_{\mathrm{MM}}(\mathbf{X})\right\}\right)} \tag{17-74}$$

Equation (17-74) shows that $\delta\nu(\phi)$ is the free energy change associated with the variation from the pure solvent to the solution where the relation $\phi = E_{\mathrm{dist}}(n) - \bar{E}$ is imposed. From Eq. (17-73), we obtain

$$\begin{aligned} \delta\mu &= \delta\tilde{\mu} + k_{\mathrm{B}}T \int \mathrm{d}\phi P(\phi) \ln\left(\frac{P(\phi)}{P_0(\phi)}\right) \\ \delta\tilde{\mu} &= \int \mathrm{d}\phi P(\phi)\delta\nu(\phi). \end{aligned} \tag{17-75}$$

The second term of Eq. (17-75) can be computed by QM/MM simulations directly. To evaluate $\delta\tilde{\mu}$, we consider the distribution function over the energy coordinate ζ. Indeed, it is possible to show that the correspondence is one-to-one from the solute–solvent interaction defined over the coordinate ζ to the resultant energy distribution function of ζ. An approximate expression for $\delta\tilde{\mu}$ can be given by a set of equations listed as

$$\begin{aligned} \delta\tilde{\mu} = &-k_{\mathrm{B}}T \int \mathrm{d}\zeta \left\{[\rho(\zeta) - \tilde{\rho}_0(\zeta)] + \beta\tilde{\omega}(\zeta)\rho(\zeta)\right. \\ &\left. - \tilde{F}(\zeta)[\rho(\zeta) - \tilde{\rho}_0(\zeta)]\right\}, \end{aligned} \tag{17-76}$$

where $\rho(\zeta)$ is the ensemble average of $\hat{\rho}(\zeta)$ in the solution and

$$\tilde{\rho}_0(\zeta) = \int \mathrm{d}\phi P(\phi)\tilde{\sigma}_0(\zeta; \phi), \tag{17-77}$$

$$\tilde{\omega}(\zeta) = -k_{\mathrm{B}}T \ln\left(\frac{\rho(\zeta)}{\tilde{\rho}_0(\zeta)}\right) - \zeta, \tag{17-78}$$

$$\tilde{\sigma}_0(\zeta; \phi) = \frac{\int \mathrm{d}\mathbf{X}\delta\left(\phi - \left[E_{\mathrm{dist}}(n) - \bar{E}\right]\right) \sum_i \delta\left(\zeta - [\upsilon(n, \mathbf{x}_i) - \upsilon(\tilde{n}, \mathbf{x}_i)]\right) \times \exp\left\{-\beta\left[E_{\mathrm{QM/MM}}(\tilde{n}, \mathbf{X}) + E_{\mathrm{MM}}(\mathbf{X})\right]\right\}}{\int \mathrm{d}\mathbf{X}\delta\left(\phi - \left[E_{\mathrm{dist}}(n) - \bar{E}\right]\right) \exp\left\{-\beta\left[E_{\mathrm{QM/MM}}(\tilde{n}, \mathbf{X}) + E_{\mathrm{MM}}(\mathbf{X})\right]\right\}}, \tag{17-79}$$

$$\tilde{F}(\zeta) = \begin{cases} \beta\tilde{\omega}(\zeta) + 1 + \dfrac{\beta\tilde{\omega}(\zeta)}{\exp[-\beta\tilde{\omega}(\zeta)] - 1} & [\text{when } \tilde{\omega}(\zeta) \leq 0] \\ \dfrac{1}{2}\beta\tilde{\omega}(\zeta) & [\text{when } \tilde{\omega}(\zeta) \geq 0] \end{cases} . \tag{17-80}$$

In constructing Eq. (17-80) the weight factor α given by Eq. (17-55) is simply set to unity here. This is possible because the "excluded volume region", where ζ is very large, is absent in the present treatment. The correlation matrix over the energy coordinate ζ is then not necessary to be computed. Thus, the simulation for the pure solvent system can be shortened considerably. Eqs. (17-75), (17-76), (17-77), (17-78), and (17-79) are actually not affected by the constant shift of the variable ϕ. Thus, although Eq. (17-67) states that $\bar{E}$ is set to the ensemble average of the stochastic variable $E_{dist}(n)$, the computation of $\delta\mu$ with Eqs. (17-75), (17-76), (17-77), (17-78), (17-79), and (17-80) can be carried out simply by regarding ϕ as the $E_{dist}(n)$ value.

In this subsection, we presented an approximate scheme to evaluate the contribution $\delta\mu$ of the electron density fluctuation to the excess chemical potential. Although we saw that this contribution is minor for a QM water molecule in ambient and supercritical water, it should emphasized that $\delta\mu$ can be treated quantitatively in the method of energy representation. Actually, the treatment of the electron density fluctuation is not directly possible in the PCM and RISM-SCF methods. Furthermore, the approximate $\delta\mu$ is exact to second order in the solvent density and in the electron density fluctuation. Thus, when the effect of the electron density fluctuation is weak, the calculation of $\delta\mu$ is expected to be accurate.

The computational procedure for the QM/MM-ER is summarized as follows.

(P1) An ordinary QM/MM simulation is carried out to obtain the average distortion energy $\bar{E}$ and $\tilde{n}(\mathbf{r})$ which are described by Eqs. (17-67) and (17-68), respectively.

(P2) The energy distribution functions $\rho_0(\varepsilon)$, $\chi_0(\varepsilon, \eta)$, and $\rho(\varepsilon)$ for pure solvent and solution systems are computed for the QM solute with fixed density $\tilde{n}(\mathbf{r})$ to obtain $\Delta\bar{\mu}$ of Eq. (17-60) that gives major contribution to the total excess chemical potential. Note that $\bar{E} = \langle E_{\text{dist}} \rangle$ as indicated by Eq. (17-67).

(P3) The effect of the electron density fluctuation can be approximately estimated by performing additional QM/MM simulations that compute distribution functions $\tilde{\rho}_0(\zeta)$ and $\rho(\zeta)$ with respect to the energy coordinate $\zeta = \upsilon(n, \mathbf{x}_i) - \upsilon(\tilde{n}, \mathbf{x}_i)$. These distribution functions are used as inputs to the approximate functional.

In practical implementation of QM/MM-ER, the procedures (P1) and (P2) would be sufficient to compute the free energies with substantial accuracy. As was demonstrated in the previous paper [60], delocalization of electron distribution in space significantly affects the energetics of solvation. The effect of the electron density fluctuation can be safely neglected when one computes the free energy differences between reactants and products in chemical reactions in solution since the cancellations of the effect will take place.

17.5. APPLICATION OF THE QM/MM-ER APPROACH

In the previous papers, we applied QM/MM-ER to various systems to examine the efficiency of the method [19,63,64,38,65,66]. Here, we present the results of a few applications. At first, we employ the QM/MM-ER approach to compute solvation free energy of a QM water molecule described by DFT in an MM water solvent [19]. Second, the method is utilized to compute free energy change associated with a proton transfer in glycine in aqueous solution [64]. The results are compared with those obtained by experiments and the accuracy and efficiency of the QM/MM-ER approach is discussed.

17.5.1. Solvation Free Energy of a Water Molecule

To examine the efficiency and the accuracy of the QM/MM-ER approach we applied it to the computation of the excess chemical potential of a QM water solute immersed in MM water solvent. The QM/MM-ER simulations were performed for two thermodynamic conditions of water solutions; ambient water (AW: T = 300 K, ρ = 1.0 g/cm^3) and supercritical water (SCW: T = 600 K,[1] ρ = 0.3 g/cm^3). The solvent was represented by 255 water molecules of TIP4P model [67] of which reliability is well established. The electronic structure of the QM water molecule is obtained by KS-DFT that utilizes the real-space grid and the BLYP functional. The kinetic energy operator in the Kohn–Sham equation was expressed by the fourth-order finite difference method (L = 4 in Eq. (17-10)) and the effective potentials for the valence electrons were constructed from the Kleinman–Bylander non-local pseudopotentials (Eq. (17-6)). The Hartree potential (Eq. (17-11)) of the electron was computed by utilizing the fast Fourier transforms (FFT). The geometry of the QM water molecule used in the QM/MM simulation was optimized by the Gaussian 98 package by means of DFT with the BLYP functional. The basis set used is the correlation-consistent valence double zeta with polarization (aug-cc-pVDZ). The obtained geometrical parameter is OH = 0.975 Å, and HOH = 104.2°. The QM solute was placed at the center of the cubic QM cell in which 32 grids with equi-intervals were placed on each axis. The grid spacing h of the QM cell was set at 0.287 a.u. (0.152 Å), which corresponds to a cutoff energy of 60 a.u. The atomic core regions were reinforced by the double grids of which spacing was set at 0.2 h. Such a QM cell was embedded in the center of an MM simulation cell with periodic boundary conditions. The molecular configurations for the solvent were sampled in *NVT* ensemble through molecular dynamics simulations where Newtonian equations of motion for each particle were solved by the leap-frog algorithm [42] with a time step 1.0 fs and the velocity rescaling was used for the temperature control. For the TIP4P molecule, which is the four-site model, the Lennard-Jones (LJ) site is placed at the O atom (σ = 3.15 Å, ε = 0.155 kcal/mol), and the negative point charge q_M is placed near the O atom and the positive point charges q_H at hydrogens (q_M = –1.04, q_H = 0.52 in the unit of

[1] The reduced temperature of 600 K for TIP4P model is estimated as T_r = 1.07.

elementary charge). The LJ potential between MM water molecules is given in the form of Eq. (17-23). The long-range interaction between MM charges was calculated by the Ewald method [68] and a cutoff distance of the LJ potential was set at half of the box length.

The average electronic distortion energy $\bar{E}$ and the electron density $\tilde{n}(\mathbf{r})$ given, respectively, by Eqs. (17-67) and (17-68) were obtained by the 50-ps QM/MM simulation after 5-ps equilibration. Subsequently, the QM/MM simulation for the solute with the electron density fixed at $\tilde{n}(\mathbf{r})$ was performed to construct the energy distribution functions $\rho(\varepsilon)$, $\rho_0(\varepsilon)$, and $\chi_0(\varepsilon,\eta)$ given, respectively, by Eqs (17-47), (17-48), and (17-49); 100 and 200 ps simulations were carried out for the solution and the pure solvent systems, respectively. We note that the energy distribution functions were constructed for the solvent molecules of which oxygen was inside a sphere of 9 Å radius centered at the oxygen of the QM water molecule. The energy distribution functions $\rho(\varepsilon)$, $\rho_0(\varepsilon)$ for the MM water molecules in the AW and the SCW are presented in Figures 17-7 and 17-8, respectively. $\rho_{\mathrm{np}}(\varepsilon)$ is the energy distribution functions for the solute with non-polarized electron density (electron density at the isolation). Note that these functions are normalized with respect to the bulk number densities. In the solution of AW, there exists a distinct peak around –5 kcal/mol in the energy coordinate due to the hydrogen bonding. Further, it is shown that the

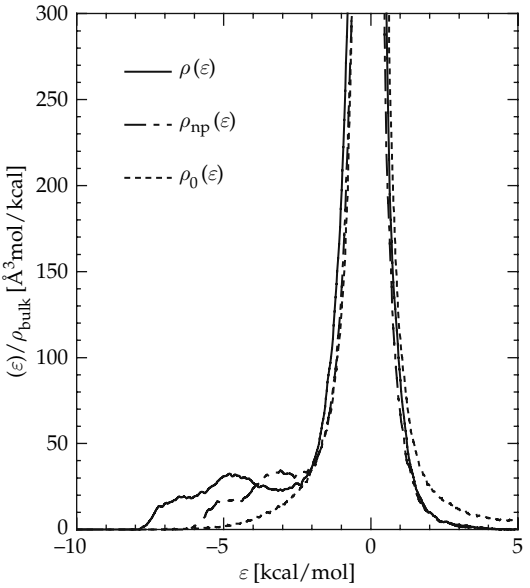

Figure 17-7. Energy distribution functions for the water molecule in ambient water (AW: T = 300 K, ρ = 1.0 g/cm^3). $\rho(\varepsilon)$, $\rho_{\mathrm{np}}(\varepsilon)$ are for the solution, and $\rho_0(\varepsilon)$ is for the pure solvent systems. $\rho_{\mathrm{np}}(\varepsilon)$ is the distribution function for the QM solute with non-polarized electron density. The distribution functions are normalized by the bulk number density ρ_{bulk}

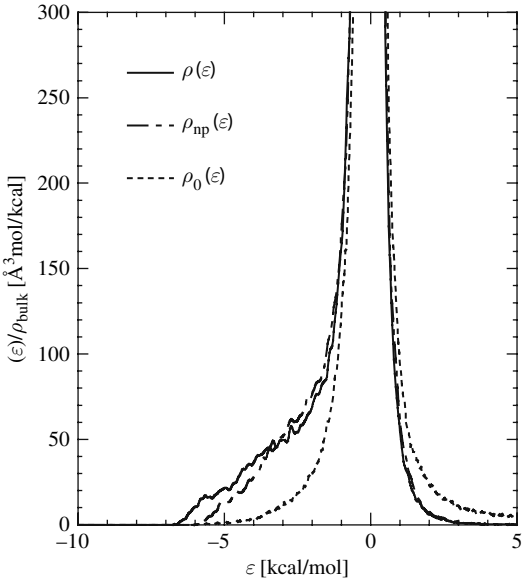

Figure 17-8 Energy distribution functions for the water molecule in the supercritical water (SCW: T = 600 K, ρ = 0.3 g/cm^3). Notations are synonymous with Figure 17-7

solute polarization gives significant effect on the energy distribution functions. In the SCW, on the other hand, the peak is smeared due to the high temperature and low density of the solution. These distribution functions were substituted in Eq. (17-52) to compute free energy contribution $\Delta\bar{\mu}$ originating from pairwise interaction in the solute–solvent interaction (Eq. (17-60)). The additional QM/MM simulations were also performed to compute free energy $\delta\mu$ described in Eq. (17-61) due to the many-body effect in the QM object. For the computation of $\delta\mu$ the energy distribution was constructed on the energy coordinate $\zeta = \upsilon(n, \mathbf{x}_i) - \upsilon(\tilde{n}, \mathbf{x}_i)$ as described in Section 17.4.2.

The results of the QM/MM-ER simulations are summarized in Table 17-2. $\Delta\bar{\mu}_{\mathrm{np}}$ is the free energy change due to the solvation of the non-polarized solute, for which

Table 17-2. Solvation free energies of water molecule and their components computed by the QM/MM-ER method. Units are in kcal/mol

Thermodynamic states	$\Delta\mu$					
	$\bar{E}$	$\Delta\bar{\mu}_{\mathrm{np}}$	$\Delta\bar{\mu}_{\mathrm{pol}}$	$\delta\mu$	$\Delta\mu$	$\Delta\mu^{\mathrm{a}}_{\mathrm{exp}}$
AW	3.5	–4.5	–4.8	–1.2	–7.0	–6.3
SCW	1.0	–2.0	–0.6	–0.9	–2.5	–2.2[b]

[a] see footnote [2]
[b] experimental value is taken at the same reduced temperature as the TIP4P value.

the distribution $\rho_{\rm np}(\varepsilon)$ was used. It can be readily recognized that the free energy $\Delta\bar{\mu}_{\rm np}$ makes a major contribution both in the AW and SCW. On the contrary, the net contribution of the electron polarization, which may be given by $\Delta\bar{\mu}_{\rm pol} - \bar{E}$, makes much smaller contribution to the total solvation free energy. The free energy changes $\delta\mu$ due to the electron density fluctuation of the QM solute in the AW and the SCW were estimated as –1.2 and –0.9 kcal/mol, respectively. An attention should be paid on the fact that the free energy $\delta\mu$ in the SCW almost amounts to 40% of total solvation free energy and is comparable to that in the AW despite the fact that the distortion energy $\bar{E}$ in the SCW is much smaller than that in the AW. This result can be understood in terms of the asymmetric hydration in the SCW. Absolute of $\delta\mu$ becomes larger when the instantaneous electron density $n(\mathbf{r})$ in the solution deviates largely from the average distribution $\tilde{n}(\mathbf{r})$. In the SCW, due to its density fluctuation, it often takes place that only one hydrogen atom of a solute water molecule makes a hydrogen bond with another solvent molecule. Such an asymmetric hydration gives rise to the deviation of $n(\mathbf{r})$ from $\tilde{n}(\mathbf{r})$ since the average distribution $\tilde{n}(\mathbf{r})$ is always symmetric. Thus, it has been revealed that the electron density fluctuation plays a role in the solvation free energy especially in the SCW. As a sum of these contributions, the total excess chemical potentials of the QM water molecules in the AW and the SCW have been obtained as –7.0 and –2.5 kcal/mol, respectively. These values are in excellent agreement with those determined by experiments[2], indicating that the present new method is quite efficient and sufficient in accuracy.

A rational way to examine the accuracy of the present methodology is to compare the results with those obtained by a numerically exact method to compute free energy change. Of course, the same levels of theory of quantum chemistry and the same potential parameters in the MM force field must be used in the computation. Such a calculation is possible in principle, however, it is very much costly to perform in practice. Actually, it requires two orders of magnitude more computational cost than the QM/MM-ER to accomplish the free energy perturbation calculation along with the QM/MM interactions. So we bypassed to compute explicit QM/MM interaction by reducing the electron density $\tilde{n}(\mathbf{r})$ to a set of point charges placed on the nucleus of the solute. Assuming that the set of point charges correctly reproduces the electrostatic field formed by $\tilde{n}(\mathbf{r})$, the free energy perturbation calculation using the point charges provides the free energy change that can be compared with the value $\Delta\bar{\mu}_{\rm np} + \Delta\bar{\mu}_{\rm pol}$ obtained by the QM/MM-ER method. The set of point charges were optimized by the least square fittings so that they reproduce the electrostatic potentials of $\tilde{n}(\mathbf{r})$ at the sample points. We obtained the charges –0.90 and +0.45 at oxygen and hydrogen, respectively. The free energy perturbation using these point charges gives the value of –8.8 kcal/mol for the AW, which excellently agrees with that given by QM/MM-ER ($\Delta\bar{\mu}_{\rm np} + \Delta\bar{\mu}_{\rm pol} = -9.3{\rm kcal/mol}$).

---

[2] The International Association for the Properties of Water and Steam, 1997, IAPWS Industrial Formulation 1997 for the Thermodynamic Properties of Water and Steam, Erlangen, Germany.

17.5.2. Free Energy Change Associated with a Proton Transfer Process

The purpose of the present work is to compute the free energy change associated with the isomerization of glycine in aqueous solution as a benchmark test of the QM/MM-ER method. It is well known that glycine takes a neutral form (NF) at isolation while it takes a zwitterionic form (ZW) in the aqueous solution by a proton translocation. There has been a lot of works both in the gas phase and in aqueous solutions [69,70,71,72,73,74,75,76]. In general the computational error in the free energy calculation can be considered to be proportional to the magnitude of the solute–solvent interaction energy. The affinity of NF-glycine to the polar solvent will be much smaller than that of ZW-glycine, hence, the computation of the free energy change for the isomerization from NF to ZW serves as a severe test. The results will be compared with those obtained by the SCRF (self-consistent reaction field) calculation and the classical molecular simulations.

The free energy change δG_{aq} for the chemical reaction in solution can be described in terms of the reaction free energy δG_{gas} in gas phase and the solvation free energies of the solutes at the initial and the final state of the reaction, thus,

$$\delta G_{\mathrm{aq}} = \delta G_{\mathrm{gas}} + \Delta\mu\,(\mathrm{ZW}) - \Delta\mu\,(\mathrm{NF})\,. \tag{17-81}$$

In Eq. (17-81), $\Delta\mu$ (ZW) and $\Delta\mu$ (NF) are, respectively, the solvation free energies of the ZW and the NF form of glycine. Since the free energy difference δG_{gas} can be accurately computed by a sophisticated method based on the DFT or the molecular orbitals theory, the accuracies of the solvation free energies of the solute molecules dominate the reliability of the free energy difference δG_{aq}.

The geometry of glycines in the form of ZW and NF were optimized by using the Gaussian 03 package [77] with B3LYP/aug-cc-pVDZ level of theory. The presence of the water solvent in the optimization was mimicked by the PCM with the dielectric constant $\varepsilon = 78.39$. The schematic illustration of the molecular structure for the NF and ZW glycines are shown in Figures 17-9(a) and 17-9(b), respectively. Subsequently the frequency analyses were performed to compute zero-point vibrational energies and also the free energies corresponding to the vibrational and the rotational motion of the solutes. There is no need to consider the effect of the translational molecular motion since the reaction proceeds without any associations or fragmentations. The molecular geometries we obtained are in good agreement with those identified by Tuñón et al. [73]. The energy difference between the two structures determined by B3LYP functional was also estimated by the CCSD(T) calculation to examine the accuracy of the DFT calculations. The basis-set dependence of the energetics was examined by using the valence triples basis set (aug-cc-pVTZ).

The computational details for the QM/MM simulation were almost common to those for the simulation described in Section 17.5.1. The major change was made in the setup of the real-space grids of the QM cell. The number of grid points for each axis was increased to 64 from 32 where the grid spacing h was set at $h = 0.152$ Å. The thermodynamic condition of the MM water solvent was set at $T = 300$ K, $\rho = 1.0$ g/cm^3. The LJ parameters in AMBER95 force field were employed

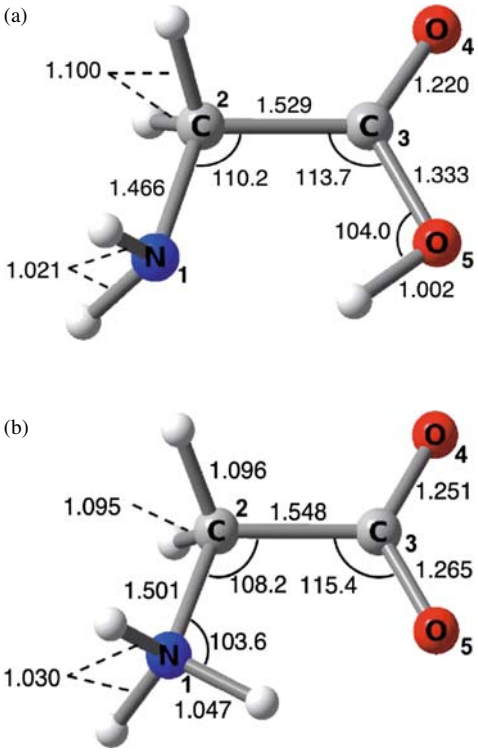

Figure 17-9 Ball and stick representation of the glycine (**a**) in the neutral form and (**b**) in the zwitterionic form. The distances are in the units of angstrom and the angles are in degrees

to describe the LJ interaction of glycine. The size and energy parameters between unlike atoms were determined by the Lorentz–Berthelot mixing rule. Other details for the QM/MM simulation are common to those used in the calculation shown in the previous subsection. We refer the readers to the notation given above for further information.

The energy differences between the ZW and the NF form of glycine in the gas phase were computed by various methods including the molecular-orbital theory. The energy changes δE_{gas}, the zero-point energy change δE_{ZPE}, and the free energy change δG_{vibrot} associated with the molecular vibration and rotation are summarized in Table 17-3. The vibrational and rotational free energy change gives minor contribution to the energy difference between the ZW and the NF glycine, however, the effect of the zero-point vibrational energy is not negligible. The contributions from δG_{vibrot} and δE_{ZPE} amount to $\sim$1.2 kcal/mol. In accord with the general trend, the DFT calculation with the BLYP functional underestimates the reaction energy as compared to that with the B3LYP functional that gives the close value to

Table 17-3. Energy and free energy differences computed by various methods between the ZW and the NF form of glycine in the gas phase. Units are in kcal/mol

	B3LYP			BLYP	CCSD(T)
	δG_{vibrot}	E_{ZPE}	E_{gas}	E_{gas}	E_{gas}
δ(NF→ZW)	0.29	0.89	21.52	19.36	22.26

CCSD(T)/aug-cc-pVDZ calculation. Note that sum of these energies gives the free energy change δG_{gas} in Eq. (17-81), i.e., $\delta G = \delta G_{\text{gas}} + \delta G_{\text{ZPE}} + \delta G_{\text{vibrot}}$. Hence, δG_{gas} is estimated to be 22.7 kcal/mol within the framework of the DFT/B3LYP calculations. The basis-set dependence of the energy difference was also examined by employing the valence-double (aug-cc-pVDZ) and triple (aug-cc-pVTZ) exponents for the Gaussian-type orbitals in the BLYP calculations and it was found that the difference is only about 0.1 kcal/mol. Hence, we concluded that the valence-double basis set is adequate in accuracy for the present application. The energy difference δE_{gas} between the ZW and the NF was computed as 21.3 kcal/mol by our real-space-grid package that employs the BLYP functional. The value is exceptionally closer to that from the B3LYP functional than the BLYP calculation by Gaussian 03. Anyway we adopted the value of B3LYP (21.5 kcal/mol) as the energy difference in E_{gas}.

The energy distribution functions $\rho(\varepsilon)$, and $\rho_0(\varepsilon)$ for the solutes NF and ZW with the electron densities $\tilde{n}(\mathbf{r})$ given by Eq. (17-68) are shown in Figures 17-10 and 17-11. The energy distribution functions $\rho_{\text{np}}(\varepsilon)$ for the solutes at isolations are also drawn in the figures. The energy distribution functions are normalized by the bulk number density. A notable feature is that the peak due to the hydrogen bonding between the solute and the solvent can be found in $\rho(\varepsilon)$ for NF (Figure 17-10) around $\varepsilon = -7$ kcal/mol. The corresponding peak for the ZW is more prominent and it shifts to lower region of the energy coordinate (Figure 17-11). On the other hand, the peaks of the energy distribution functions $\rho_{\text{np}}(\varepsilon)$ for the non-polarized solutes are located in the region of the substantially higher energy coordinate than the distributions $\rho(\varepsilon)$, implying that the electronic polarization of the solute plays an essential role in the intermolecular interactions. Especially for the ZW, the peak becomes more pronounced by the solute polarization which may strengthen the zwitterionic character of the solute. Actually, the dipole moment of the ZW increases from 10.4 to 15.1 Debye by the solute insertion to the solvent. The solvation free energies and their components for the NF and ZW forms of glycine are summarized in Table 17-4.

Electronic deformation energy $\bar{E}$ defined by Eq. (17-67) for the ZW is found to be much larger than that for the NF, which clearly corresponds to the larger induced dipole of the ZW (change of the dipole moment by 4.7 Debye). The term $\Delta\bar{\mu}_{\text{np}}$ in Table 17-3 is the solvation free energy of the solute with the electron density fixed at its isolation and $\Delta\bar{\mu}_{\text{pol}}(= \Delta\bar{\mu} - \Delta\bar{\mu}_{\text{np}})$ is the contribution due to the electronic polarization. It is of interest to note that $\Delta\bar{\mu}_{\text{pol}}$ is comparable to or larger than $\Delta\bar{\mu}_{\text{np}}$. Thus, the electronic polarization greatly affects the solvation. The solute polarization,

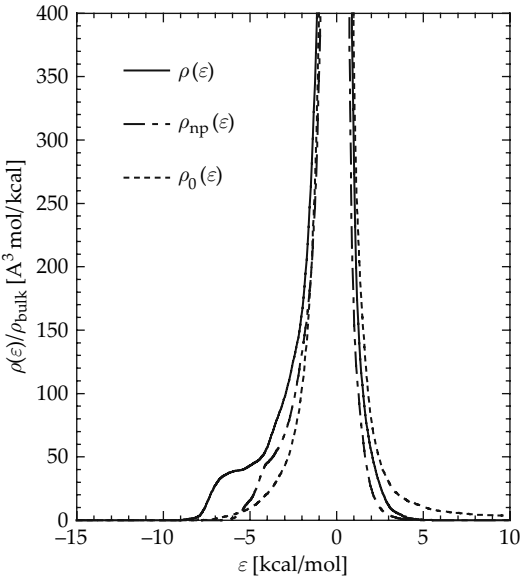

Figure 17-10. Energy distribution functions for glycine in neutral form (NF). $\rho(\varepsilon)$, $\rho_{np}(\varepsilon)$ are for the solution, and $\rho_0(\varepsilon)$ for pure solvent system. $\rho_{np}(\varepsilon)$ is the distribution function for the QM solute with non-polarized electron density. The distribution functions are normalized by the bulk number density ρ_{bulk}

of course, is concomitant with the destabilization in the electronic energy. Hence, the net polarization contribution can be estimated as the sum of $\bar{E}$ and $\Delta\bar{\mu}_{pol}$. The net polarization contribution of the ZW is estimated to be –10.5 kcal/mol, while that of the NF is –4.1 kcal/mol. The contribution of the electronic fluctuation $\delta\mu$ for the ZW was computed as –4.2 kcal/mol, while that for the NF as –3.0 kcal/mol. It was demonstrated that $\delta\mu$ gives non-negligible contribution to the total solvation free energy for both molecular species as revealed for the solvation free energies of water molecules presented in the previous section. The major contribution to the solvation free energy is found to be given by the non-polarized solute, while the electron polarization and the fluctuation give minor but significant contributions. As a result, the free energy difference δG_{aq} between the ZW and the NF was computed as –7.8 kcal/mol according to Eq. (17-81) where the values of B3LYP calculation was adopted for the free energy difference δG_{gas} in the gas phase. When we take the energy difference E_{gas} obtained by our real-space grid package, δG_{aq} becomes –8.0 kcal/mol. Thus, it was demonstrated that the free energy change computed by QM/MM-ER is in quite excellent agreement with the reported experimental values, –7.3 or –7.7 kcal/mol [75,76]. Furthermore, the other values on energetics also show satisfying agreement with computational or experimental data obtained by other groups. The energy difference in the solute–solvent interaction energies between the ZW and the NF was estimated to be –80.2 kcal/mol in the present calculation, which

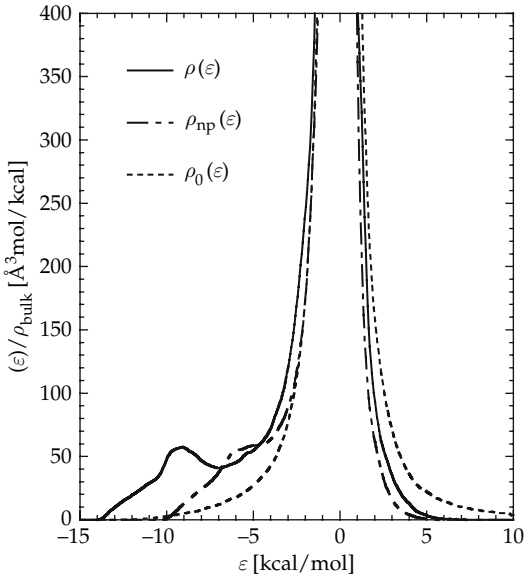

Figure 17-11. Energy distribution functions for glycine in zwitterionic form (ZW). Notations are synonymous with the Figure 17-10

is almost comparable to the value –77.1 kcal/mol given by other QM/MM simulations [72]. Another available data determined experimentally is the heat of transfer of glycine from gaseous state to the solution. The experimental value is $\Delta H = -19.2 \pm 1$ [74], while our estimation is equal to –20.4 kcal/mol. As shown in Eq. (17-81), the calculation of a free energy change associated with a reaction in solution is given by the subtraction of the solvation free energies between the product and the reactant. Hence, the computational error associated with the methodology is often cancelled due to the subtraction procedure. In the present application, however, the product ZW largely differs from the reactant NF in the affinity to the polar solvent molecules and the cancellation of error is considered to be small. It should also be emphasized that the present approach requires only the LJ parameters for the solutes and the

Table 17-4. Solvation free energies for the NF and the ZW form of glycine computed by the QM/MM-ER approach. Units are in kcal/mol

Species	$\Delta\mu$				
	$\bar{E}$	$\Delta\bar{\mu}_{\mathrm{np}}$	$\Delta\bar{\mu}_{\mathrm{pol}}$	$\delta\mu$	$\Delta\mu$
NF	9.3	–8.5	–13.4	–3.0	–15.6
ZW	21.2	–31.4	–31.7	–4.2	–46.1

solvent as empirical parameters and requires no extra parameter tunings. Thus, the QM/MM-ER approach was found to be efficient and accurate for the calculation of the free energy change associated with a chemical event in aqueous solution. Additionally, we also performed the polarizable continuum model (PCM) calculations by using the Gaussian 98 package to make comparisons. The solvation free energies for the ZW and the NF glycine were obtained as –30.8 and –9.5 kcal/mol, respectively, from which the reaction free energy was estimated as 1.4 kcal/mol. In this estimation the value of 22.7 kcal/mol obtained by B3LYP calculation was adopted as the free energy difference in the gas phase. Thus, the PCM approach, which neglects the explicit shapes of the molecules that constitutes the solvent, gives a qualitatively incorrect result that the NF glycine is more stable in aqueous solution than the ZW glycine. The faithful representation of the short-range interactions such as hydrogen bondings will be crucial in describing the solvation free energies.

Here we address the issue of the effect of the simplification in the molecular interaction on the solvation free energy. To do this the electron density of the solute is reduced to a set of point charges alloted to atomic sites. Then, the classical Monte Carlo simulation is performed to obtain the solvation free energy of the solute represented by a set of interaction sites. The purpose of the analysis is to examine the effect of the diffuse nature of the electronic distribution. At first, we optimized the point charges by the least-square fittings so that they reproduce the electrostatic potential formed by the solute with the average electron density $\tilde{n}(\mathbf{r})$. The reliability of the optimized set of charges was assessed by comparing its dipole moment with that of the solute with the electron density $\tilde{n}(\mathbf{r})$. The dipole moment of the NF with the density $\tilde{n}(\mathbf{r})$ is 8.7 Debye and that with the point charges is 8.7 Debye, showing an excellent agreement. Similarly the dipole moment due to the point charges of the ZW is 15.0 Debye, which agrees well with that of the solute with the realistic electron density (15.1 Debye). Thus, the sets of fractional charges were found to realize the important electronic property of the solute.

By employing the sets of point charges, the energy distribution functions were constructed through classical Monte Carlo simulations. Then the solvation free energies were computed by the method of the energy representation, which can be directly compared to the free energy $\Delta\bar{\mu}\left(=\Delta\bar{\mu}_{\mathrm{np}}+\Delta\bar{\mu}_{\mathrm{pol}}\right)$ in Table 17-3 for the NF and the ZW. The solvation free energies $\Delta\bar{\mu}$ by the point charge representation were computed as –78.9 and –29.3 kcal/mol for the ZW and the NF, respectively. It should be noted that the electronic distortion and the fluctuation energy cannot be determined within the framework of the classical representation without polarizability. It is very clear that the simulations with point charge model significantly overestimate the solvation free energies in magnitude as compared with the QM/MM-ER approach. The discrepancy between these methodologies is $\sim$16 kcal/mol for the ZW and $\sim$7 kcal/mol for the NF. As a result the classical simulations give the reaction free energy in solution as –26.9 kcal/mol. As was exhibited in Figure 17-6, the method of the energy representation with the functional used in the present application was found to give results that agree well with those obtained by the numerically exact method for various solutes. Therefore, the significant discrepancy in the free energy

change can be attributed to the artificial simplification of the electron distribution of the solute. It is obvious that the reduced set of point charges is not adequate to reproduce the solvation free energy and hence it sometimes leads to the significant errors in the free energy changes associated with chemical reactions in solution.

The origin of such discrepancy noted above was investigated in terms of the radial distribution functions (RDF) around the atoms of interest in the ZW specie. The RDFs for oxygens of water molecules around N (see Figure 17-9) of the ZW are presented in Figure 17-12. The peak position and the height of the RDF for the classical simulation agree well with those given by the QM/MM simulation. This suggests that the reduced set of fractional charges successfully reproduce the local solvation around the cationic site (NH_3-group) of ZW glycine. On the contrary, as shown in Figure 17-13, the significant disagreement between the two approaches appears in the RDFs for water oxygen around anionic site of glycine. O4 in carboxyl group has a large negative charge (–0.92) in the ZW. Obviously the peak height given by the classical simulation is erroneously emphasized as compared with the QM/MM simulation. These observations are fully consistent with the results obtained by previous QM/MM simulations where RDFs and solute–solvent interaction energies were studied for the solutes H_2O and OH^- in aqueous solution [60]. It was revealed by the simulations that the point-charge representation can faithfully realize the RDF generated by a QM/MM method for H_2O, but it fails seriously in the simulation of the

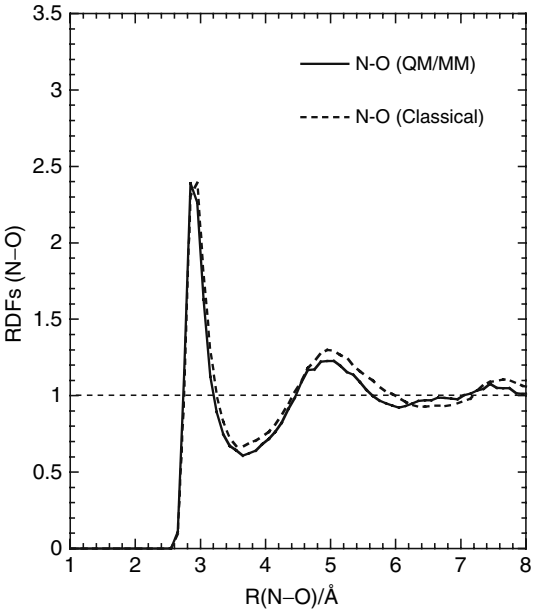

Figure 17-12. Radial distribution functions (RDFs) of the oxygen of water solvent around the nitrogen in the neutral glycine (NF). The solid line is for the solute with average electron density and the broken line is for the solute with a set of point charges

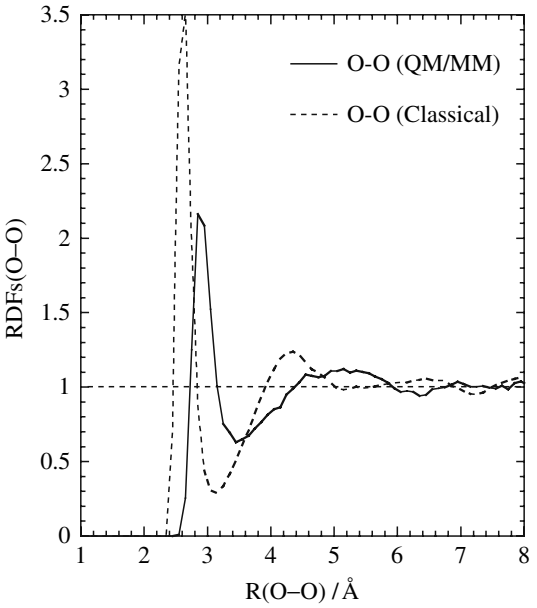

Figure 17-13. Radial distribution functions (RDFs) of the oxygen of water solvent around the oxygen in the carboxyl group in the zwitterionic glycine (ZW). Notations are synonymous with Figure 17-12

anionic molecules. This result suggests that the excess charge on the anionic system is delocalized in space and that the neglect of the charge volume effect will give rise to the significant discrepancy. The source of the error in the present calculation is common to that in the system of OH anion. The excess charge on the carboxyl group in ZW glycine flows into space, which disables the reduced set of point charges to reproduce soundly the detailed electrostatic field formed by the continuous electron density. Thus, we have attributed the discrepancy of the classical simulations to the neglect of the charge volume effect for the excess electron. The reason why the deviation in the NF is much smaller than in the ZW is, of course, that the NF does not undergo significant charge polarization.

REFERENCES

1. Berne BJ, Ciccotti G, Coker DF (eds) (1998) Classical and quantum dynamics in condensed phase simulations, World Scientific, Singapore
2. Szabo A, Ostlund NS (1982) Modern quantum chemistry, Macmillan, New York
3. Parr RG, Yang W (1989) Density-functional theory of atoms and molecules, Oxford University Press, Oxford
4. Kohn W, Sham L (1965) Phys Rev 140:A1133
5. Car R, Parrinello M (1985) Phys Rev Lett 55:2471

6. Gao J, Thompson MA (eds) (1998) Combined quantum mechanical and molecular mechanical methods, American Chemical Society, Washington DC
7. Wu SY, Jayanthi CS (2002) Phys Rep 358:1
8. Yang W (1991) Phys Rev Lett 66:1438
9. Prodan E, Kohn W (2005) PNAS 102:11635
10. Zwanzig RW (1954) J Chem Phys 22:1420
11. Chandler D, Andersen HC (1972) J Chem Phys 57:1930
12. Hirata F, Rossky PJ (1981) Chem Phys Lett 83:329
13. Hansen JP, McDonald IR (1986) Theory of simple liquids, 2nd edn. Academic Press, London
14. Matubayasi N, Nakahara M (2000) J Chem Phys 113:6070
15. Matubayasi N, Nakahara M (2002) J Chem Phys 117:3605; erratum (2003) J Chem Phys 118:2446
16. Matubayasi N, Nakahara M (2003) J Chem Phys 119:9686
17. Tomasi J, Persico M (1994) Chem Rev 94:2027
18. Ten-no S, Hirata F, Kato S (1994) J Chem Phys 110:7443
19. Takahashi H, Matubayasi N, Nakahara M, Nitta T (2004) J Chem Phys 121:3989
20. Beck TL (2000) Rev Mod Phys 72:1041
21. Hirose K, Ono T, Fujimoto Y, Tsukamoto S (2005) First-principles calculations in real-space formalism, Imperial College Press, London
22. Thomas LH (1927) Proc Camb Phil Soc 23:542
23. Fermi E (1927) Rend. Accad. Lincei, 6:602
24. Hohenberg P, Kohn W (1964) Phys Rev B 136:864
25. Slater JC (1951) Phys Rev 81:385
26. Dirac PAM (1930) Proc Camb Phil Soc 26:376
27. Lee C, Yang W, Parr RG (1988) Phys Rev B 37:785
28. Colle R, Salvetti O (1975) Theor Chim Acta 37:329
29. Kleinman L, Bylander DM (1982) Phys Rev Lett 48:1425
30. Chelikowsky JR, Troullier N, Saad Y (1994) Phys Rev Lett 72:1240
31. Chelikowsky JR, Troullier N, Wu K, Saad Y (1994) Phys Rev B 50:11355
32. Jing X, Troullier N, Dean D, Binggeli N, Chelikowsky JR, Wu K, Saad Y (1994) Phys Rev B 50:12234
33. Barnett RN, Landman U (1993) Phys Rev B 48:2081
34. Becke AD (1988) J Chem Phys 88:2547
35. Ono T, Hirose K (1999) Phys Rev Lett 82:5016
36. Dunning TH Jr (1989) J Chem Phys 90:1007
37. Becke AD (1988) Phys Rev A 38:3098
38. Hori T, Takahashi H, Nitta T (2005) J Theor Comp Chem 4:867
39. Ruiz-Lopez MF (ed) (2003) Combined QM/MM calculations in chemistry and biochemistry. J Mol Struct (THEOCHEM) 632: special issue
40. Takahashi H, Hori T, Hashimoto H, Nitta T (2001) J Comp Chem 22:1252
41. Takahashi H, Hori T, Wakabayashi T, Nitta T (2001) J Phys Chem A 105:4351
42. Allen MP, Tildesley DJ (1987) Computer simulation of liquids, Oxford University Press, Oxford
43. Frenkel D, Smit B (2002) Understanding molecular simulation, from algorithms to applications, 2nd edn. Academic Press, London
44. Beutler TC, Mark AE, van Schaik RC, Gerber PR, van Gunsteren WF (1994) Chem Phys Lett 222:529
45. Resat H, Mezei M (1994) J Chem Phys 101:6126
46. Zacharias M, Straatsma TP, McCammon JA (1994) J Chem Phys 100:9025
47. Lu N, Singh JK, Kofke DA (2003) J Chem Phys 118:2977

48. Shirts MR, Pande VS (2005) J Chem Phys 122:144107
49. Matubayasi N, Reed LH, Levy RM (1994) J Phys Chem 98:10640
50. Singer SJ, Chandler D (1985) Mol Phys 55:621
51. Kovalenko A, Hirata F (1999) J Chem Phys 110:10095
52. Kast SM (2001) Phys Chem Chem Phys 3:5087
53. Freedman H, Truong TN (2003) Chem Phys Lett 381:362
54. Freedman H, Truong TN (2004) J Chem Phys 121:12447
55. Balbuena PB, Johnston KP, Rossky PJ (1995) J Phys Chem 99:1554
56. Balbuena PB, Johnston KP, Rossky PJ (1996) J Phys Chem 100:2706
57. Matubayasi N, Liang KK, Nakahara M (2006) J Chem Phys 124:154908
58. Takahashi H, Hori T, Wakabayashi T, Nitta T (2000) Chem Lett 3:222
59. Takahashi H, Hashimoto H, Nitta T (2003) J Chem Phys 119:7964
60. Takahashi H, Takei S, Hori T, Nitta T (2003) J Mol Struct (THEOCHEM), 632:185
61. Hori T, Takahashi H, Nitta T (2003) J Chem Phys 119:8492
62. Hori T, Takahashi H, Nitta T (2003) J Comput Chem 24:209
63. Takahashi H, Kawashima Y, Nitta T, Matubayasi N (2005) J Chem Phys 123:124504
64. Takahashi H, Satou W, Hori T, Nitta T. (2005) J Chem Phys 122:044504
65. Hori T, Takahashi H, Nakano M, Nitta T, Yang W (2005) Chem Phys Lett 419:240
66. Hori T, Takahashi H, Furukawa S, Nakano M, Yang W (2007) J Phys Chem B 111:581
67. Jorgensen WL, Chandrasekhar J, Madura JD, Impey RW, Klein ML (1983) J Chem Phys 79:926
68. Ewald P (1921) Ann Phys 64:253
69. Andzelm J, Kölmel C, Klamt A (1995) J Chem Phys 103:9312
70. Tortonda FR, Pascual-Ahuir JL, Silla E, Tuñón I, Ramírez F (1998) J Chem Phys 109:592
71. Nagaoka M, Okuyama-Yoshida N, Yamabe T (1998) J Phys Chem A 102:8202
72. Tuñón I, Silla E, Ruiz-López MF (2000) Chem Phys Lett 321:433
73. Tuñón I, Silla E, Millot C, Martins-Costa MTC, Ruiz-López MF(1998) J Phys Chem A 102:8673
74. Gaffney JS, Pierce RC, Friedman L (1977) J Am Chem Soc 99:4293
75. Haberfield P (1980) J Chem Edu 57:346
76. Wada G, Tamura E, Okina M, Nakamura M (1982) Bull Chem Soc Jpn 55:3064
77. Frisch MJ et al (2002) Gaussian 03, Revision B.05, Gaussian, Inc., Pittsburgh PA

CHAPTER 18

QUANTIFYING SOLVATION EFFECTS ON PEPTIDE CONFORMATIONS: A QM/MM REPLICA EXCHANGE STUDY

GUSTAVO M. SEABRA[1], ROSS C. WALKER[2], AND ADRIAN E. ROITBERG[1]

[1] *Quantum Theory Project and Department of Chemistry, University of Florida, 2234 New Physics Building #92, P.O. Box 118435, Gainesville, FL 32611-8435, USA, e-mail: roitberg@ufl.edu*

[2] *San Diego Supercomputer Center, University of California, San Diego, 9500 Gilman Drive #0505, La Jolla, CA 92093-0505, USA*

Abstract: We present replica exchange molecular dynamics calculations of the conformational space of alanine dipeptide, both in the gas phase and in water using both a classical force field potential and several commonly used semi-empirical QM/MM Hamiltonians implemented within the latest version of the AMBER software suite. We present results comparing the performance of each method with experimental data for Ramachandran conformational distributions, NMR *J* coupling estimates and radial distribution functions for the peptide–solvent interactions

18.1. INTRODUCTION

Small peptides are often used as model systems in investigations of conformational properties of biological molecules. For example, recent experimental results suggest that the backbone preferences in proteins are already present in blocked aminoacids, with obvious important consequences to protein folding and dynamics [1,2]. Studying the conformational properties of small peptides is an outstanding experimental and theoretical challenge, since such small and flexible systems are often better described as ensembles of fast interconverting conformers [3]. Interactions with the environment are very important, and results from gas-phase experiments and calculations can seldom be extrapolated to the more biologically relevant condensed phase.

From a theoretical perspective, general force fields, being designed to reproduce the properties of large biological systems, might have difficulties in the simulation of small molecules. On the other hand, high-level ab initio calculations are possible only for a small number of conformations in vacuum or in the presence of implicit solvent, and prohibitively expensive for extended molecular dynamics or explicit

S. Canuto (ed.), Solvation Effects on Molecules and Biomolecules, 507–518.
DOI 10.1007/978-1-4020-8270-2_18,

solvent simulations. One more affordable alternative resides in the application of hybrid quantum mechanics/molecular mechanics (QM/MM) methods in which a small part of the system (for example, the peptide) is treated quantum mechanically while the much larger environment (solvent) is explicitly considered at the molecular mechanics level. Still, the extended conformational sampling made necessary by the molecular flexibility of the peptide restricts this methodology to the use of fast semi-empirical methods, which require calibration and validation.

One such small molecule, alanine dipeptide (Ace-Ala-NMe, AD, Figure 18-1) has often been used as a model system in studies of backbone conformational equilibrium in proteins. It is composed of an alanine unit blocked by an acetyl group at the N-terminus (Ace) and a *N*-methylamide group (NMe) at the C-terminus. A number of experimental [1,3,4,5,6,7] and theoretical [8,9,10,11,12,13,14,15,16,17,18, 19,20,21,22,23,24,25], studies indicate that the potential energy surface for AD in vacuum and in solution are considerably different: while in the gas phase the global minimum is believed to be a C7eq structure ($\phi \sim -83^\circ$, $\psi \sim 73^\circ$) [16], it has only recently been shown that interaction with water favors the polyproline-II (PP_{II}, $\phi \sim -75^\circ$, $\psi \sim 150^\circ$) conformation [3,7].

AD has also been used previously to investigate the performance of the SCC-DFTB (self-consistent field, density functional tight binding) method both in gas phase [13] and in solution [15]. In the present work we use alanine dipeptide as a model to investigate the performance of the widely used semi-empirical method PM3 [26,27], as well as the effect of two different corrections to the PM3 energy function: the peptide correction (PC), which adds an empirical force field correction term to improve the description of planarity in peptide bonds and the addition of the pairwise distance-directed Gaussian (PDDG) function [28], which differentiates between a wide range of functional groups by the addition of four new parameters per atom. These methods will be referred to in the text as PM3, PM3PC and PDDG/PM3.

We applied replica exchange molecular dynamics (REMD) calculations for conformational sampling of the AD in explicit water, where the AD is treated quantum mechanically and the water molecules classically, using the TIP3P [29] model. For comparison purposes, the same calculation is done where the AD is treated by a classical force field, using our recently developed AMBER ff99SB [30] parameters.

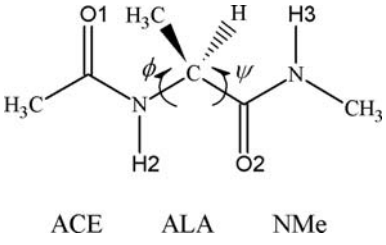

Figure 18-1. Schematic of alanine dipeptide showing the dihedral angles ϕ and ψ and the numbering used in the radial distribution functions of Figure 18-5

We compute free energy surfaces in the (ϕ,ψ) space, $^3J(H_C,H_N)$ dipolar couplings and radial distribution functions (RDF) which show that (1) PM3 is incapable of reproducing the conformational distribution of alanine dipeptide; (2) the peptide correction does not improve the results; (3) the addition of the PDDG function to PM3 can noticeably improve the energetics and (4) none of the QM methods can reproduce the experiment better than the classical ff99SB force field.

18.2. THEORY

18.2.1. Hybrid Quantum Mechanics–Molecular Mechanics (QM/MM)

In a QM/MM calculation [31,32], the system is partitioned into two regions: a QM region, typically consisting of a relatively small number of atoms relevant for the specific process being studied, and a MM region with all the remaining atoms. This scheme has been recently implemented in the Amber Molecular Dynamics package with support for various semi-empirical Hamiltonians [33,34]. The total Hamiltonian ($\hat{H}$) for such a system is written as

$$\hat{H} = \hat{H}^{\mathrm{QM}} + \hat{H}^{\mathrm{MM}} + \hat{H}^{\mathrm{QM/MM}}, \tag{18-1}$$

where $\hat{H}^{\mathrm{QM}}$ and $\hat{H}^{\mathrm{MM}}$ are the Hamiltonians for the QM and MM parts of the system, and are calculated using either the QM method chosen or the usual force field equations, respectively. The remaining term, $\hat{H}^{\mathrm{QM/MM}}$, describes the interaction between the QM and MM parts:

$$\hat{H}^{\mathrm{QM/MM}} = \hat{H}^{\mathrm{QM/MM}}_{\mathrm{vdW}} + \hat{H}^{\mathrm{QM/MM}}_{\mathrm{elect}} + \hat{H}^{\mathrm{QM/MM}}_{\mathrm{bonds}}. \tag{18-2}$$

The first term on the right hand side of Eq. (18-2) represents the van der Waals interactions between QM and MM atoms and is described classically using the same Lennard-Jones 6–12 potential used in the classical AMBER force fields:

$$E^{\mathrm{QM/MM}}_{\mathrm{vdW}} = \sum_{\alpha}^{\mathrm{QM}} \sum_{A}^{\mathrm{MM}} \left[\frac{A_{\alpha A}}{R^{12}_{\alpha A}} - \frac{B_{\alpha A}}{R^{6}_{\alpha A}} \right]. \tag{18-3}$$

It has been shown that the use of the MM parameters in this interaction does not introduce significant errors in the calculation [35].

The second term on the right hand side of Eq. (18-2) accounts for the electrostatic interaction between classical and quantum zones, and depends on the specifics of the QM implementation.

The final term in Eq. (18-2) is necessary only to describe covalent bonds that cross the boundaries of the QM and MM subsystems. The treatment of such bonds is still the topic of active research and, since the system of study used in this work does not involve bonds that cross the QM/MM boundary, it will not be discussed here. For further discussion the reader is referred to the following references [33,34,36,37,38,39].

18.2.2. Replica Exchange Molecular Dynamics

A detailed description of the replica exchange molecular dynamics algorithm (REMD) can be found in the papers of Sugita and Okamoto [40,41]. In REMD, N non-interacting copies (replicas) of a system are simulated at N different thermostat target temperatures (one each). Regular molecular dynamics is run simultaneously at each target temperature and periodically an exchange of conformation between two adjacent temperatures is attempted. Consider replica i at temperature T_n and replica j at temperature T_m are attempting to exchange; the following satisfies the detailed balance condition:

$$P_n(i)P_m(j)\rho(i, n \rightarrow j, m) = P_m(i)P_n(j)\rho(j, m \rightarrow i, n). \tag{18-4}$$

Here $\rho(i \rightarrow j)$ is the transition probability between two states i and j and $P_n(i)$ is the population of state i at temperature n (in REMD assumed Boltzmann). If the Metropolis criterion is applied, the exchange probability is obtained as

$$\rho = \min\left(1, \exp\left\{(\beta_m - \beta_n)\left[E\left(q^{[i]}\right) - E\left(q^{[j]}\right)\right]\right\}\right) \tag{18-5}$$

where positions,momenta and temperature of one replica are denoted as $\{q[i], p[i], T_n\}$, $i, n = 1, ..., N$, $\beta = 1/k_B T$ and $E(q^{[i]})$ is the potential energy of structure i. If the exchange between two replicas is accepted, the thermostat target temperatures of the two replicas are swapped and the velocities are rescaled to the new temperatures by multiplying all the old velocities by the square root of new temperature to old temperature ratio [41]:

$$v_{\text{new}} = v_{\text{old}}\sqrt{\frac{T_{\text{new}}}{T_{\text{old}}}}. \tag{18-6}$$

Upon completion of a simulation, data are collected from the appropriate temperature and compiled into an ensemble average. The weighted histogram analysis method (WHAM) [42,43,44] can also be applied to collect information from all replicas in order to obtain optimal ensemble averages. REMD accelerates convergence against regular molecular dynamics since the system is able to visit high temperature replicas and hence traverse energy barriers easier than at lower temperatures.

18.3. COMPUTATIONAL METHOD

The protocol used for the simulations was as follows. Temperature and pressure were controlled using the Berendsen weak coupling algorithm [45] with a coupling time constant of 1 ps for both temperature and pressure. All long-range interactions were calculated using the particle-mesh Ewald (PME) approach [46,47], including the newly developed QM/MM-compatible PME implementation of Walker et al. [34]. The SHAKE algorithm [48,49] was used to constrain bonds containing hydrogen in

both the QM and MM regions, allowing a time step of 2 fs to be used. The QM/MM calculations used PM3, PDDG/PM3 and PM3 with peptide correction (PM3PC), and the TIP3P [29] model for the water molecules. The van der Waals parameters from the classical force field AMBER ff99SB [30] were used for the quantum atoms in the interaction with the classical region. For comparison purposes, similar calculations were performed with the AD treated classically using the AMBER force field ff99SB [30]. All simulations were performed using a pre-release development version of AMBER v10.0.

18.3.1. System Preparation

The system was prepared using the LEaP program (part of the AMBER package). The AD solute was placed in a box with 929 water molecules for a total of 2809 atoms, with periodic boundary conditions. After initial MM minimization, the system was heated at constant volume to 300 K over 100 ps using a classical (ff99SB) potential on all atoms. The system was then equilibrated at 300 K for 1 ns using the same ff99SB potential in a constant pressure environment with a pressure target of 1 atm. The structure at the end of this classical equilibration was used as the starting point for each QM simulation method. The system was further equilibrated for 100 ps, for each method independently, at 300 K and 1 atm pressure, using a QM treatment for the alanine dipeptide. Once the necessary equilibration had been completed each respective method was run for a total of 12 ns per temperature of replica exchange.

18.3.2. REMD of Alanine Dipeptide in Explicit Water

Thirty-two replicas were used, and exchanges were attempted every 0.2 ps (100 MD steps). The temperatures (in K) were, respectively, 292.9, 300.0, 307.3, 314.8, 322.4, 330.3, 338.3, 346.6, 355.0, 363.6, 372.5, 381.5, 390.8, 400.3, 410.1, 420.1, 430.3, 440.8, 451.5, 462.5, 473.7, 485.2, 497.1, 509.2, 521.5, 534.2, 547.2, 560.6, 574.2, 588.2, 602.4, and 616.8, chosen to provide an exchange acceptance ratio of approximately 15%. The results shown here represent the final 10 ns from the total of 12 ns of REMD simulations.

18.3.3. Molecular Dynamics of Alanine Dipeptide in Vacuum

The alanine dipeptide in vacuum was created with the LEaP program. After initial minimization, the system was relaxed for 100 ps at 300.0 K using the respective QM (or MM) method, followed by 9 ns of conventional MD at 300.0 K.

18.3.4. Free Energy Surfaces

The free energy surfaces for AD at 300 K were obtained by calculating the (normalized) probability P of finding the AD in a conformation at a particular region in (ϕ, ψ)-space from the REMD/MD trajectories, then converting this number to free

energies by $G = -RT \ln(P)$, where G is the Gibbs free energy, R is the general gas constant and T is the temperature (300 K).

18.3.5. Dipolar Couplings

Dipolar couplings for each structure were calculated by following the Karplus equation:

$$^3J(H_\alpha, H_N) = A\cos^2(\phi - 60) + B\cos(\phi - 60) + C, \quad (18\text{-}7)$$

where ϕ is the angle shown in Figure 18-1, and the parameters A, B and C were taken from five different sources in the literature [50,51,52,53,54], and the results averaged.

18.4. RESULTS AND DISCUSSIONS

18.4.1. Molecular Dynamics of Alanine Dipeptide in Vacuum

It is currently accepted that there exist at least 6 minima in the energy surface of AD in vacuum, denoted by C7eq, C5, C7ax, α_R, β_L and α_L, ordered from the most to the least stable structure according to ab initio and DFT calculations [10,13,16,23,25,55,56]. Although the relative energies change slightly, the overall ordering does not depend on the level of theory. Table 18-1 shows the dihedral angles and relative energies for these structures, reproduced from Vargas et al. [23]. The geometries were optimized at the MP2/aug-cc-pVTZ level, and the relative energies extrapolated to the complete basis set limit from a series of single-point MP2/aug-cc-pVxZ calculations (x = D,T,Q) [23].

The free energy surfaces obtained from the MD simulations in vacuum are displayed in Figure 18-2. The four lowest energy minima obtained by Vargas et al. [23] are also indicated for reference as filled circles. Note that the ab initio calculations only include enthalpy, while the results presented in Figure 18-2 represent

Table 18-1. (ϕ,ψ) angles and relative energies for the different minima of alanine dipeptide, from Vargas et al. [23]. Geometries were optimized at the MP2/aug-cc-pVDZ level and energies extrapolated to MP2/CBS limit. Angles are in degrees and energy differences in kcal/mol relative to the $C7_{eq}$ minimum

Conformer	ϕ	ψ	ΔE
$C7_{eq}$	−82.6	75.8	0.00
C_5	−161.1	155.5	1.39
$C7_{ax}$	73.7	−53.7	2.66
$\delta_R(\beta_2)$	−82.3	−9.5	3.35
α_L	63.8	30.2	5.19
δ_L ($\alpha\prime$)	−164.7	−38.3	6.80

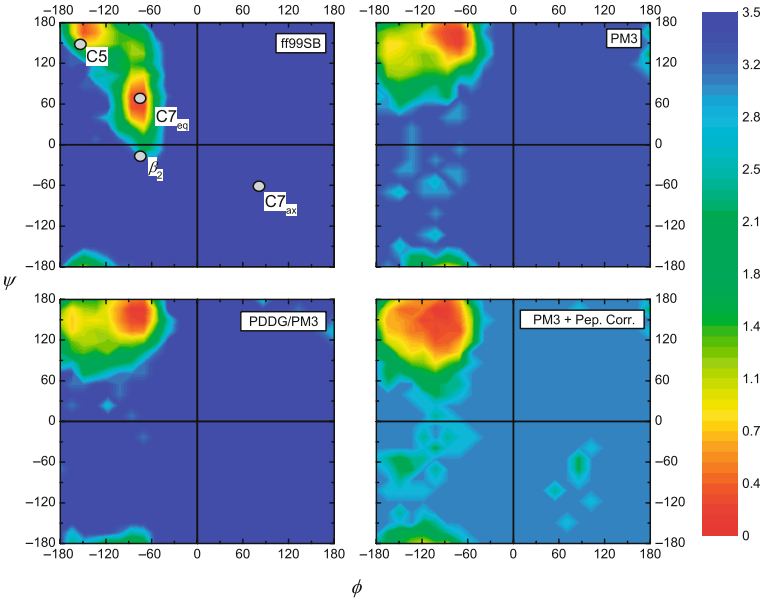

Figure 18-2. Free energy surfaces of alanine dipeptide in vacuum. Relative energies are in kcal/mol

free energies generated from the replica exchange molecular dynamics trajectories. The free energy surface from the classical calculation reproduces the position of the global minimum well and also shows a second minimum close to the C5 position as predicted by the MP2 calculations. This force field was derived from the ff94 force field [57] modified specifically to reproduce relative energy differences in alanine tetrapeptide from high-level QM calculations and so it is comforting to find it does well for our alanine dipeptide test system. Contrary to the close agreement with high-level ab initio data seen for the classical force field none of the semi-empirical methods were capable of locating the $C7_{eq}$ global minimum. This deficiency has been shown before for the case of PM3 [13]. In vacuum, PDDG/PM3 closely follows the PM3 free energy surface suffering from the same issue of a missing $C7_{eq}$ minimum. This behavior is a manifestation of the fact that, as noted by Repasky et al., the parameter sets of PDDG and PM3 are very similar, and some issues that derive from the NDDO approximations used in PM3 are maintained in PDDG, noticeably conformer energetics [28]. The addition of the peptide correction to PM3 increases the flexibility of the backbone as compared to PM3 and PDDG/PM3, as indicated by the wider basin in the free energy surface, but it is still not sufficient to recover from the PM3 limitations. The relative success of the classical force field, the sole method used here that explicitly includes peptides in the parameterization, in reproducing features of the high-level surface stresses the importance of an appropriate training set for the parameterization of the methods.

18.4.2. Replica Exchange Molecular Dynamics of Alanine Dipeptide in Explicit Water

Experimental evidence [1,2,3,4,5,7,58] indicates that interaction with the solvent molecules stabilize a polyproline-II (PP_{II}, $\phi \sim -75^{\circ}$, $\psi \sim 150^{\circ}$)-type structure. The free energy surfaces for AD in explicit water at 300 K calculated from the REMD trajectories are shown in Figure 18-3. Only the ff99SB and PDDG/PM3 surfaces show a global minimum on the PP_{II} region. Although there seems to be a minimum present around the PP_{II} region, in PM3 and PM3PC it is not the global minimum. This was also pointed out by Hu et al. [15] in a previous study. Notice that the background color, representing the highest value of the free energy, is a direct function of the number of snapshots observed and does not have a physical meaning in the context of these results.

A more direct comparison with experimental data can be achieved by calculating the average dipolar couplings from the MD ensemble. Figure 18-4 shows the dipolar couplings calculated for the alanine dipeptide as a function of simulation time using the Karplus relation from Eq. (18-7). Also shown is the experimental result of 6.06 Hz obtained for the AD molecule by Avbelj et al. at pH 4.9 [1]. The low experimental value for $^{3}J(H_{\alpha},H_{N})$ is an indication of high population of basins with ϕ angle around –75°, as present in the PP_{II} structure. The plot shows that, in the timescale of the simulation, all calculated dipolar couplings have converged, a signal that sufficient sampling has been achieved. However, none of the calculations

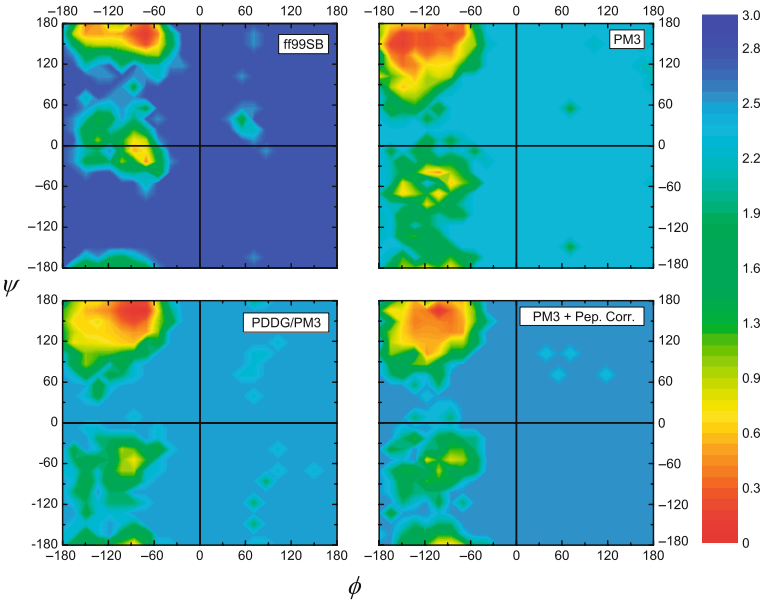

Figure 18-3. Free energy surfaces of alanine dipeptide in water. Relative energies are in kcal/mol

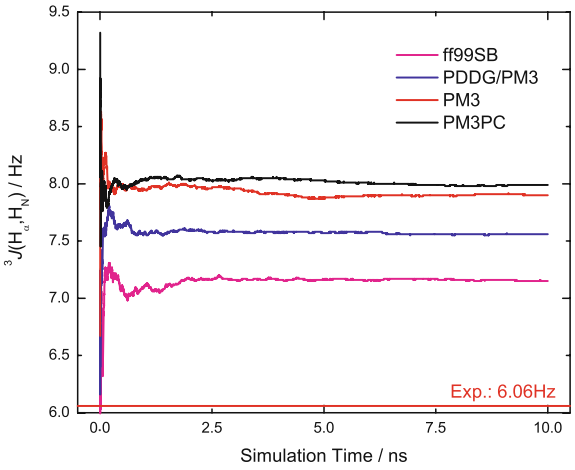

Figure 18-4. Dipolar couplings calculated for alanine dipeptide in water

were able to reproduce the experimental value, indicating an experimental minimum significantly deeper than suggested by the simulations. Indeed, a combination of experiment and molecular dynamics calculations has suggested that, for the case of the alanine zwitterion in water, the relative population of the PP_{II} basin should be higher than 99% [3]. It is interesting to note, however, that none of semi-empirical QM results is closer to experiment than the classical force field. The PDDG correction significantly improves the PM3 prediction while the peptide correction apparently has no effect in improving the prediction of dipolar couplings, in par with the results for the free energy surfaces.

18.4.3. Radial Distribution Functions

The radial distribution functions in Figure 18-5 show the distribution of water molecules around the carbonyl oxygens and amide hydrogens, as obtained from the REMD trajectories. All methods show a clear hydrogen bond between the carbonyl oxygen and water. All the QM Hamiltonians predict the H-bond at about the same distance. This interaction is stronger, however, in the classical force field, bringing the water molecule slightly closer (1.85 Å for ff99SB versus ~1.95 Å for QM methods). It has been suggested that the PP_{II} structure is favored by water molecules bridging the one carbonyl oxygen to amide hydrogen of a close residue [7]. In this case, two distinct bridges are possible: a "short" one, linking H2 to O2, and a longer one bridging O1 and H3. The classical force field is the only calculation that predicts a clear persistent H-bond between a water molecule and the amide hydrogen, which peaks at 2.05 Å for the H2 and with a broader peak between 2.15 and 2.25 for H3. The presence of this hydrogen bond may explain the higher success of the force field in reproducing the experimental results.

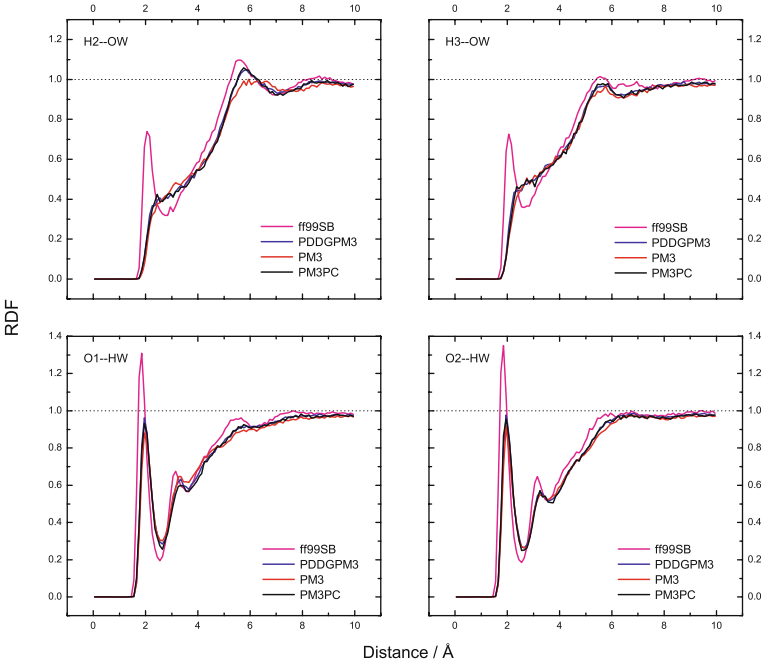

Figure 18-5. Radial distribution functions showing the distribution of water molecules around the alanine dipeptide

18.5. CONCLUSIONS

This chapter highlighted the use of replica exchange molecular dynamics calculations for the investigation of the performance of the PM3, PDDG/PM3 and PM3PC Hamiltonians as applied for the conformational equilibrium of alanine dipeptide in the gas phase and water solution, a convenient model system for the study of biological molecules.

The results presented here stress the importance of the training set used in the parameterization of the methods. The semi-empirical Hamiltonians, missing appropriate parameters in the training set, are unable to properly reproduce the conformational equilibria of the dipeptide, both in vacuum and in water. The PDDG correction to the PM3 Hamiltonian improves the description of hydrogen bonds and long-distance interactions as compared to PM3 [28], resulting in a better description of the solution structure as compared to PM3 and PM3PC. On the other hand, the peptide correction to PM3 is unable to noticeably improve the PM3 results. Being parameterized to reproduce the conformational energetics of polypeptides, the classical force field ff99SB is substantially better for these types of molecules. The results from classical calculations were closer to both high-level ab initio calculations (in the gas phase) and experiments (in water).

There is ongoing work in this group to implement and test other QM methods as well, such as the more recent RM1 [59], which is a reparameterization of the AM1 Hamiltonian [60], and PM6 [61], which involves modifications to the Hamiltonian as well as to the parameterization methods and training sets. It is expected that the newer methods should improve the QM results.

ACKNOWLEDGMENTS

The authors wish to thank the Amber developers' team for access to the development version of the Amber package. Computer resources were provided by the Large Allocations Resource Committee through grant TG-MCA05S010 to AER, the High-Performance Computing Center at the University of Florida, the San Diego Supercomputing Center and a local cluster built with a generous IBM-SUR grant. RCW also thanks SDSC Core, HPCOPS and DOE SciDAC grants.

REFERENCES

1. Avbelj F, Grdadolnik SG, Grdadolnik J, Baldwin RL (2006) Proc Natl Acad Sci U S A 103: 1272–1277.
2. Shi Z, Chen K, Liu Z, Ng A, Bracken WC, Kallenbach NR (2005) Proc Natl Acad Sci U S A 102:17964–17968.
3. Graf J, Nguyen PH, Stock G, Schwalbe H (2007) J Am Chem Soc 129:1179–1189.
4. Kang YK (2006) J Phys Chem B 110:21338-21348.
5. Kim YS, Wang J, Hochstrasser RM (2005) J Phys Chem B 109:7511–7521.
6. Lavrich RJ, Plusquellic DF, Suenram RD, Fraser GT, Walker ARH, Tubergen MJ (2003) J Chem Phys 118:1253–1265.
7. Poon CD, Samulski ET, Weise CF, Weisshaar JC (2000) J Am Chem Soc 122:5642–5643.
8. Smith PE (1999) J Chem Phys 111:5568-5579.
9. Aleman C, Leon S (2000) J Mol Struct THEOCHEM 505:211–219.
10. Apostolakis J, Ferrara P, Caflisch A (1999) J Chem Phys 110:2099–2108.
11. Beachy MD, Chasman D, Murphy RB, Halgren TA, Friesner RA (1997) J Am Chem Soc 119: 5908–5920.
12. Boresch S, Willensdorfer M, Steinhauser O (2004) J Chem Phys 120:3333–3347.
13. Cui Q, Elstner M, Kaxiras E, Frauenheim T, Karplus M (2001) J Phys Chem B 105:569–585.
14. Elstner M, Jalkanen KJ, Knapp-Mohammady M, Frauenheim T, Suhai S (2001) Chem Phys 263:203–219.
15. Han W-G, Jalkanen KJ, Elstner M, Suhai S (1998) J Phys Chem B 102:2587–2602.
16. Hu H, Elstner M, Hermans J (2003) Proteins: Struct, Funct, Genet 50:451–463.
17. Improta R, Barone V (2004) J Comput Chem 25:1333–1341.
18. Iwaoka M, Okada M, Tomoda S (2002) J Mol Struct THEOCHEM 586:111–124.
19. Kalko SG, Guardia E, Padro JA (1999) J Phys Chem B 103:3935–3941.
20. Liu P, Kim B, Friesner RA, Berne BJ (2005) Proc Natl Acad Sci U S A 13749–13754.
21. Marrone TJ, Gilson MK, McCammon JA (1996) J Phys Chem 100:1439–1441.
22. Tobias DJ, Brooks CL (1992) J Chem Phys 96:3864–3870.
23. Vargas R, Garza J, Hay BP, Dixon DA (2002) J Phys Chem A 106:3213–3218.

24. Wei D, Guo H, Salahub DR (2001) Phys Rev E: Stat, Nonlin, Soft Matter Phys 64:011907/011901–011907/011904.
25. Wang Z-X, Duan Y (2004) J Comput Chem 25:1699–1716.
26. Stewart JJP (1989) J Comput Chem 10:209–220.
27. Stewart JJP (1989) J Comput Chem 10:221–264.
28. Repasky MP, Chandrasekhar J, Jorgensen WL (2002) J Comput Chem 23:1601–1622.
29. Jorgensen WL, Chandrasekhar J, Madura JD, Impey RW, Klein ML (1983) J Chem Phys 79:926–935.
30. Hornak V, Abel R, Okur A, Strockbine B, Roitberg A, Simmerling C (2006) Proteins: Struct, Funct, Bioinform 65:712–725.
31. Warshel A, Levitt M (1976) J Mol Biol 103:227–249.
32. Field MJ, Bash PA, Karplus M (1990) J Comput Chem 11:700–733.
33. Seabra GM, Walker RC, Elstner M, Case DA, Roitberg AE (2007) J Phys Chem B 111:5655–5664.
34. Walker RC, Crowley MF, Case DA (2008) J Comput Chem 29:1019–1031.
35. Riccardi D, Li G, Cui Q (2004) J Phys Chem B 108:6467–6478.
36. Konig PH, Hoffmann M, Frauenheim T, Cui Q (2005) J Phys Chem B 109:9082–9095.
37. Reuter N, Dejaegere A, Maigret B, Karplus M (2000) J Phys Chem A 104:1720–1735.
38. Zhang YK, Lee TS, Yang WT (1999) J Chem Phys 110:46–54.
39. Gao JL, Amara P, Alhambra C, Field MJ (1998) J Phys Chem A 102:4714–4721.
40. Mitsutake A, Sugita Y, Okamoto Y (2001) Biopolymers 60:96–123.
41. Sugita Y, Okamoto Y (1999) Chemical Physics Letters 314:141–151.
42. Kumar S, Rosenberg JM, Bouzida D, Swendsen RH, Kollman PA (1992) Journal of Computational Chemistry 13:1101–1021.
43. Gallicchio E, Andrec M, Felts AK, Levy RM (2005) Journal of Physical Chemistry B 109:6722–6731.
44. Chodera JD, Swope WC, Pitera JW, Seok C, Dill KA (2007) Journal of Chemical Theory and Computation 3:26–41.
45. Berendsen HJC, Postma JPM, van Gunsteren WF, DiNola A, Haak JR (1984) J Chem Phys 81:3684–3690.
46. Darden T, York D, Pedersen L (1993) J Chem Phys 98:10089–10092.
47. Essmann U, Perera L, Berkowitz ML, Darden T, Lee H, Pedersen LG (1995) J Chem Phys 103:8577–8593.
48. Ryckaert J-P, Ciccotti G, Berendsen HJC (1977) J Comput Phys 23:327–341.
49. Miyamoto S, Kollman PA (1992) J Comput Chem 13:952–962.
50. Wang AC, Bax A (1996) J Am Chem Soc 118:2483–2494.
51. Pardi A, Billeter M, Wuthrich K (1984) J Mol Biol 180:741–751.
52. Ludvigsen S, Andersen KV, Poulsen FM (1991) J Mol Biol 217:731–736.
53. Vuister GW, Bax A (1993) J Am Chem Soc 115:7772–7777.
54. Schmidt JM, Blümel M, Löhr F, Rüterjans H (1999) Journal of Biomolecular NMR 14:1–12.
55. Perczel A, Farkas O, Jakli I, Topol IA, Csizmadia IG (2003) J Comput Chem 24:1026–1042.
56. Philipp DM, Friesner RA (1999) J Comput Chem 20:1468–1494.
57. Cornell WD, Cieplak P, Bayly CI, Gould IR, Merz KM, Ferguson DM, Spellmeyer DC, Fox T, Caldwell JW, Kollman PA (1995) J Am Chem Soc 117:5179–5197.
58. Schweitzer-Stenner R, Measey TJ (2007) PNAS 6649–6654.
59. Rocha GB, Freire RO, Simas AM, Stewart JJP (2006) J Comput Chem 27:1101–1111.
60. Dewar MJS, Zoebisch EG, Healy EF, Stewart JJP (1985) J Am Chem Soc 107:3902–3909.
61. Stewart J (2007) J Mol Model 13:1173–1213.

Index

A

Ab initio molecular dynamics (AIMD), 41, 92
Absorption spectra, 39, 135, 136, 149, 155, 176, 178, 180, 185, 435, 447, 448, 449
  de-excitation pathways in acrolein, 148
Ace-Lala-NME, 388, 389, 391
Acetone, dipole moment with iteration step, 181
Acetonitrile, 76, 85, 118, 119
Acrolein, ground and excited states, 148
Adsorption, 322, 324, 329, 333, 334, 336, 341, 343
  processes on clay mineral surfaces, 324
    cluster approach, 324
    periodic approach, 324
  structures of H_2O, HAc, Ac^-, 2,4-D and 2,4-D, 341
    interaction energies, 339, 343, 344
Alanine dipeptide model
  in gas phase, lowest energy conformation $C^{eq}{}_7$ of, 389
  surrounded by water molecules from first solvation shell, 390
Al(III), hydrated, 266
Alkaloids of pharmaceutical value, 436
Analytical algorithms, development
  to compute solvation energy derivatives, 25
Anti-Hermitian operator, 359
Apparent surface charges (ASC), 4
Applequist scheme, 42
Aqueous solution, polypeptides in, 387
  Ace-Lala-NME, 388, 391
  helix formation in ace-lala$_n$-NME peptides with n = 4–20, 391
ASEP/MD
  CI and STC of molecules in solution using, 144
  defined, 138
  fundament of, 138
  scheme of method, 139
  set of charges for potential, 139
Asymmetric solvation
  of PBQ, 237
Atom-centred basis sets (ACBS), 226, 227, 228, 230, 231
Atomic contributions, 384
Atomic fraction(s), 305
Atomic natural orbital (ANO) basis sets, 228
Atomic polarizabilities (Bohr^3)
  from various fits, 55
Atomic radii, 28, 65, 68, 106
Auto-correlation function *C(k)*
  of energy, 160, 165, 175, 185
Auxiliary function, 369
Average solvent electrostatic configuration (ASEC), 183, 184
Average solvent electrostatic potential (ASEP)
  obtained from molecular dynamics data, 138
    see also ASEP/MD
Axilrod–Teller term, 44

B

Baker–Campbell–Hausdorff expansion, 360
Band gap convergence hydrated fullerene, 177
Basis set superposition error (BSSE), 43, 49, 68, 92, 325, 388, 415, 421, 423
Benzene
  dimer, 67, 70, 71, 72, 74
    interaction of, 72
    interaction energies and derivative dimmers, 72
    structures of various, 71, 72
  partition coefficient of, 286

temperature dependence of partitioning of, 287
Benzophenone molecule, MC configuration of, 169
Binding–unbinding reaction of CO in myoglobin, 205
Blue shift, 13
Boltzmann factor(s), 76, 78, 162, 296, 470
Bonding potentials, 250
Born–Oppenheimer many-body vacuum, Hamiltonian, 351
Born–Oppenheimer molecular dynamics (BOMD), 115, 116, 125, 131

C

Caffeine
molecular structures of, 436
solvent density maps in CO_2, 439
$C^{\alpha}H\cdot\cdot O$ H-bond energy, 415
Car–Parrinello (CP) method, 224
Car–Parrinello (CP) simulations, 253
Car–Parrinello molecular dynamics (CPMD), 185
Cavitation
free energy, 89
Cavity
boundary, 40
limit conditions at, 25
definition, 27
formation, 282, 283
molecular volume, 27
Central processor (CP) time
for simulations, 248
CHARMM expression, 68
CHELPG analysis, 140, 180, 374
Chemical potential
entropic component, 290, 291
excess, 282, 293, 295, 296, 297, 298, 317, 486, 487, 488, 491, 492, 495
and Flory–Huggins model, 286
as functions of pressure, 295
ideal gas, 282
at infinite dilution for methane and propane in polystyrene, 296
and probability density, 202
of solvent and solute, 316
standard-state, 281, 282
sum of contributions from pure solute, 282
Chemical reactions
environment effects on, 1
experiment and interpretation, 25
Chemical solvent model, explicit quantum, 215
applications, examples of, 216
asymmetric salvation, 237
polarization and repulsion, coupled, 235
solute–solvent interaction(s), 232, 238, 241
model, QMSTAT, 215, 219, 241
intermolecular interactions, 215, 216, 217, 219, 223, 224, 241
parametrization and simulation protocol, 232
quantum chemical methods, 216, 218, 226, 232, 242
Classical force field(s), 41, 42, 142, 161, 162, 176, 218, 224, 232, 235, 237, 241, 457, 507, 508, 511, 513, 515, 516
Classical models, 73, 263, 323, 467
Classical solution model
vs. Flory–Huggins model, 286
coupling of center of mass one molecule, 288
effect of internal degrees of freedom, 288
effect of molecular shape and architecture, 290
Classical systems, total energy for, 355
Cluster approach, 324
time dependent, 368–369
Collapse transition
phenomenological theory, 311
CO–Mb reaction
CO–heme–histidine complex with schematic view of Mb, 205
rototranslational constraint in, 206
Complete active space second-order perturbation (CASPT2), 148, 149, 150, 233
Complete active space self-consistent field (CASSCF) method, 229
Complete active space state interaction (CASSI) method, 229, 230
Computer simulation methods, 315, 317
Conductor-like screening model (COSMO), 160, 323, 324
Conductor-polarized continuum model (CPCM), 410
Conical intersections and singlet–triplet crossing location, 143
energies in vacuum and in solution, 146
scheme, 144
"Continuum model of Nancy," *see* Self-consistent reaction field (SCRF), model
Continuum models, 2, 4, 18, 19, 23, 24, 25, 32, 33, 34, 35, 40, 41, 59, 85, 93, 104, 105,

137, 138, 139, 159, 181, 209, 217, 253, 260, 323, 374, 390, 407, 408, 410, 413, 414, 417, 418, 426, 458, 501
Core region
force acting on particle in, 263
Correlation (program), 167
CO_2 systems, theoretical investigations for, 451
Coulomb interactions, 59, 250, 252, 254, 255, 256, 257, 260, 261, 262, 263, 267, 269, 274, 356, 361, 391, 472
Coupled cluster-molecular mechanics response method (CC/MM)
effective one-electron operators, 371
function, 367
linear, 370
matrices and vectors for linear and quadratic, 371
optimization, 365, 366
symmetrizer, 371
time-dependent energy functional, 370
Coupled cluster singles and doubles (CCSD), 374
Coupled cluster wave function
time dependent, 368
Coupling
entropy, 289
polarization and repulsion, 237
distribution of coupling term, 236
energies computation, 264
positive/negative, 236

D

Dalton program package, 374
Damping, 54, 60, 61, 86, 222, 225, 233, 234
Debye times for SCW, experimental and simulated, 444
De-excitation pathways in acrolein, 148
absorption spectra, 149
emission spectra, 151
in gas phase, 152
non-radiative excited state decay, 152
geometries of minima, and minimal energy CI and STC points, 152
rdf for S_0 and S_1 states, 149
H(water)–O(acrolein), 149
O(water)–O(acrolein), 149
Degrees of freedom
classical, 201
computation, 234
effect of internal, 288
Flory–Huggins model *vs.* classical solution model, 286
of solvent, 42, 92, 137, 140, 446, 481
translational, 288
De-Mon code, 24
Density functional theory (DFT)
linear response theory, 349
many-body polarization, results, 86
QMCF MD approach, 263, 274
shortcomings, 266
Density matrix, 8, 9, 50, 62, 227, 230, 231, 392, 457, 460
Deuterium kinetic energy
time evolution of, 127, 130
DFT, *see* Density functional theory (DFT)
DFT/MM
energy functional, 356
potential, 358
DFT(X)/DPM, 14
DICE program, 121, 171
Dielectric continuum
bulk effects, 58
atom in, 40
models, 137, 138, 139, 374, 417
Dielectric depletion, 241
Dielectric effect, 387
Dielectric relaxation methods, 313
Diels–Alder reaction, 25
Dipole interaction tensor, 15, 54, 353
Dipole moment
with iteration step, acetone, 181
of water and ammonia molecule, 118, 131
of water molecule on hydrogen bonds, 120
Dipole time–correlation function, 443
Direct reaction field (DRF)
applications, 74
chemistry in solution, 89
(hyper-) polarizabilities and macroscopic properties in solution, 84
polarization in excited states of symmetric ethylenes, 74
spectra, 76
bulk effects: dielectric continuum, 58
dispersion interaction in, 47, 78, 226
electrostatic potentials: point charges, 49
implementations, 45
macroscopic and microscopic properties, 65
many-body polarization, 45, 49, 51, 59, 86
perturbation theory, 39, 43, 45, 46, 49, 63
validation, 67, 74, 92
benzene dimmer, 67, 70, 71, 72, 74
many-body interactions, 43, 73
water dimmer, 67, 68, 69, 70
Discrete polarizable method (DPM)
differences/similarities with PCM, 16

polarizable and structured environment, 7
reaction field, 15, 16, 17
See also Polarizable continuum model (PCM)
Discrete solvent models, 41, 217
Dispersion interaction (solute and solvent)
in DRF, 47, 78, 226
Distribution function for pair energy of water, 475
DRF model, 44, 67, 73, 84, 85, 86, 88
DRF/QM/MM method
working expression, 59
Dual-mode sorption theory
and pressure, 292

E

Effective potential (GSBP partitions), 386
Ehrenfest theorem, 361
Electrical and osmotic equilibria, ions in, 248
Electric field, due to induced dipole moments, 357
Electron binding energies
dependence of central water molecule on number of hydrogen bonds, 123
Electron correlation lengths in SCW, 447
Electronic contribution, 62, 353
Electronic Hamiltonian, 144, 193, 216, 219, 352
Electronic properties of hydrogen bond networks
charge fluctuations and proton transfer, 124
Born–Oppenheimer molecular dynamics, 115, 116, 124, 125, 131
dynamics of PT in phenol–water clusters, 125
proton (deuterium) transfer and fluctuations of HB network, 127
hydrogen bond network and electronic properties of water, 115
and dipole moment of water, 118
electron binding energies, 115, 116, 122, 123, 131
polarization effects and charge fluctuations, 116
dipole moment in liquid phase, 116, 117
in hydrogen bonding liquids, 116
Electrostatic component, 105
Electrostatic contribution, 220, 283
Electrostatic entropy term, 109
Electrostatic interactions
between QM/MM, 7, 117, 352, 353, 386, 390
solute–solvent energy, 108, 110, 283, 316
Electrostatic potentials
in inner region, 386
Laplace's equation, 25, 26
operator, 3
point charges, 49
direct reaction field (DRF), 44
drawbacks, 51, 186, 262, 458, 478
Mulliken population analysis, 50
Poisson's equation, 25
Emission spectra
of C153, time-resolved, 316
de-excitation pathways in acrolein, 148
time evolution of excited state and dynamics of solvent, 136
Energy
contribution(s), 42, 63, 258, 262, 329, 354, 355, 356, 384, 494
difference gradient vector, 143
solute's multipole moments, 27
for system, 335
in terms of MOs, contributions to, 62
Energy representation
average and standard error, 484
solvation free energy, comparison, 483
theory of solutions in
density-functional theory, 475
distribution functions in solution, 473
free-energy perturbation and thermodynamic integration methods, 469
method, 479
radial distribution functions and reference interaction site mode, 478
Enthalpy
electrostatic contribution, 106
of salvation, 106
thermochemical analysis of hydration of neutral solutes, 103
Entropy
coupling, 288, 289
electrostatic, 109
orientational, 288
of solvation, 104
total configurational, 284
translational, 290, 291
Environmental effects, methods to treat, 385–387
Equilibrium conditions *vs.* non-equilibrium conditions
Equilibrium solvation
and configurational space of each state, 142
Equilibrium spatial correlations, 450, 451
Ewald method, 149, 493
Ewald summation schemes, 263

Explicit quantum chemical solvent model
applications, examples of, 234
asymmetric salvation, 237, 238
polarization and repulsion, coupled, 235
solute–solvent interactions, 238, 241
model, QMSTAT
intermolecular interactions, 219
parametrization and simulation protocol, 232
quantum chemical method, 215, 216, 217, 218, 219, 220, 226, 229, 232, 237, 242
statistical mechanical method, 215, 217, 219, 231
External potential, 25, 26, 46, 50, 257, 262, 459, 486
Eyring theory, 205

F
Fast-Fourier transformation (FFT), 461
FEP *see* Free energy perturbation (FEP)
Finite field (FF), 75, 350
First-order autoregressive/ Markovian chain, 166
First-principles molecular dynamics (FPMD) method, 456
Flory–Huggins model, 286
and chemical potentials, 291
theory, 286, 287, 288, 289, 291
volume-fraction relation, 286
vs. classical solution model, 286
coupling of center of mass of one molecule to another, 288
effect of internal degrees of freedom, 288
effect of molecular shape and architecture, 290
Flory's theory, 279, 280
Fluctuation-induced chemical reaction, 115
Fluorescence band
blue shift, 151
Fluorescence spectrum, 148, 238
Flux density vector, 202
Fock matrix, 227
Fock operator, 27
Forces
acting on particle in core region, 263
acting on QM, 262
different absolute values of QM/MM, 261
on embedded particle, 259
Hessian expressions and, 142
implementation in molecular dynamics framework, 264
interaction between particular point charge and QM atom, 259
on solute molecule, 141
treatment in combination with embedding, 259
Fourier transformation(s), 359, 360, 361, 461, 463
Fractional molecule, 298
Franck–Condon (FC)
non-equilibrium situation of solvent, 154
principle, 145
solvent situation, 154
Free-energy
barriers, 203, 207, 208, 210
change, 196, 199, 200, 469, 470, 471, 472
differences, 207, 208, 234
of mixing, 285
reaction surface, 196
ensemble average, 197
provided by PMM and MD simulation, 206
singlet and quintet reaction, 206
Free energy of solvation (ΔG_{sol})
electrostatic and non-electrostatic components in water, 108, 109, 112
Free energy perturbation (FEP)
and thermodynamic integration methods, 469, 470, 471, 472, 475, 479
Frequency dependent absorption coefficients, 443

G
Gases in polymers, very dilute solutions of, 279
Gauge including atomic orbitals (GIAOs), 8
Gaussian charge distribution, 58, 60, 61, 468
Gaussian series of programs, 24
Generalized gradient approximation (GGA), 325, 465
Generalized self-consistent reaction field (GSCRF), 219
Geometries of partially solvated F_3CH and OH_2, and complex $F_3CH\cdots OH_2$, 414
GEPOL cavities, 106
Gibbs free energy
change in phases difference in salvation, 286
of formations of complexes in solution ($\square G_{sol}$), 326
interaction enthalpies for gas/liquid phases using BLYP/SVP_{+sp} approach, 327
Gibbs–Helmholtz relationship, 106, 108
Global salvation, 324, 329, 330, 332, 344
Global solvent effect, 332

Gradient-corrected approximation (GGA), 175
Grand equilibrium method
  solubility of gases in polystyrene, 295
GSBP partitions
  advantage, 387
Gss(r), 437, 438

H
Hamiltonian
  Born–Oppenheimer many-body vacuum, 351
  matrix, perturbed, 192, 193, 196, 206, 210
    on Born–Oppenheimer (BO) surface, 192, 193
  molecular electronic, 352
  operator, 5, 45, 216
    perturbational potential, 257
  solute molecular, 138, 139, 147
  of solute system, 3
  standard one-electron, 373
Hartree–Fock level
  simulation, 266
Hartree term, 357
Heat of mixing, 284, 285
Helmholtz free energy
  statistical mechanical expression for, 281
  of system, 141
  of total NVT system, 202
Heme–CO thermal dissociation, 209
Henry's law, solubility coefficient, 292
Hessian expressions
  force and, 142
  mean field approximation (MFA), 142
Highest occupied molecular orbital (HOMO), 122, 177
Humic substances (HS)
  organic functional groups as models for, 325
    binary complexes of 2,4-dichlorophenoxyacetic acid (2,4-D), 329
    binary complexes with acetic acid and acetate, 325, 326
Hybrid quantum mechanical/molecular mechanical (QM/MM) approach, 455, 457, 467
Hydrated fullerene, top of valence band of, 177
Hydration
  energetics of, 425, 426
  enthalpy and entropy, 107
    change in non-electrostatic component, 107, 110, 111
    electrostatic and non-electrostatic terms of free energy, 103, 110
    free energy, 103, 108, 109, 110
    non-electrostatic components of, 107
  of neutral solutes, enthalpy, 103
  sites, 424, 425, 426
    energetic cooperativity of imidazole, 425
  thermochemical analysis of, 103, 108
    non-electrostatic term, 103, 108, 110, 112
Hydrogen bonded solute–solvent clusters, 124
Hydrogen bonded systems, solvation of
  biologically important H-bonds, 414
    alanine and methylalanine, optimized, 416
    amino acids, 409
    dipeptide, 409
    intermolecular H-bond energies between dipeptide and formamide, 418
  CH··O and OH··O H-bonds, 409, 410
    B3LYP/6-31+G level for C7 dipeptide, 418
    B3LYP interaction energies, 413
    dipole variant, 410
    interaction energies for complexes combining F_3CH and HOH, 412
    solvation energies for $F_3CH{\cdot\cdot}OH_2$, 411
  cooperativity
    clusters, 424
    energetic cooperativity of hydration sites of imidazole, 425
    energetics of H-bonds, 410, 421
    energetics of hydration, 425, 426
    energetics of mean H-bonds, 423
    hydration sites around imidazole molecule, 424
    interaction energies between imidazole and pairs of water molecules, 428
    interaction energies between imidazole and water molecule, 427
    MP2/6-31+G** H-bond energies, 422
    one-dimensional chains, 419
    pentameric chains of HOH, H_2CO, and HFCO molecules, 420
  early applications of rudimentary SCRF, 409
    $HCOOH{\cdot\cdot}NHCH_2$ complex, orientation of H-bond within, 410
Hydrogen bond (HB)
  biologically important, 414
    amino acids, 407, 409, 415, 426
    dipeptide, 389, 390, 409, 417
  dipole moment of water molecule, 24, 115, 120, 124
  electron binding energies, 115, 116, 122, 123, 131

energies of $F_3CH{\cdot\cdot}OH_2$ and $HOH{\cdot\cdot}OH_2$ complexes, 414
of hydroxyl groups, classification, 307
networks, 115, 116, 119, 120, 121, 127, 131
chemical reactivity in, 115, 116
Hydrogen bonding
B3LYP/SVP$_{+sp}$ optimized structures of 2,4-D hydrogen-bonded complexes, 331
central water molecule on, dependence of, 122, 123
charge fluctuations in, liquids, 119
computational modeling of, 322
computed complex formation energies (in kcal/mol) for 2,4-D and 2,4-D^{--}, 330
defined, 273
and dipole moment of liquid water, 120
distribution per water molecule, 121
effects of heptane, DMSO and water on, 327
and electron binding energies, 122
electron binding energies of central water molecule on, dependence of, 123
electronic density of states on, dependence of, 123, 124
and neutral complexes, 326, 327
polarization effects and charge fluctuations, 116
Hydrogen bond networks, electronic properties
charge fluctuations and proton transfer, 124
Born–Oppenheimer molecular dynamics, 115, 116, 124, 125, 131
dynamics of PT in phenol–water clusters, 125
proton (deuterium) transfer and fluctuations of HB network, 127
hydrogen bond network and electronic properties of water, 115
and dipole moment of water, 120
electron binding energies, 115, 116
polarization effects and charge fluctuations, 115, 116, 122, 123, 131
dipole moment in liquid phase, 116, 117
in hydrogen bonding liquids, 116, 117, 119
Hydrogen bonds and solvent effects in soil processes
binary complexes of 2,4-dichlorophenoxyacetic acid (2,4-D), 329
models for humic substances, 325
binary complexes with acetic acid and acetate, 326
simulation methods,324
soil minerals and their surfaces, 333
broken clay surfaces with water and model organic molecules, 339
2,4-D with octahedral kaolinite surface, 336
goethite surface, 321, 340, 341, 343, 344
surfaces of isolated kaolinite layer, 333

I

Ideal gas, chemical potential of, 282
INDO/CIS method
transition energies calculated with, 176
Indole, fluorescence spectrum of, 238
Infinite dilution conditions, statistical mechanics in, 194
Interaction energy
achieving, 49
between imidazole and pairs of water molecules, 428
water molecule, 427
related to induced dipole moments, 353
structures of H_2O, HAc, Ac^-, 2,4-D and 2,4-D^-, adsorption, 341
Interaction tensor
dipole, 15, 353
screened dipole, 54
Interface-specific effect, 241
Intermolecular forces, theory of, 216
Internal conversion (IC), 136
Internal potential, 26
Intersystem crossing (ISC), 136, 151, 155
Intramolecular proton transfer in aqueous malonaldehyde, 209
Intrinsic reaction coordinate (IRC), 209
Ion–water interaction
degrees of freedom in scanning, 250
Isolated kaolinite layer
hydrophilic (octahedral), 334
hydrophobic (tetrahedral), 344

J

Jacobian matrix, transformation of, 373

K

Kaolinite(s)
hydrogen-bonded interactions, 333
interaction energies of single water molecule and monomolecular water layer, 337
interactions of 2,4-D with octahedral, 336
MD snapshot of water layer confined between two, 337

structural model of isolated, 334
surface interactions of, 336
two views of optimized structure of 2,4-D interacting with octahedral surface of, 338
Kohn–Sham (KS)
determinant, 359
equation(s), 9, 384, 461, 467, 492
Hamiltonian
Fourier transformation of first-order perturbed, 361
matrix elements, 461
operator, 9, 27, 357
effective, 357
modifications to, 358
Kohn–Sham density functional theory (KS-DFT), 455, 456, 459

L

Lagrangian
CC/MM, 365
CC quasienergy, 369
variational, 364
Langevin dipoles, 138
Langmuir mechanism, 293
Laplace's equation
with suitable boundary conditions, 105
LCAO approach *see* Linear combination of atomic orbitals (LCAO) approach
Legendre polynomials, 26
Lennard–Jones (LJ) potentials
nonpolar solvation dynamics of dense, 314
Linear combination of atomic orbitals (LCAO) approach, 461
Linear response theory
coupled cluster/molecular mechanics, 349
response theory, 367
density functional theory/molecular mechanics model, 349, 356, 358
response functions, 358
molecular properties, 349, 350, 364, 376, 377
quantum mechanics and molecular mechanics model, 351
solvated acetone, calculations on, 374
transition energy in gas phase, 375
Local density approximation (LDA), 175, 325, 460
Lorenz–Lorentz equation, 55, 66
Lowdin–Sokalski–Poirier distribution, 29

M

Macroscopic electric field
power series in, 66
Macroscopic polarization, 66, 67
Many-body polarization
density functional theory (DFT) results, accuracy, 57
point charge, 54, 58
Markovian chain, 166
MDC-q charges for some molecules, 52
Mean field approximation (MFA)
advantage of, 138
simplifying gradient and Hessian expressions, 142
Mean ligand residence times (MRT), 266, 269, 272, 273
Metropolis–Monte Carlo (MMC) algorithm, 231
Microsolvation, 323, 324, 329, 330, 332, 343
MidasCpp program package, 374
Minimal energy conical intersection (MECI), 143
Minimum-distance distribution function (MDDF), 163, 168
Minimum energy pathways (MEPs), 381, 382, 397, 398, 399
Mixed quantum-classical methods, 446
MM framework
approach, problems, 382
MM molecule
electric field, 4, 353
induced dipole moment for, 353
Mode coupling theory, 314
Molecular configurations for solvated electron polymer, 448
Molecular dispersion coefficient, 233
Molecular dynamics (MD) simulations
for calculation of phase equilibria, 294
(CP) type simulations, 253
DFT(X)/PCM, 14
methodologies for simulating liquid systems, 249
implementation of consistent embedding in QMCF MD approach, 263
molecular mechanics, 254
quantum mechanical charge field framework, 255
quantum mechanical/molecular mechanical scheme, 254
quantum mechanics, 254
results of QMCF MD simulations, 265
Molecular dynamics/quantum mechanics (MD/QM)
of water dipole moment, 117
Molecular mechanics (MM)

advantages, 250
linear response theory, 367
treatment of environment in, 382
Molecular structures
of caffeine, theophylline, and theobromine, 436
Møller–Plesset
second-order perturbation theory (MP2), 43
MOLSIM program package, 374
Monkorst–Pack scheme, 325
Monte Carlo (MC)
cycles, 166
free energy perturbations (FEP), 108
Metropolis method, 164, 165, 166
simulations
of acetone in water
of benzophenone in water, 165
See also Molecular dynamics (MD) simulations, 249, 387
MPE approach
parameterized expression for, 33
on reactivity focused on modifications of frontier orbitals, 25
solvent effects on chemical/physico-chemical properties, 24, 34
MST-PCM continuum method, 105
Mulliken analysis, wave functions, 53
Mulliken population analysis, 50
Mulliken–Sokalski–Poirier, 29
Multicentre multipole expansion (MME)
introduced error, 221
Multipole(s), 7, 23, 24, 26, 27, 28, 29, 30, 31, 32, 34, 35, 46, 47, 50, 51, 71, 74, 116, 117, 120, 138, 178, 193, 220, 221, 222, 228, 230, 358, 387, 409
Multipole expansion(s), 23, 28, 29, 30, 35, 46, 47, 138, 220, 221, 222, 230
Multipole moment expansion (MPE) solvent continuum model
accuracy, 24
basic equations, 25
cavity definition, 27
comparison with other solvent models, 33
development, 24
distributed multipoles, 28–29
non-electrostatic contributions, 33
solvation energy convergence, 29
Multipole moments
components of, 29
energy, 27
solute's energy, 27
"Multi-scale" methods, 381, 386

N
Nitrogen nuclear shielding(s), 9, 10, 12, 17, 18
diagonal components, and corresponding isotropic value in pyrimidine, 17
solvent effects on, 12
of diazines, 9
and nitrogen lone pair natural population, 12
NMR spectroscopy, 7, 408
Non-adiabatic processes, 136
Non-bonding interactions, 250
Nonelectrostatic contributions, 283
Non-electrostatic perturbation, 223, 242
Non-equilibrium conditions *vs.* equilibrium conditions, 137
Non-polar SCF
effects from adding co-solvent, 440
solvation of alkaloids in SC-CO_2, 435
Nonpolar solutes
blue and red shifts, 170
convergence of shift, 171
hydration effects on structure, band gap and UV-vis spectrum of C_{60}, 175
solvent effects on the UV-vis spectra of benzene, 171
Non-radiation pathways
IC and ISC, 136
and solvent, 136
Non-spherical first shell coordination number, 438
Normalized non-equilibrium response function for electron energy gap in SCA, 450
N-particle distribution function (PDF), 231
NPT ensemble simulation, 295
$N\pi^+$ *transition*, 77
Nuclear magnetic shielding tensor, components of, 8
Nuclear shieldings
of diazines, nitrogen, 9
correlation between calculated and experimental N, 11, 12
graphical representation, 10
QM/continuum and QM/MM errors, 18
QM evaluation of NMR, 7

O
Octahedral *vs.* tetrahedral surfaces, 334
One-electron
interaction operator, 365
operators, effective, 365, 371, 372
CC/MM interactions, 371
ONIOM in Gaussian, 324
ONIOM method, 254

Onsager formalism, 408
Onsager function, 412, 413, 426
Onsager's theory, 27
O–O radial distribution function gOO and O–H radial distribution function gOH, 474
Optical absorption spectra for solvated electron, 449
Order-*N* approach, 457
Orientational distribution functions (ODFs)
  mutual orientation of plane normals of aromatic rings, 302
Orientational entropy, 288
Overlapping charge distributions, energies of, 49

P

Packing strain, 224
Para-benzoquinone (PBQ)
  asymmetric solvation structures in, 235
  with four water molecules, 237
  potential energy involving polarizability, 238
  solvation in aqueous solution, 237
Parametrization, 104, 106, 108, 172, 232, 233, 235, 350, 359, 391, 394
Particle distribution function, 217, 231, 235
Particle insertion method, 470, 471
Particle-mesh Ewald (PME) approach, 510
Pauli exclusion principle
  QM/MM method of Rode, 224
Pauli principle, 48, 49, 63, 78, 215
PBQ, *see Para*-benzoquinone (PBQ)
PCM, *see* Polarizable continuum model (PCM)
Pd(II), hydration structure, 268
Periodic approach, 324
Perturbation theory, 39, 43, 45, 46, 49, 63, 68, 93, 224, 307, 324, 367
Perturbed matrix method (PMM)
  basic derivations, 192
  singlet and quintet reaction free-energy surfaces, 206
Phase-isolated form, time-dependent wave function, 368
Phenol–water clusters
  proton transfer (PT) dynamics in, 116
    and fluctuations of HB network, 127
    ionized, 115, 116, 124, 127, 131
Phenoxyacetic acid (PAA) derivatives, 322
Phosphorescence band
  blue shift, 151
  energy of singlet and triplet states, 151
Phosphorescence spectrum, 135, 148
Photoacidity, 124
Photophysical/photochemical process, 136
Pierotti's scaled particle theory, 105
Point charges, 2, 3, 4, 5, 15, 29, 30, 34, 44, 45, 49, 51, 54, 58, 59, 61, 72, 73, 92, 139, 144, 161, 179, 180, 181, 183, 186, 219, 220, 225, 253, 255, 257, 258, 259, 260, 261, 262, 263, 265, 274, 351, 374, 382, 387, 458, 467, 468, 478, 485, 486, 492, 495, 501, 502, 503
Poisson's equation, 25
Polarizability
  atomic, 42
  for compounds, 56
  molecular, 4, 42, 53, 71, 72, 140
  solvent
    damping, 222
    and QMSTAT, 224, 233, 235
  static, 56,
  Taylor expansion of total energy in external field, 56
  of water molecules in aqueous solution, 219
Polarizable continuum model (PCM)
  differences/similarities with DPM, 16
  dipole moment of acetone, 181
  isolated and "solvated," comparison, 13
  iterative polarization, 183
  reaction field, 15, 16, 17
  of surrounding solvent, 253
  See also Discrete polarizable method (DPM), 4
Polarizable force fields, 42, 43, 140, 179, 387
Polarizable model, 117, 141, 443
Polarization effects
  and charge fluctuations, 116
    dipole moment in liquid phase, 116, 117
    in hydrogen bonding liquids, 116, 119
  energy, 52, 238, 354
  interaction, 4
Polar SCFs
  dielectric behavior SC-water, 441
  excess electrons in – equilibrium aspects, 445
  excess electrons in – solvation dynamics, 449
Polymers
  nonpolar solute in nonpolar solvent, 283
  polar solute in polar solvent, 283
    poly(vinyl alcohol) (PVA), 300, 304
    PVA – hydrophilic polymer, 306
  solvent effect, 307, 309
    collapse dynamics, 309
    in solution, 307
  in solvents, solution of, 279, 280, 299, 317

hydrogen bonding in polar polymer–solvent mixtures, 305
mixtures of nonpolar polymers with nonpolar solvents, 300
mixtures of polar polymers with polar solvents, 304
solvation of oxygen atoms of poly(vinyl alcohol), 304
solvent competition for solvation of PVA, 306
transfer of polymer *vs.* globular molecule, 290
volume of, 293
Polymers solvation
classical thermodynamics of salvation, 280
collapse transition, 307, 309, 311
comparison of Flory–Huggins and classical solution theories, 286
coupling of center of mass of a molecule to another, 288
effect of internal degrees of freedom, 288
effect of molecular shape and architecture, 290
computer simulations and mechanisms of salvation, 315
concentrated solutions of polymers in solvents, 299
dynamics of polymer collapse, 309
polymer size in solution, 307
polymer solutions, 279, 280, 284, 288, 290, 307, 313, 317
sorption of gases in polymers, 279, 292, 294
grand equilibrium method, 295
statistical mechanics of salvation, 281
time-dependent solvation response, 311
experimental methods, 312
theoretical studies, 314
Polypeptides in aqueous solution
Ace-Lala-NME, 388, 391
helix formation in ace-lala$_n$-NME peptides with n = 4–20, 391
'Potential embedding', 256
Potential energy of system, 281
Programs Turbomole, 324
Projector-augmented wave (PAW), 325
Proton transfer (PT) dynamics
in aqueous malonaldehyde, intramolecular, 209
Born–Oppenheimer molecular dynamics, 116, 124
and fluctuations of HB network, 116
ionized clusters, 125, 126, 127
in phenol–water clusters, 125
and fluctuations of HB network, 124
ionized, 115, 116, 124, 127, 131
reactions in complex environments, 397
free energy simulations using multi-scale approaches, 399
minimum energy pathways (MEPs), 397, 398
time evolution at deuterium position of electrostatic field, 128, 129
electrostatic field fluctuation, 129
time evolution of deuterium kinetic energy, 130
time evolution of O–D and D–O distances between phenol oxygen and deuterium, 126
Pseudo-potential
defined, 223
purpose in QMSTAT, 223
Pt(II)
hydration structure, 268
Push–pull ethylene derivatives, 25
PVA solvation
hydrogen bonds of hydroxyl groups, classification, 305, 306
solvent competition for, 306
spatial extension of, 308
time evolution of the radius of gyration of, 309
Pyrazine (1,4-diazine), 9, 10
Pyridazine (1,2-diazine)
cluster structure and corresponding PCM cavity, 11
largest solvent effect, 12
Pyrimidine (1,3-diazine)
diagonal components, and corresponding isotropic value, of nitrogen nuclear shielding tensor in, 17

Q

QMCF ansatz
improvement, 267
shortcomings, 258, 259
QMCF MD approach
advantages of, 272
density functional theory, 266
hydration shells, 266, 269, 271, 273
ion formed by 'core region', 266, 270
ion–oxygen RDFs of Al(III) and Zn(II), 266, 267
in aqueous solution, 266
and LAXS, 274
Pd(II) and Pt(II) in aqueous solution, 268

QM/MM to, 266, 268
Al(III), hydrated, 266
Zn(III), hydrated, 266–267
re-evaluation of hydrated ions, 265
results of simulations, 265
simulation in aqueous solution
of $Hg^{2+}{}_2$, 271
of TiO^+, 272
simulation of TiO^+ in aqueous solution, 272
simulations, 247, 265, 266, 268, 269, 270, 271, 272, 273
QM/continuum
approaches, 3, 4, 6, 19
errors with respect to experiments for N nuclear shielding of diazines, 18
polarity *versus* H-bond, 10
versus QM/MM, 14
'QM core', 256
'QM layer', 256
QM/MM
hybrid method, 161, 170
MD simulations
Coulombic forces and, 268
ion–oxygen RDFs of Al(III) and Zn(II) in aqueous solution, 266, 267
methodologies, 171, 179, 180, 185, 254, 265, 274, 469, 485
Coulombic interactions between, 257, 267, 274
energy, 355
Hamiltonian in, 44
illustration of, 351
interactions between molecules and structured environments, 350
ion-oxygen radial distribution functions, 266, 267
ion-oxygen RDFs of Al(III) and Zn(II), 266, 267
linear response function, 362
separate treatment of Coulombic interaction, 260, 261
sequential, 185
total energy of system, 356
transition region, 257, 264, 267
polarizable, 4
nuclear shielding of diazines, 10
potential energy curves, 70
versus QM/continuum, 14
semi-empirical (SE) methods, 382, 385
QM/MM-ER approach
energy and free energy differences, 498
energy distribution functions, 458, 491, 494, 499, 501
for glycine in neutral form, 499
for glycine in zwitterionic form, 500
for water molecule in ambient water, 493
for water molecule in supercritical water, 494
free energy change associated with proton transfer process, 496
glycine in neutral form and zwitterionic form, 497
radial distribution functions (RDFs), 458, 474, 478, 479, 502
solvation free energy
for NF and ZW form of glycine, 496, 500
of water molecule, 496
QM/MM methods for simulation of condensed phase processes
methods to treat environmental effects, 385
of non-natural peptides: β and α/β-peptides, 393
gas-phase benchmark, 393
solution results, 395
proton-transfer reactions in complex environments, 397
free energy simulations using multi-scale approaches, 399
minimum energy pathways (MEPs), 397
SCC-DFTB
performance of, 385
small polypeptides in aqueous solution, 387
Ace-Lala-NME, 388
helix formation in ace-lala$_n$-NME peptides with n = 4–20, 391
QM/MM method with theory of solutions, combination of
contribution of many-body effect, 489
division of total solvation free energy, 486
QM/MM simulations, 42, 178, 247, 261, 264, 382, 390, 391, 392, 393, 400, 402, 457, 486, 487, 490, 491, 492, 493, 494, 496, 497, 500, 502
QM/MM to
QMCF MD approach, 266, 268
Al(III), hydrated, 266
Zn(III), hydrated, 266–267
QMSTAT
advantages of, 241
applications, examples of, 234
asymmetric solvation from many-body interactions, 237
polarization and repulsion are coupled in some monatomic ions, 235

solute–solvent interactions in *La* and *Lb* excited states of indole, 238
CAS state interaction (CASSI) method, 229
compact many-state model, 218
error introduced, 221
intermolecular interactions, 219
parametrization and simulation protocol, 232
solute–solvent potentials to CASPT2 potentials, fitting, 233
purpose in pseudo-potential, 223
quantum chemical methods, 226
complete active space self-consistent field (CASSCF) method, 229
Hartree–Fock (HF) formulation, 218
simulations with the state-based, 232
statistical mechanical method, 231
two-dimensional projection of modelled system in, 218
using Metropolis–Monte Carlo (MMC) algorithm, 231
using non-periodic boundary condition, 220
with water as solvent, 219
QM system
electronic electric field operator, 353
polarization energy for, 354
polarization energy interacting with MM polarization site, 354
QM theory of chemical shielding, 8
Quantifying solvation effects on peptide conformations
alanine dipeptide, 507, 508, 509, 511, 512, 513, 514, 515, 516
computational method, 510
dipolar couplings, 512
free energy surfaces, 511
molecular dynamics of alanine dipeptide in vacuum, 511
REMD of alanine dipeptide in explicit water, 511
system preparation, 511
results and discussions, 512
angles and relative energies for different minima of alanine dipeptide, 512
dipolar couplings calculated for alanine dipeptide in water, 515
free energy surfaces of alanine dipeptide in vacuum, 513
free energy surfaces of alanine dipeptide in water, 514
molecular dynamics of alanine dipeptide in vacuum, 512
radial distribution functions, 515
replica exchange molecular dynamics of alanine dipeptide in explicit water, 514
theory
hybrid quantum mechanics–molecular mechanics (QM/MM), 509
replica exchange molecular dynamics, 510
Quantum calculations, 138, 139, 148, 149, 161, 162, 407, 408, 415
Quantum chemical approach, 217, 323, 455, 456, 457, 459, 461, 463, 465, 467, 469, 471, 473, 475, 477, 479, 481, 483, 485, 487, 489, 491, 493, 495, 497, 499, 501, 503
Quantum chemical approach to free energy calculation
application of QM/MM-ER approach, 492
free energy change associated with proton transfer process, 496
solvation free energy of water molecule, 492
combination of QM/MM method with theory of solutions
contribution of many-body effect, 489
division of total solvation free energy, 486
real-space grid QM/MM approach, 459
hybrid quantum mechanical/molecular mechanical (QM/MM) approach, 467
Kohn–Sham density functional theory, 459
Kohn–Sham DFT with real-space grids, 461
theory of solutions in energy representation, 469
density-functional theory, 475
distribution functions in solution, 473
free-energy perturbation and thermodynamic integration methods, 469
method of energy representation, 479
radial distribution functions and reference interaction site mode, 478
Quantum Hamiltonian, 161
Quantum mechanical/molecular mechanical (QM/MM) approach, *see* QM/MM
Quantum mechanical (QM)
charge field framework
charge field approach, 255
electrostatic embedding and periodic box, 257

general electrostatic embedding scheme for QM/MM simulations, 261
and classical subsystems, interactions between, 352
description, 261, 269
Quantum mechanics
disadvantage, 252
linear response theory and molecular mechanics model, 351
region surrounded by MM point charges, 258
Quasi-classical canonical partition function,141
Quasienergy
time-dependent, 368
time dependent CC, 369, 370
Quenching, 78, 81, 136, 310

R

Radial distribution function (RDF)
for aromatic groups for PS–benzene solutions, 300, 301
between center of mass of C_{60} and water, RDF(CM), 167
distribution of water molecules around alanine dipeptide, 516
energy representation theory and reference interaction site mode, 478
Hg(I)–oxygen and Hg(I)–hydrogen, 271
ion–oxygen
of Al(III) and Zn(II) in aqueous solution, 266, 267
QM/MM-ER approach, 502
QM/MM methodologies
ion-oxygen, 266, 267
ion-oxygen of Al(III) and Zn(II), 266, 267
Radiationless processes, 137
Radiative and non-radiative excited state decays, solvent effects on
de-excitation pathways in acrolein, 148
absorption spectra, 149
emission spectra, 151
non-radiative excited state decay, 152
free energy differences, 146
fundament of ASEP/MD method, 138
ground and excited state gradients, 141
on IC and ISC, inattention of – reasons, 136
Radiative decay *vs.* non-radiative decay pathways, 136
Raoult's law, 284
Reaction coordinate (RC), 192
Reaction energies, 329, 385
Reaction field
nonzero components at nitrogen nuclei in pyrimidine, 16
Reaction kinetics
calculating, using reaction free energy, 203
diffusion equation, 201
kinetics of reactant, 208
reaction rate constants, evaluation, 203
time dependence of three chemical state probabilities and, 203
Reaction potential(s), 2, 4, 59, 61, 70, 75, 85, 93, 139
Realistic liquid state, 248
Real-space grid approach, advantages, 462
Real-space QM cell in case of 4-CPU parallel computation, 462
Red shift, 77, 83, 136, 150, 155, 170, 171, 176, 178, 241
Reference interaction site model (RISM) method
drawbacks, 478, 479
radial distribution functions and, 478
Relay matrix, 52, 59
Replica exchange molecular dynamics (REMD), 508, 510, 514
RISM/SCF
method, 138
Rototranslational configurations, 195, 196

S

SCC-DFTB
energy terms, 384
performance of, 385
total energy, 383, 385
SC-CO_2, 433, 434, 435, 436, 439, 440, 441, 452
SCFs, *see* Supercritical fluids (SCFs)
Schrödinger equation
time-dependent
from time dependent CC wave function, 369
SCRF, *see* Self-consistent reaction field (SCRF)
Self-consistent charge density functional tight binding (SCC-DFTB)
energy terms, 384
Self-consistent field (SCF) approach, 3
Self-consistent reaction field (SCRF)
model, 23, 24
Self-energy, 63, 354
Semiempirical molecular orbital (MO), 249
Semi-empirical (SE) methods, 382, 385
Sequential MC-QM method, 323
Sequential MC (SMC)/sequential MD (SMD), 44

Sequential MD, 44, 67
Sequential QM/MM (S-QM/MM)
  applications, 170
    average solvent electrostatic configuration, 183
    including solute polarization, 178
    nonpolar solutes, 170
  disadvantage, 178
  methodology, 161
    description of statistical analyses, 162
  solvent effects in electronic and structural properties of solutes, 159, 160
  and TDDFT QM model, 161
  vs. QM/MM simulation, 160
Sequential statistical mechanics/quantum mechanics (SM/QM), 117
Simulation protocol, 232, 265, 387
Singlet–triplet crossing (STC)
  energy difference gradient vector, 143
Slater–Kirkwood
  approximation, 48
  expression, 64
Smoothing factor, 264
Soil(s), 321, 322, 323, 325, 326, 327, 329, 331, 333, 335, 337, 338, 340, 343, 344, 434
Soil organic material (SOM), 322
Solubility coefficient
  for CO_2 in PS in zero-pressure, 297
  to excess chemical potentials, 293
  in zero-pressure limit, 293, 297
Solute
  density, 201, 281, 282
  distortion energy of, 147, 150
  electronic wavefunction (ψ)), 3
  force on, 141
  molecular Hamiltonian, 138, 139, 147, 155
  polarization
    and acetone, 84
    Benzophenone, 182
    charge distribution of acetone equilibrated with water environment, 181
Solute–solvent clusters
  hydrogen bonded, 124
Solute–solvent interactions
  distributions of ϕ for first and second excited states, 239
  electrostatic, 110, 138, 155, 221, 283, 316
  energy, 24, 27, 139, 144, 147, 150, 151, 155, 266, 315, 437, 458, 483, 484, 496, 499, 502
    between the final and initial states, difference in, 147
    final expression for polarizable solvent, 147
    non-vertical transition, 148
    vertical transitions, 148
  in excited states of indole, 238
  interactions at surface – counter-acting effects, 241
  intermolecular, 103, 217
  in *La* and *Lb* excited states of indole, 238
  shift distributions for absorption and fluorescence, 234, 240
Solute wave function, 229
Solvated system(s), 6, 8, 9, 10, 177, 249, 407, 408
Solvation dynamics, 312, 313, 314, 315, 316, 317, 435, 441, 449, 450
Solvation effects, importance of, 247
Solvation/embedding
  strategies, 1–2
Solvation energy
  convergence, 29
    in MPE method, 31
    speed in multipole expansion of, 30
  monocentric multipole moment development, 31
Solvation enthalpy, 106, 283
  See also Enthalpy, of salvation, 106, 107
Solvation free energy, 486, 492
Solvation in polymers
  classical thermodynamics of salvation, 280
  collapse transition, 307, 309, 311
  comparison of Flory–Huggins and classical solution theories, 286
    coupling of center of mass of one molecule to another, 288
    effect of internal degrees of freedom, 288
    effect of molecular shape and architecture, 290
  computer simulations and mechanisms of salvation, 315
  concentrated solutions of polymers in solvents, 299
  normalized response function, 313
  polymer solutions, 284
  solvent effect on
    dynamics of polymer collapse, 309
    polymer size in solution, 307
  sorption of gases in polymers, 292
    grand equilibrium method, 295
    molecular simulation methods for calculation of phase equilibria, 294
  statistical mechanics of salvation, 281

time-dependent solvation response, 311
electronic excitation, 312
experimental methods, 312
theoretical studies, 314
Solvation in supercritical fluids
non-polar SCF
effects from adding co-solvent, 440
solvation of alkaloids in SC-CO_2, 435
polar SCFs
dielectric behavior SC-water, 441
excess electrons in – equilibrium aspects, 445
excess electrons in – solvation dynamics, 449
Solvation models for molecular properties
focussed models, 2
QM/continuum, 4
QM/MM, 3
modeling solvent effects on properties, 6
application to solvated systems: N nuclear shieldings of diazines, 9
QM/continuum: Polarity *vs.* H-bond, 10
QM evaluation of NMR nuclear shieldings, 7
QM/MM *vs.* QM/continuum, 14
Solvation of hydrogen bonded systems
biologically important H-bonds, 414
alanine and methylalanine, optimized, 416
amino acids, 415
dipeptide, 417
intermolecular H-bond energies between dipeptide and formamide, 418
CH··O and OH··O H-bonds
B3LYP/6-31+G level for C7 dipeptide, 418
B3LYP interaction energies, 413
dipole variant, 410
interaction energies for complexes combining F3CH and HOH, 412
solvation energies for F3CH··OH2, 411
cooperativity
clusters, 424
energetic cooperativity of hydration sites of imidazole, 425
energetics of H-bonds, 410, 421
energetics of hydration, 425, 426
energetics of mean H-bonds, 423
hydration sites around imidazole molecule, 424
interaction energies between imidazole and pairs of water molecules, 428
interaction energies between imidazole and water molecule, 427
MP2/6-31+G H-bond energies, 422
one-dimensional chains, 419
pentameric chains of HOH, H_2CO, and HFCO molecules, 420
early applications of rudimentary SCRF, 409
$HCOOH··NHCH_2$ complex, orientation of H-bond within, 410
Solvation process, 147, 280, 286, 292, 312, 469, 471
Solvation shell
and free-energy functions for caffeine–CO_2 systems, 438
in terms of *g(r),* and *gss(r)*, 437
Solvatochromic shifts
of absorption band of acetone, 180
of transition, 172
transition of benzene in water, 173, 174
Solvent
continuum models, 23, 407
density maps for CO_2+5% ethanol, 440
dynamics, 137, 314
effects, 39, 323
influence on different geometries, 152
and relative energies of minima and crossing points, 154
role in chemical reactions in solution, 115
Solvent distortion energy (ΔG_{solv}), 147
Solvent effects on properties, modeling, 6
application to solvated systems: N nuclear shieldings of diazines, 9
QM/continuum: polarity *versus* H-bond, 10
QM/MM *versus* QM/continuum, 14
effects of H-bonding, 12
isolated and "solvated" PCM systems, comparison, 13
on nitrogen nuclear shielding of diazines, 10
QM evaluation of NMR nuclear shieldings, 7
additive corrections to shielding arising, 7
Solvent electric field, 4
Solvent electrostatic configuration, 183, 184
Solvent-induced dipole moments, 75
Solvent-induced shift, 15, 374, 375, 376, 377
Solvent models, three-way picture of, 217
Solvent perturbation operator, 220
Solvent reorganization energy, 283, 284
Solvent shells
nearest neighbor of benzene molecules and phenyl groups, 301
Solvent shift (δ)

magnitude of, 136
on solute embedded in polarizable solvent, 147
values and its components in kcal/mol, 150
Solvent situation
equilibrium/non-equilibrium, 154
at FC point, 154
Solvent–solute
interaction energy, 24, 27, 139, 144, 147, 150, 151, 155, 266, 315, 437, 458, 483, 484, 496, 499, 502
Solvent–solvent
interactions, 42, 161, 162, 175, 217, 220, 231, 254, 283, 284, 438, 476, 477
reorganization energy, 283, 284
Solvent structure
by RDF, 300
Sorption isotherms
for CO_2 in polystyrene, 299
computing, 298
Spectra
circular dichroism spectrum of $[Co(en)_3]^{3+}$ in water, 83
DRF for applying, 76
$n \rightarrow \pi^*$ transition in acetone, 76
N-(1-pyrenyl)-methyluracil-5-carboxamide-1-aminopyrene (PAU_{Me}), 78
visible spectrum of Fe-$(PyPepS)_2^{--}$, 81
Spectroscopical properties, MPE method for analysis of, 24
Speedup and parallel efficiency, 465
Split valence polarization (SVP), 324
Standard self-consistent field (SCF) approach, 3
State average CASSCF (SA-CASSCF), 229
State parameters and static dielectric properties for SPC/E water, 442
Static dielectric constant, 25
Static polarizability, 56, 233
Statistical analyses, sequential QM/MM (S-QM/MM)
statistical correlation or statistical inefficiency, 180
Statistical inefficiency, 159, 160, 162, 163, 165, 166, 185
Statistical mechanical method, 231
Statistical mechanical modeling of chemical reactions
applications, 205
binding–unbinding reaction of CO in myoglobin, 205
intramolecular proton transfer in aqueous malonaldehyde, 209
free-energy reaction surface, 196
modeling reaction kinetics
diffusion equation, 201
evaluation of reaction rate constants, 203
PMM basic derivations, 192
statistical mechanics in infinite dilution conditions, 194
Statistical mechanics of salvation, 281
Statistical simulations
methods, 249
molecular dynamics (MD), 249
Monte Carlo (MC) framework, 249
Steric interference, 289
Subsystem treated using DFT, energy of, 356
Sudden polarization
biradical state, 74
tetraphenylethylene (TPE), experiments on, 74
Supercritical fluids (SCFs)
equations, 27
non-polar SCF
effects from adding co-solvent, 440
solvation of alkaloids in SC-CO_2, 435
polar SCFs
dielectric behavior SC-water, 441
excess electrons in – equilibrium aspects, 445
excess electrons in – solvation dynamics, 449
Supercritical water (SCW), 434, 435, 441, 492, 494
Supermatrix notation, 52
Supermolecular interactions, fitting of model potentials to
disadvantages, 44
Supermolecular model, 41
SVP, *see* Split valence polarization (SVP)
Symmetrizer CC/MM, 371
Symmetry-adapted perturbation theory (SAPT), 49, 224
Systems
energy of, split into three, 141
Helmholtz free energy of, 141
interaction between two, 43
polarizability, 54

T

Tautomeric equilibrium, 90, 170, 209
Tautomeric intramolecular proton transfer
schematic picture of, 209
Taylor expansion, 56, 462

Test-particle insertion method, 295, 317
Theophylline, molecular structures, 436
Thermochemical analysis of the hydration of neutral solutes
  enthalpy of salvation, 106
  experimental data and computational details, 107
  MST-PCM continuum method, 105
  thermochemical analysis of hydration, 108
Thermodynamic integration methods
  energy representation and free-energy perturbation, 469
  Quantum chemical approach to free energy calculation and free-energy perturbation, 469
Thermodynamics of solvation, classical, 280
Thole's model, 42, 56, 72
'Three-body' energies, 43
Three-body interactions, 73
Three-body terms
  and three-body potentials, 252
Time-resolved spectroscopy, 450
Transition energy, 13, 81, 148, 172, 375
Transition structure (TS), 25
Translational entropy, 290, 291
Turbomole methods, 324

U

UV-vis spectra
  absorption, 149
  of C_{60} in water, 175
  solvent effects of formaldehyde and acetone, 180

V

Van der Waals cavity, 110, 111
Van der Waals contributions
  MM/MM energy, 355
Van der Waals forces, 283, 386, 392
Van der Waals interactions, 42, 104, 283, 388, 392, 509
Van der Waals term, 106
Vapor pressure, 281, 284
VASP (program), 325
Vector (CC/MM) interactions, 371
Vertical electron affinity
  of ammonia and water, 120
Vibrational relaxation, 311, 434
Volume fraction, 285

W

Water dimer
  experimental radial distribution of water, 68
  potential energy surface for obtained at RHF/DZP, 70
Water–water intermolecular potential, 220
Wave function
  coupled cluster
    time-dependant, 367
  phase-isolated, time-dependent, 368
  solute, 229
  time-dependent, 367
Widom's test-particle method, 298